Institute of Rock Structure and Mechanics
of the Czech Academy of Sciences
and
National Institute for Earth Physics, Măgurele, Romania

Czech-Romanian Seismology Workshop:
AdriaArray local experiment in Vrancea (Romania)

December 5th - 6th 2023, Conference centre of IRSM CAS, Prague

Programme:

Tuesday 5th December 2023

09:30 – 09:35	Welcome and Opening (Lucia Fojtíková, Renata Lukešová, IRSM CAS)
09:35 – 10:45	Felix Borleanu (INFP): Investigations and new insights on earthquake generation mechanisms, seismic activity and lithospheric structure at the bending of the Southeastern Carpathians Vrancea region)
10:45 – 11:00	Coffee break
11:00 – 12:00	Václav Vavryčuk (IG CAS): Tectonic stress from focal mechanisms (Part 1 - Theory)
12:00 – 13:30	Lunch break
13:30 – 13:45	Renata Lukešová (IRSM CAS): First preliminary result from new AdriaArray data in Vrancea
13:45 – 15:00	Václav Vavryčuk (IG CAS): Tectonic stress from focal mechanisms (Part 2 - Applications I)
15:00 – 15:15	Coffee break
15:15 – 16:30	Václav Vavryčuk (IG CAS): Tectonic stress from focal mechanisms (Part 3 - Applications II)

Wednesday 6th December 2023

09:30 – 09:50	Lucia Fojtíková, Kristian Csicsay (SAV): Earthquake near Humenné on October 9, 2023
09:50 – 10:35	Jiří Vackář (IRSM CAS) – BayesISOLA
10:35 – 10:50	Coffee break
11:00 – 12:00	Jiří Málek, Lucia Fojtíková (IRSM CAS): Attenuation of seismic waves in Reykjanes peninsula (Iceland)
12:00 – 13:30	Lunch break
13:30 – 14:15	Jiří Zahradník (FMP CUNI): Earthquake complexity studied with multiple point-source ISOLA
14:15 – 15:00	František Gallovič (FMP CUNI): Present and future applications of dynamic rupture modeling in earthquake research
15:00 – 15:15	Coffee break
15:15 – 16:30	Vladimír Plicka (FMP CUNI): Empirical Green's function (EGF) method to calculate Apparent Source Time Functions (ASTFs)

This workshop is part of the Dynamic Planet Earth research program Strategy AV21

Contact person: Dr. Renata Lukešová
Department of Seismotectonics, IRSM of CAS
tel.: +420776026159, email: lukesova@irsm.cas.cz
www.irsm.cas.cz/renata.gazdova

Czech Academy of Sciences

STRATEGY AV21
Top research in the public interest

Institute of Rock Structure and Mechanics of the CAS
and National Institute for Earth Physics, Măgurele, Romania
invite to

Czech-Romanian seismology workshop:

ADRIA-ARRAY LOCAL EXPERIMENT IN VRANCEA (ROMANIA)

December 5th - 6th 2023

Conference hall of IRSM CAS
Prague, V Holesovickach 94/41

Contact person: Dr. Renata Lukešová
Department of Seismotectonics, IRSM of CAS
Tel.: +420776026159, Email: lukesova@irsm.cas.cz
www.irsm.cas.cz

Czech Academy of Sciences
STRATEGY AV21
Top research in the public interest

WORKSHOP IS PART
OF THE RESEARCH PROGRAM
DYNAMIC PLANET EARTH - STRATEGY AV21

INFP USMH AdriaArray

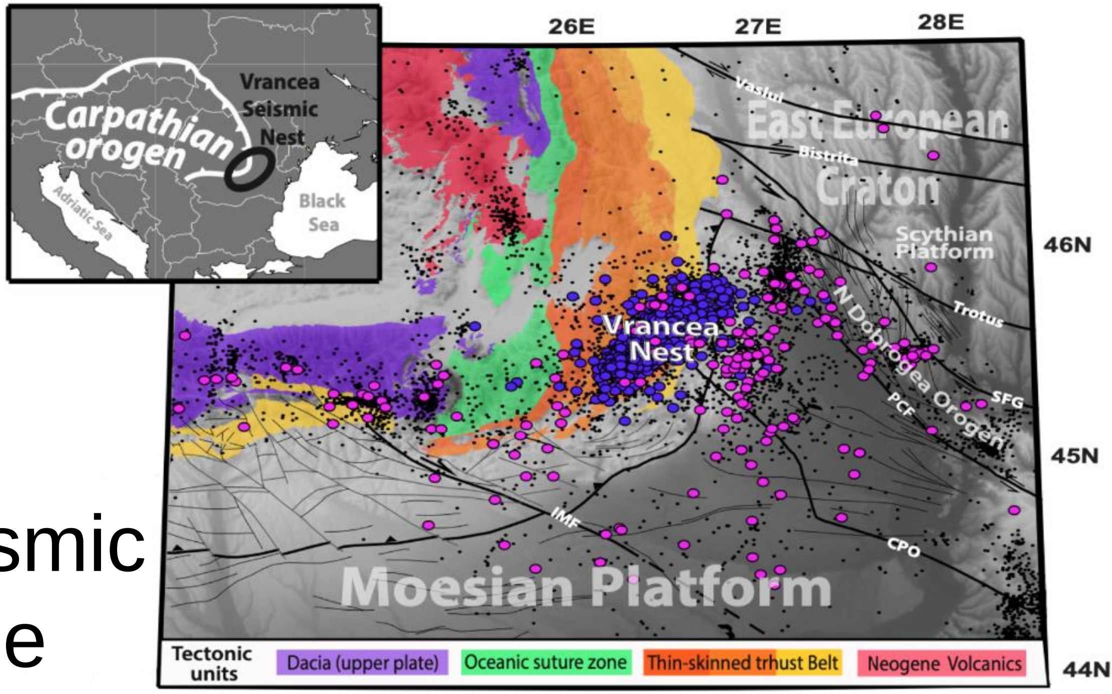

Investigations and new insights on earthquake generation mechanisms, seismic activity and lithospheric structure at the bending of the Southeastern Carpathians (Vrancea region)

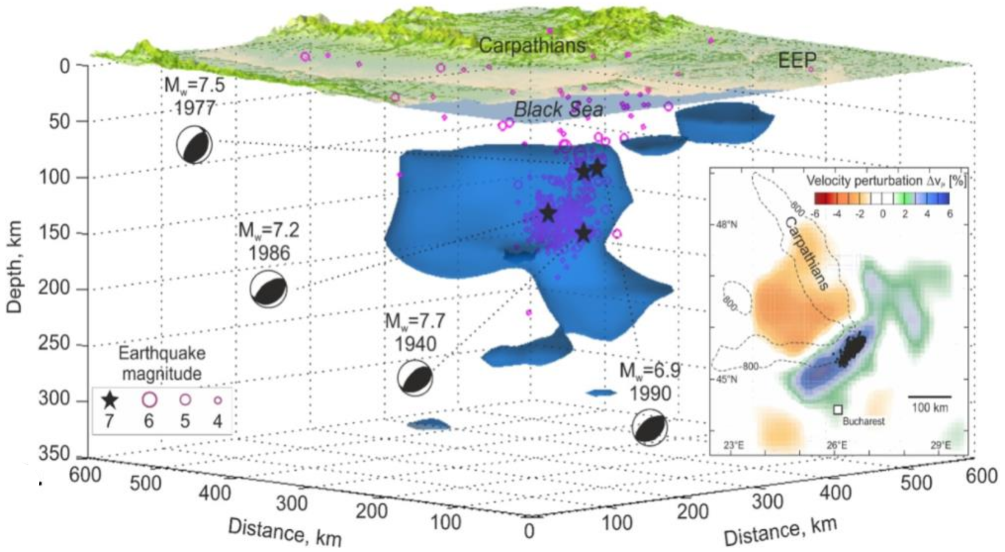

Felix Borleanu[(1)] & co-authors

1) National Institute for Earth Physics, Măgurele, Romania (NIEP - felix@infp.ro)

Romanian Seismic Network – past to present

Analog Seismic Network **1977-1995**

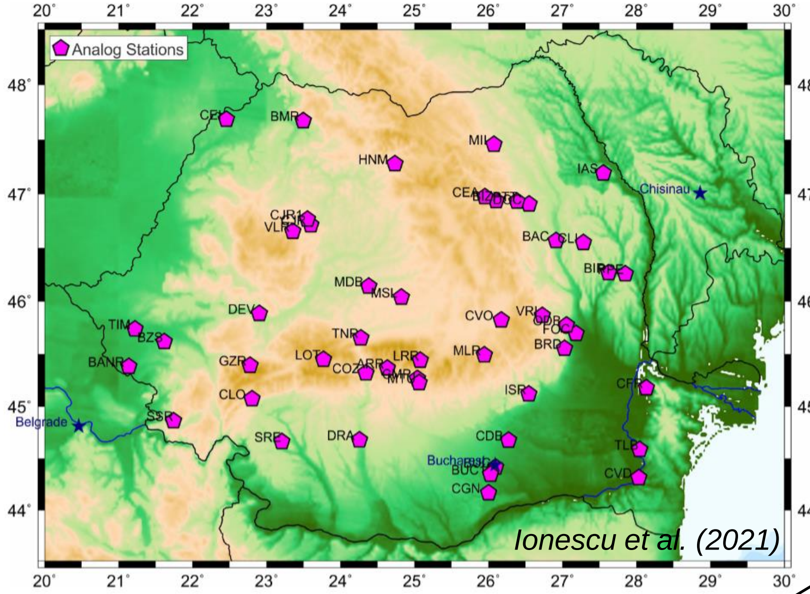

Digital Seismic Network **2023**

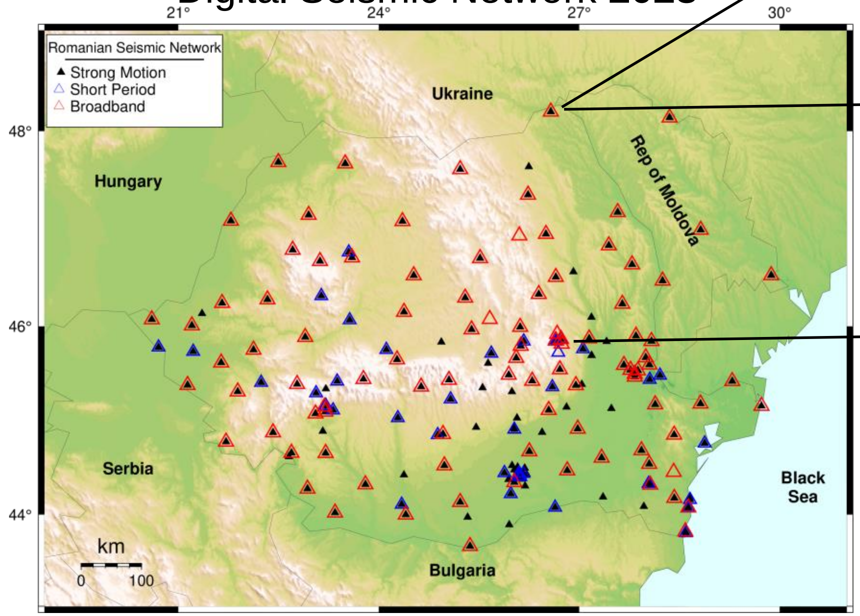

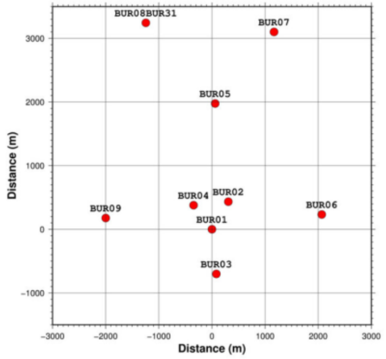

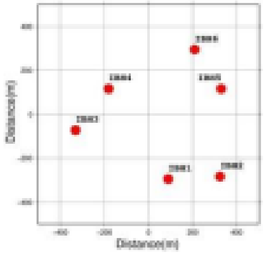

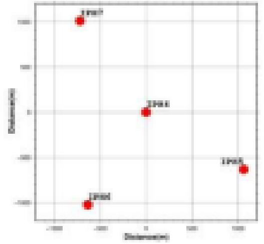

Romanian Seismic Network & AdriaArray **2023**

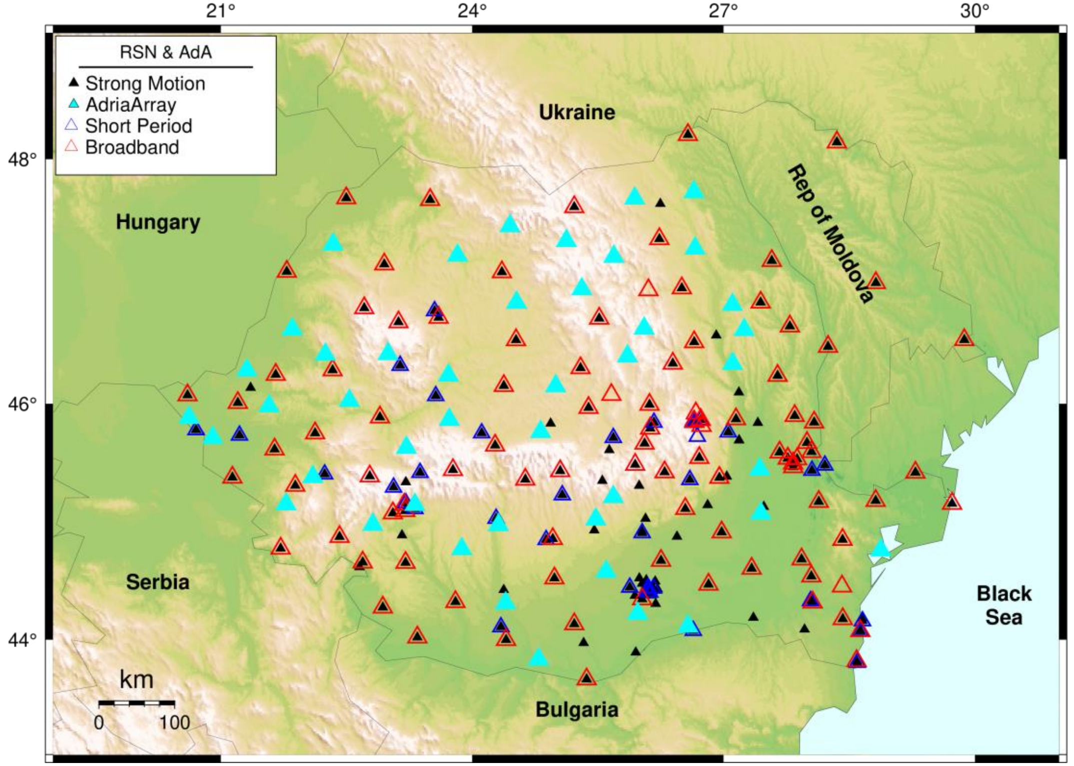

- **154** single broadband and short-period stations;
- **175** stations (EpiSensor-2g full scale) with 21 stations deployed in the Bucharest area;
- **1** seismic array – BURAR;
- **2** infrasound arrays (BURARI and PLORI);
- **44** temporary stations deployed within AdriaArray;

Romanian Seismic Network – Data Acquisition & Processing - **Seiscomp3**

- data acquisition;
- data quality control;
- real-time data exchange;
- network status monitoring;
- real-time data processing;
- easy access to relevant information stations, waveforms and recent earthquakes;
- issuing event alerts;
- waveform archiving;
- waveform data distribution;
- automatic event detection and location;
- interactive event detection and location;
- event parameter archiving;
- real time Moment Tensor estimation;

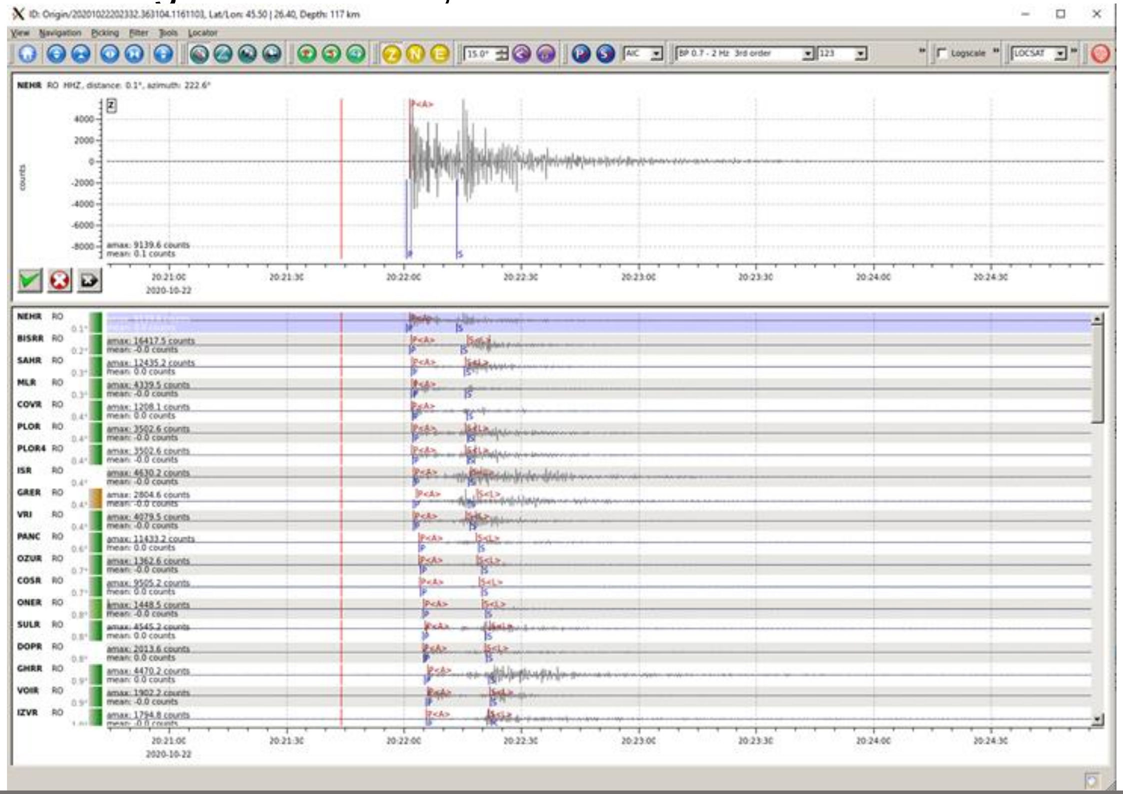

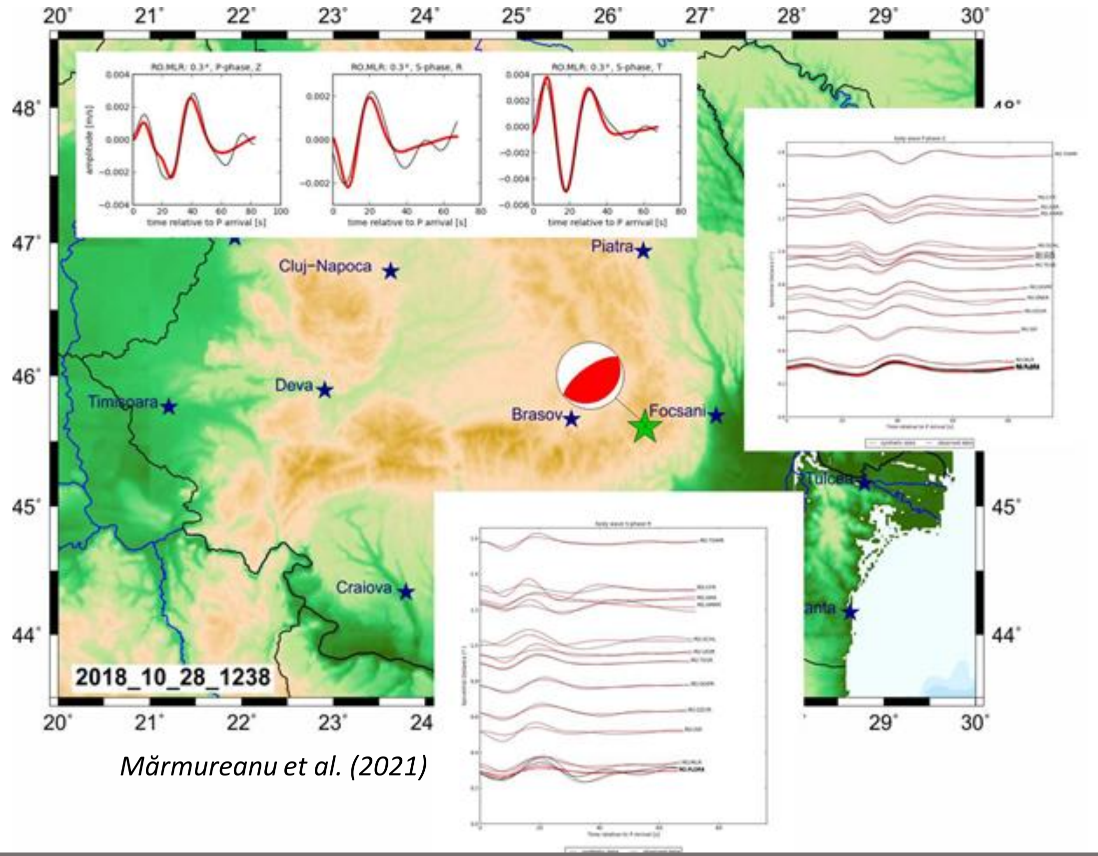

Mărmureanu et al. (2021)

Romanian Seismic Network – Data Acquisition & Processing - **Antelope 5.7**

Automatic processing:
- P-wave picking;
- event association;
- event location;
- computation of magnitude;
- sending e-mail / SMS alerts;

Offline processing:
- P & S-waves picking;
- event association;
- computation of magnitude;
- creation of database;
- sending reports/ bulletins

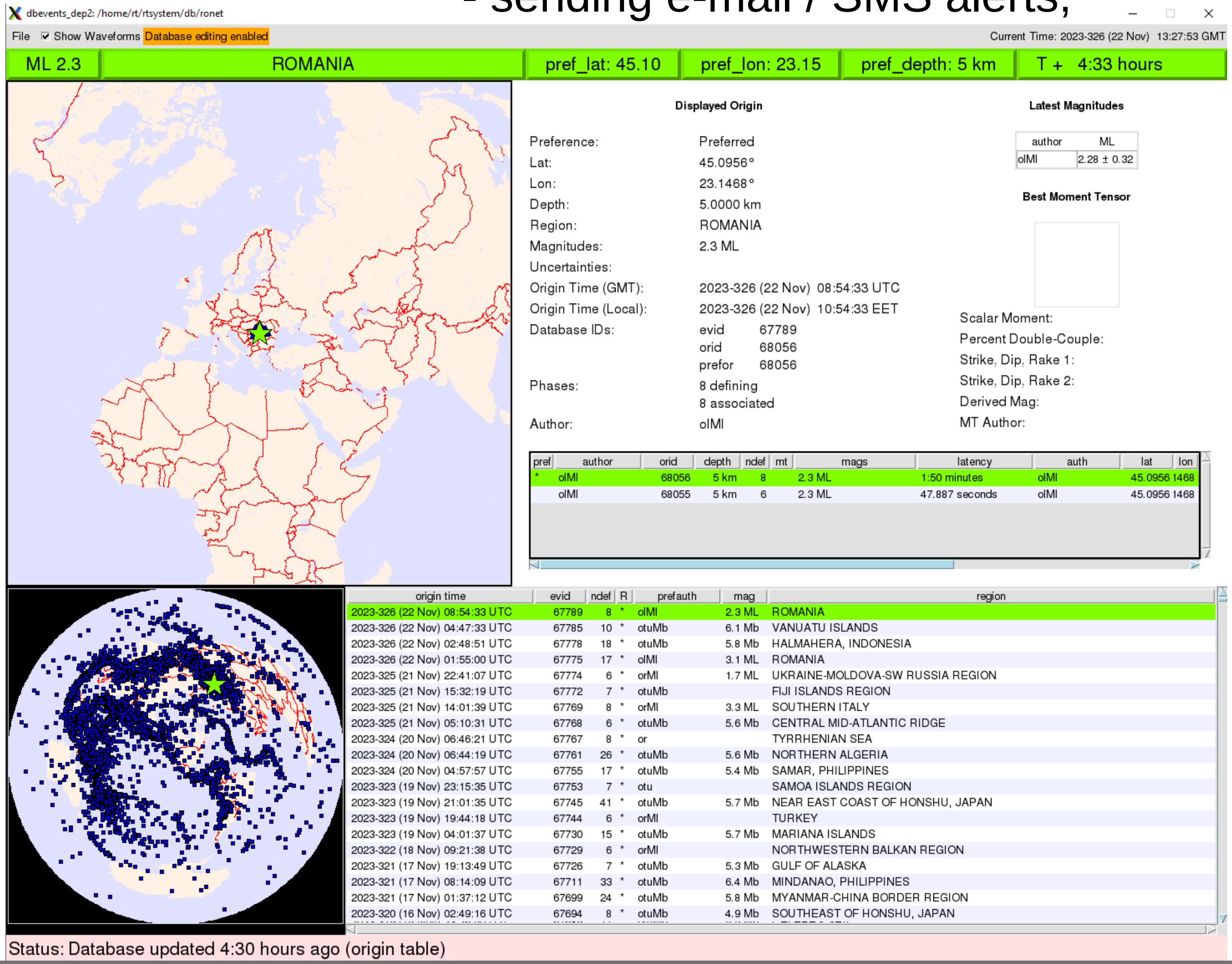

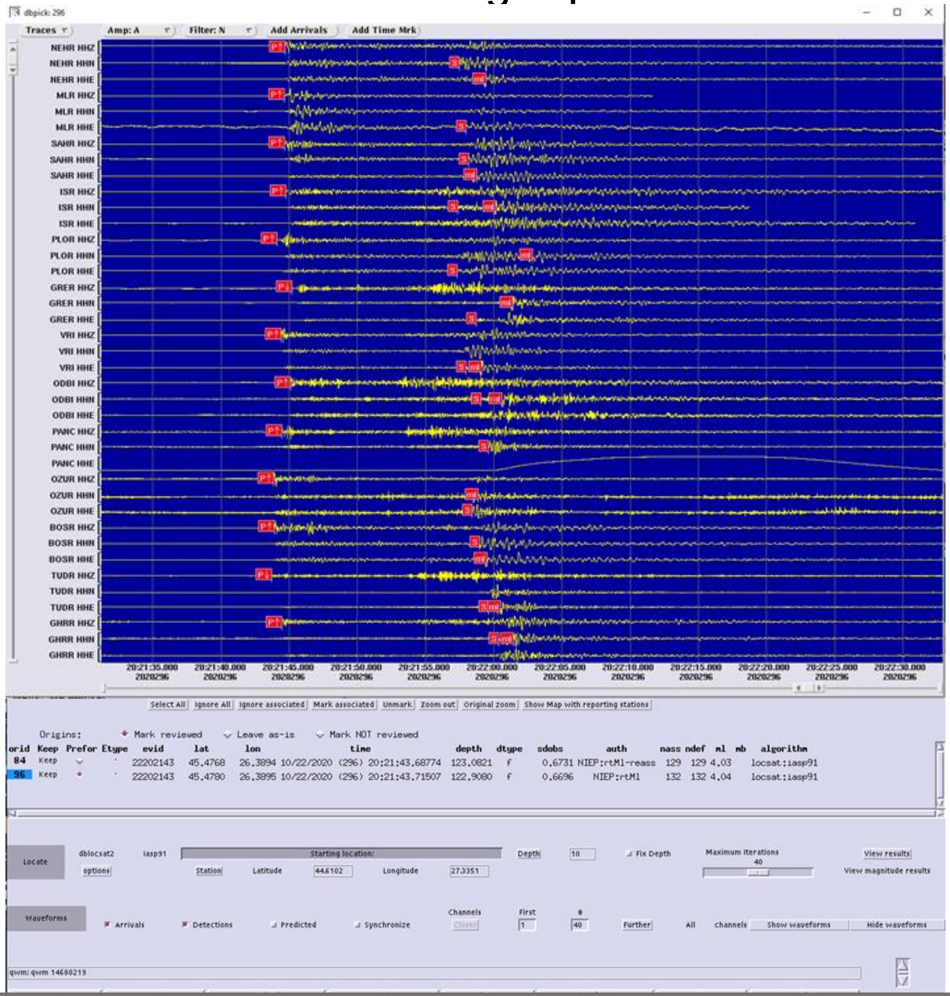

Romanian Seismic Network – **Earthquake early warning (EEW)**

- Current Operational EEW System (since 2013) uses a network of 35 stations centered on Vrancea providing location and magnitude focusing only on the intermediate-depth events;
- 25 – 35 s warning for Bucharest;

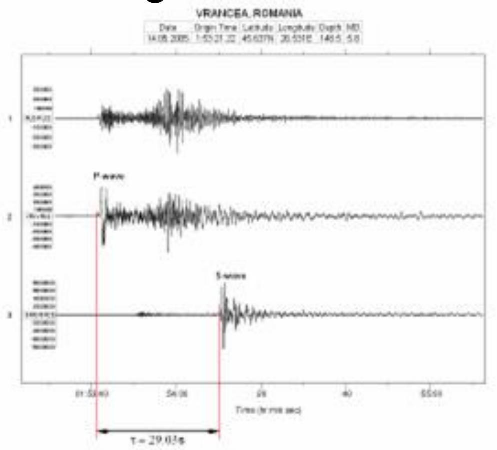

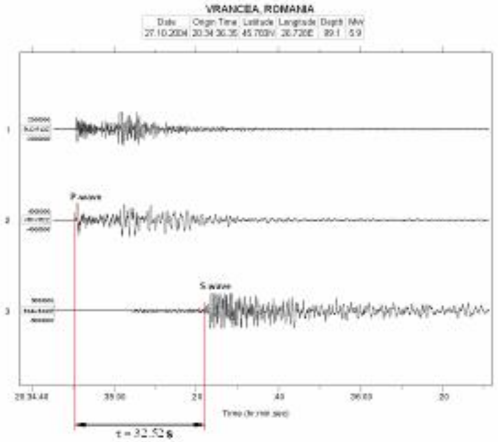

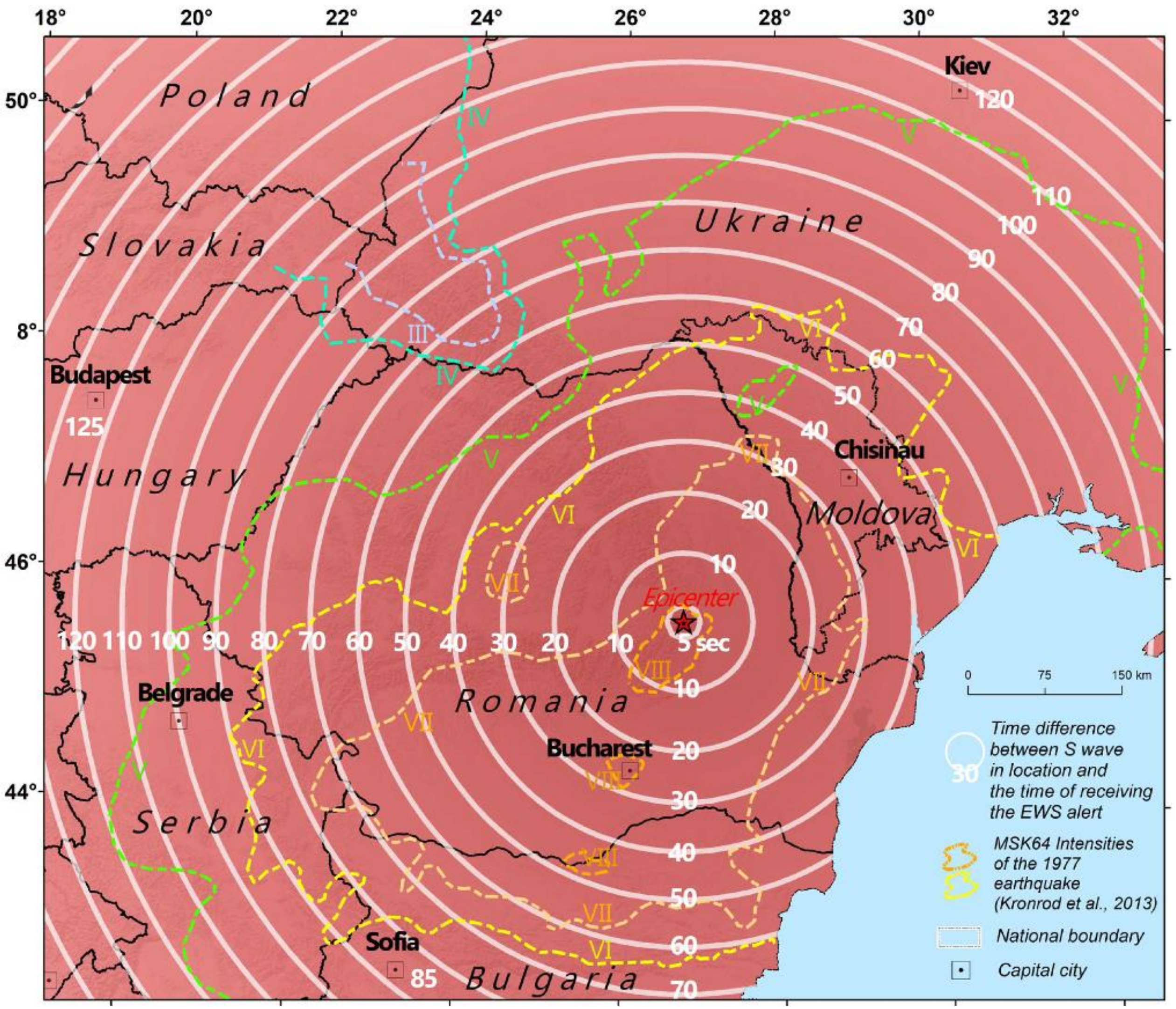

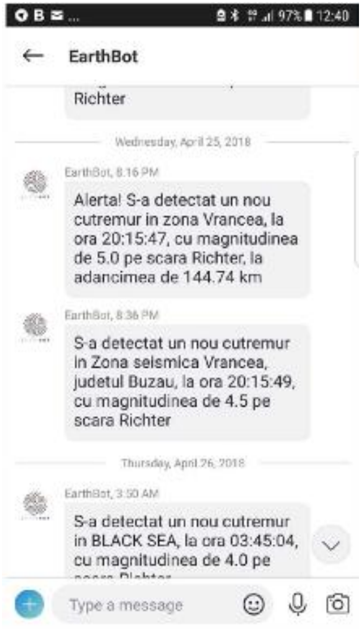

Mărmureanu et al. (2021)

Romanian Seismic Network - **Data Exchange & Services – EIDA NODE**

- NIEP has been an EIDA primary node since 2014;
- NIEP has a seismic data archive of around 25 TB;

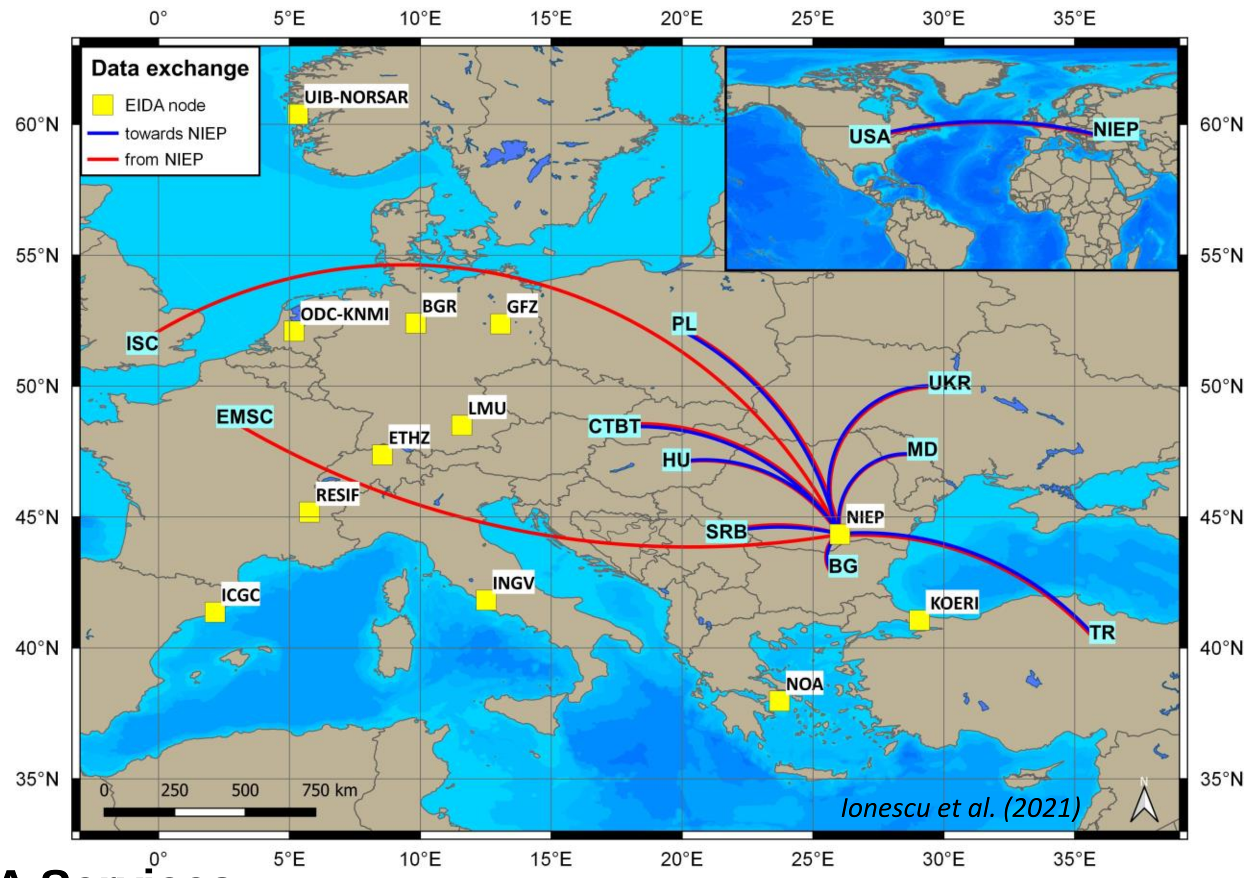

Seismic networks within the EIDA node:

- RO - NIEP, National Seismic Network from Romania;
- MD - Digital Seismic Network from Moldova;
- BS - The Seismic Network from Bulgaria;
- UD – The Seismic Network from Ukraine;

NIEP – EIDA Services:

- FDSNWS - Dataselect (miniSEED): http://eida-sc3.infp.ro/fdsnws/dataselect/1/
- FDSNWS Station (station metadata): http://eida-sc3.infp.ro/fdsnws/station/1/
- Routing service: http://eida-sc3.infp.ro/eidaws/routing/1/
- WFCatalog: http://eida-sc3.infp.ro/eidaws/wfcatalog/1/

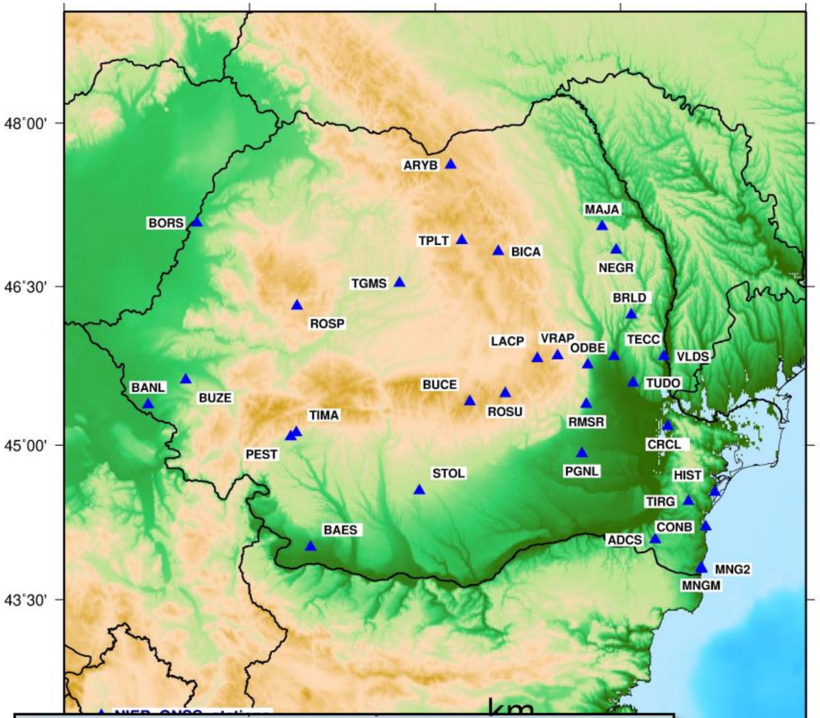

GNSS Network

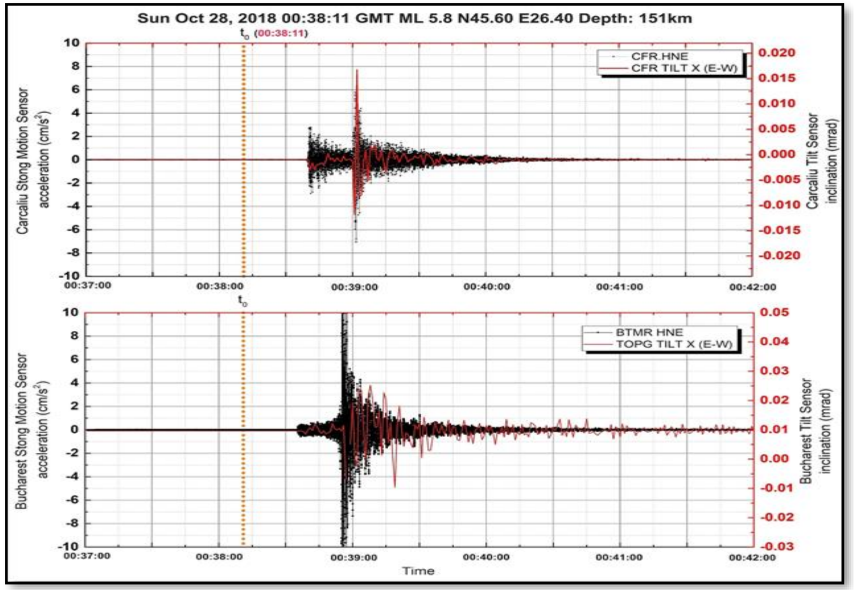

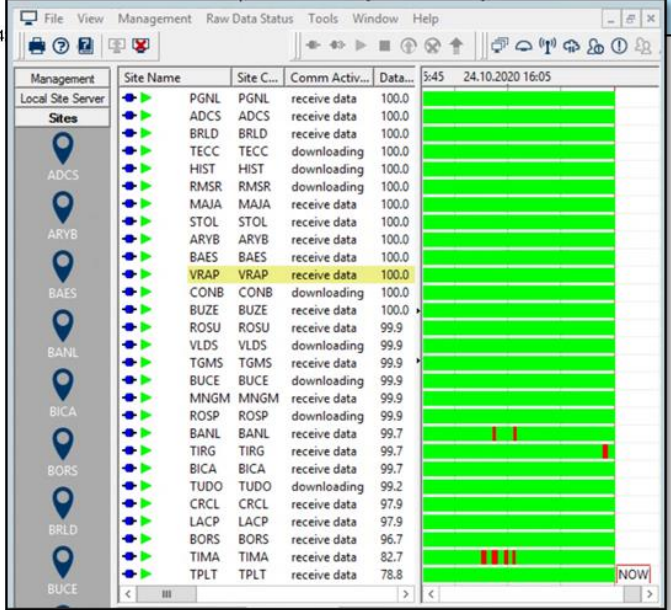

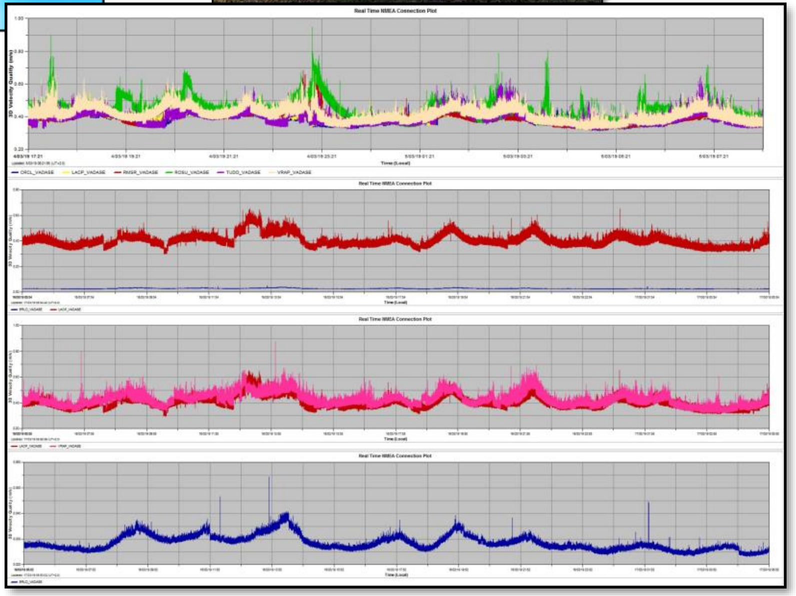

- **33** Real-time **GNSS** stations;
- **4** Real-time **TILT** Sensors;
- **12 VADASE 10Hz** Real-time velocity recordings
  (Variometric Approach for Displacements Analysis Stand-alone Engine);
- **4** National **MoU** data exchange collaborations;
- **> 140** National GNSS stations processed;

NIEP Infrastructures (cont.)

Mobile Geophysical Instrument Pool

- Seismic (Surface vibrator source Elvis VII, Geode Exploration Seismograph, ATOM 3C wireless units, Nanometrics seismic stations, Raspberry Shake 3D);
- Georadar - Akula 9000C (GCB 100/300/700 MHz antennas);
- Magnetometers (G-862RBS, G-864);
- A10 absolute gravimeter;
- Interferometers (Hydra-G, IBIS-FM EVO);
- Rezistivity imaging instruments (Syscal Pro, FullWaver);

Research interests & cooperation

- Information, knowledge and technologies sharing;
- Establish co operations and scientific exchange;
- Capacity building;
- Scholarship, education and training;

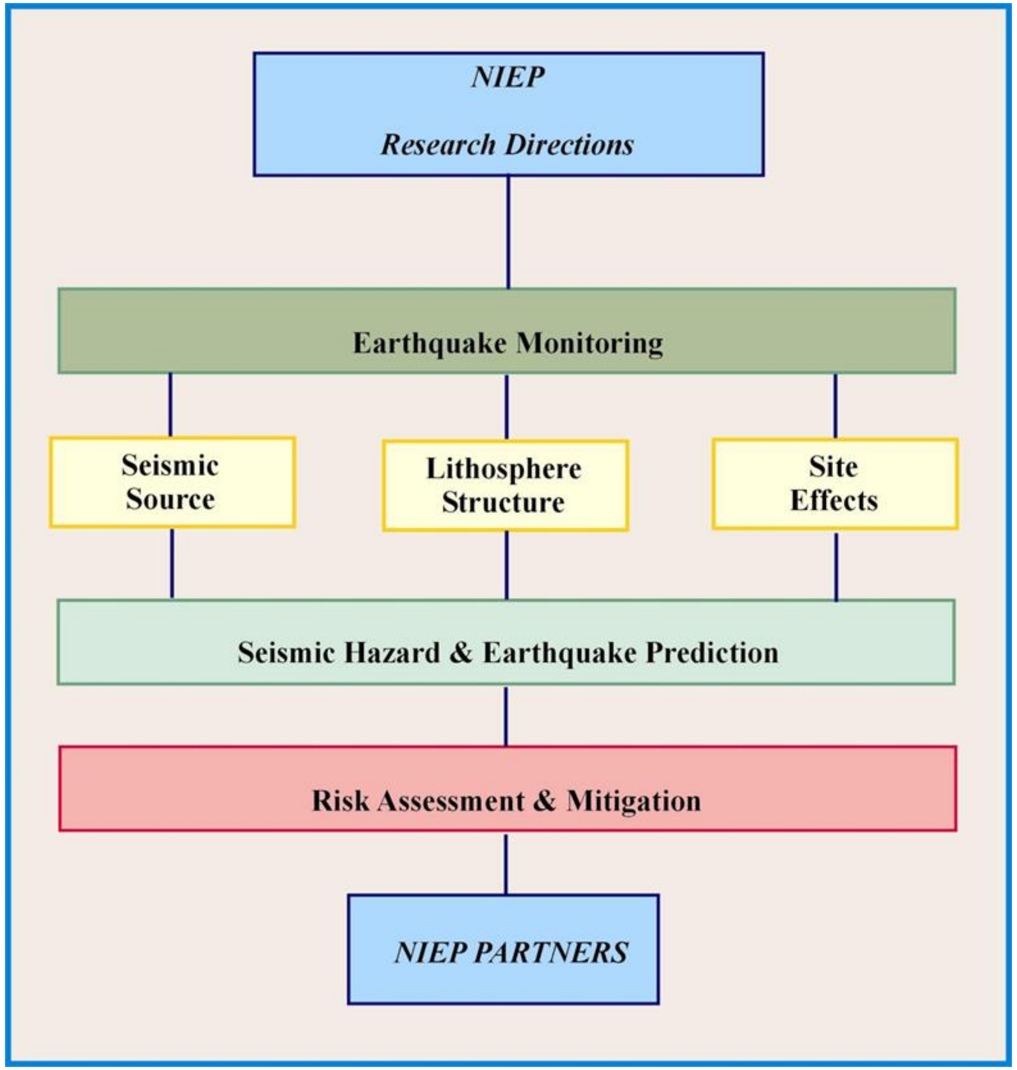

Complex tectonic factors shape the region of Eastern Europe

- Movement towards north of the Adria Plate leads to a transfer of deformations to the west and east;

- The evolution of Carpathians orgen and Pannonian Basin in Neogene is characterized by the relative movement of two independently-moving microplates;

- The effects of the Black Sea opening split the NW inland into several slivers by creating major faults trending NW-SE;

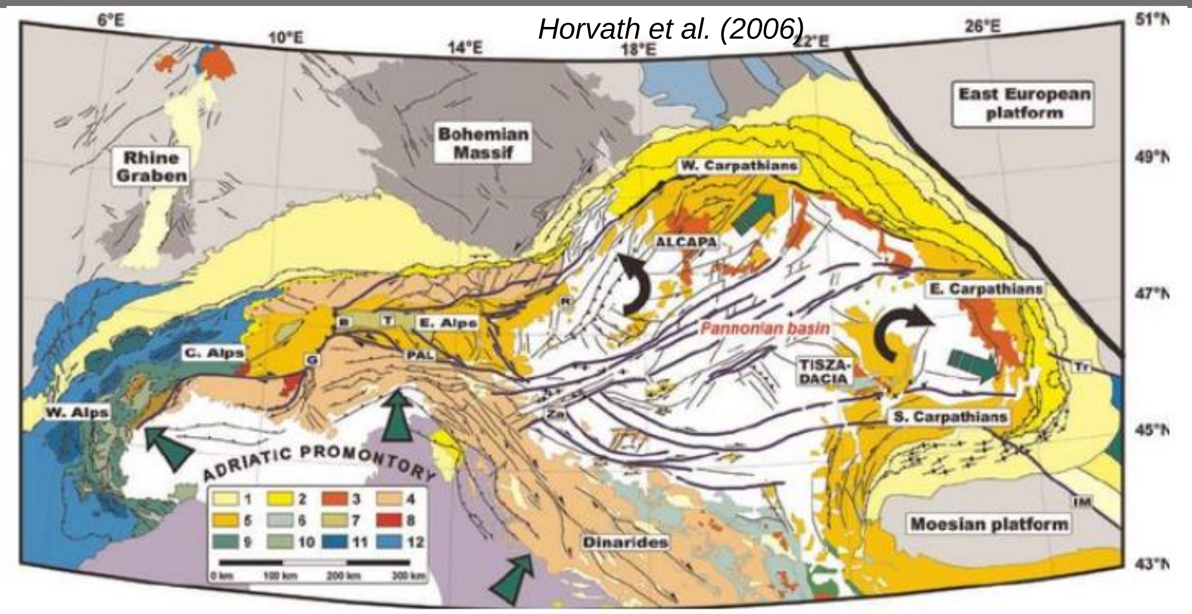

Horvath et al. (2006)

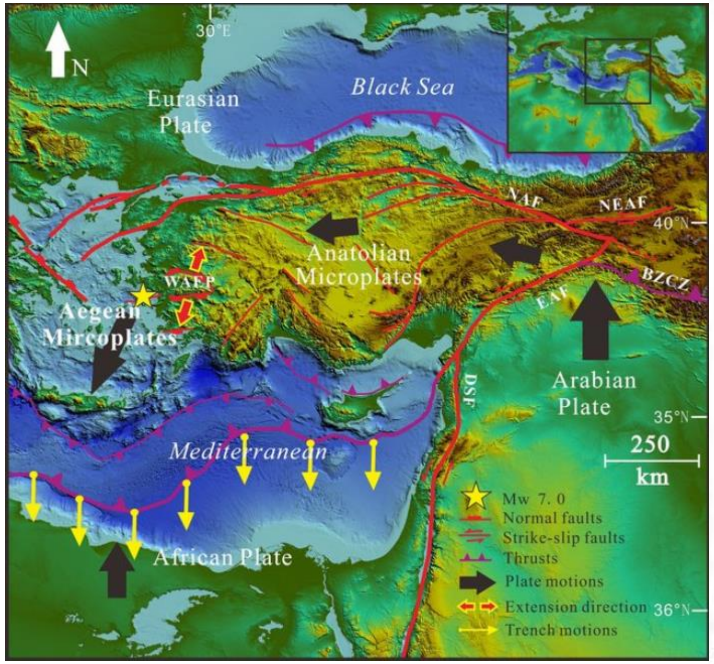

Meng et al. (2021)

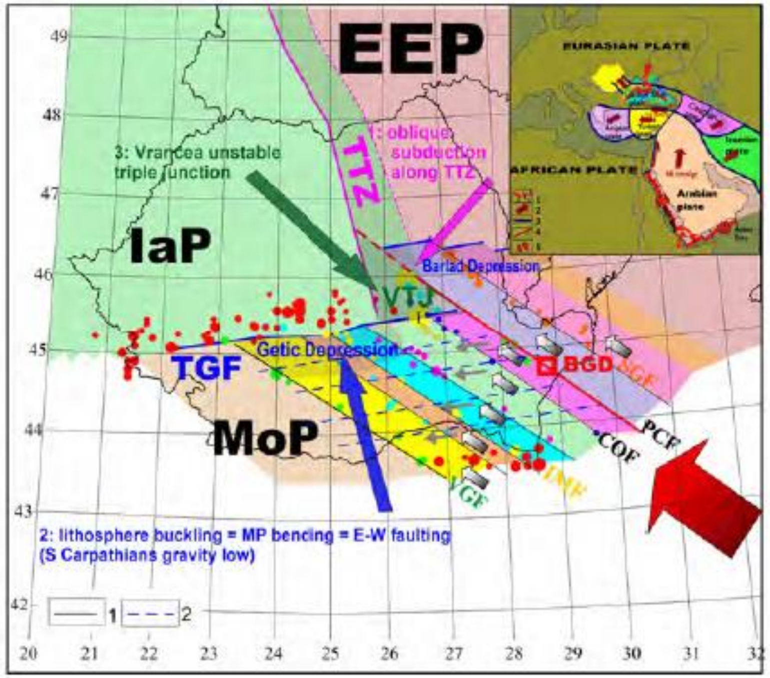

Besutiu (2013)

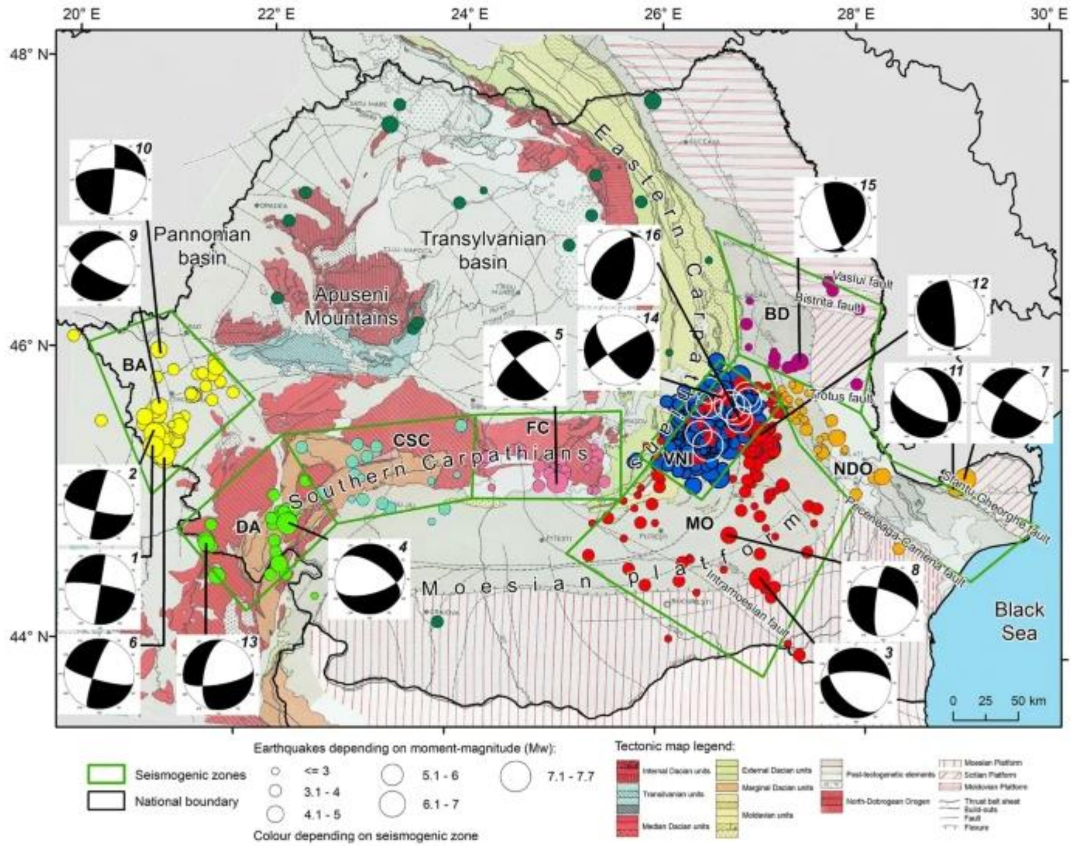

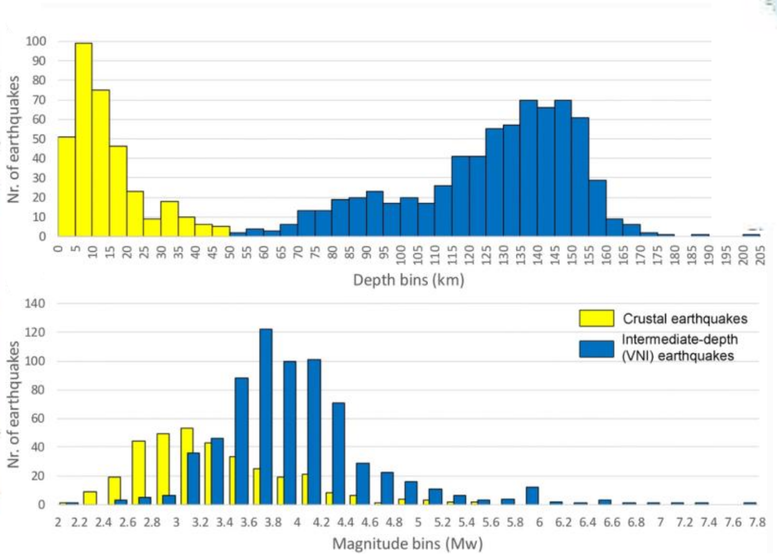

Bala et al. (2019)

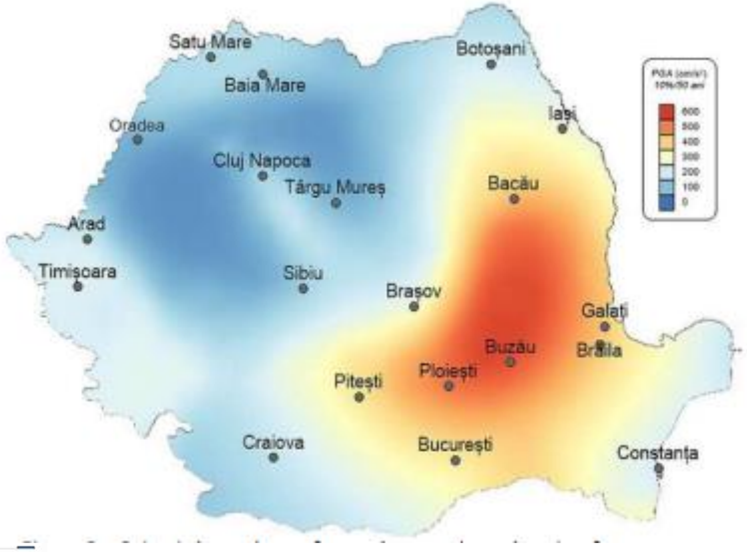

Pavel et al. (2016)

- Romania has a significant seismic activity, especially in the Vrancea seismic zone, which is characterized by the occurrence of earthquakes with magnitudes greater than 7;
- The crustal earthquakes are smaller and more sporadic, spreading along the South Carpathians orogeny, Carpathians foreland and Pannonian depression;

Seismic activity in the Vrancea region

- Vrancea - the most concentrated seismic area in Europe;

  ~ 30 x 70 x 130 km^3

- The moment release rate is as high as the moment release rate of Southern California (Wenzel et al., 1998);

  ~1.2 x 10^{19} Nm/year - (60 – 180 km);
  ~5.3 × 10^{15} Nm/year - (1 – 60 km);

- The strong earthquakes are exclusively located at intermediate depths (60-170 km), while the shallow events are below magnitude Mw 5.5;

- The rate of seismicity indicated the occurrence of 2-4 shocks with magnitude Mw ≥ 7.0 per century;

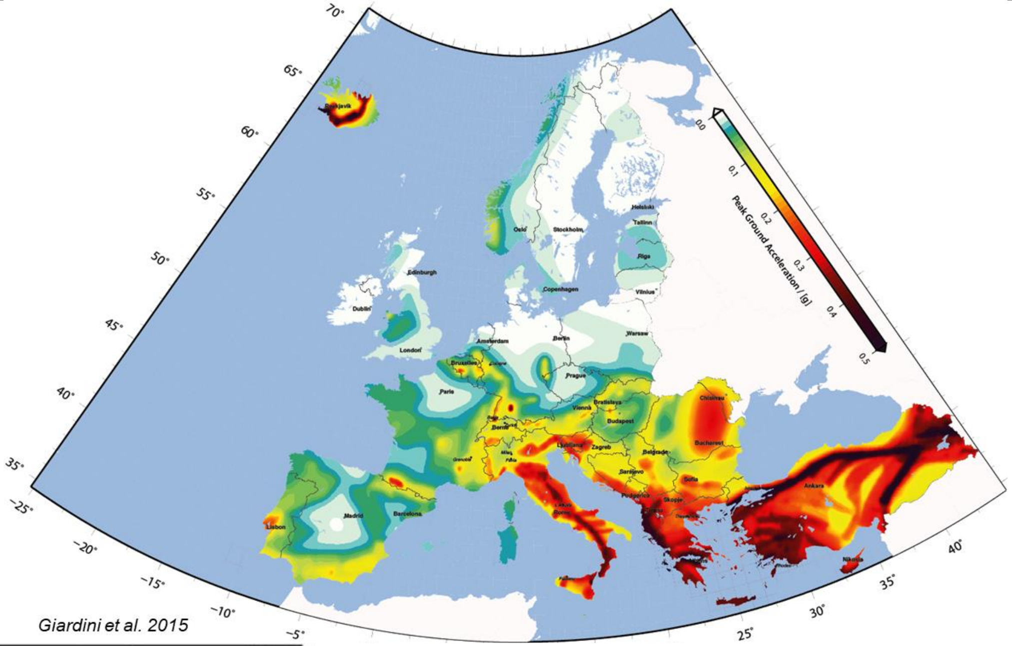

Giardini et al. 2015

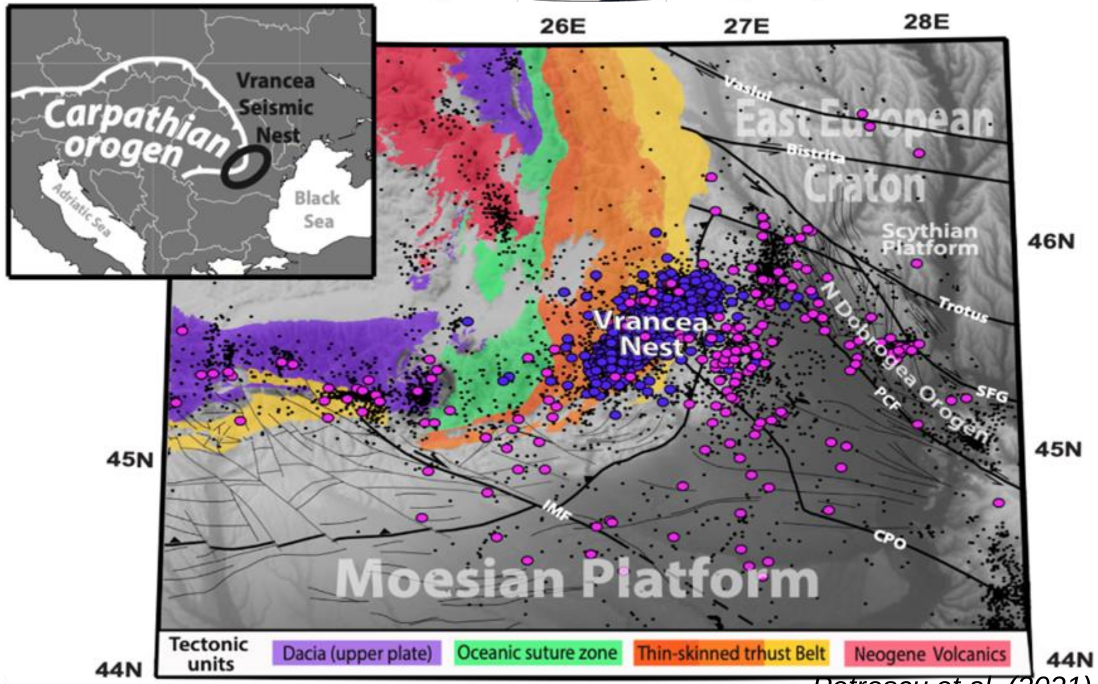

Petrescu et al. (2021)

Seismic activity in the Vrancea region (cont.)

- The tendency of big earthquakes M > 7 to occur in clusters: periods of intense activity interrupted by intervals of low seismic activity.

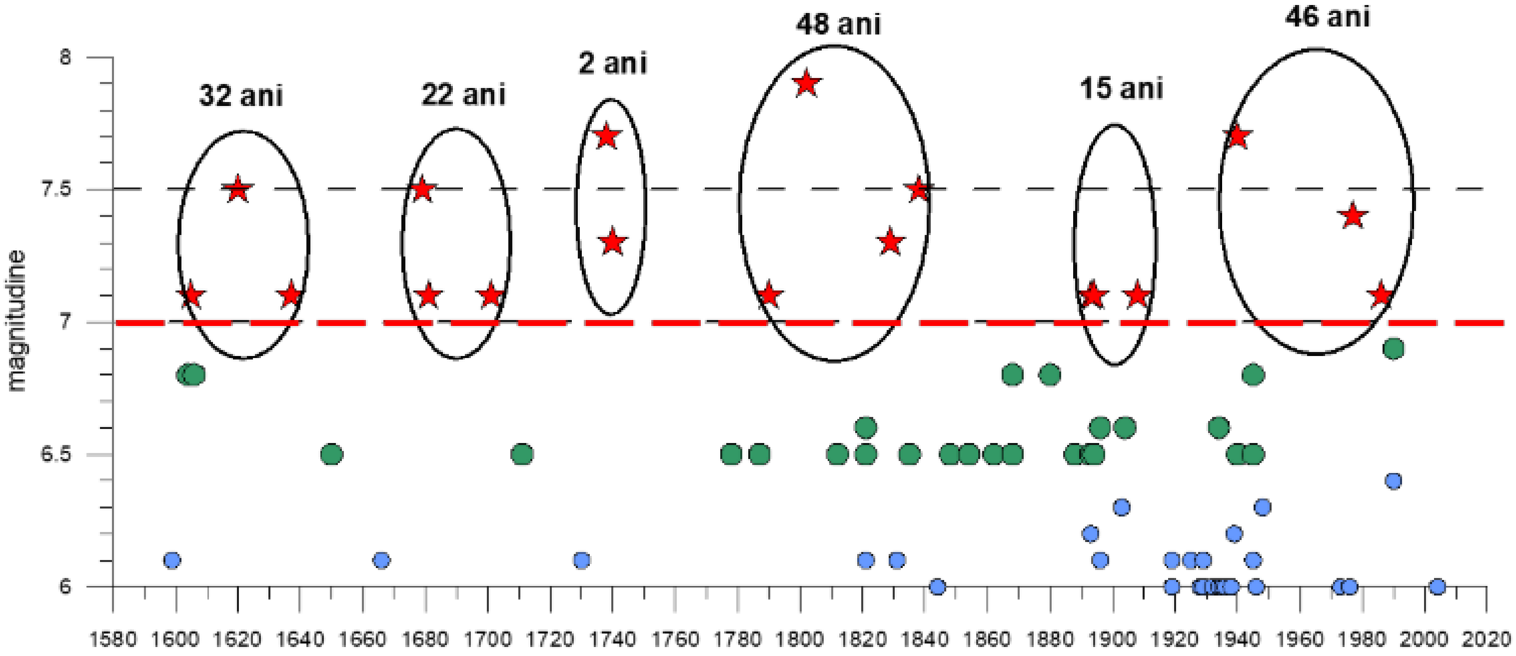

Radulian et al. (2023)

○ In the framework of the Mediterranean Basin area, the Vrancea source belongs to the type of sources of intermediate depth located in arch-type structures;

○ The subcrustal seismicity in the Vrancea region is confined to a narrow ~100km (height) × 70 × 30km volume in the upper mantle beneath the SE Carpathians ;

○ Three remarkable nests in the world are located in Bucaramanga (Colombia), Hindu Kush (Afghanistan), and Vrancea (Romania);

○ Earthquake nests are anomalous clusters because they are not necessarily located in or related to classic oceanic subduction systems at active plate margins;

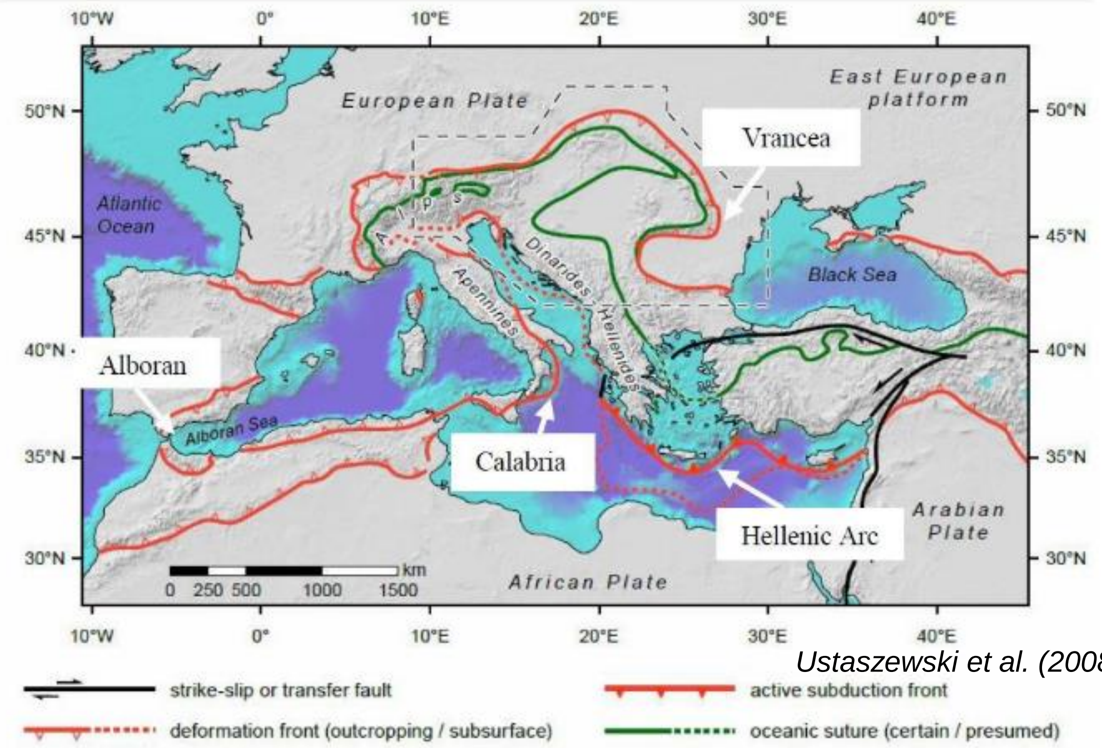

Ustaszewski et al. (2008)

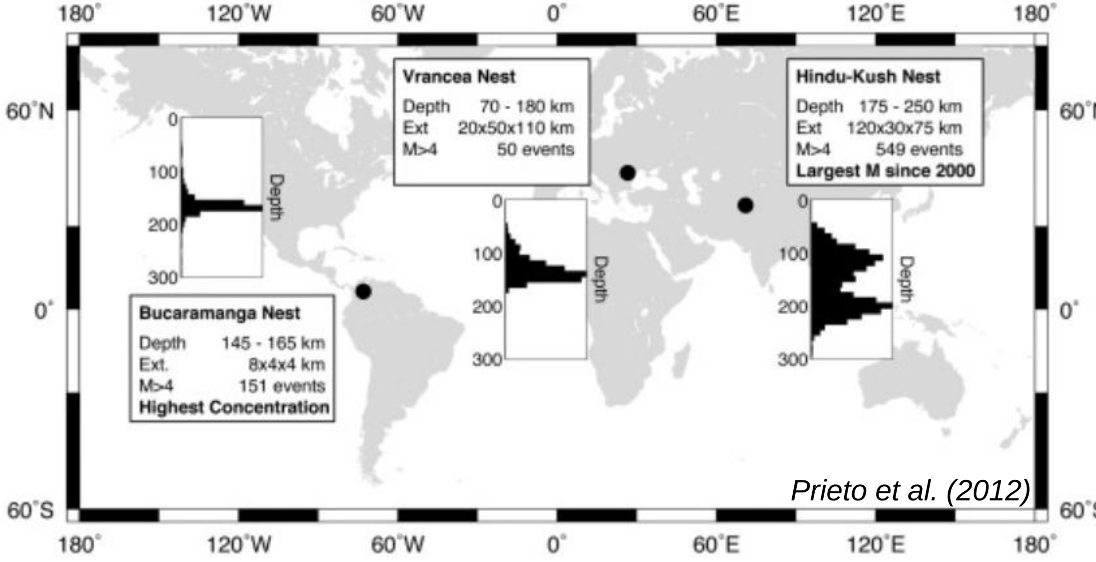

Prieto et al. (2012)

- The seismicity distribution is clustered in a narrow epicentral area elongated along NE-SW direction;
- The seismicity in the subducting slab is significantly more abundant and stronger than that in the overriding crust;

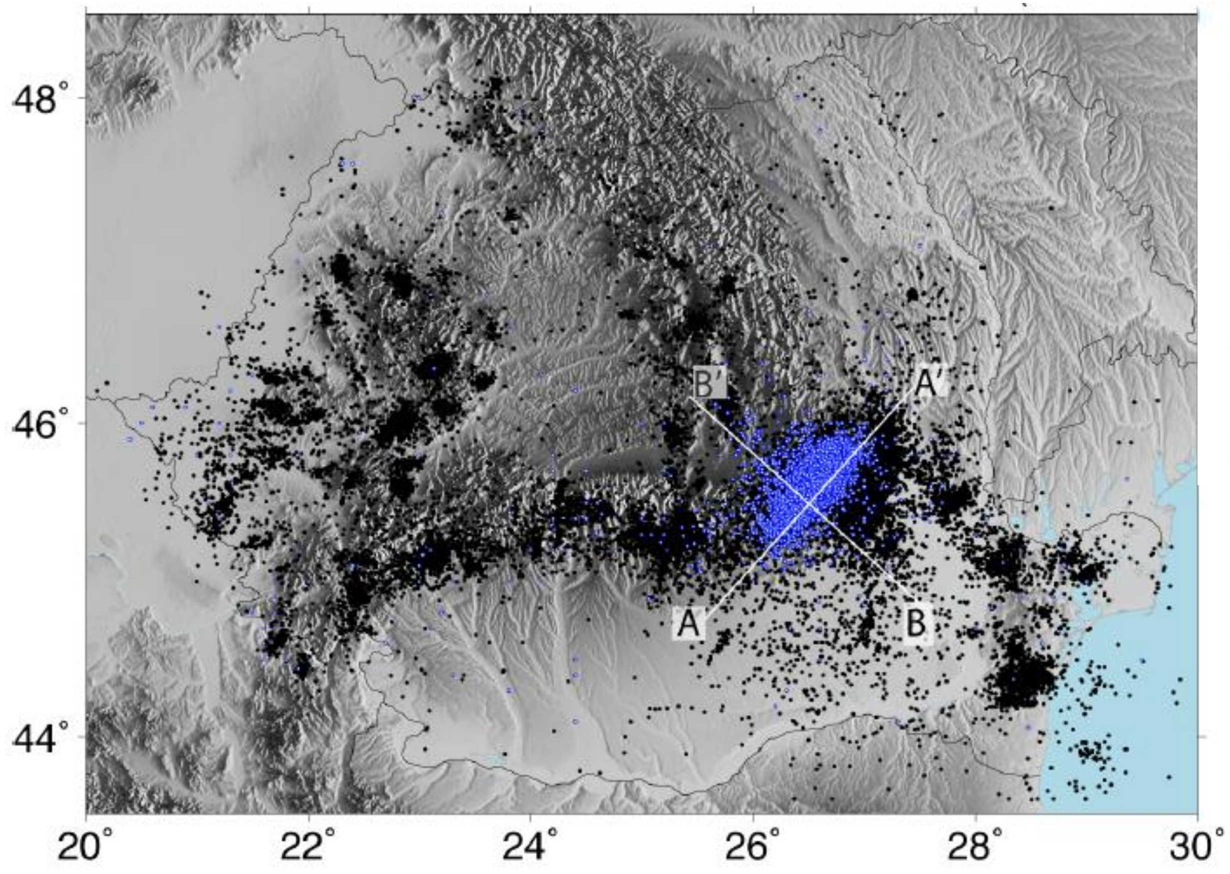

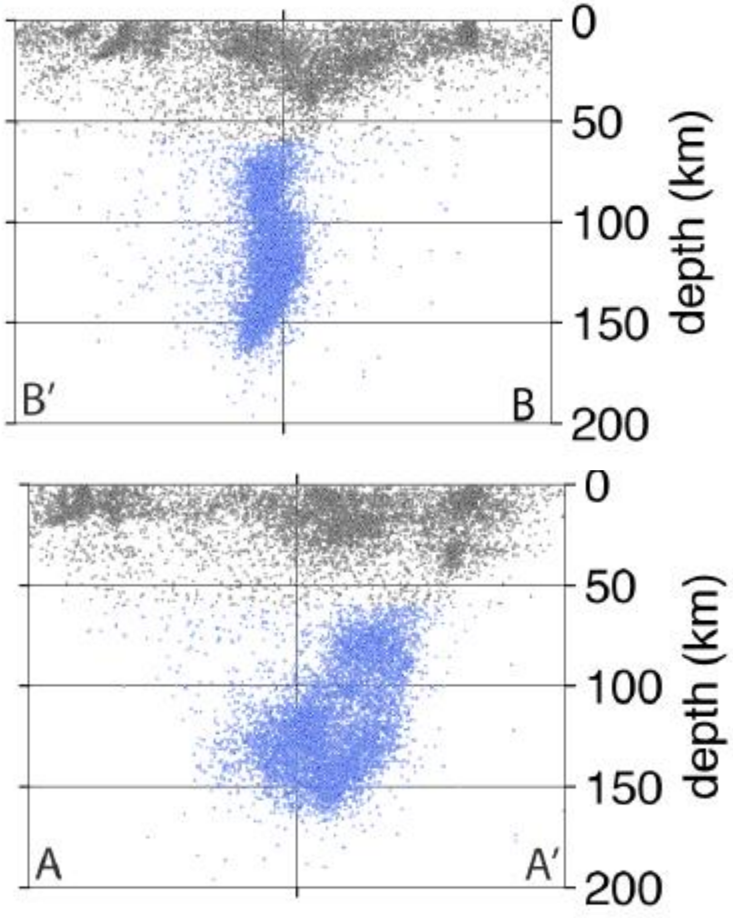

Poiata et al. (2022)

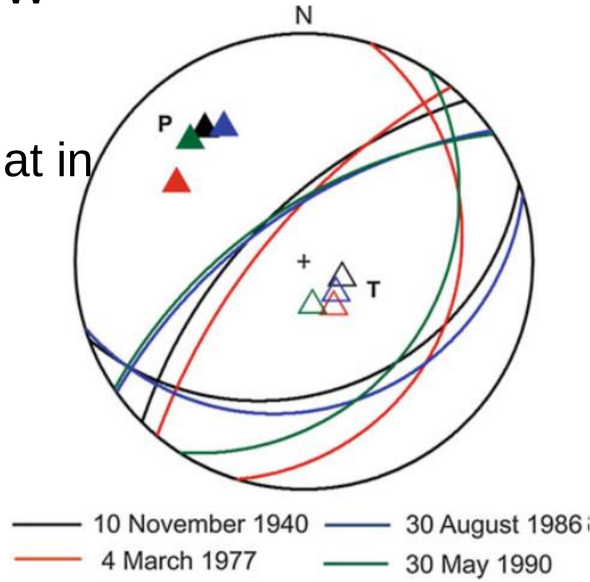

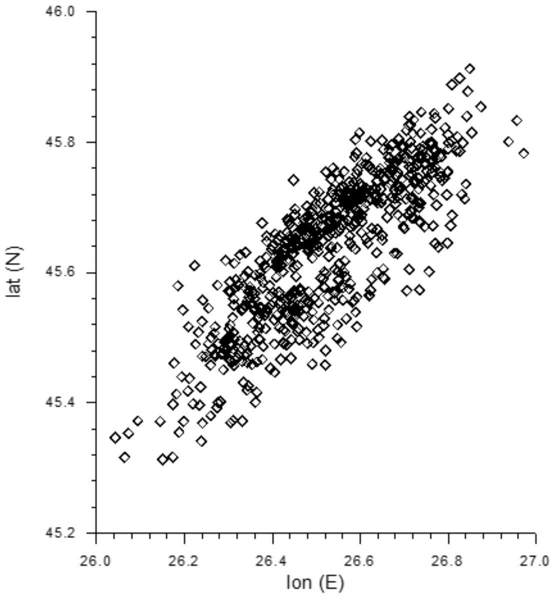

Radulian et al. (2023)

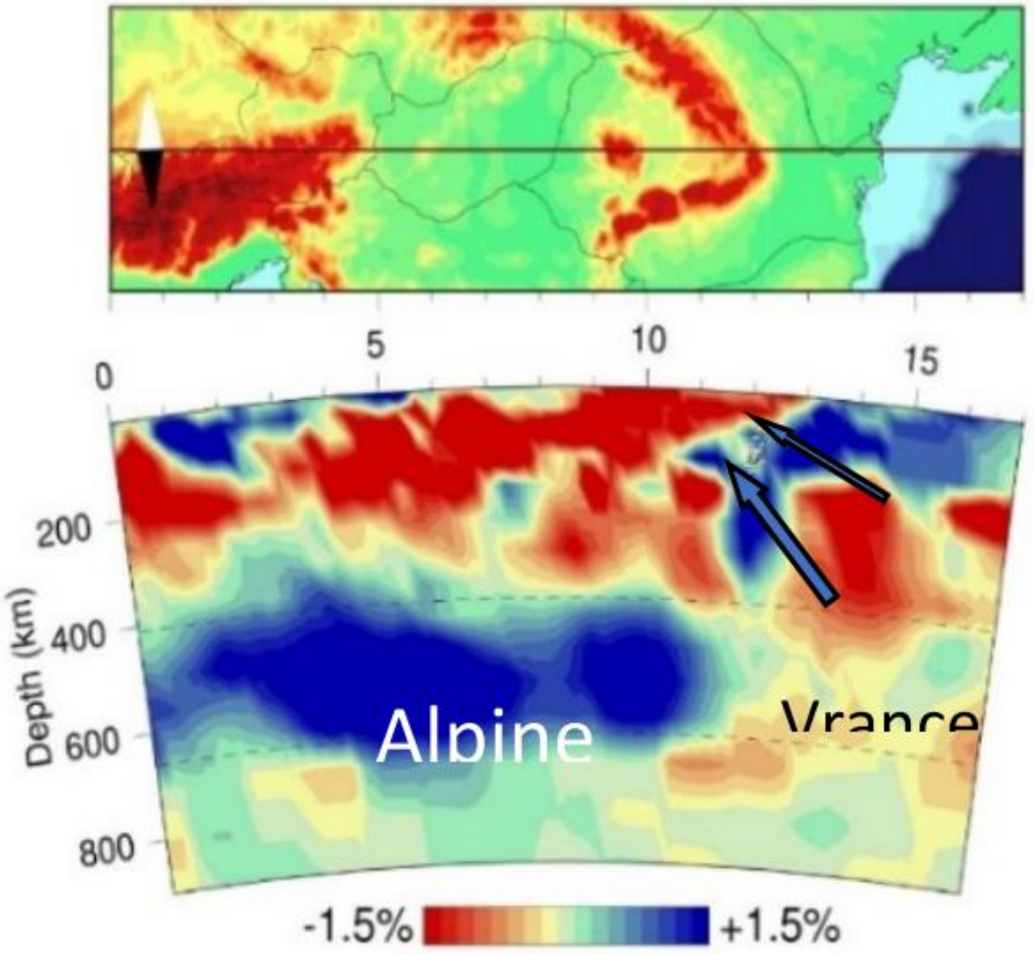

Wortel and Spakman, (2000)

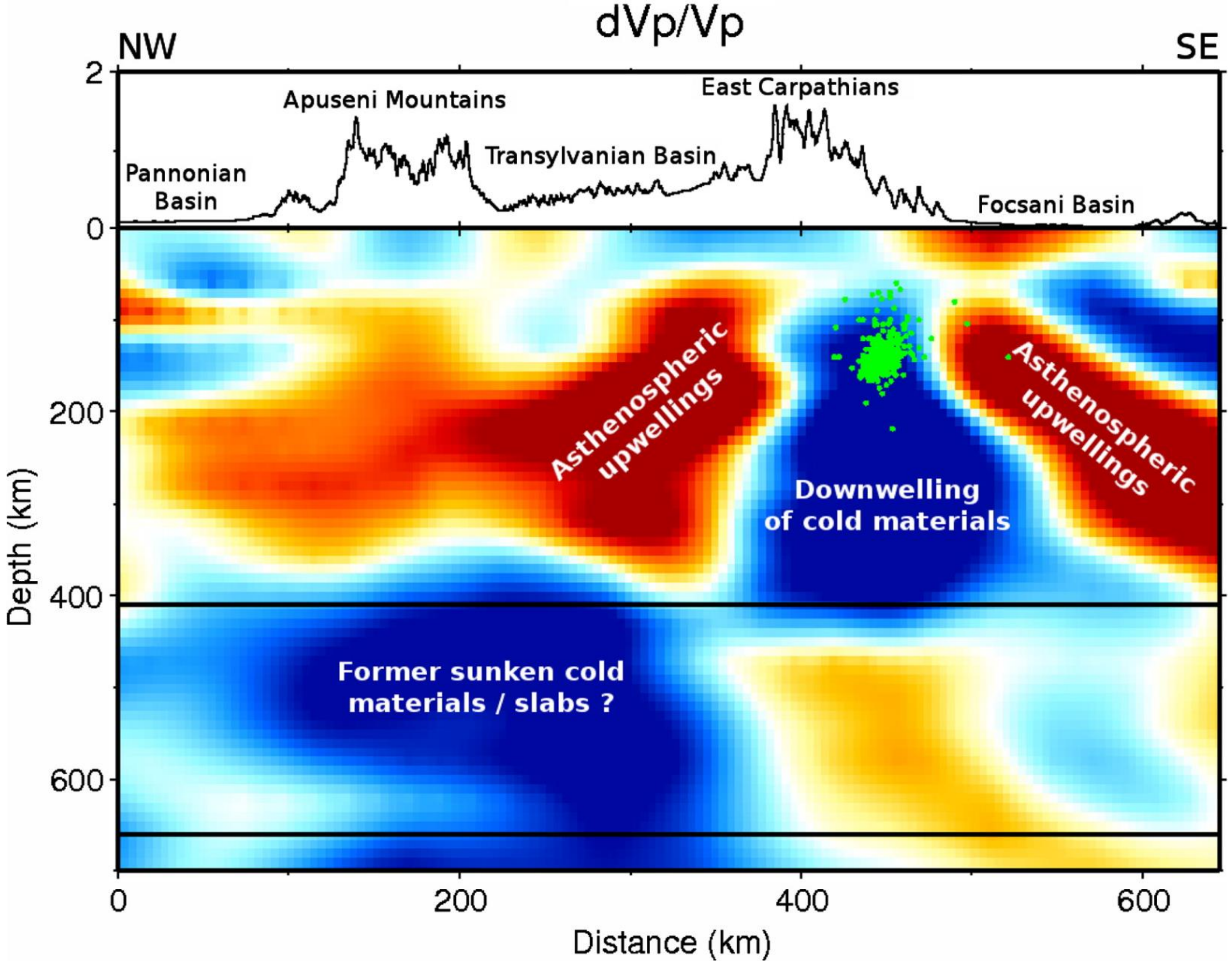

Ren et al. (2012)

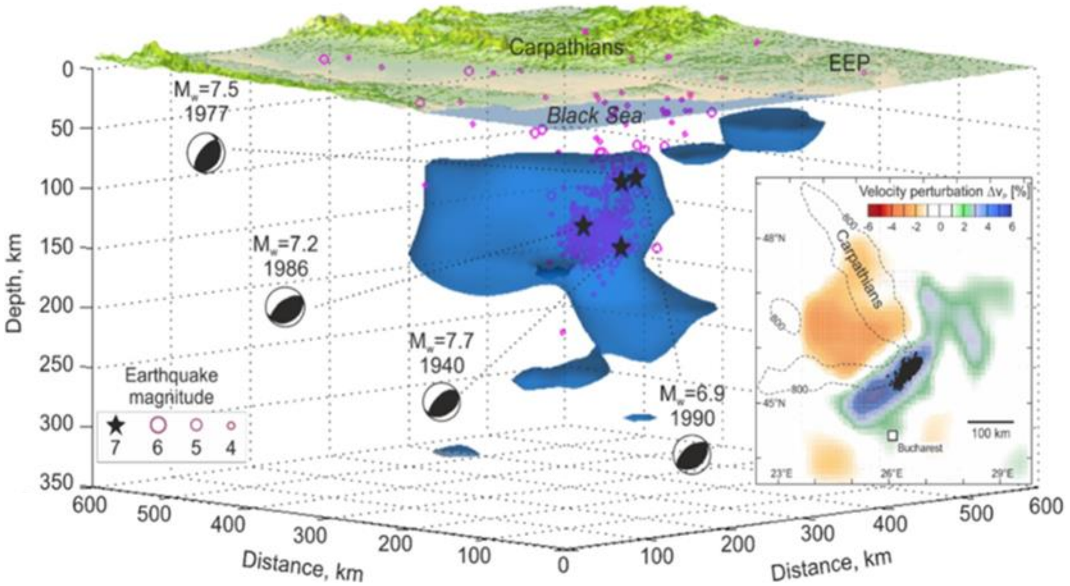

Martin et al. (2006)

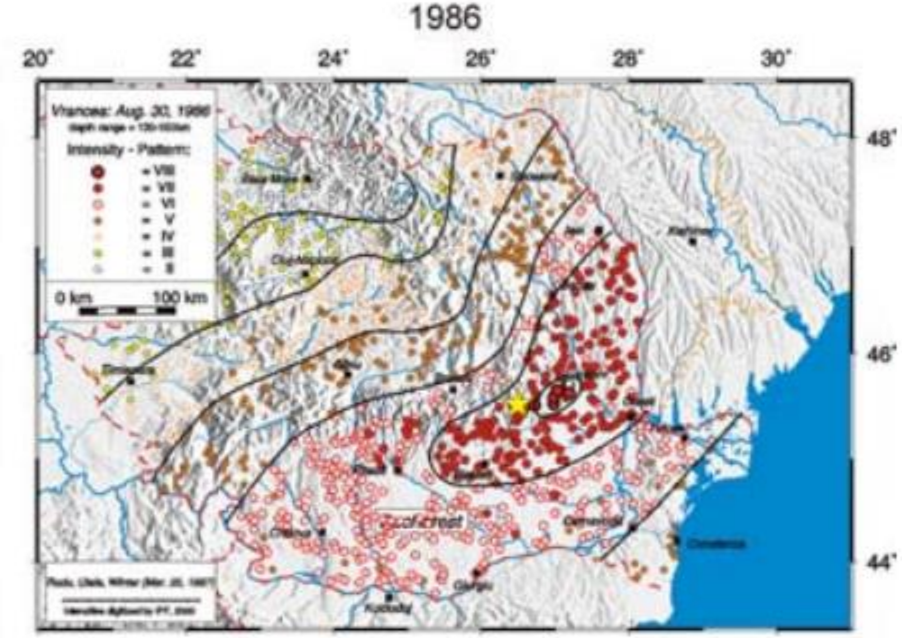

08/30/1986; H = 131 km; Mw = 7.1

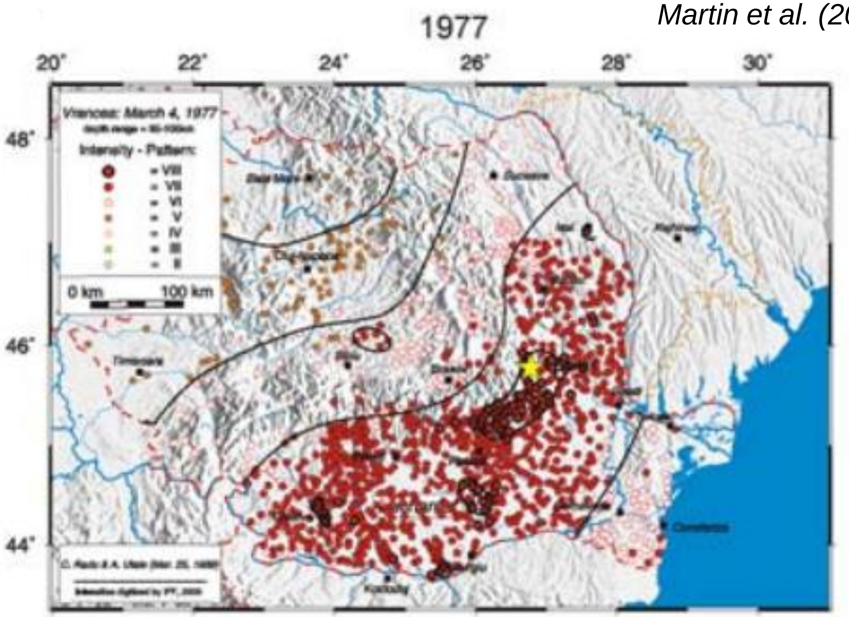

03/04/1977; H = 94km; Mw = 7.4

Sokolov et al. (2006)

- The earthquakes affect very large areas with a predominant NE-SW orientation;
- NE-SW enhancement of effects coincides with the geometry of seismicity and of the fault-plane solutions;
- The radiation of seismic waves seems to be influenced by the depth of earthquake

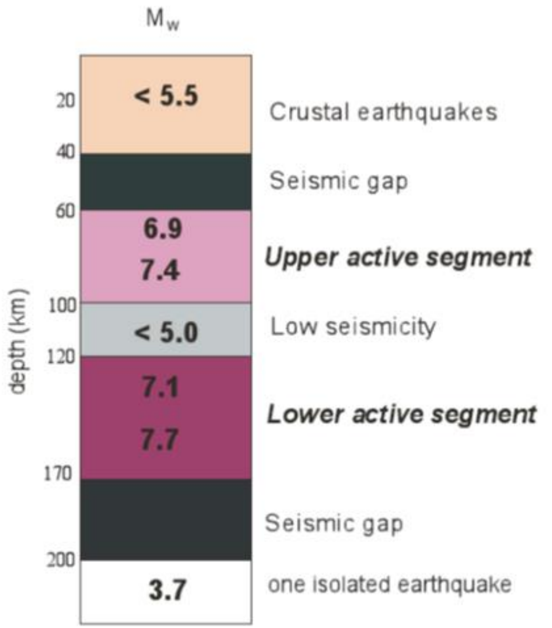

- Seismic activity history in time indicate two active segments;
- Decoupling hypothesis between the two segments and that the processes that trigger major earthquakes;

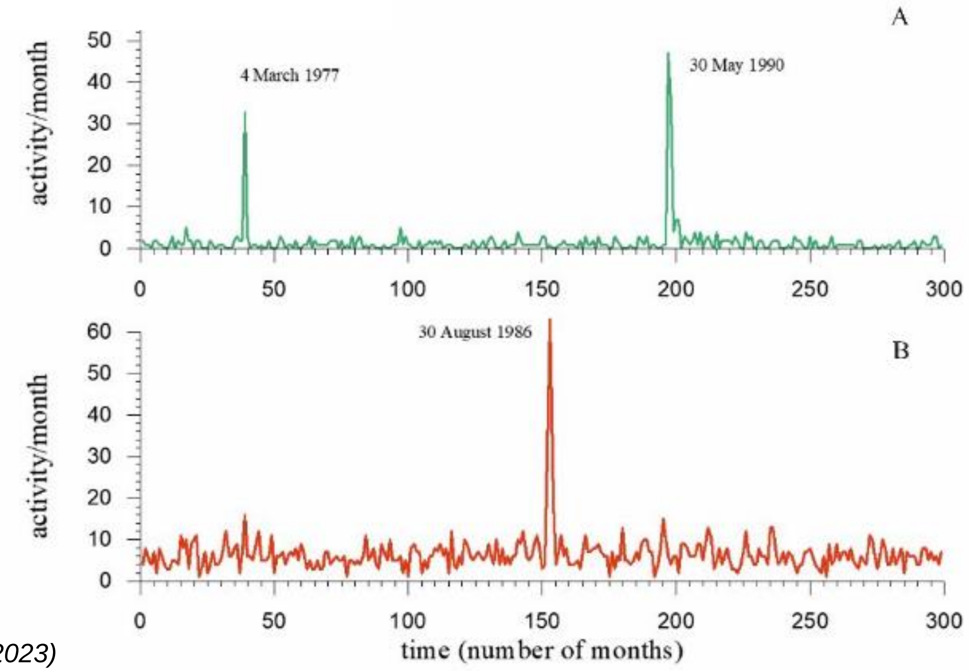

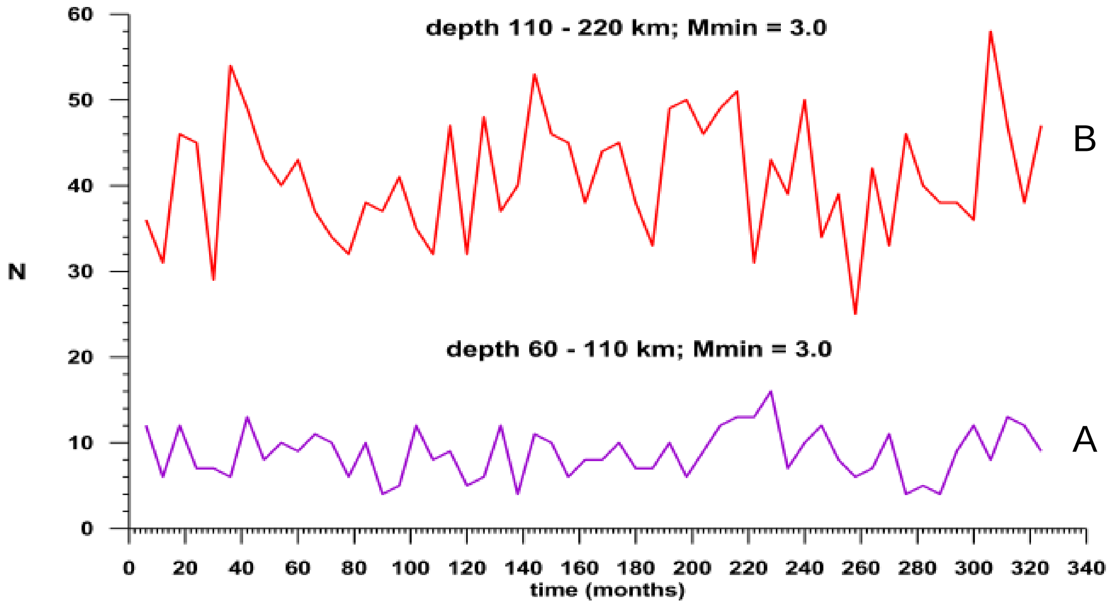

Radulian et al. (2023)

Resistant or not resistant material?

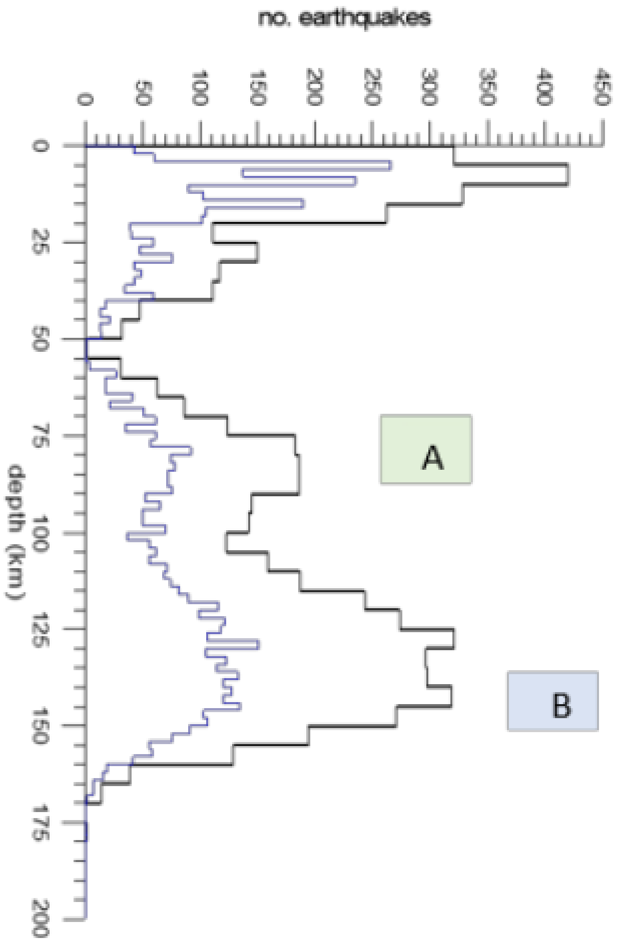

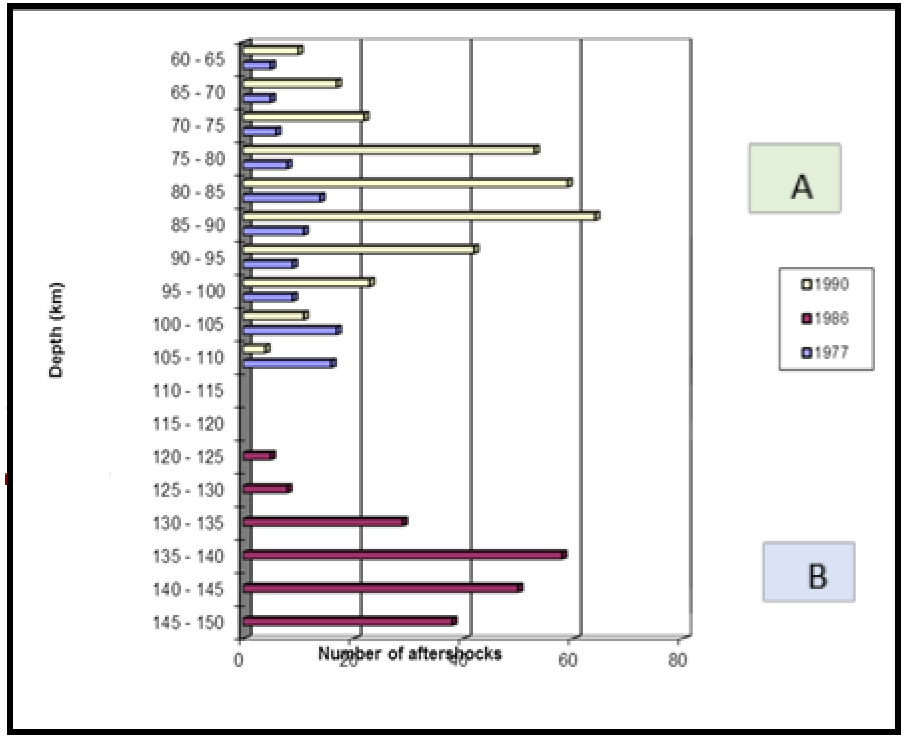

1977 1990
2004

1940
1986

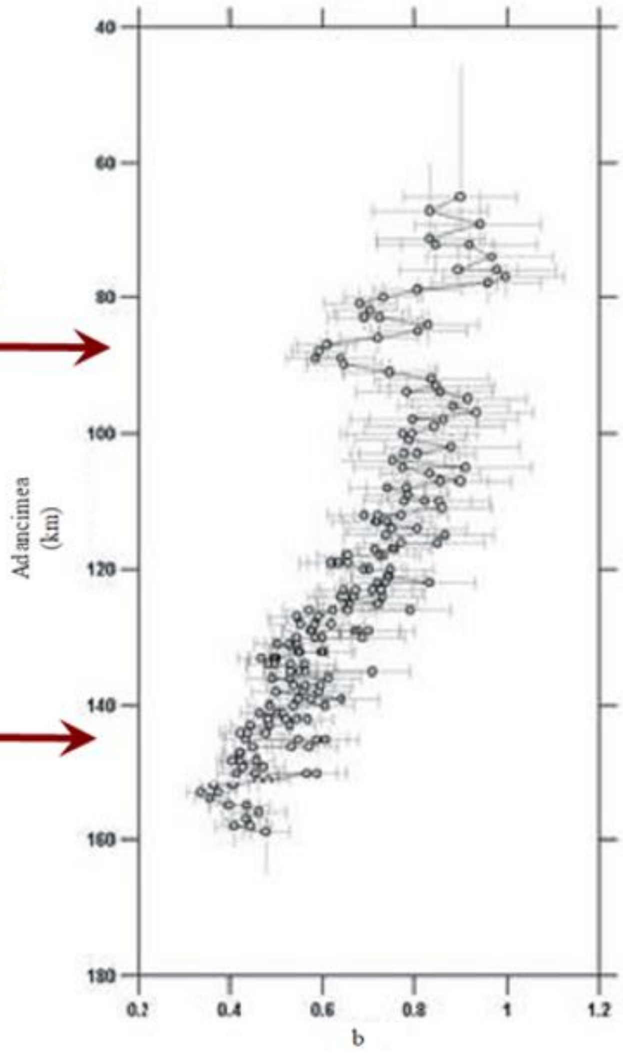

Radulian et al. (2023)

MOMENT TENSOR SOLUTION

HYPOCENTER LOCATION (RONDC)

```
Origin time 20210525 21:30:37.20
Lat 45.5321 Lon 26.5226 Depth 131
```

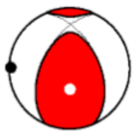

CENTROID

```
Trial source number : 5 (Fixed Epicenter inversion)
Centroid Lat (N)45.5321 Lon (E)26.5226
Centroid Depth (km) : 130
Centroid time : +0.45 (sec) relative to origin time

Moment (Nm) : 2.990e+15
Mw : 4.3
VOL% :0
DC% :90.7
CLVD% :9.3                                         SNR   CN   FMVAR  STVAR
Quality :A1
Var.red.:(for stations used in inversion):0.6     NaN   3.7   3±2    0.17
Var.red.(for all stations)                :0.6
```

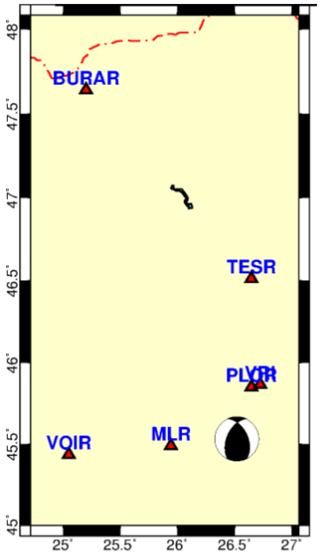

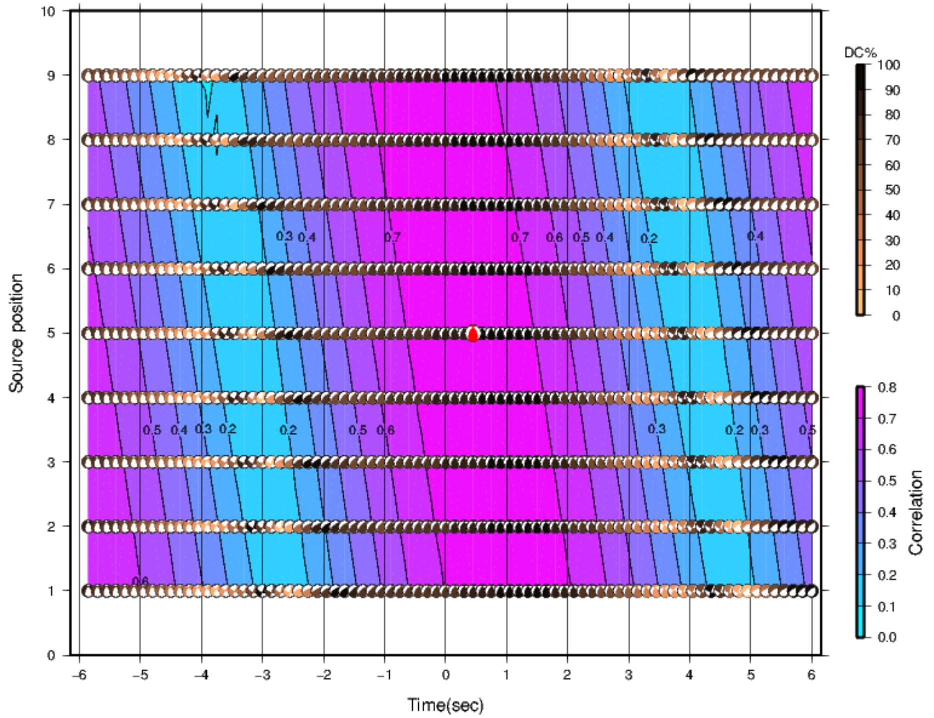

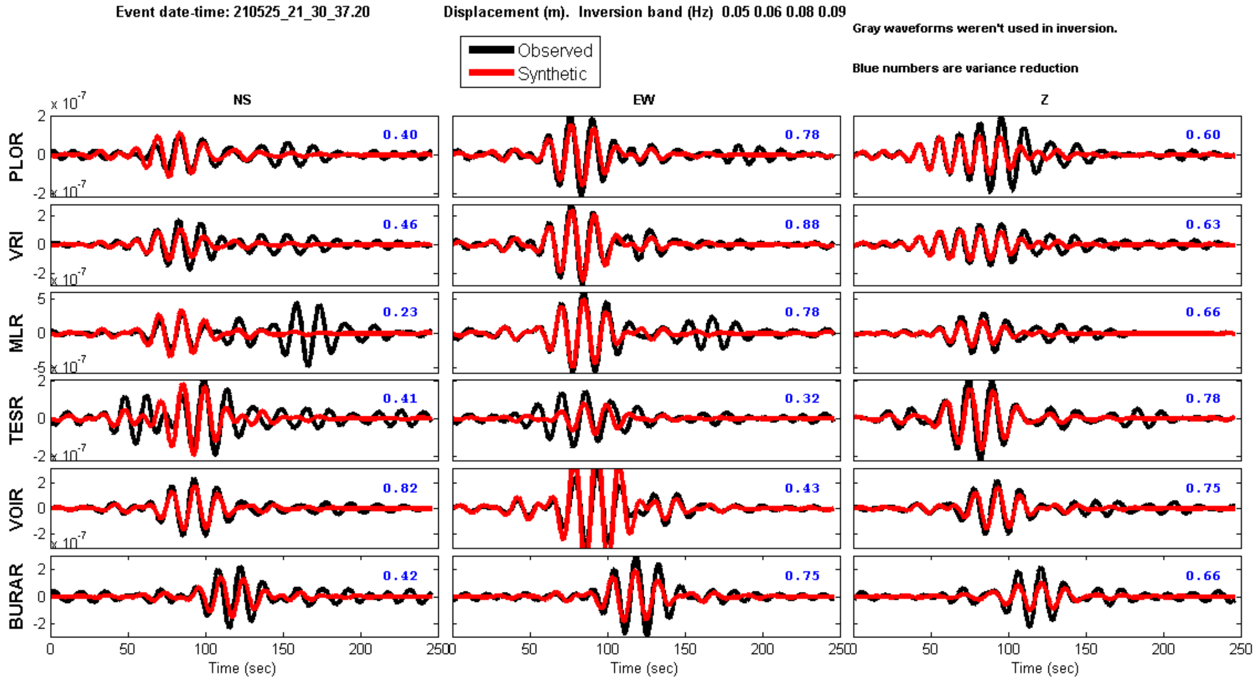

- REFMC catalogue comprising 193 focal mechanisms from the 1952–2012 (Radulian et al., 2019);
- RSN catalogue comprises 437 solutions, for events with magnitude ranges of 2.7 ≤ Mw ≤5.6 and depth interval of 60 ≤ H(km) ≤ 162, that occurred from 2005 to 2020 (Craiu et al., 2022);
- FWC catalogue comprises 46 solutions for events that occurred from 2014 to 2023 ISOLA –www.infp.ro;

- Source parameters of 81 intermediate-depth earthquakes (2.9 ≤ MW ≤ 5.3) were determined based on the inversion of the P-wave displacement spectra and spectral ratios method;

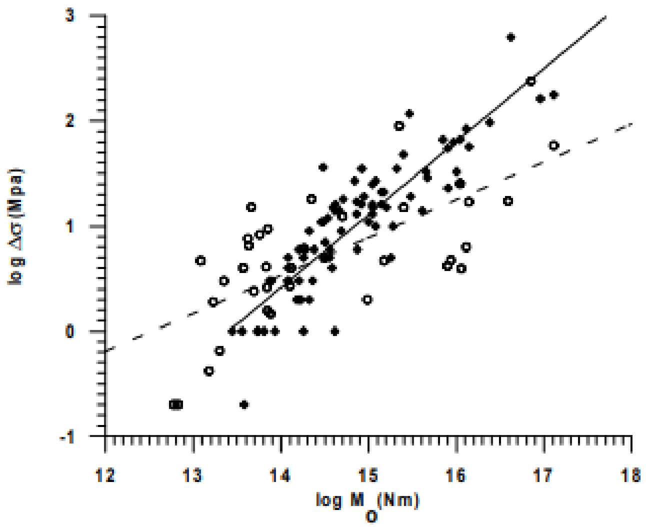

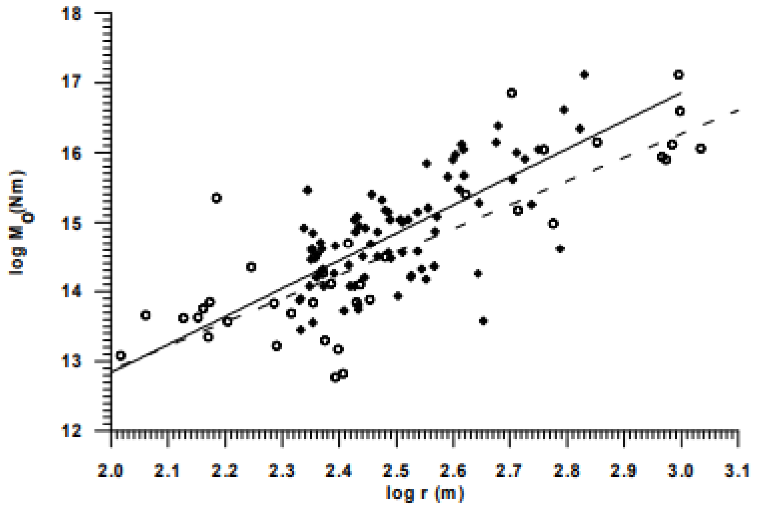

60 ≤ H(km) ≤ 110 km

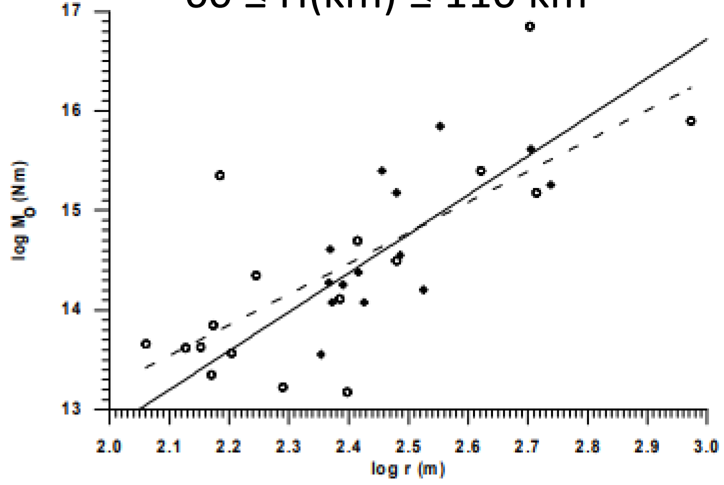

110 ≤ H(km) ≤ 200 km

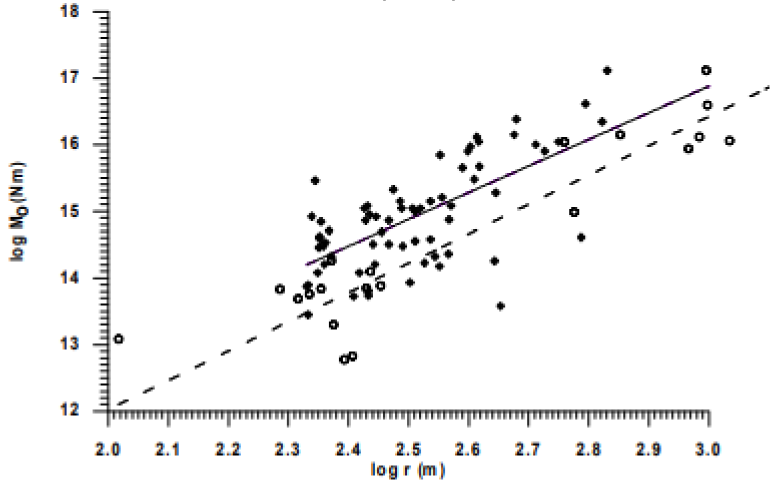

Popescu et al. (2003)

Dehydration embrittlement – Hydrated minerals expel water into rock pores increasing pore fluid pressure. If the permeability is insufficient to relieve increasing fluid pressure rocks undergo weakening and embrittlement leading to shear fracturing and a sudden stress drop (Frohlich 2006);

Thermal runaway –If heat generation inside a deforming rock is faster than its transport the rock becomes unstable and prone to brittle failure (Ogawa, 1987);

Transformational faulting – Minerals can undergo phase transformation resulting in fine grained rock that is easier to deform (Ferrand et al., 2017);

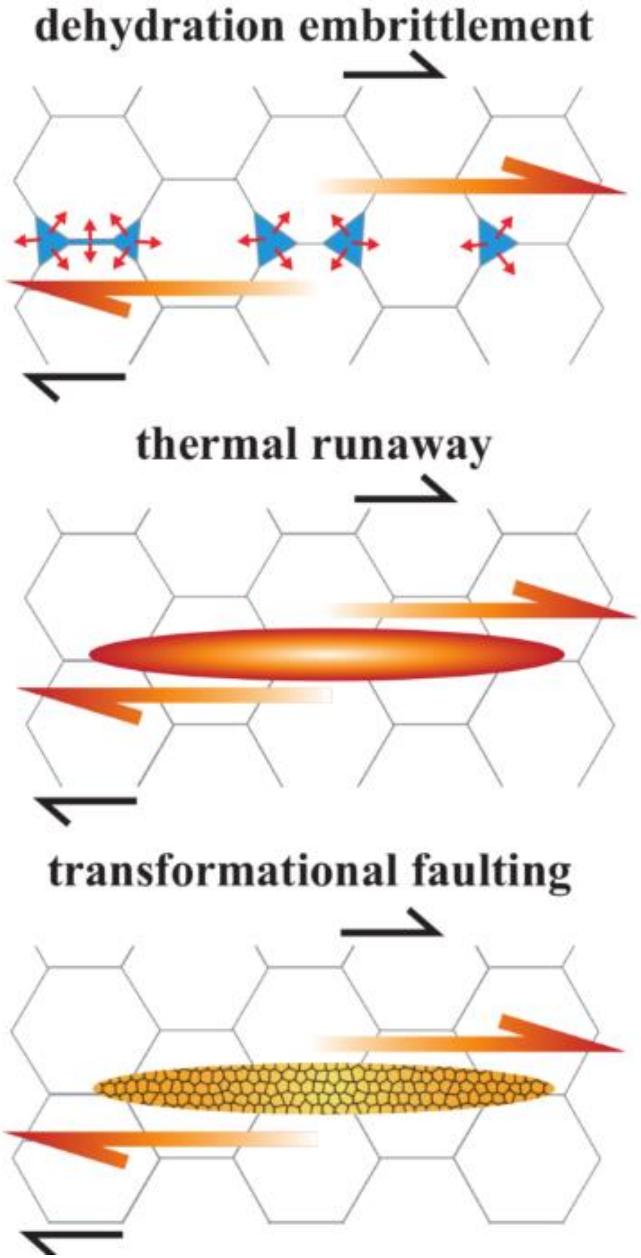

https://blogs.egu.eu/divisions/gd/2019/11/13/enigmas-at-depth

Dehydration embrittlement

Water enters the oceanic lithosphere especially along bending faults and reworked transform faults and it captured inside minerals;

The subducted slab is a subject of high pressure and temperatures causing hydrated minerals to release water;

The presence of fluids in Vrancea could imply that the slab is oceanic in origin;

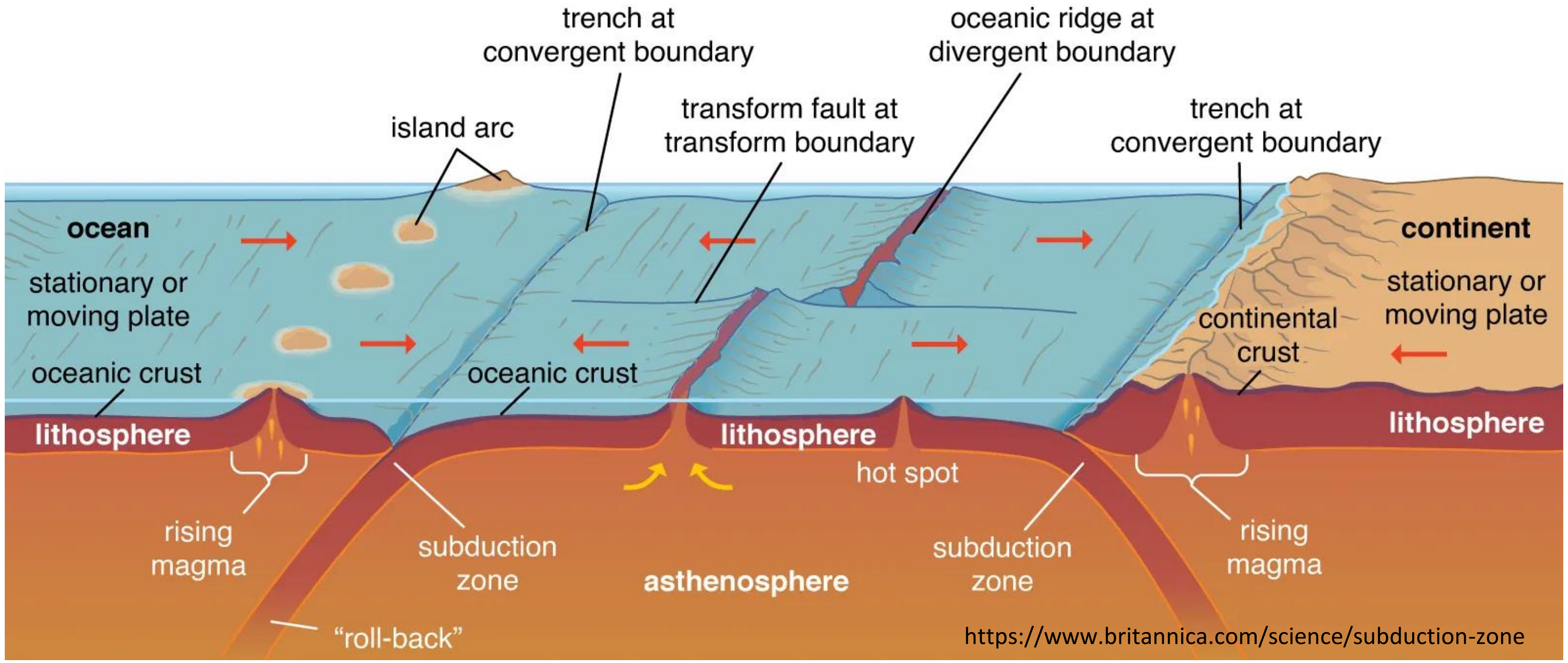

Oceanic slab subduction and break-off

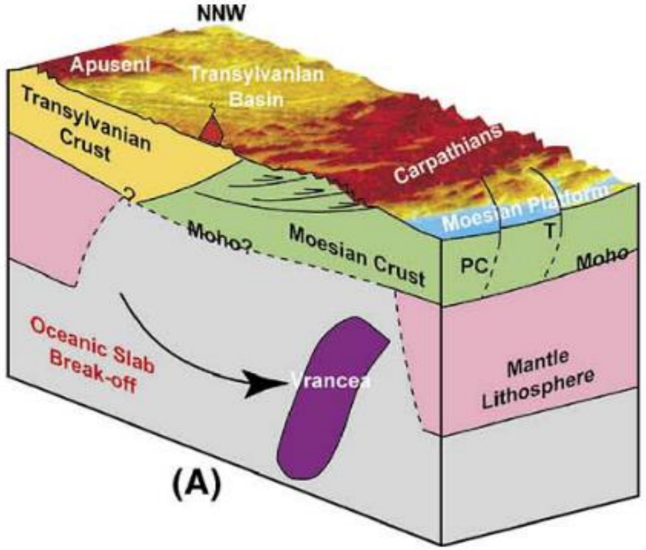

Oceanic slab subduction and progressive tear

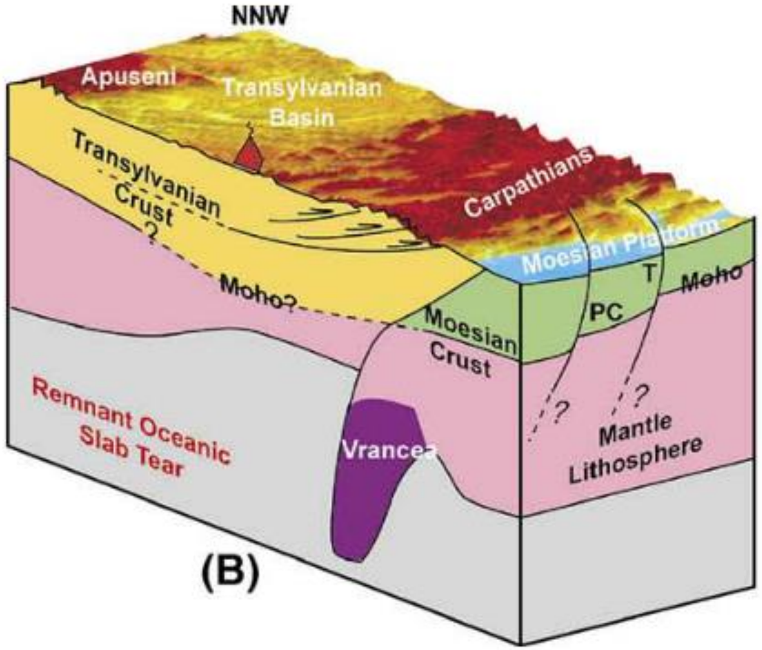

Lithospheric drip

Lorinczi and Houseman (2009)

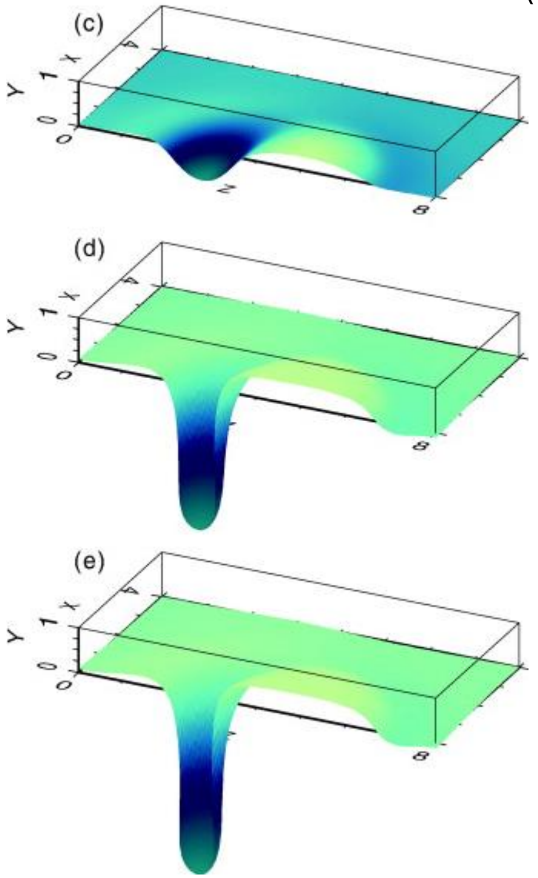

Continental lithospheric delamination

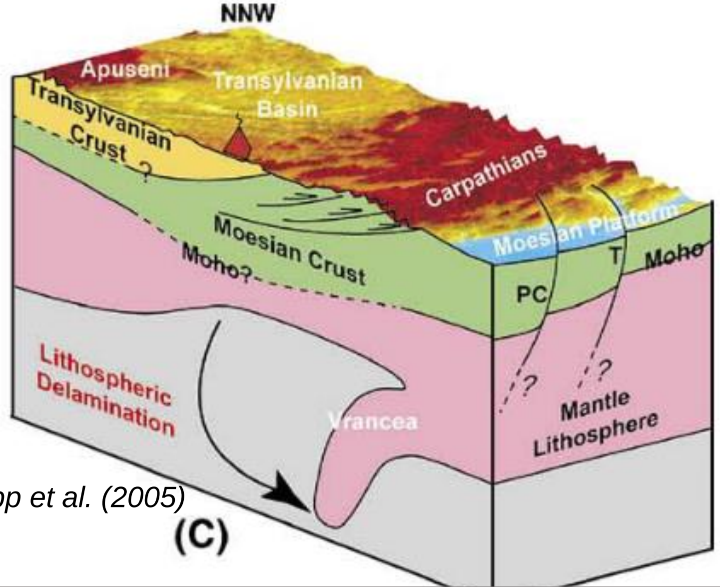

Knapp et al. (2005)

Unstable triple junction

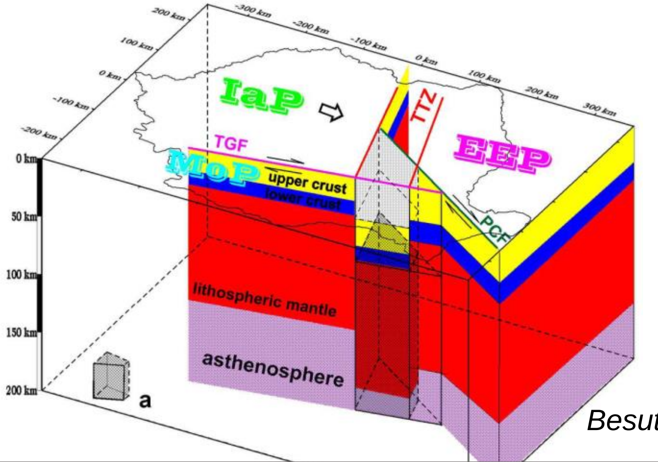

Besutiu, (2001)

Dehydration embrittlement

- Earthquakes distribution is controlled by temperature with material hotter than 600^0C being aseismic;

- A delaminated continental lithosphere root would still be aseismic at lower depths unless brittle failure is assisted;

- Ferrand & Manea (2021) modelled the thermodynamic stability limits for the minerals typical of the uppermost mantle oceanic crust and lower continental and found a good correlation between Vrancea subcrustal earthquakes and antigorite dehydratation;

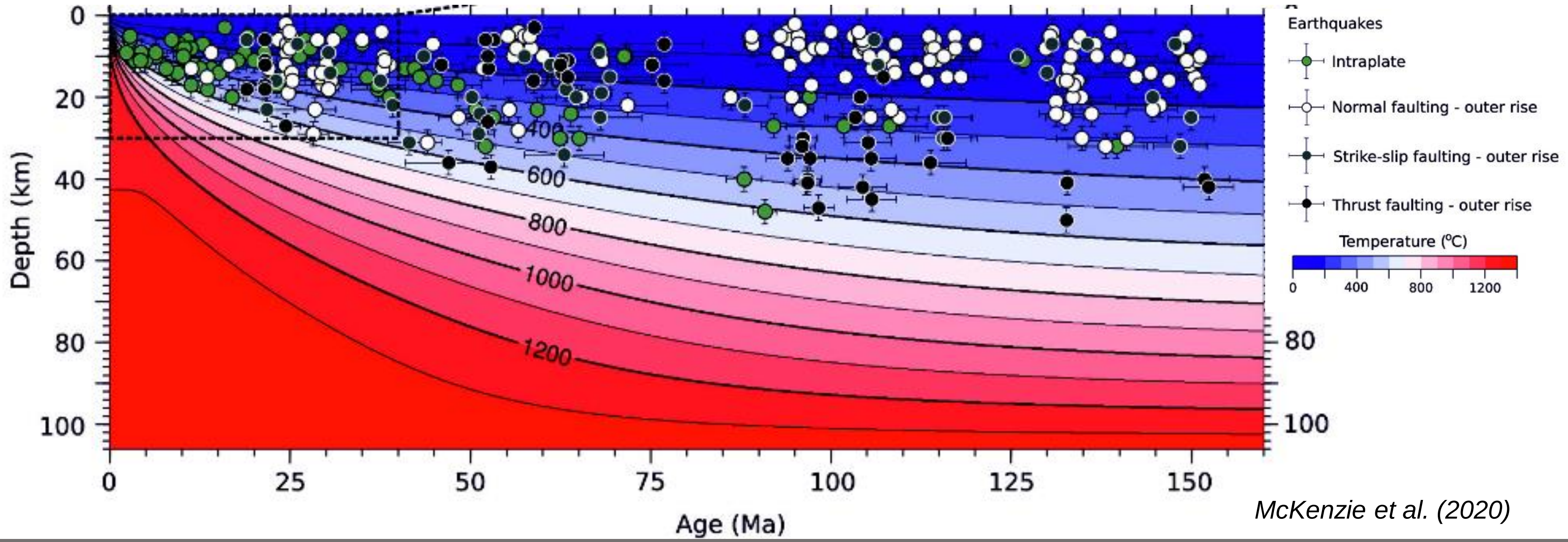

McKenzie et al. (2020)

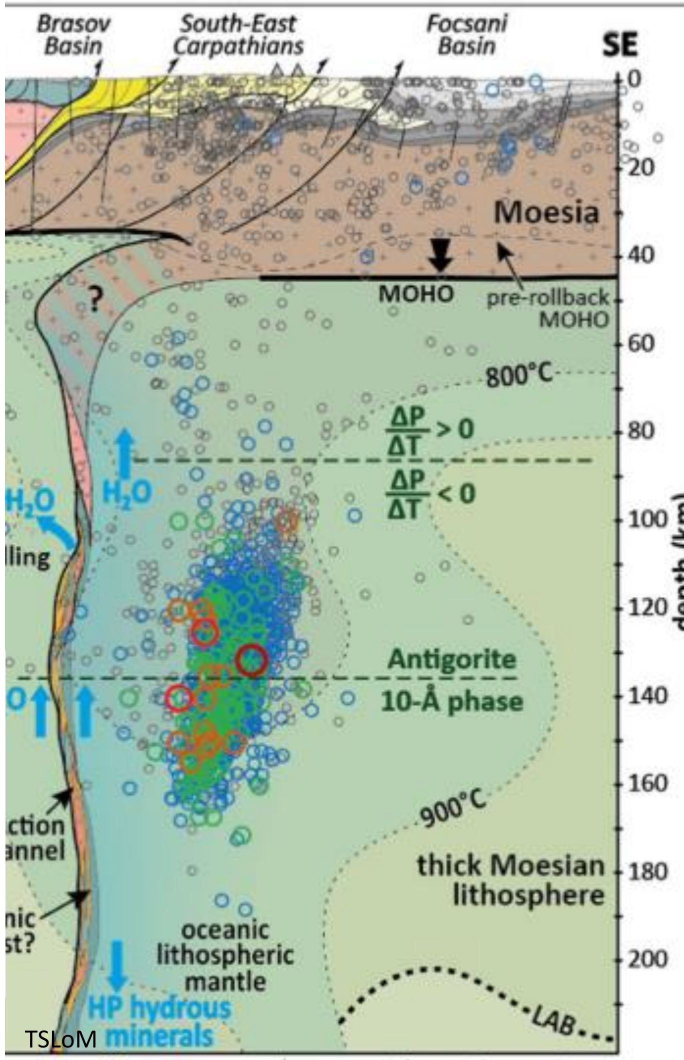

Ferrand & Manea (2021)

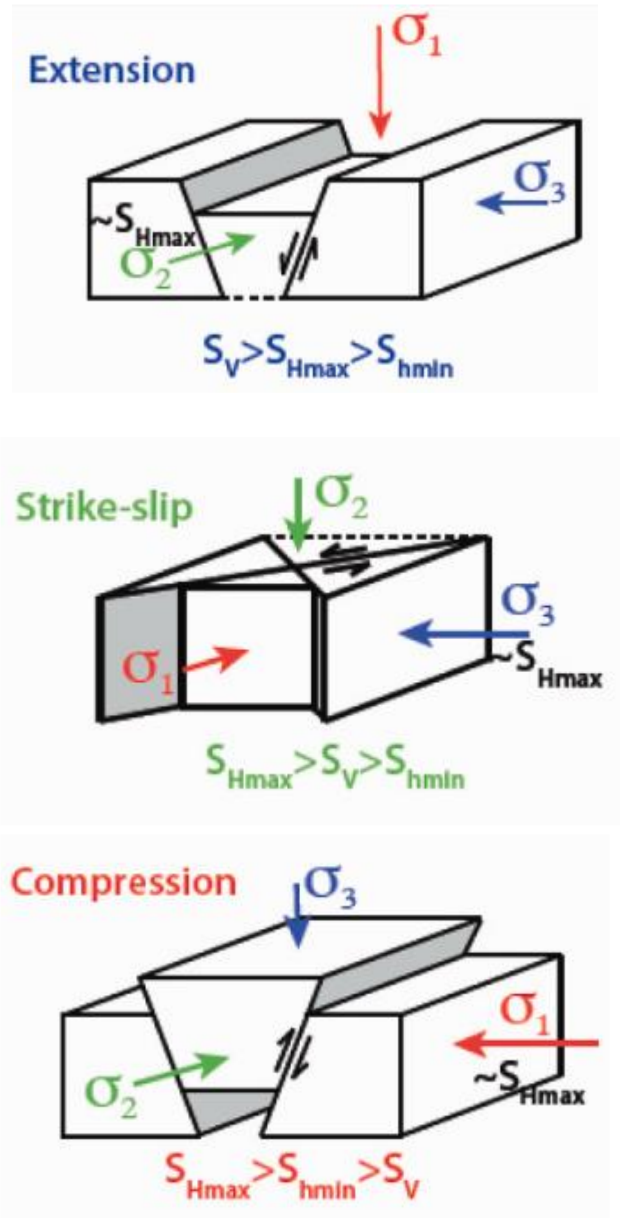

$$R = \frac{\sigma 1 - \sigma 2}{\sigma 1 - \sigma 3}$$

R low - extension

R high - compression

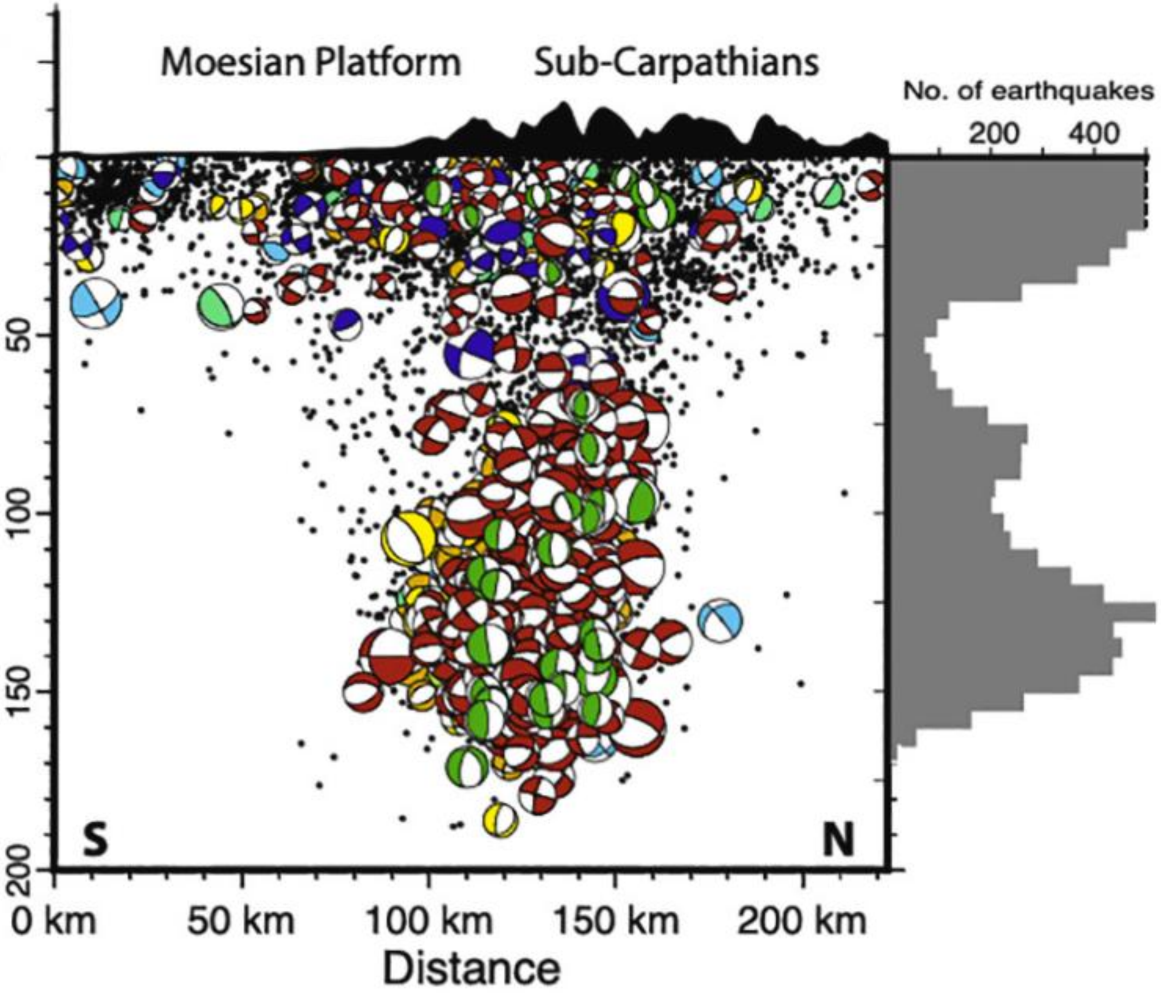

Petrescu et al. (2021)

- Relative stress ratio changes may be used as an indicator of fluid presence in seismic zones;
- Subcrustal earthquakes were divided into a 3D cubic grid 0.2^0x0.2^0x30km with 20% depth overlap;
- Invert clusters of focal mechanisms to obtain $\sigma 1$, $\sigma 2$ *and* $\sigma 3$ and R using MSATSI software (Martinez Garcon et al., 2014);

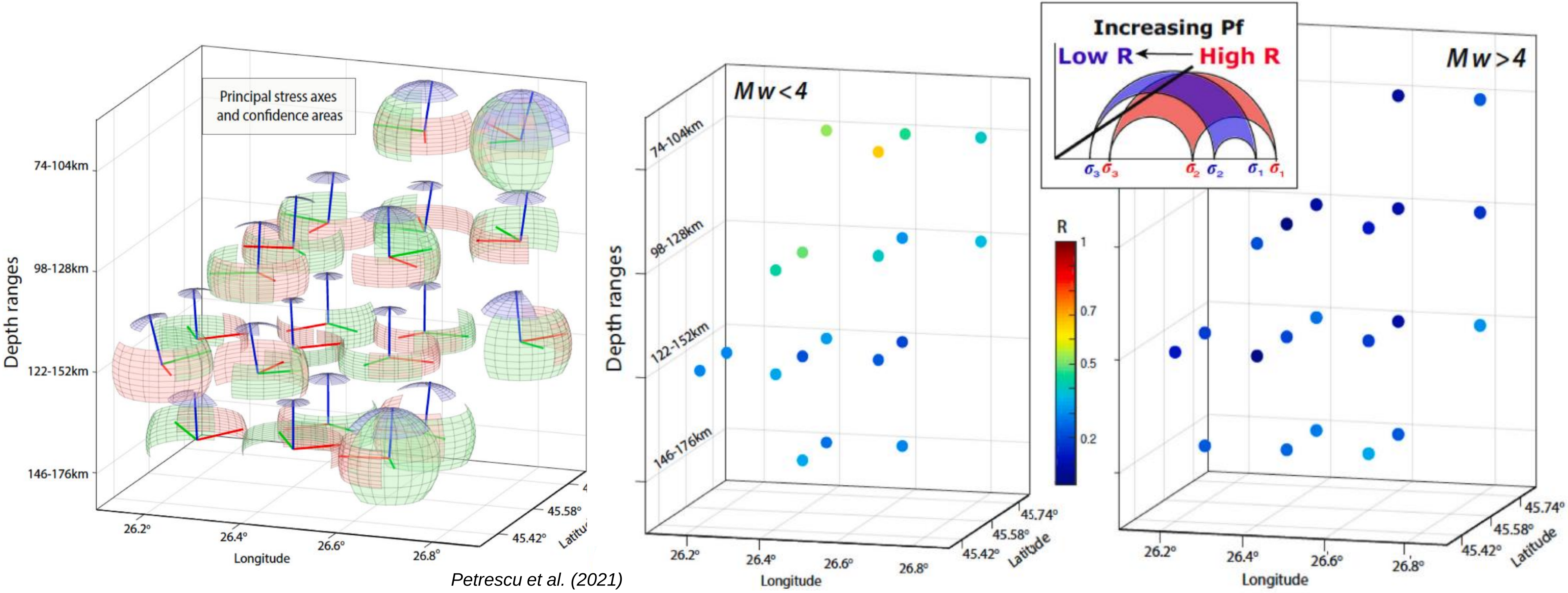

Petrescu et al. (2021)

- R changes from 0.3 to 0.7 for Mw<4 and M>4 earthquakes suggest that small earthquakes are more clearly associated with preferential vertical elongation in the slab, while larger earthquakes could be generated by other mechanisms such as dehydration embrittlement;

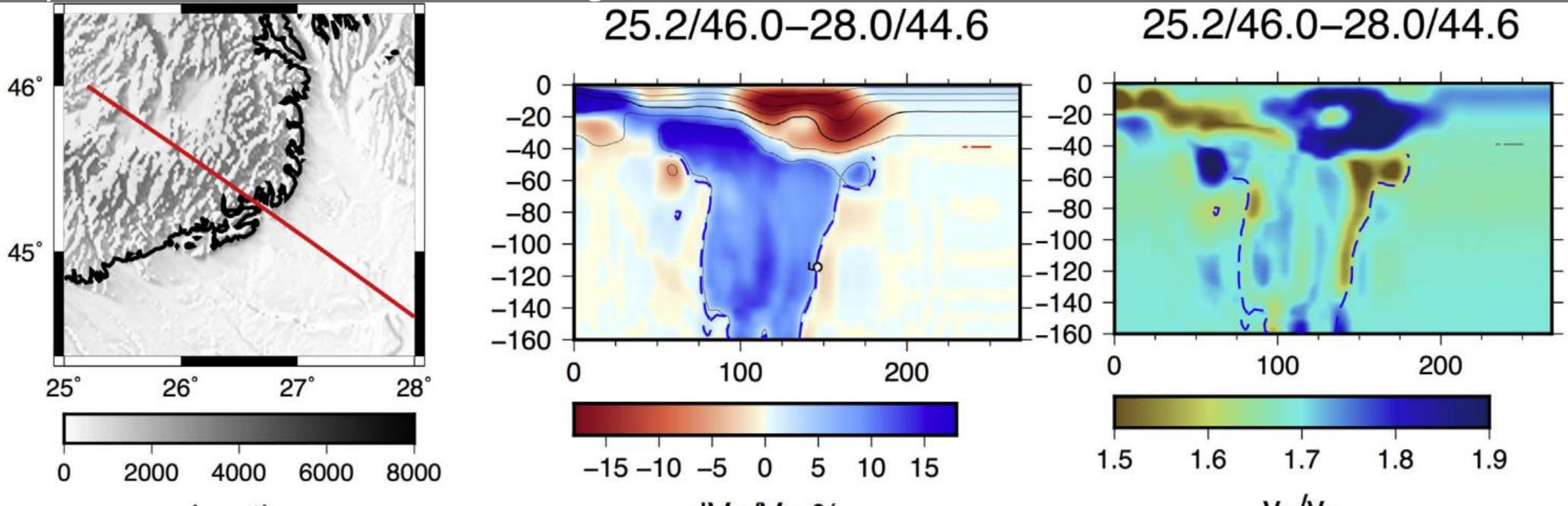

Baron and Morelli, (2017)

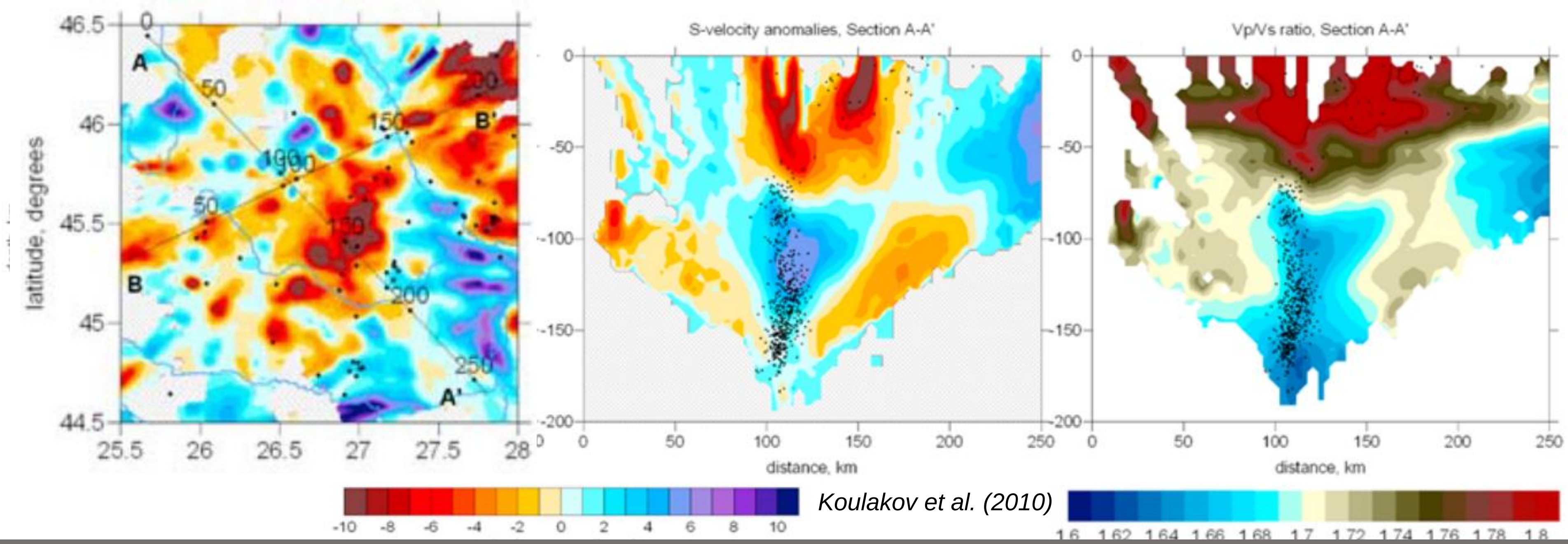

Koulakov et al. (2010)

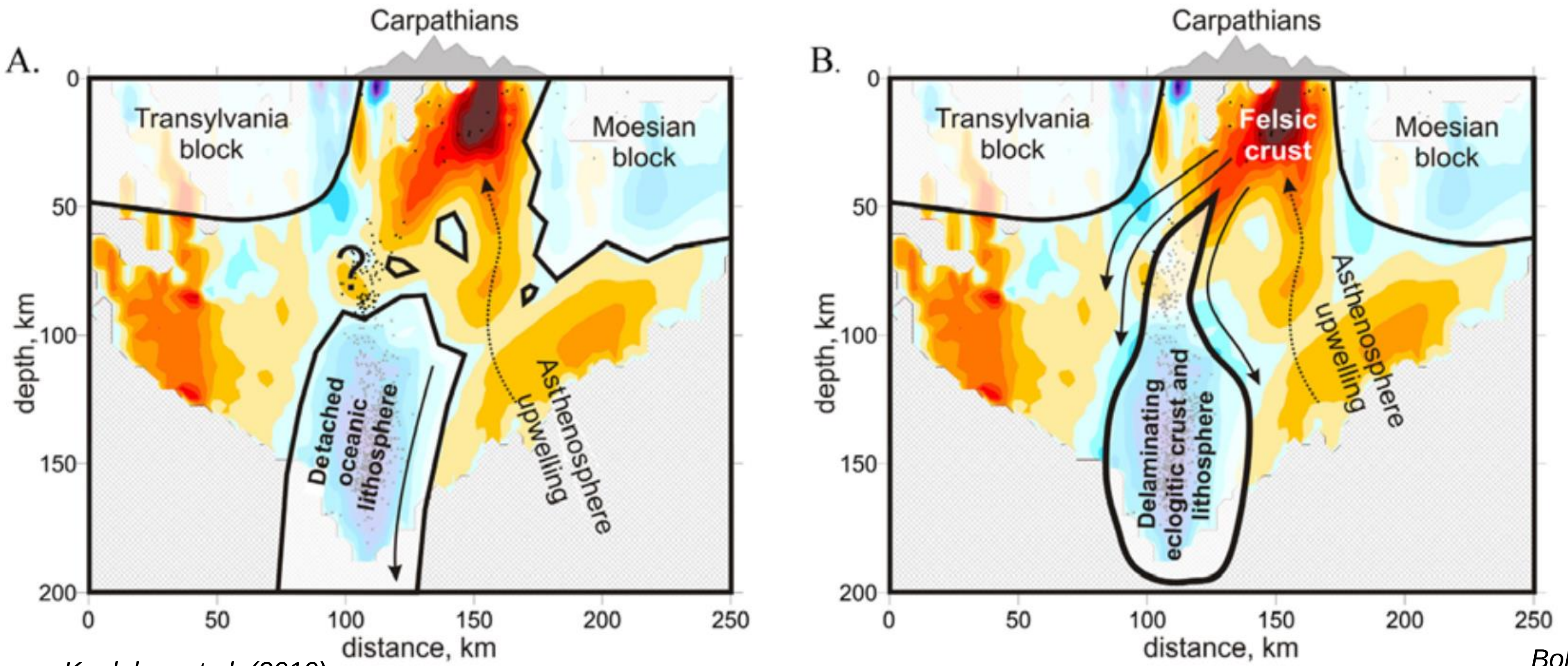

Koulakov et al. (2010)

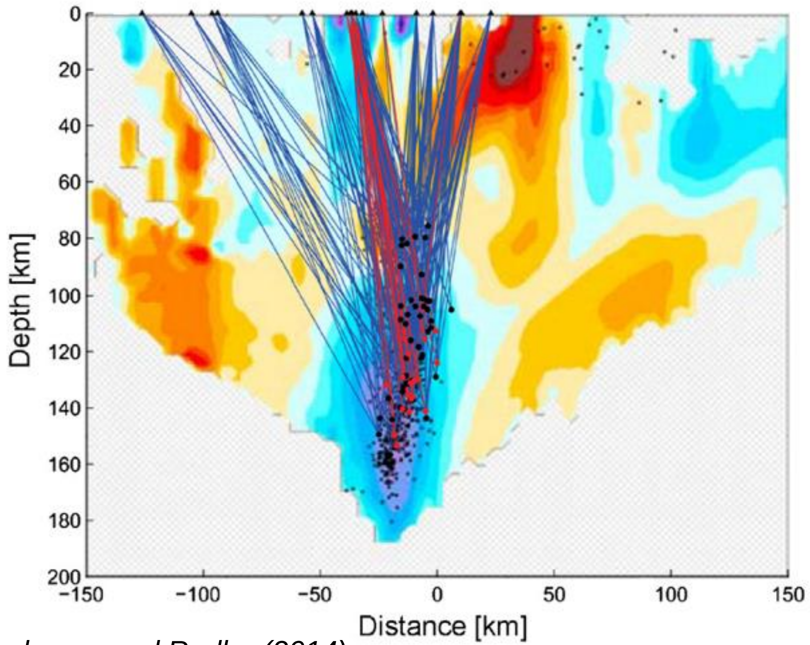

Bokelmann and Rodler (2014)

Transylvanian Basin vs. Romanian Plain

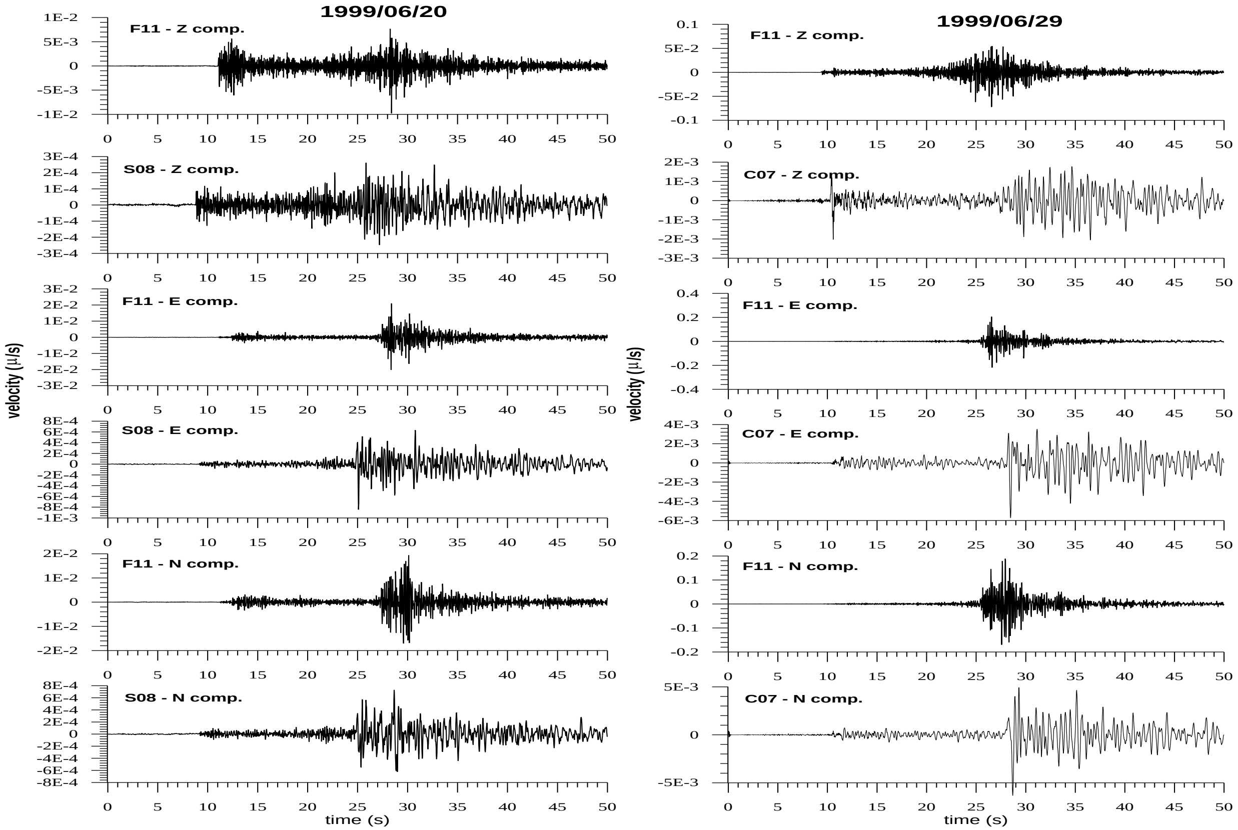

Radulian et al. 2006

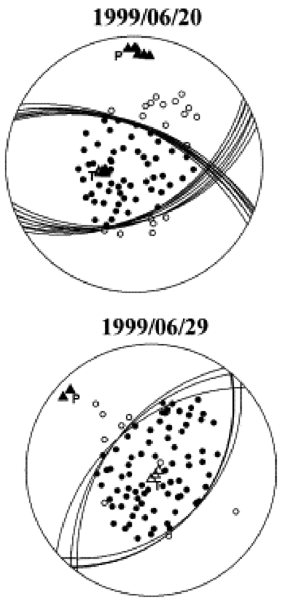

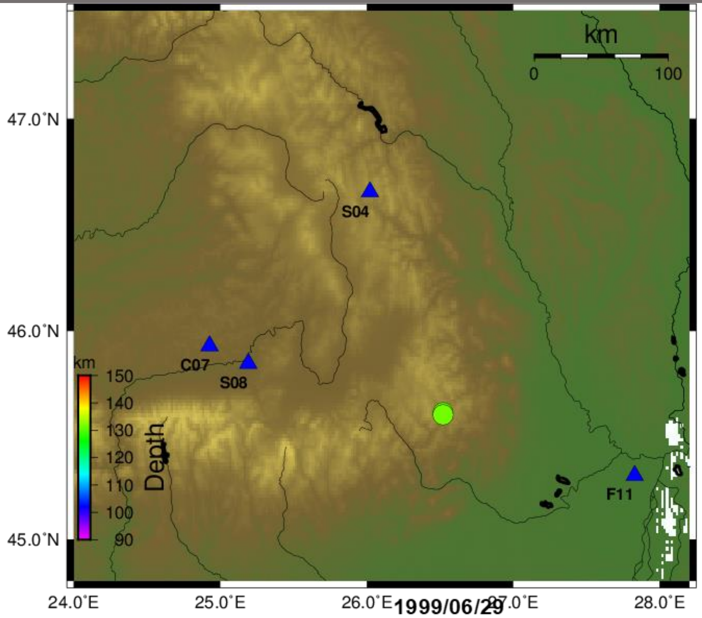

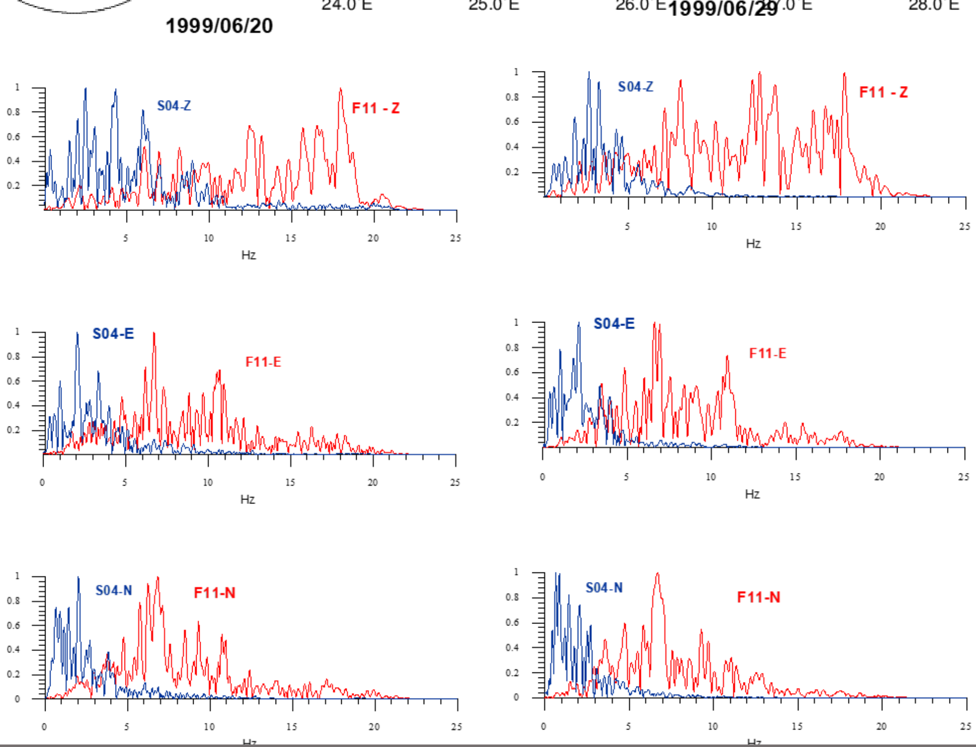

- In the Transylvanian Basin and the Eastern Carpathians amplitudes decrease significantly and high frequencies are also attenuated in contrast to the foreland platform;

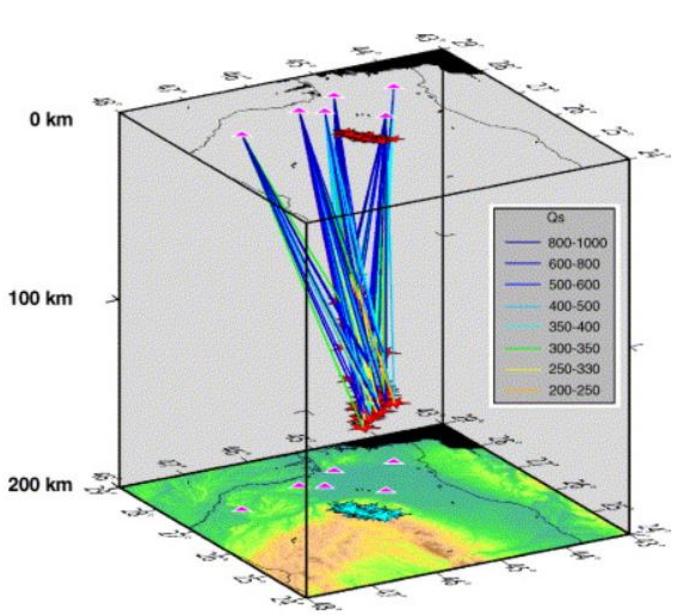

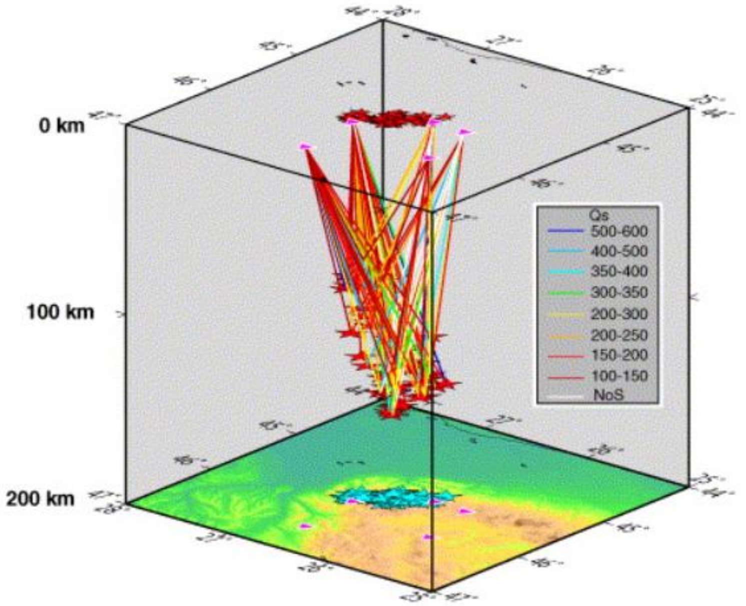

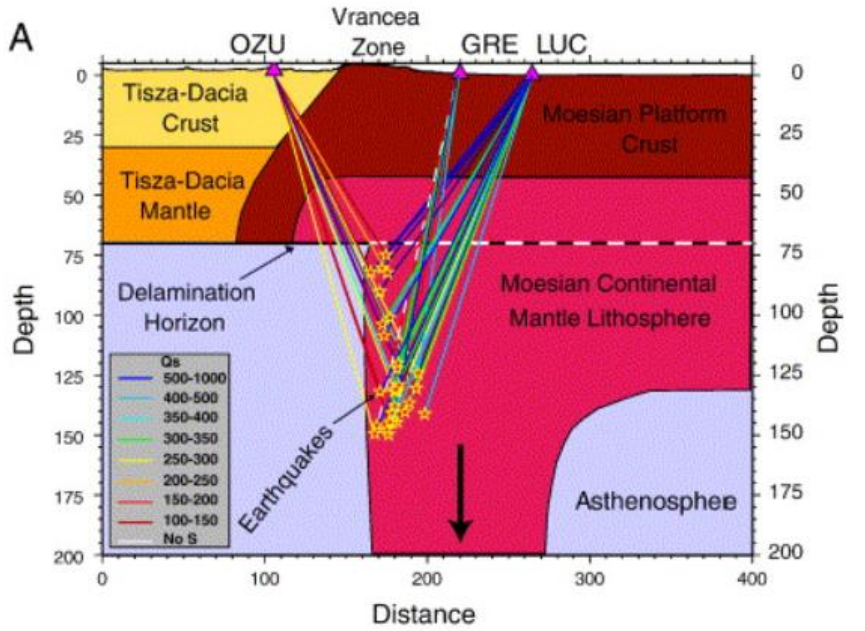

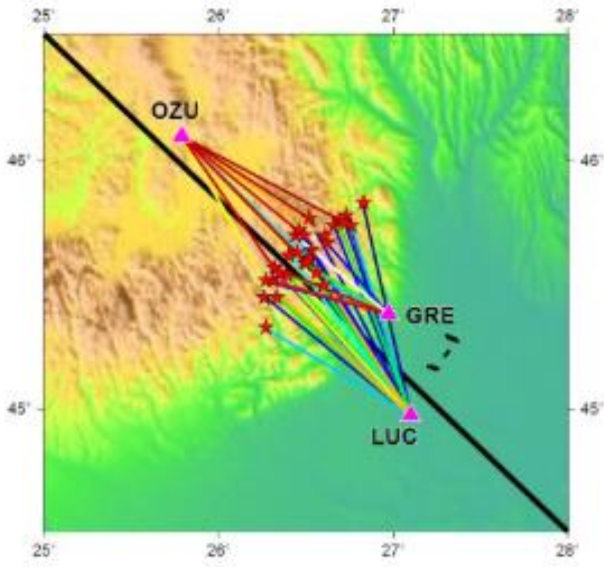

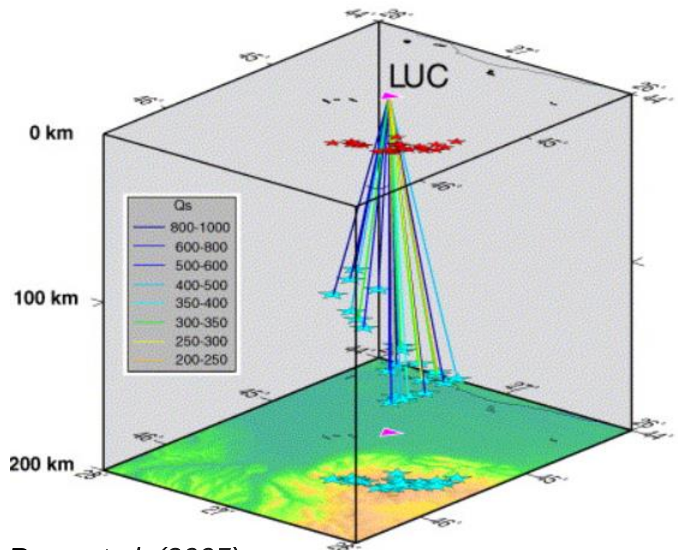

Ruso et al. (2005)

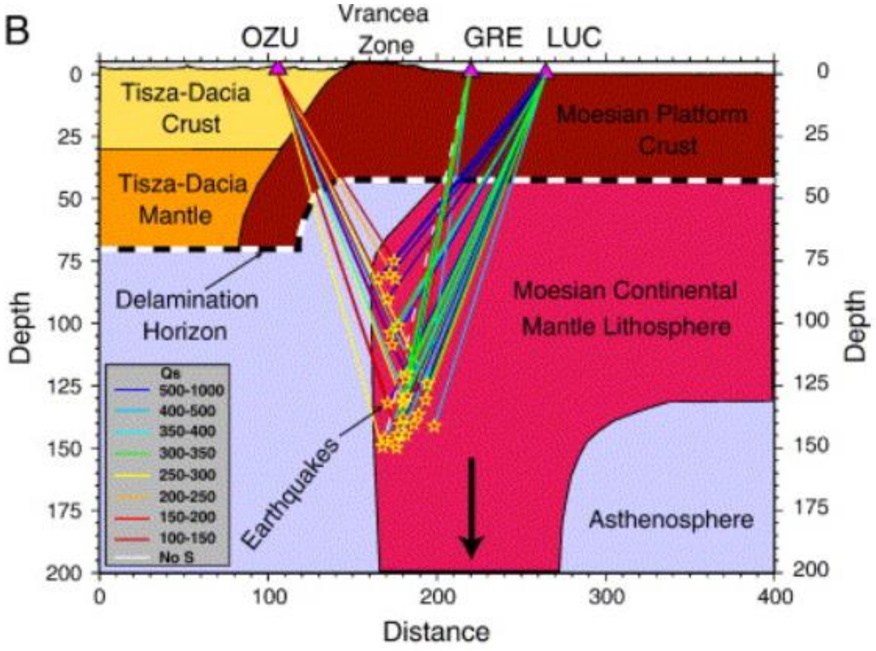

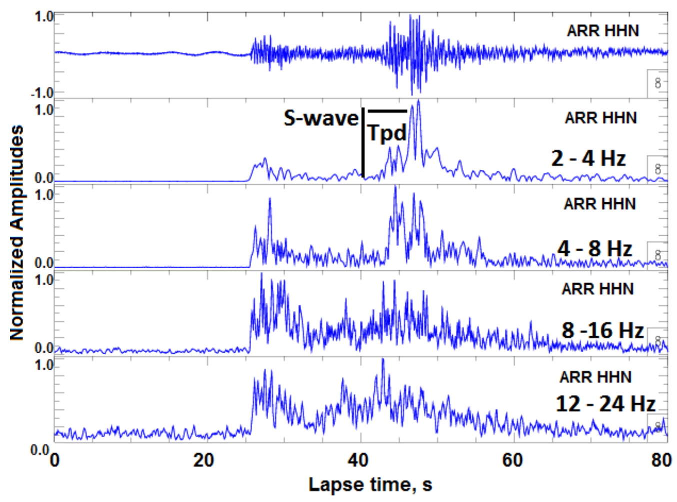

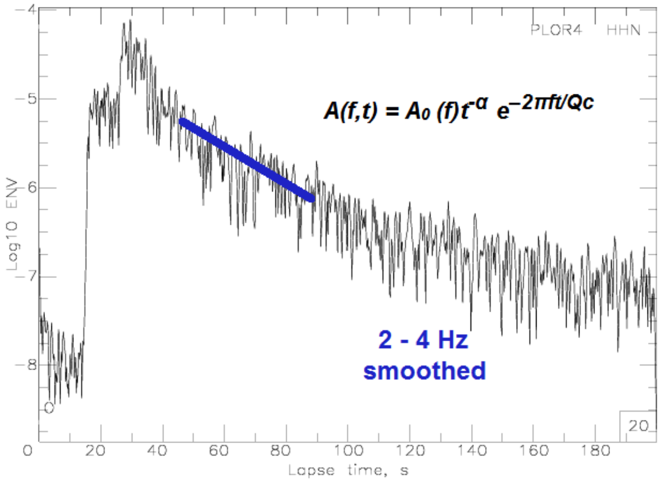

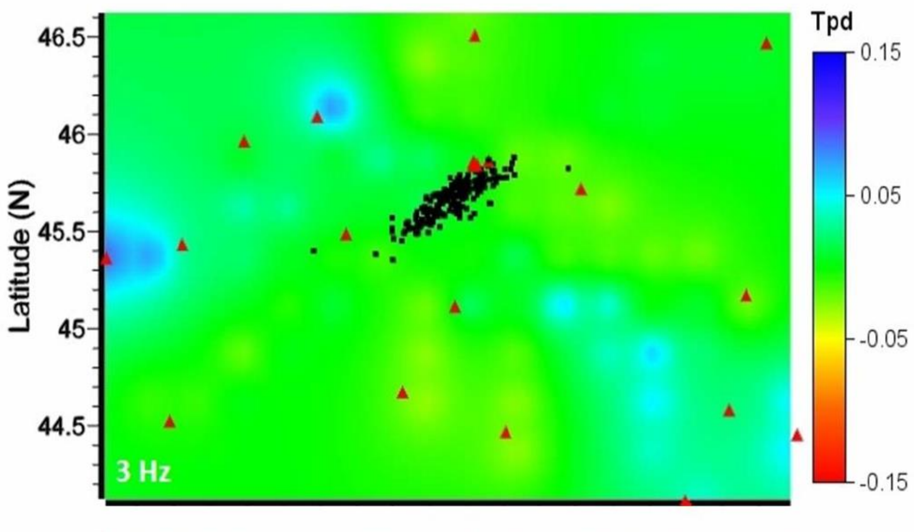

Borleanu et al. (2017)

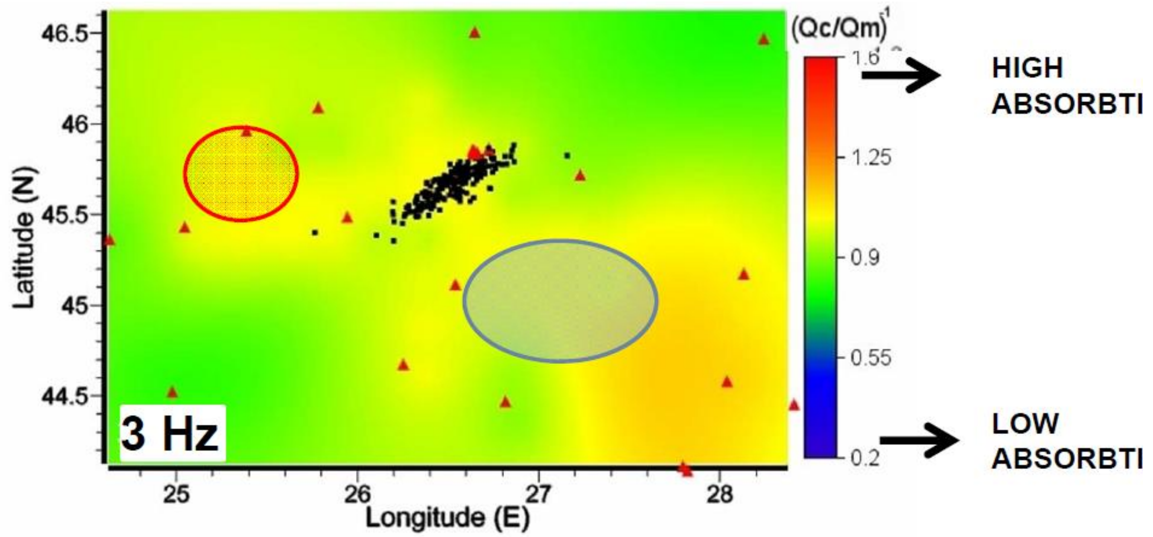

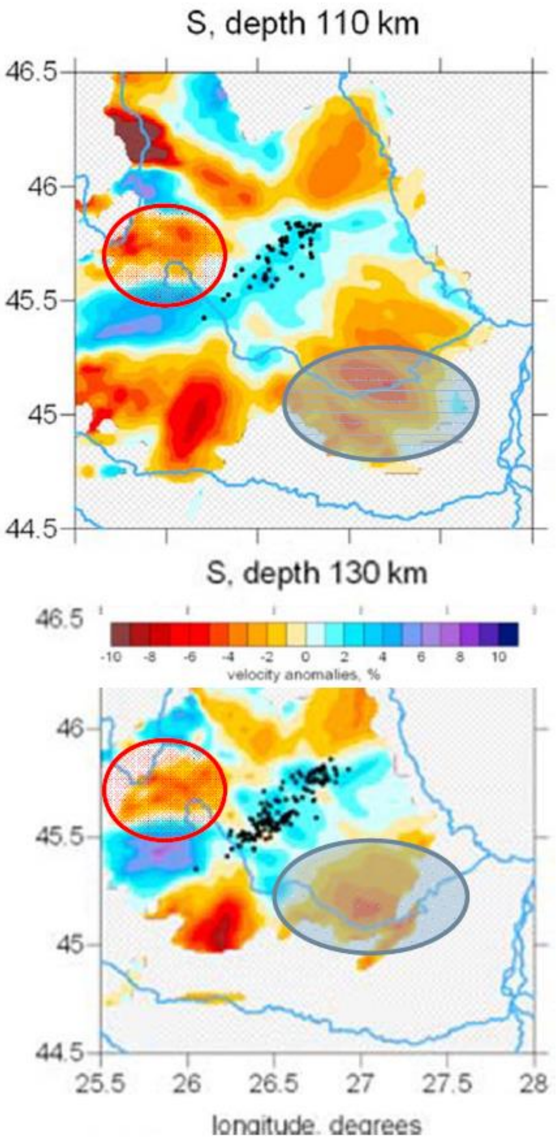

- The high absorption regions match to the low velocity areas found in the previous tomographic images;

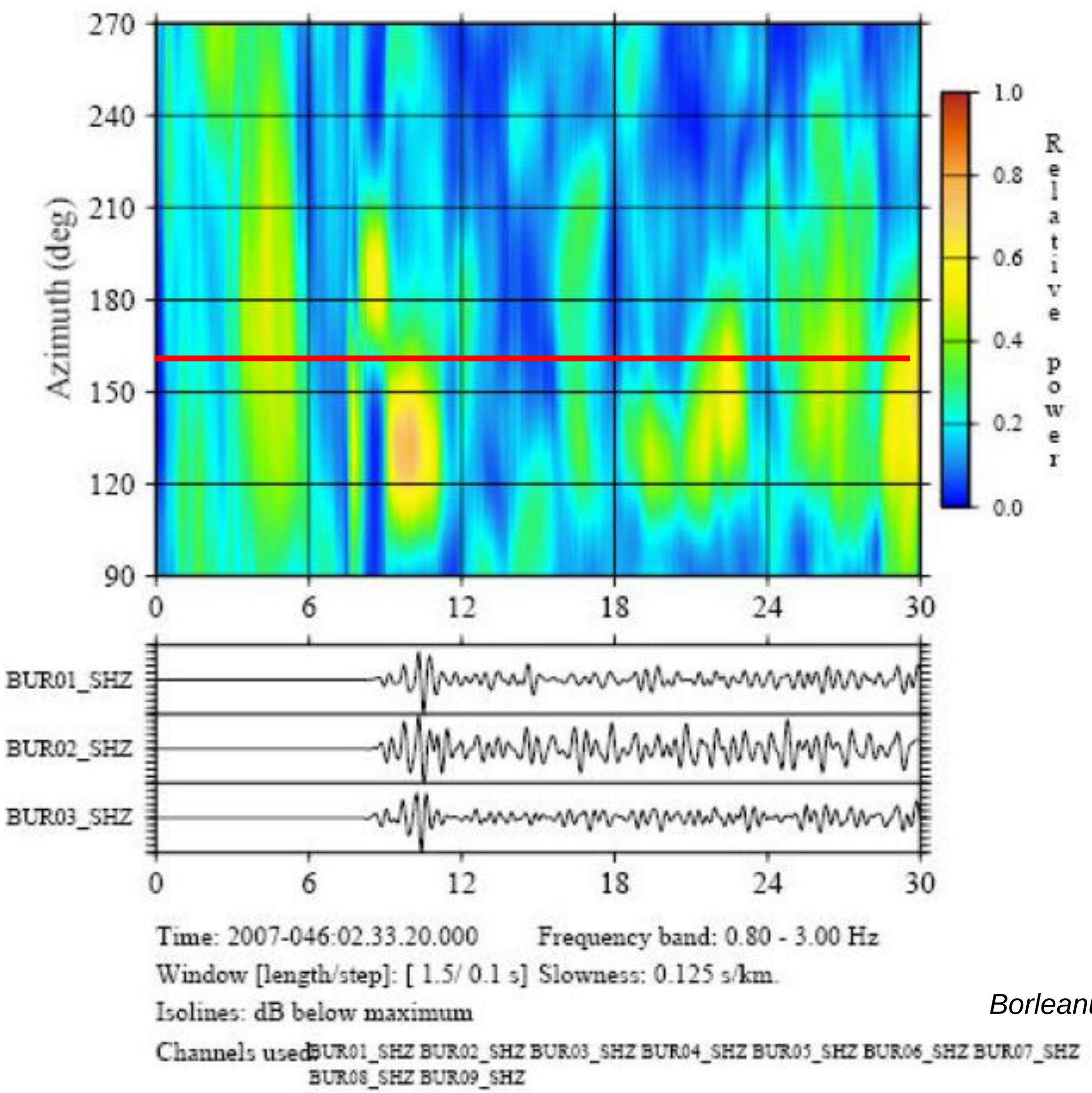

15/02/2007:02:32, H=100km

Borleanu et al. (2013)

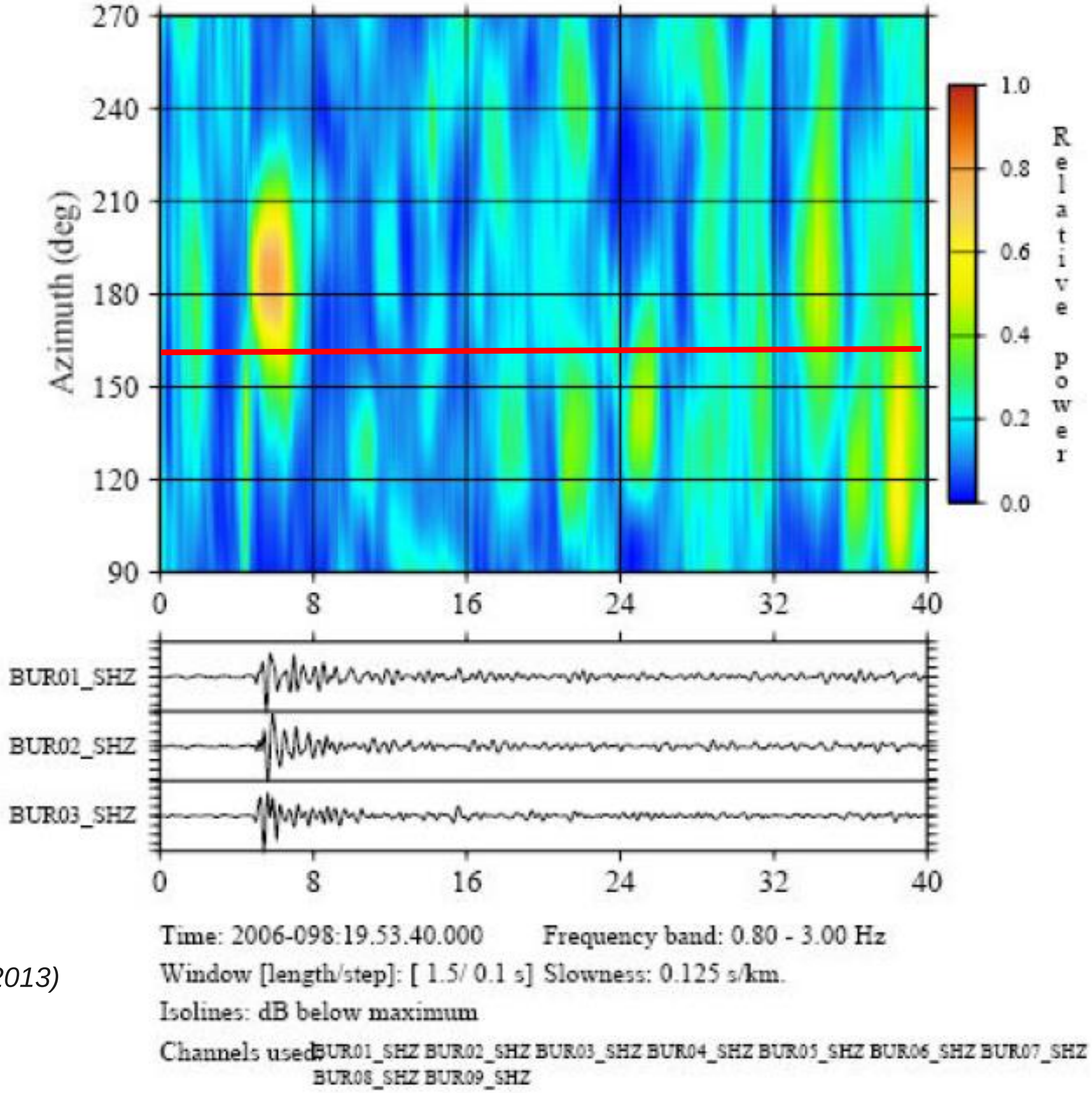

08/04/2006:19:53, H=150km

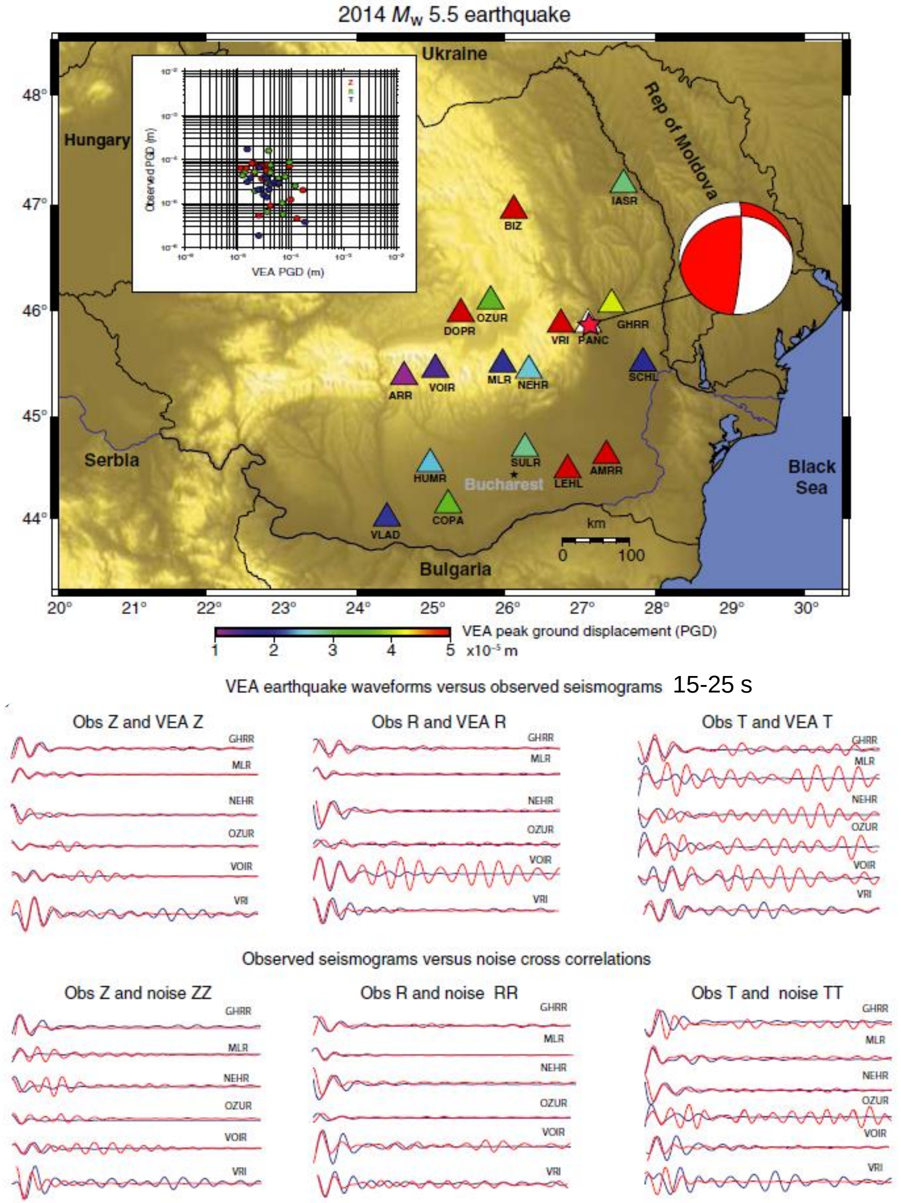

Petrescu et al. (2023)

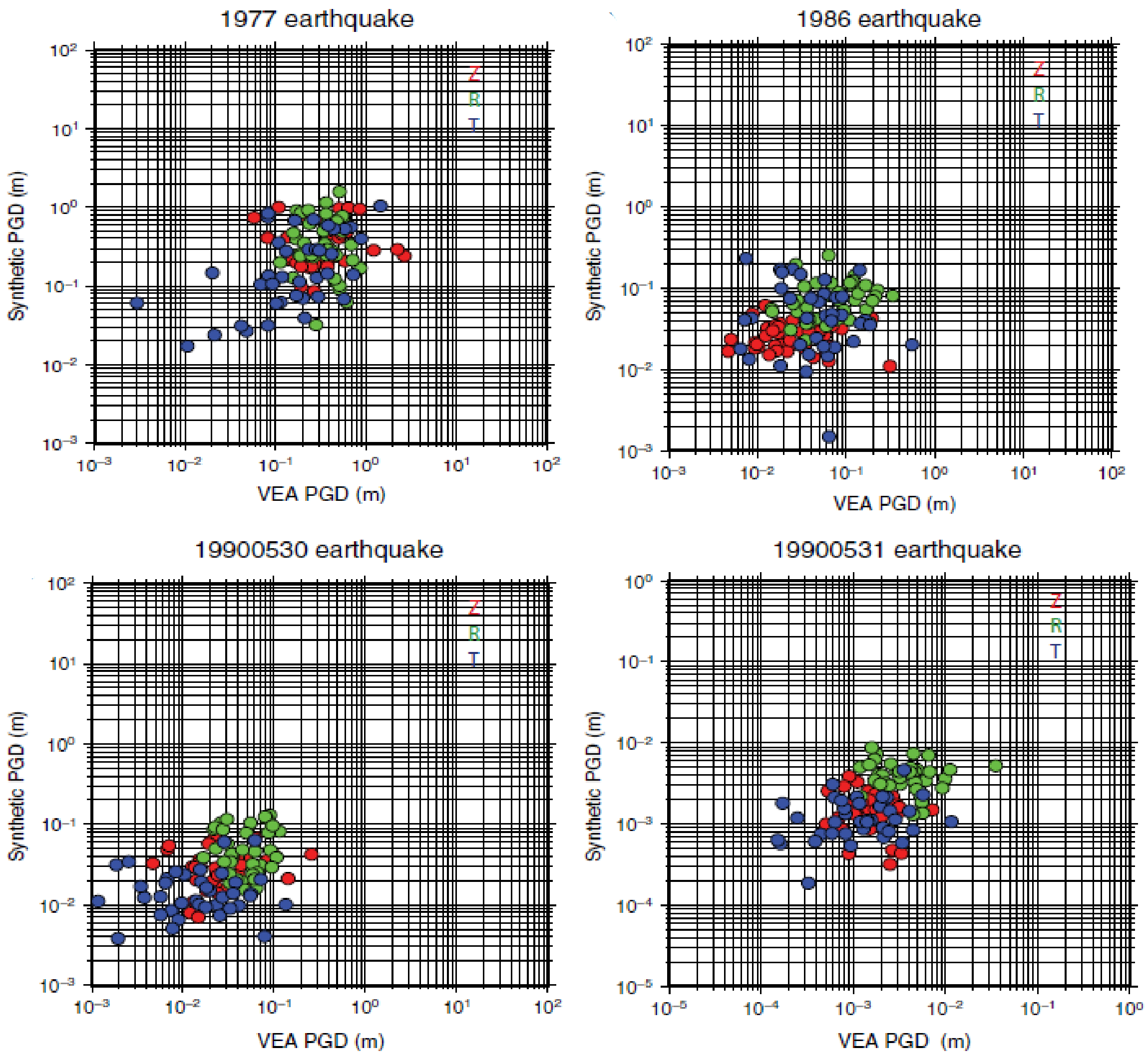

- Gaining a more comprehensive insight into the unique earthquake threat is an important research objective. Substantial progress in comprehending the challenges we encounter is achievable within the framework of AdriaArray;

- The Vrancea area functions as a natural laboratory, with each new study adding another piece to the puzzle. These collective research efforts aim to construct a holistic picture of the continuous processes that shape this complex region;

- The seismic energy release increases significantly with depth, which appears to be the primary source controlling the geodynamics of the entire system;

- The tomography results, independent of the data employed emphasize the presence of a high-velocity lithospheric body in the mantle, but do not provide enough information on its origin;

- The attenuation characteristics highlight significant perturbations beneath the Vrancea region. Examining the reasons behind these perturbances and enhancing the resolution of their spatial-temporal distributions will improve our capacity to model intricate processes, including retreat, break-off, and rotation. This, in turn, will contribute to a better understanding of recent events at the bend of the South-Eastern Carpathians arc and enhance our ability to predict seismic hazards and risks resulting from strong earthquakes in the Vrancea area.

BayesISOLA: full waveform MT inversion in Bayesian framework

RNDr. Jiří Vackář, Ph.D.

December 6, 2023
Czech-Romanian Workshop

1. Key features of BayesISOLA
   - Purpose and target of BayesISOLA
   - Bayesian formulation of the problem
   - Covariance matrix of the noise
2. User interface
3. Applications
   - Switzerland
   - Apparent Non-Double-Couple Components as Artifacts of Moment Tensor Inversion
   - A New Automated Procedure to Improve Moment Tensor Solution and Its Application for Light-Moderate Earthquake ($M \leq 5.5$) in the North Banda Arc Region

Purpose of BayesISOLA

BayesISOLA is a tool for fully automated MT inversion.

WAVEFORMS $\longrightarrow$ 

Target applications:

- large data sets of previously recorded events,
- various tests and sensitivity analysis, and
- component for other software.

Reference paper:
J. Vackář, J. Burjánek, F. Gallovič, J. Zahradník, and J. Clinton (2017). Bayesian ISOLA: New Tool for Automated Centroid Moment Tensor Inversion, *Geophys. J. Int.*, 210(2), 693—705.

Input data and method

input data

- (filtered) waveforms
- Green's functions (options described later)

method

- full waveform inversion in L-2 norm
- weighting by covariance matrix of noise / Green's functions

output

- full or deviatoric (iso = 0) moment tensor
- posterior probability density function

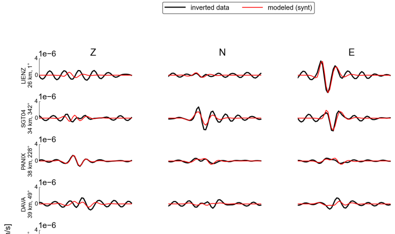

Key features of BayesISOLA

Key features of `BayesISOLA` code:

- Automated data retrieval (files / fdsnws)
- Green's functions using `Axitra` or IRIS `Syngine` web service
- Disturbance detection: `MouseTrap` code [Vackář et al., 2015]
- Automated frequency ranges
- Full-waveform inversion in space-time grid around hypocenter
- MT results accompanied by their uncertainties
- Extensive output: various figures are automatically plotted

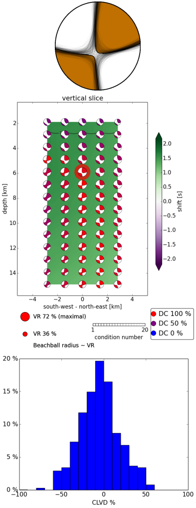

Technical solution and availability

- Programmed in Python, using `ObsPy`, `matplotlib` etc.
- object-oriented and well documented code
- parallelized
- open-source (GNU/GPL licence)
- code at `GitHub`:
  `https://github.com/vackar/BayesISOLA`
- documentation:
  `http://geo.mff.cuni.cz/~vackar/BayesISOLA/`

Bayesian formulation

Bayesian formulation is used to get full probability distribution of the result.

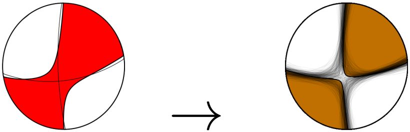

Bayesian formulation of mixed linear – non-linear problem:

- Grid search over space and time (4 variables; non-linear problem)
- Least-square solution of MT components in each grid point (6 variables; linear problem)
- Faster and/or more accurate than Monte Carlo and gradient methods

Least-square solution in a grid point

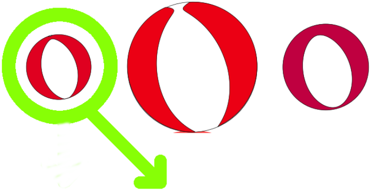

Solution in a grid point i (x_i, y_i, z_i, t_i)
Inverse problem with no a priori information [Tarantola, 2005]:

$$\widetilde{\mathbf{m}} = \left(\mathbf{G}^T \mathbf{C}_D^{-1} \mathbf{G}\right)^{-1} \mathbf{G}^T \mathbf{C}_D^{-1} \mathbf{d}_{obs}$$

- model parameters (result)
- data vector
- forward problem matrix (Green's functions)
- data covariance matrix (will be described later)

Noise covariance matrix

The data covariance matrix is calculated from auto-/cross-covariance of before-event noise.
The data covariance matrix works as automated frequency filter and station weighting to emphasize the high-SNR data.

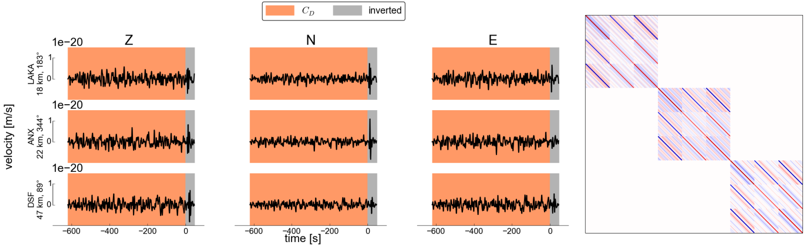

Covariance matrix of Green's functions uncertainty

Geophysical Journal International

Geophys. J. Int. (2016) **207,** 1012–1029
doi: 10.1093/gji/ggw320
Advance Access publication 2016 August 25
GJI Seismology

Fast and cheap approximation of Green function uncertainty for waveform-based earthquake source inversions

M. Hallo and F. Gallovič

Faculty of Mathematics and Physics, Charles University, Prague, Czech Republic. E-mail: hallo@karel.troja.mff.cuni.cz

command line / script usage

BayesISOLA code example. To use it in your own project you need just lines setting necessary inputs and parameters.

```
import BayesISOLA
inputs = BayesISOLA.load_data(outdir = 'output/example_2_fdsnws')
inputs.read_event_info('input/example_2_fdsnws/event.isl')
inputs.set_source_time_function('step')
inputs.read_network_coordinates('input/example_2_fdsnws/network.stn')
inputs.read_crust('input/example_2_fdsnws/crustal.dat')
inputs.load_streams_fdsnws(['http://eida.ethz.ch/fdsnws/',], t_before=360, t_after=100)
grid = BayesISOLA.grid(
        inputs,
        location_unc = 1000, depth_unc = 3000, # m
        time_unc = 1, # s
        step_x = 200, step_z = 200, # m
        max_points = 500,)
data = BayesISOLA.process_data(
        inputs, grid,
        threads = 8,
        use_precalculated_Green = 'auto',
        fmax = 0.15, fmin = 0.02)
cova = BayesISOLA.covariance_matrix(data)
cova.covariance_matrix_noise(crosscovariance=True)
solution = BayesISOLA.resolve_MT(data, cova, deviatoric=False)
plot = BayesISOLA.plot(solution)
```

BayesISOLA as a module of Integrated Seismic Program

Roberto Cabieces Diaz (Spanish Navy Observatory) included `BayesISOLA` in `ISP`, a GUI for seismology.

`https://projectisp.github.io/ISP_tutorial.github.io/`

Reference paper:

R. Cabieces, A. Olivar-Castaño, T. C. Junqueira, J. Relinque, L. Fernandez-Prieto, J. Vackář, B. Rösler, J. Barco, A. Pazos, and L. García-Martínez (2022). Integrated Seismic Program (ISP): A New Python GUI-Based Software for Earthquake Seismology and Seismic Signal Processing. *Seis. Res. Lett.* 93 (3), 1895–1908.

Real test: 16 years of Swiss data

Analyzed 16 years of $M > 3$ events from Swiss Digital Seismic Network (113 events)

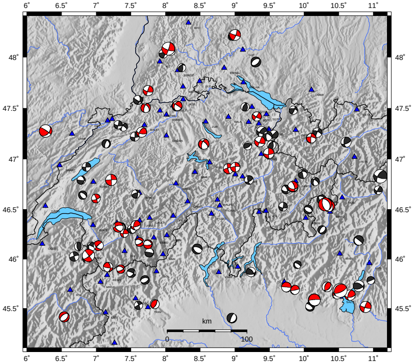

- Quality comparable to manual processing
- Capable to invert slightly weaker events

Apparent Non-Double-Couple Components as Artifacts of Moment Tensor Inversion

Boris Rösler[1*], Seth Stein[1,2], Adam Ringler[3], Jiří Vackár[4]

[1]Department of Earth and Planetary Sciences, Northwestern University, Evanston IL 60208 USA

[2]Institute for Policy Research, Northwestern University, Evanston IL 60208 USA

[3]United States Geological Survey, Albuquerque, NM, USA

[4]The Czech Academy of Sciences, Prague, Czech Republic.

*Corresponding author: boris@earth.northwestern.edu

Submitted to SRL

Main question: Are non-DC components in GCMT catalog realistic or just artefact of the inversion?

Mid-Atlantic ridge earthquake

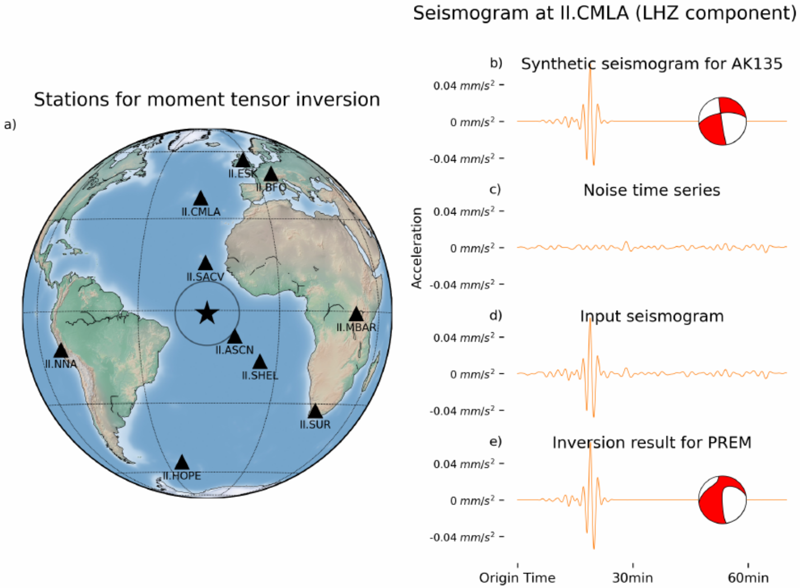

A New Automated Procedure to Improve Moment Tensor Solution and Its Application for Light-Moderate Earthquake (M ≤ 5.5) in the North Banda Arc Region

Yehezkiel Halauwet[1,2], Afnimar[3]*, Wahyu Triyoso[3], Jiří Vackář[4], Gatut Daniarsyad[1,5], Daryono[5], Herlina A. A. M. Narwadan[2], M. Luqman Hakim[5]

[1]Faculty of Earth Sciences and Technology, Bandung Institute of Technology (ITB), Ganesha 10 Street, Bandung, West Java 40132, Indonesia

[2]Agency for Meteorology, Climatology, and Geophysics (BMKG), Ambon 97122, Indonesia

[3]Seismology & Geodynamic Laboratory, Faculty of Mining and Petroleum Engineering, Bandung Institute of Technology (ITB), Ganesha 10 Street, Bandung, West Java 40132, Indonesia

[4]Institute of Rock Structure and Mechanics, Czech Academy of Sciences, Prague, Czechia

[5]Agency for Meteorology, Climatology, and Geophysics (BMKG), Jakarta 10610, Indonesia

**Corresponding author's email: afnimar@itb.ac.id*

Submitted to GJI

Main goal: Moment tensor solutions of a large dataset from tectonically complicated region in Indonesia

C_D usage	Covariance Matrix	MT Uncertainty
$C_d + C_t$	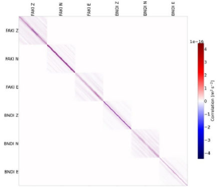	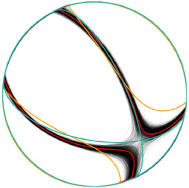
C_d	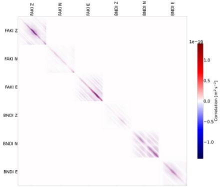	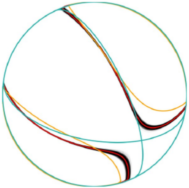
C_t	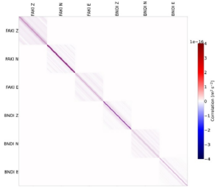	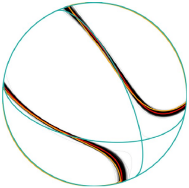

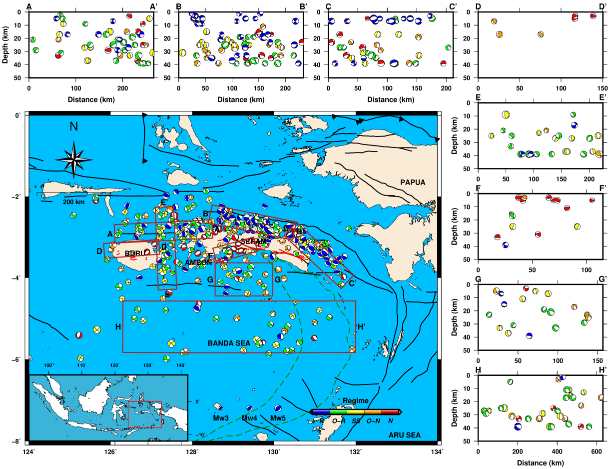

Figure 17. Distribution of quality A and B focal mechanism solutions and cross-sections on several large structures and focal mechanism clusters. Focal mechanism color indicates fault regime: reverse (blue), oblique-reverse (green), strike-slip (yellow), oblique-normal (orange), and normal (red).

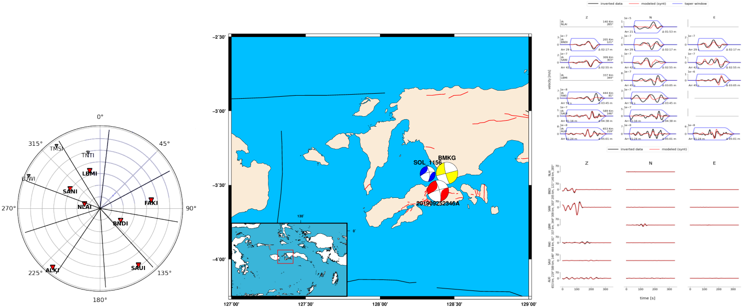

Figure 19. Details of the solution of the 11 October 2013 earthquake, Mw 4.7 (blue focal mechanism), and the focal mechanism of the Ambon-Kairatu earthquake (Mw 6.5, 26 September 2019) from GCMT (red) and BMKG (yellow). The polar plot depicts the azimuth coverage of the observation stations. Red and black waveforms represent the synthetic and observation data on the original waveform fittings (right-top) and standardized data (right-bottom).

Conclusions

- BayesISOLA is autemated tool for MT inversion
- It is quite unique in the following:
  - Bayesian formulation of inverse problem is used: we get the posterior probability density function
  - The uncertainty of data is quantified by a covariance matrix
  - Covariance matrix from before-event noise or Green's function covariance matrix can be used
  - Grid-search is combined with least-square solution
- It can be used from ISP GUI or Python script

http://geo.mff.cuni.cz/~vackar/BayesISOLA/

Earthquake complexity studied with multiple point-source ISOLA – a review

Jiří Zahradník

Charles University, Prague, Czech Republic

Long-lasting cooperation

The presentation is based on articles of the last 6 years published with co-authors from Greece, Turkey, France, China, and the Czech Republic.

Part 1:
Moment tensors in theory and practice

An example of a non-DC representing

real (=true, genuine) departure from shear faulting.

Seismic records (ground motion) and description of fault-process with a point-source moment tensor, MT

Ground motion | Response of the Earth | Fault(source) MT

$$u_i = G_{ip,q} * \left(\int_{\Sigma} m_{pq} d\Sigma \right) = G_{ip,q} * M_{pq}$$

MTs can be dominated by double-couple forces, i.e., DC component (=shear faulting)

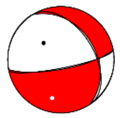

<u>or</u>

MTs display some (real or apparent) departures from shear faulting characterized by non-DC components (CLVD and ISO)

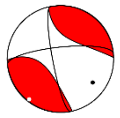

Moment-tensor uncertainty
(for a fixed time and position of centroid)

$$d = Gm$$

$$\tilde{m} = (G^T C_d^{-1} G)^{-1} G^T C_d^{-1} d$$

$$C_m = (G^T C_d^{-1} G)^{-1}$$

$$PDF(m) = \frac{1}{c} \exp\left(-\frac{1}{2} (d - G\tilde{m})^T C_d^{-1} (d - G\tilde{m}) \right)$$

d = data, m= MT parameters
G = Green's function
Cd y Cm = covariance matrices
PDF = probability density function
(6-dimensional Gaussian for full MT)

Knowing Cd, we can estimate Cm.
Knowing Cm, we can draw samples from the PDF, i.e. group of plausible solutions near the best-fitting solution.
(=analogy of 'clouds' in NonLinLoc)

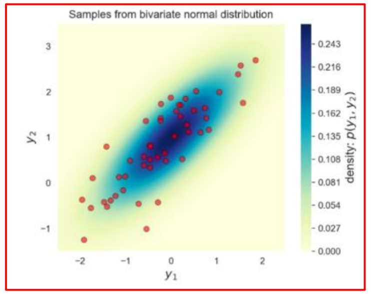

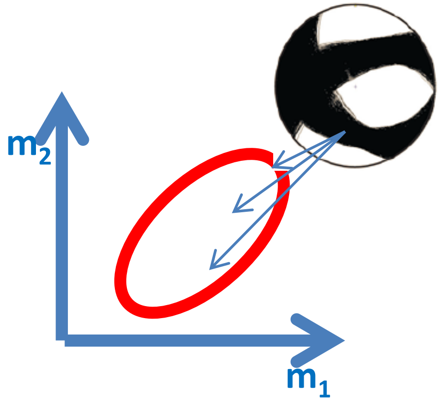

Knowing the 'cloud', we construct histograms …

Korea nuclear test 2017, mainshock and aftershock (8 minutes later): RAW DATA with "mirror symmetry"

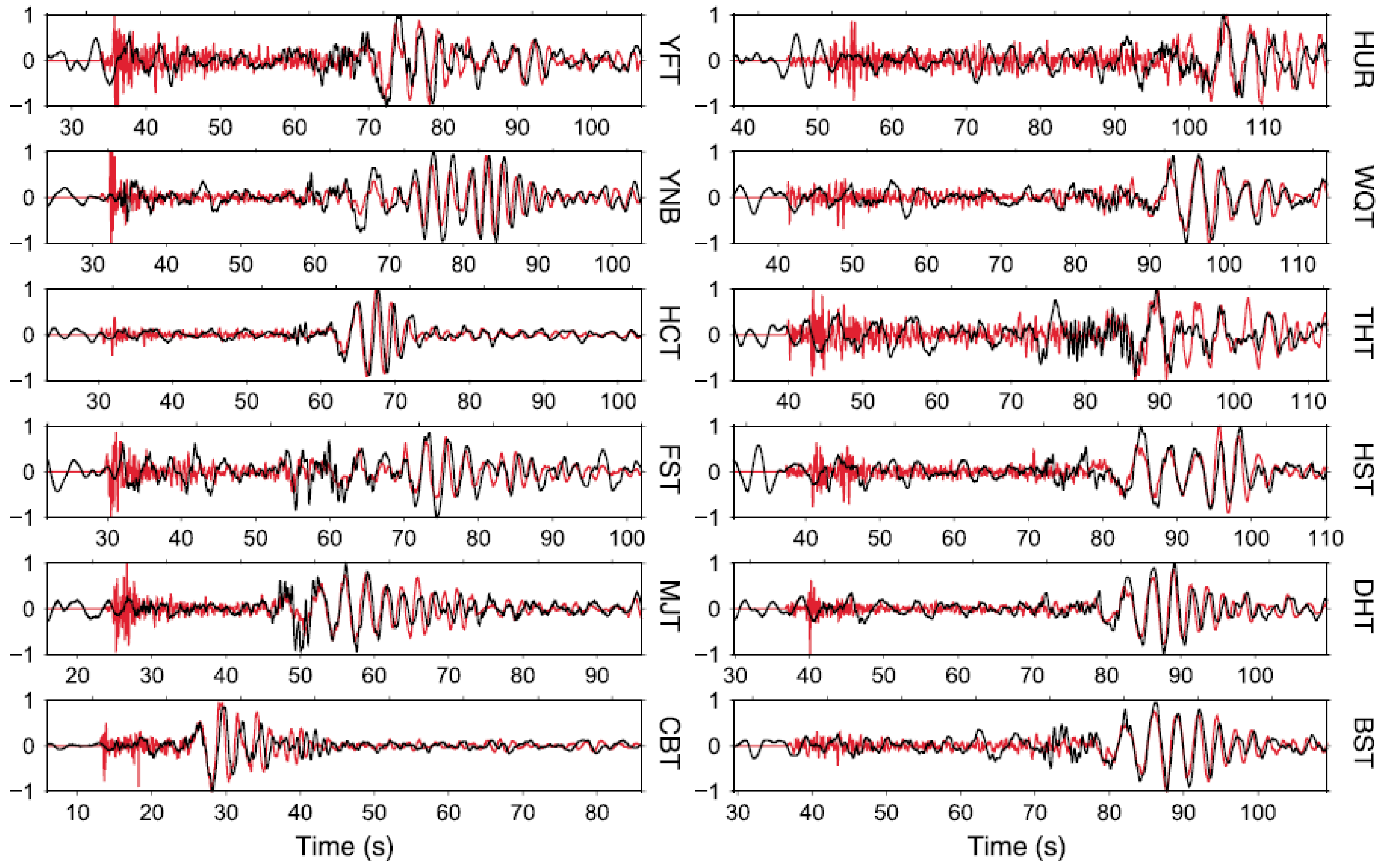

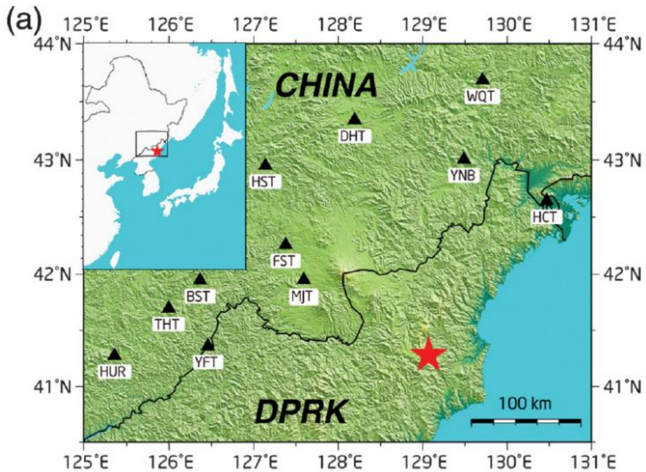

Mainshock (red) and

aftershock (black),
NORMALIZED
to the same amplitude
and plotted
with OPPOSITE SIGN

Interpretation: mainshock = detonation, aftershock = collapse of cavity

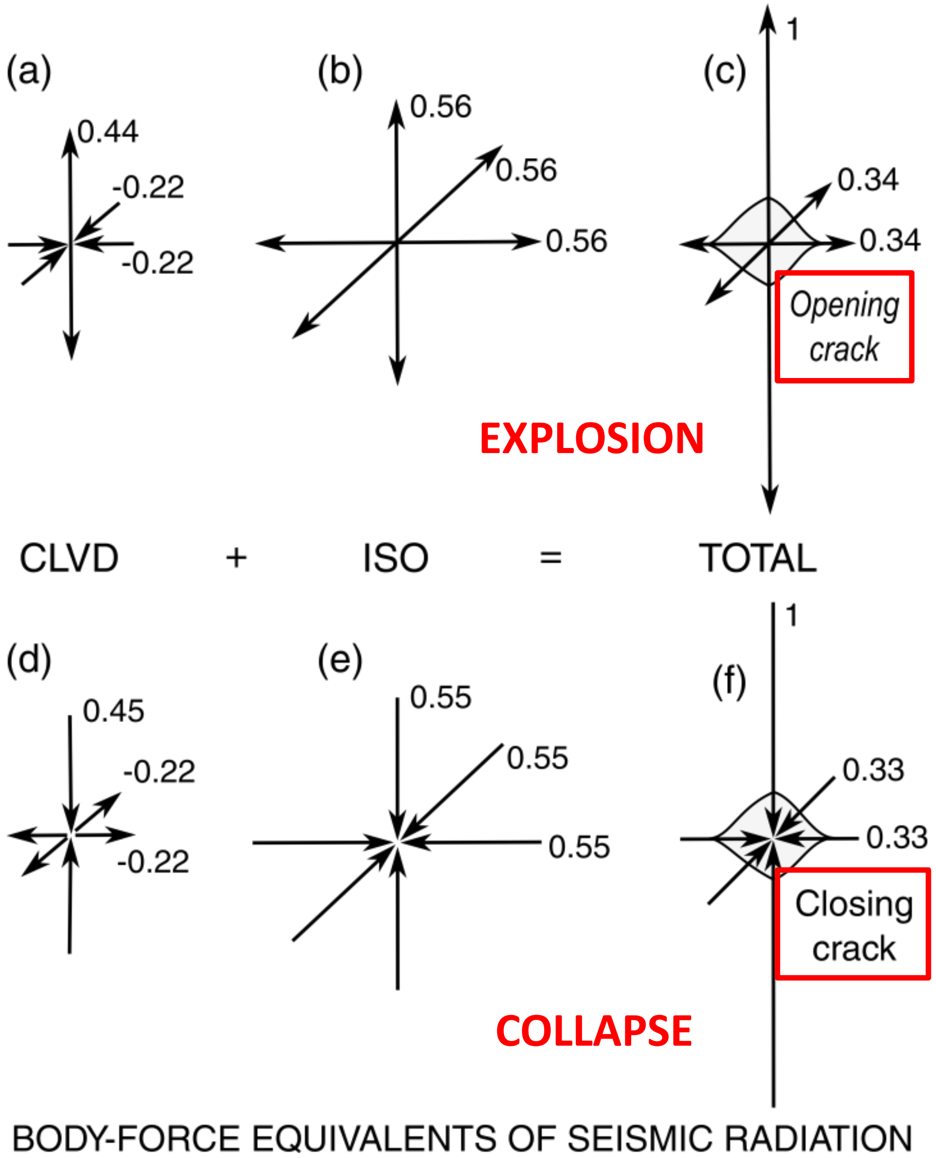

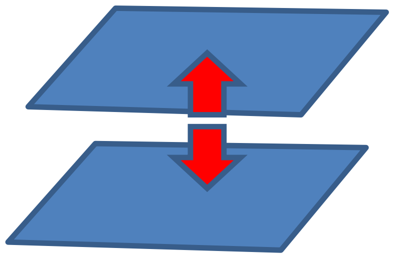

Model explains the mirror symmetry of seismograms for the two stages

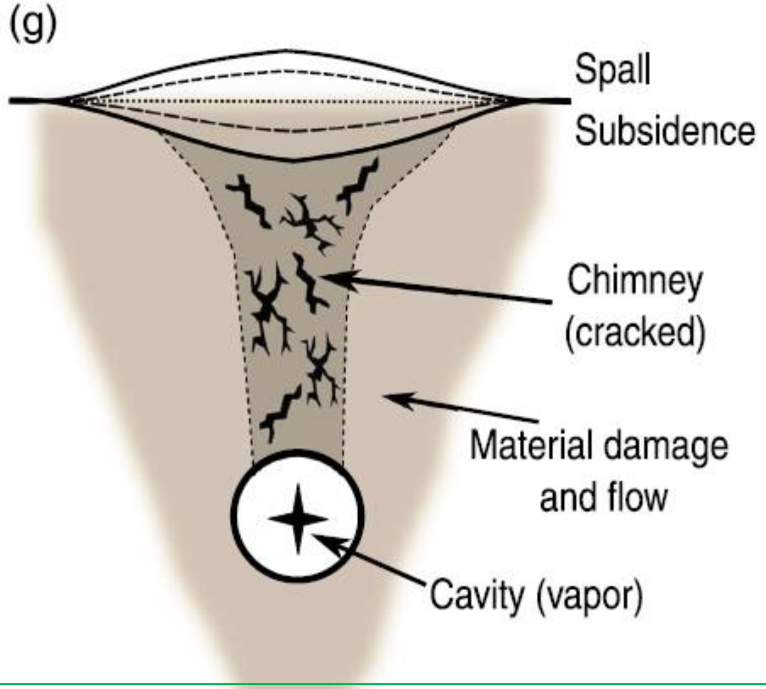

Liu J, Li L., Zahradník J, Sokos E, Liu C., Tian X. (2018): North Korea's 2017 test and its nontectonic aftershock. ***Geophys Res Lett*** **45**.

Source-type plots: Korea nuclear test 2017

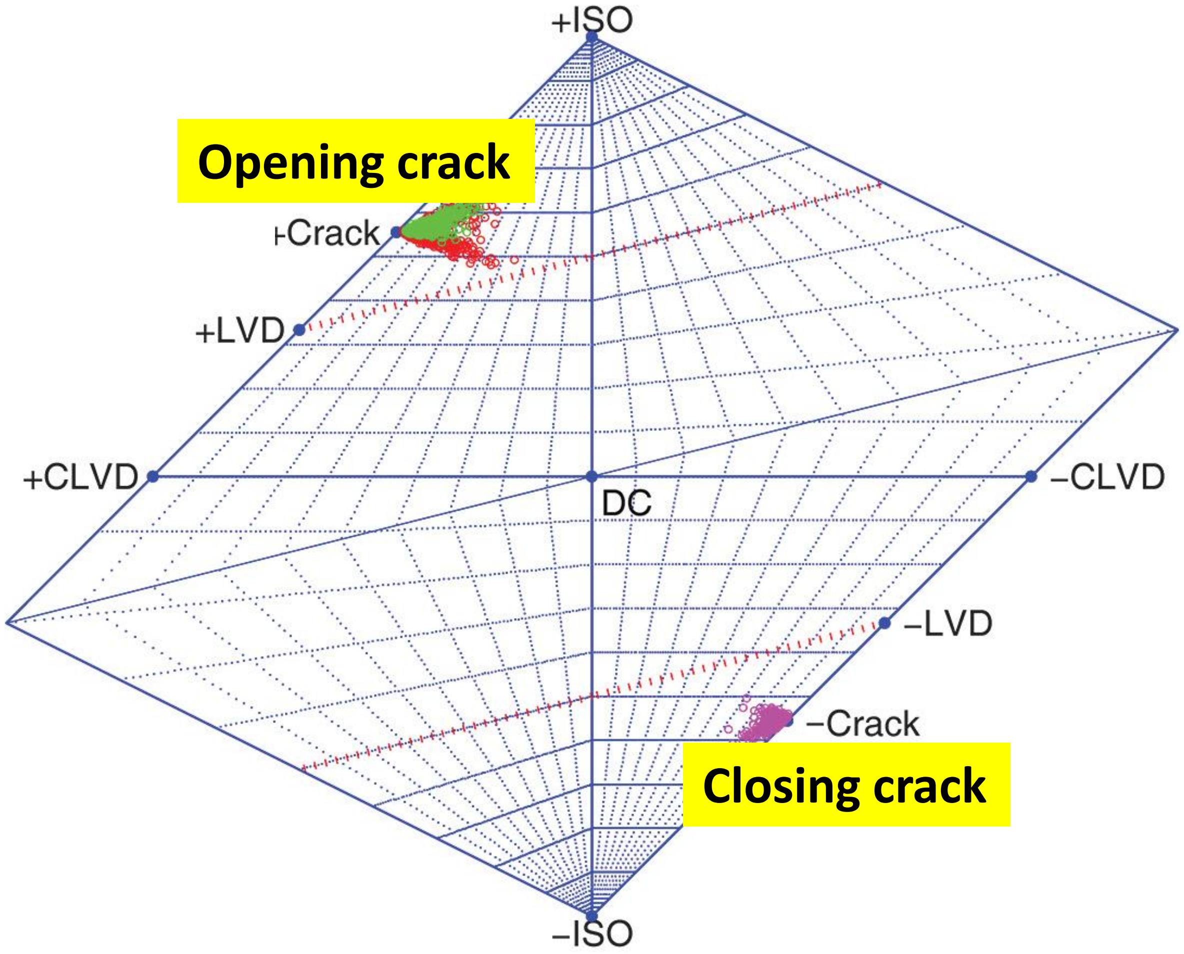

Beachball

All P-polarities
with these MT's
are <u>compressions</u>
<u>(not only pure explosion)</u>

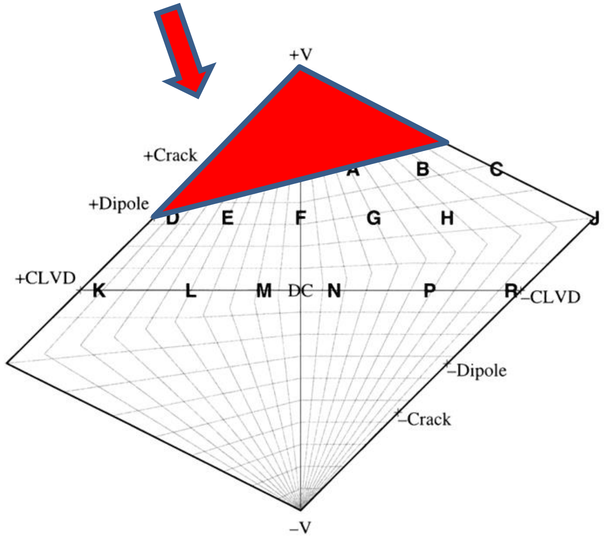

Hudson et al. (1989), Julian et al. (1998)

Part 2:
Deviatoric earthquakes

Are they possible? What is their physical meaning?

Source-type plot: Deviatoric earthquakes (ISO ~0)

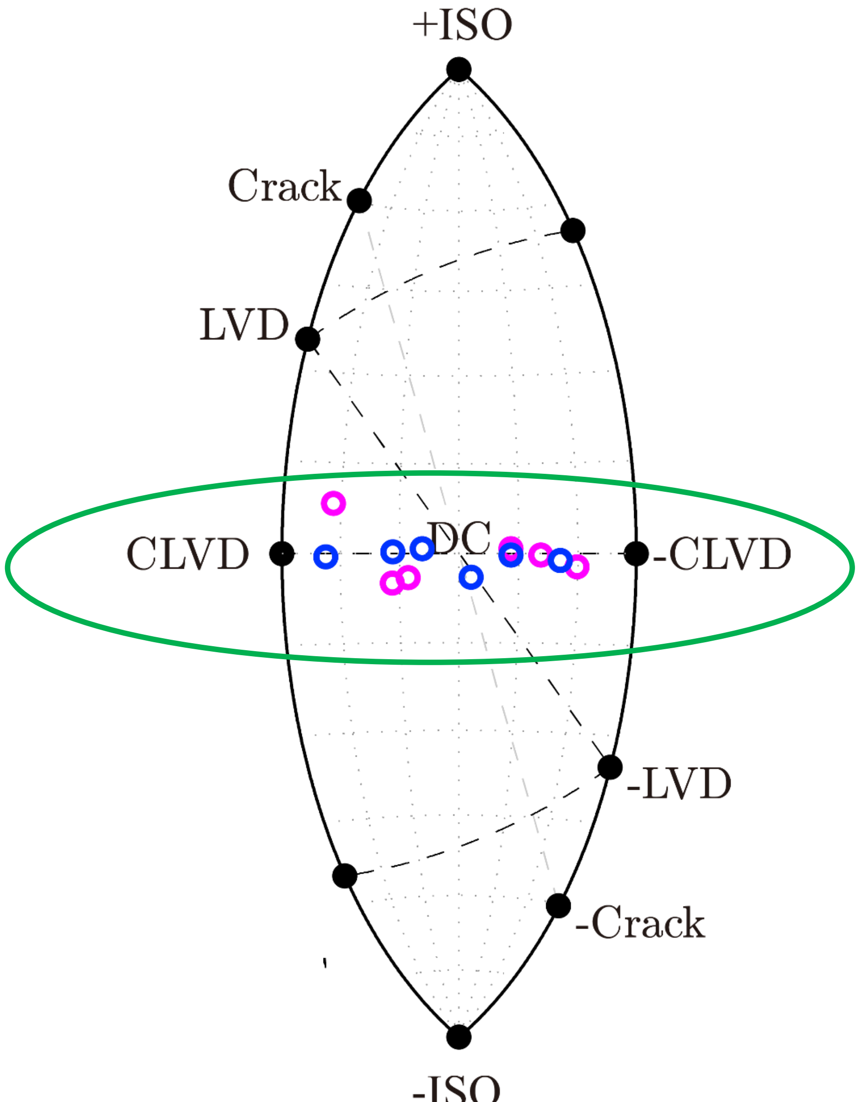

Alternative explanations:

0. Noise in results, all is in fact DC
1. Pure DC in anisotropic medium
2. Mixed-type DC's
3. Classical non-DC model with auxetic near-fault material
4. A new source model

e.g. X. Markenscoff, explains CLVD (+ DC) in isotropic media with standard Poisson's ratio

Part 3a: Multi-type faulting (example in Marmara Sea)

ISO~0 and large CLVD as an apparent (≠ true) departure from shear faulting.

The non-DC% can be explained as a 100% shear faulting on fault segments with different mechanisms.

The 2019 Mw 5.7 Silivri earthquake in the Marmara Sea seismic gap

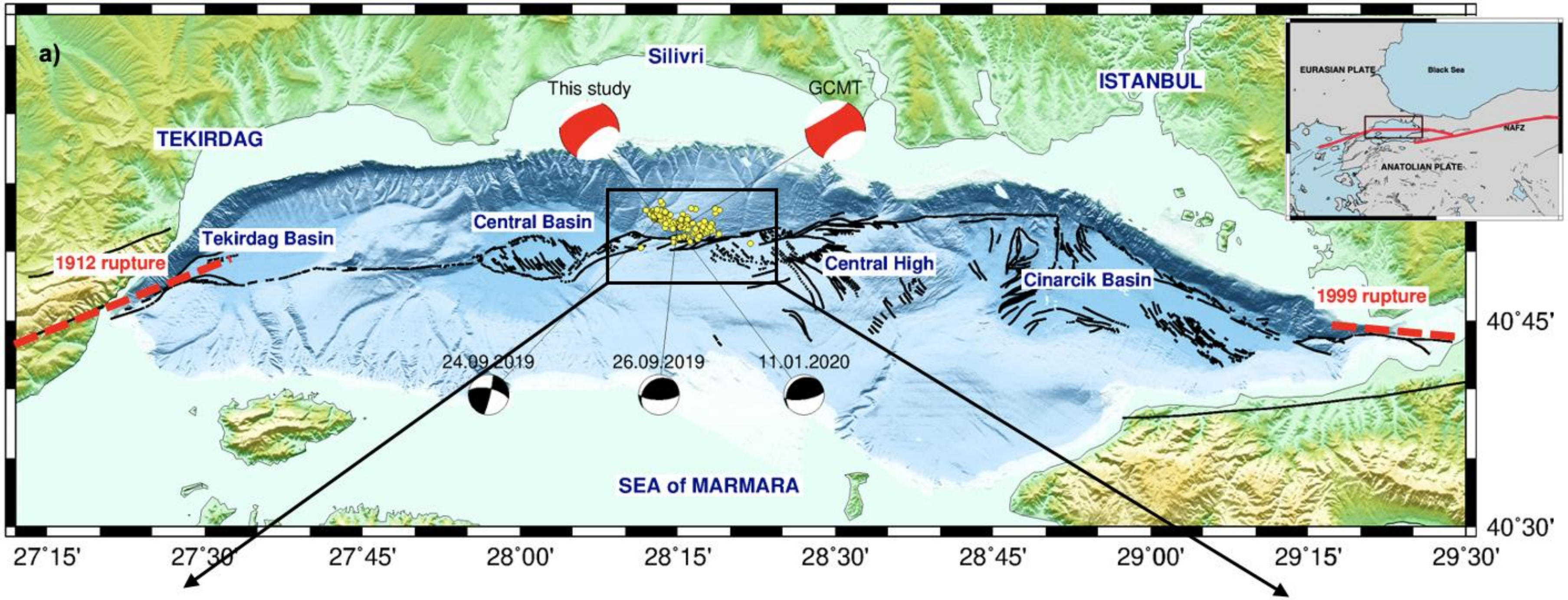

Turhan, F., D. Acarel, V. Plicka, M. Bohnhoff, R. Polat, J. Zahradník:
Coseismic faulting complexity of the 2019 Mw5.7 Silivri earthquake in the central Marmara seismic gap, offshore Istanbul
Seismological Research Letters, 2022
https://doi.org/10.1785/0220220111

The 2019 Mw 5.7 Silivri earthquake in the Marmara Sea seismic gap

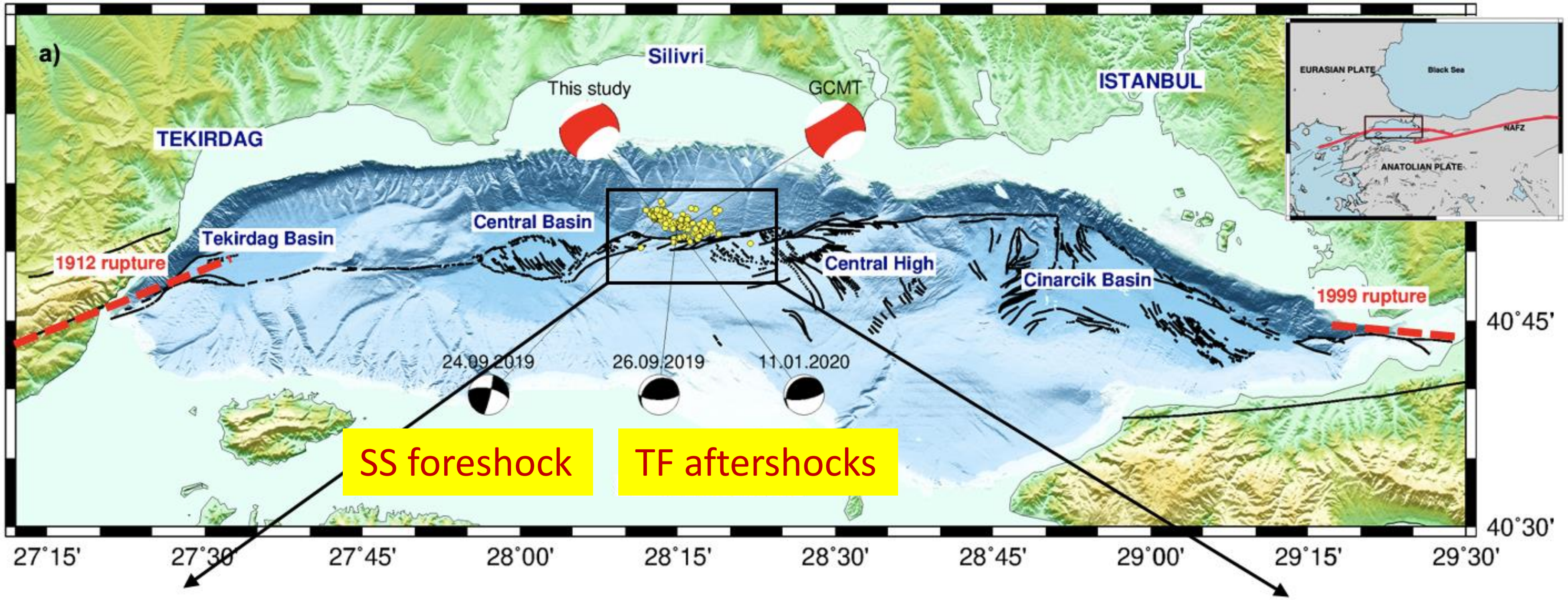

Turhan, F., D. Acarel, V. Plicka, M. Bohnhoff, R. Polat, J. Zahradník:
Coseismic faulting complexity of the 2019 Mw5.7 Silivri earthquake in the central Marmara seismic gap, offshore Istanbul
Seismological Research Letters, 2022
https://doi.org/10.1785/0220220111

Prerequisite: High-quality networks

Stations for complete waveform inversion

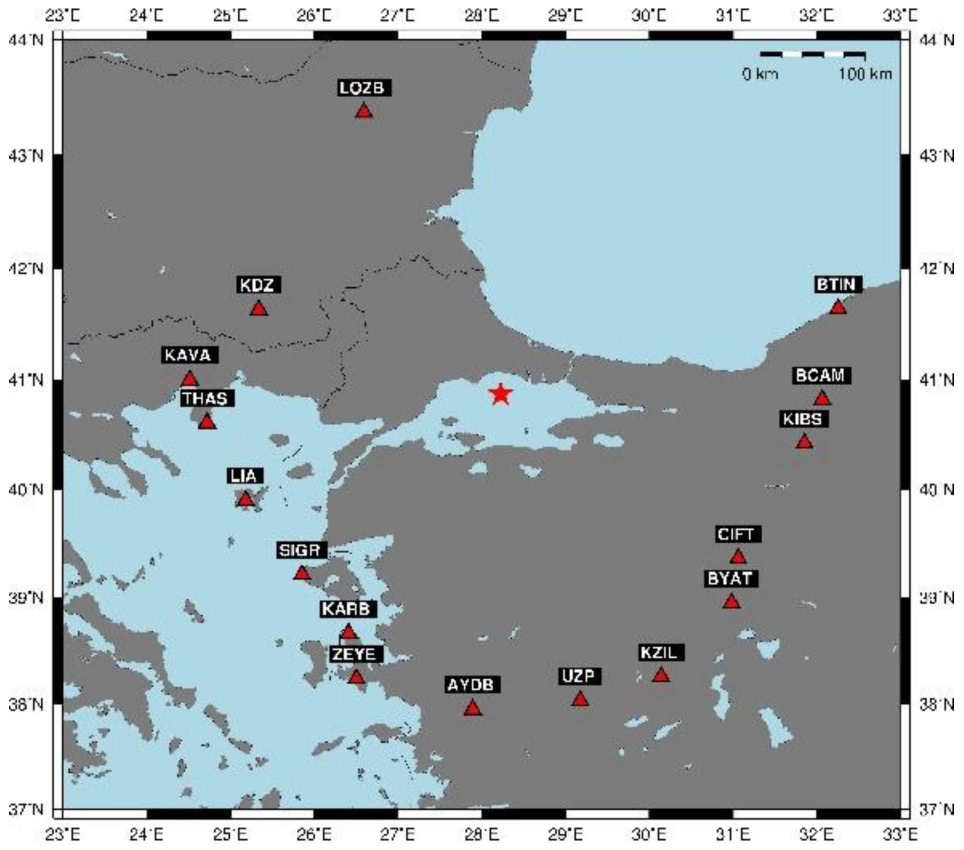

and for P-wave polarity reading.

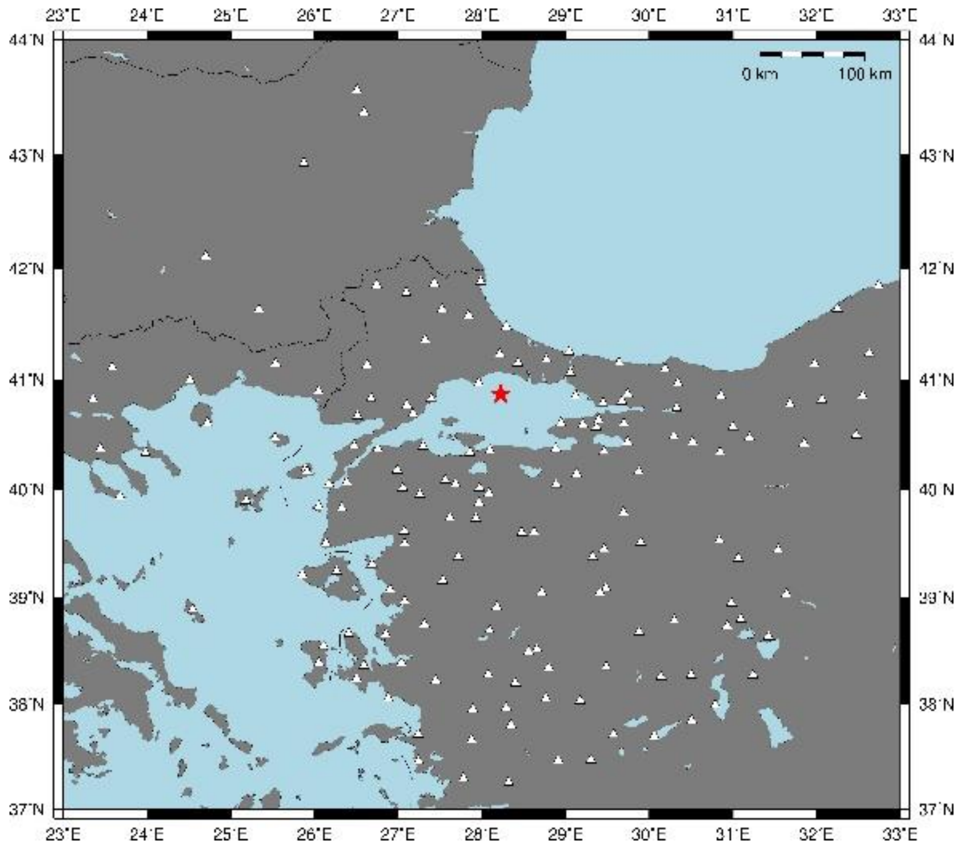

A nearby calibration event: Foreshock Mw 4.4 is an almost 100% DC event

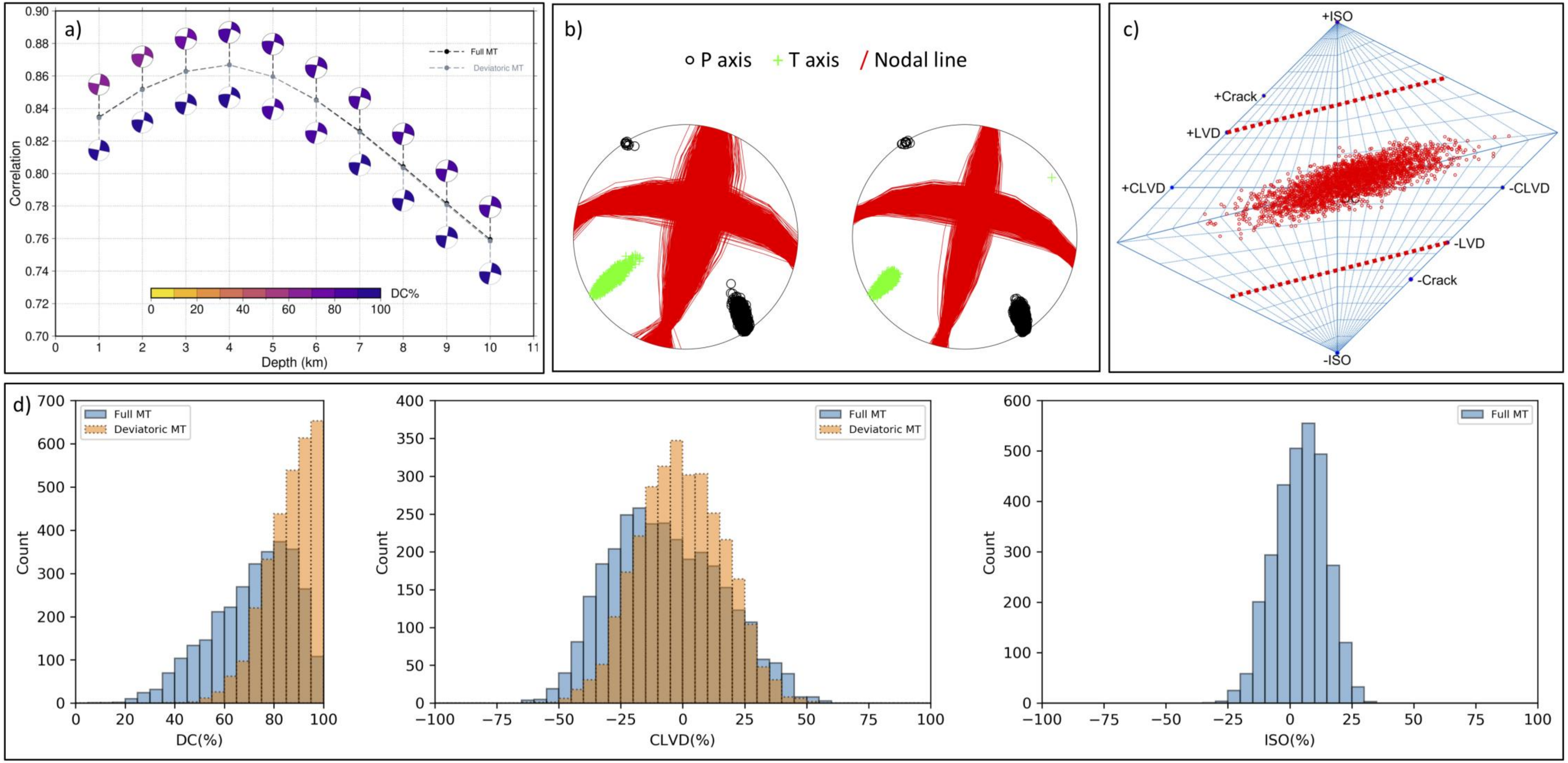

Mainshock has a large non-DC part (a large negative CLVD and ISO ≈ 0)

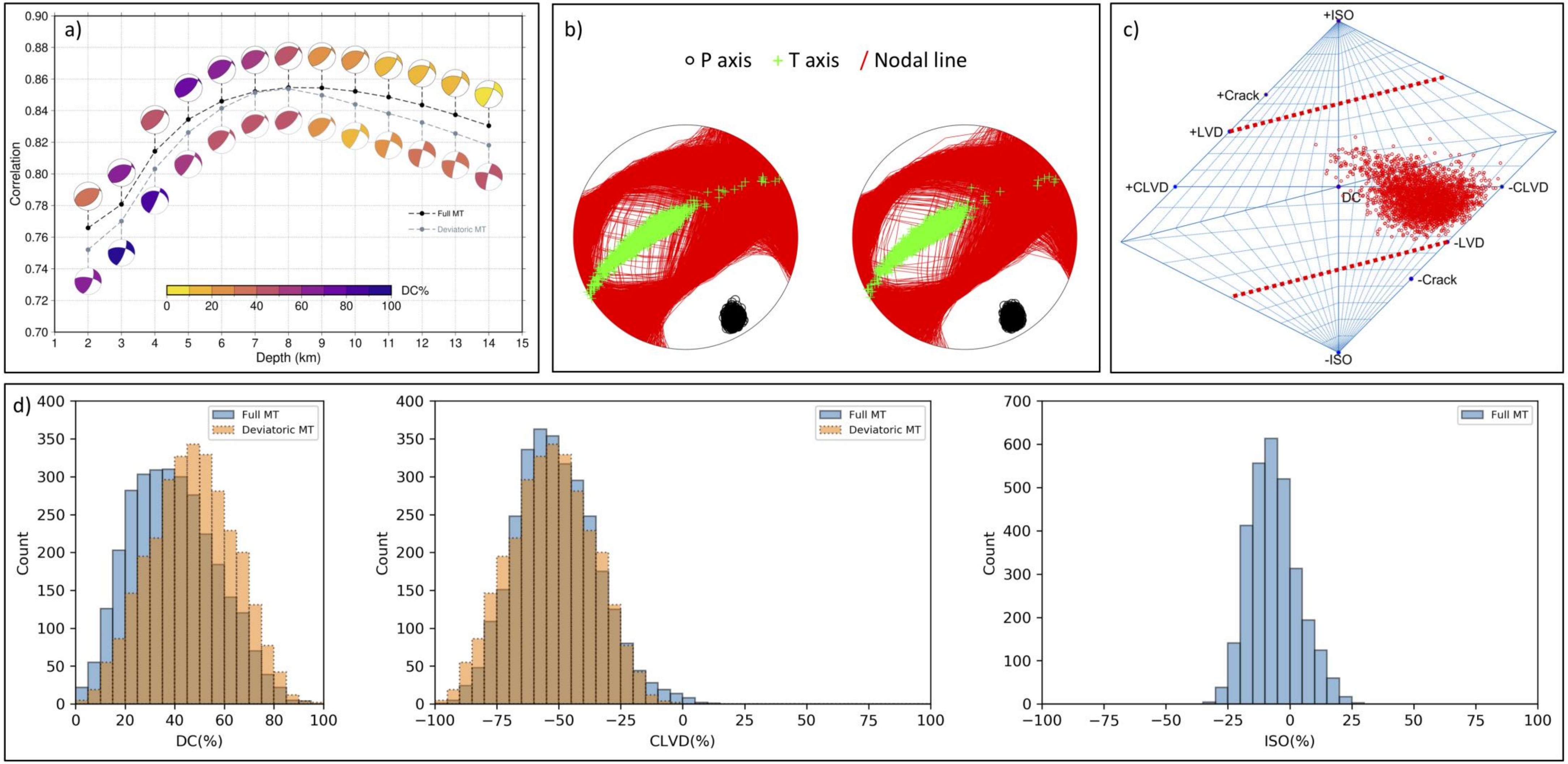

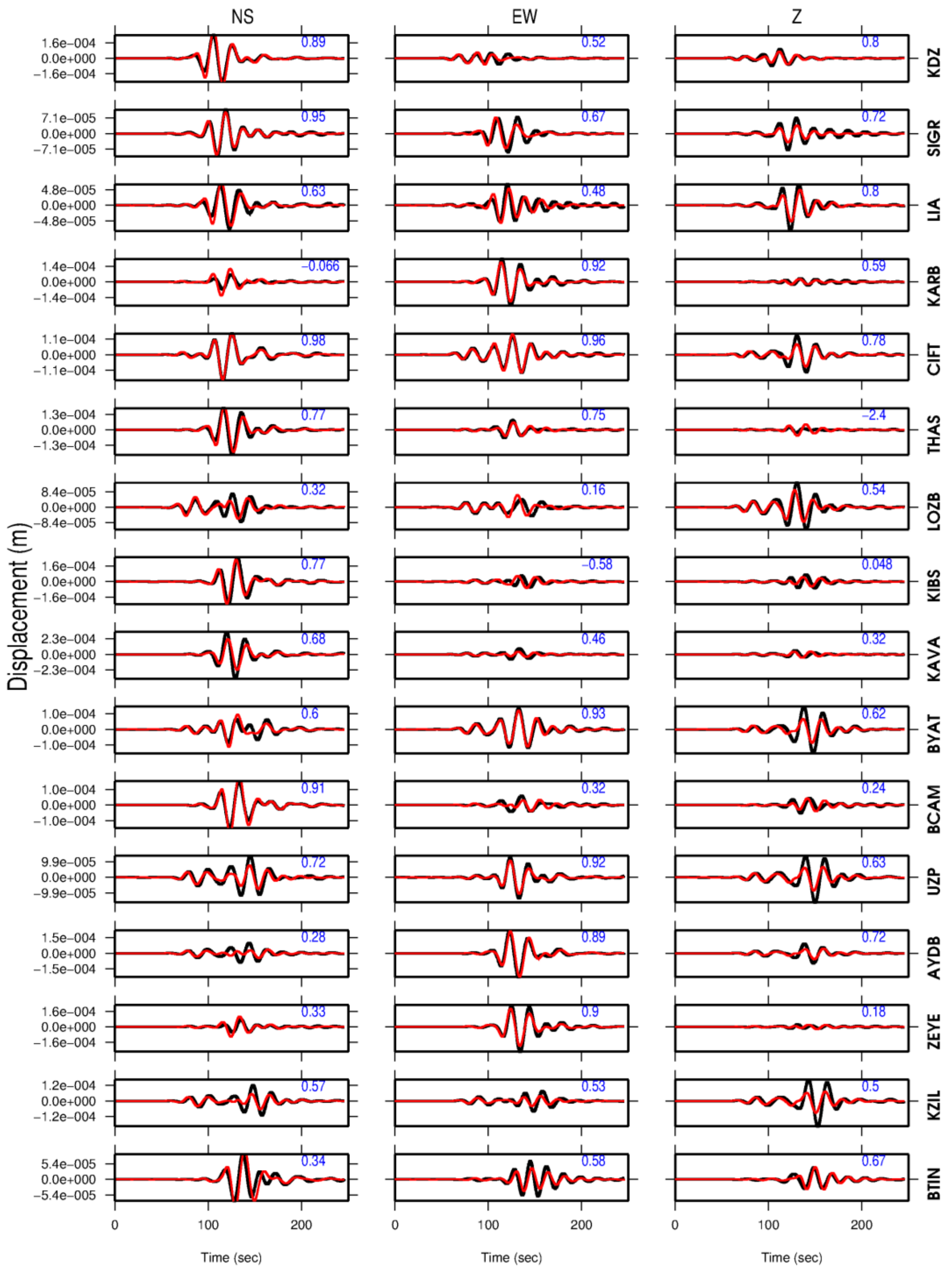

Mainshock waveform modeling

(here 0.03-0.06 Hz
with VR=0.73
without any artificial
time alignment)

Such a perfect fit
at 16 stations
is a necessary condition
for reliable non-DC.

First-motion polarities do NOT agree with full MT.

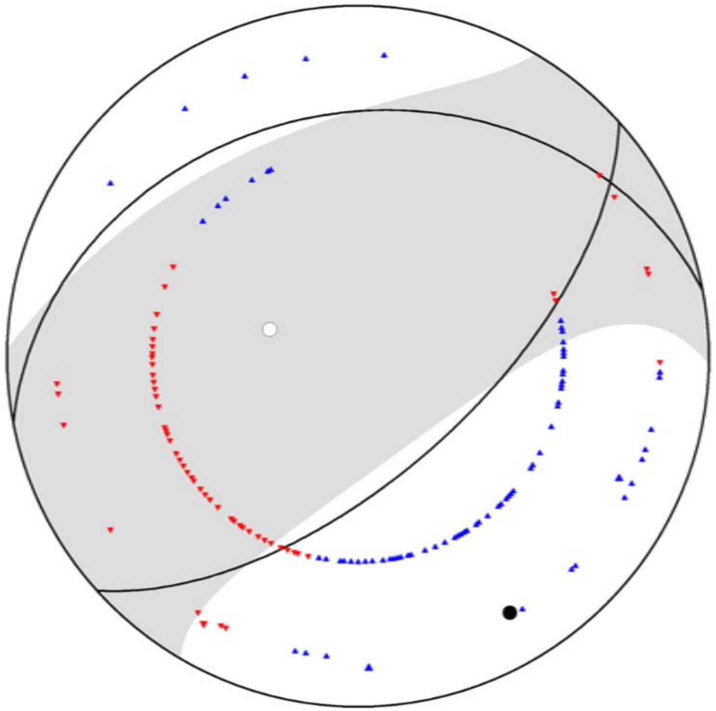

First-motion polarities do NOT agree with full MT.
However, they inform that the earthquake started as strike-slip (in agreement with the Main Marmara Fault)

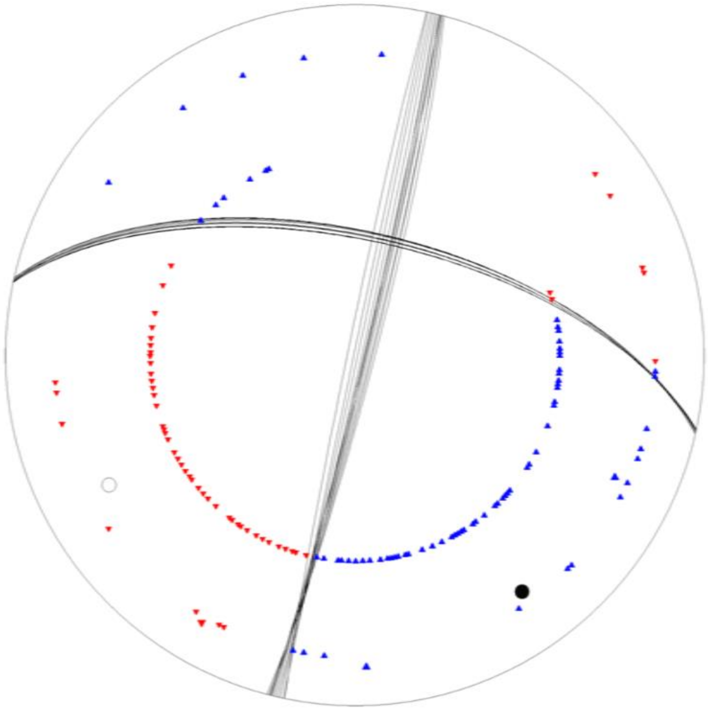

First-motion polarities do NOT agree with full MT. However, they inform that the earthquake started as strike-slip (in agreement with the Main Marmara Fault)

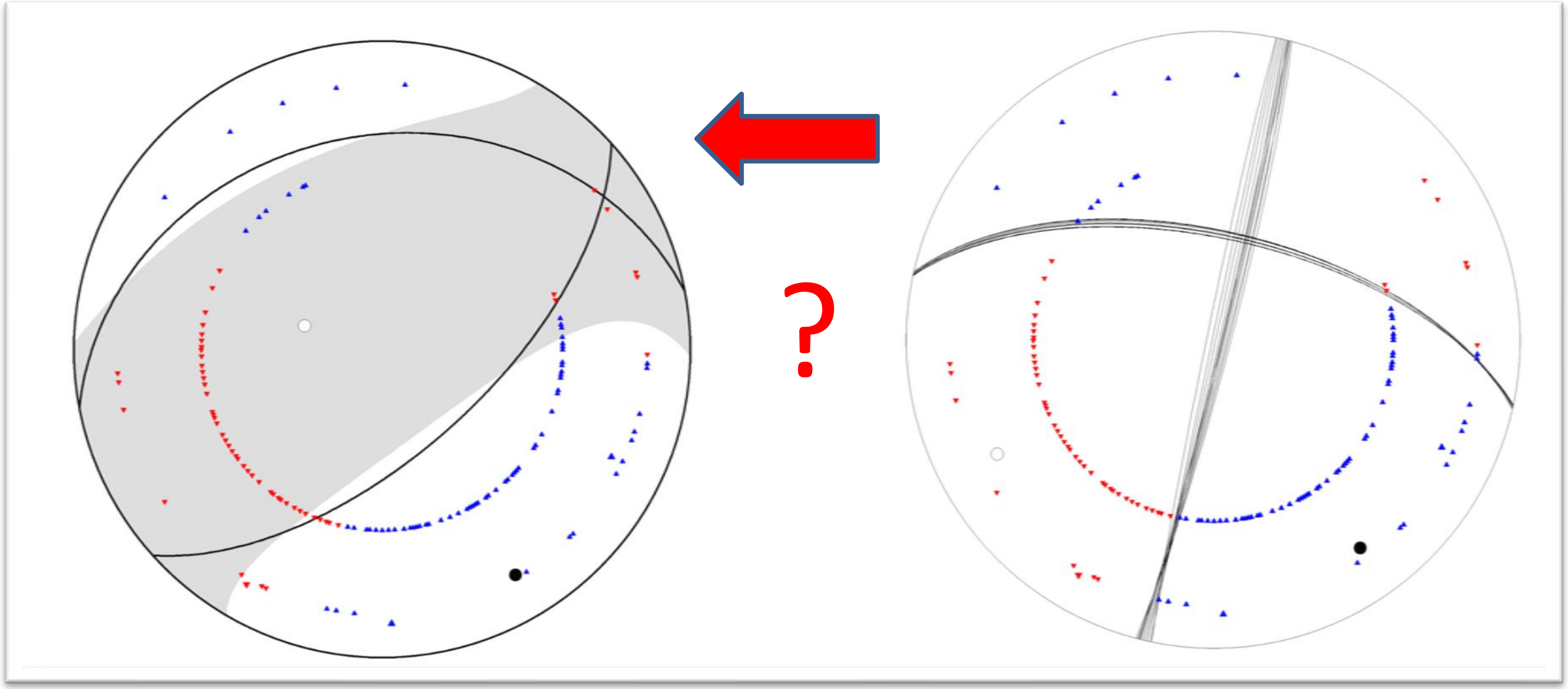

Then how the rupture continued after the initial SS to produce the full MT?

A "hint": Formal decomposition of MT into the "major" and "minor" DC

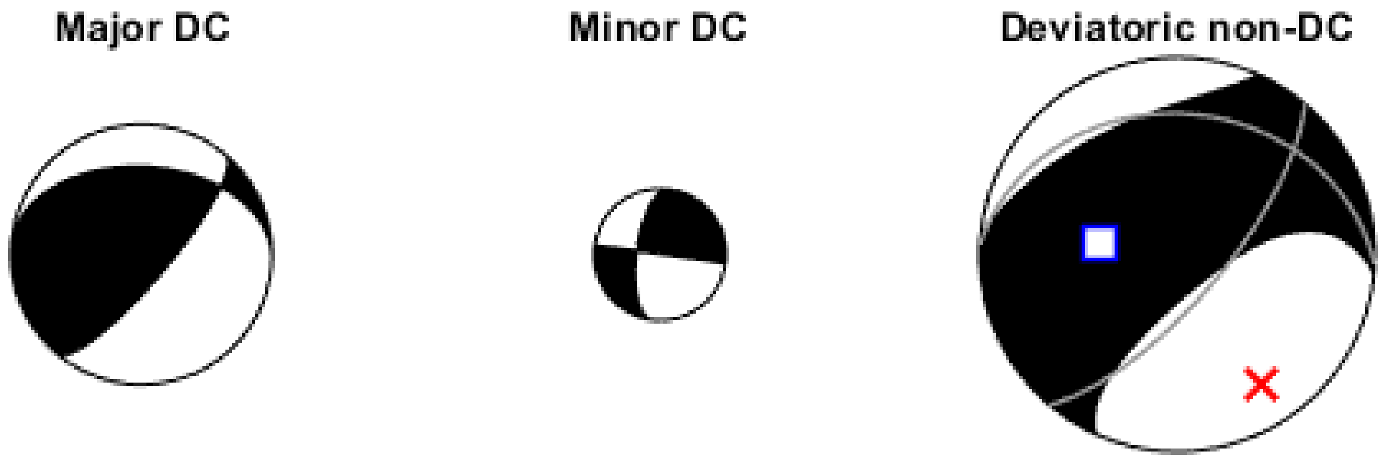

Thrust fault + Strike-slip fault = Apparent non-DC full MT

Multi-point approximation by “iterative deconvolution”

Observed ground motion o(t)

Invert o(t) for the 1st subevent s1(t), create residual data o(t)-s1(t)

Invert residual data for the 2nd subevent s2(t), … etc.

Final source model =
1st subevent + 2nd subevent + …

Final synthetic data s1(t) + s2(t) + …

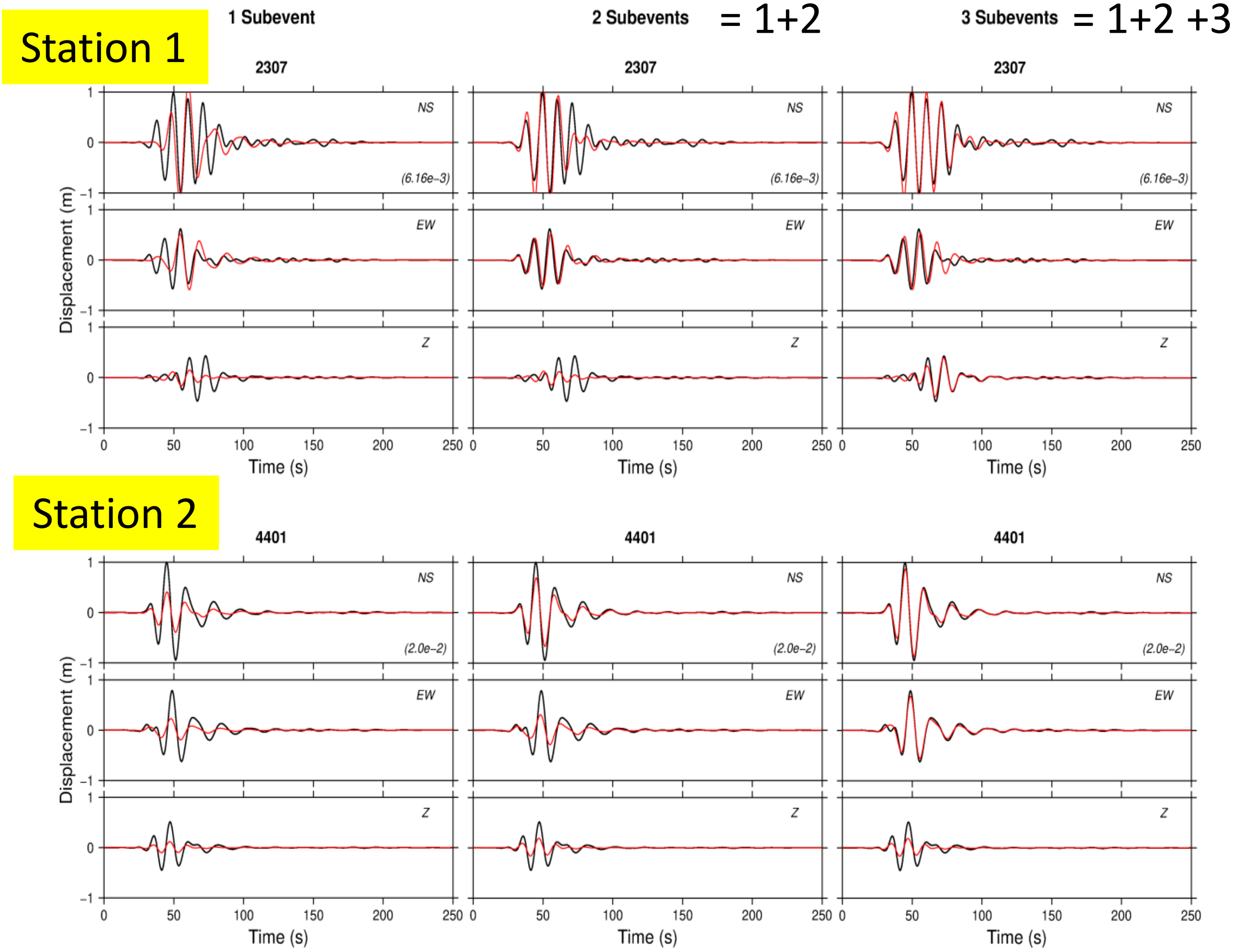

Instead of relying on formal decomposition we inverted waveforms for two DC subevents (applying a DC-constraint)

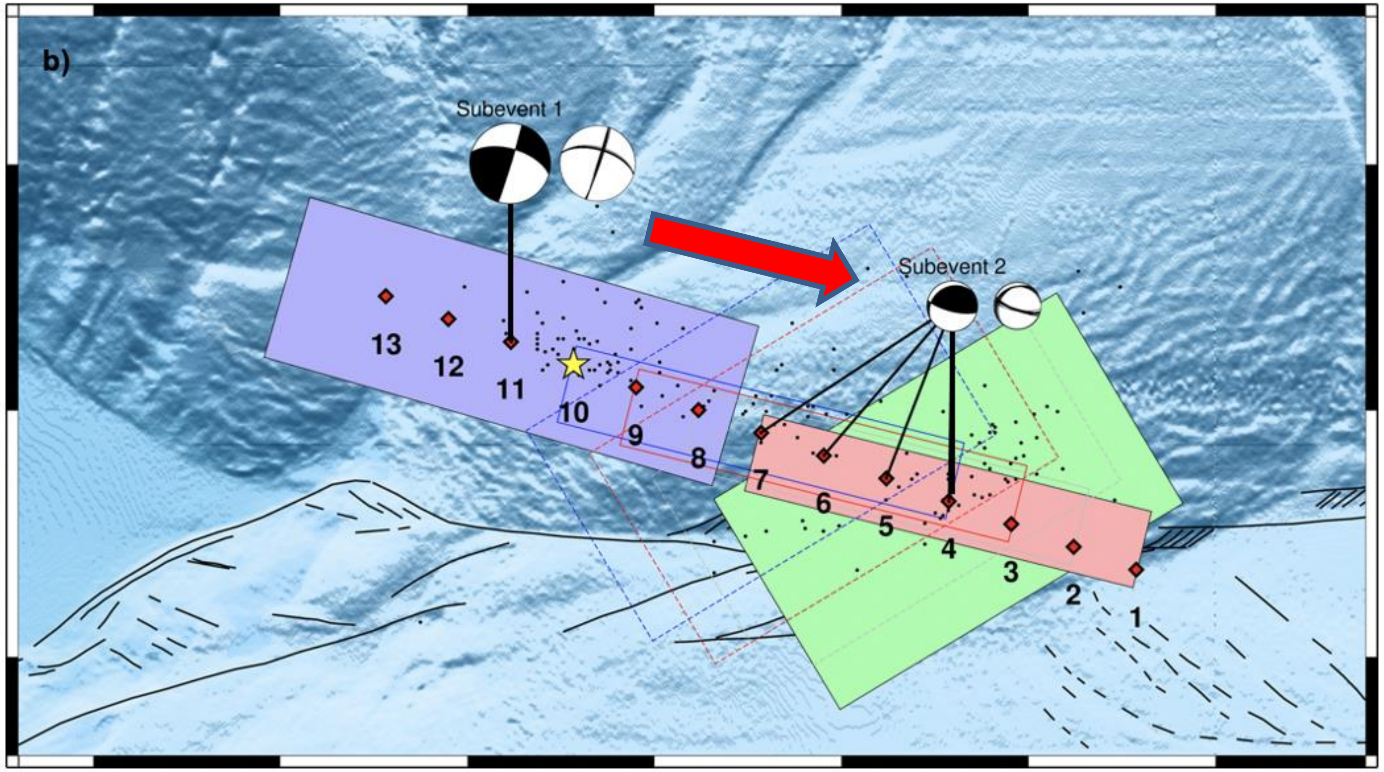

We confirmed that after a strike-slip fault, a secondary (weaker and later) thrust-fault subevent occurred during the mainshock.

Two fault segments activated within ~ 6 km and ~2 seconds.

Rupture propagation to SE.

TF important for tsunami generation of a future M 7 event.

Analogy from Japan, transpression

Hallo *et al. Earth, Planets and Space* *(2019) 71:34*
https://doi.org/10.1186/s40623-019-1016-8

Earth, Planets and Space

FULL PAPER **Open Ac**

Seismotectonics of the 2018 northern Osaka M6.1 earthquake and its aftershocks: joint movements on strike-slip and reverse faults in inland Japan

Miroslav Hallo[1*], Ivo Opršal[2], Kimiyuki Asano[3] and František Gallovič[1]

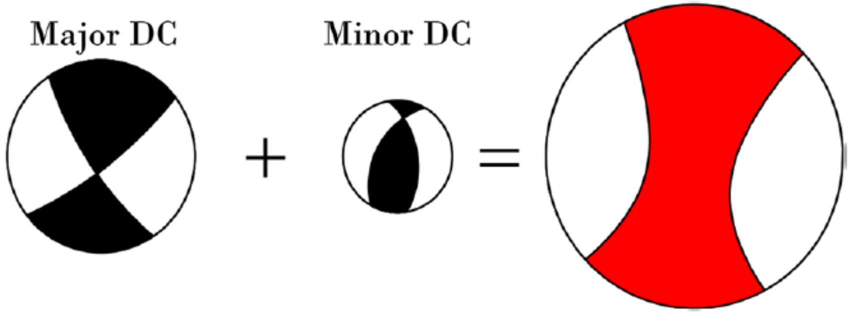

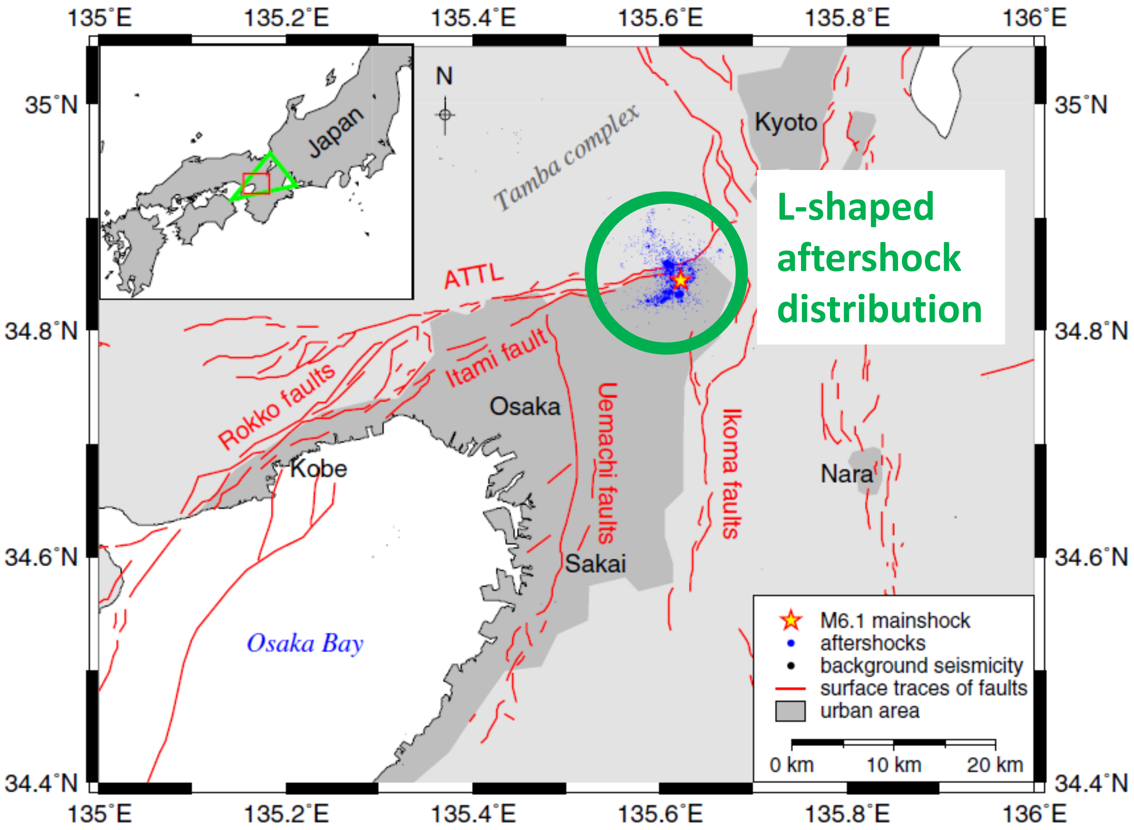

Mixing SS and TF, L-shape = two faults

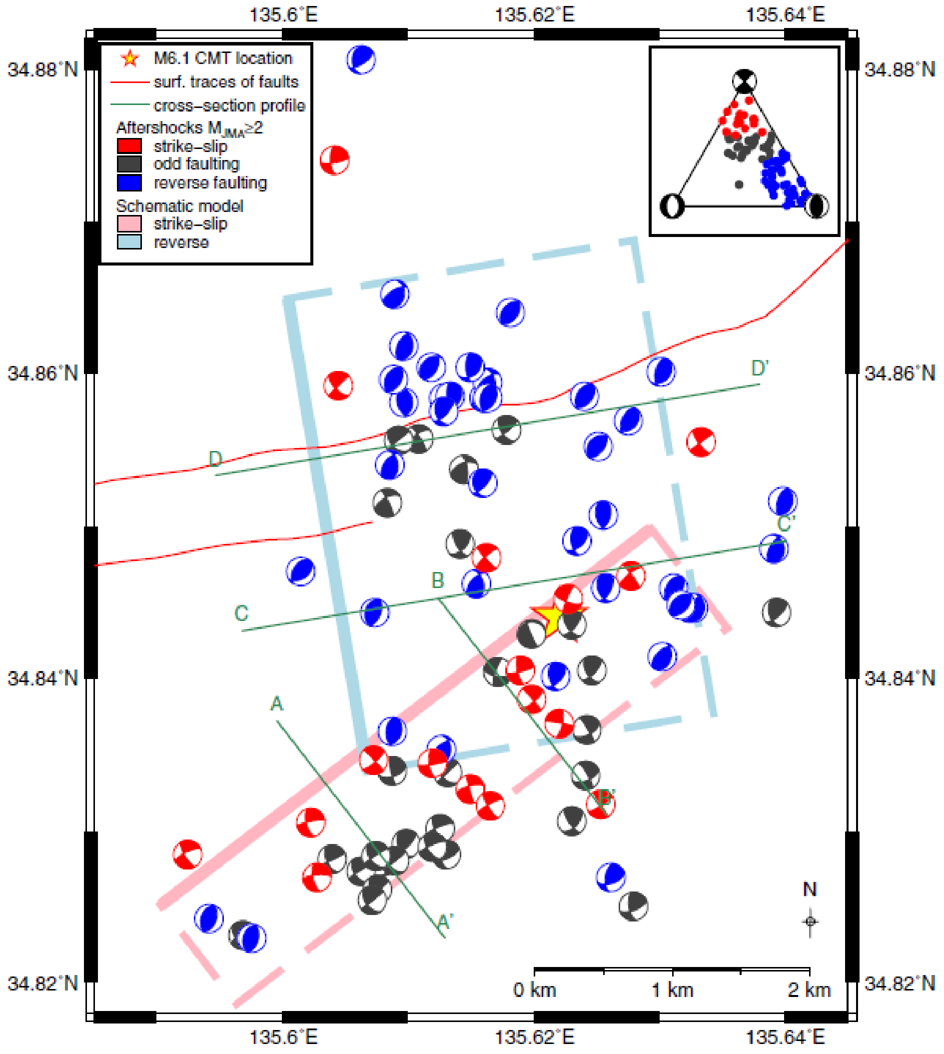

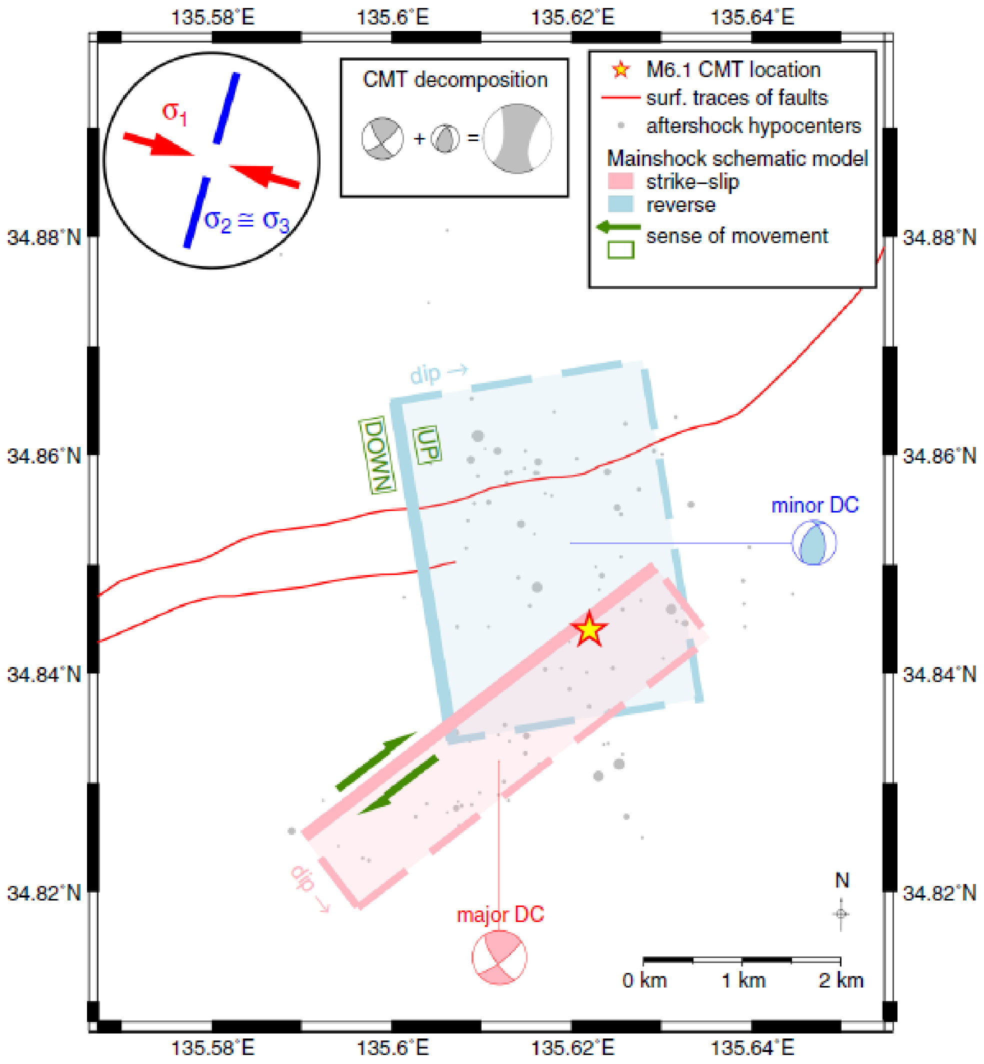

Only one principal stress axes is stable (σ 1)

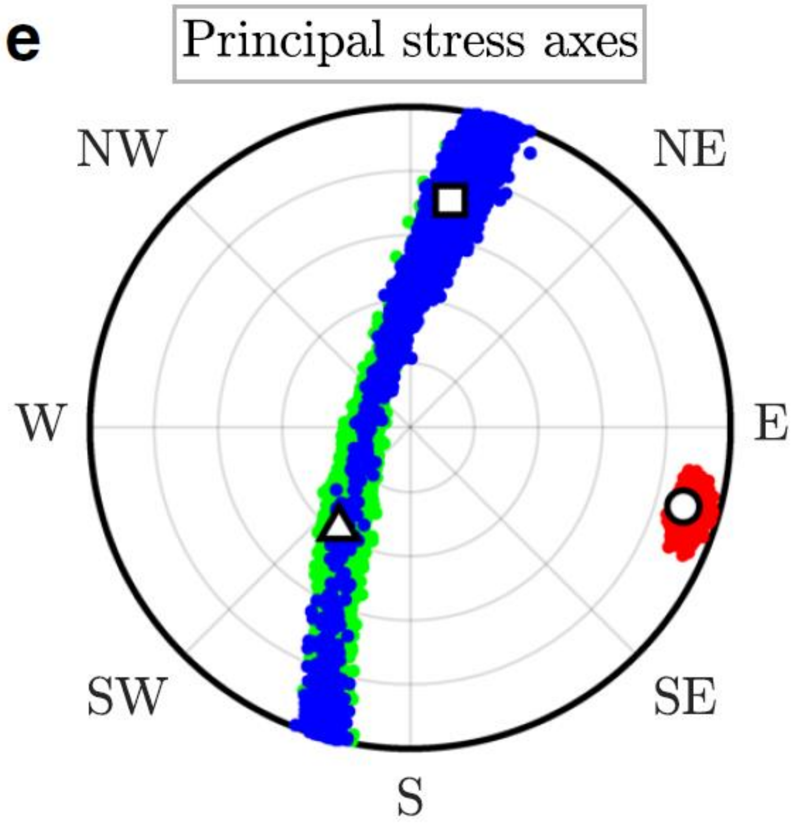

Two almost same eigenvalues = **indeterminacy** of two principal stress axes σ 2 (blue), σ 3 (green)

σ 1 … well constrained … common P axis of Maj/Min DC

x

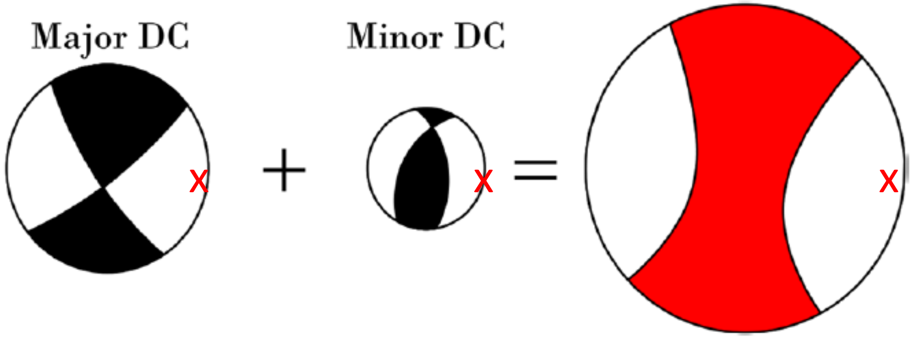

Part 3b: Multi-type faulting in salt-mine district Sichuan Basin, China

Another Non-DC as an apparent (≠ true) departure from shear faulting.

An application with importance in anthropogenic earthquake triggering.

The 2019 Mw 5.7 earthquake in Sichuan - huge non-DC explained as a mixed-type doublet

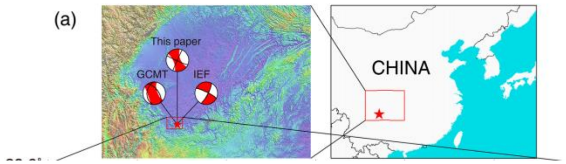

GCMT reported the DC part as low as DC=2%

We calculated full MT and obtained a large (negative) CLVD and an almost zero ISO=VOL.

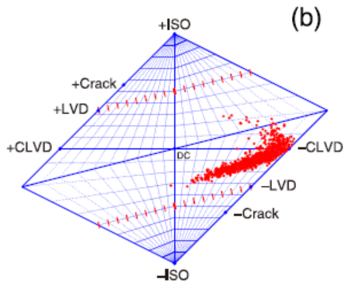

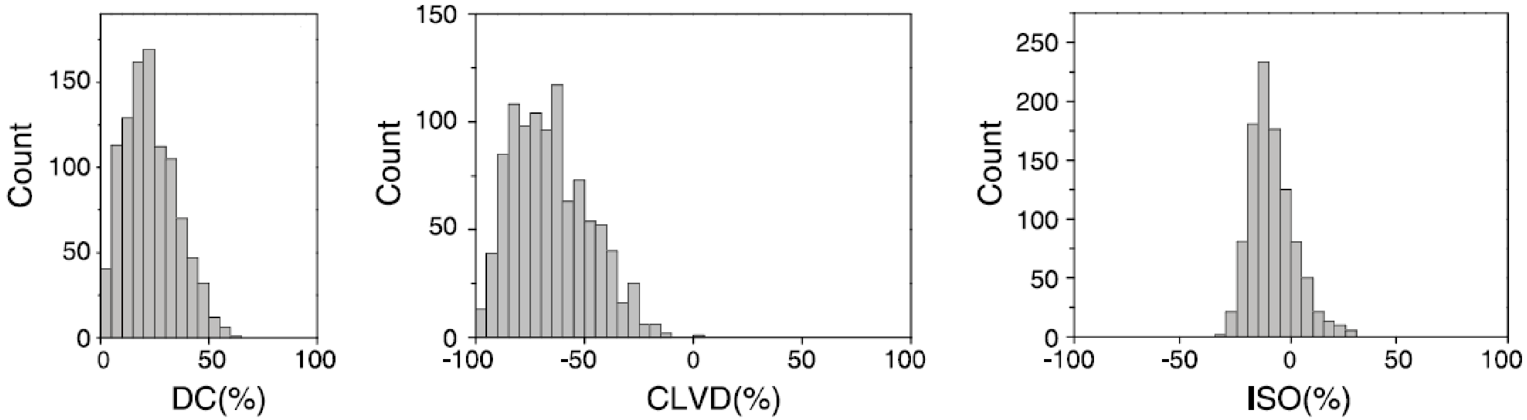

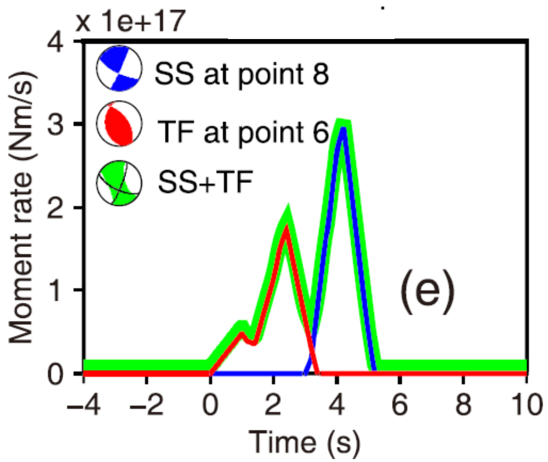

We explained the event as *two different 100% DC faults*, **Strike-Slip and Thrust-Fault**, approximately ~3-9 km and ~3 s from each oth

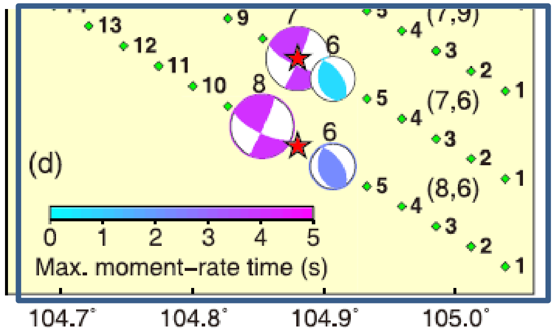

Liu, J. and Zahradník,J. (2020).
***Geophys. Res. Lett.*, 47, e2019GL085408**

First-motion polarities provide a perfect coverage but they disagree with full MT ….

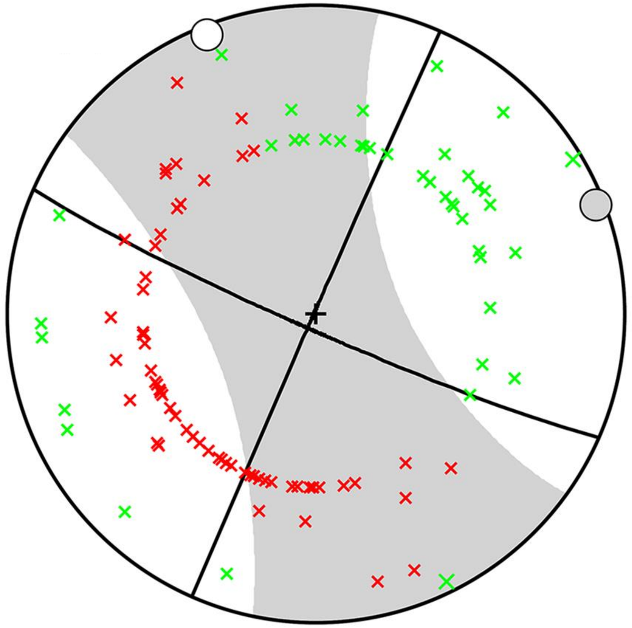

Full MT+DC

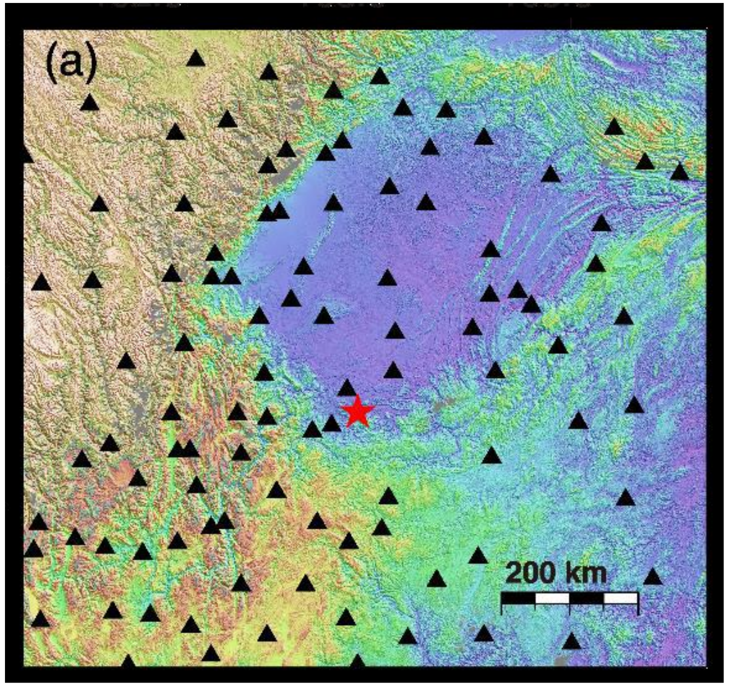

First-motion polarities disagree with full MT but confirmed that the earthquake started as a thrust fault

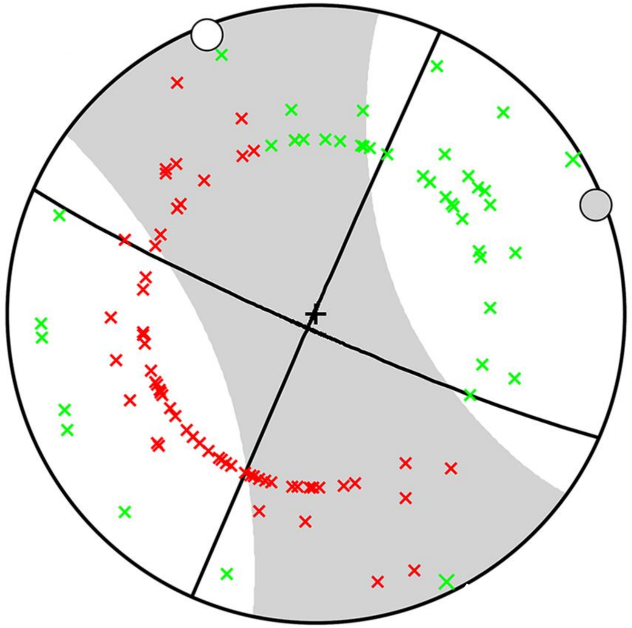

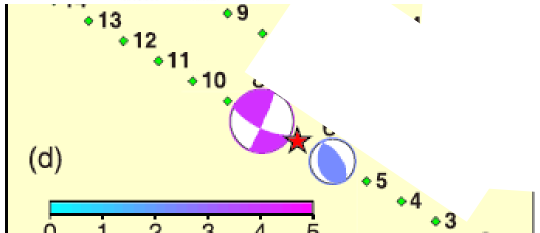

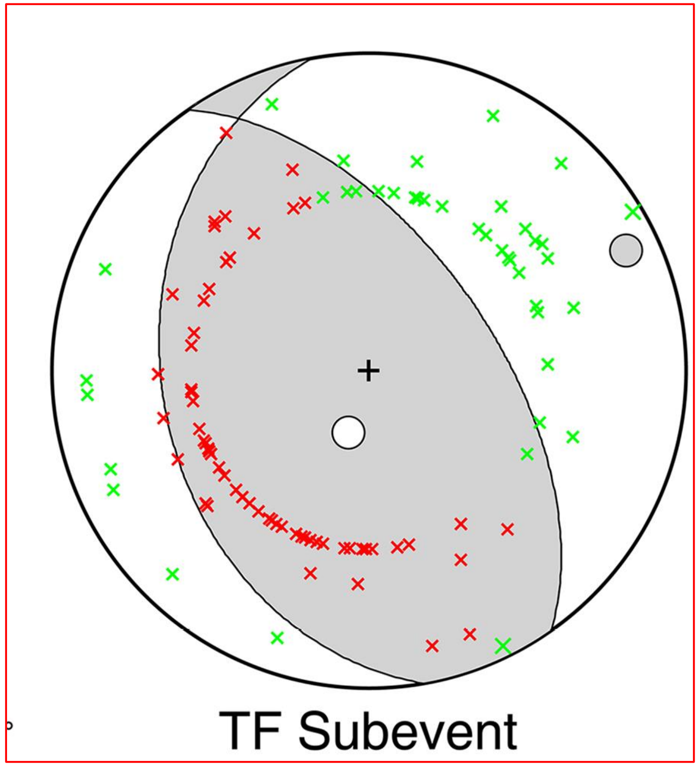

Practical importance of the revealed SS fault

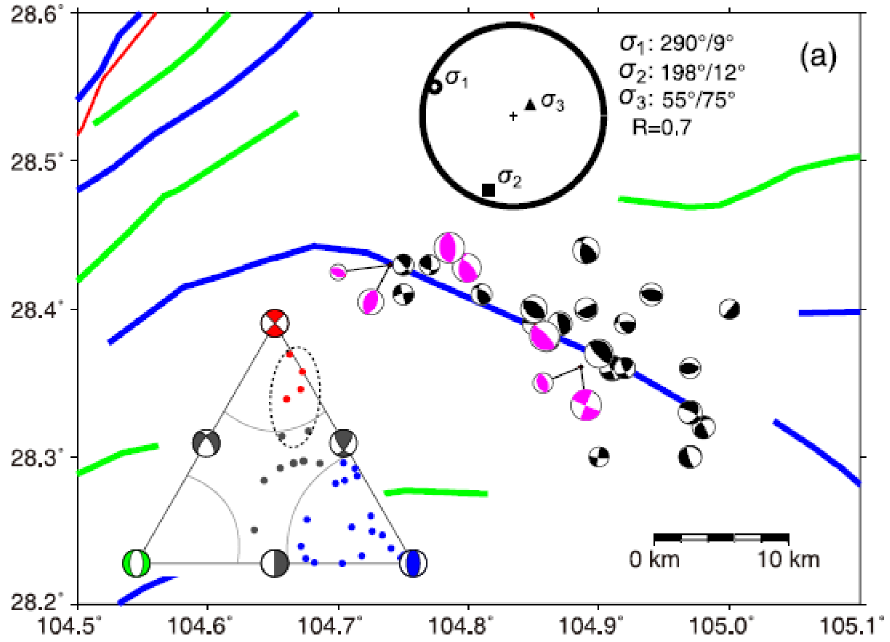

Active SS faults have not often occurred in the region.
According to regional stress field,
<u>SS faults seem to be stable, far from</u>
<u>the Coulomb failure envelope.</u>

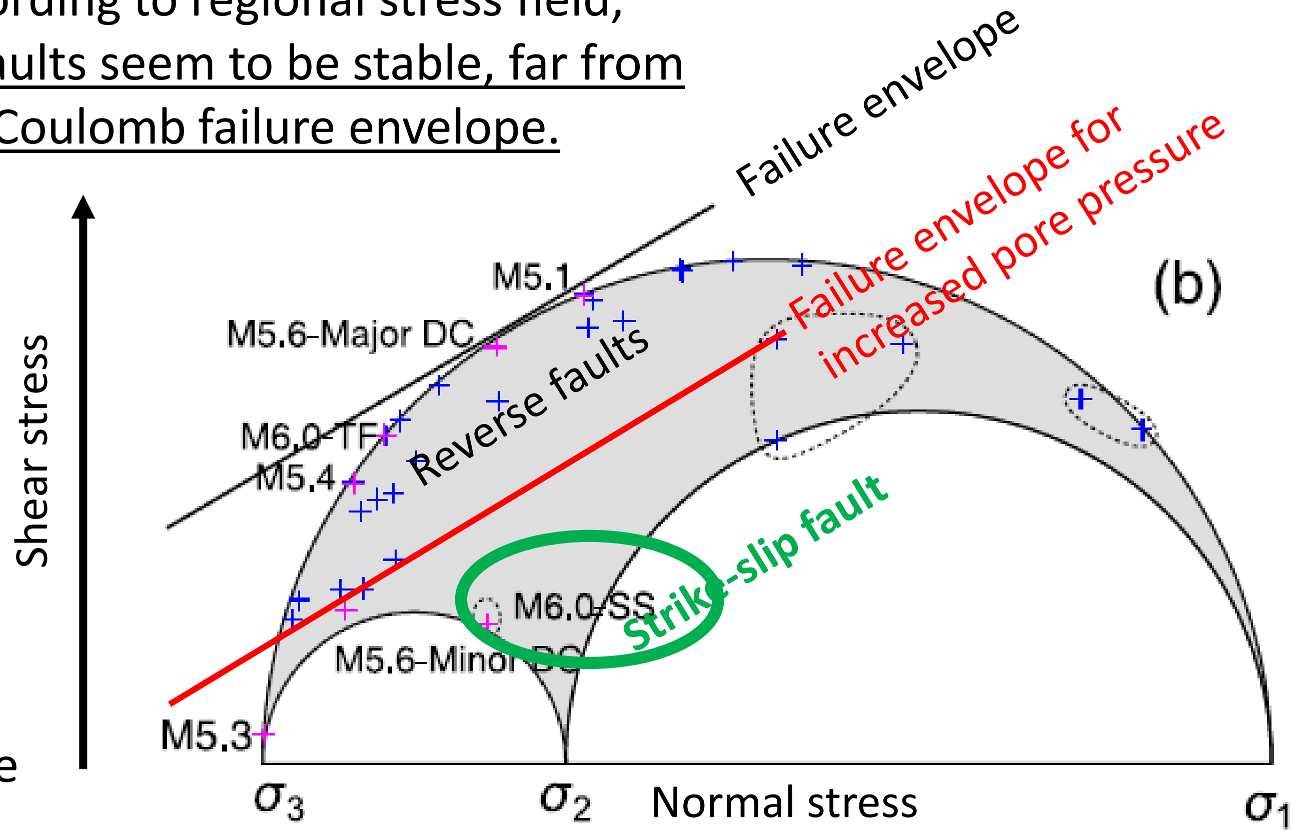

Nevertheless, SS ruptured there, and since there are many water injections in the salt-mines

the SS fault was probably activated by **elevated pore-water pressure**. Anthropogenic triggering.

Part 3c: Multi-type faulting near Zakynthos Island

Complex zone at western termination of Hellenic subduction, near Kefalonia transform.

The 2018 Mw 6.8 Zakynthos

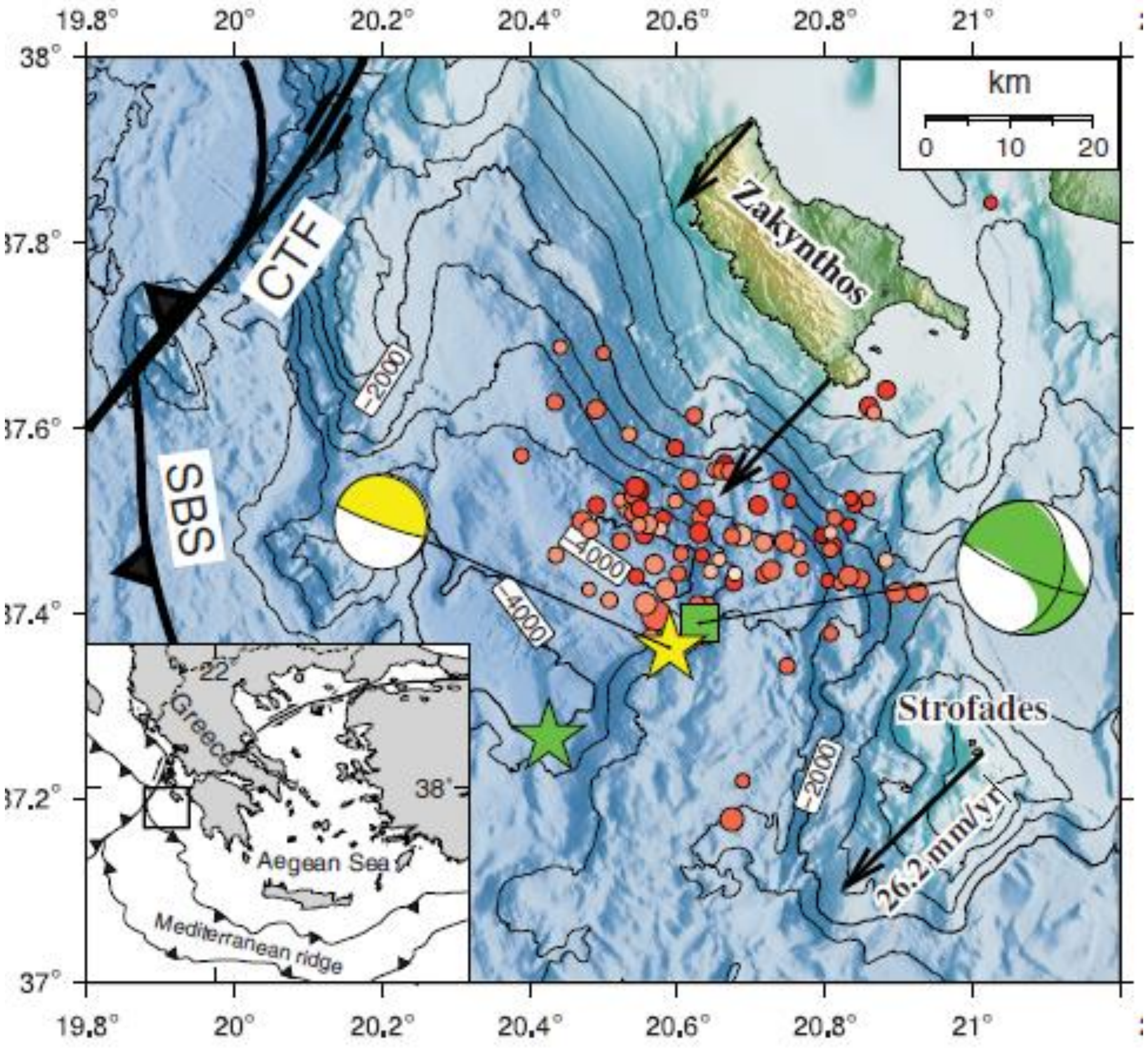

Full MT of the mainshock (green beachball):
DC ~ 40%, CLVD ~ −60%

Note also a low-dip (dip 10°) reverse faulting during foreshock (yellow beachball)

Sokos, E., F. Gallovič, . C.P. Evangelidis, A. Serpetsidaki, V. Plicka, J. Kostelecký, and J. Zahradník (2020):
The 2018 Mw 6.8 Zakynthos, Greece, Earthquake: Dominant Strike-Slip Faulting near Subducting Slab, ***Seismol. Res. Lett.*** 91, 721–732, https://doi.org/10.1785/0220190169

The 2018 mainshock likely consisted of two fault segments:
a low-dip thrust, and a dominant moderate-dip, right-lateral strike-slip

Kinematic slip inversion of F. Gallovič

SS was a dominant faulting style "between" two TF episodes

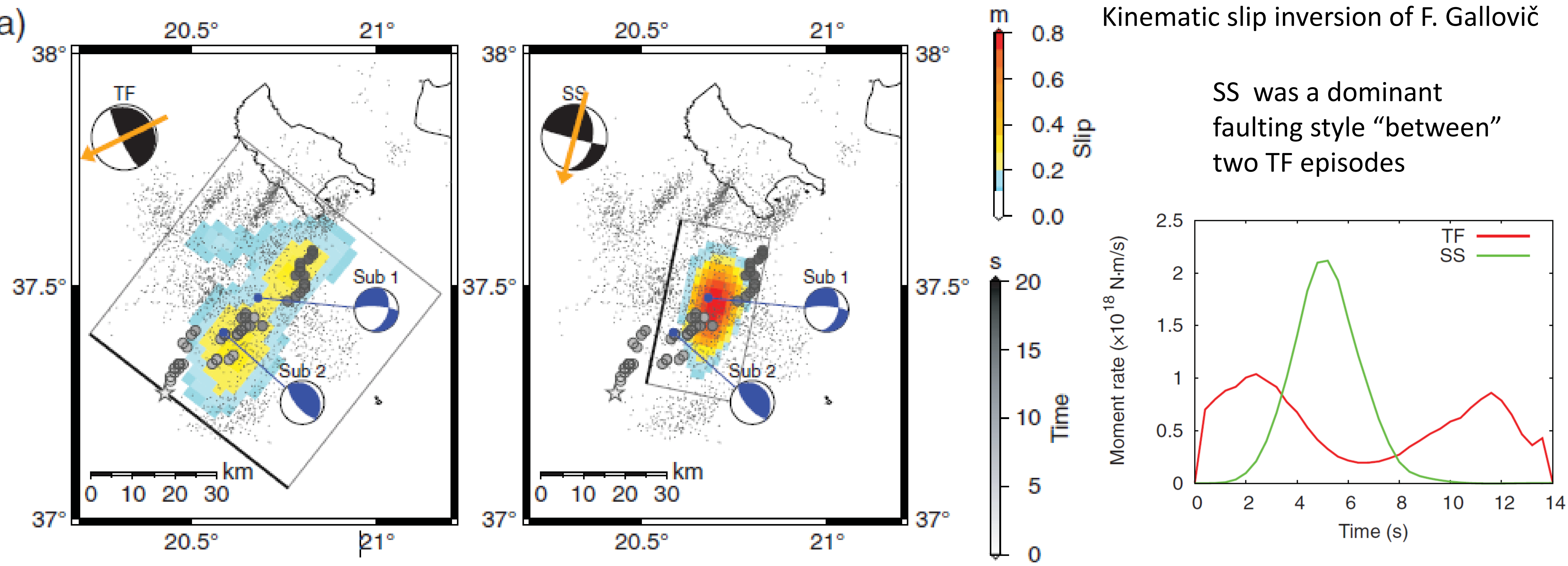

Part 4: Something else - a single-type faulting, yet complex

DC ~ 100%

Part 4a: Single-type complex faulting in Turkey 2020

Eastern Anatolia Fault, a “predecessor”
of the Mw7.8 of 2023

The 2020 Mw 6.8 earthquake in Turkey

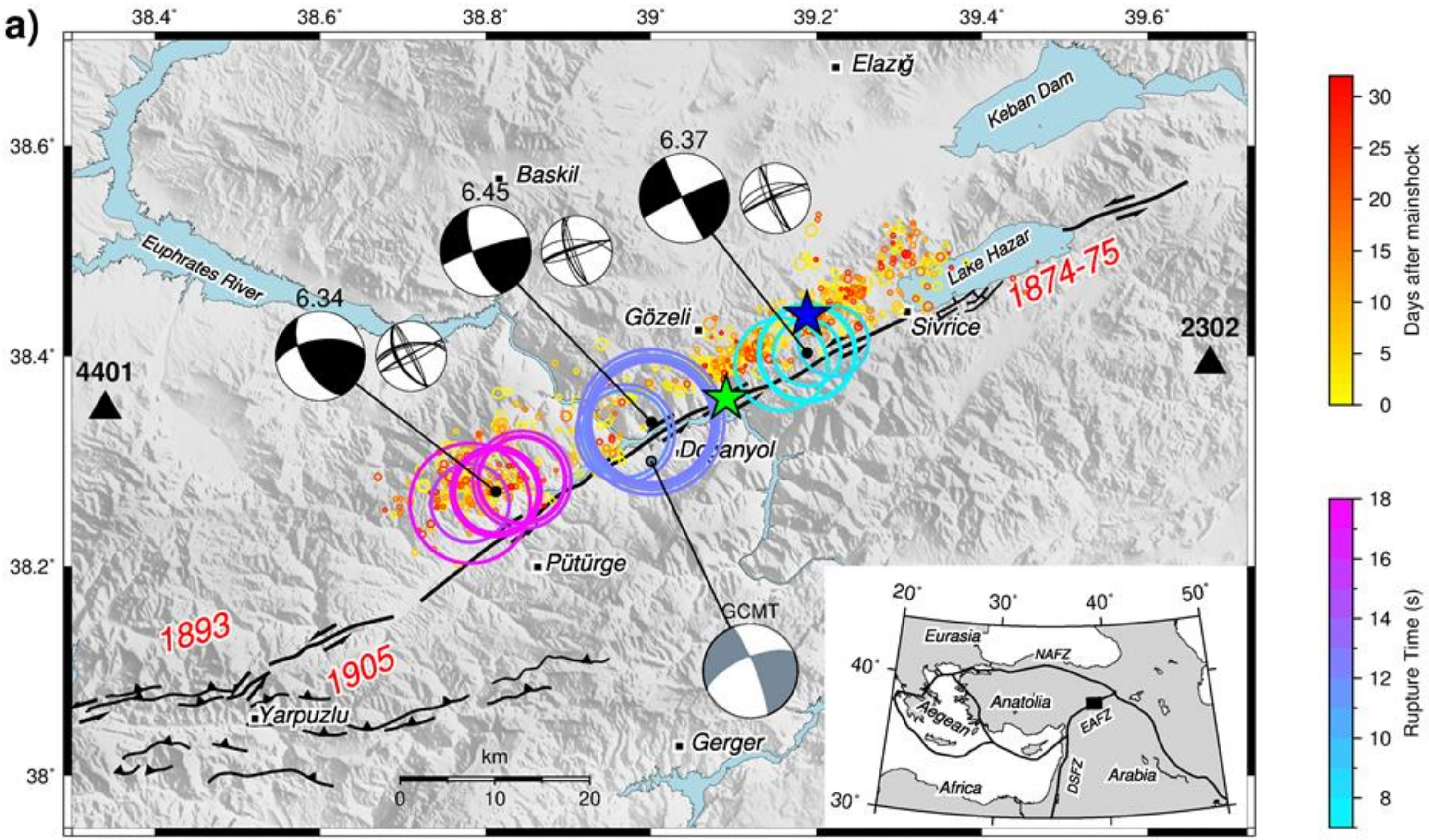

Using ISOLA we suggested
three main 100% DC
strike-slip
source episodes
and this geometry enabled
advanced *dynamic* source modeling
of F. Gallovič.

Gallovič, F., Zahradník, J., Plicka, V., Sokos, E., Evangelidis, C., Fountoulakis, I. and Turhan, F. (2020). Complex rupture dynamics on an immature fault during the 2020 Mw 6.8 Elazığ earthquake, Turkey. ***Commun Earth Environ*** 1, 40

Multi-point approximation by "iterative deconvolution"

Observed ground motion o(t)

Invert o(t) for the 1st subevent s1(t), create residual data o(t)-s1(t)

Invert residual data for the 2nd subevent s2(t), … etc.

Final source model =
1st subevent + 2nd subevent + …

Final synthetic data s1(t) + s2(t) + …

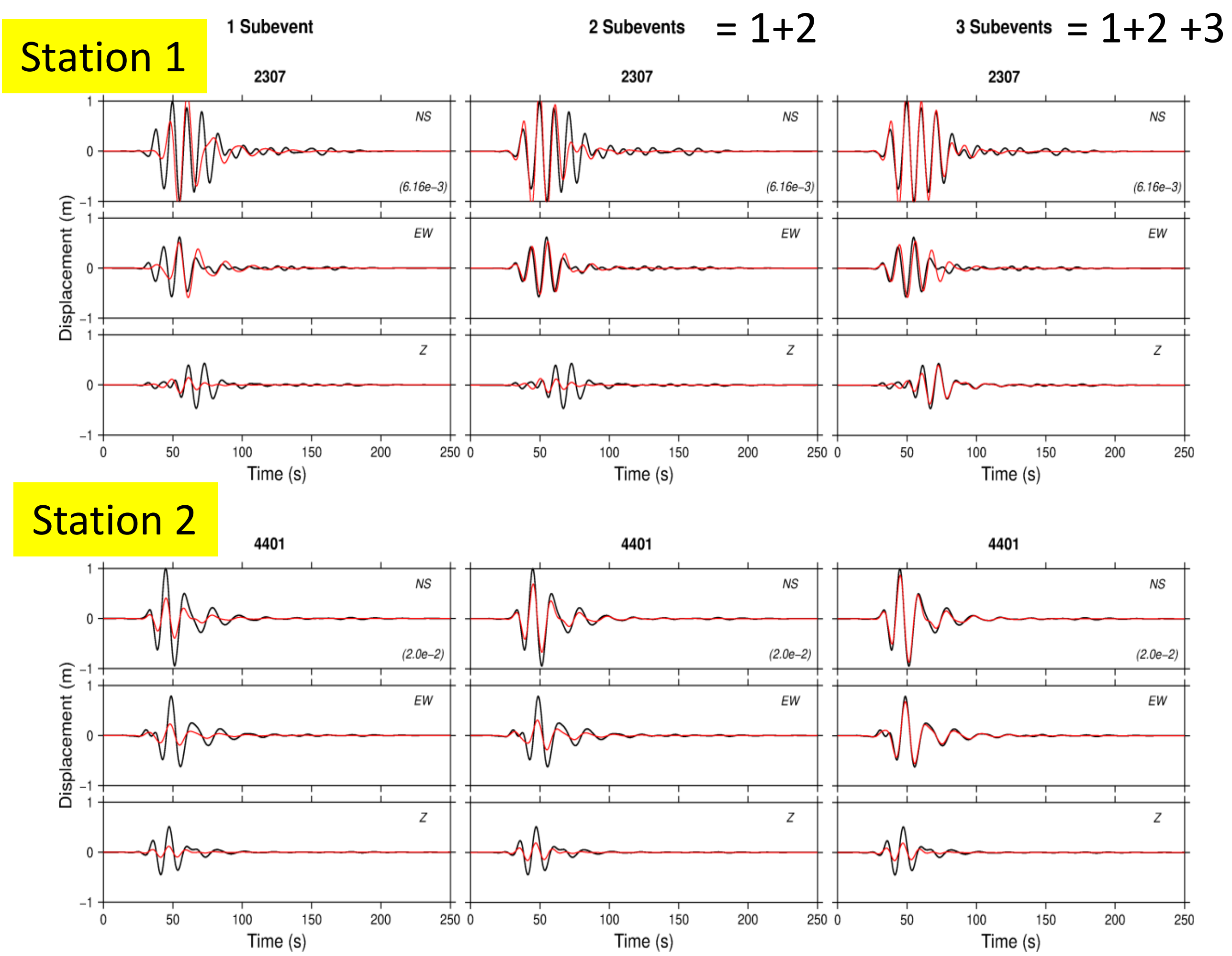

Part 4b: A deeply rooted shallow rupture on a less known normal fault

Corinth Rift, Greece

„A single beachball, with both nodal planes being partial ruptures“

The Mw 5.3 largest event of the 2020-2021 Corinth-Gulf seismic crisis

JGR Solid Earth

An example of a strong international cooperation in Corinth Rift Laboratory

An Atypical Shallow Mw 5.3, 2021 Earthquake in the Western Corinth Rift (Greece)

Jiří Zahradník[1], El Madani Aissaoui[2], Pascal Bernard[2], Pierre Briole[3], Simon Bufféral[3], Louis De Barros[4], Anne Deschamps[4], Panagiotis Elias[5], Christos P. Evangelidis[6], Ioannis Fountoulakis[6], František Gallovič[1], Vasilis Kapetanidis[7], George Kaviris[7], Olga-Joan Ktenidou[6], Sophie Lambotte[8], Olivier Lengliné[8], Helene Lyon-Caen[3], Mark Noble[9], Vladimír Plicka[1], Alexis Rigo[3], Zafeiria Roumelioti[10], Anna Serpetsidaki[10], Efthimios Sokos[10], and Nicholas Voulgaris[7]

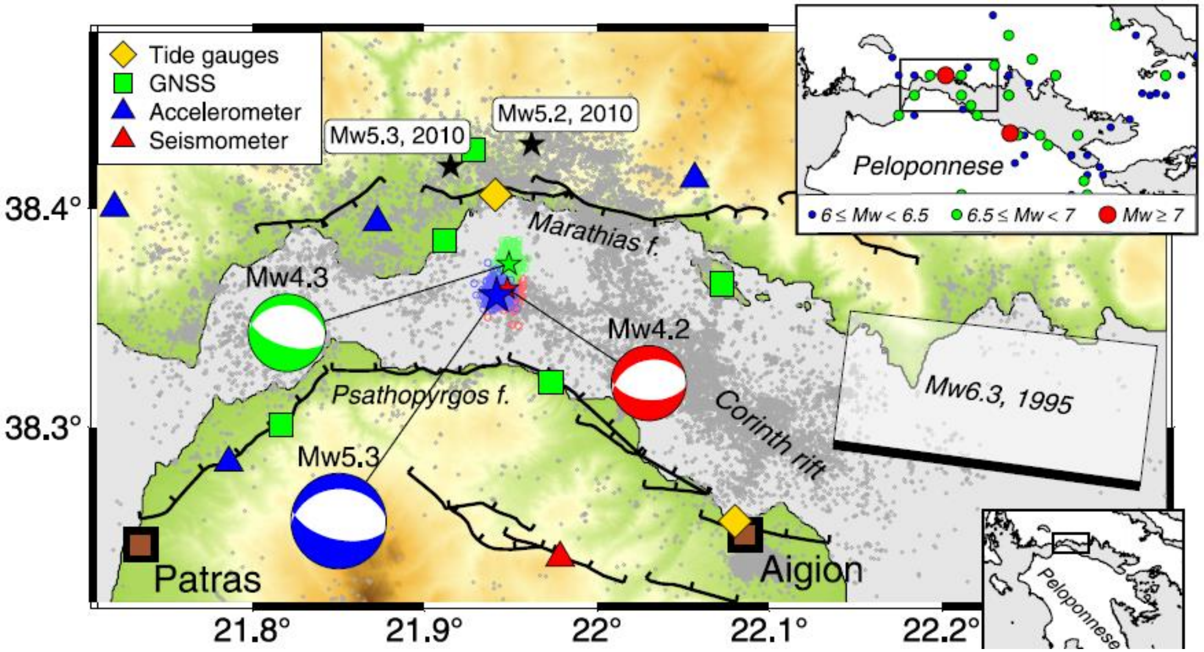

Seismic, GNSS, InSAR and tide-gauge data were combined to reveal the source process.

Note: major rift-bordering major normal faults were NOT activated !

Multidisciplinary data interpreted as a shallow rupture of an offshore normal fault, rooted in detachment, antithetic to Psathopyrgos

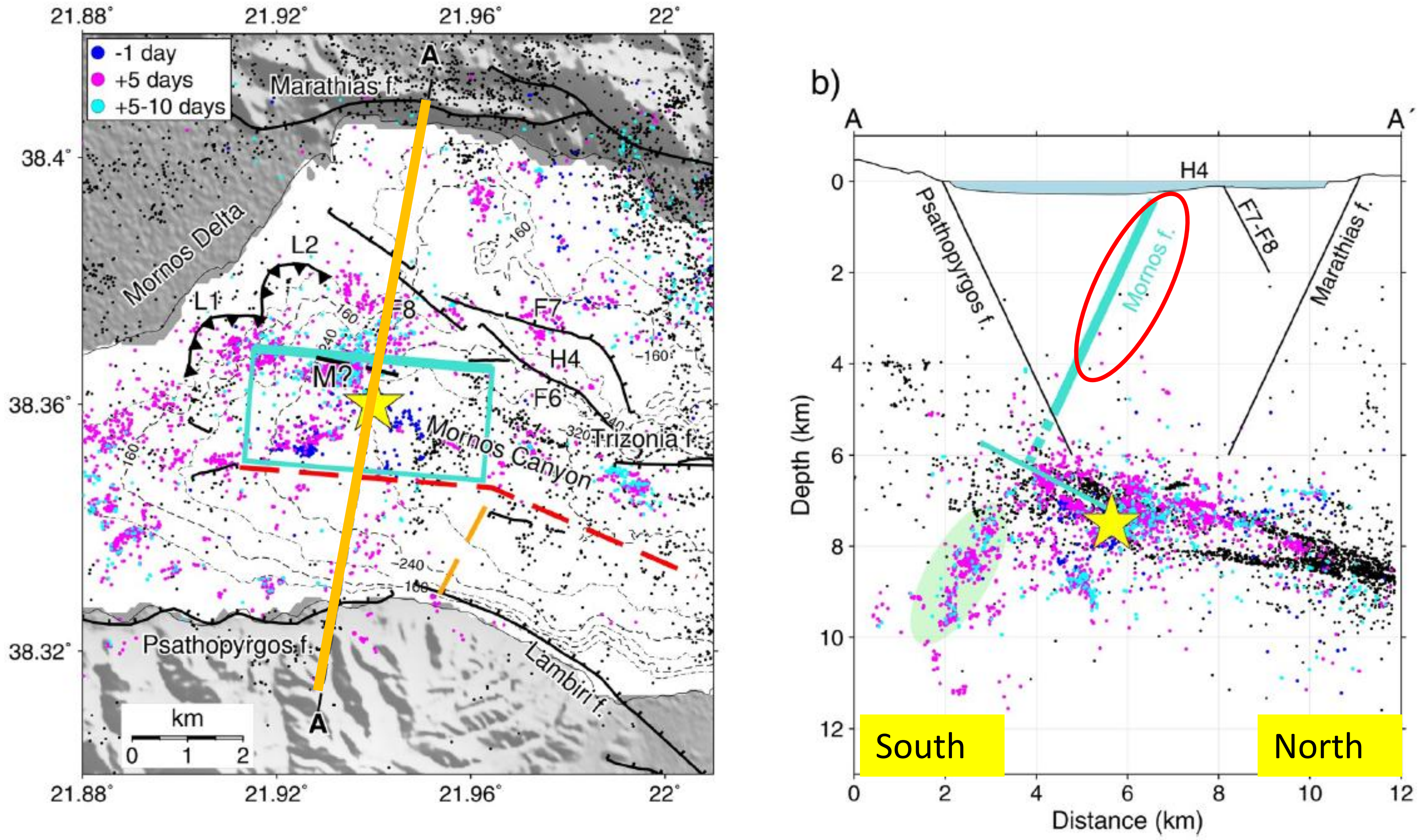

Multidisciplinary data interpreted as a shallow rupture of an offshore normal fault, rooted in detachment, antithetic to Psathopyrgos

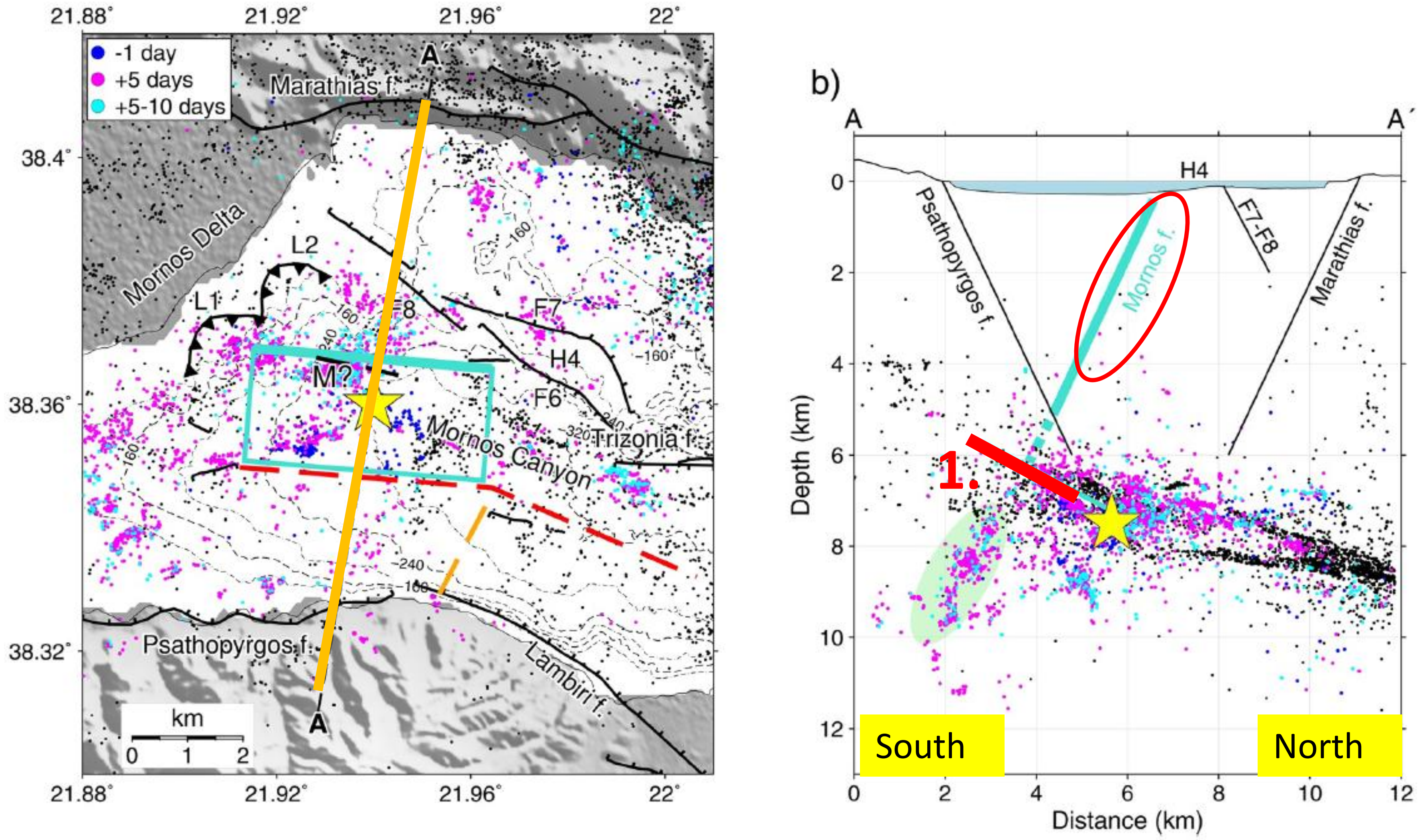

1. Rupture started on detachment surface (where small events typically occur)

Multidisciplinary data interpreted as a shallow rupture of an offshore normal fault, rooted in detachment, antithetic to Psathopyrgos

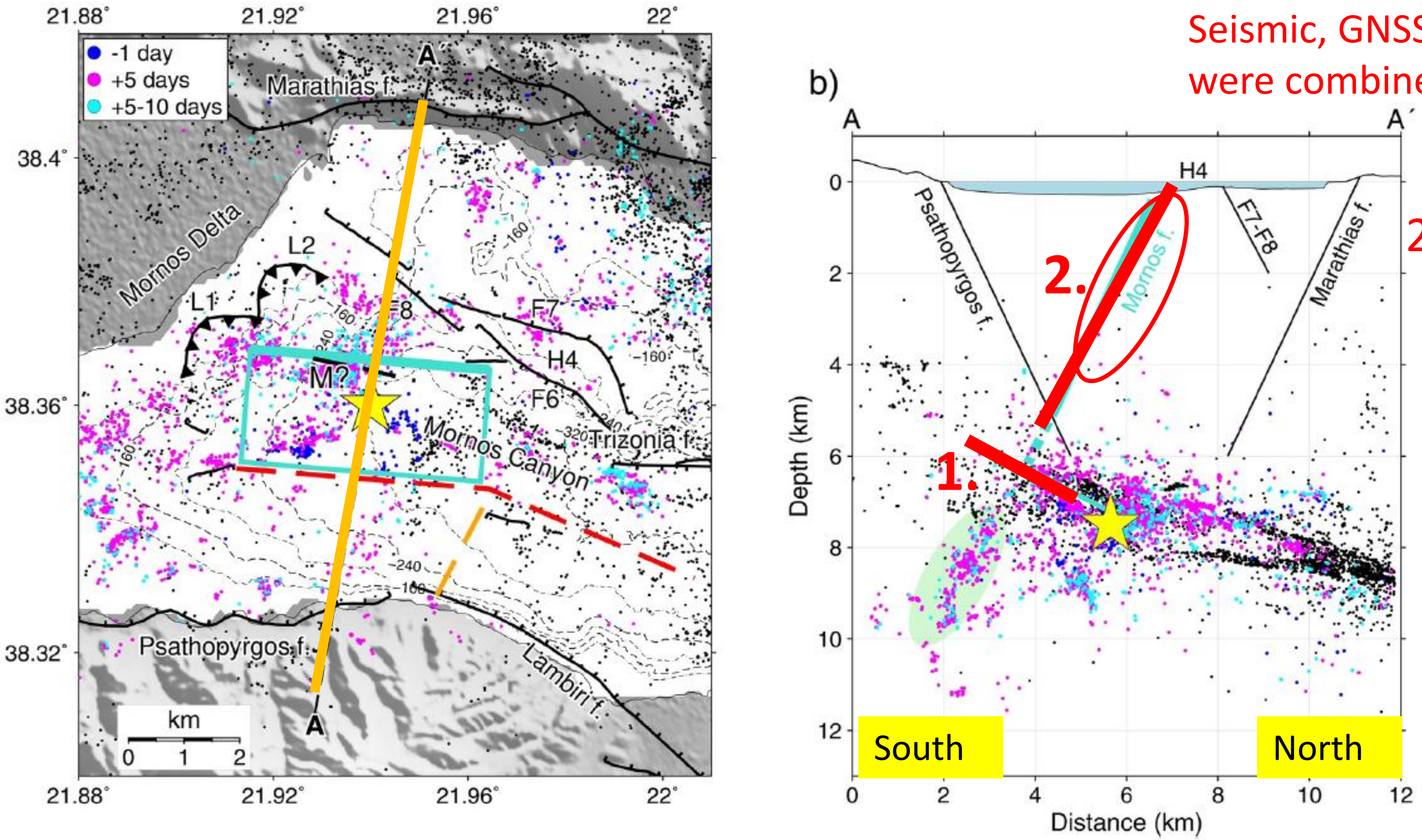

Seismic, GNSS, InSAR and tide-gauge data were combined to reveal the source process.

2. Dominant ruptured evolved at unusual shallow depth

1. Rupture started on detachment surface (where small events typically occur)

"A single beachball – both nodal planes are fault planes"

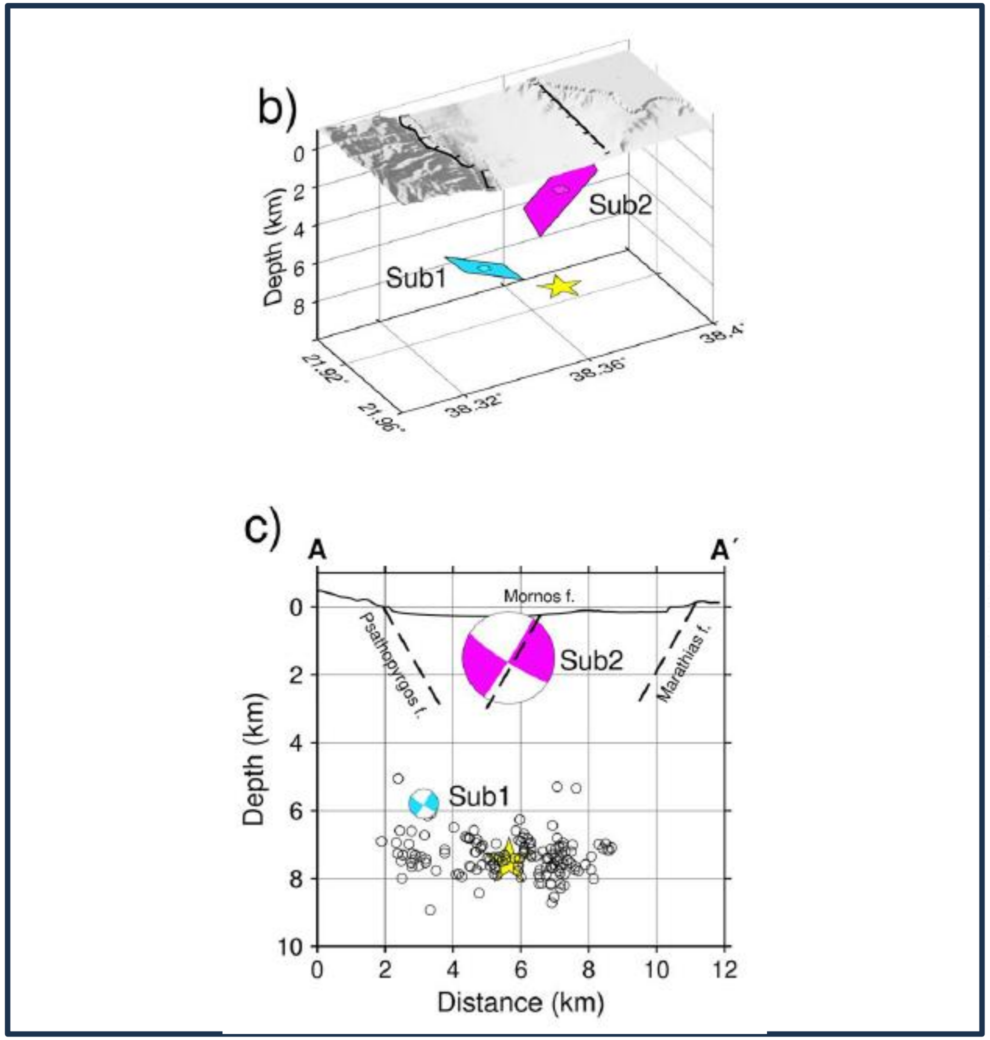

Seismic, GNSS, InSAR and tide-gauge data were combined to reveal the source process.

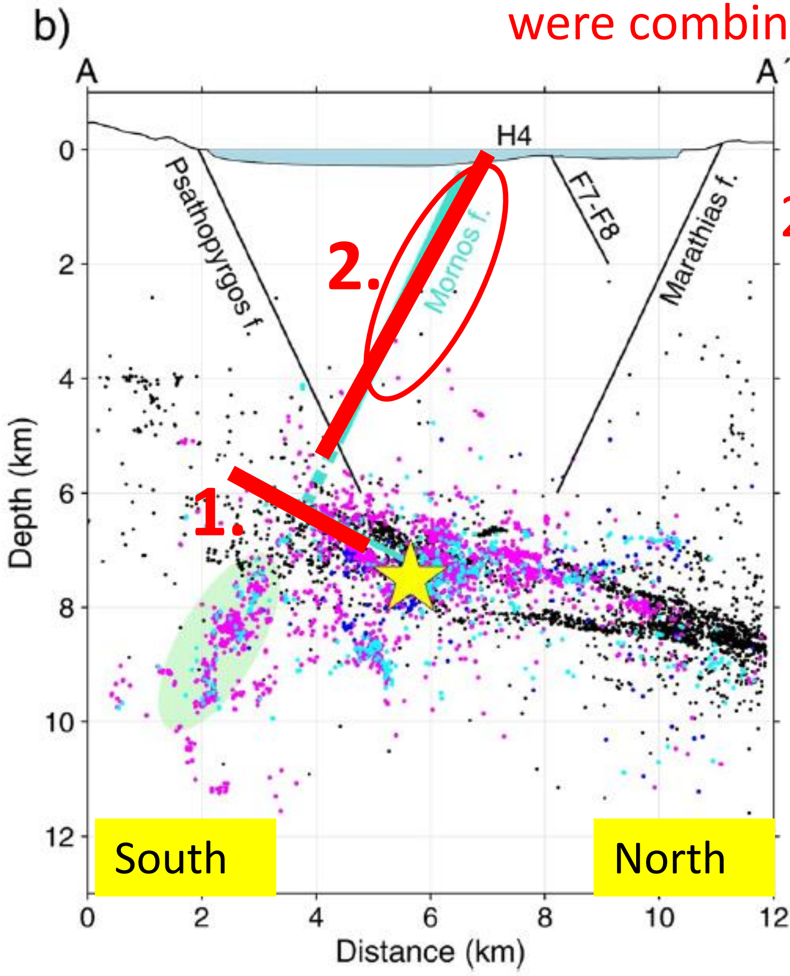

2. Dominant ruptured evolved at unusual shallow depth

1. Rupture started on detachment surface (where small events typically occur)

Part 4c: A very large fault system
“everything is posible”
(single- or multiple-type faultng)

Eastern Anatolia Fault, Turkey 2023

The Mw 7.8 Turkey eq. 2023

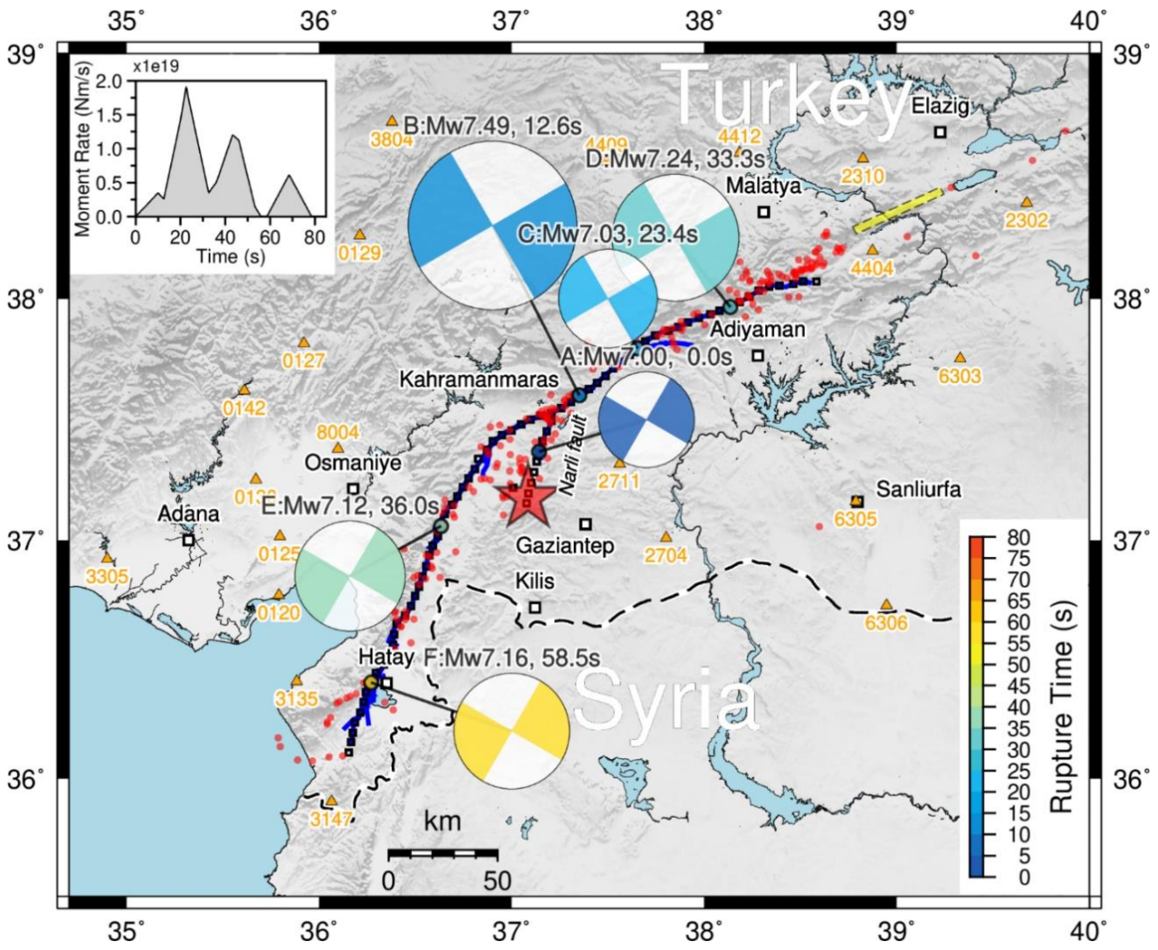

Multi-point subevents reveal:

1) Change of the fault strike between the major SW and NE segments

2) Asymmetric bilateral rupturing

3) Patch-like space-time structure

The Mw 7.5 Turkey eq. 2023 (9 hours later)

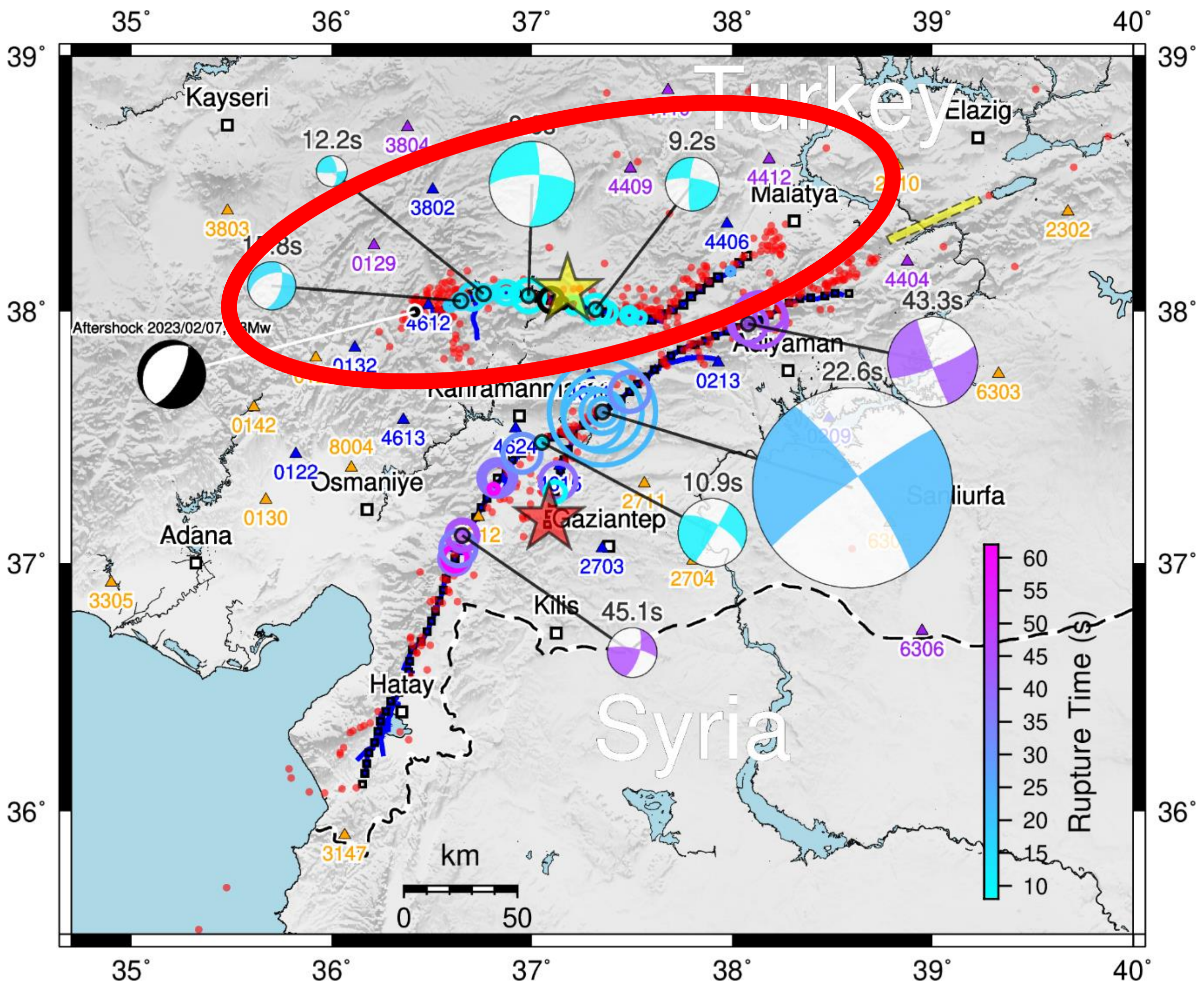

Multi-point subevents reveal:

1) A more compact rupture

2) Partial mixed-type faulting in the western part of the Mw 7.5.

The Mw 7.8 and 7.5 Turkey eqs. 2023

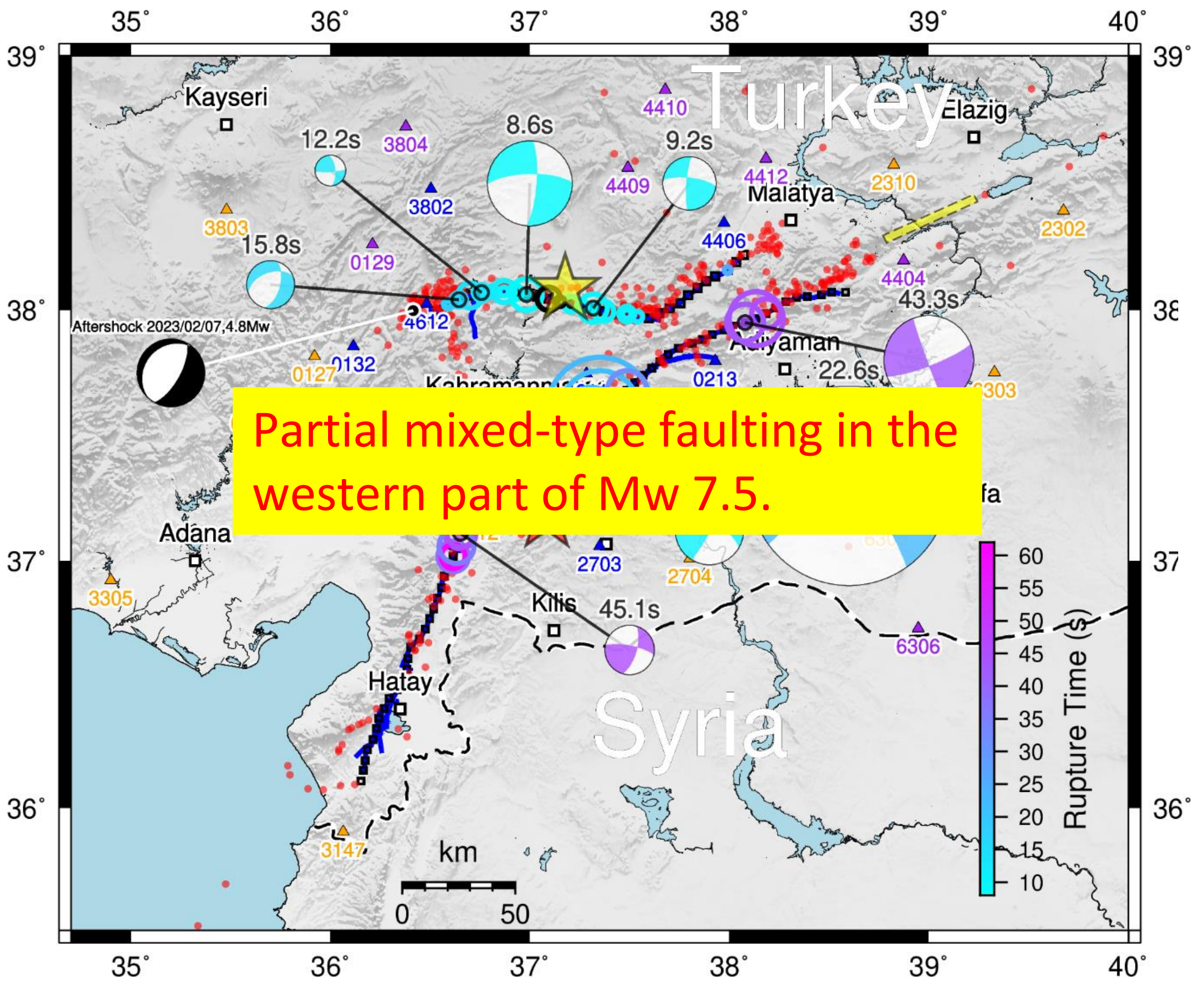

Partial mixed-type faulting in the western part of Mw 7.5.

Agreement with aftershocks:

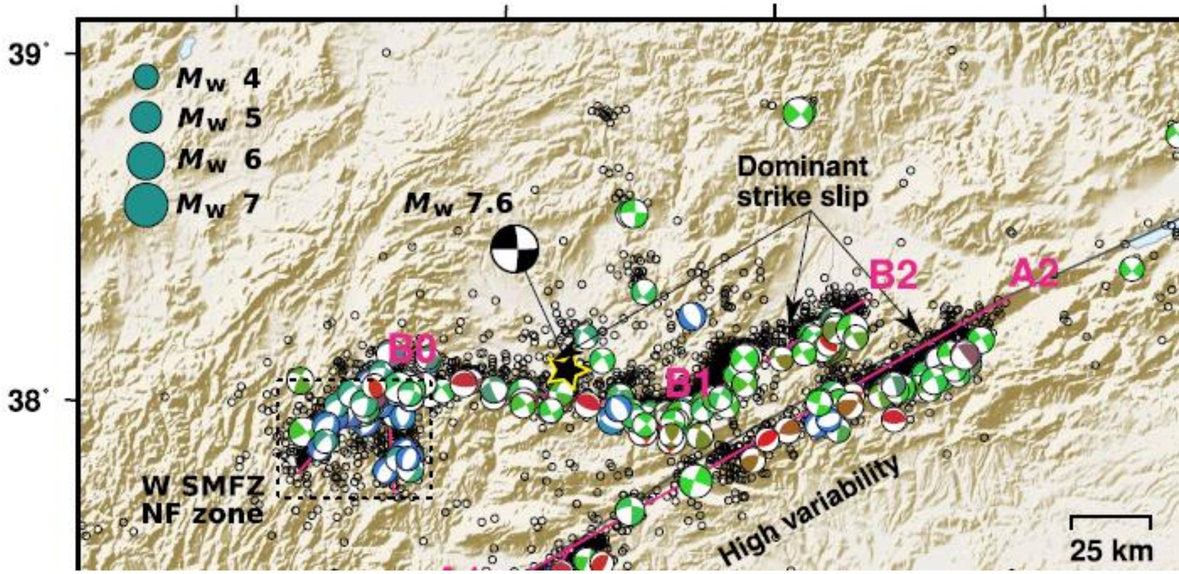

G.M. Petersen et al. , 2023

Summary and outlook

- Multi-type faulting is a combination of a few 100% DC faults of different mechanisms, e.g., strike-slip and reverse (or normal), whose full MTs has ISO=0 and large |CLVD|.
- The opposite is not true! Not all events with ISO=0 and large |CLVD| are multi-type faulting.
- Multi-type faulting events help decipher fault zones, e.g. transpression.
- Single- and multi-type faulting is important for detecting segmented faults.
- Detected segmentations improve hazard assessment, mainly for blind faults.
- Future tasks: How complex are deep-focus and intermediate-depth events?

Thanks for your attention!

For full acknowledgment of all data and services used here, see the published papers.

Summary and outlook

- Multi-type faulting is a combination of a few 100% DC faults of different mechanisms, e.g., strike-slip and reverse (or normal), whose full MTs has ISO=0 and large |CLVD|.
- The opposite is not true! Not all events with ISO=0 and large |CLVD| are multi-type faulting.
- Multi-type faulting events help decipher fault zones, e.g. transpression.
- Single- and multi-type faulting is important for detecting segmented faults.
- Detected segmentations improve hazard assessment, mainly for blind faults.
- Future tasks: How complex are deep-focus and intermediate-depth events?

Present and future applications of dynamic rupture modeling in earthquake research

František Gallovič
Dept. of Geophysics, MFF, Charles University

In cooperation with:
Ľ. Valentová Krišková, A.-A. Gabriel, J. Premus, J.-P. Ampuero, …

Earthquake finite-fault modeling

Beyond a point-source model:

- Kinematic rupture model:
  - Slip rates functions along the fault
  - Linear relation with ground motions (via the representation theorem)
  - Easy to handle, standard in earthquake modeling

Kinematic description of tectonic faulting

- The rupture front spreads from the hypocenter over the fault.
- The development of slip (discontinuity of displacement) is accompanied by the emission of seismic waves.
- The rupture process is controlled by friction and is significantly heterogeneous, even with several areas of large slip (asperities).

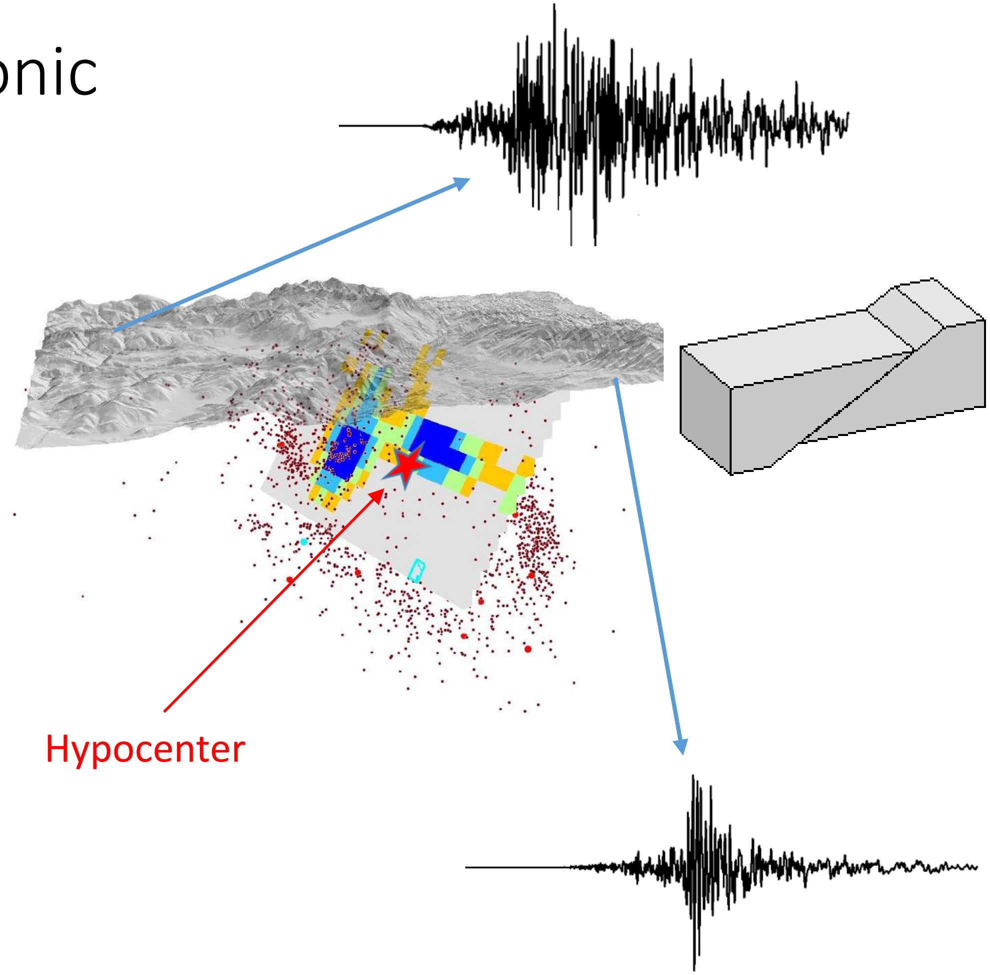

Fault plane

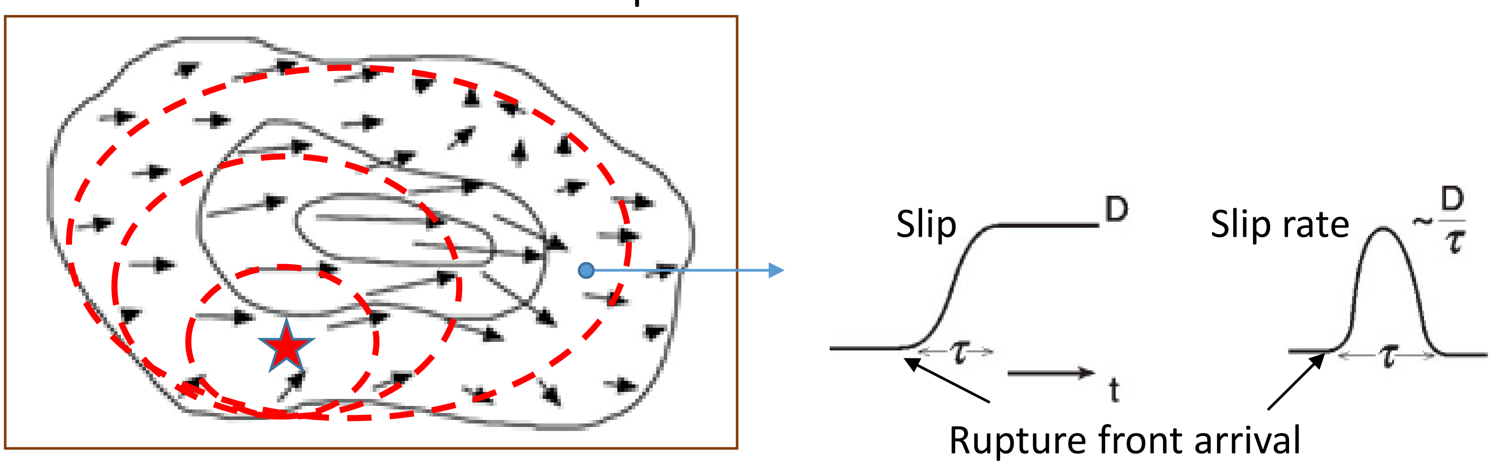

Uncertainty of slip the inversion

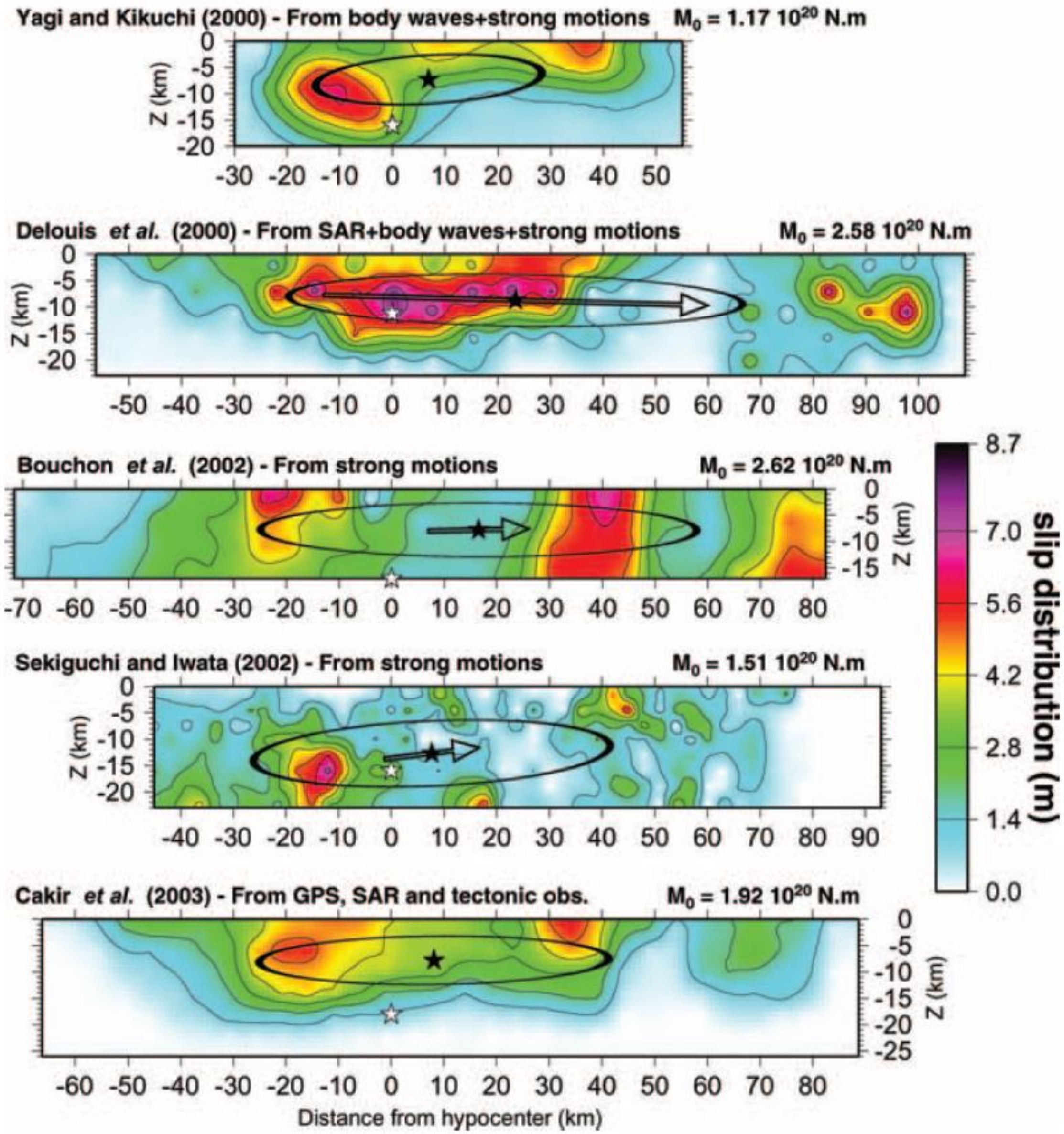

Clévédé et al. (2004)
M7.4 1999 Izmit, Turkey

Comparison of slip models inverted by various authors

What is the source of their discrepancies?

Our interpretation (Gallovič and Ampuero, 2015): the differences are due to differences in components from the null space of the representation theorem (linear projection)

How to extract the rupture model from the null space?

- Regularization of the solution in kinematic inversions:
  - Spatial smoothing of the slip rates (e.g., Hartzell & Heaton, 1983; Asano et al., 2005; Gallovič et al., 2015)
  - Assumption of slip rate shape with sought (spatially variable) parameters such as rupture time, rise time, slip (e.g., Archuleta, 1984; Ji et al., 2002; Halló and Gallovič, 2020)
- Drawback: kinematic approach does not guarantee physical consistency of the model in terms of friction (e.g., Burjánek and Zahradník, 2007)
- Solution: Use *elastodynamic equation* and *a friction law* as physical constraints

  => dynamic slip inversions

Dynamic slip inversion

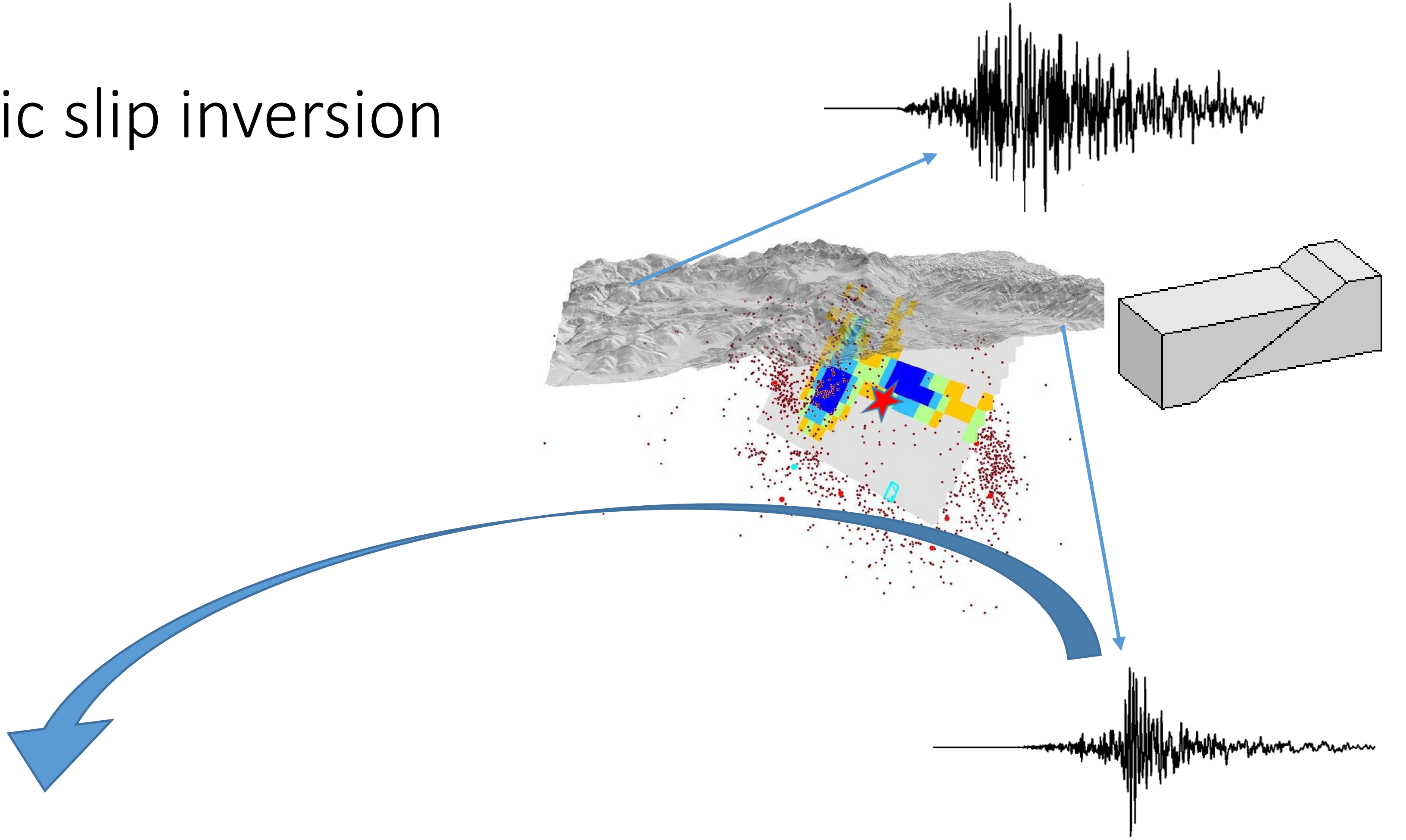

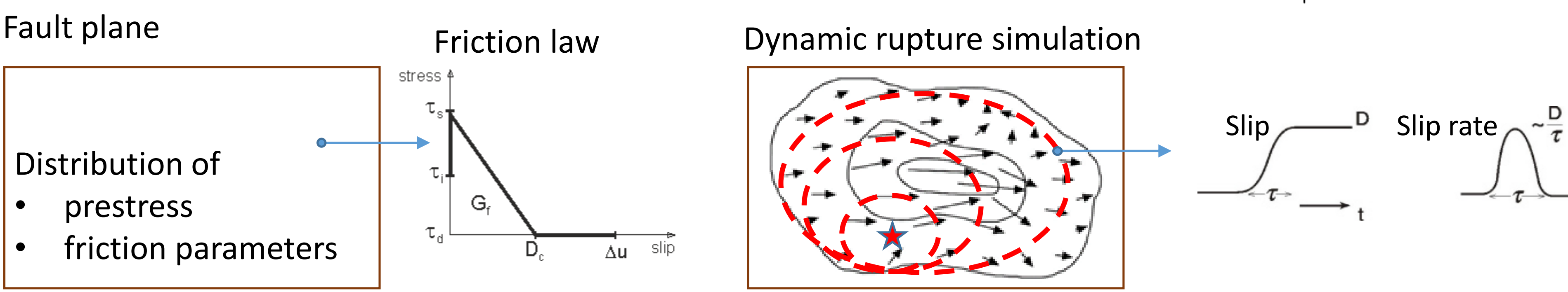

Dynamic rupture simulation in 3D

- Elastic continuum, small deformations, Lagrange coordinates
- Equation of motion (momentum conservation law)

$$\rho \dot{\boldsymbol{v}} = \boldsymbol{f} + \nabla \cdot \boldsymbol{\sigma}$$

- Hook's law for isotropic solid

$$\dot{\boldsymbol{\sigma}} = \lambda \mathbf{I} \nabla \cdot \boldsymbol{v} + \mu \left(\nabla \boldsymbol{v} + (\nabla \boldsymbol{v})^T \right)$$

$\boldsymbol{v}$ – velocity
ρ – density
$\boldsymbol{f}$ – forces
$\boldsymbol{\sigma}$ – stress tensor
λ, μ – Lamé's param.

- Solution by, e.g., finite differences on staggered grids

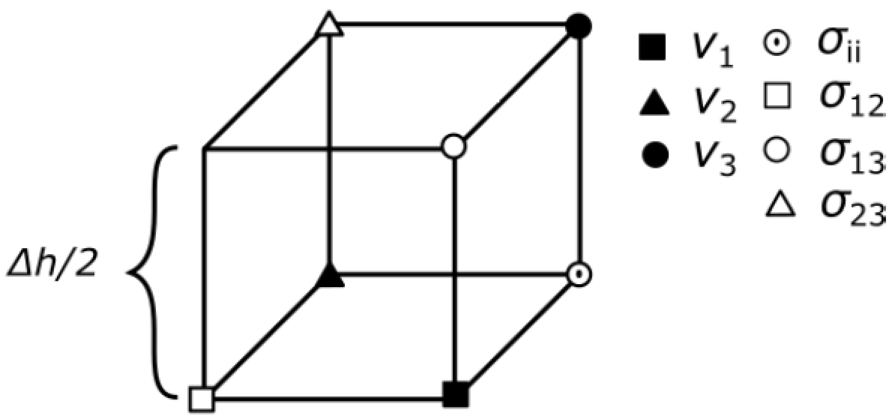

- Free surface and nonreflecting boundaries (e.g., PML)

Fault as a boundary condition

- Relationship between stress and friction:

$$|\boldsymbol{T}| \leq f(\Delta u, \Delta \dot{u}, \ldots)$$

- Traction-at-split-node method (Dalguer and Day, 2007)

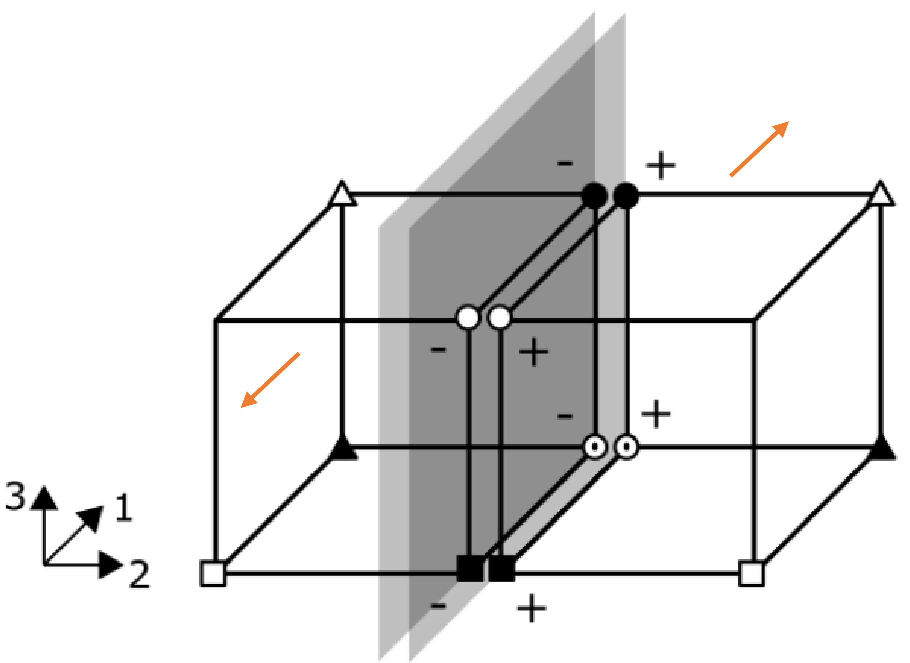

Friction law – one of the simplest choices is the *slip-weakening friction*:

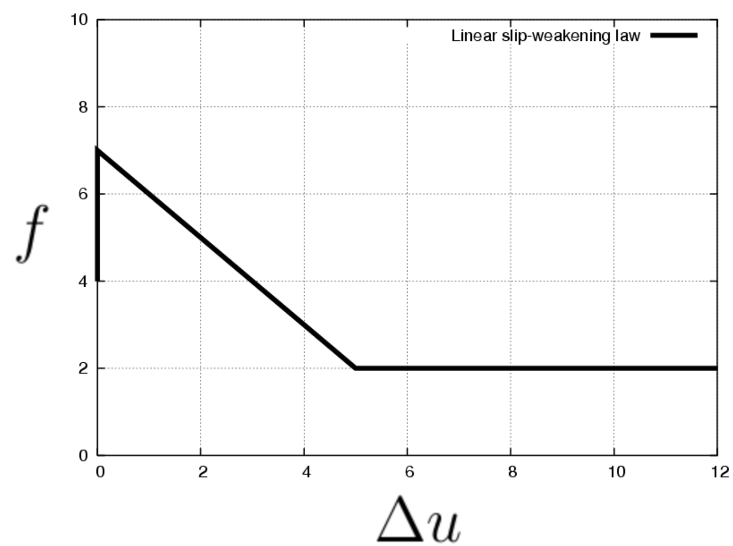

(Ida, 1972; Andrews, 1976)

Forward solver (speed matters)

- **Dynamic rupture** by FD3D_TSN (Premus et al., SRL, 2020)
  - 4^{th} order finite differences on a Cartesian box (Madariaga et al., 1998)
  - Vertical fault reaching free surface
  - 1D layered velocity model (VM1)
  - Friction law implemented by the Traction-at-Split-Node method (Dalguer and Day, 2007)
  - Symmetry conditions permit to solve the problem on half of the domain
  - Box covers just the fault – only slip rates are saved (waveforms are calculated externally)
  - Nonreflecting boundaries by Perfectly matched layers
  - Ported to GPU – up to 10x faster performance (w.r.t. CPU)

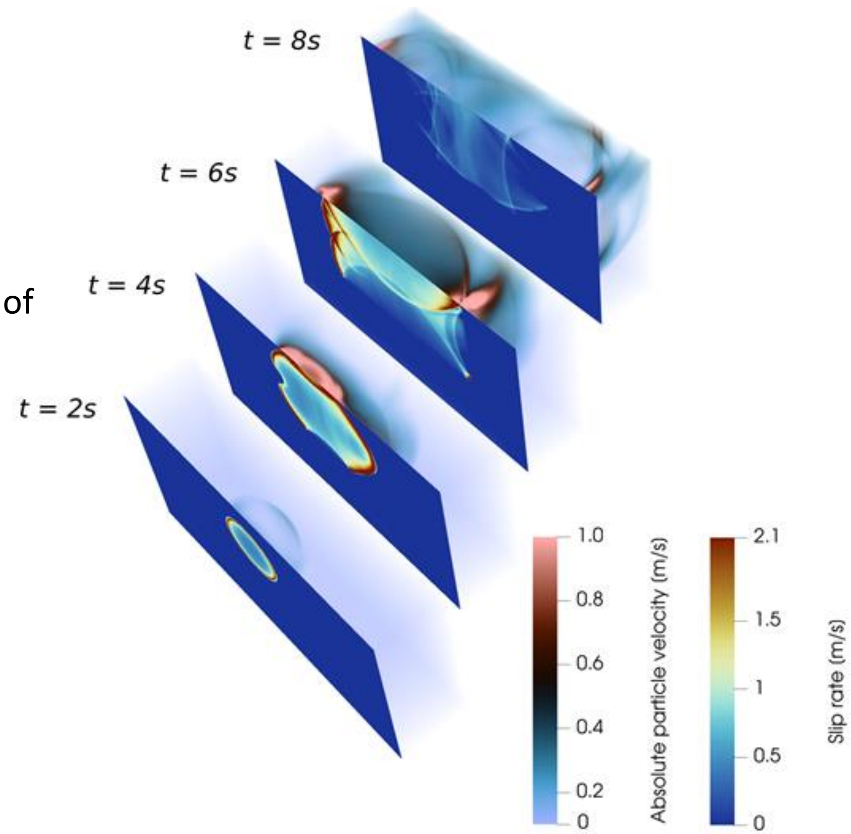

- **Wave propagation** by Axitra (Bouchon, 1981; Coutant, 1989)
  - 1D layered velocity model (VM1)
  - Pre-calculated Green’s functions on a coarser grid, respecting the „true“ fault geometry
  - Representation theorem is used to obtain station waveforms

Example of rupture propagation simulation

- FD3D_TSN (*Premus et al., 2020*)
- Community test with heterogeneous dynamic parameters
- Fault size 30x15km (grid step 100m)
- 12s of rupture propagation calculated in:
  - 3min on 1 CPU (Intel i9-9900K)
  - 20s on 1 GPU (Nvidia RTX 2700); ported using OpenACC in nvfortran
- Freely available on GitHub

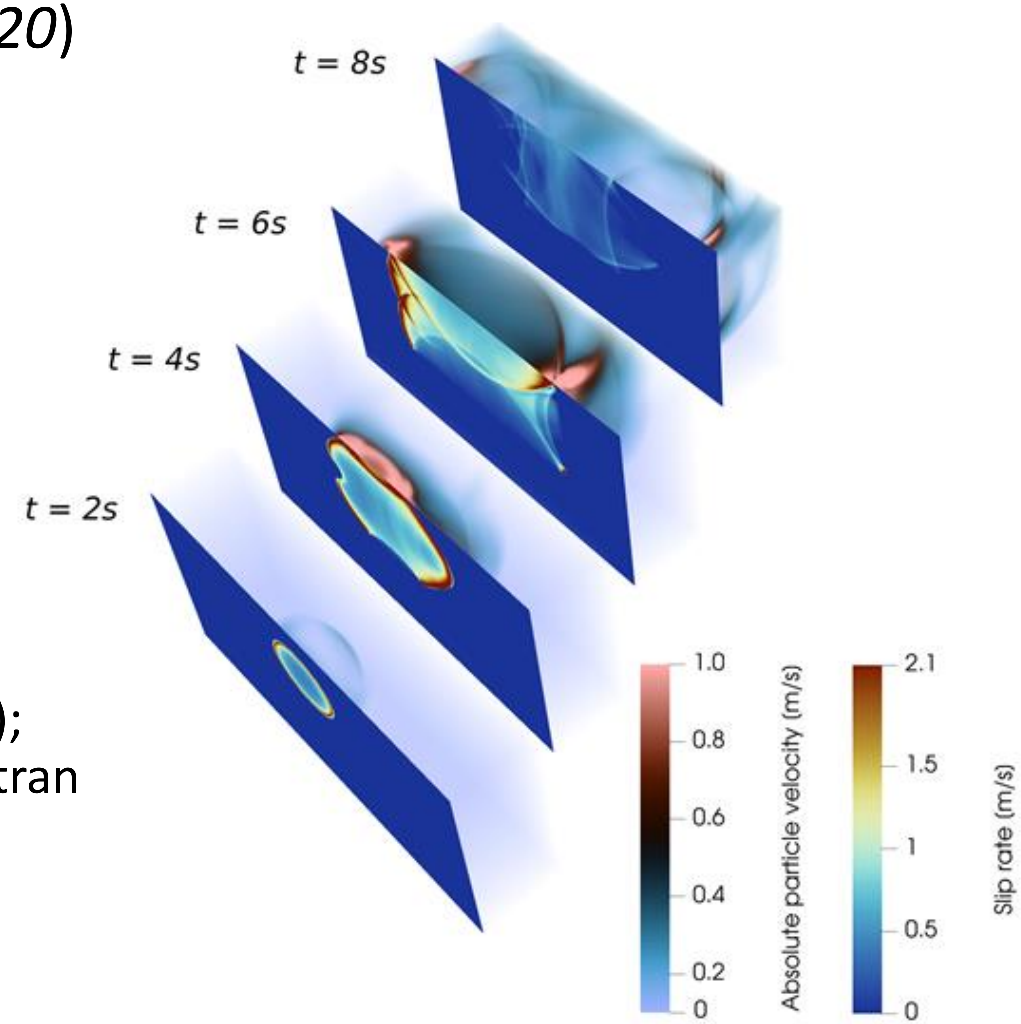

Earthquake finite-fault modeling

Beyond a point-source model:

- Kinematic rupture model:
  - Slip rates functions along the fault
  - Linear relation with ground motions (via the representation theorem)
  - Easy to handle, standard in earthquake modeling

- Dynamic rupture model (physics-based):
  - Friction law + elastodynamics
  - Non-linear relation with ground motions (via rupture simulation and representation theorem)
  - Cumbersome in some applications, still waiting for a widespread use

Dynamic rupture inversions

Dynamic slip inversions

- Problems:
  - The rupture simulation is computationally demanding, typically solved on supercomputers -> it is necessary to use a fast solver even at the cost of simplifying assumptions
  - The relation between seismograms and model parameters is strongly nonlinear -> it is necessary to use general optimization/sampling techniques (e.g., of Monte Carlo type)

- State-of-the-art:
  - Dynamic models are built "manually" by setting the parameters based on the results of kinematic slip inversions (Song and Duan, 2023; Ma et al., 2008; Peyrat et al., 2001; Olsen et al., 1997; Ide and Takeo, 1996; etc.)
  - Simplified models are considered in dynamic inversions (e.g., elliptic patch with constant parameters, Twardzik et al., 2014; Ruiz and Madariaga, 2011; *Kostka et al., 2022*)
  - Full dynamic inversion performed only few times (Peyrat a Olsen, 2004; Fukuyama a Mikumo, 1993) -> our contributions

Our applications of Bayesian dynamic source inversions so far

- 2019 Mw6.2 Amatrice (Central Italy)
  - Gallovič et al. (JGR 2019b)
- 2020 Mw 6.8 Elazığ (Turkey)
  - Gallovič et al. (CommEE 2020)
- Mw 6.0 2014 South Napa (California)
  - Premus et al. (Science Advances, 2022)
- 2017 Mw 6.3 Lesvos (Greece)
  - Kostka et al. (GJI 2022)
- 2011 and 2016 Mw 5.8 Ibaraki twins (Japan)
  - Gallovič (in prep.)
- 2004 Mw Parkfield (California)
  - Schliwa et al. (in prep.)

The 2020 Elazığ (Sivrice), Turkey, earthquake

Gallovič et al. (Comm. Earth & Env., 2020)

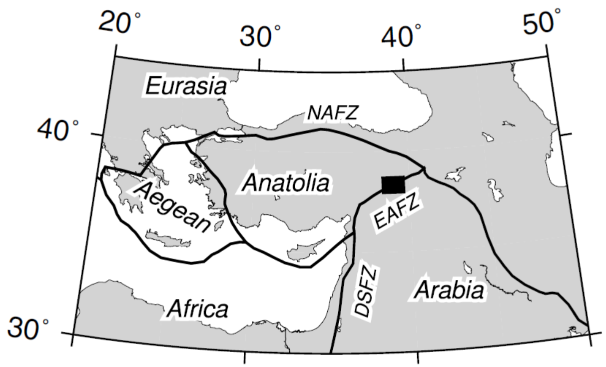

AFAD MINISTRY OF INTERIOR DISASTER AND EMERGENCY MANAGEMENT PRESIDENCY

T.C. İÇİŞLERİ BAKANLIĞI
AFET ve ACİL DURUM YÖNETİMİ BAŞKANLIĞI
Deprem Dairesi Başkanlığı

2020 Elazığ earthquake

UTC time	2020-01-24 17:55:14
ISC event	617204417
USGS-ANSS	ComCat
Local date	24 January 2020
Local time	20:55 TRT (UTC+3:00)
Duration	40 seconds
Magnitude	6.7 M_w[1]
Depth	10.0 km (6 mi)
Epicentre	38.390°N 39.081°E
Fault	East Anatolian Fault
Type	Strike-slip
Max. intensity	VIII (*Severe*)
Aftershocks	Numerous 17 with a M_w 4.0 or greater Largest: M_w 5.1 at 16:30 UTC, 25 January 2020
Casualties	41 fatalities, 1,600+ injuries

Wikipedia

Mainshock relocation

- Two nucleations?

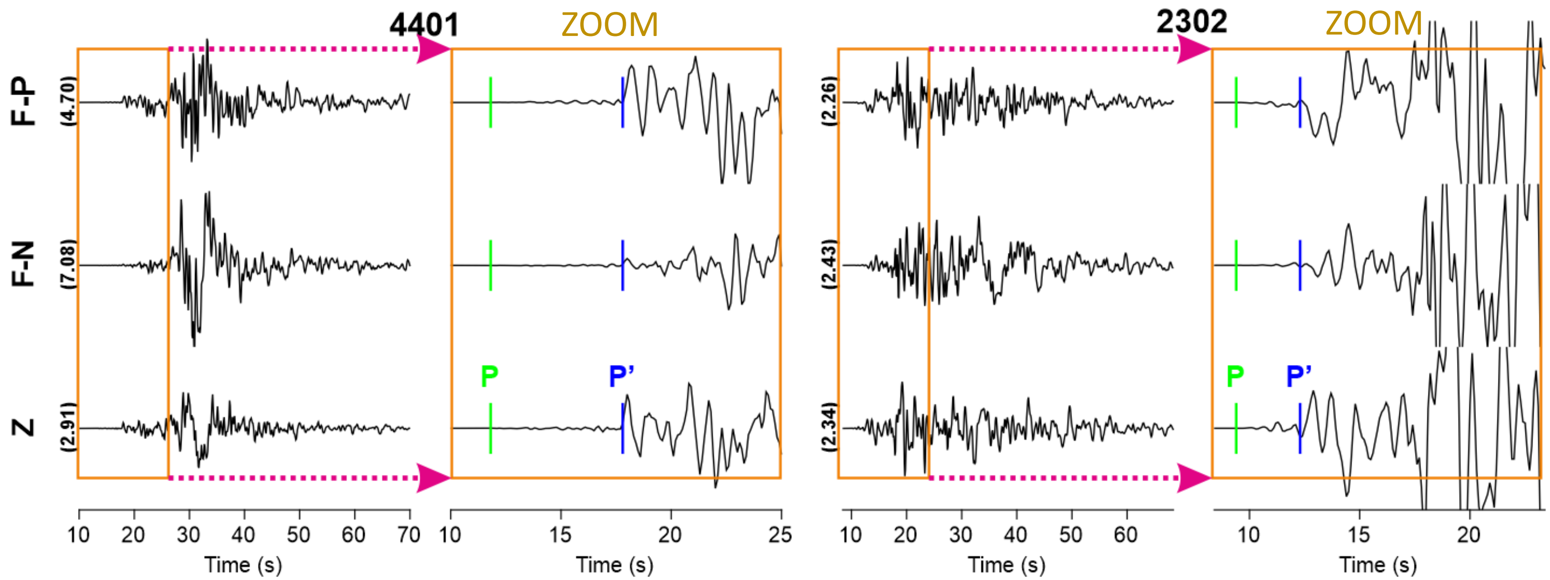

Velocity waveforms (0.05-2.5Hz)

Data from Disaster and Emergency Management Authority Presidential of Earthquake Department (AFAD)

Mainshock relocation

- P-onsets from 10 strong-motion (SM) and 8 broadband (BB) records at distances <110 km.
- NonLinLoc probabilistic method in several velocity models with significant effect mainly upon the source depth (preferred model VM1 by Acarel et al., 2019).
- Epicenter well constrained with +/−2 km uncertainty in the NNW-SSE direction, depth poorly constrained between 10 and 20 km; S-minus-P travel time difference of 3.9 s at the nearest SM station (2308) suggests depth of 12–14 km.
- Certain SM stations with large time residuals (obviously due to GPS time error) excluded them from the relocation; for waveform modeling, two important SM stations with the large residuals corrected.
- P'-onsets -> hypocenter H' at 0-10 km depth and ~4.5 s after the origin time.

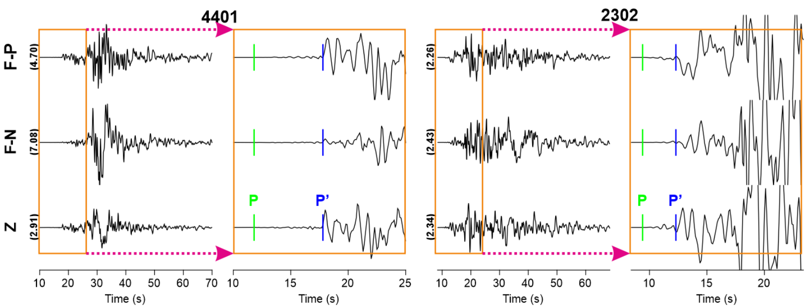

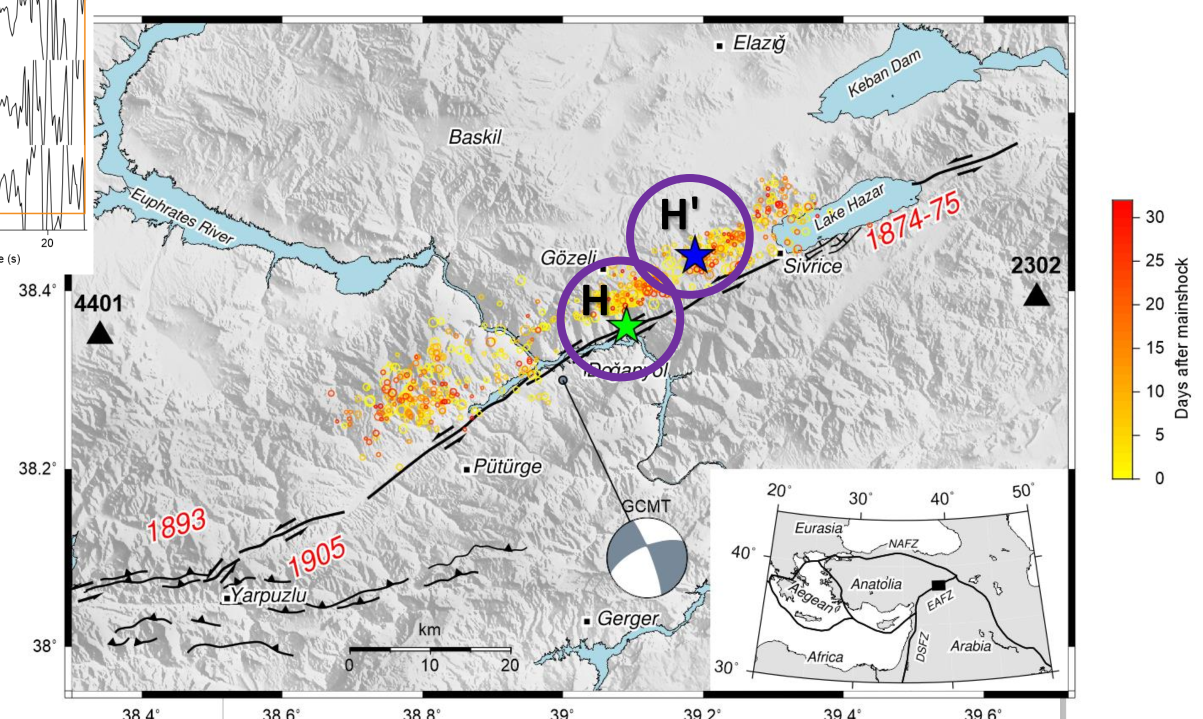

Multiple-point source (MPS) model

- Focal mechanisms of the subevents are remarkably similar (despite being free in the inversion).
- The focal mechanism of the latest subevent appears to have a gentler fault dip (in agreement with aftershocks) and a thrust-faulting component.
- The first-motion polarities of P point to left-lateral strike-slip faulting mechanism of initial nucleation (too weak to be captured by a subevent).

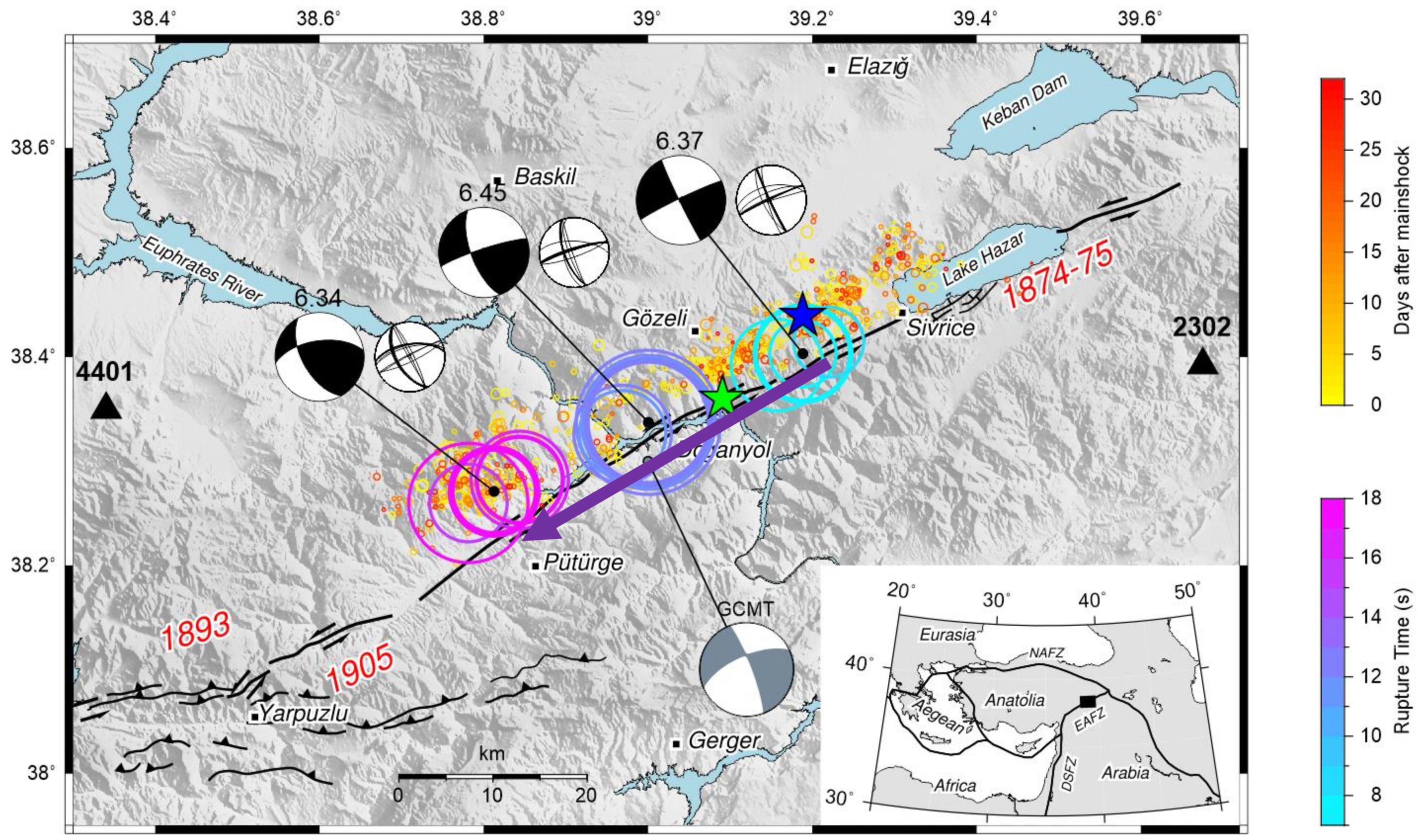

Rupture propagation (slip rates)

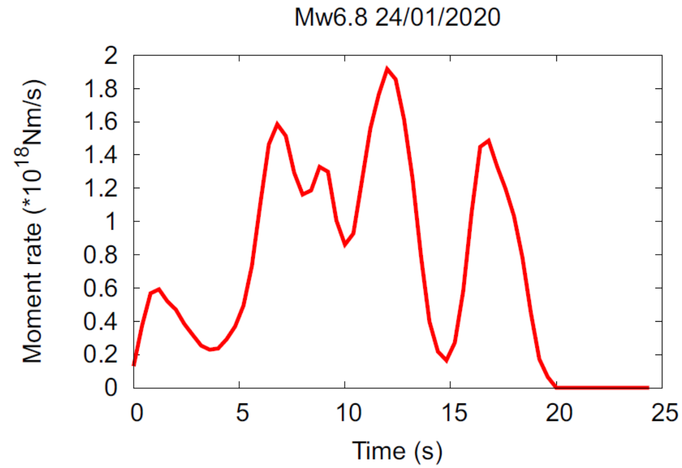

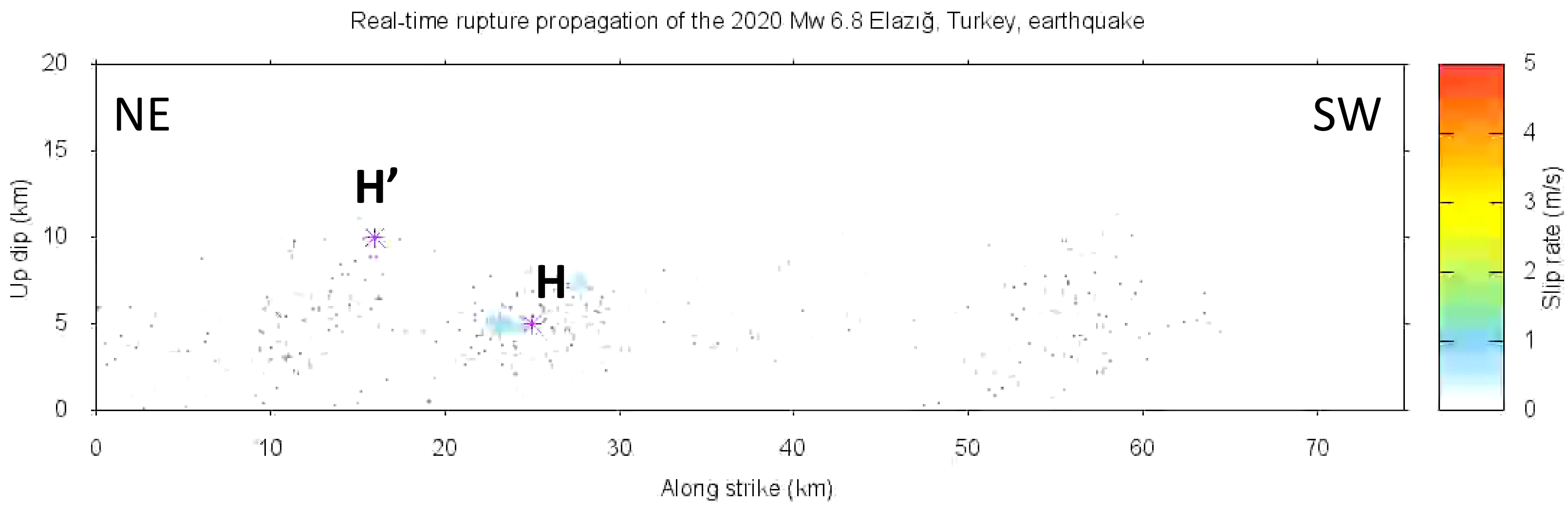

2020 Elazığ (Sivrice), Turkey

Maximum a-posteriori model
(after weeks of multi-GPU runs,
visiting ~1M models)

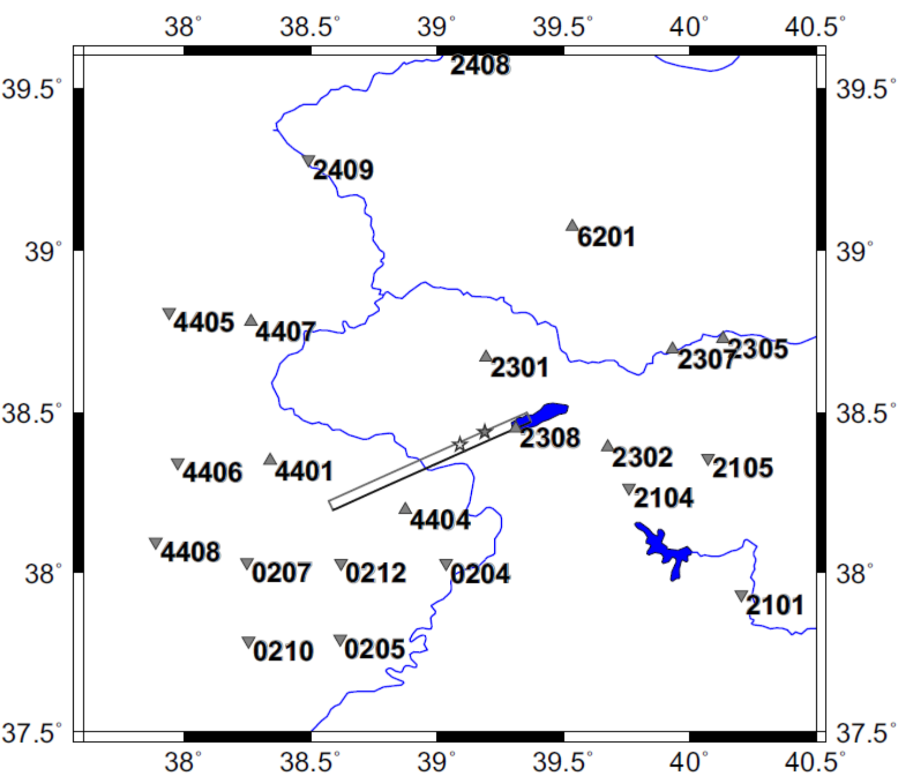

Data from Disaster and Emergency Management Authority
Presidential of Earthquake Department (AFAD)

Kinematic and dynamic parameters of the rupture model

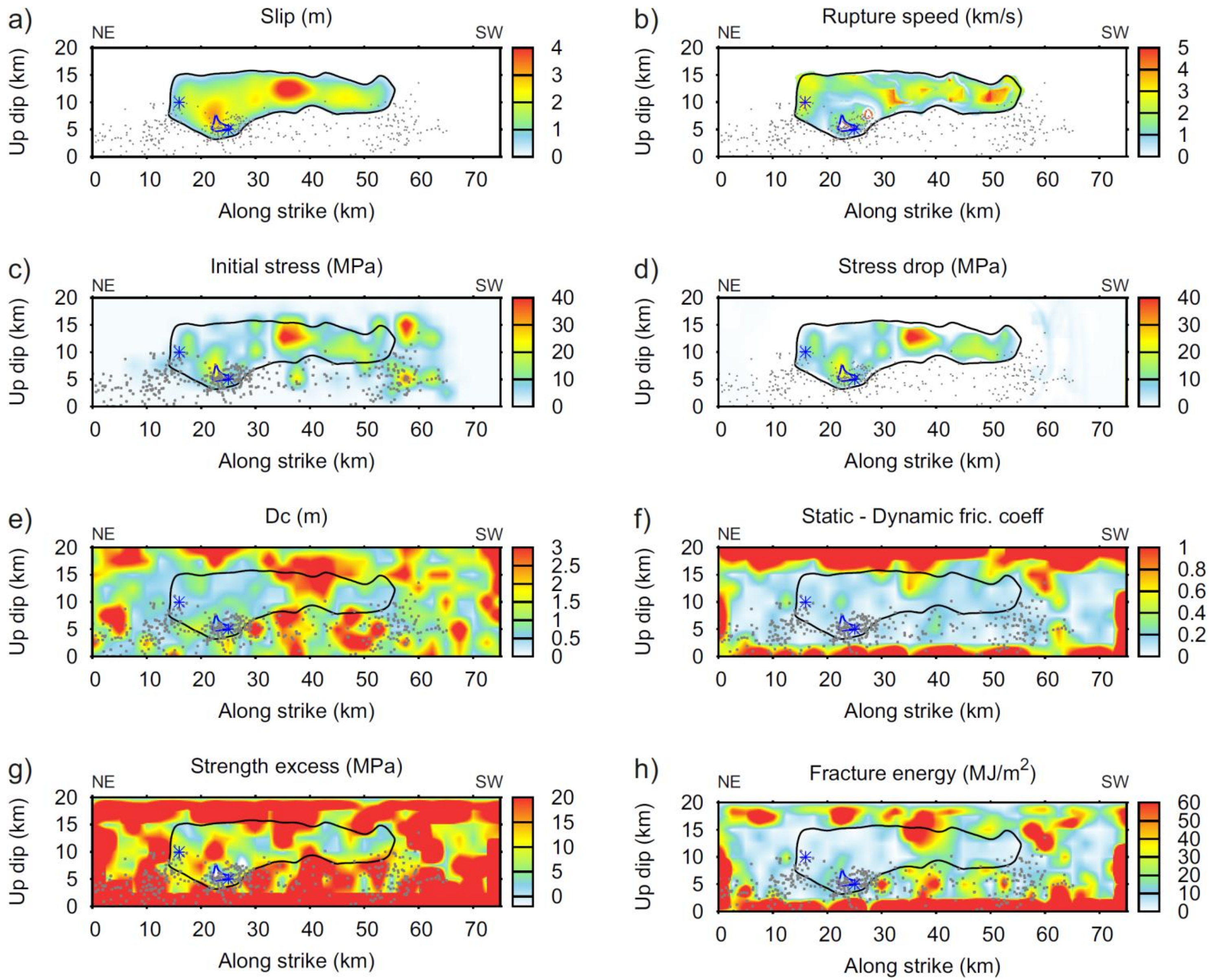

Inversion of ASTFs (China Sea deep event)

INTER-EXCELLENCE II (MŠMT) project on

Dynamics of subducting slabs and origin of deep-focus earthquakes

ASTFs obtained by EGF method

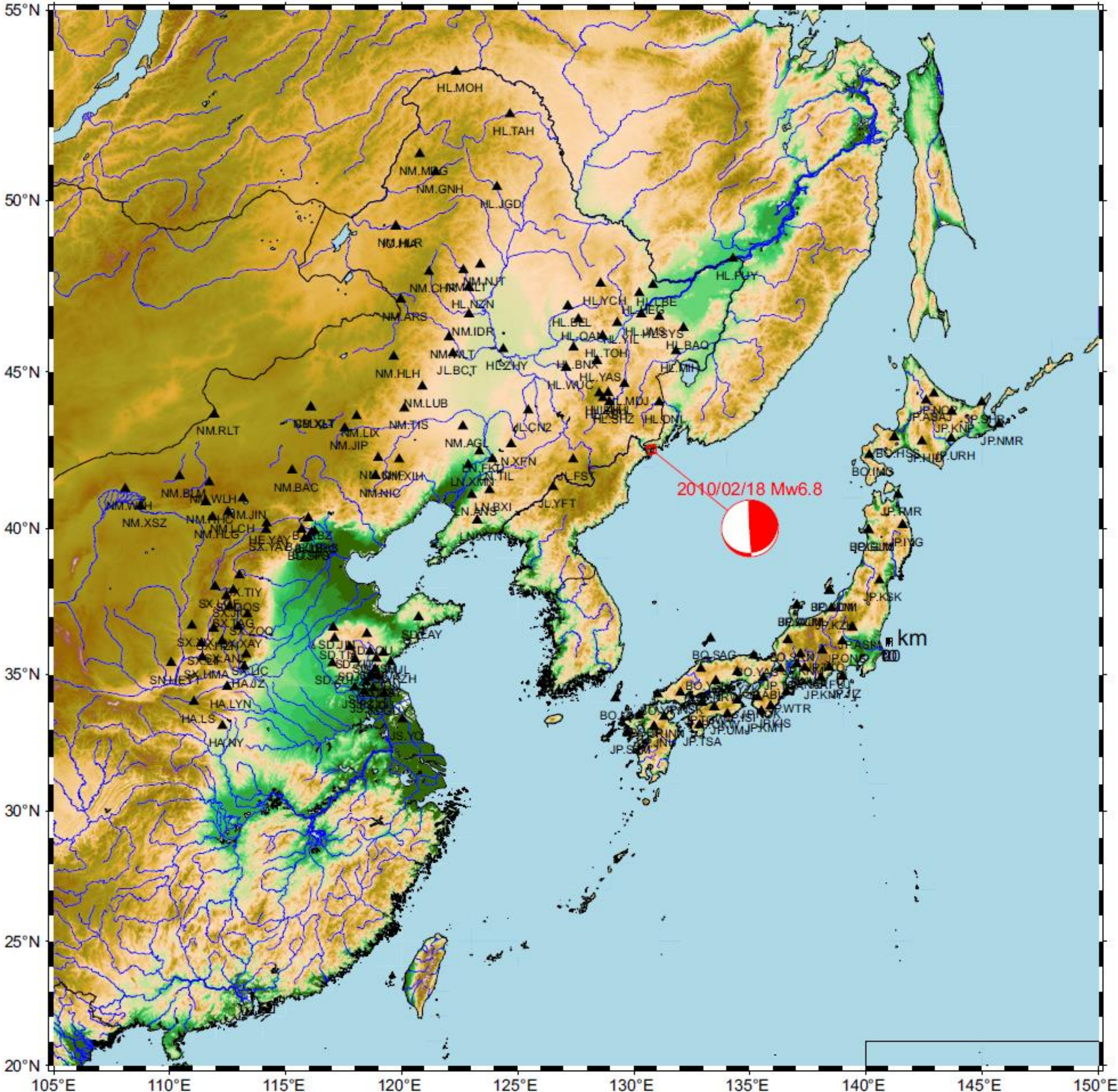

China Sea deep earthquake

- Parameters of the event
  - Depth 574 km
  - Origin time: 2010-02-18, 01:13:18
  - Mw6.8
  - Subhorizontal fault plane likely within metastable olivine wedge (MOW) in the deepest tip of Pacific slab under Northeastern China
- Assumed parameters of the model
  - Friction law: Slip weakening
  - Normal stress: 21GPa, const.
  - Velocity model: Vp=10.16km/s, Vs=5.52km/s, const.
- Dynamic rupture inversion of apparent source time functions (ASTFs) obtained by EGF deconvolution (Plicka et al., 2022).

ASTF fit

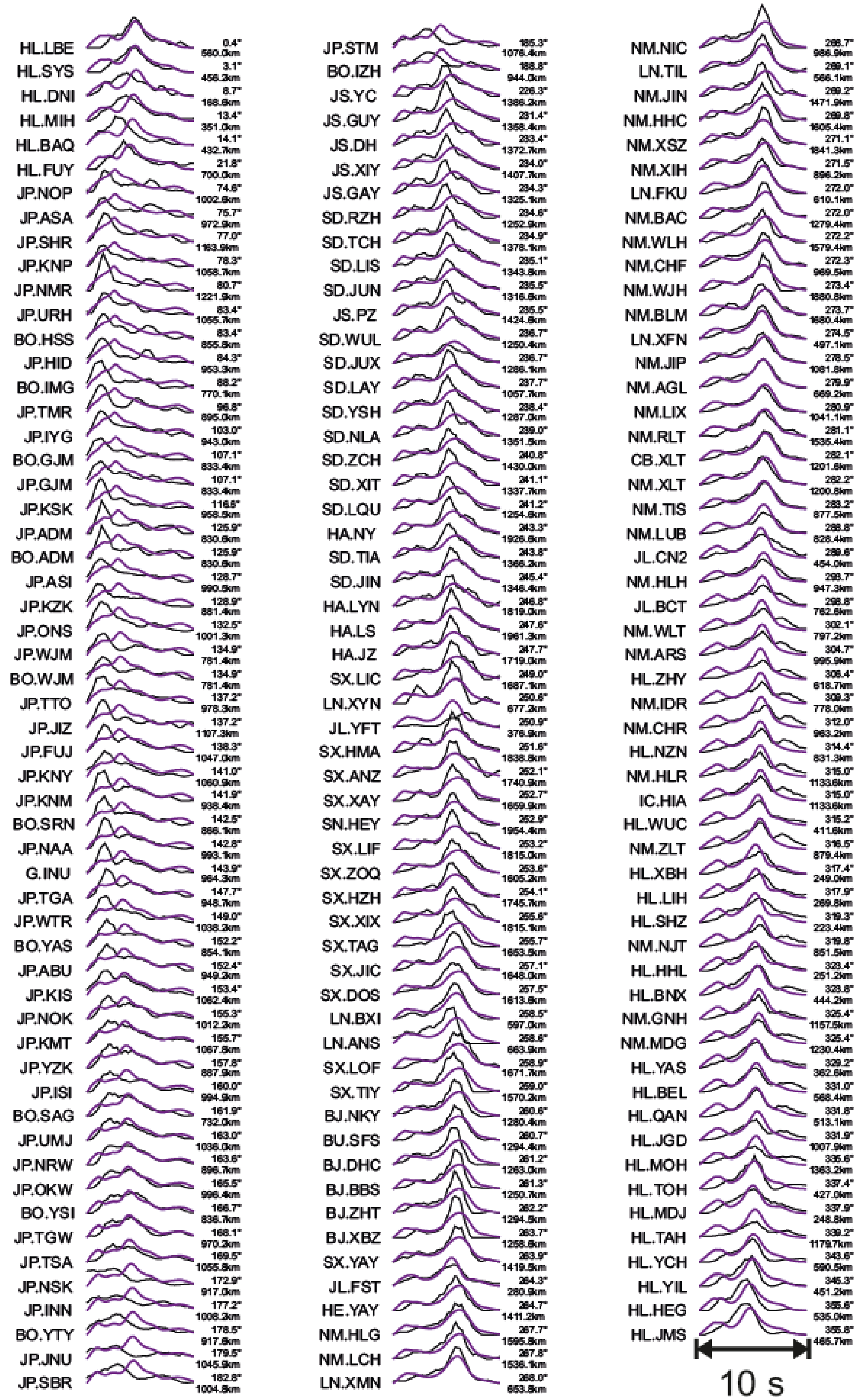
HL.LBE
HL.SYS
HL.DNI
HL.MIH
HL.BAQ
HL.FUY
JP.NOP
JP.ASA
JP.SHR
JP.KNP
JP.NMR
JP.URH
BO.HSS
JP.HID
BO.IMG
JP.TMR
JP.IYG
BO.GJM
JP.GJM
JP.KSK
JP.ADM
BO.ADM
JP.ASI
JP.KZK
JP.ONS
JP.WJM
BO.WJM
JP.TTO
JP.JIZ
JP.FUJ
JP.KNY
JP.KNM
BO.SRN
JP.NAA
G.INU
JP.TGA
JP.WTR
BO.YAS
JP.ABU
JP.KIS
JP.NOK
JP.KMT
JP.YZK
JP.ISI
BO.SAG
JP.UMJ
JP.NRW
JP.OKW
BO.YSI
JP.TGW
JP.TSA
JP.NSK
JP.INN
BO.YTY
JP.JNU
JP.SBR
JP.STM
BO.IZH
JS.YC
JS.GUY
JS.DH
JS.XIY
JS.GAY
SD.RZH
SD.TCH
SD.LIS
SD.JUN
JS.PZ
SD.WUL
SD.JUX
SD.LAY
SD.YSH
SD.NLA
SD.ZCH
SD.XIT
SD.LQU
HA.NY
SD.TIA
SD.JIN
HA.LYN
HA.LS
HA.JZ
SX.LIC
LN.XYN
JL.YFT
SX.HMA
SX.ANZ
SX.XAY
SN.HEY
SX.LIF
SX.ZOQ
SX.HZH
SX.XIX
SX.TAG
SX.JIC
SX.DOS
LN.BXI
LN.ANS
SX.LOF
SX.TIY
BJ.NKY
BU.SFS
BJ.DHC
BJ.BBS
BJ.ZHT
BJ.XBZ
SX.YAY
JL.FST
HE.YAY
NM.HLG
NM.LCH
LN.XMN
NM.NIC
LN.TIL
NM.JIN
NM.HHC
NM.XSZ
NM.XIH
LN.FKU
NM.BAC
NM.WLH
NM.CHF
NM.WJH
NM.BLM
LN.XFN
NM.JIP
NM.AGL
NM.LIX
NM.RLT
CB.XLT
NM.XLT
NM.TIS
NM.LUB
JL.CN2
NM.HLH
JL.BCT
NM.WLT
NM.ARS
HL.ZHY
NM.IDR
NM.CHR
HL.NZN
NM.HLR
IC.HIA
HL.WUC
NM.ZLT
HL.XBH
HL.LIH
HL.SHZ
NM.NJT
HL.HHL
HL.BNX
NM.GNH
NM.MDG
HL.YAS
HL.BEL
HL.QAN
HL.JGD
HL.MOH
HL.TOH
HL.MDJ
HL.TAH
HL.YCH
HL.YIL
HL.HEG
HL.JMS
10 s

ASTF fit

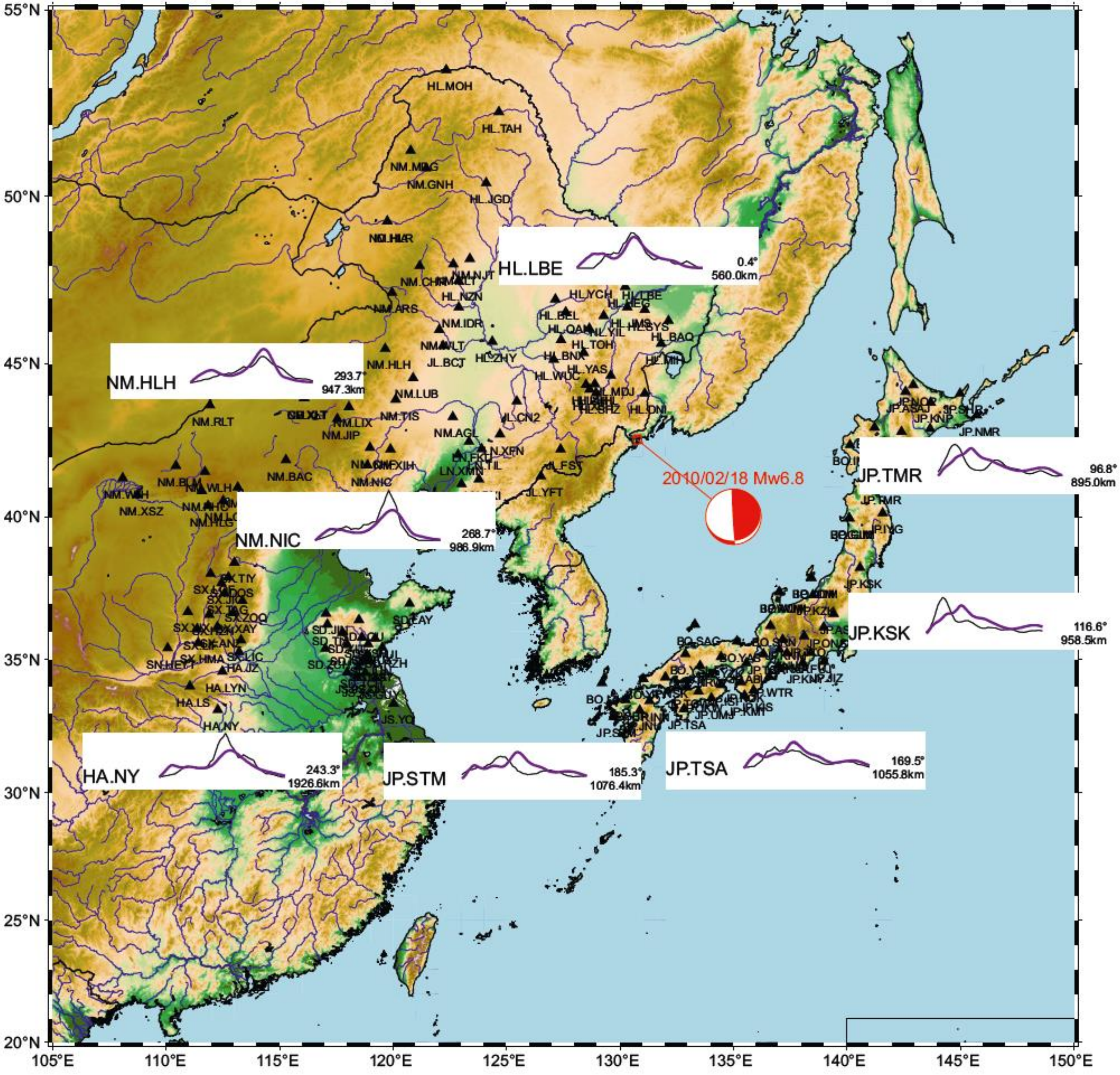
HL.LBE 0.4° 560.0km
NM.HLH 293.7° 947.3km
NM.NIC 268.7° 986.9km
JP.TMR 96.8° 895.0km
JP.KSK 116.6° 958.5km
HA.NY 243.3° 1926.6km
JP.STM 185.3° 1076.4km
JP.TSA 169.5° 1055.8km
2010/02/18 Mw6.8
HL.MOH
HL.TAH
NM.GNH
HL.JGD
NM.ARS
NM.IDR
NM.LUB
NM.TIS
NM.AGL
NM.RLT
NM.JIP
NM.BAC
NM.XSZ
JL.YFT
HL.YCH
HL.BEL
HL.TOH
HL.BNX
HL.YAS
HL.DNI
HL.MDJ
HL.BAQ
HL.MIH
JL.BCT
HL.ZHY
HA.LYN
HA.LS
HA.NY
SD.CAY
JS.YC
JP.NMR
JP.TMR
JP.KSK
JP.TSA
BO.SAG
JP.WTR
55°N
50°N
45°N
40°N
35°N
30°N
25°N
20°N
105°E
110°E
115°E
120°E
125°E
130°E
135°E
140°E
145°E
150°E

Slip distribution and rupture evolution (MAP model)

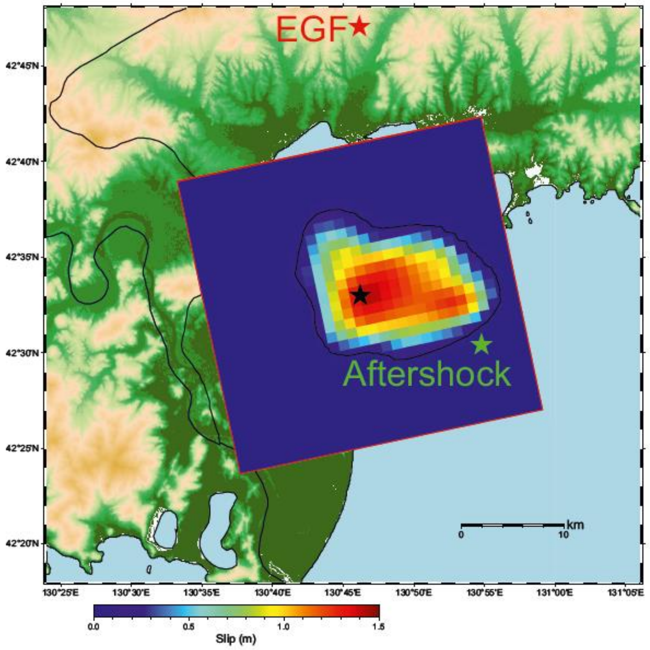

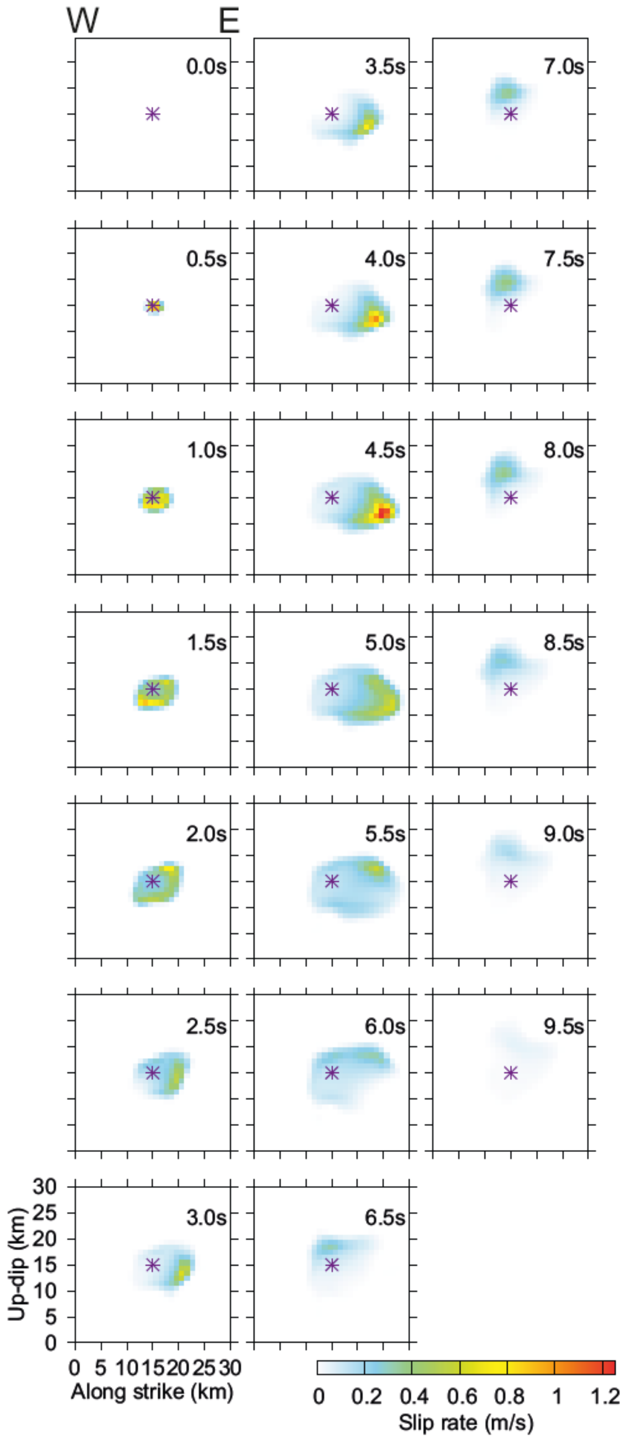

Uncertainty analysis

(from 3270 accepted models)

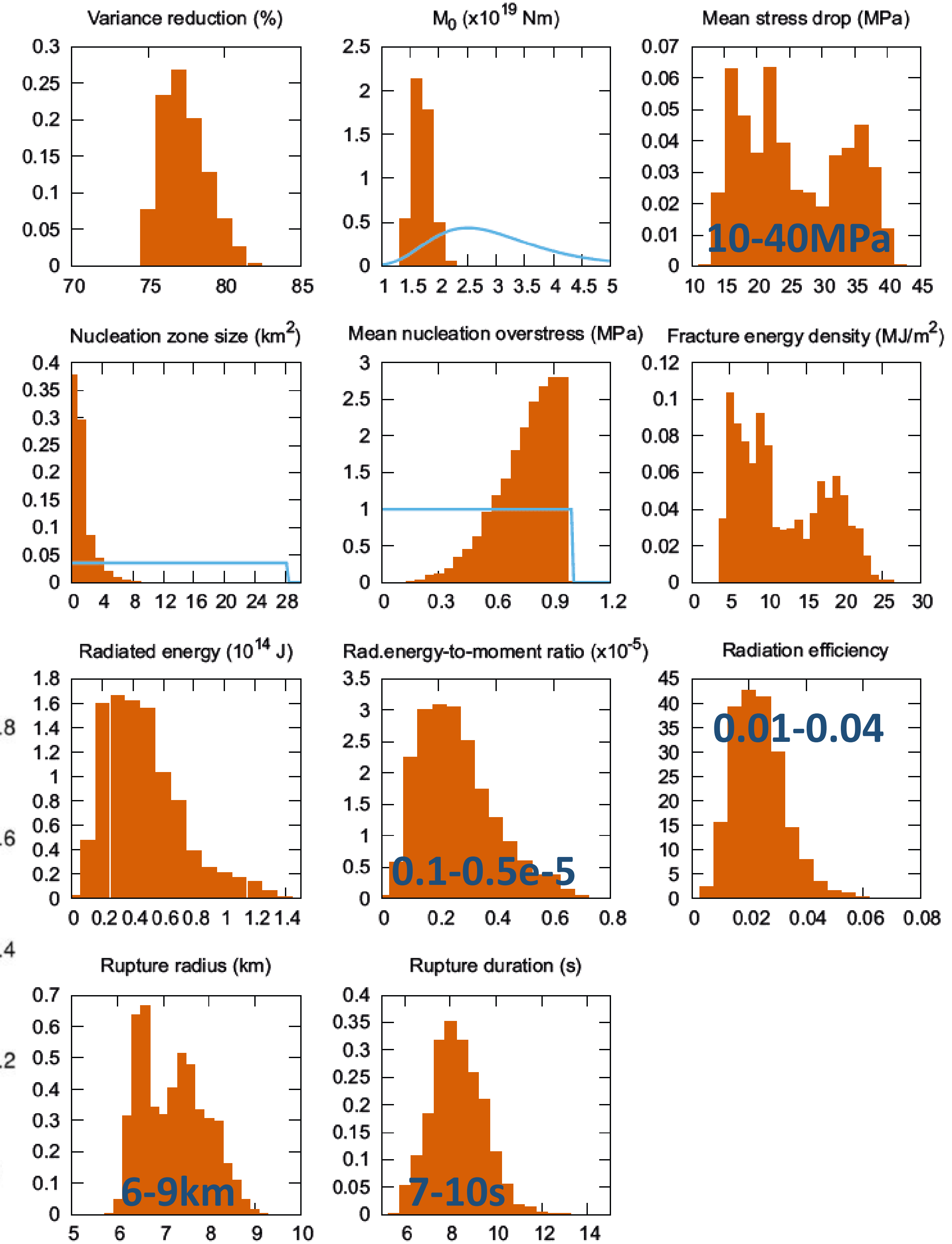

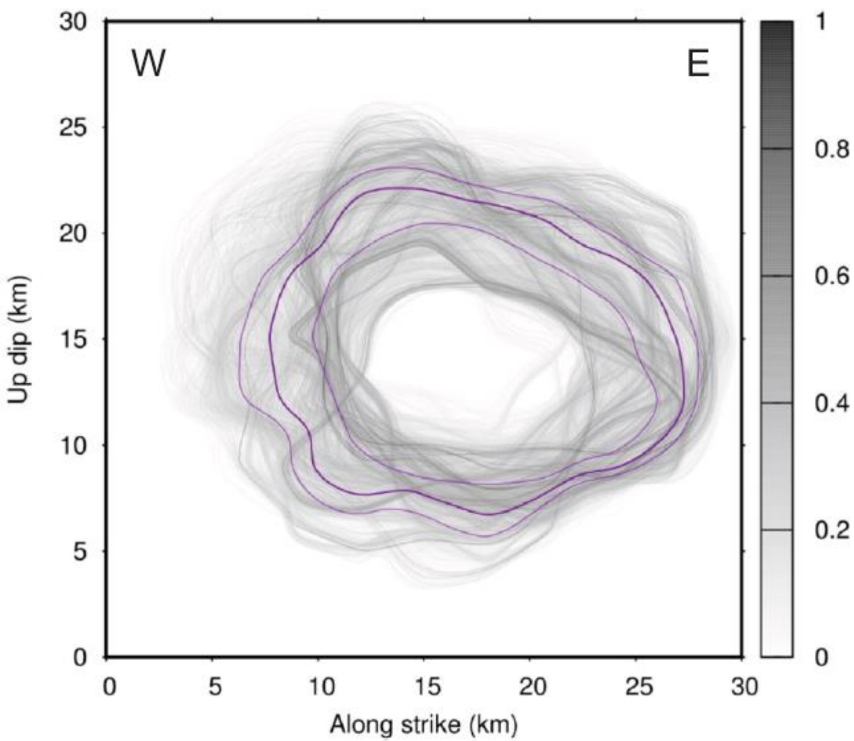

Stress drop variability

Gallovič, F., Valentová, Ľ. (2020). Earthquake stress drops from dynamic rupture simulations constrained by observed ground motions, Geophys. Res. Lett. 47, e2019GL085880.

Properties of the model ensemble

- Calculation performed on a farm of 12 GPUs and supercomputer IT4I in Ostrava (Czech Republic) using FD3D_TSN (Premus et al., 2020)
  - Number of models saved: ~1700
  - Number of models visited: ~250k
- Magnitudes range from 5.8 to 6.8
- Fit of GMPEs at various periods after normalization to Mw6.5:

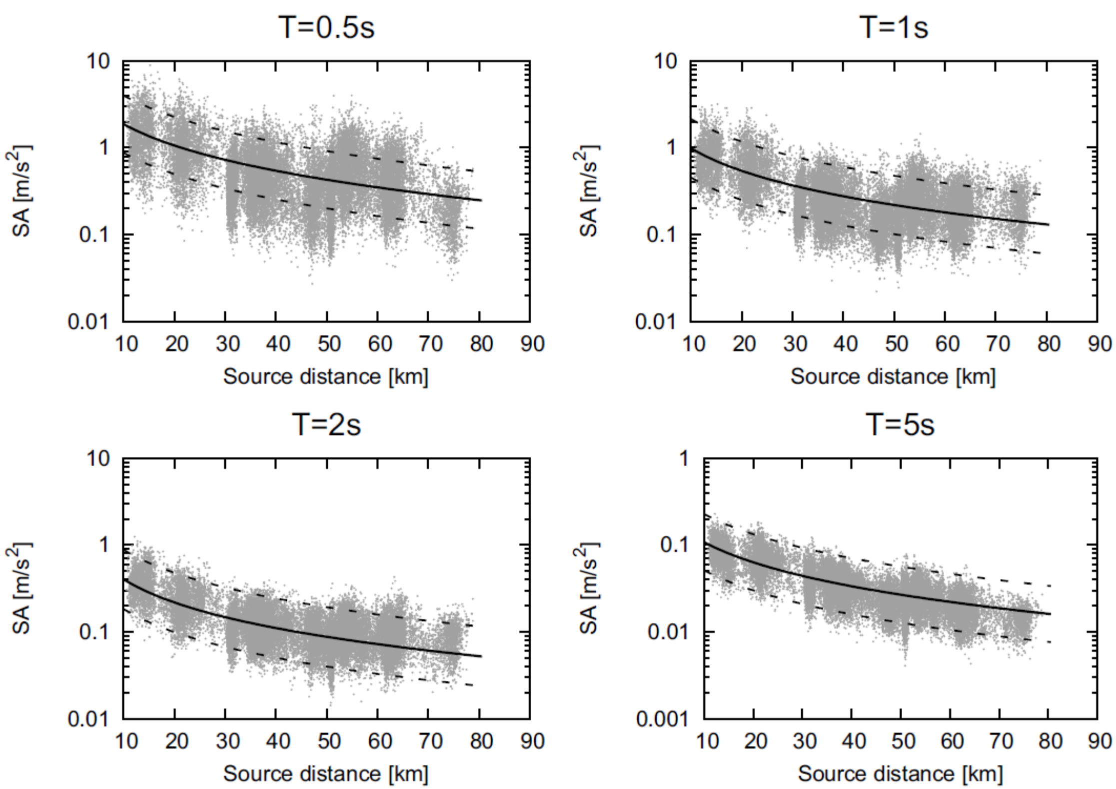

GMPE within-event variability ~ 0.4

Properties of the model ensemble

- Examples of moment rate functions for Mw 6.2:
  - Duration 4-10s
  - Single/multiple peaks

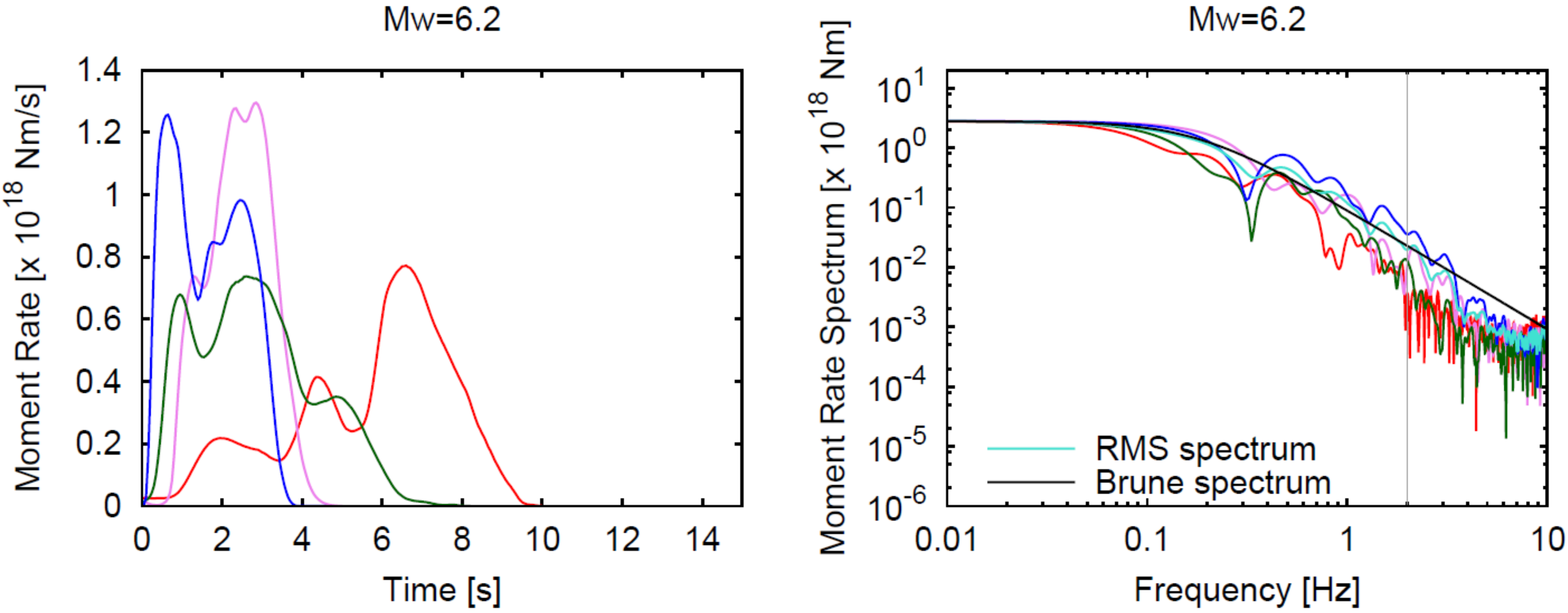

Properties of the model ensemble

- Examples of moment rate functions for Mw 6.2:
  - Duration 4-10s
  - Single/multiple peaks

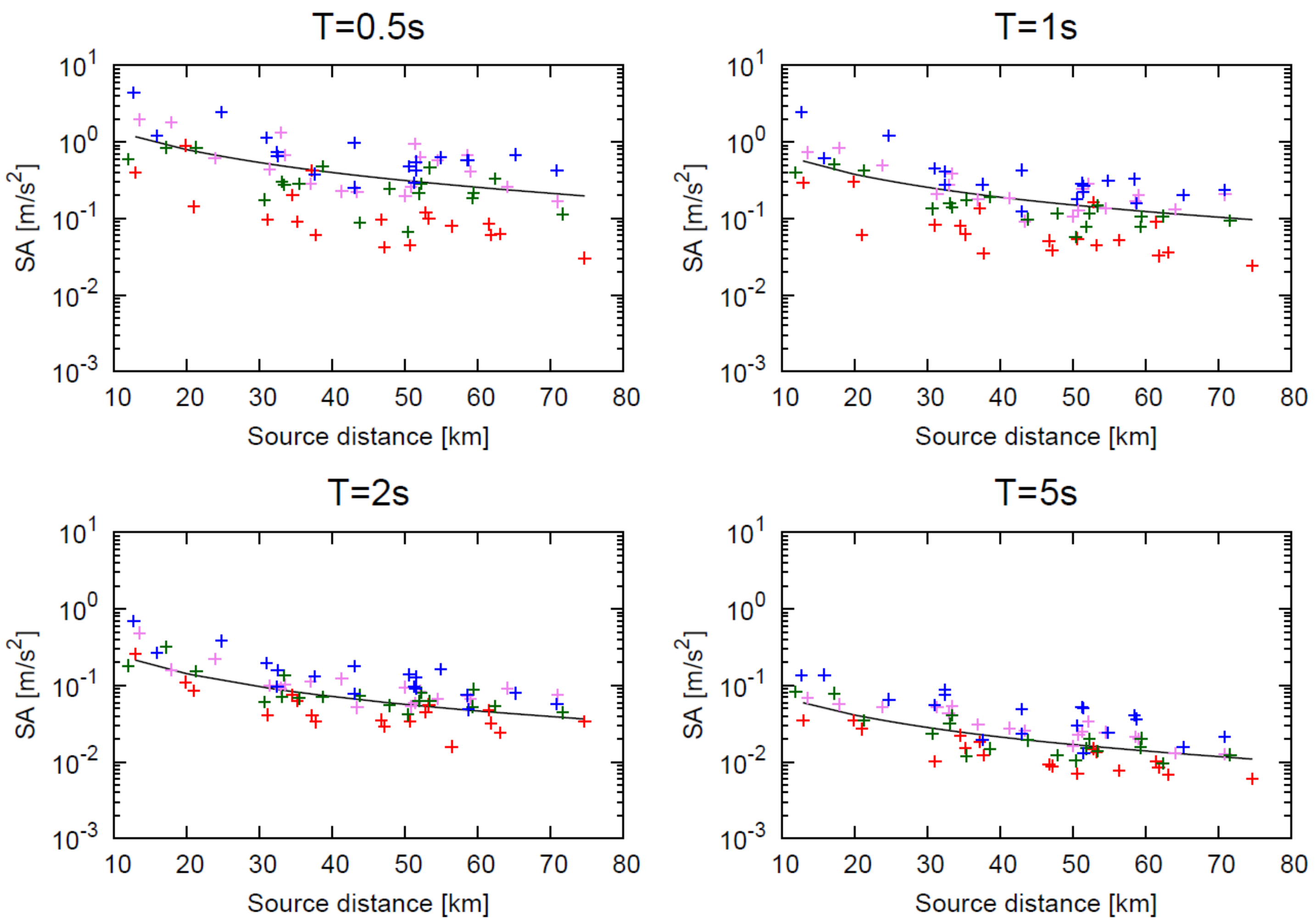

Synthetic database of dynamic ruptures

- The dynamic parameters are heterogeneous on the fault to permit complex rupture propagation

Examples of Mw6.2

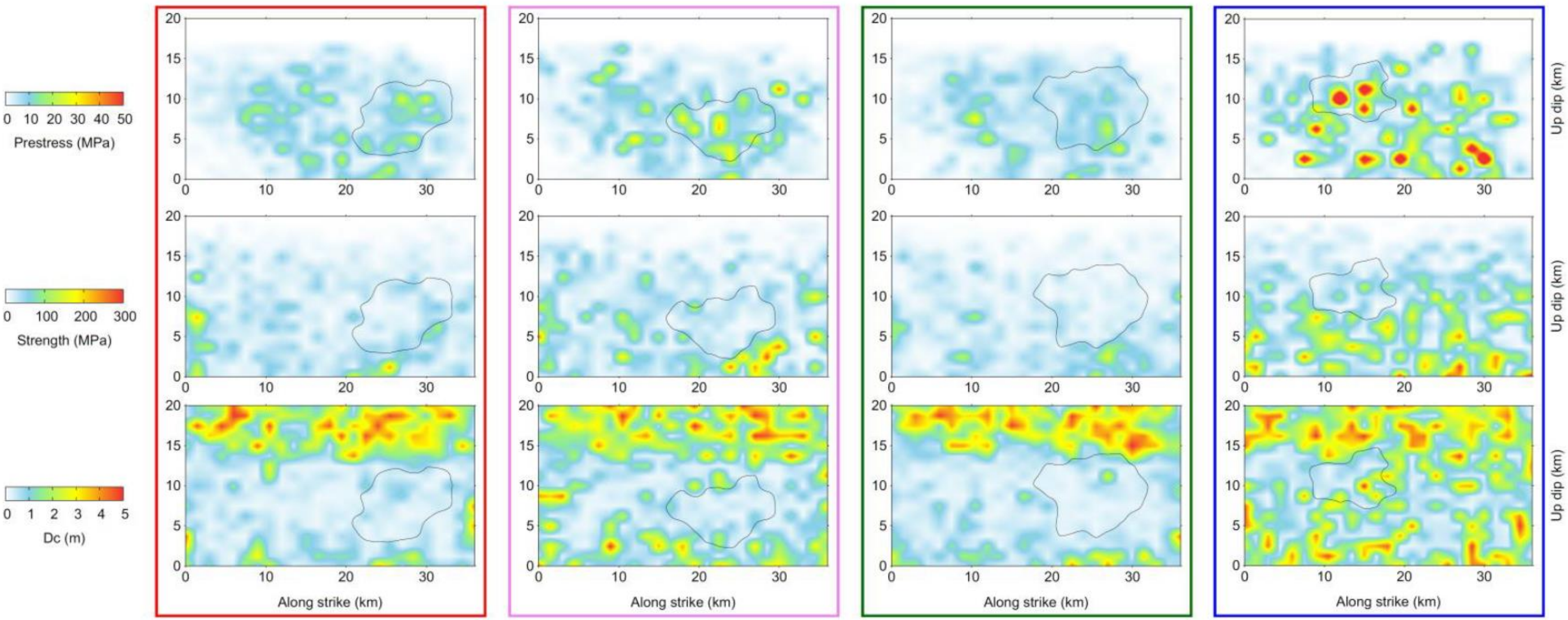

Synthetic database of dynamic ruptures

Examples of Mw6.2

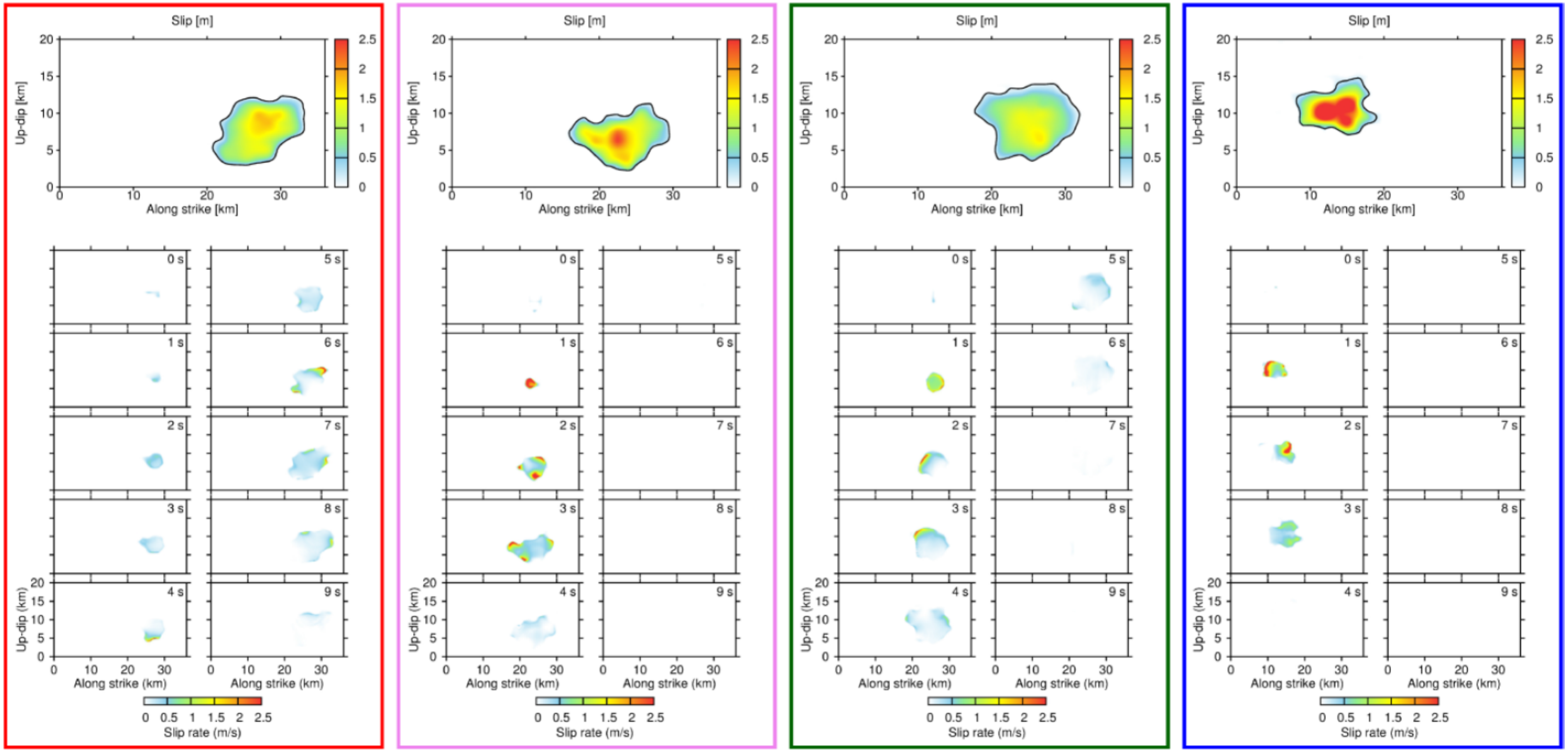

Stress drop variability

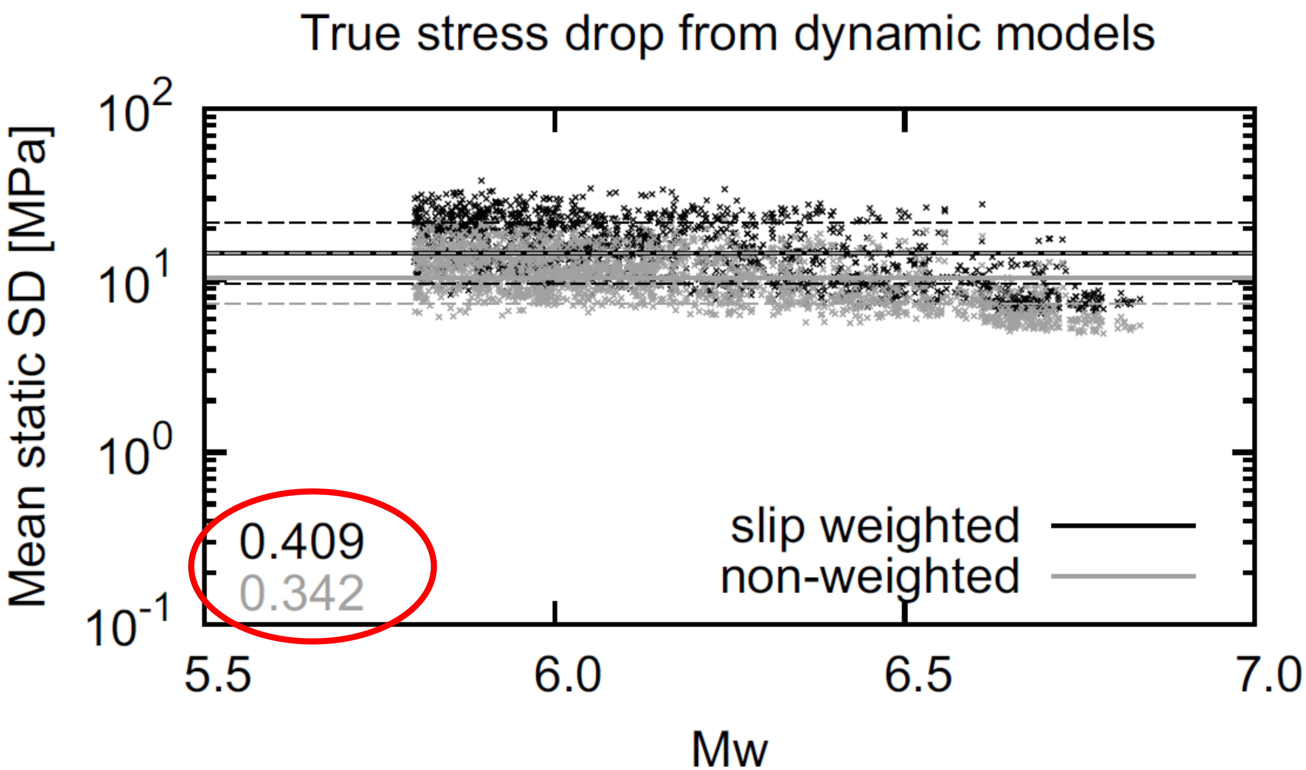

$$\Delta\tau_s = \frac{\int \Delta\tau D \, dS}{\int D \, dS}$$

$$\Delta\tau_{s_{nw}} = \frac{1}{S}\int \Delta\tau \, dS$$

Stress drop variability

- Variability of the effective stress drop variability comparable with real-data observations (~1.0, Courboulex et al., 2016)
- However, it is ~3x larger than the actual on-fault stress drop.

$$\Delta\tau_{e_f} = \frac{7}{16} M_0 \left(\frac{f_c}{k_2 v_s}\right)^3$$

$$\Delta\tau_{e_T} = \frac{7}{16} M_0 \left(\frac{1}{k_1 v_s T}\right)^3$$

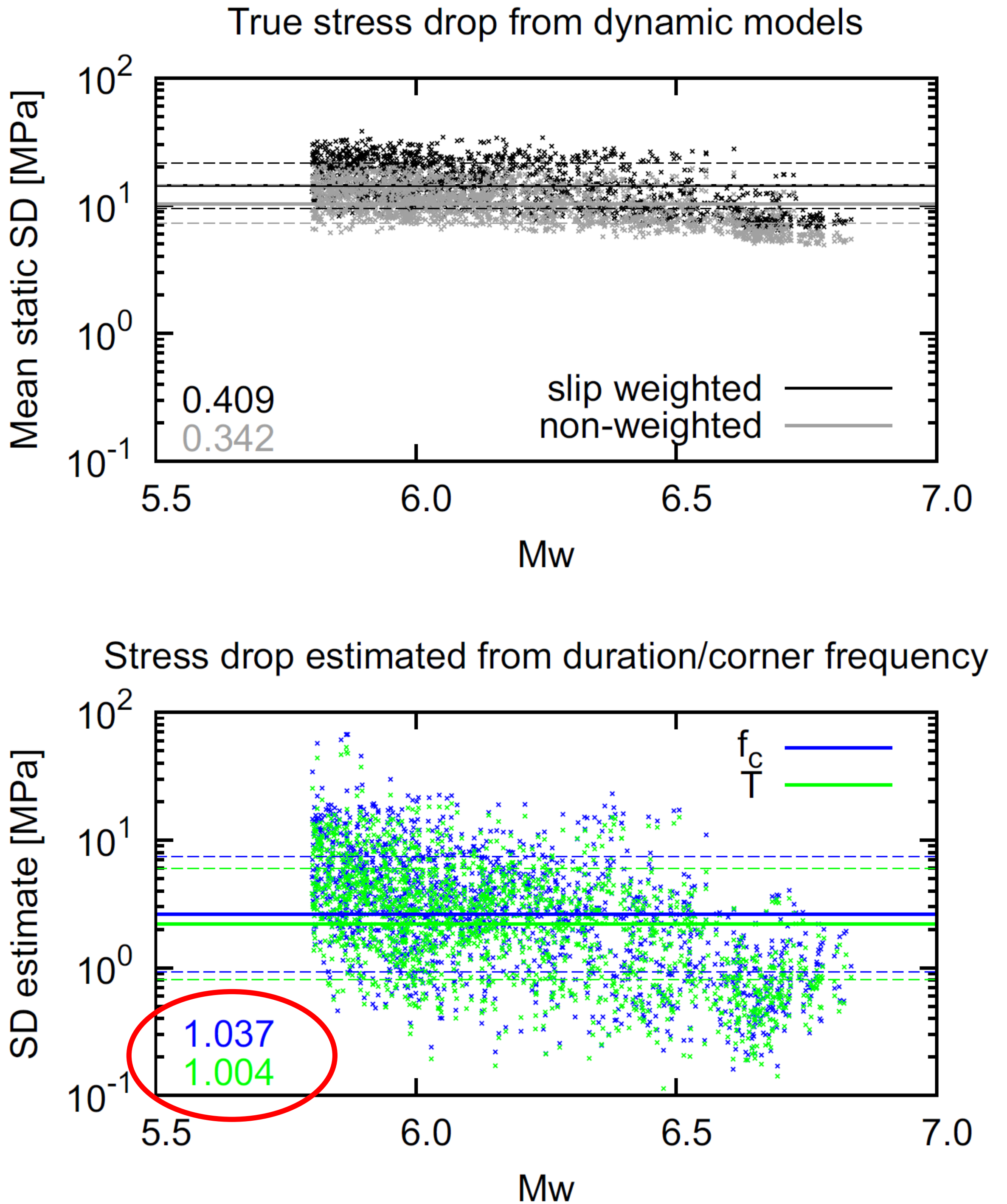

Dependence of PGV on stress drop

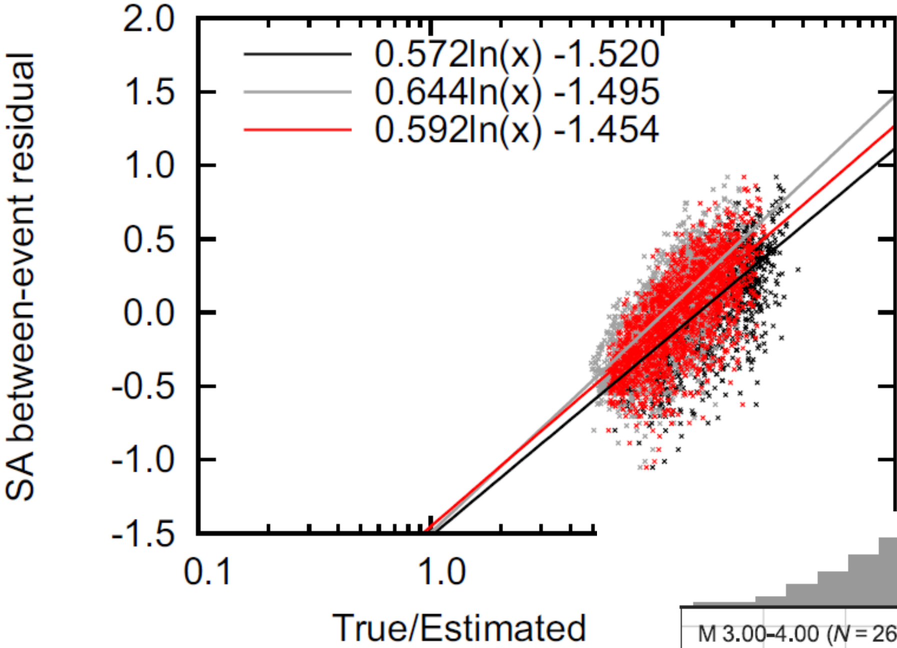

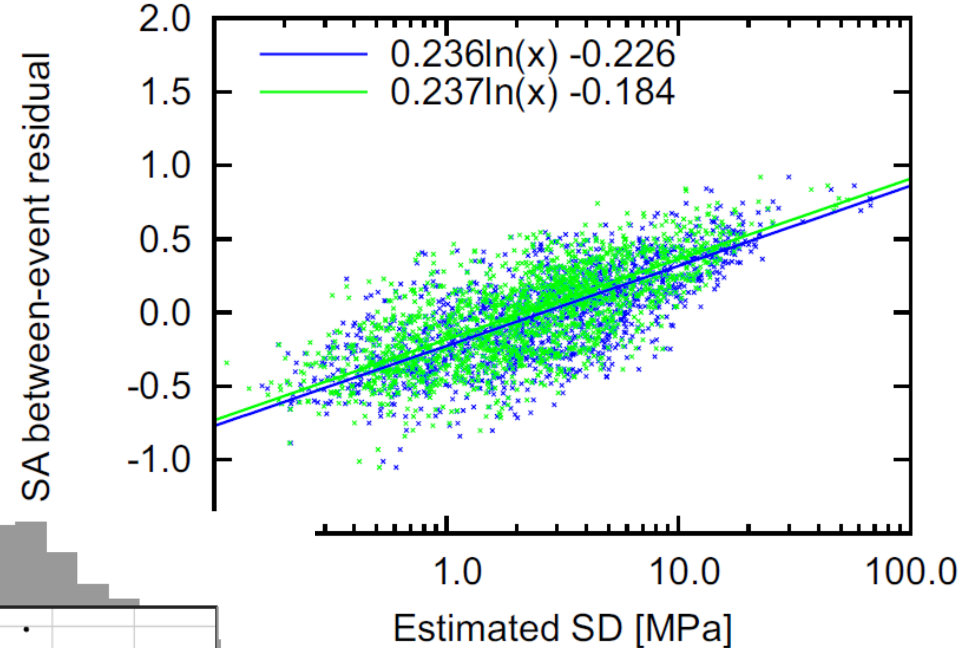

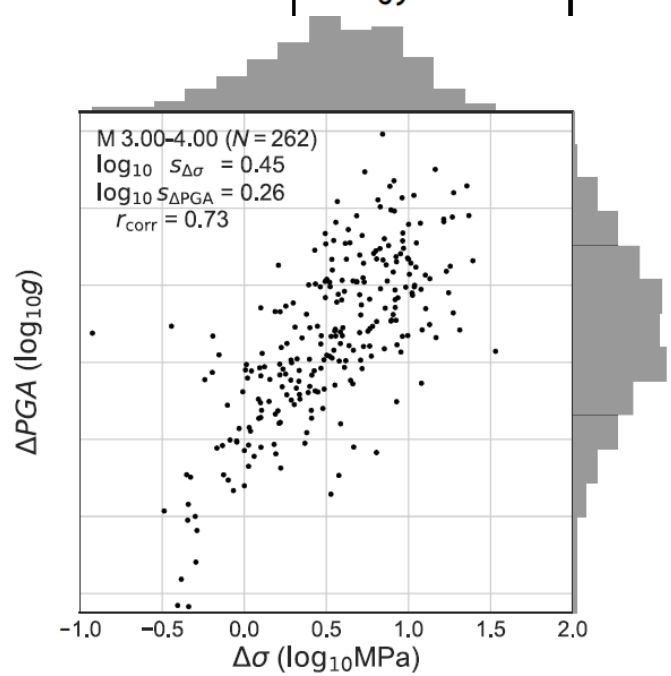

Real-data observation
(Trugman and Shearer, 2018)

Towards broadband ground motion simulations

Gallovič, F., Valentová, Ľ. (2023). Broadband strong ground motion modeling using planar dynamic rupture with fractal parameters, J. Geophys. Res. Solid Earth 128, e2023JB026506.

Rupture with (approx.) constant Vr

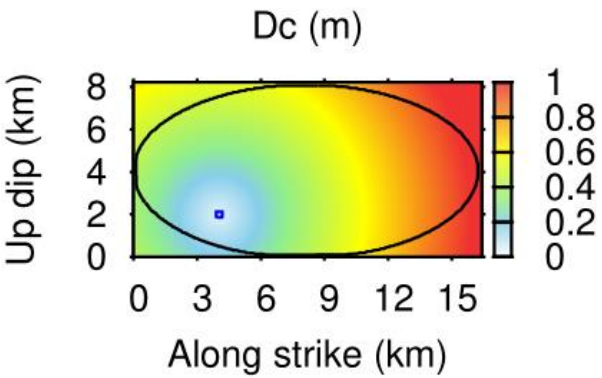

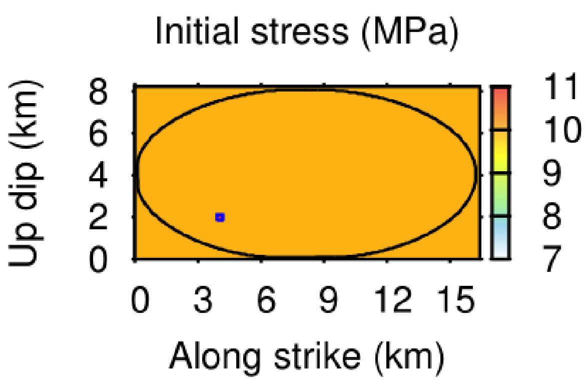

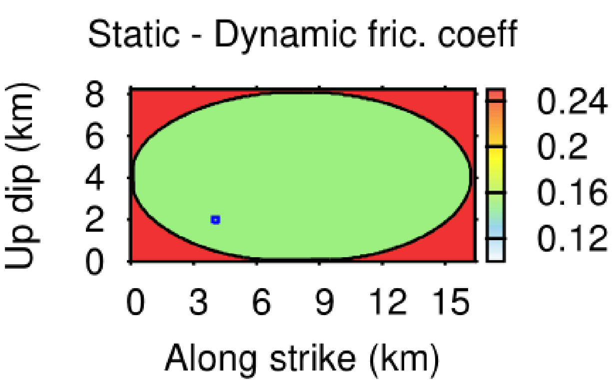

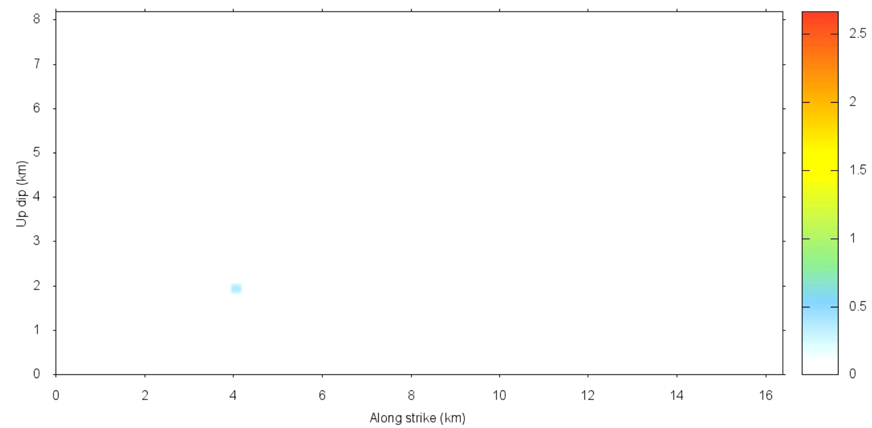

Rupture simulation up to 10 Hz in 30 mins on a GPU using efficient code FD3D_TSN for planar rupture (Premus et al., 2020)

Rupture with (approx.) constant Vr

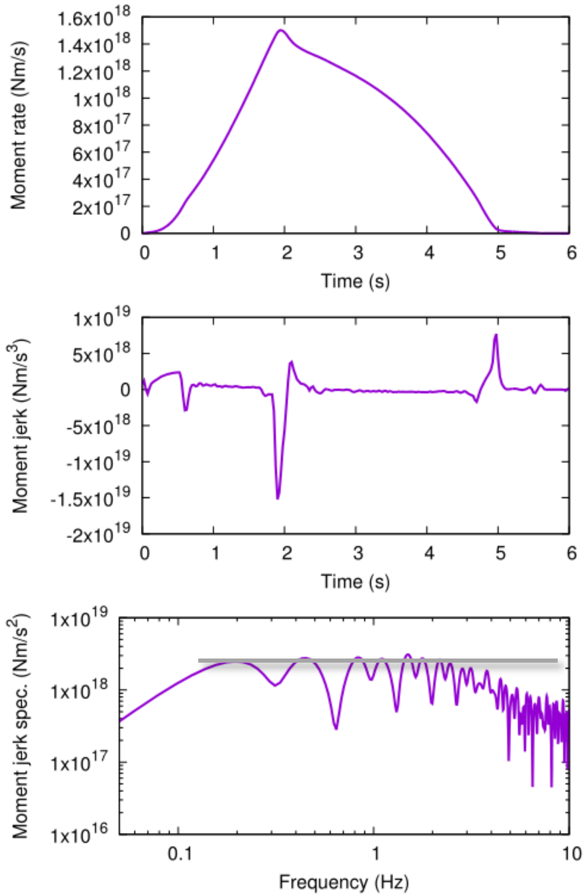

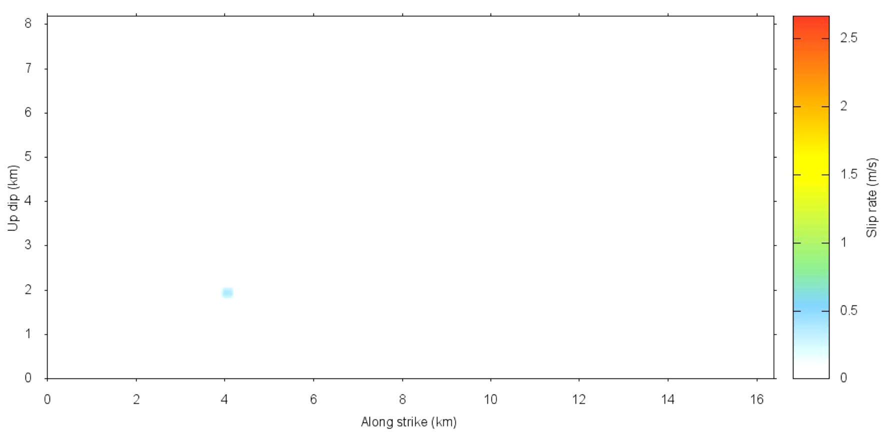

Rupture simulation up to 10 Hz in 30 mins on a GPU using efficient code FD3D_TSN for planar rupture (Premus et al., 2020)

Taufiqurrahman et al. (GRL, 2022)

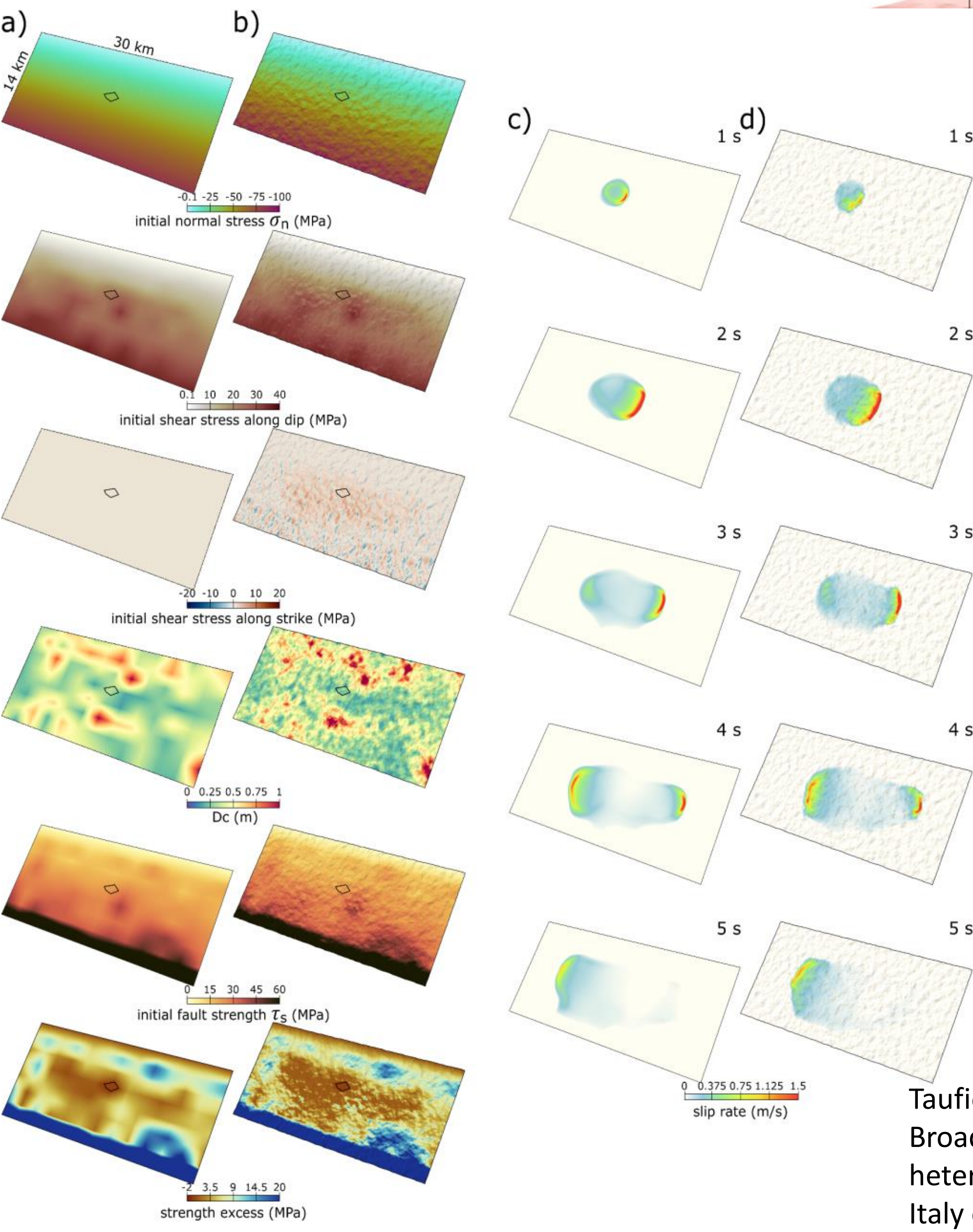

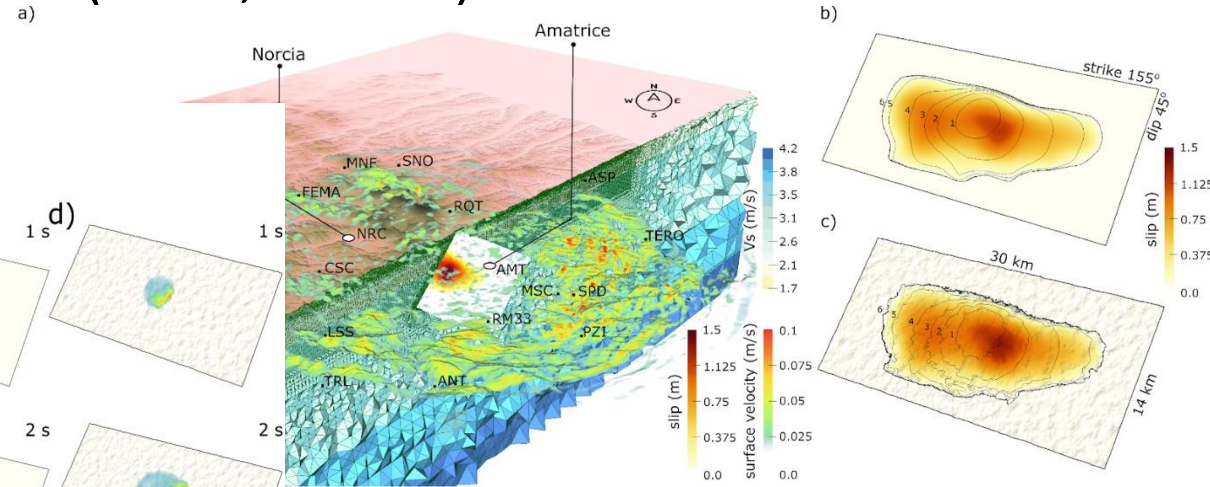

“ More than 80 million elements. ”

“Simulating 40 s of a broadband Amatrice dynamic rupture earthquake scenario using SeisSol requires 4 hours on 256 **nodes** of the SuperMUC-NG supercomputer.”

Taufiqurrahman, A.-A. Gabriel, T. Ulrich, Ľ. Valentová, F. Gallovič (2022). Broadband dynamic rupture modeling with fractal fault roughness, frictional heterogeneity, viscoelasticity and topography: the 2016 Mw 6.2 Amatrice, Italy earthquake, Geophys. Res. Lett. 49, e2022GL098872.

Fractal Gc model of Ide and Aochi (2005)

- Rupture starts from a small patch with small D_c associated with weak radiation.
- Events stop spontaneously without requiring a special stopping mechanism.
- Average fracture energy general increase as the rupture grows =>
  - Rupture velocity locally exceeds the shear wave speed but globally remains subshear
  - Fracture energy scales linearly with rupture size, in agreement with empirical studies
- Relation between size and frequency of events is a power law (explained by the triggering probability between patches).
- Initial phase of the moment rate does not predict the final magnitude due to the statistically self-similar random triggering growth.
- Properties of initial accelerating phase of moment rates agrees with an empirical statistical model (Renou et al., 2022).

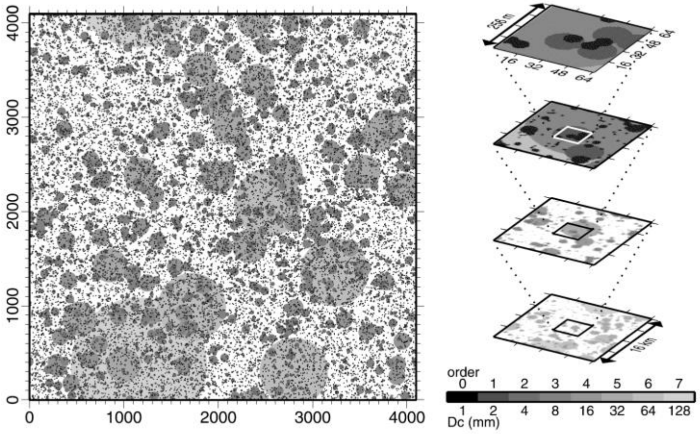

Figure 3. An example of D_c distribution in two dimensions using a set of circular patches. We randomly distribute eight different orders of patches in 4096 × 4096 model space with periodic boundaries, which we consider to be 16 km × 16 km. This model space is treated as four subspaces of different scale through three renormalizations as shown at the right.

Multiscale Dc model

Gallovič and Valentová (2023)

↓r_n ↓D_c ↑T_{ini} ↓$\Delta\mu$

Smooth

Fractal

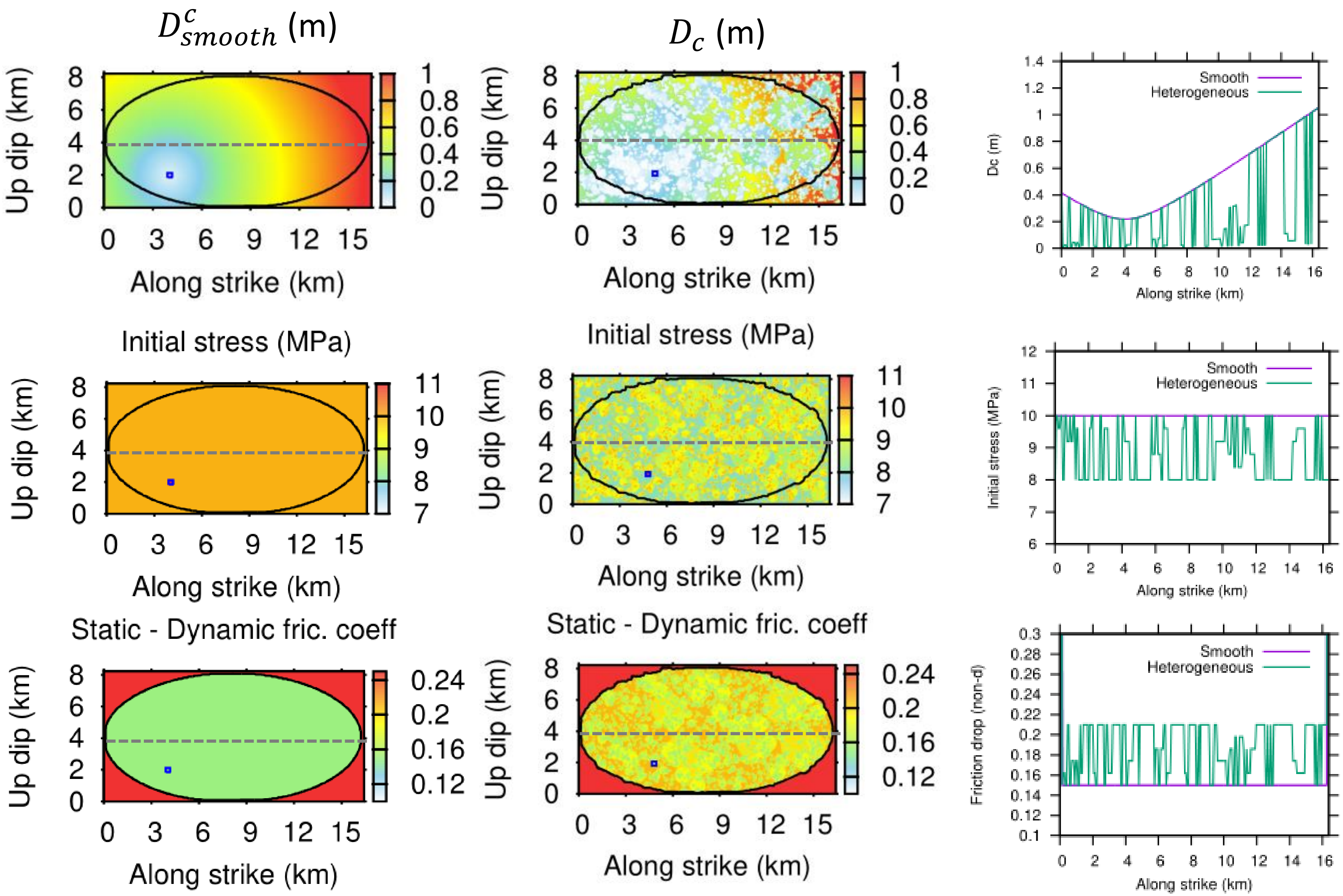

Example – elliptical rupture

Solver: FD3D_TSN (Premus et al., 2020)	
Spatial discretization	32 m
FD half-domain size (along strike x normal x along-dip)	512 x 300 x 256
Duration of slip-rate functions	10 s
Time step	0.001 s
Computation time (single GPU)	**30 min**

Smooth

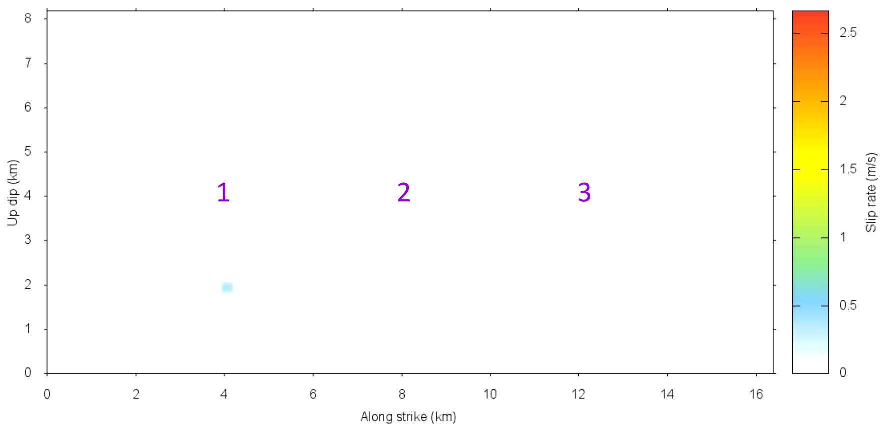

Fractal

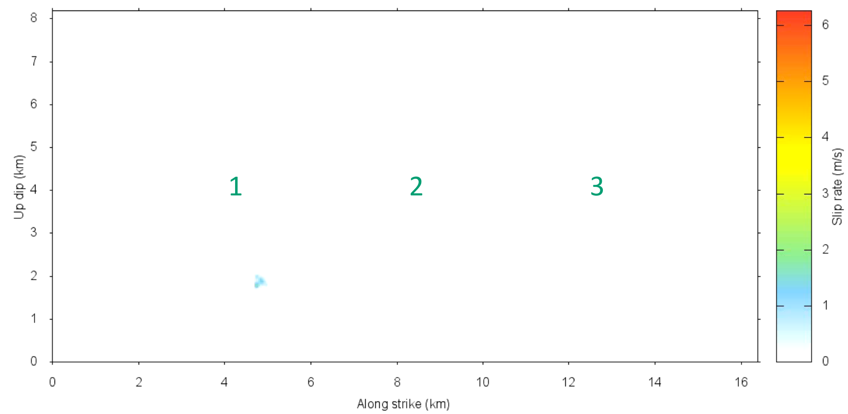

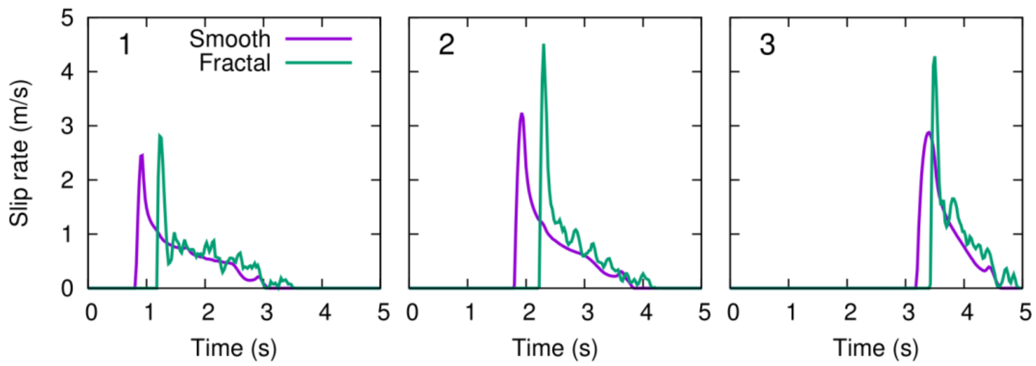

Example – elliptical rupture

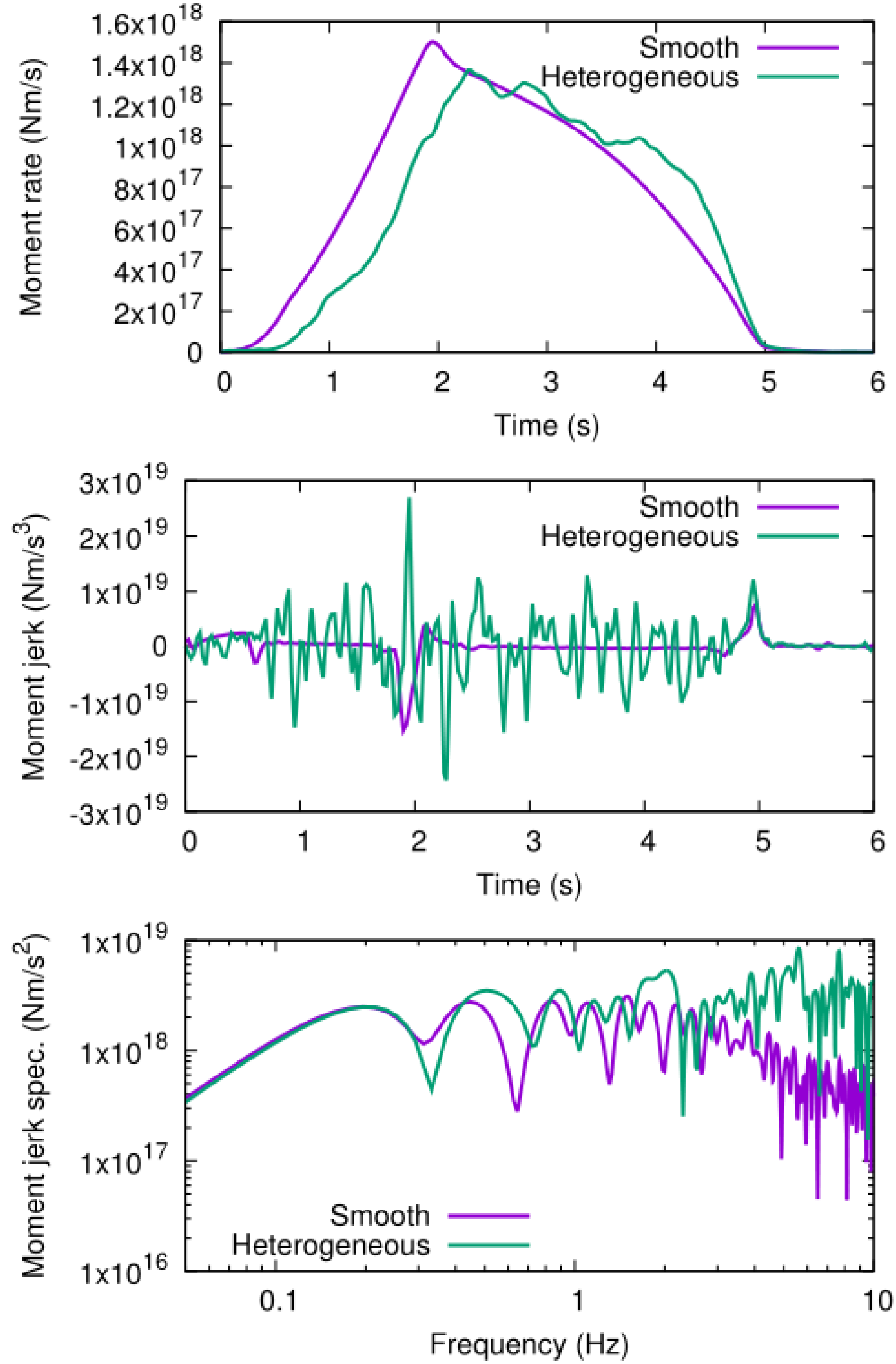

-> The model radiates omega-squared during the whole rupture propagation due to the random acceleration and deceleration of the rupture (Madariaga, 1977)

Example – Amatrice

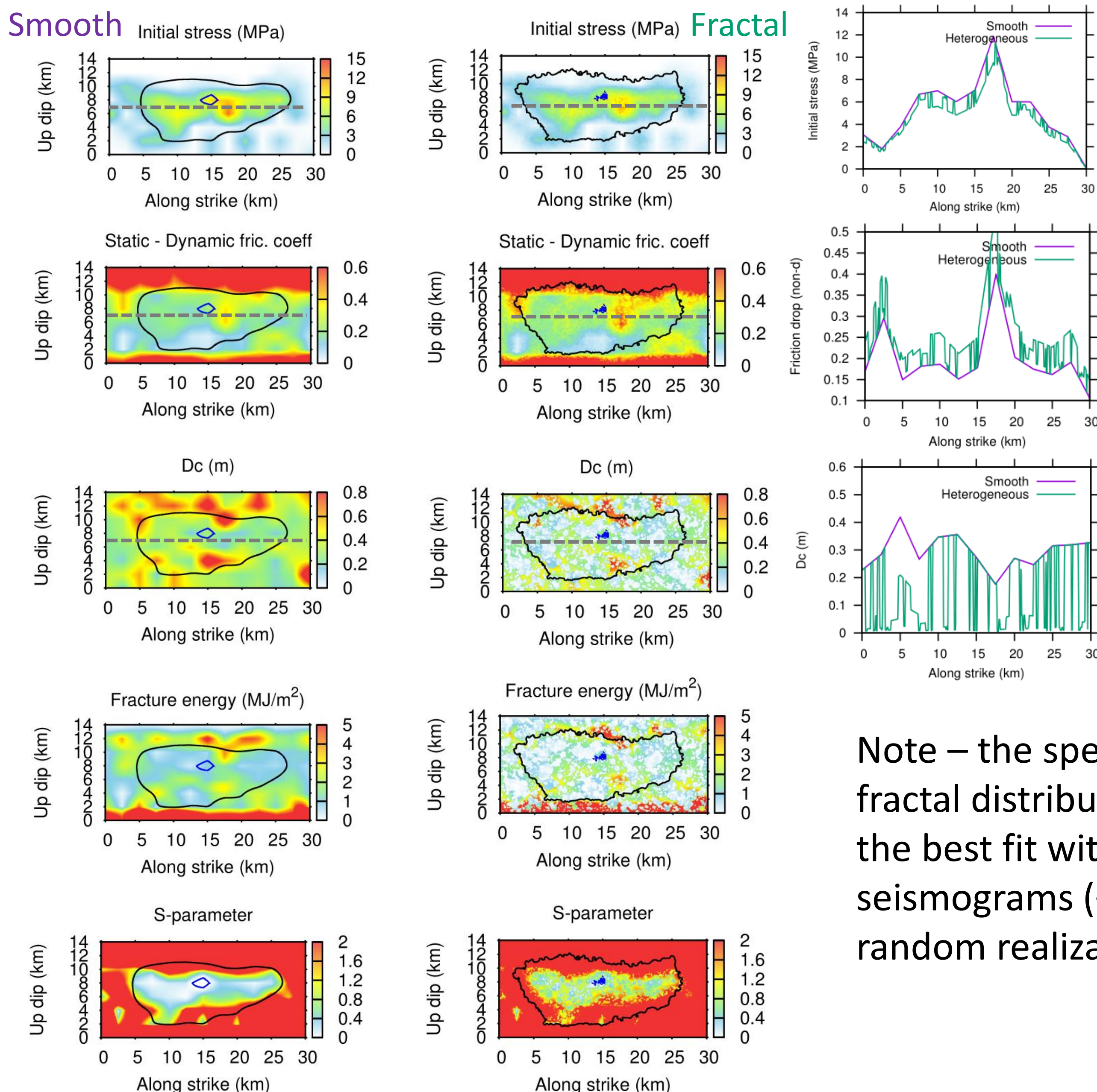

Note – the specific realization of the fractal distribution found to obtain the best fit with low-frequency seismograms (<0.5Hz) out of 500 random realizations.

Gallovič et al. (2019)

Example – Amatrice

Smooth

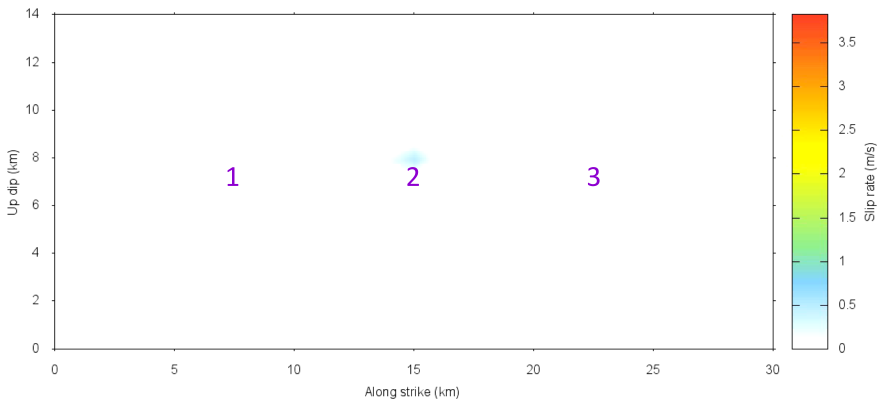

Fractal

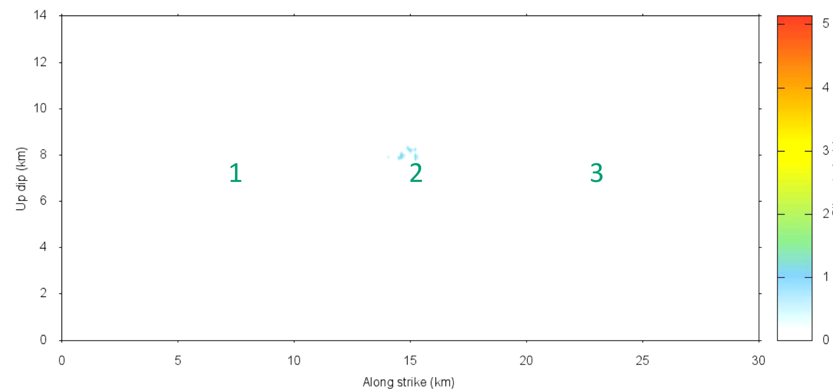

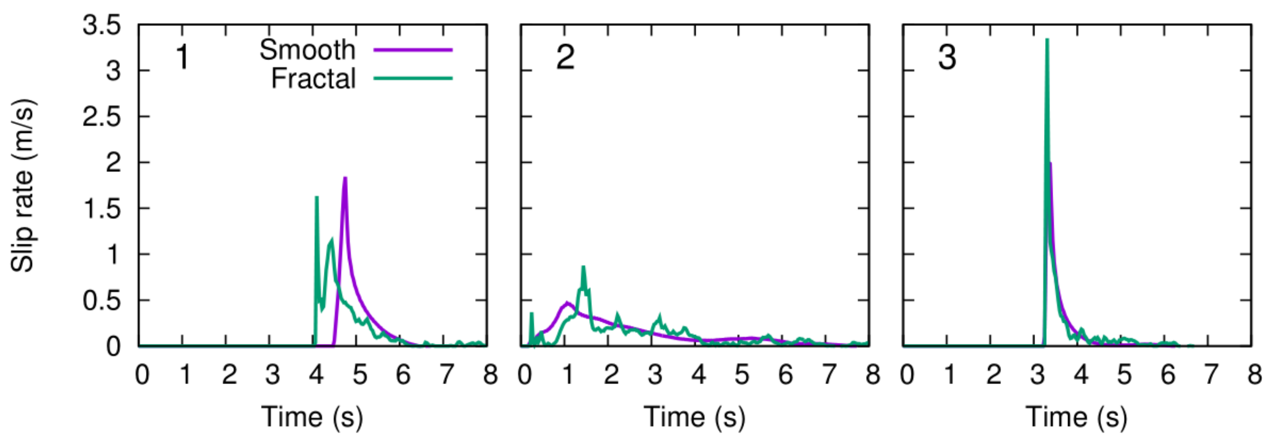

FD3D_TSN performs the calculation in about 30 minutes up to 10 Hz on a single GPU

Example – Amatrice

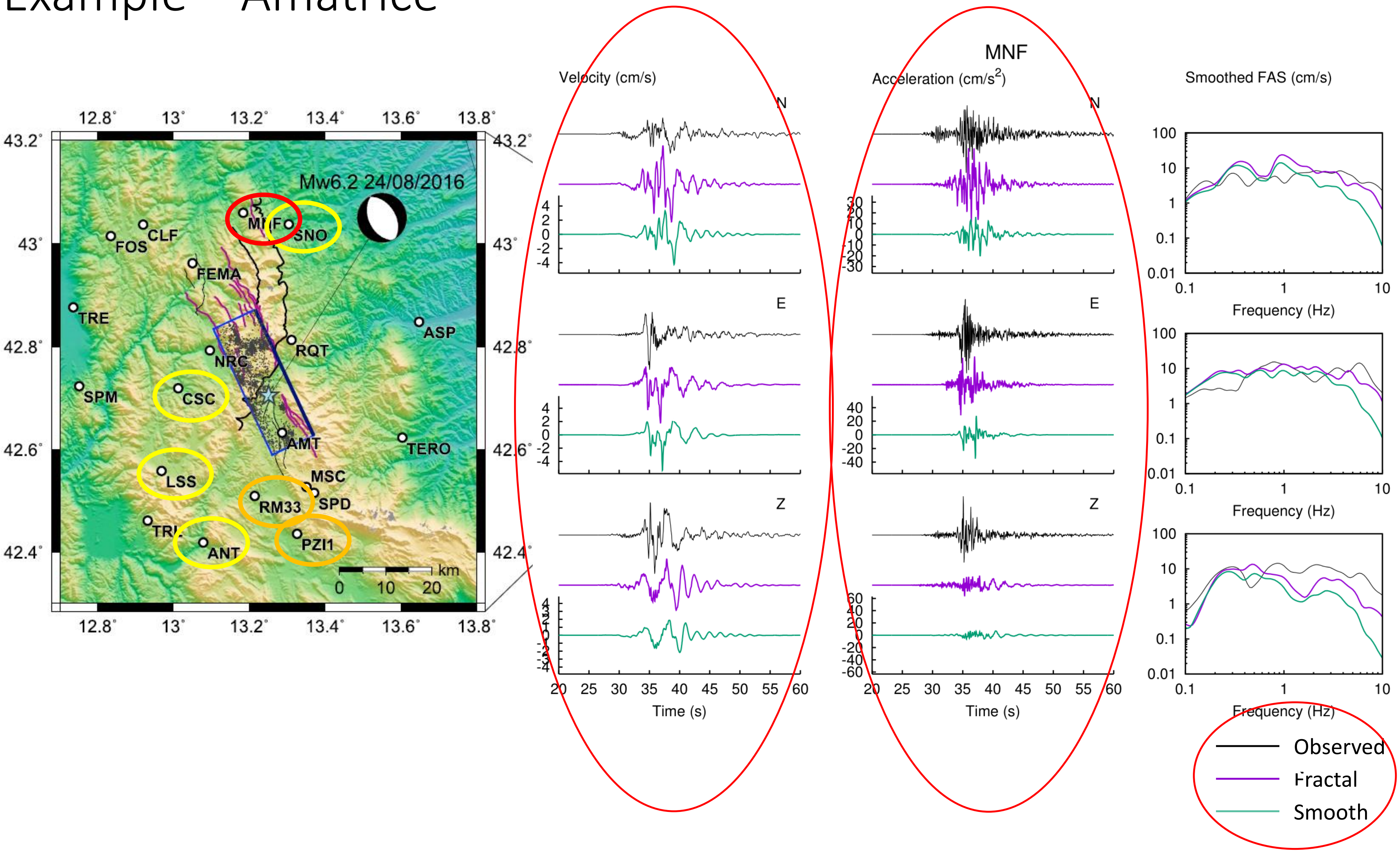

Example – Amatrice

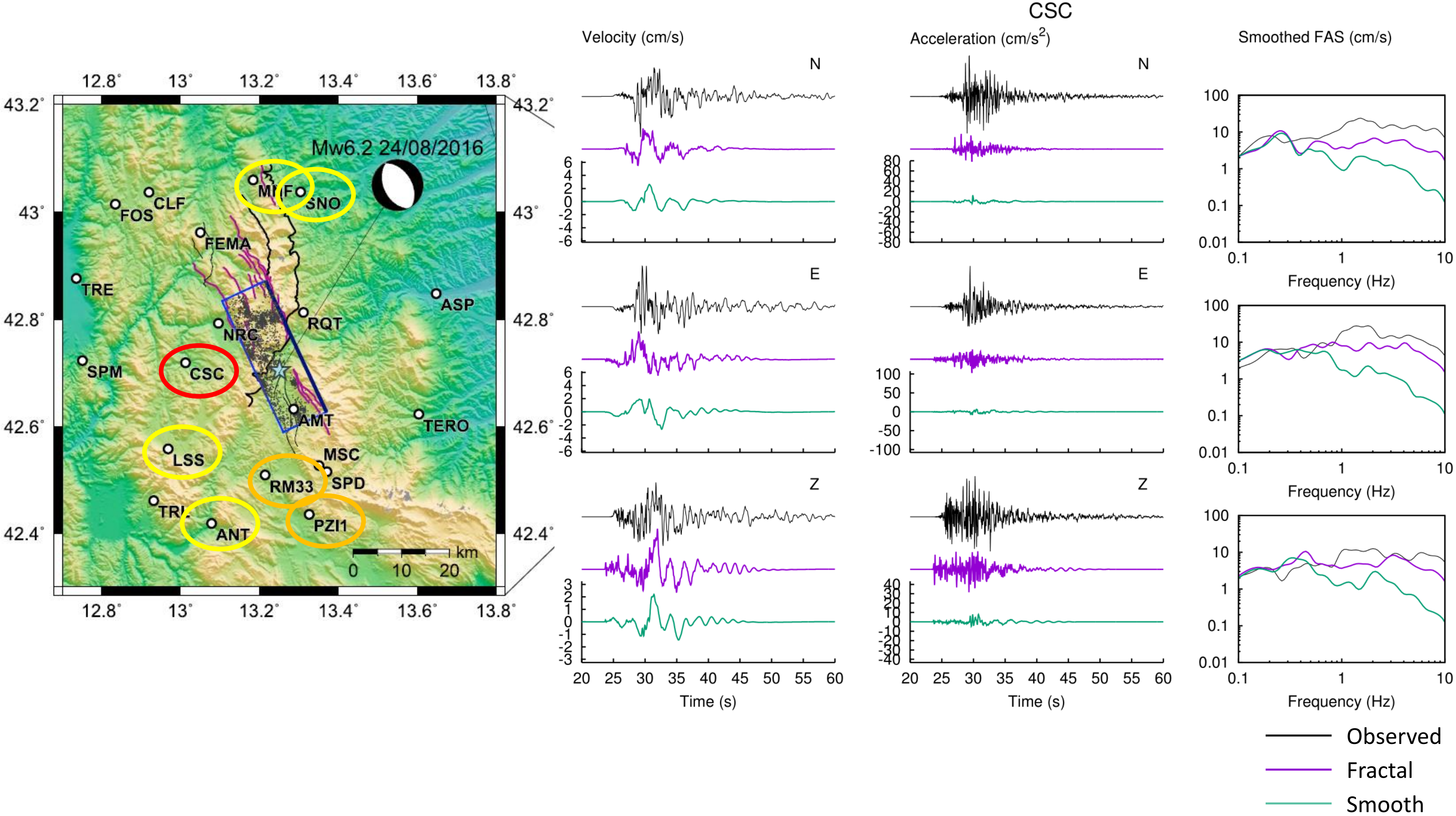

Example – Amatrice

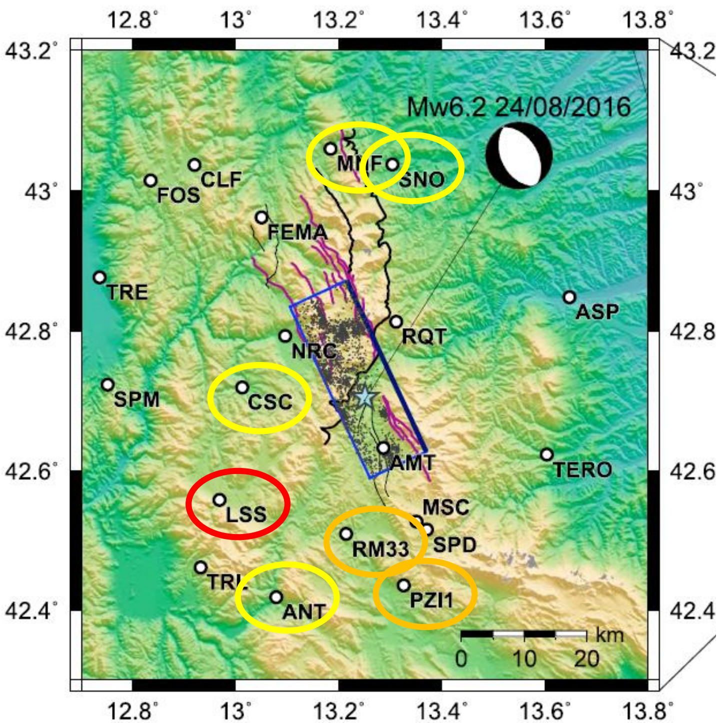

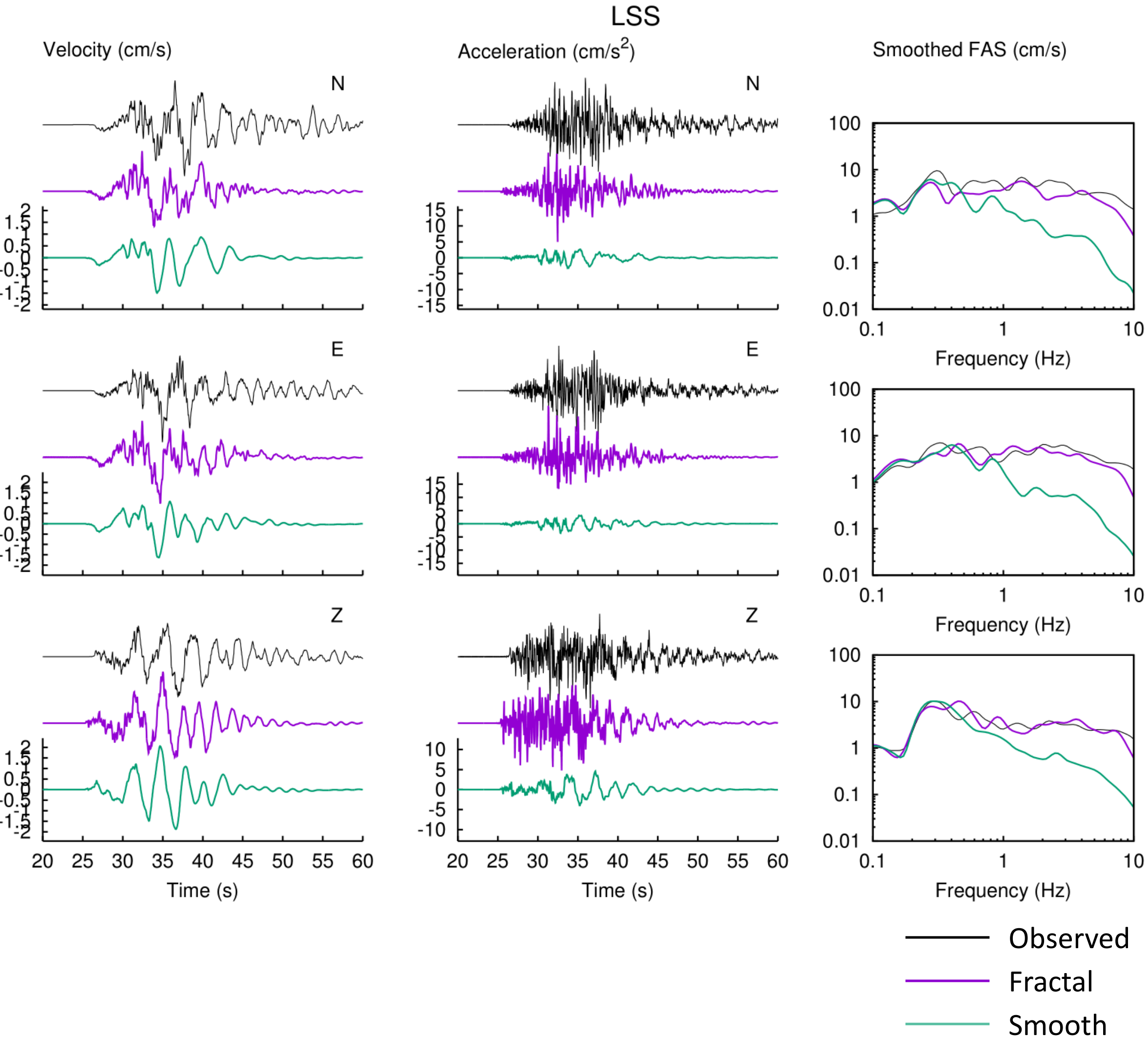

Example – Amatrice

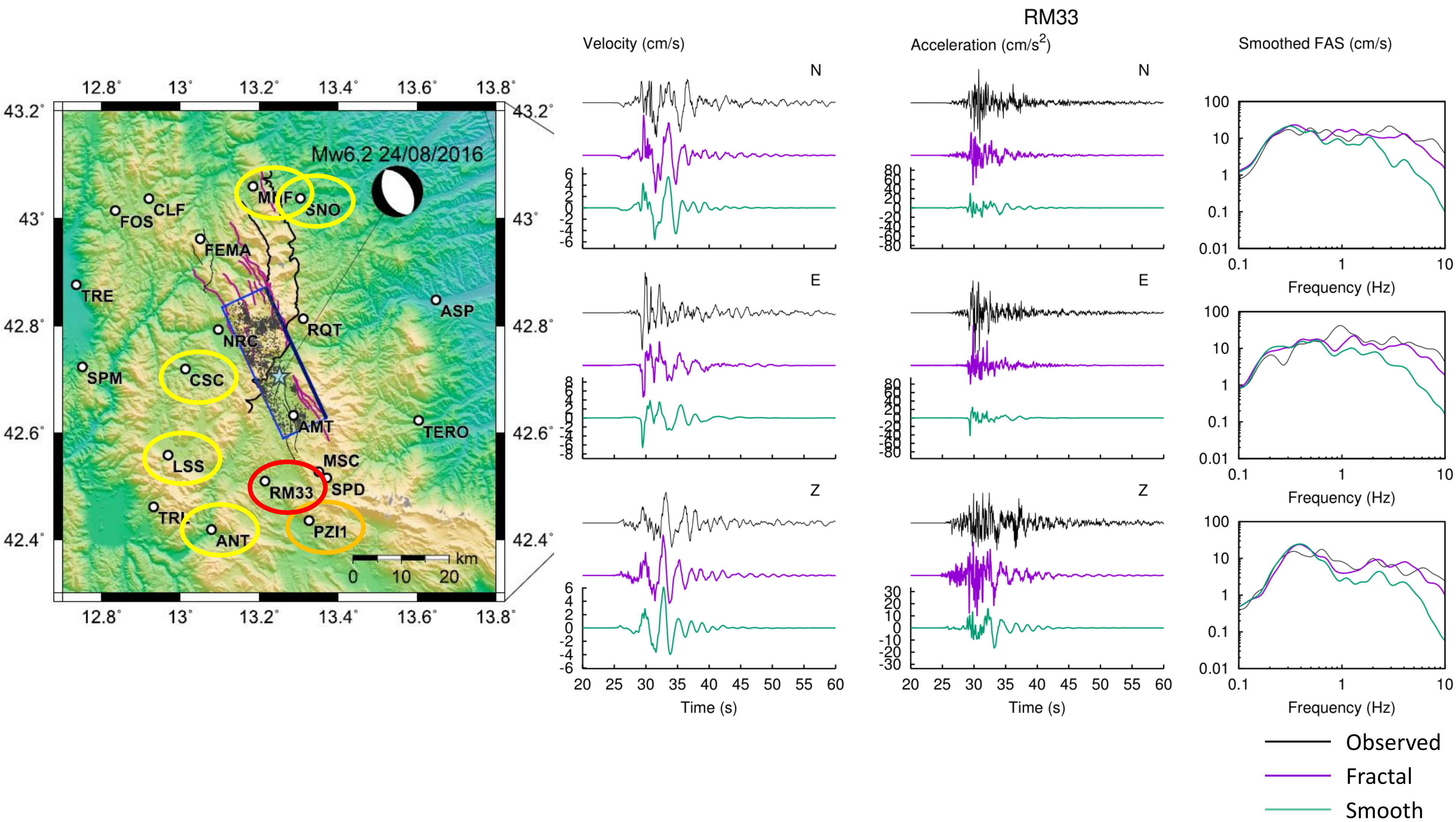

Example – Amatrice (comparison with Ground Motion Model)

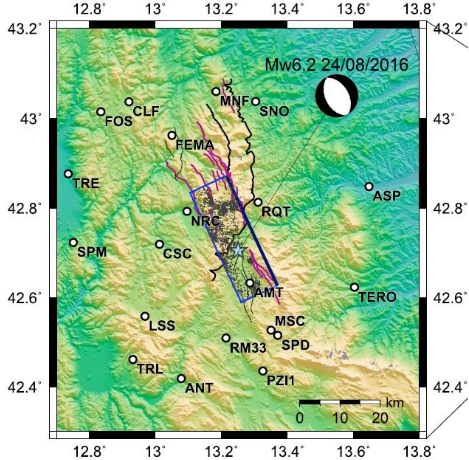

Smooth

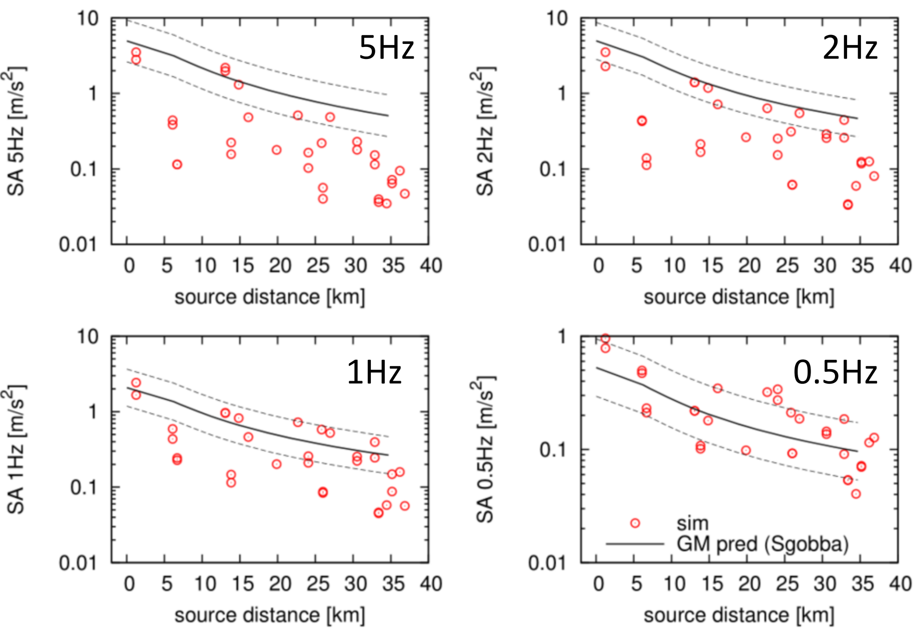

GM pred: Sgobba et al. (2021)

Example – Amatrice (comparison with Ground Motion Model)

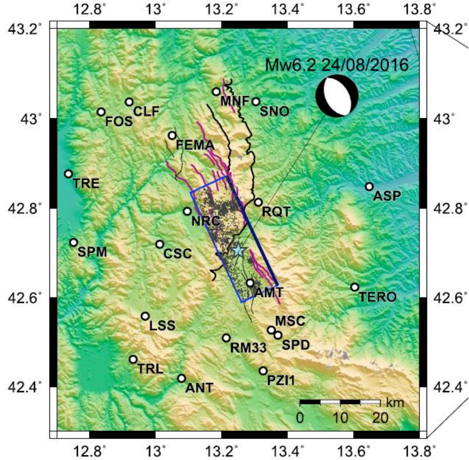

Smooth

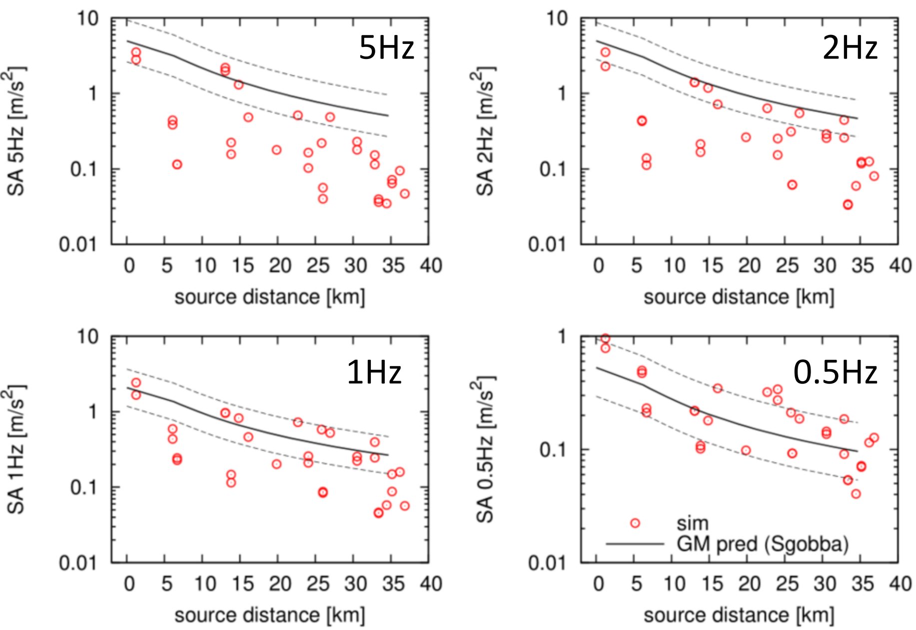

Fractal

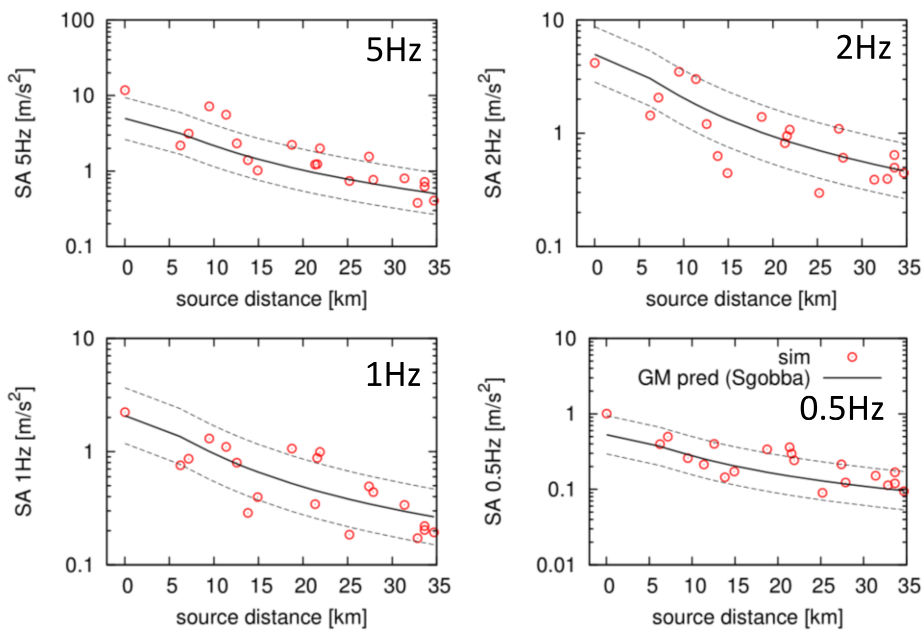

GM pred: Sgobba et al. (2021)

Outlook

Future applications of dynamic source modeling:

- Beyond kinematic inversions: Dynamic rupture inversions of well-recorded events from observed data using synthetic (or empirical) Green's functions
- Beyond Brune source spectral modeling: Dynamic source inversion of apparent source time functions or spectra directly for stress drop and other source parameters (rupture size, radiation efficiency)
- Beyond kinematic broadband simulations: Earthquake rupture scenario simulations constrained by GMM

Limitations of the dynamic modeling:

- Computationally very intense task
- At present, our rupture simulation code is limited only to buried ruptures or vertical faults

First preliminary result from new AdriaArray data in Vrancea

Renata Lukešová

Vrancea zone

AlpArray + PACASE + AdriaArray

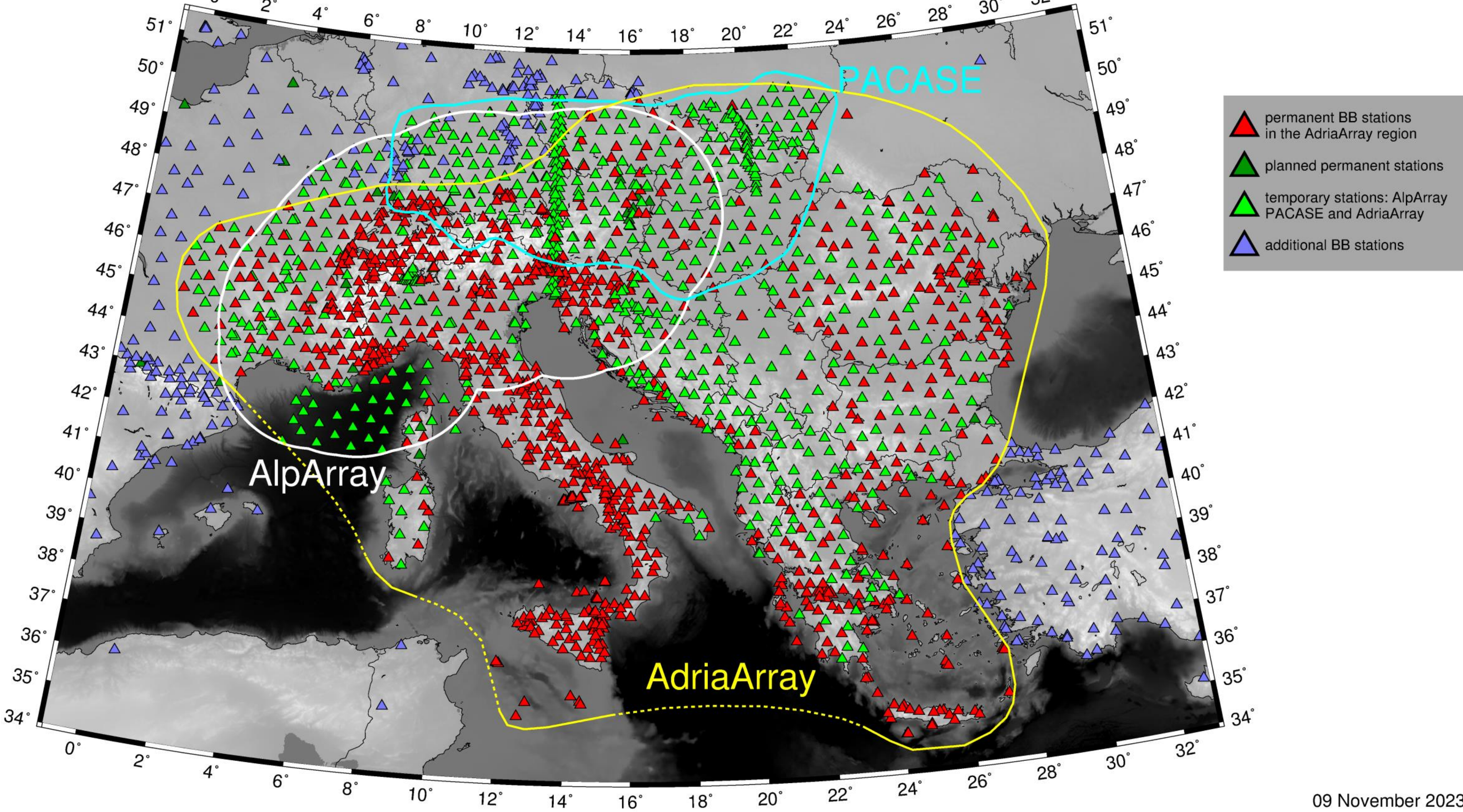

AdriaArray - Local experiments: Denser network in Romania

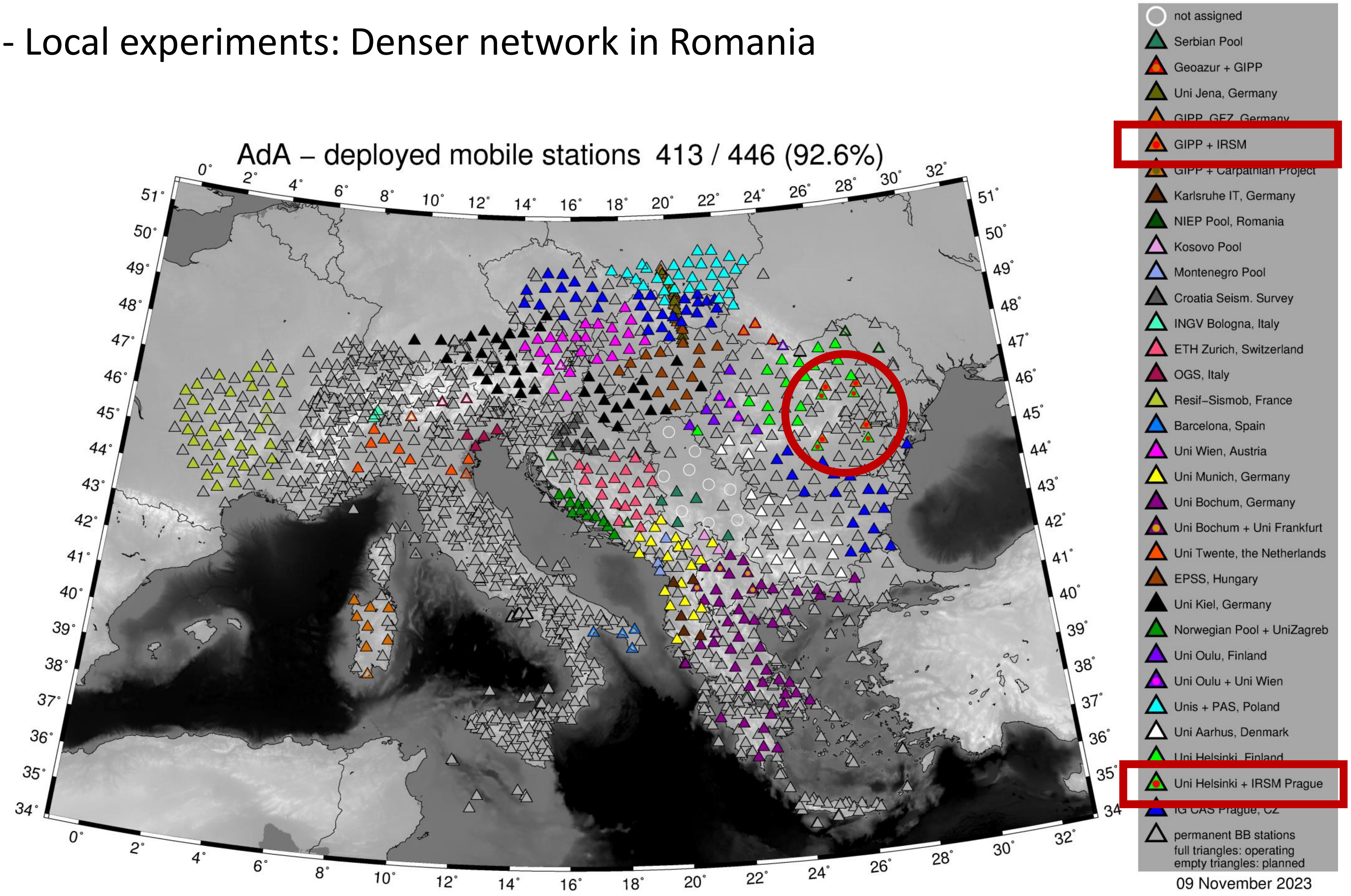

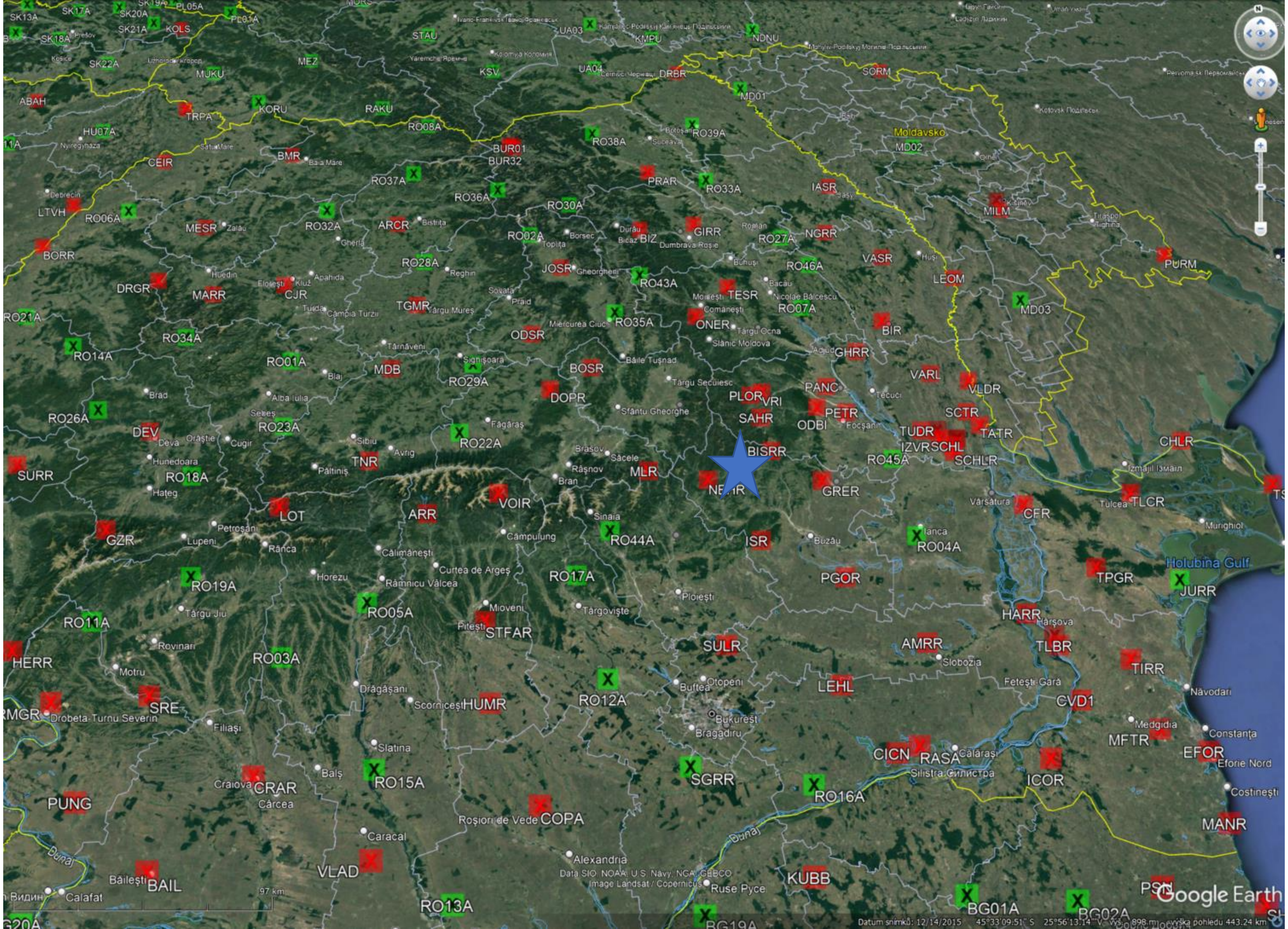

SK13A
SK17A
SK20A
SK21A
SK18A
SK22A
KOLS
PL05A
PL01A
STAU
UA03
KMPU
NDNU
MEZ
MUKU
KSV
UA04
DRBR
SORM
MD01
ABAH
TRPA
KORU
RAKU
RO08A
BUR01
BUR32
RO38A
RO39A
Moldavsko
MD02
HU07A
CEIR
BMR
RO37A
RO36A
PRAR
RO33A
IASR
MILM
LTVH
RO06A
MESR
RO32A
ARCR
RO30A
RO02A
BIZ
GIRR
RO27A
NGRR
BORR
RO28A
JOSR
RO43A
RO46A
VASR
LEOM
PURM
DRGR
MARR
CJR
TGMR
TESR
RO07A
MD03
RO21A
RO34A
ODSR
RO35A
ONER
BIR
RO14A
RO01A
MDB
RO29A
BOSR
GHRR
VARL
VLDR
DOPR
PLOR
VRI
PANC
PETR
SCTR
RO26A
DEV
RO23A
SAHR
ODBI
TUDR
TATR
RO22A
IZVR
SCHL
CHLR
BISRR
RO45A
SCHLR
SURR
RO18A
TNR
MLR
NEHR
GRER
TLCR
LOT
VOIR
ARR
CFR
GZR
RO44A
ISR
RO04A
RO19A
RO17A
PGOR
TPGR
Holubina Gulf
JURR
RO05A
RO11A
STFAR
HARR
HERR
RO03A
SULR
AMRR
TLBR
TIRR
RO12A
LEHL
RMGR
SRE
HUMR
CVD1
MFTR
CICN
RASA
EFOR
ICOR
CRAR
RO15A
SGRR
RO16A
PUNG
COPA
MANR
VLAD
KUBB
BAIL
RO13A
BG01A
BG02A
PSN
G20A
BG19A
Debrecen
Nyíregyháza
Satu Mare
Baia Mare
Zalău
Gherla
Bistrița
Huedin
Apahida
Cluj
Turda
Câmpia Turzii
Reghin
Târgu Mureș
Sovata
Praid
Toplița
Borsec
Durău
Bicaz
Dumbrava Roșie
Roman
Buhuși
Bacău
Nicolae Bălcescu
Comănești
Moinești
Târgu Ocna
Slănic Moldova
Miercurea Ciuc
Băile Tușnad
Târgu Secuiesc
Sfântu Gheorghe
Târnăveni
Blaj
Alba Iulia
Sighișoara
Brad
Sebeș
Făgăraș
Orăștie
Cugir
Deva
Hunedoara
Hațeg
Sibiu
Avrig
Păltiniș
Brașov
Săcele
Râșnov
Bran
Sinaia
Câmpulung
Petroșani
Lupeni
Rânca
Călimănești
Curtea de Argeș
Râmnicu Vâlcea
Horezu
Mioveni
Pitești
Târgoviște
Ploiești
Buzău
Focșani
Tecuci
Adjud
Huși
Iași
Chișinău
Tiraspol
Tighina
Ismail
Tulcea
Vărsătura
Murighiol
Ianca
Slobozia
Hârșova
Fetești-Gară
Năvodari
Medgidia
Constanța
Eforie Nord
Costinești
Călărași
Silistra Силистра
Otopeni
Buftea
București
Bragadiru
Târgu Jiu
Rovinari
Motru
Drobeta-Turnu Severin
Filiași
Drăgășani
Scornicești
Slatina
Balș
Craiova
Cârcea
Caracal
Roșiori de Vede
Alexandria
Ruse Русе
Băilești
Calafat
Видин
Dunai
97 km
Data SIO, NOAA, U.S. Navy, NGA, GEBCO
Image Landsat / Copernicus
Google Earth
Datum snímků: 12/14/2015 45°33'09.51" S 25°56'13.14" V výš. 898 m výška pohledu 443.24 km

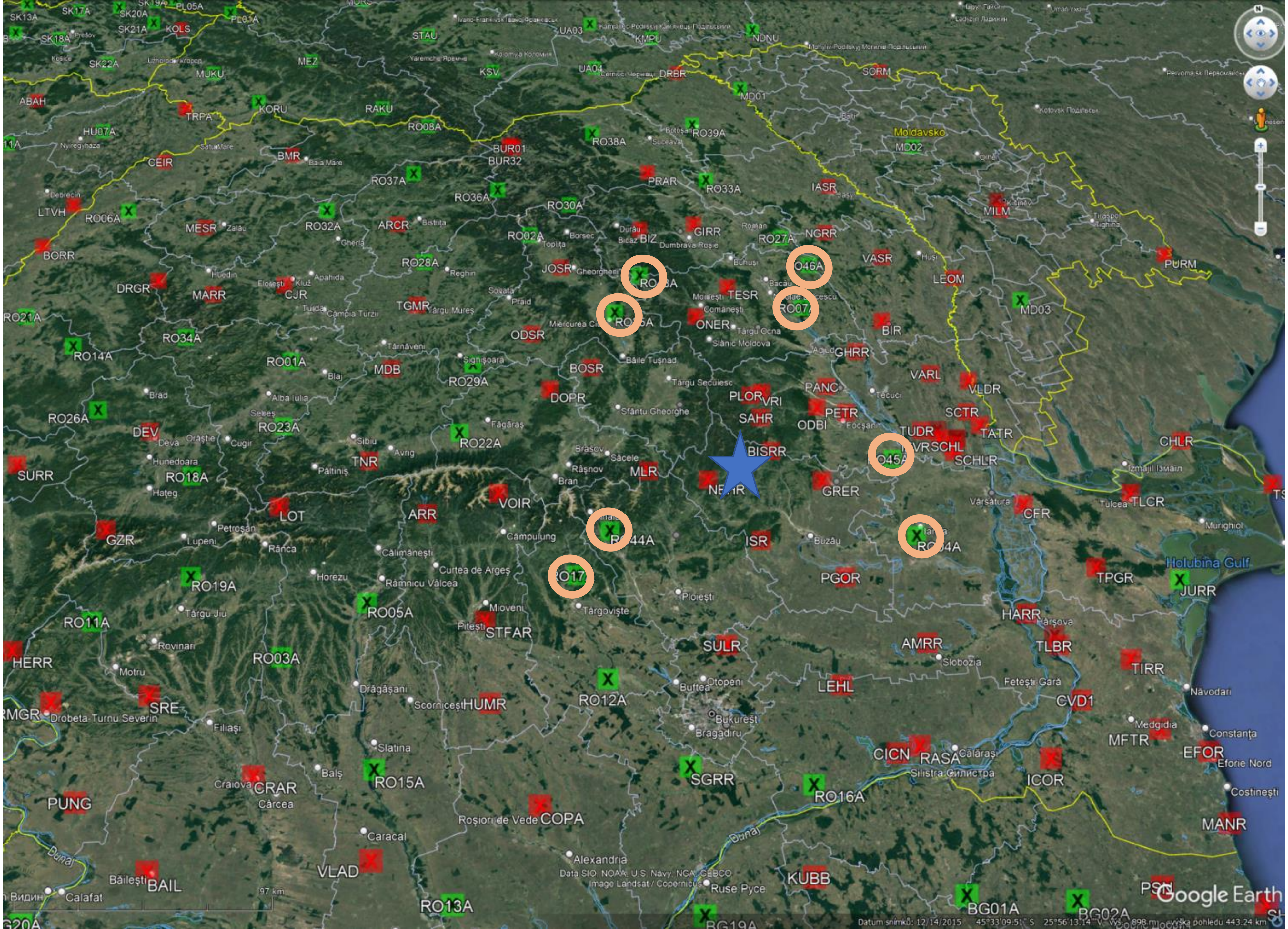

SK13A
SK17A
SK20A
SK21A
SK18A
SK22A
KOLS
PL05A
PL01A
STAU
UA03
KMPU
NDNU
MEZ
MUKU
KSV
UA04
DRBR
SORM
ABAH
KORU
RAKU
TRPA
MD01
HU07A
RO08A
BUR01
BUR32
RO38A
RO39A
Moldavsko
MD02
CEIR
BMR
RO37A
PRAR
RO33A
IASR
RO36A
RO30A
MILM
LTVH
RO06A
MESR
RO32A
ARCR
BIZ
GIRR
RO02A
RO27A
NGRR
PURM
BORR
RO28A
JOSR
VASR
LEOM
DRGR
MARR
CJR
TESR
TGMR
ONER
BIR
MD03
RO21A
ODSR
RO34A
RO14A
GHRR
RO01A
MDB
BOSR
VARL
VLDR
RO29A
DOPR
PANC
PLOR
PETR
SCTR
RO26A
SAHR
ODBI
TUDR
TATR
CHLR
DEV
RO23A
RO22A
BISRR
SCHLR
SURR
TNR
RO18A
MLR
GRER
TLCR
LOT
VOIR
ARR
CFR
GZR
ISR
RO19A
PGOR
TPGR
Holubina Gulf
JURR
RO05A
RO11A
STFAR
HARR
SULR
AMRR
TLBR
HERR
RO03A
TIRR
LEHL
RO12A
CVD1
SRE
HUMR
MFTR
CICN
RASA
EFOR
CRAR
RO15A
SGRR
ICOR
PUNG
RO16A
COPA
MANR
VLAD
KUBB
BAIL
BG01A
BG02A
RO13A
Google Earth

BACKBONE STATIONS (RO04A, RO07A, RO17A, RO35A)
sensor: Guralp 3ESPC 120s 100Hz 2x1000 V/m/s
digitizer: Guralp minimus (4-channel)
sampling frequency: 100 Hz

The digital data recorded by these stations are transmitted in real time to the NIEP node of EIDA.


GOOWEI
ENERGY


minimus
RUT240
R140761


minimus
FEB42


SCOALA GENERALA
CLASELE I-IV
JUD ALBA

LOCAL EXPERIMENT STATIONS (RO43A, RO44A, RO45A, RO46A)
GIPP (Geophysical Instrument Pool Potsdam) - GFZ Potdsdam
sensor: Trillium Compact - Model TC120-SV1 (16838)
digitizer: Earth Data EDR-210
sampling frequency: 100 Hz

The digital data recorded by these stations are transmitted in real time to the NIEP node of EIDA.




Vrancea – example of measured data

Earthquake M = 4.1   2023-07-30 04:20:06.5 UTC   Depth 123 km

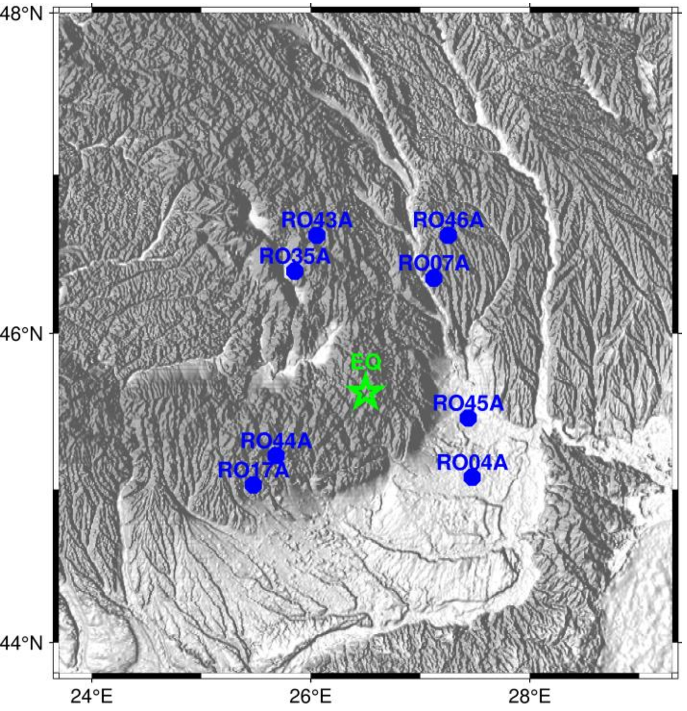

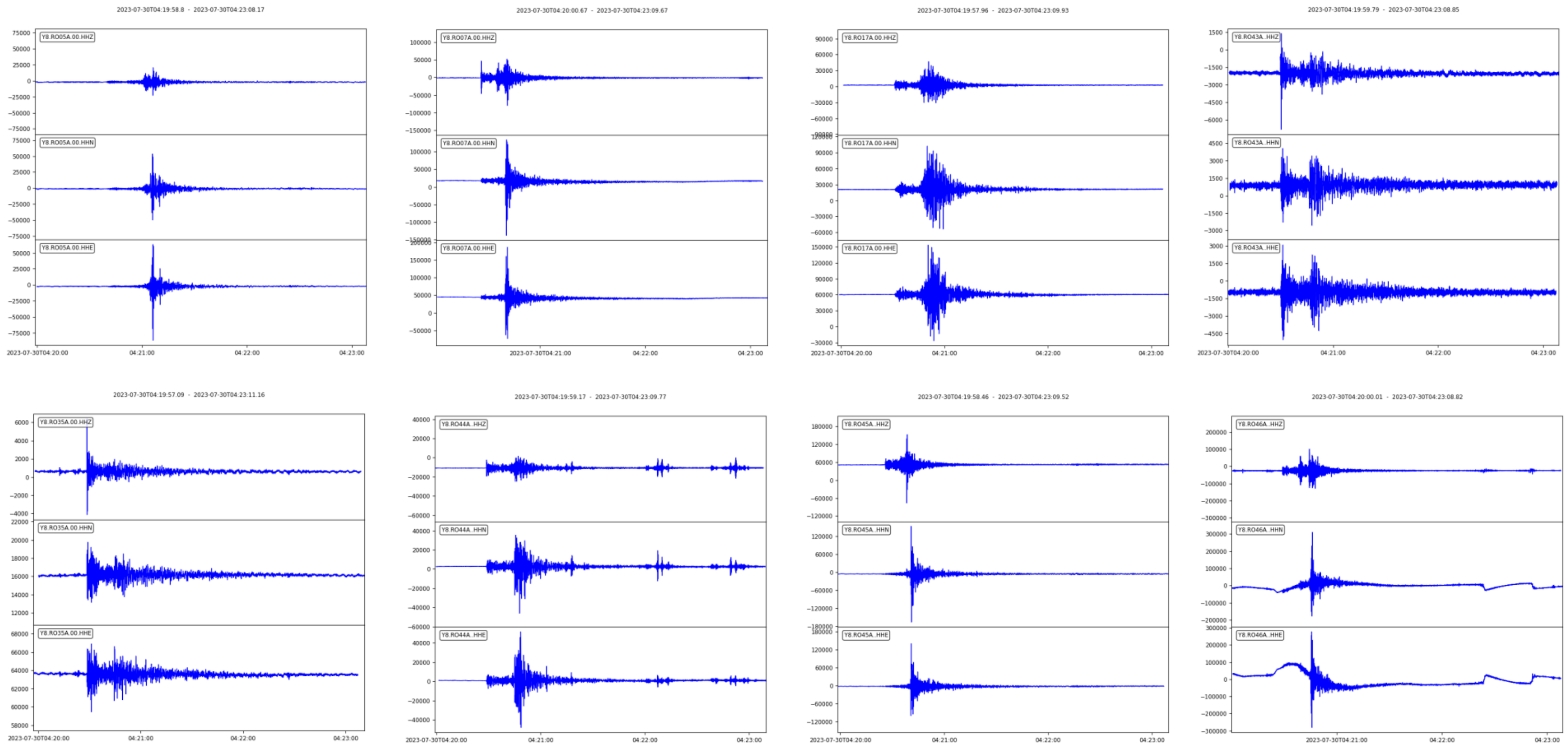

CSEM EMSC

Centre Sismologique Euro-Méditerranéen
Euro-Mediterranean Seismological Centre

Magnitude	4.6
Region	ROMANIA
Date time	2023-12-03 22:05:48.6 UTC
Location	45.637 ; 26.407
Depth	137 km
Distance	62 km E of Braşov, Romania / pop: 27 26 km N of Nehoiu, Romania / pop: 11

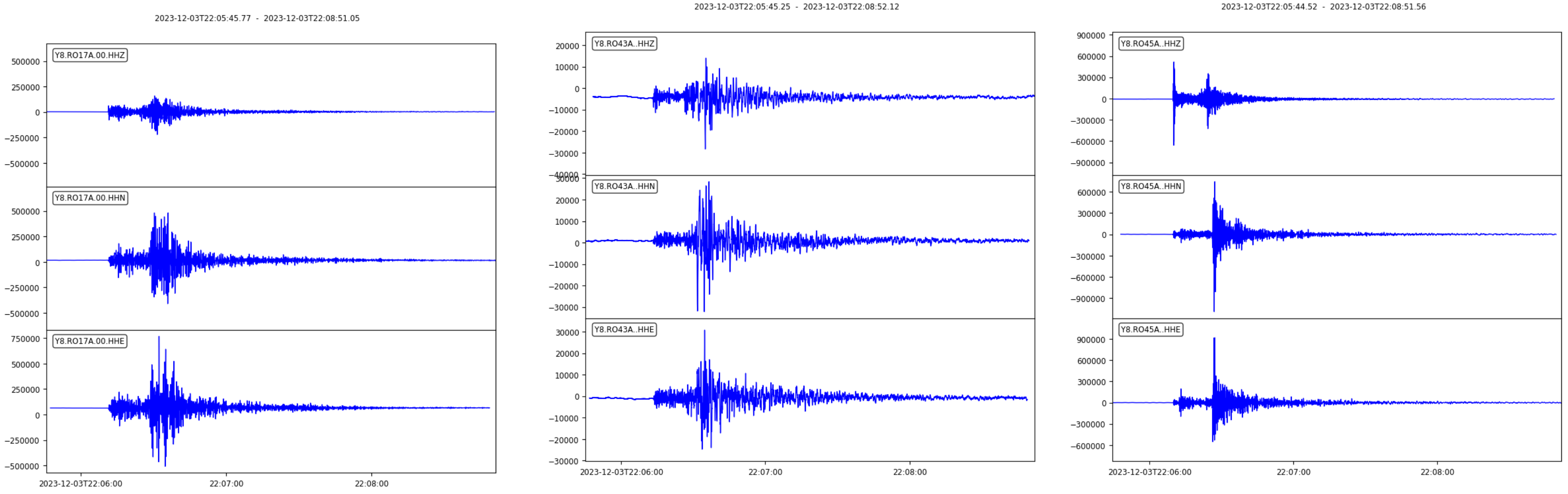

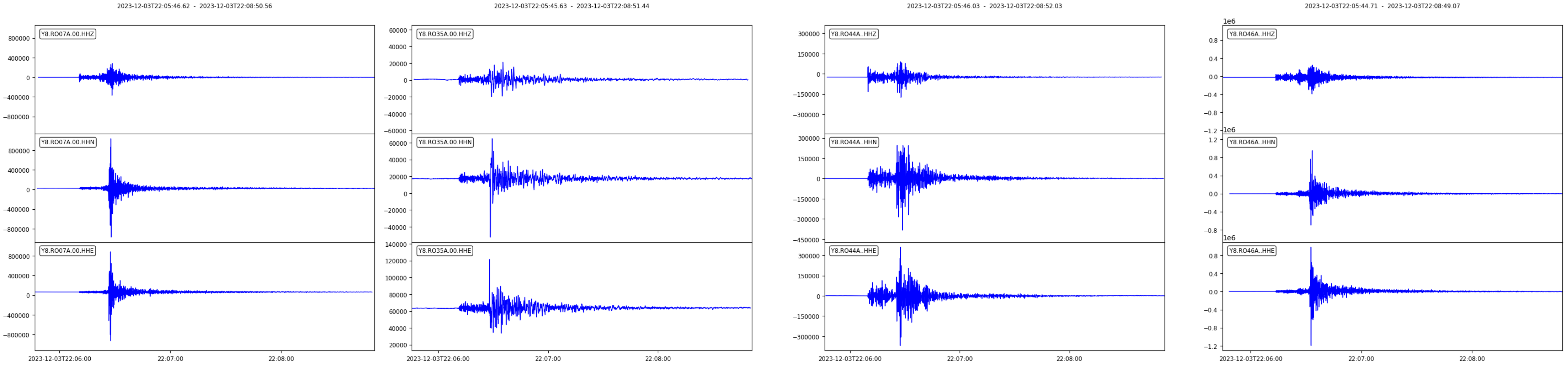

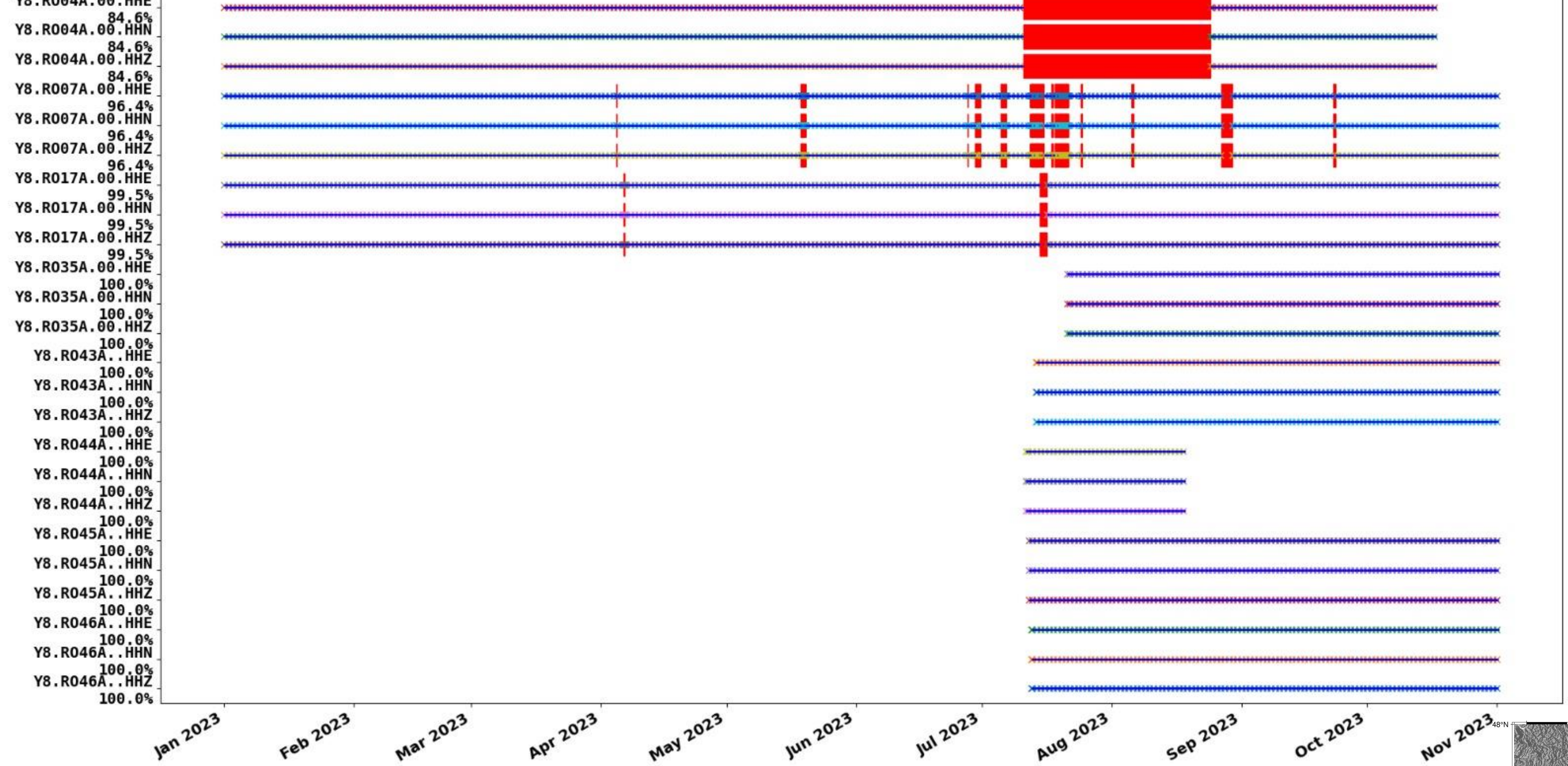

Y8.RO04A.00.HHE
84.6%
Y8.RO04A.00.HHN
84.6%
Y8.RO04A.00.HHZ
84.6%
Y8.RO07A.00.HHE
96.4%
Y8.RO07A.00.HHN
96.4%
Y8.RO07A.00.HHZ
96.4%
Y8.RO17A.00.HHE
99.5%
Y8.RO17A.00.HHN
99.5%
Y8.RO17A.00.HHZ
99.5%
Y8.RO35A.00.HHE
100.0%
Y8.RO35A.00.HHN
100.0%
Y8.RO35A.00.HHZ
100.0%
Y8.RO43A..HHE
100.0%
Y8.RO43A..HHN
100.0%
Y8.RO43A..HHZ
100.0%
Y8.RO44A..HHE
100.0%
Y8.RO44A..HHN
100.0%
Y8.RO44A..HHZ
100.0%
Y8.RO45A..HHE
100.0%
Y8.RO45A..HHN
100.0%
Y8.RO45A..HHZ
100.0%
Y8.RO46A..HHE
100.0%
Y8.RO46A..HHN
100.0%
Y8.RO46A..HHZ
100.0%
Jan 2023
Feb 2023
Mar 2023
Apr 2023
May 2023
Jun 2023
Jul 2023
Aug 2023
Sep 2023
Oct 2023
Nov 2023

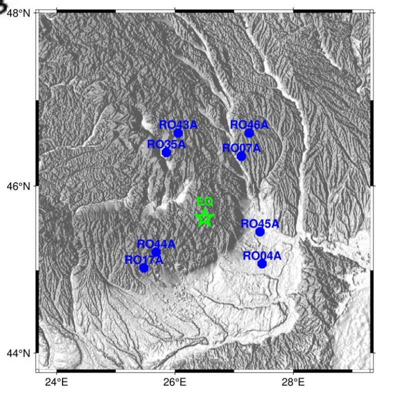

RO43A
RO46A
RO35A
RO07A
RO45A
RO44A
RO17A
RO04A
48°N
46°N
44°N
24°E
26°E
28°E

Probabilistic power spectral density (PPSD)

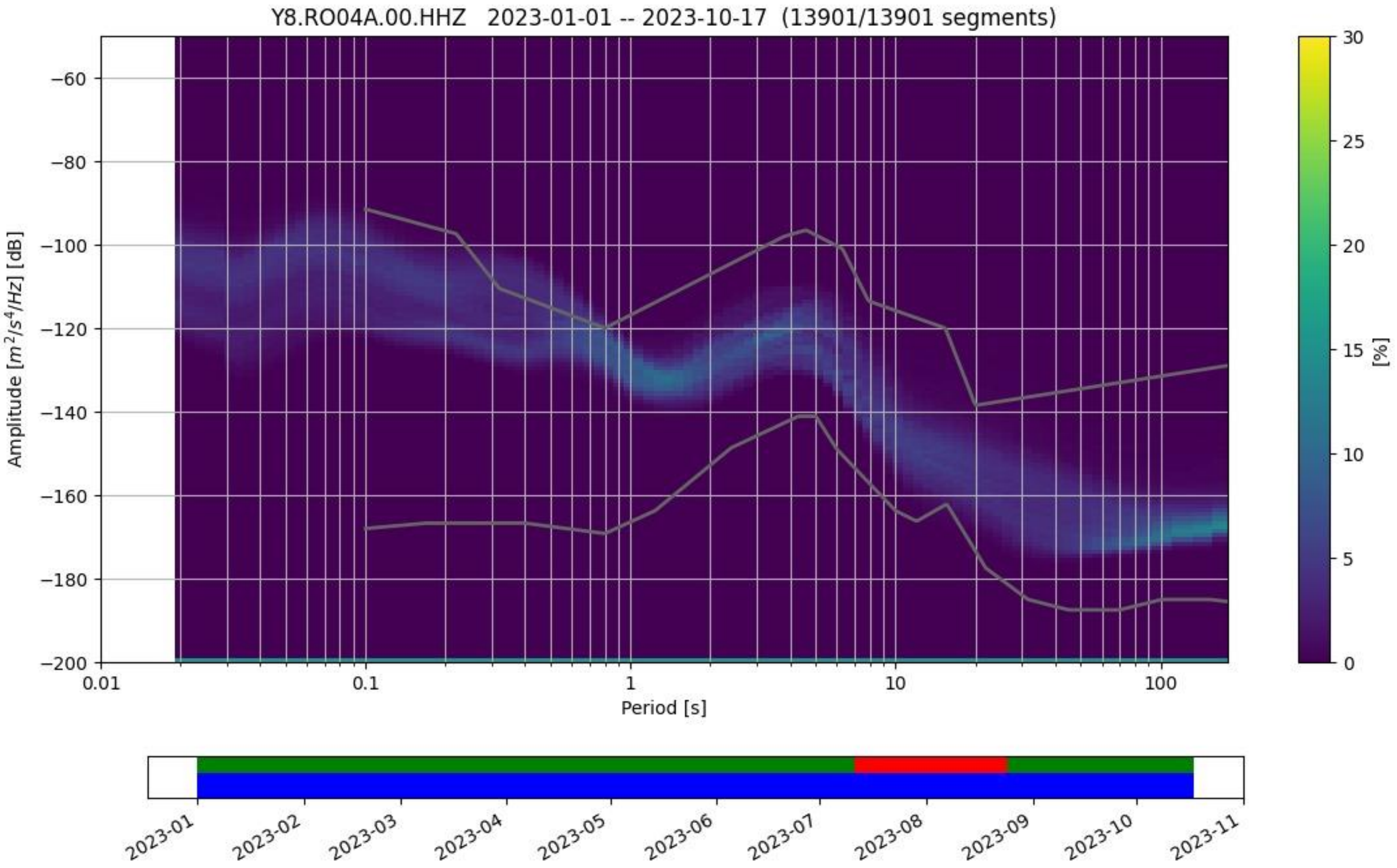

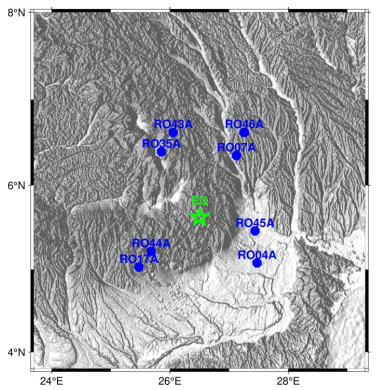

Probabilistic power spectral density (PPSD)

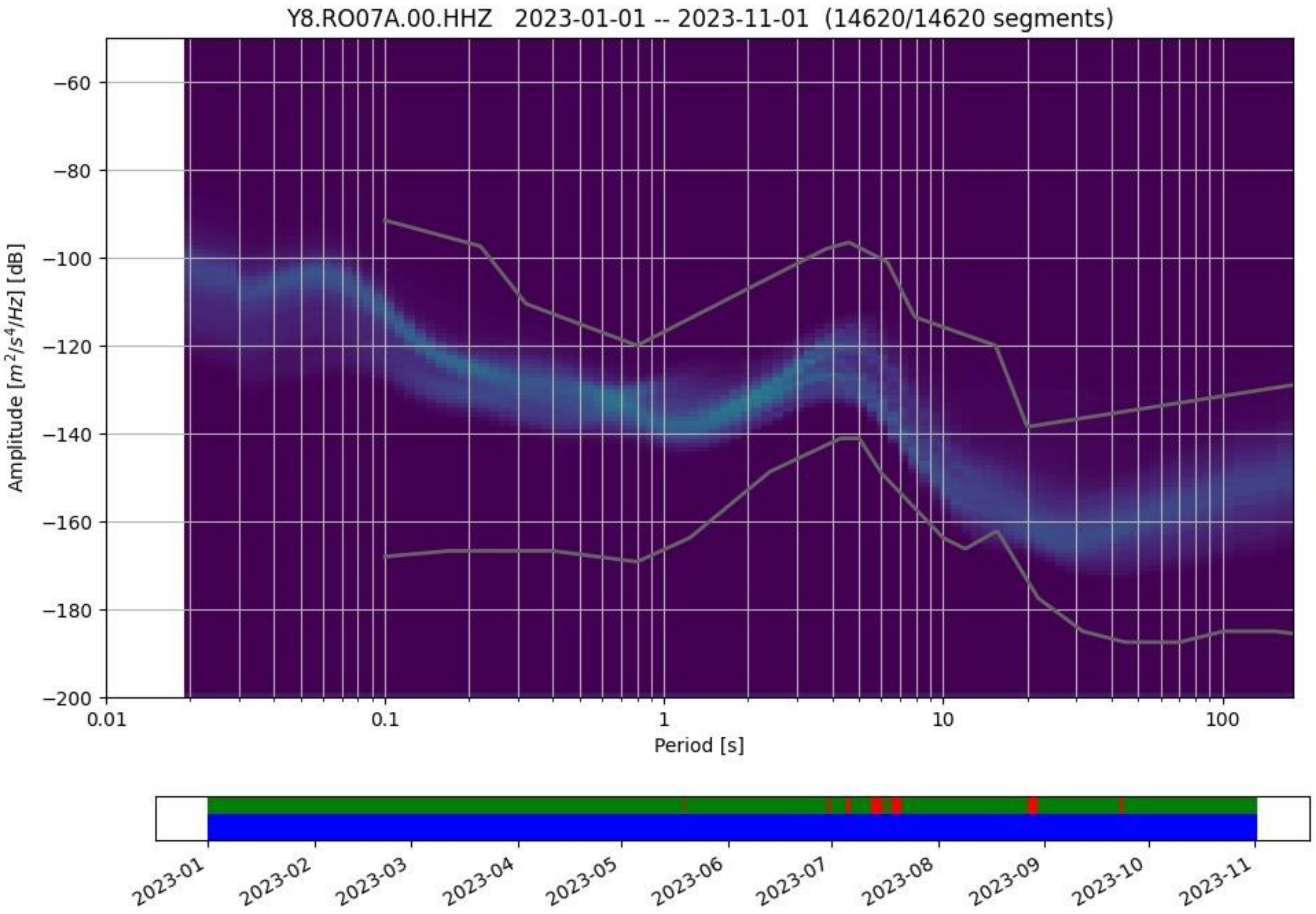

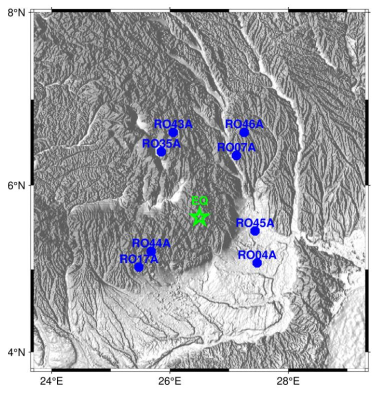

Probabilistic power spectral density (PPSD)

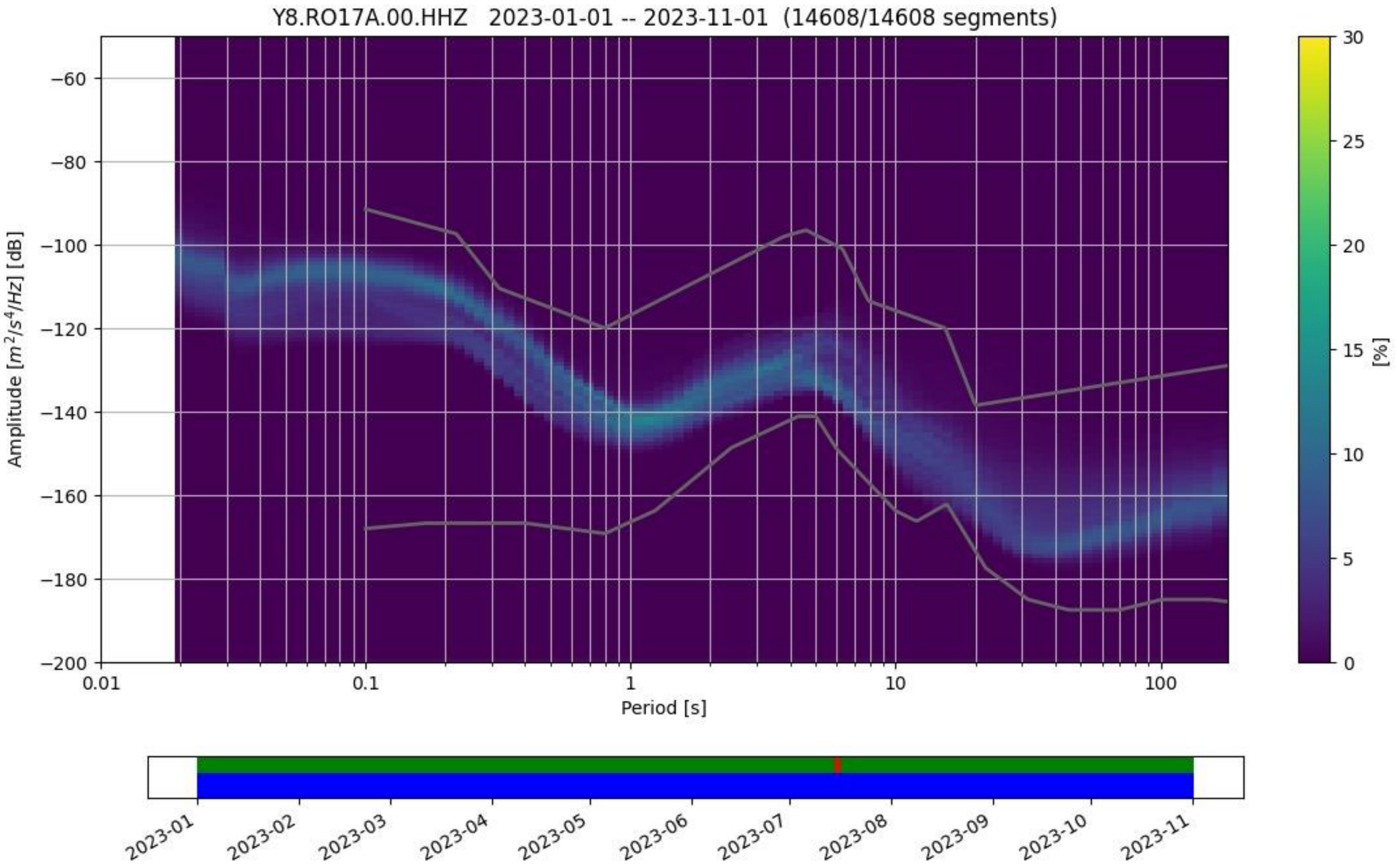

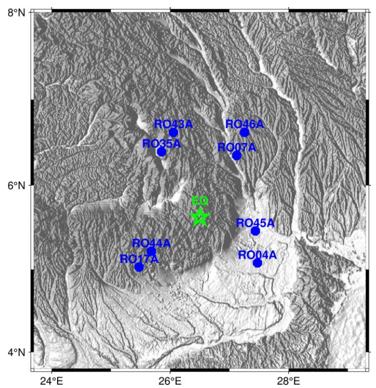

Probabilistic power spectral density (PPSD)

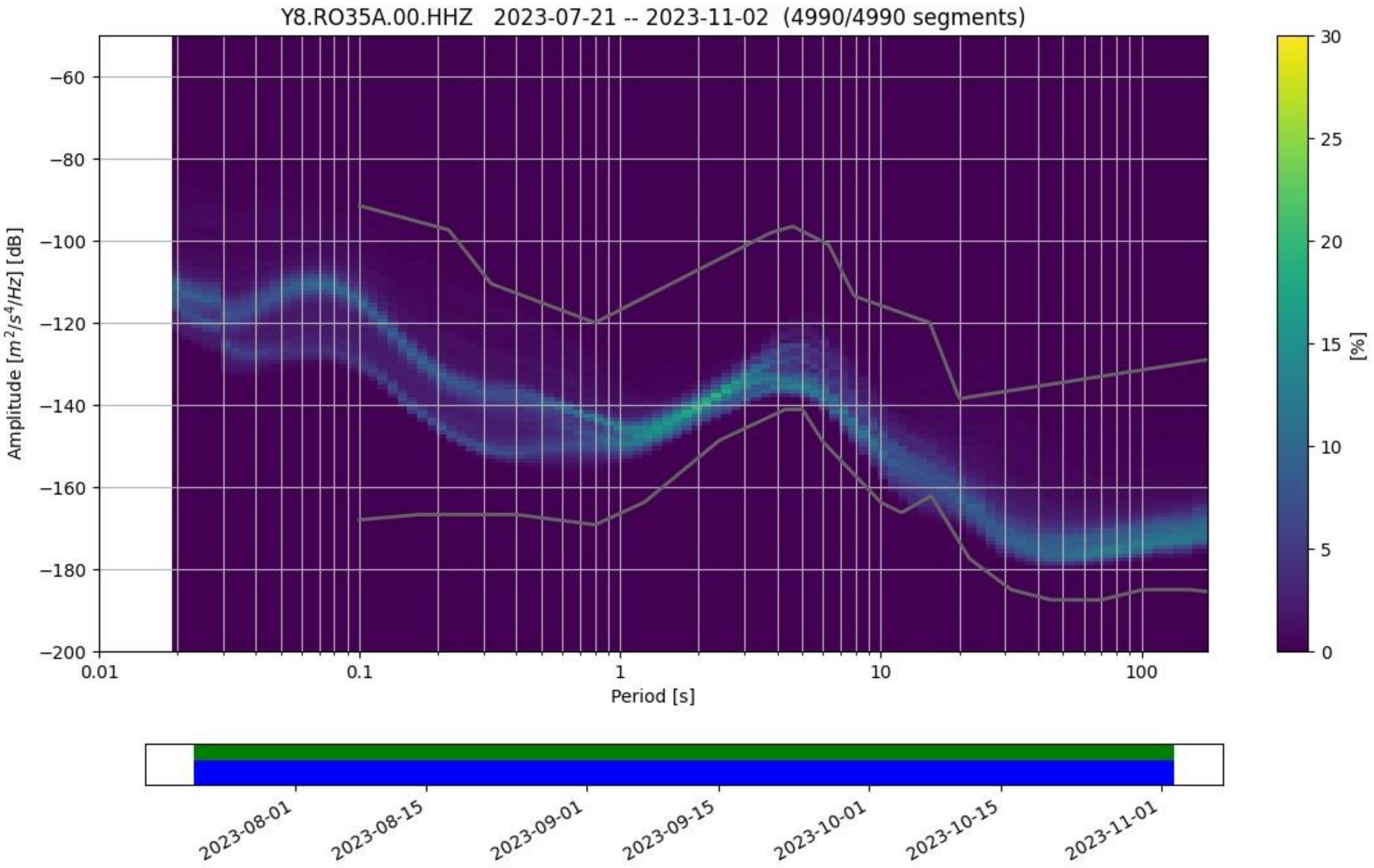

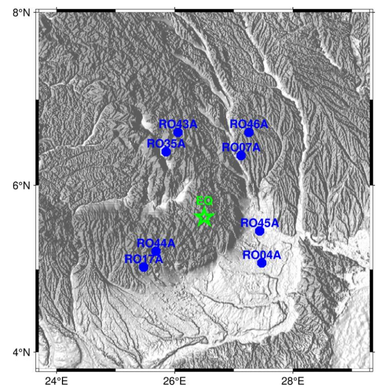

Probabilistic power spectral density (PPSD)

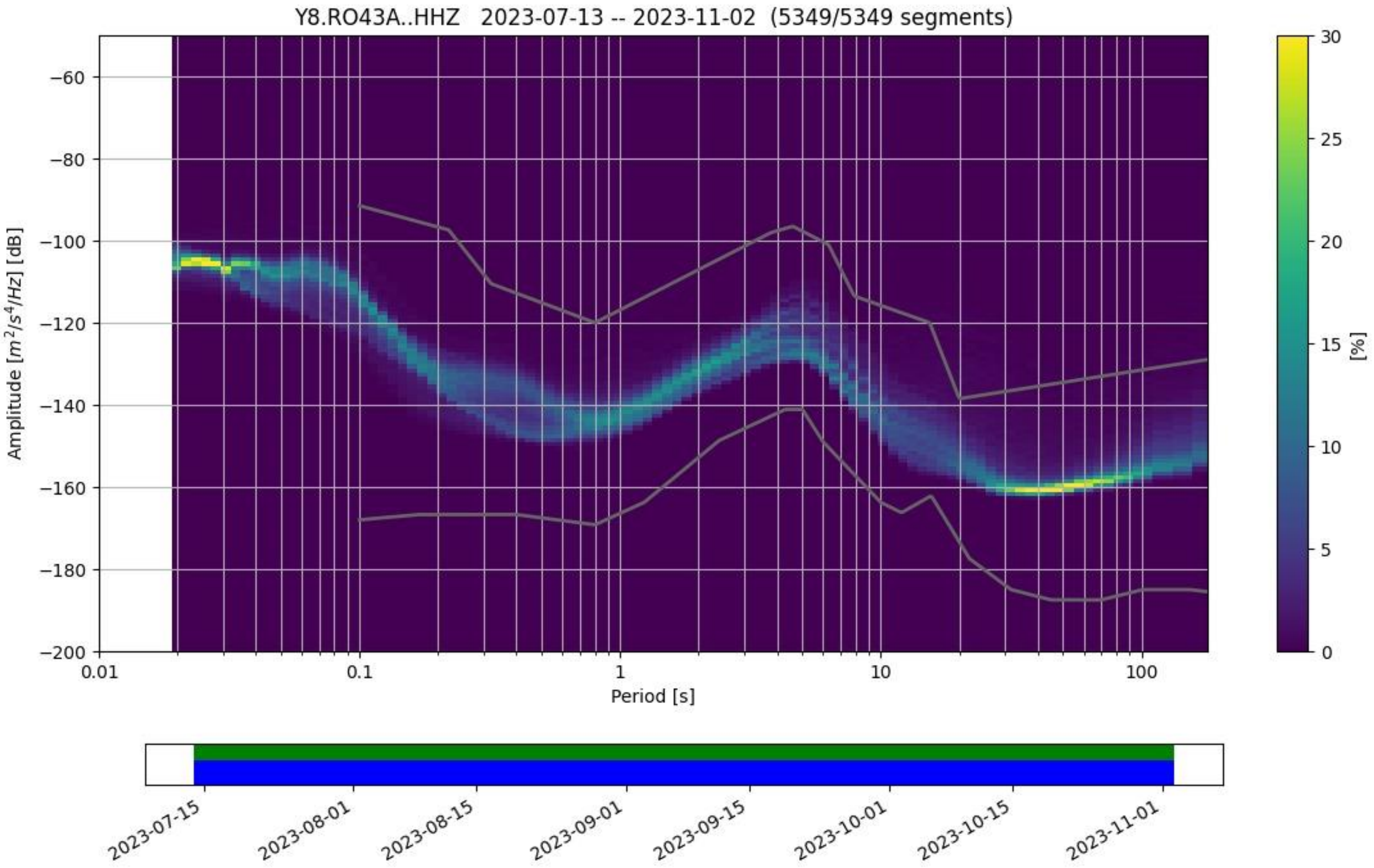

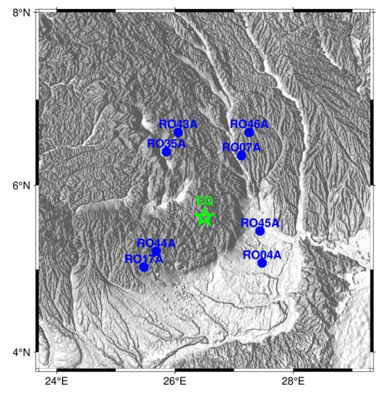

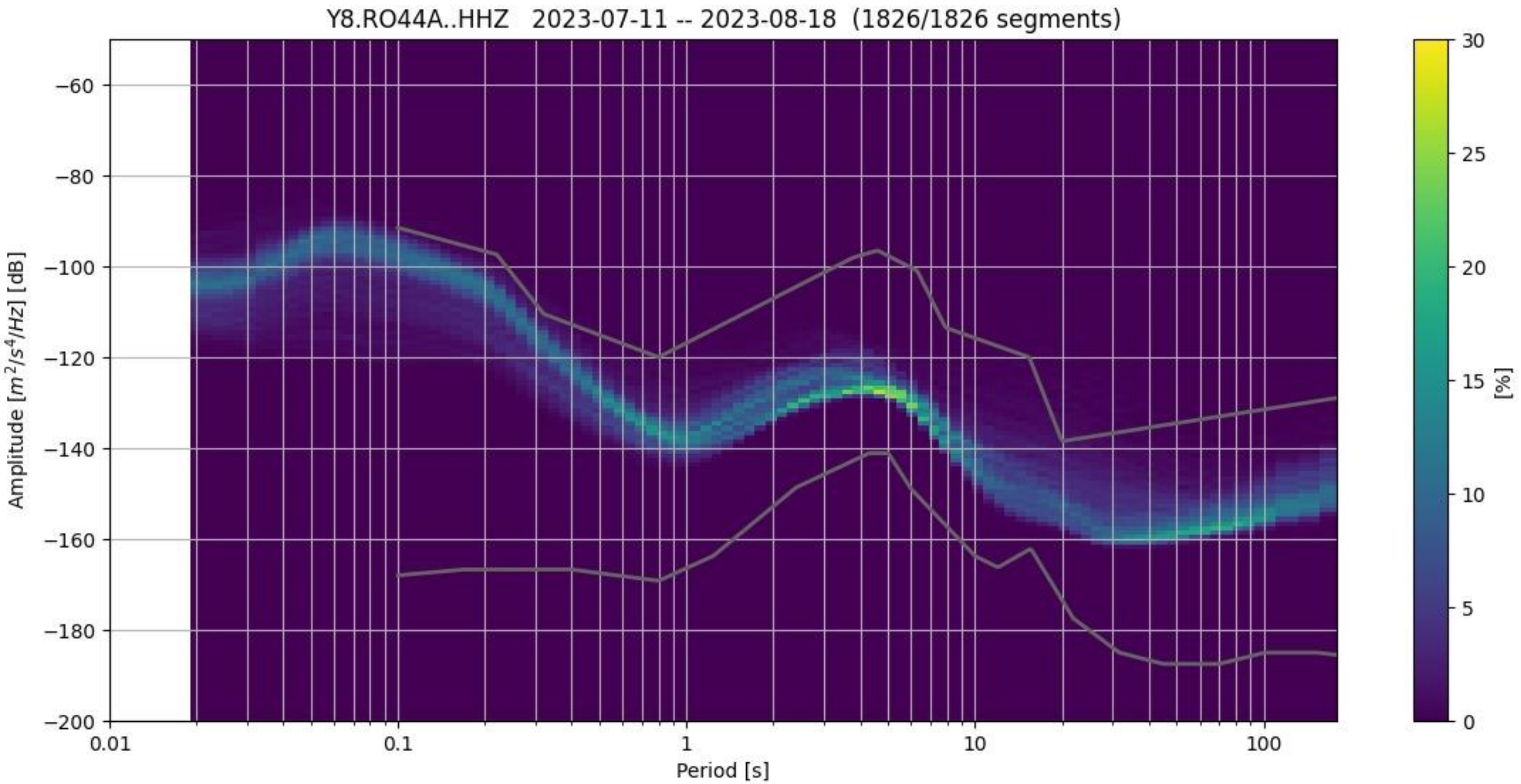
Y8.RO44A..HHZ   2023-07-11 -- 2023-08-18 (1826/1826 segments)
Amplitude [$m^2/s^4/Hz$] [dB]
−60
−80
−100
−120
−140
−160
−180
−200
0.01
0.1
1
10
100
Period [s]
30
25
20
15
10
5
0
[%]

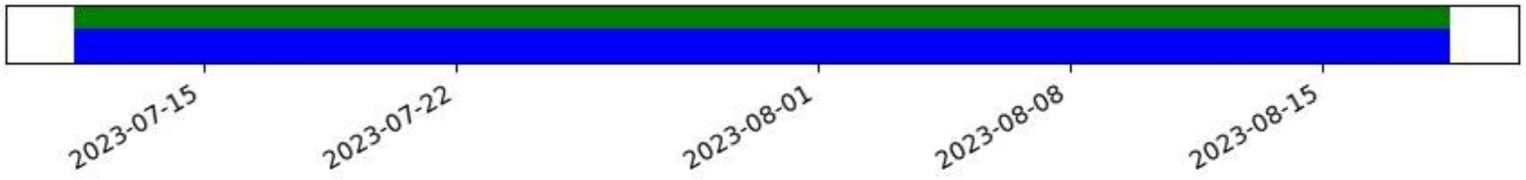
2023-07-15
2023-07-22
2023-08-01
2023-08-08
2023-08-15

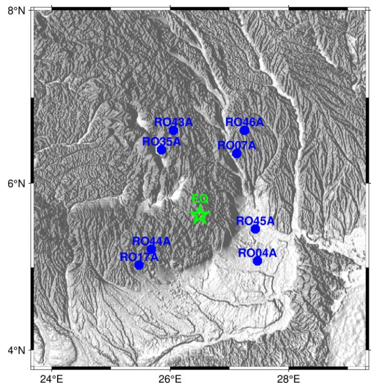
8°N
6°N
4°N
24°E
26°E
28°E
RO43A
RO46A
RO35A
RO07A
EQ
RO45A
RO44A
RO17A
RO04A

Probabilistic power spectral density (PPSD)

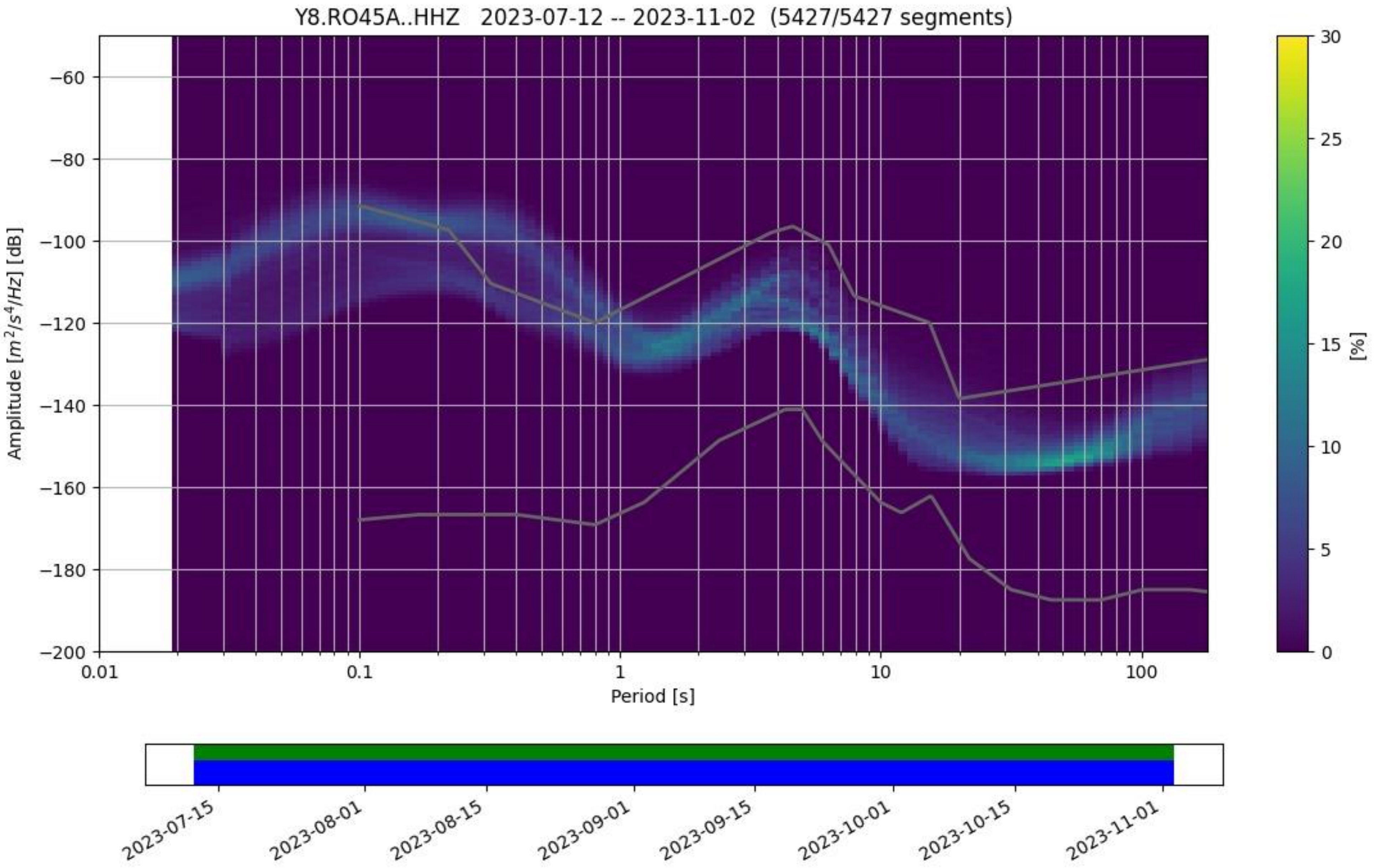

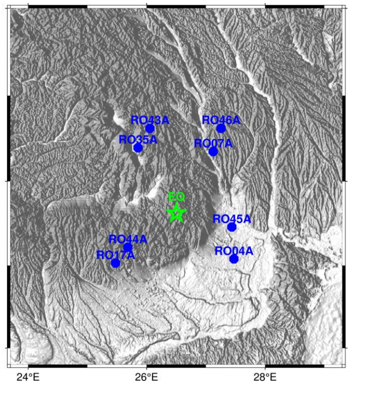

Probabilistic power spectral density (PPSD)

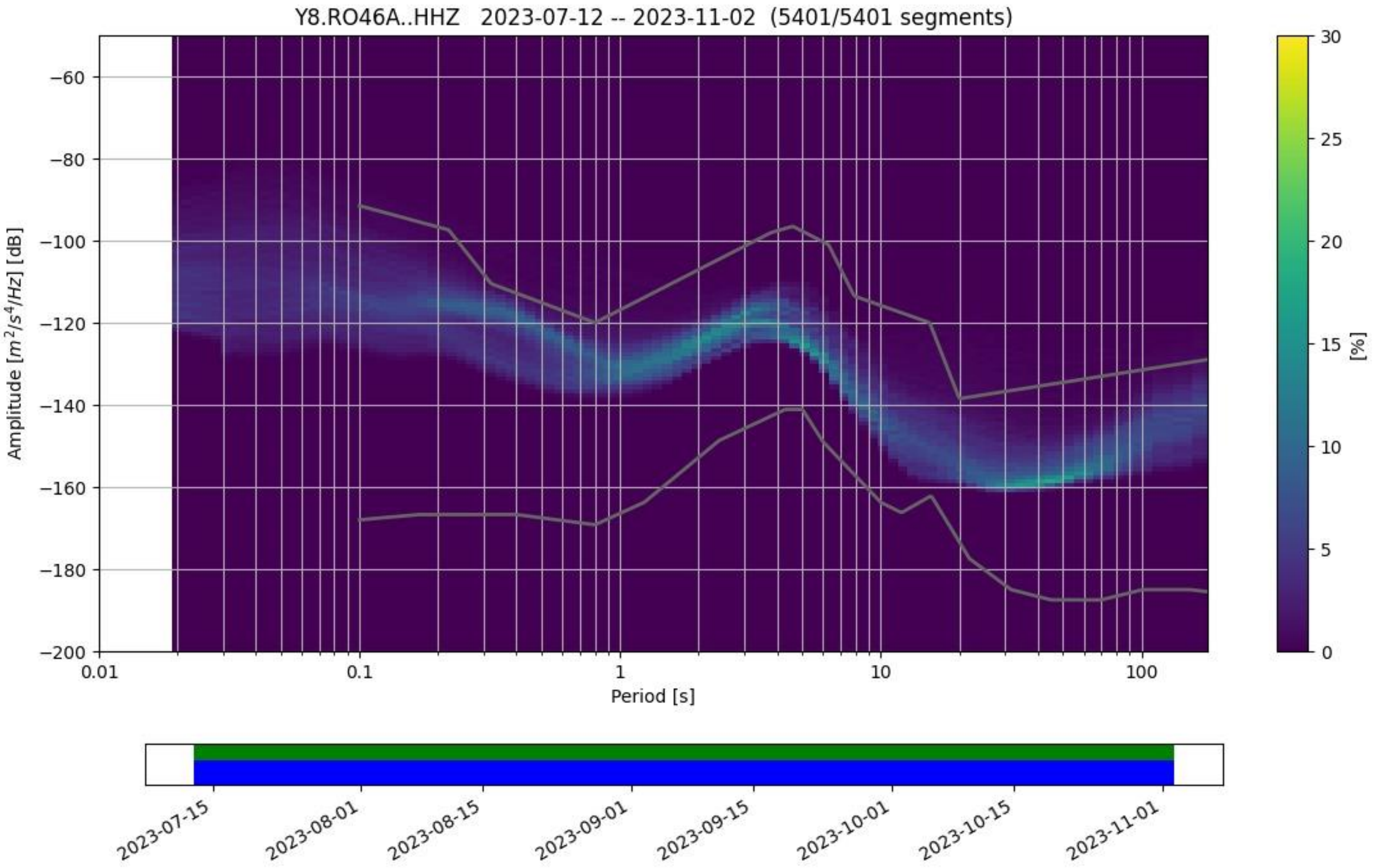

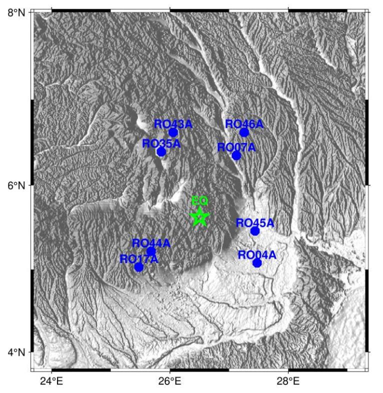

AdriaArray

AdriaArray - Mission

AdriaArray is a multi-national effort to cover the Adriatic Plate and its active margins in the central Mediterranean by a dense regional array of seismic stations to understand the causes of active tectonics and volcanic fields in the region. Plate-scale observations are complemented by local and LargeN experiments in key areas. The AdriaArray region reaches from the Massive Central in the west to the Carpathians in the east, from the Alps in the north to the Calabrian Arc and mainland Greece in the south. The deployment of seismic stations and scientific research is coordinated by the AdriaArray Seismology Group based on FAIR and open data exchange. Analyses of seismicity and multi-scale passive seismic imaging will lay the ground for a physical understanding and modelling of plate deformation and associated geohazards.

AdriaArray - Logo

The logo was discussed at the third AdriaArray international workshop in Dubrovnik, Croatia, on 3-5 April 2023. The logo was approved during the AdriaArray Splinter meeting (EGU General Assembly on April 27th, 2023). Several versions (by Claudia Piromallo and Hana Kampfová Exnerová) are available and can be downloaded from the AdriaArray GitHub repository.

AdriaArray - Current deployment

How to access the data?

Permanent stations, temporary stations with open access as well as metadata (stationXML) are available to AdriaArray members and non members through EIDA nodes.

In order to access the embargoed AdriaArray data, EIDA Token is needed. The token act as login and passwords while requesting waveforms.

EIDA Token

- The seismic data will be available to the participants through EIDA nodes.
- The metadata are openly available, but accessing the embargoed waveforms requires an authentification.

In order to get a token that would give you access to the embargoed AdriaArray data, the procedure is the following:

1. **Register to B2Access**

   If you already have a B2Access account, go to 2) If you do not have a B2Access account, please visit this link

   Please go to the link "No account, sign up". You need to create a B2Access user account (either with a username or with a certificate, up to you, no difference here). The most important is that you need to click "Select group:" and **request to be part of EPOS**. Otherwise, you won't be able to access the data.

2. **Granting permission.**

   Then, please let the representative of Working Group 'Communication and Outreach' know which email was registered, to be added to the AdriaArray group.

   Some nodes (as NIEP) require a manual update of the email list, and it may take a few more days to access the full database (i.e. Y8 network code).

   With this token, you should have access to all the AdriaArray data that are online. Any token generated before being added to the EPOS group will not give you access to the embargoed data. The representative of Working Group 'Communication and Outreach

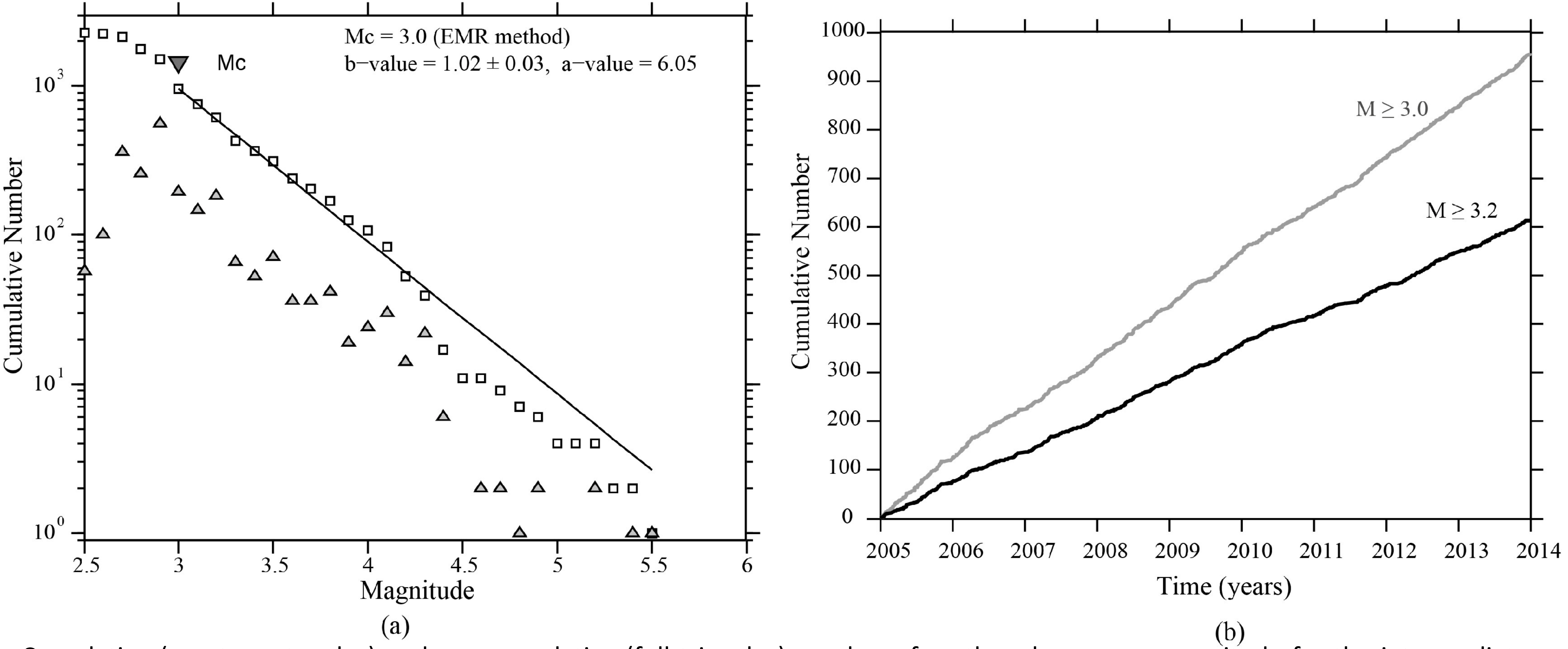

Cumulative (empty rectangles) and non-cumulative (full triangles) number of earthquakes versus magnitude for the intermediate-depth Vrancea earthquakes (ROMPLUS catalog, 60–220 km depth), period **2005–2013**, M ≥ 3.0. The earthquake data are complete above Mc = 3.0 (indicated by an inverted triangle). The black curve is a fit to the data, with the a- and b-values of the frequency-magnitude relation determined using a maximum likelihood procedure. (**b**) Cumulative number of earthquakes with time (years), for two threshold magnitudes (3.0 and 3.2).

Enescu, B.; Ghita, C.; Moldovan, I.-A.; Radulian, M. Revisiting Vrancea (Romania) Intermediate-Depth Seismicity: Some Statistical Characteristics and Seismic Quiescence Testing. Geosciences 2023, 13, 219. https://doi.org/10.3390/geosciences13070219

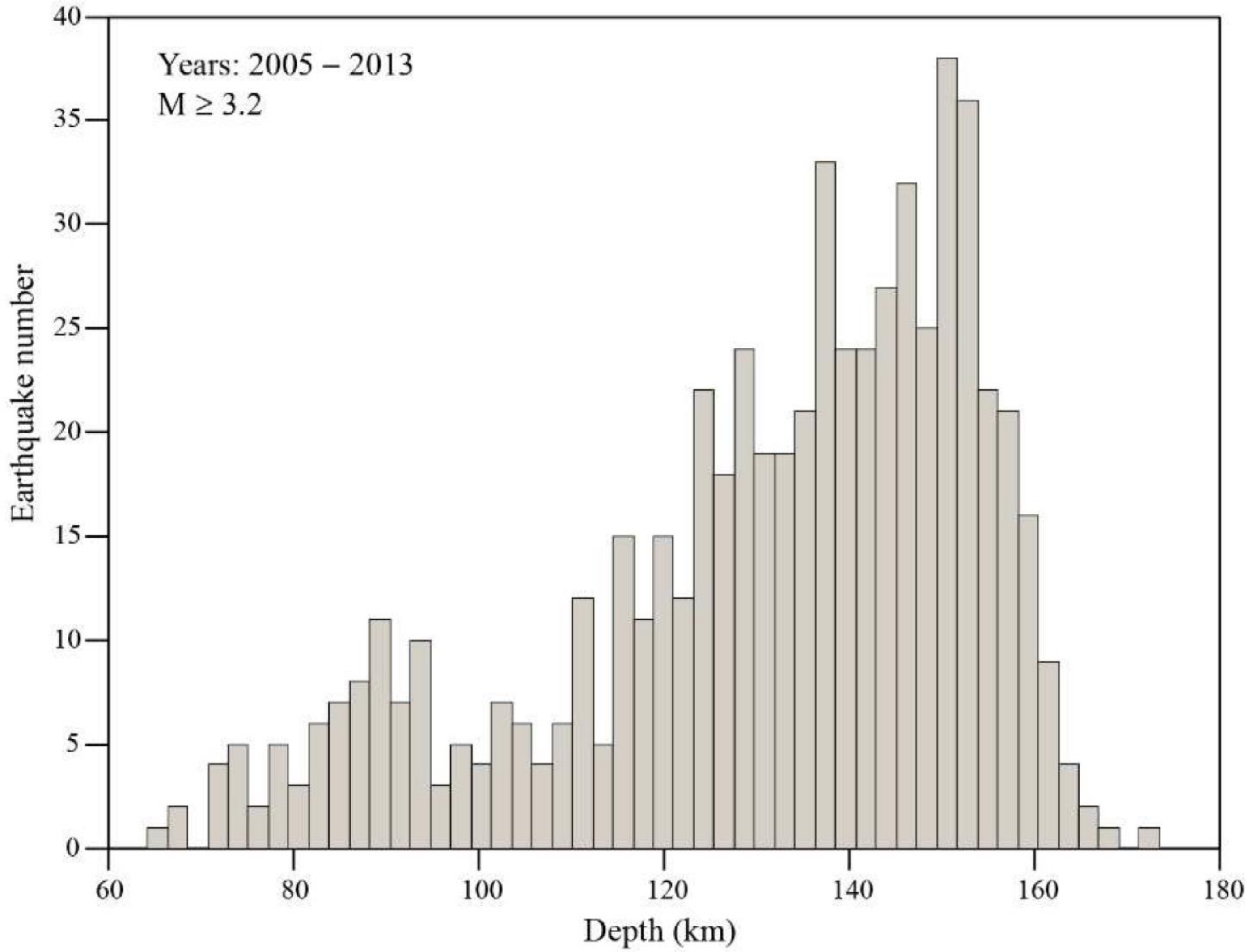

Histogram of earthquakes (2005–2013, M ≥ 3.2) as a function of depth for Vrancea intermediate-depth earthquakes.

Enescu, B.; Ghita, C.; Moldovan, I.-A.; Radulian, M. Revisiting Vrancea (Romania) Intermediate-Depth Seismicity: Some Statistical Characteristics and Seismic Quiescence Testing. Geosciences 2023, 13, 219. https://doi.org/10.3390/geosciences13070219

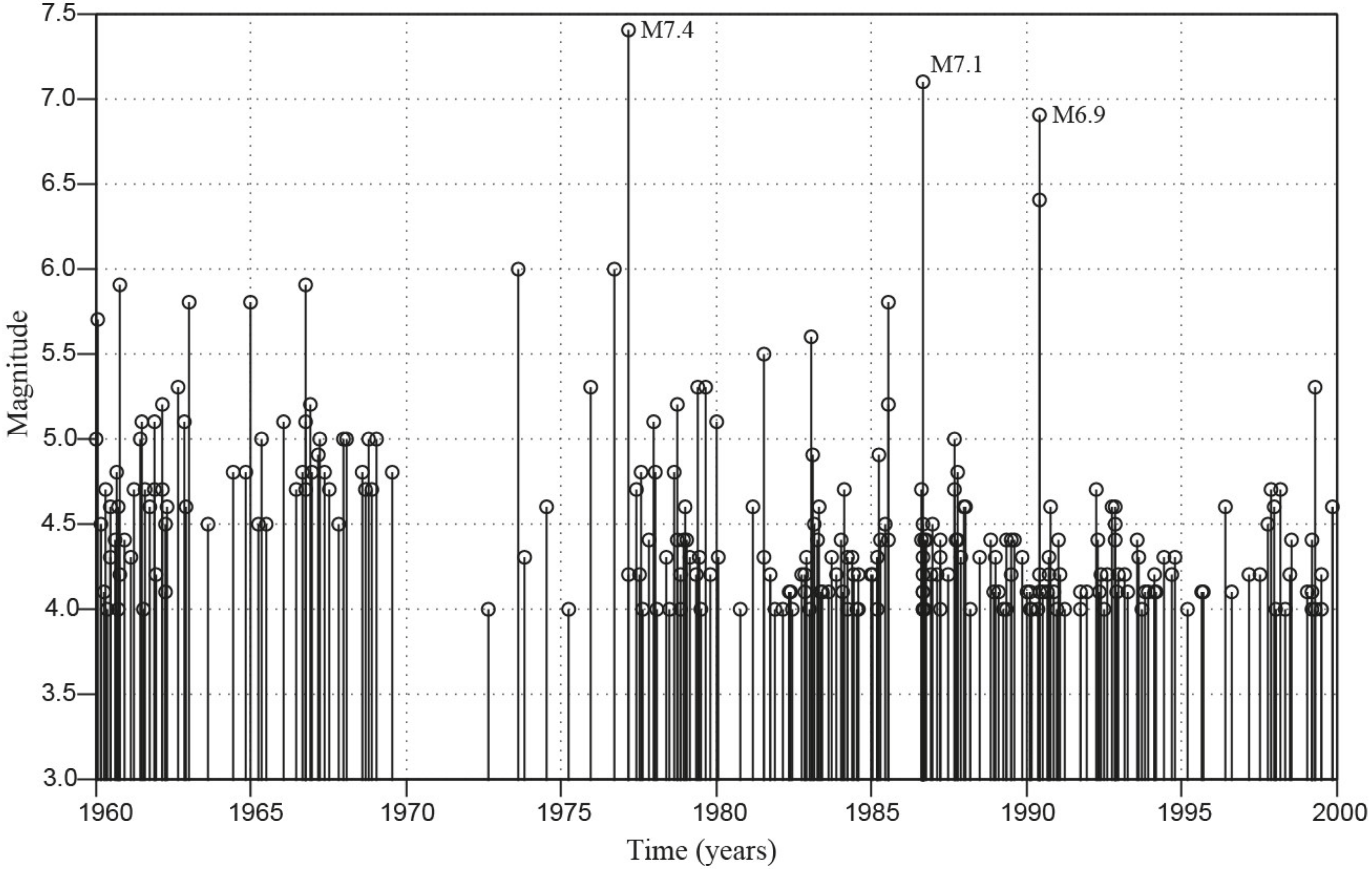

Magnitude versus time for the intermediate-depth Vrancea earthquakes, from 1960–1999. The threshold magnitude is M = 4.0. The three largest earthquakes during the studied period are marked in the figure (1977 M7.4, 1986 M7.1, and 1990 M6.9 Vrancea earthquakes).

Team:
Mgr. Lucia Fojtíková, Ph.D.,
Mgr. Renata Lukešová, Ph.D.,
RNDr. Jiří Málek, Ph.D.
RNDr. Václav Vavryčuk, DrSc.,
Mgr. Jan Valenta, Ph.D.,
RNDr. Jiří Vackář, Ph.D.
Mgr. Martin Mazanec - PhD student
Mgr. Milosz Wcislo (Mgr) - PhD student

Methodologies:

Precise location of microearthquakes: For the determination of P and S wave onsets, we will apply recently developed methods, e.g., a normalized cross-correlation of effective functions for clustering different seismic sequences (e.g., Vlček et al., 2018). Microearthquakes will be located using the double-difference technique. The expected number of events is many tens of thousands every year, therefore automated procedures have to be applied.

Methodologies:

Focal mechanisms: Focal mechanisms will be computed using different approaches, e.g., BayesISOLA, which are automated method for determination of the source mechanism with uncertainties described in Bayesian formulation (Vackář et al., 2017) and/or the method: Cyclic Scanning of the Polarity Solutions (CSPS), which can be efficiently adopted where weak events are recorded (Fojtíková and Zahradník, 2014). We will attempt to calculate the full moment tensors even for microearthquakes. The agreement between nodal planes of the individual sources and possible source clustering on planar faults will be investigated. The superior station coverage of the area, providing a reference focal-mechanism solution, is a unique opportunity to investigate and test methodologies for calculating moment tensors in a sparse network (which is modeled as a subset of the reference station network).

Methodologies:

Existence of seismic tremors: Seismic tremors are typical for regions with active volcanic activity. However, non-volcanic tremors were also detected in many regions. For instance, episodic tremors have been correlated with rupture characteristic in subducting oceanic lithosphere (Burlini et al., 2009). The most probable hypothesis is that non-volcanic tremors are connected with movement of crustal fluids. The presence or absence of seismic tremors and their localization can significantly contribute to the debate about nature of the seismicity in the Vrancea region.

Methodologies:

Tomography based on direct P and S waves from local earthquakes: New data obtained from AdriaArray enables one to construct a more precise and reliable model for Vrancea seismic zone from the surface to 180 km depth - the depth range of the hypocenters. Inversion for a velocity model from travel times generated by local microearthquakes needs a special technique because there is a strong trade-off between hypocenter locations and the velocity model. It is a non-linear inverse problem, which is solved iteratively with the relocation of all earthquakes at each iteration (Málek et al. 2005, Málek et al., 2023). A very fast isometric method was developed for this inverse problem which enables one to compute hundreds of parameters of the velocity model while using millions of onset times of direct P and S waves. This method will be enhanced in the scope of our project. We will determine a velocity model that predicts precise travel times. More precise absolute locations of hypocenters can be determined from this model.

Methodologies:

Amplitude tomography and site-specific GMPE dependent on the hypocenter depth:

Isometric inversion method will be used also for amplitude tomography based on amplitudes of direct P and S waves – it will be used for the Vrancea seismic zone though the hypocenters for Vrancea are much deeper than in Iceland. With this approach, we can find a 3D attenuation (Qp and Qs) model of the region. We will be looking closely for low-value anomalies of Qs, which could imply the presence of partially melted rocks or even the presence of magma.

A second objective will be a site-specific Ground Motion Prediction Equation (GMPE) for the region. This is essential for seismic hazard assessment. For the Vrancea region, it is important to find the sensivitive of the GMPE on hypocenter depth because the strong earthquakes have originated at various depths. Analysis of seismic attenuation from seismic body waves will provide additional information about the tectonic structures in the Vrancea region. Varying depths of the hypocenter will allow us to determine Q in the source area (Wcisło et al., 2018). Q anomalies are often significantly stronger than velocity anomalies. Additionally, the increase/decrease in seismic velocities is not necessarily tied to a corresponding change in seismic attenuation (Pham et al., 2002). Therefore, analysis of QP/QS ratio in the region can provide complementary information - particularly in regards to the discussion about possible slab detachment from the crust.

Děkuji za pozornost!
Vă mulțumim pentru atenție!

Akademie věd České republiky

STRATEGIE AV21
Špičkový výzkum ve veřejném zájmu

Tectonic stress from focal mechanisms: Theory

Václav Vavryčuk

Institute of Geophysics, Prague

Tectonic stress and its graphical representation

Basic properties of the stress tensor

Stress tensor

$$\boldsymbol{\tau} = \begin{bmatrix} \tau_{11} & \tau_{12} & \tau_{13} \\ \tau_{21} & \tau_{22} & \tau_{23} \\ \tau_{31} & \tau_{32} & \tau_{33} \end{bmatrix}$$

$\tau_{ij} = \tau_{ji}$ tensor is symmetric

Traction

$$T_i = \tau_{ij} n_j$$

force acting on plane with normal **n** produced by stress in the body

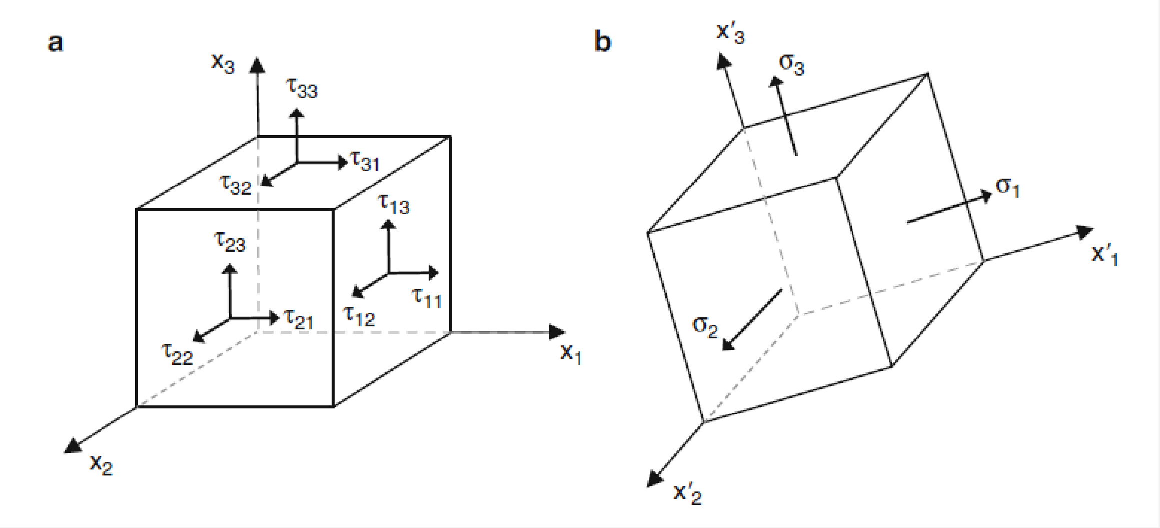

transformation into the principal coordinate system

$$\boldsymbol{\tau} = \begin{bmatrix} \sigma_1 & 0 & 0 \\ 0 & \sigma_2 & 0 \\ 0 & 0 & \sigma_3 \end{bmatrix}$$

$$\sigma_1 \geq \sigma_2 \geq \sigma_3$$

Vavryčuk (Encyclopedia Earth. Eng., 2015)

Mohr's circle diagram - definition

Traction: $T_i = \tau_{ij} n_j$

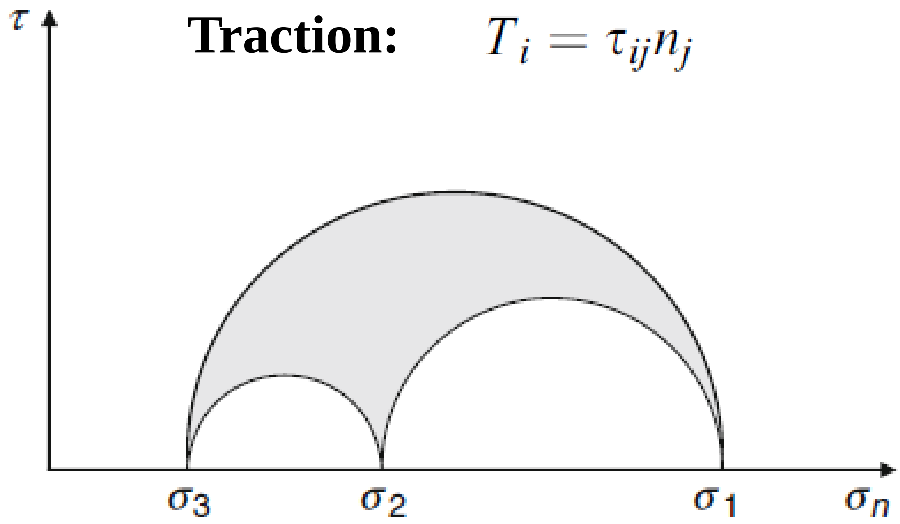

$$\sigma_n = \sigma_1 n_1^2 + \sigma_2 n_2^2 + \sigma_3 n_3^2,$$

$$\tau^2 = \sigma_1^2 n_1^2 + \sigma_2^2 n_2^2 + \sigma_3^2 n_3^2 - \sigma_n^2.$$

σ_1 means compression and it is negative

$|\mathbf{n}| = 1$ is the normal to the fault plane

τ is shear traction, σ_n is normal traction

- traction generated on any plane in the body is constrained
- only combinations of shear and normal tractions lying in the shaded area are allowed

Vavryčuk (Encyclopedia Earth. Eng., 2015)

Mohr's circle diagram - derivation

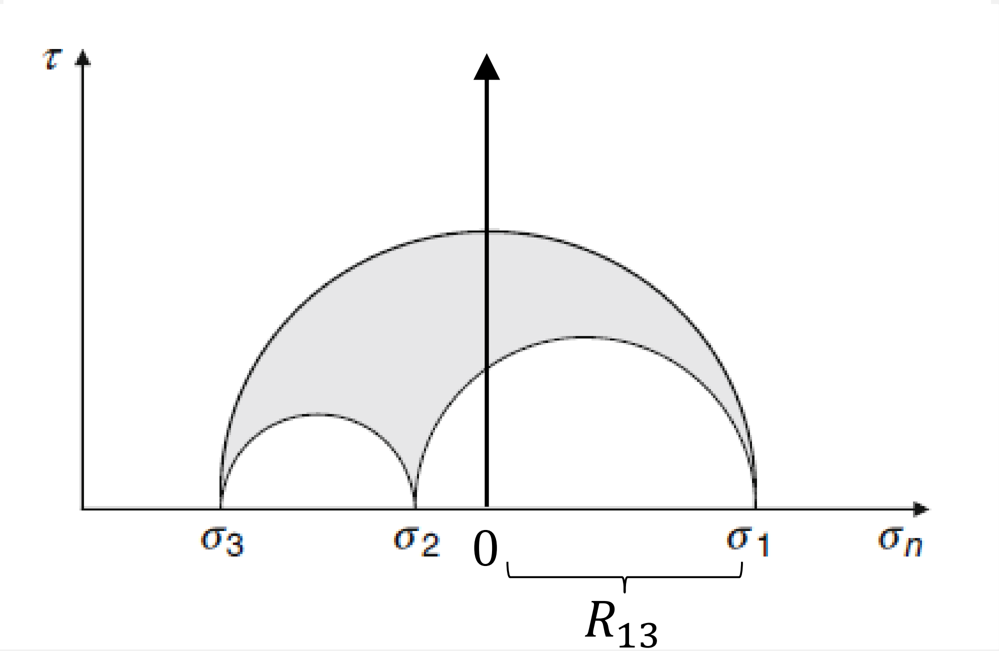

$$\sigma_n = \sigma_1 n_1^2 + \sigma_2 n_2^2 + \sigma_3 n_3^2,$$

$$\tau^2 = \sigma_1^2 n_1^2 + \sigma_2^2 n_2^2 + \sigma_3^2 n_3^2 - \sigma_n^2.$$

σ_1 means compression and it is negative

$|\mathbf{n}| = 1$ is the normal to the fault plane

Constraints:

$$\sigma_n^2 + \tau^2 \leq R_{13}^2 \qquad R_{13} = \frac{\sigma_1 - \sigma_3}{2}$$

$$\sigma_n^2 + \tau^2 \geq R_{12}^2 \qquad R_{12} = \frac{\sigma_1 - \sigma_2}{2}$$

$$\sigma_n^2 + \tau^2 \geq R_{23}^2 \qquad R_{23} = \frac{\sigma_2 - \sigma_3}{2}$$

Vavryčuk (Encyclopedia Earth. Eng., 2015)

Mohr's circle diagram versus pore pressure

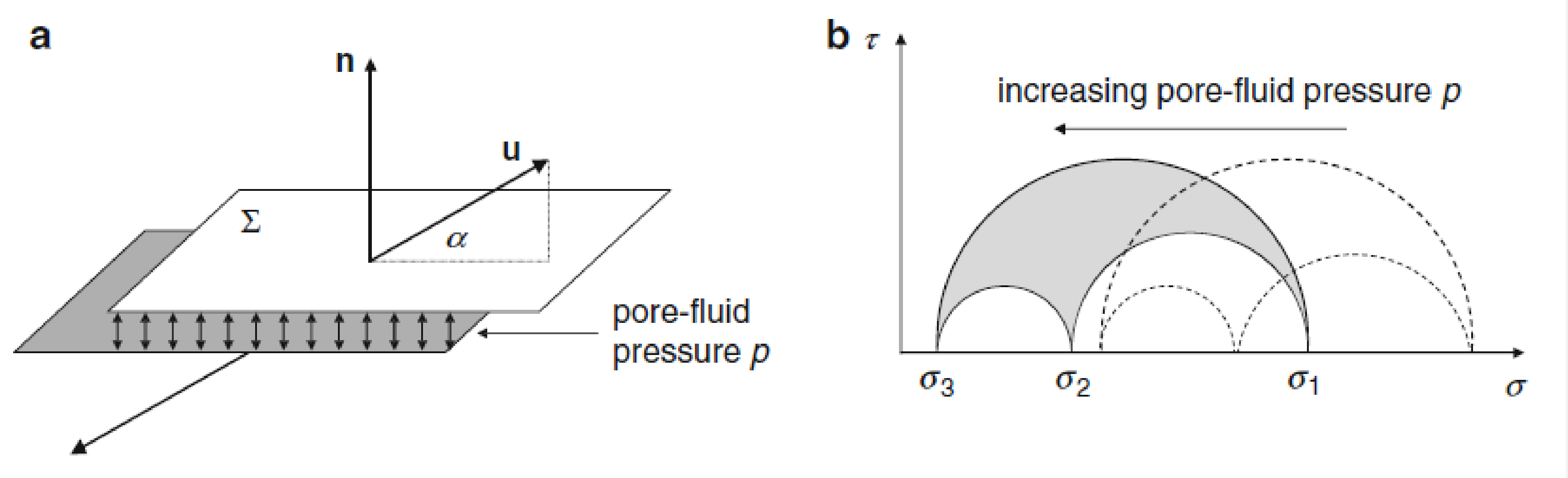

$$\sigma = \sigma_n - p,$$

effective normal traction in the porous medium

- increasing pore fluid pressure diminishes the effective normal
- increasing pore fluid pressure moves the diagram to the left
- decreasing ore fluid pressure moves the diagram to the right

Vavryčuk (Encyclopedia Earth. Eng., 2015)

Mohr-Coulomb failure criterion

When the fracture is activated?

$$\tau > \tau_c = S + k\underbrace{(\sigma_n - p)}_{\sigma}$$

τ_c – critical shear traction

S – cohesion

k – friction

σ_n – normal traction

p – pore pressure

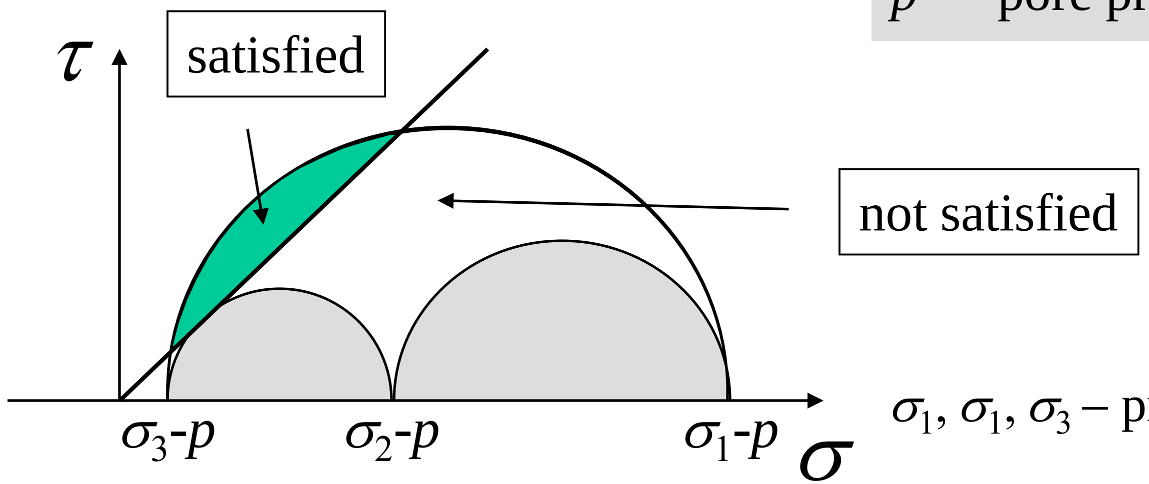

σ_1, σ_1, σ_3 – principal stress values

τ - shear traction

σ - effective normal traction

The origin of σ depends on p !

Pore pressure & types of earthquakes

a) No earthquakes

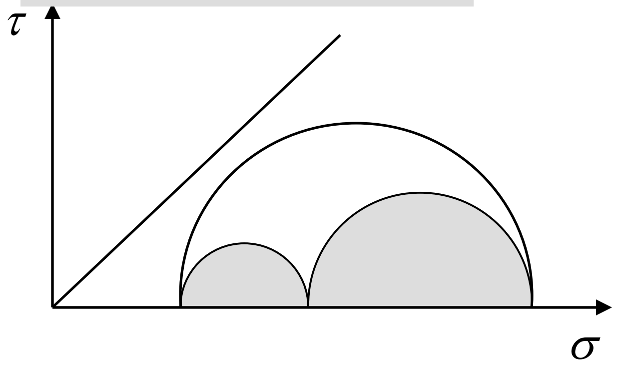

b) Shear earthquakes

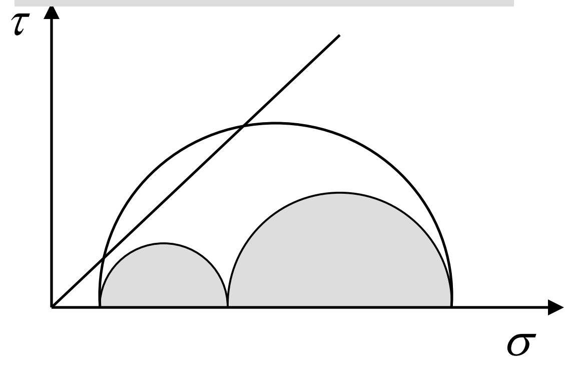

c) Shear & tensile earthquakes

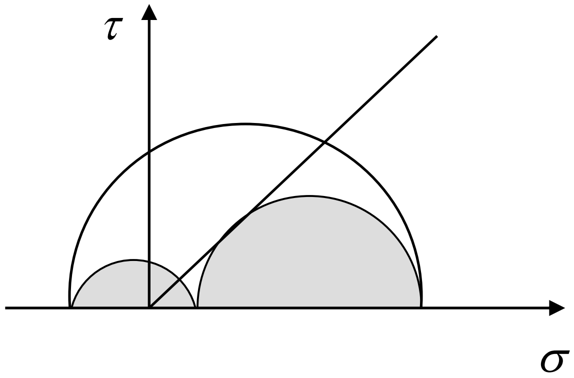

Pore pressure:

a) low

b) high

c) very high

Principal faults and principal earthquakes

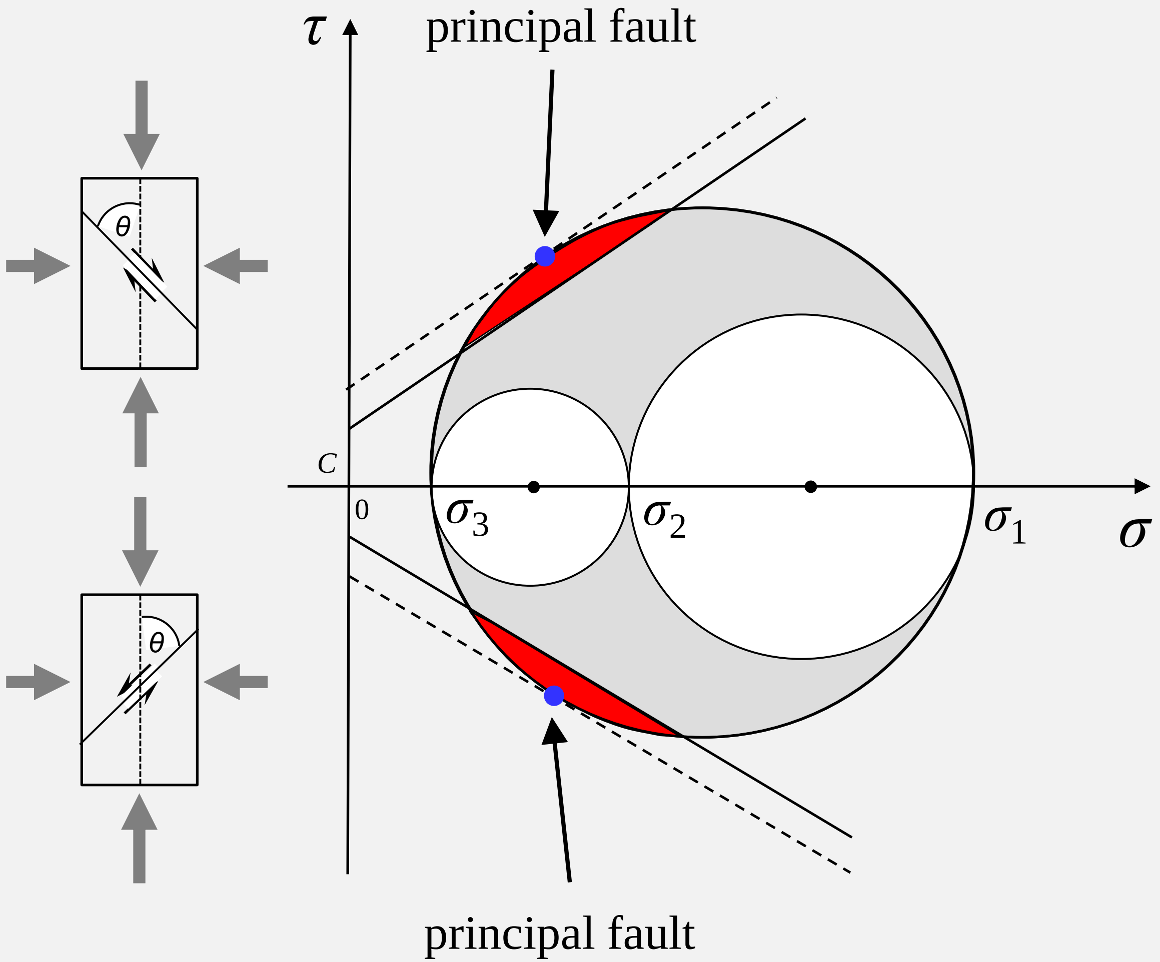

Principal earthquakes, P/T axes and stress

Principal focal mechanisms

Principal focal mechanisms – the mechanisms which occur on the most unstable (optimally oriented) fault planes

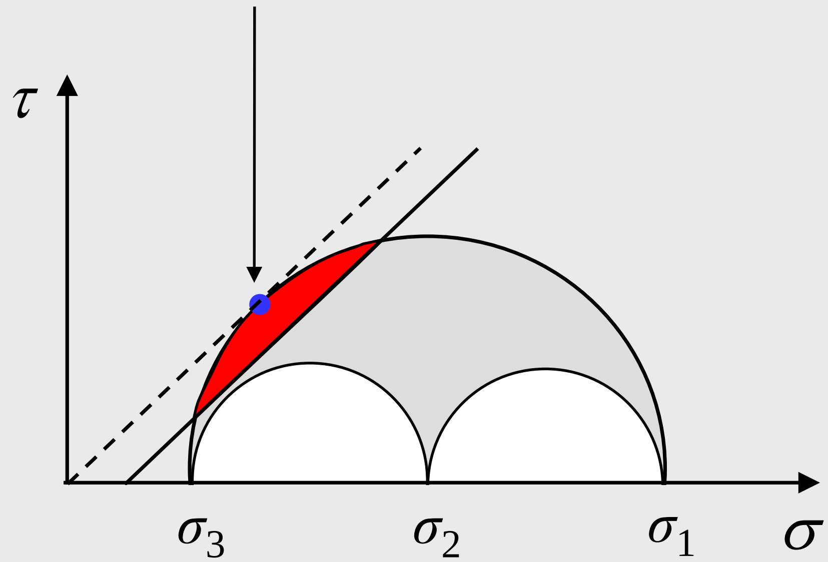

shape ratio = 0.5
friction = 0.6

Principal nodal lines and P/T axes

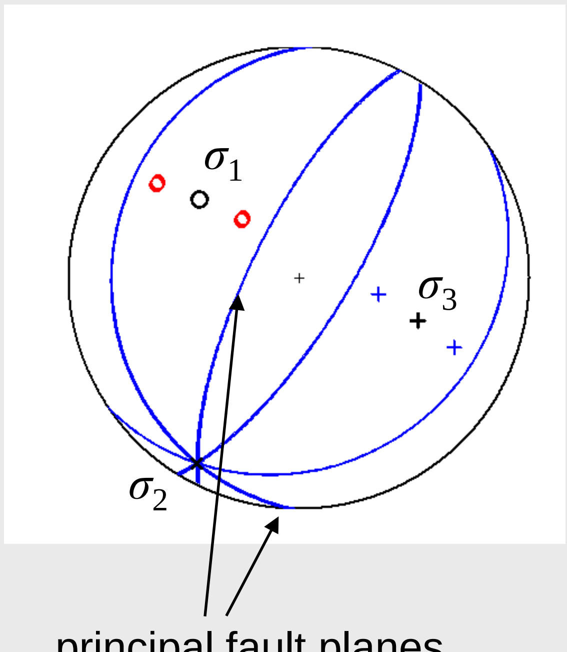

Principal faults and principal earthquakes

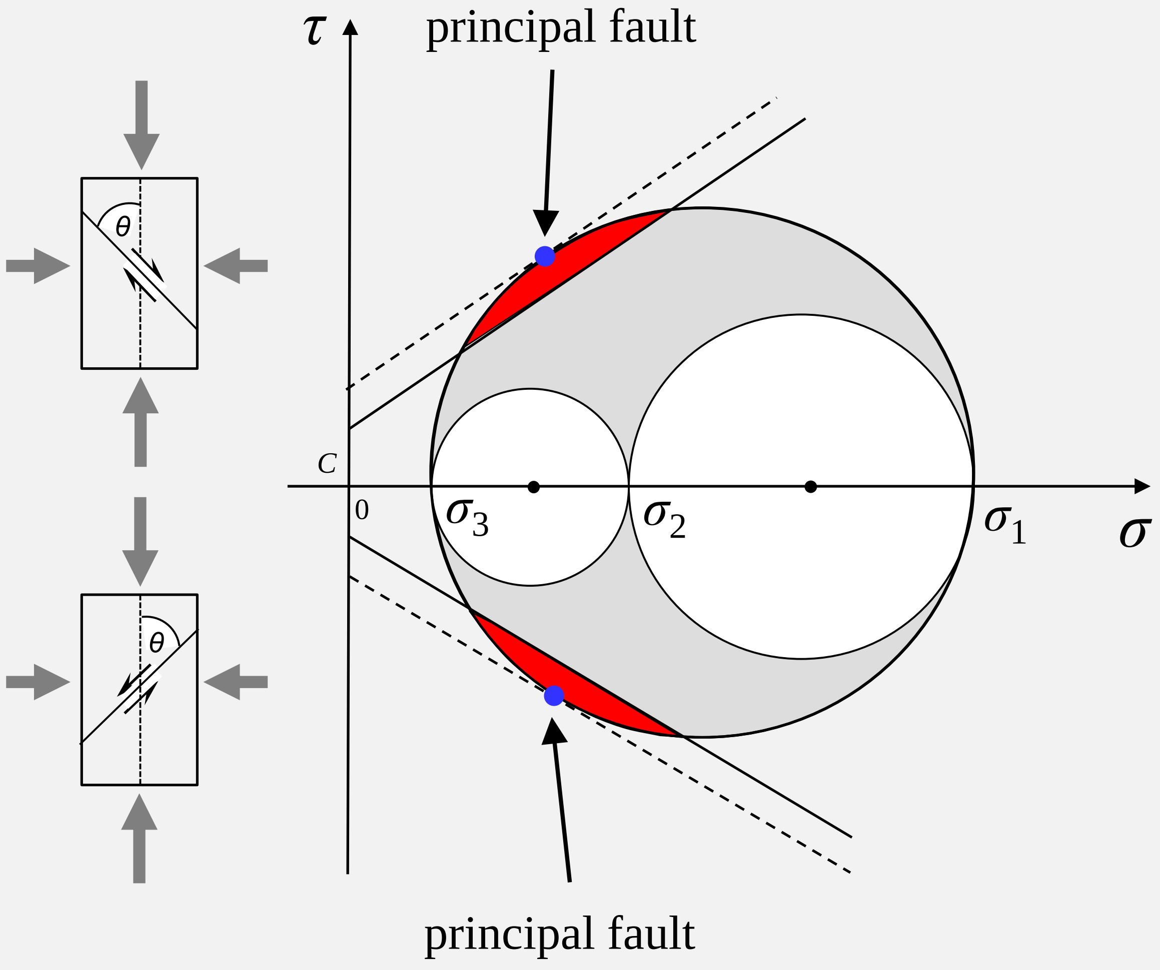

Failure criterion in the Mohr's circle diagram

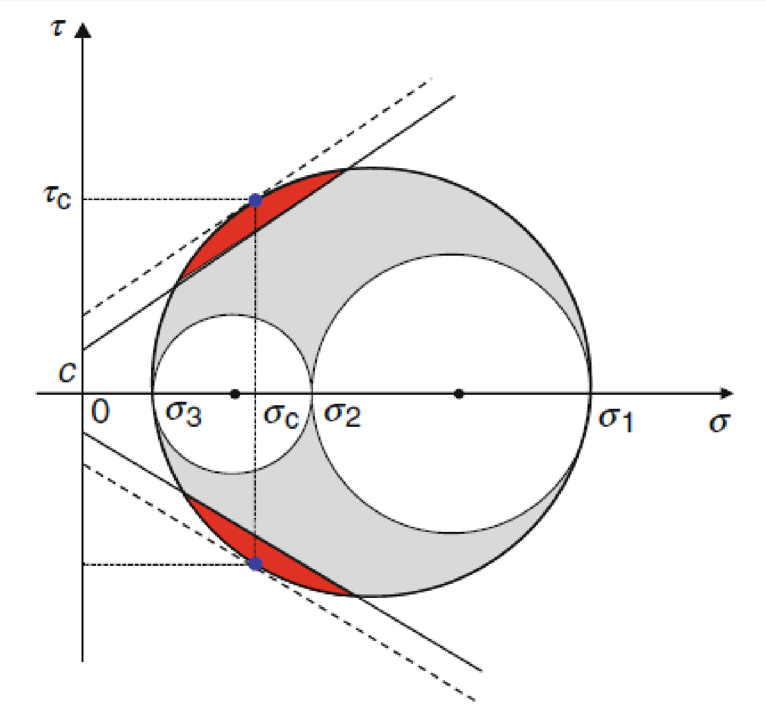

Mohr-Coulomb failure criterion

$$\tau_c = C + \mu\sigma,$$

$$\tau_c = C + \mu(\sigma_n - p),$$

fault is activated when shear stress exceeds critical value τ_c

Fault instability

$$I = \frac{\tau - \mu(\sigma - \sigma_1)}{\tau_c - \mu(\sigma_c - \sigma_1)},$$

- increasing pore fluid pressure activates more fault planes
- decreasing ore fluid pressure reduces the number of activated fault planes

Vavryčuk (Encyclopedia Earth. Eng., 2015)

Principal focal mechanisms

Principal focal mechanisms – the mechanisms that occur on the most unstable (optimally oriented) fault planes

Principal nodal lines

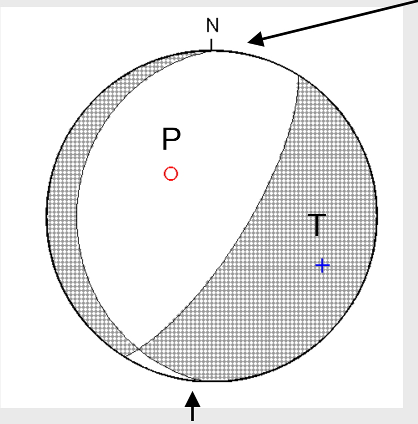

principal
fault plane

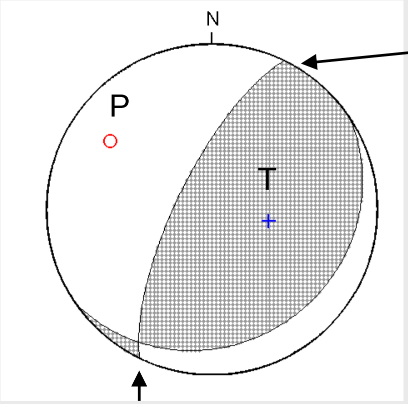

principal
fault plane

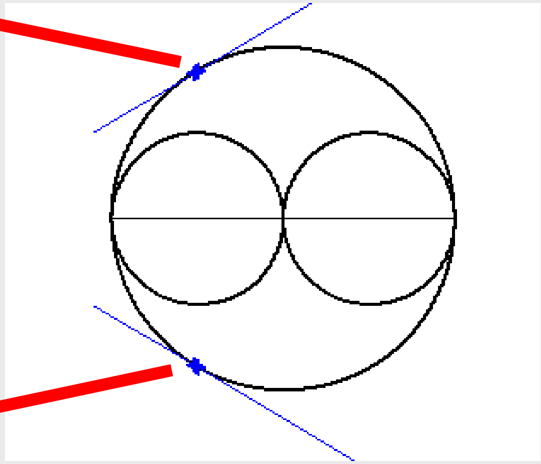

Principal focal mechanisms

Principal focal mechanisms – the mechanisms that occur on the most unstable (optimally oriented) fault planes

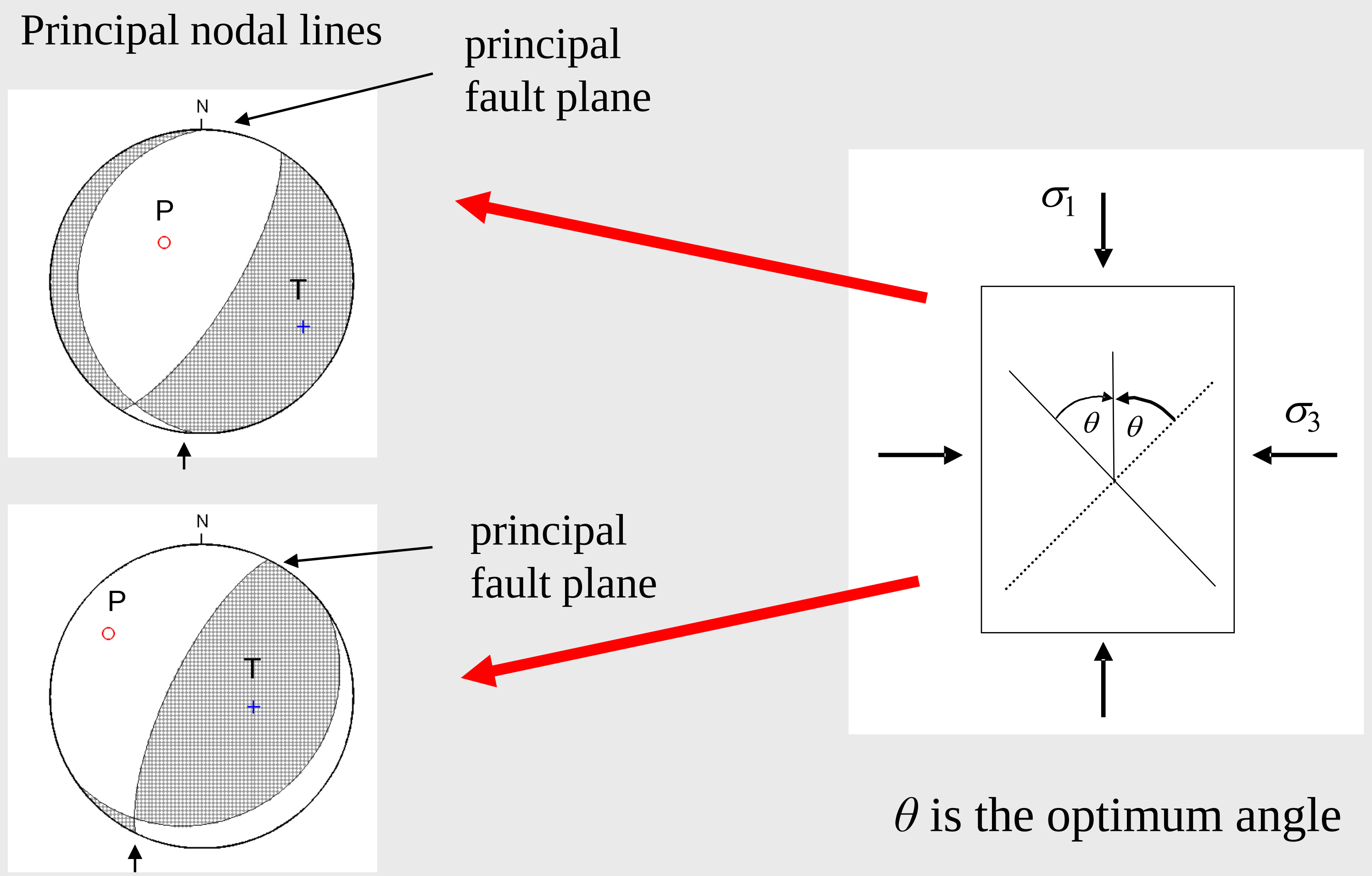

Principal focal mechanisms versus friction

Mohr's diagram	Nodal lines	P/T axes

shape ratio = 0.6

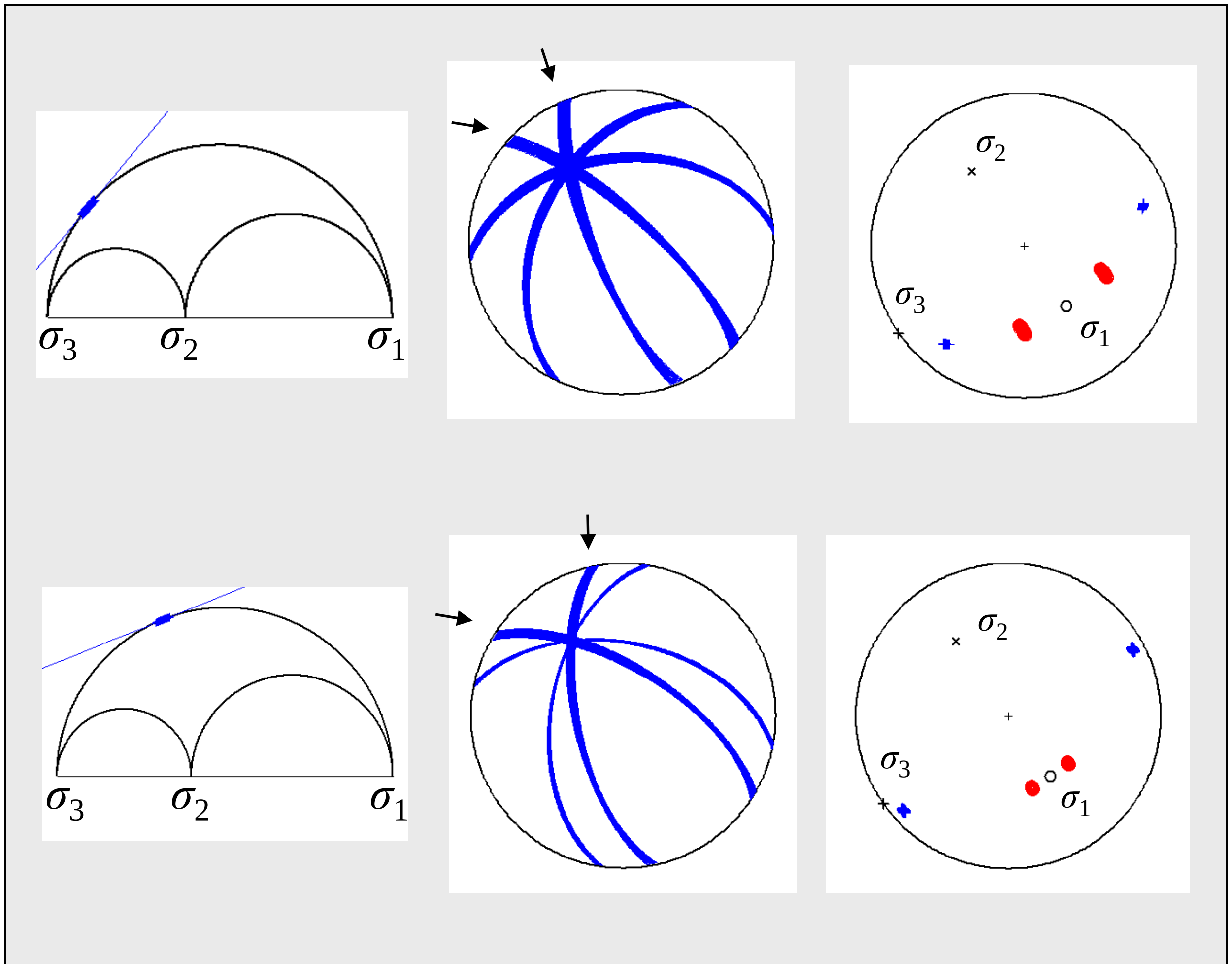

friction = 1.2

friction = 0.4

Butterfly wings

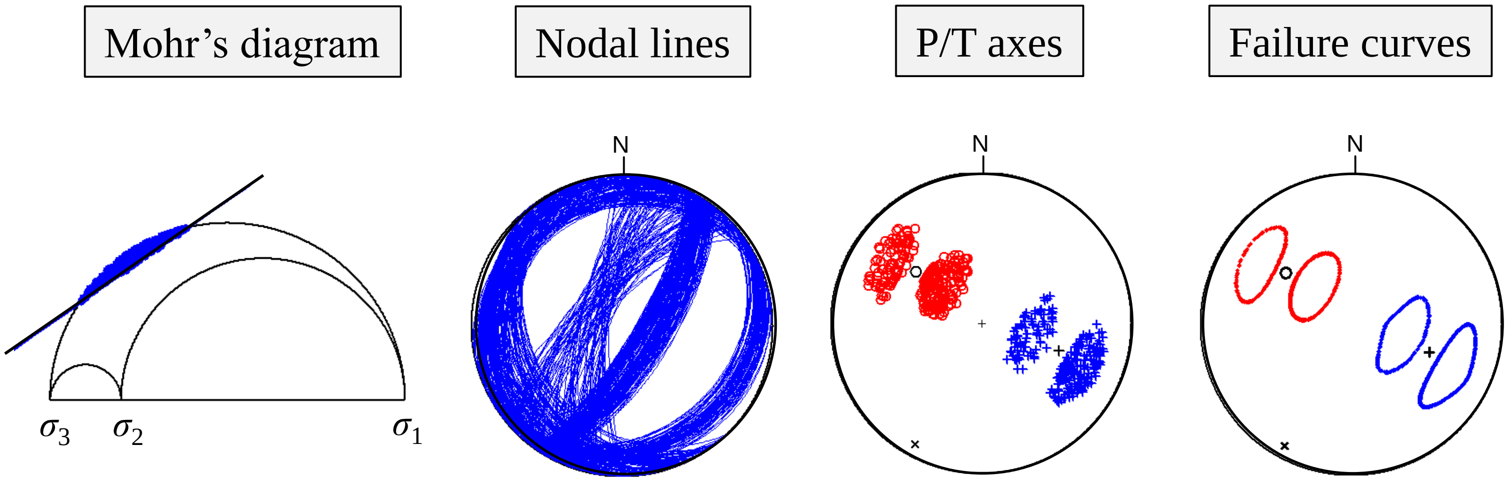

shape ratio = 0.8, friction = 0.7

Vavryčuk (EPSL, 2011)

P/T axes under various stress conditions

Procedure

Assumptions:

- Tectonic stress in the focal area is homogeneous
- Pore pressure, cohesion and friction on faults is constant

Modeled parameters:

- Orientation of faults satisfying the Mohr-Coulomb failure criterion
- Statistical properties of focal mechanisms: nodal lines, P/T axes

Statistical distribution of focal mechanisms

Tectonic stress

$$R = \frac{\sigma_1 - \sigma_2}{\sigma_1 - \sigma_3}$$

Mohr's diagram

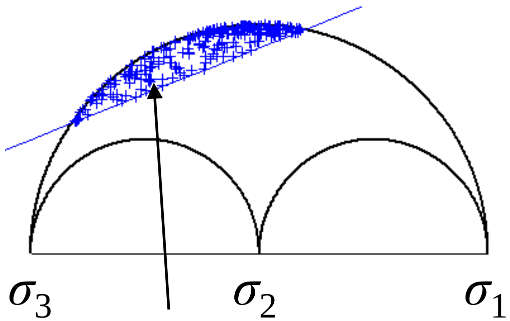

randomly distributed faults satisfying the failure criterion

orientation of principal axes

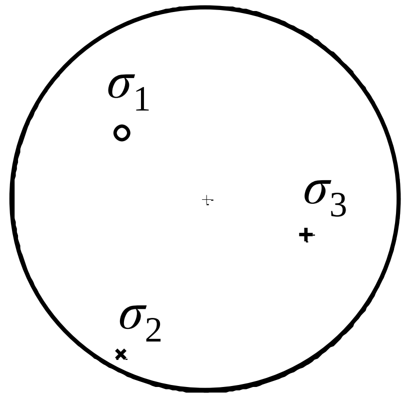

shape ratio = 0.5
friction = 0.5

Focal mechanisms

→ slip is along the traction on the fault

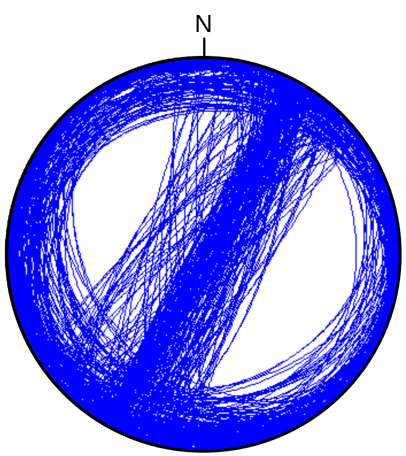

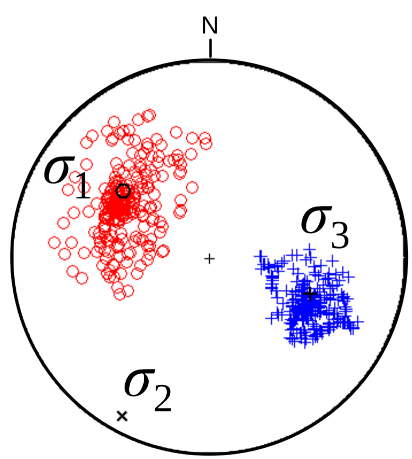

N = 250

o - P axis
+ - T axis

Failure curves I

Mohr's diagram	Nodal lines	P/T axes

shape ratio = 0.5
friction = 0.5

All unstable faults

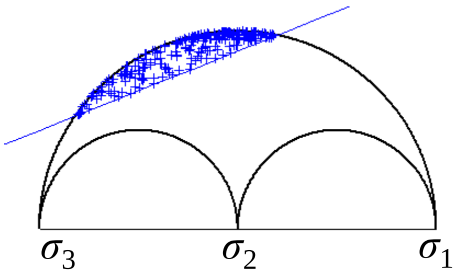

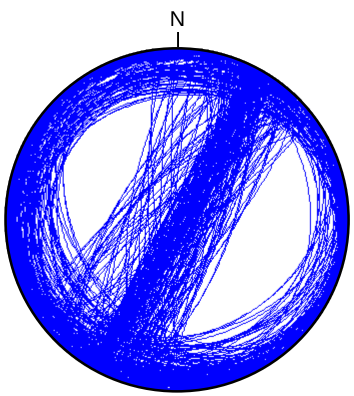

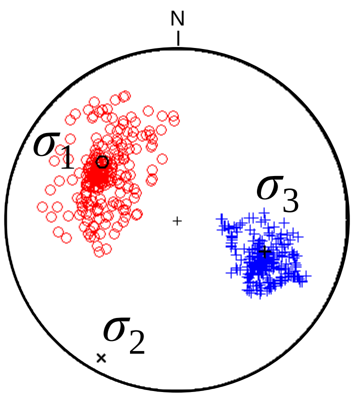

How to trace the shape of the P/T clouds?

Failure curves II

Mohr's diagram	Nodal lines	P/T axes

shape ratio = 0.5
friction = 0.5

All unstable faults

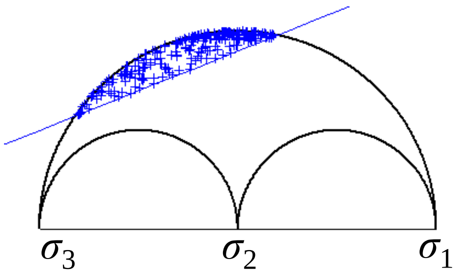

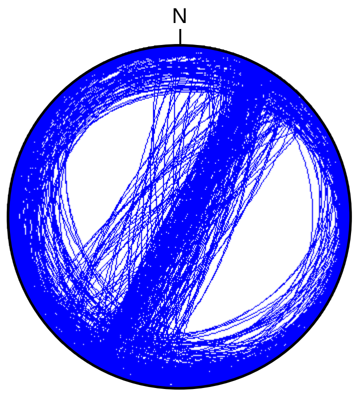

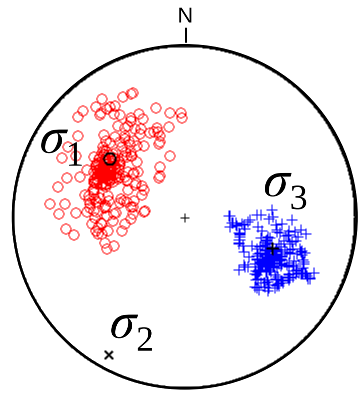

How to trace the shape of the P/T clouds?

Boundary unstable faults

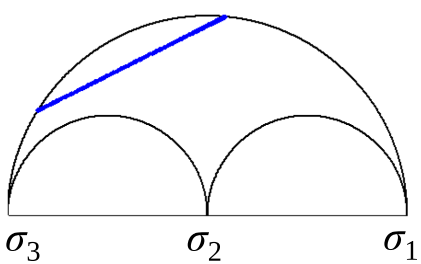

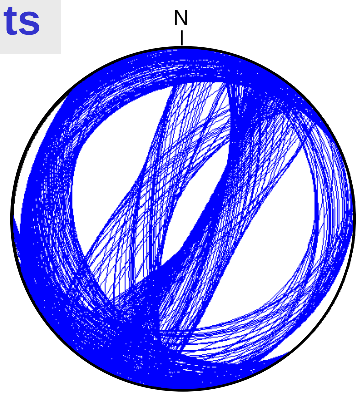

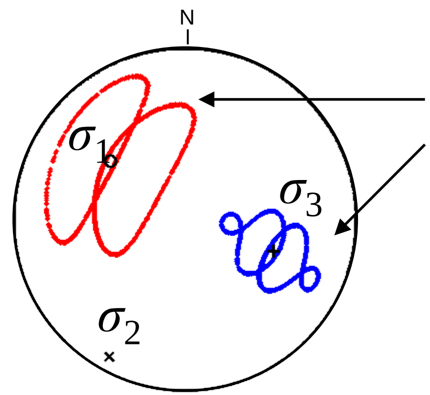

failure curves
(butterfly wings)

Friction dependence

Mohr's diagram	Nodal lines	P/T axes	Failure curves

shape ratio = 0.5

friction = 0.3

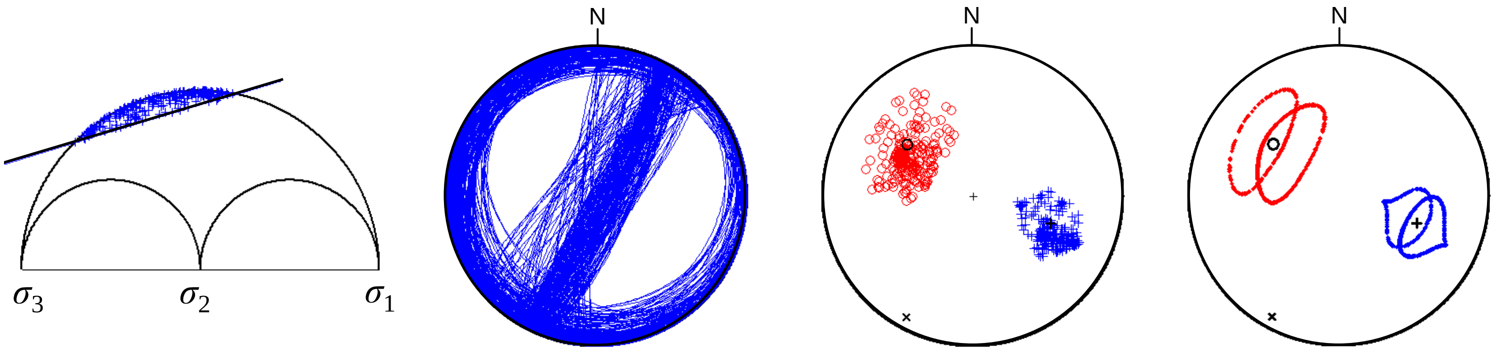

friction = 1.0

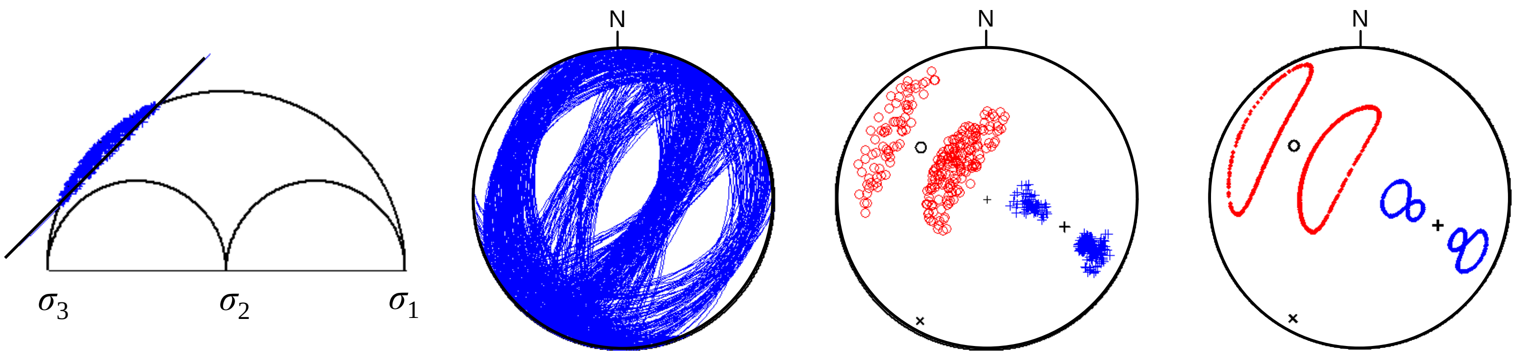

Shape ratio dependence

Mohr's diagram	Nodal lines	P/T axes	Failure curves

friction = 0.7

Shape ratio = 0.2

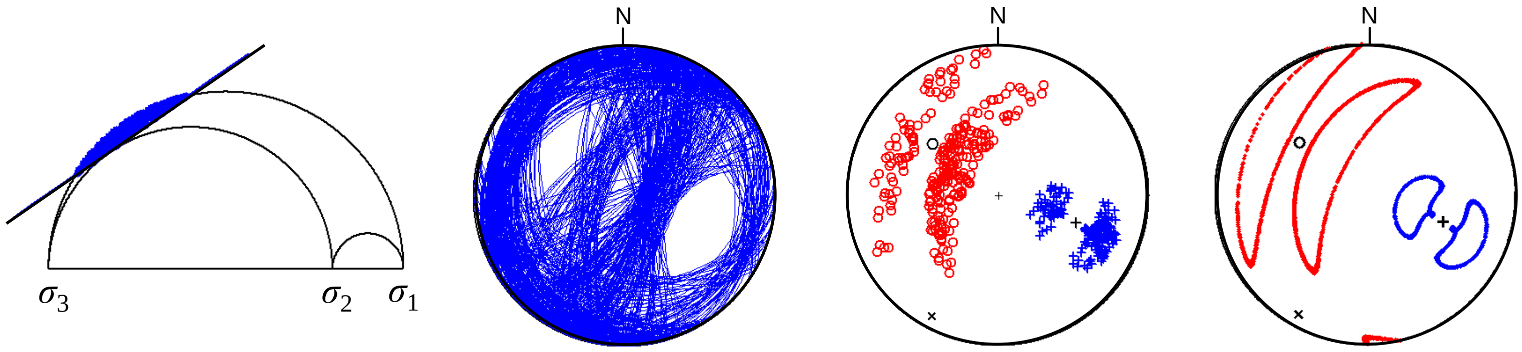

Shape ratio = 0.8

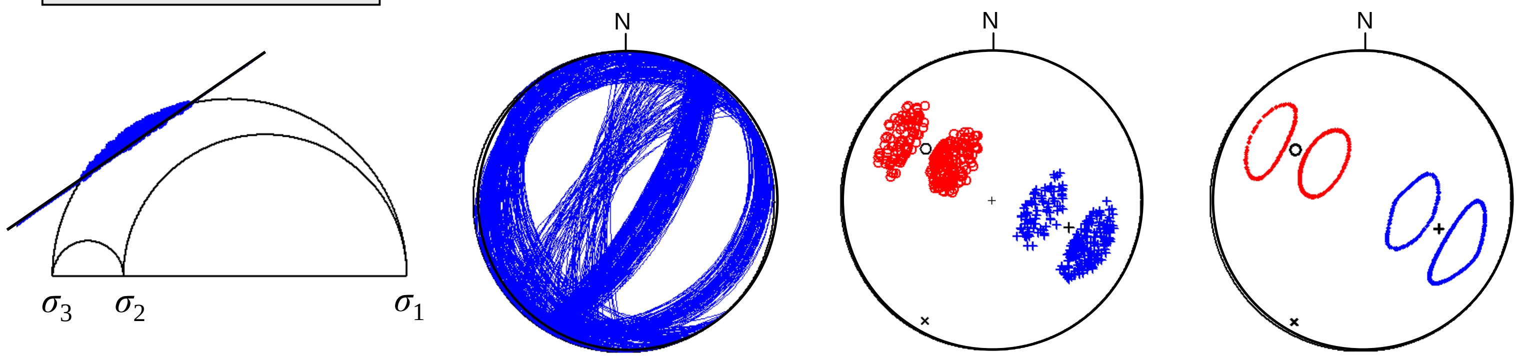

Pore pressure dependence

Mohr's diagram	Nodal lines	P/T axes	Failure curves

friction = 0.7
shape ratio = 0.5

High pore pressure

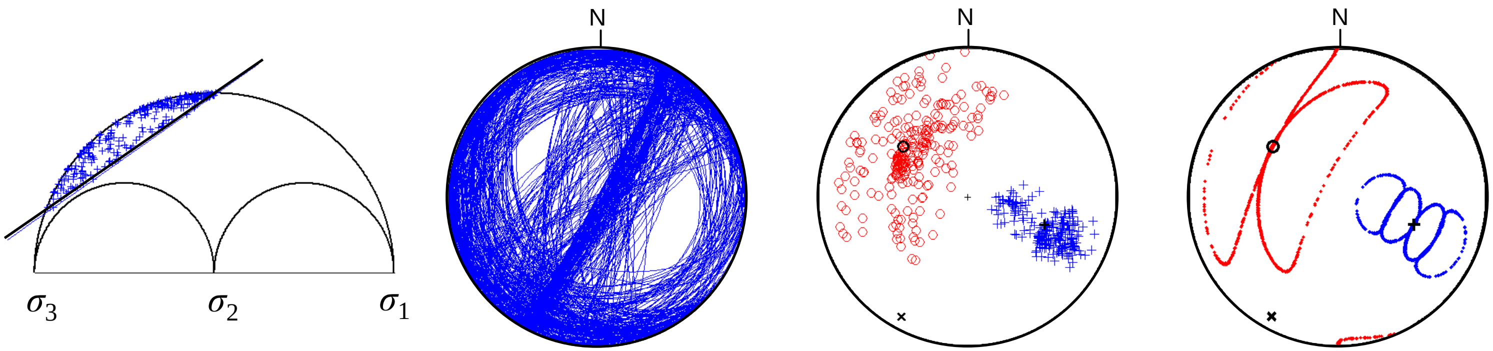

Low pore pressure

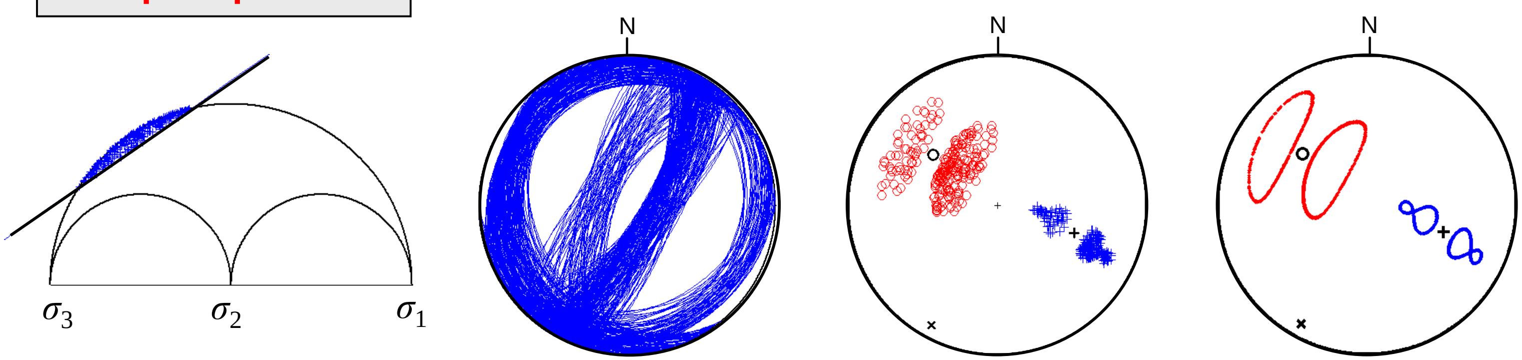

Error dependence

Noise free	Error = 10°	Error = 20°	Error = 30°

P/T axes

friction = 0.6, shape ratio = 0.5

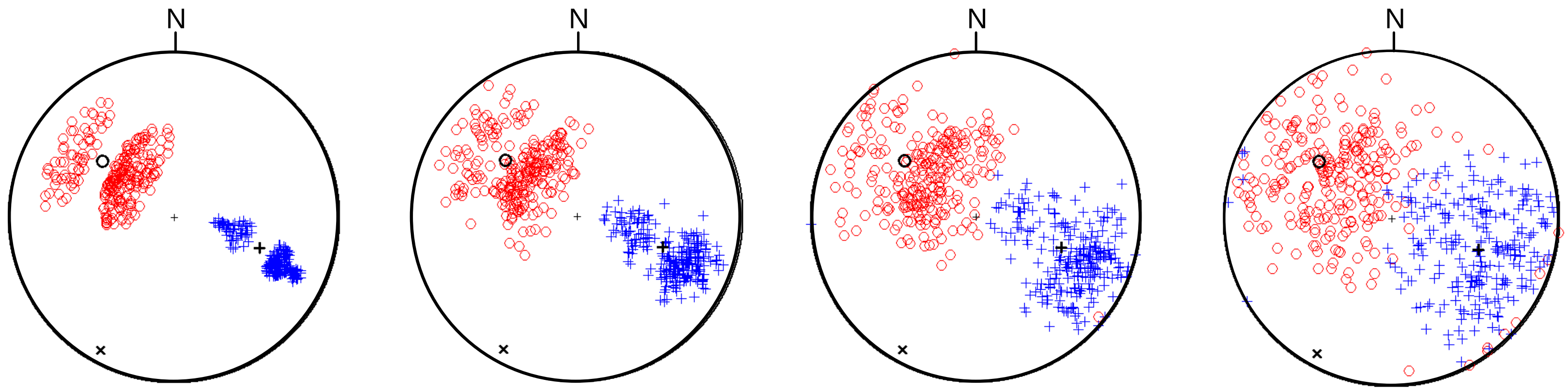

Nodal lines

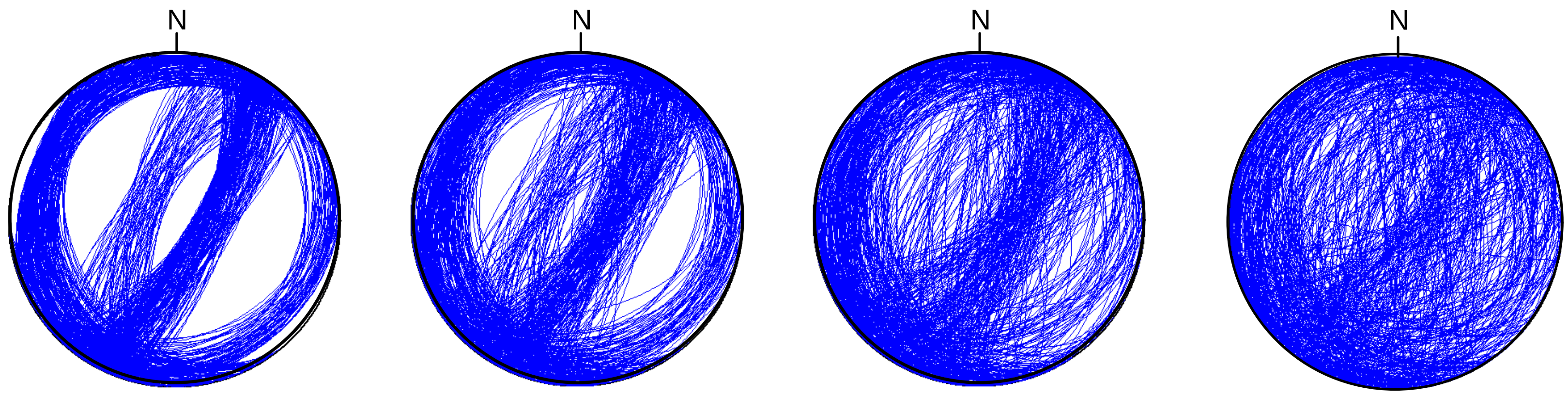

Inversion for stress: assumptions and methods

Faults in tectonic stress field

Based on the orientation of fractures we observe the following **types of faulting:**

- Shear faulting
- Tensile faulting
- Combined shear-tensile faulting

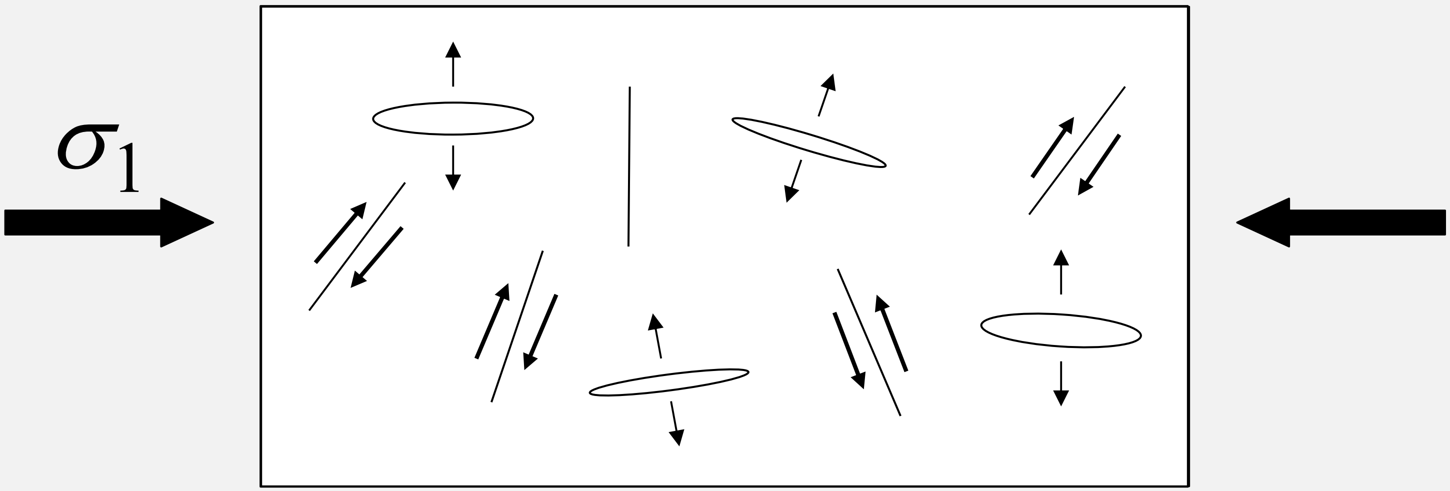

Fluid injection in KTB in 2000: focal mechanisms

Focal mechanisms always display some variety

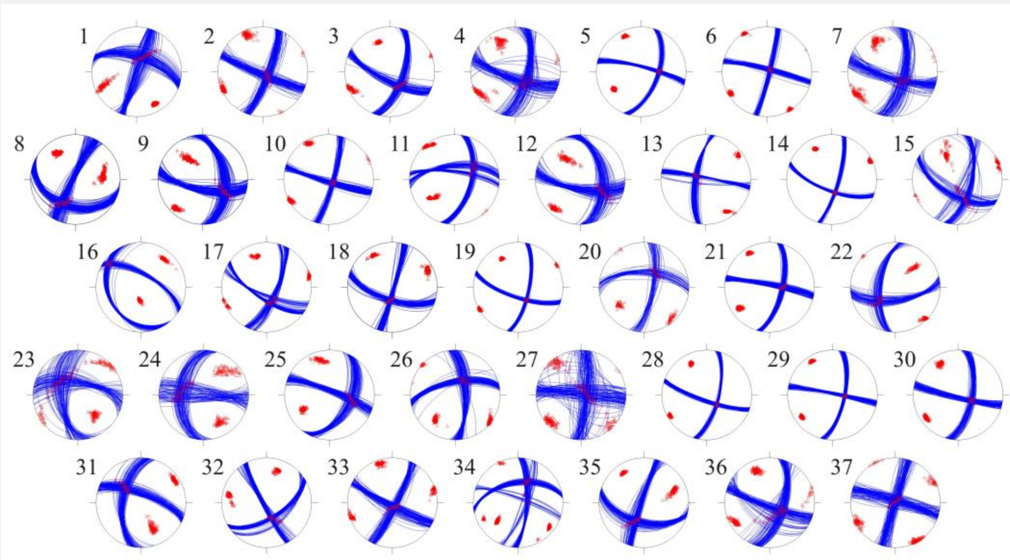

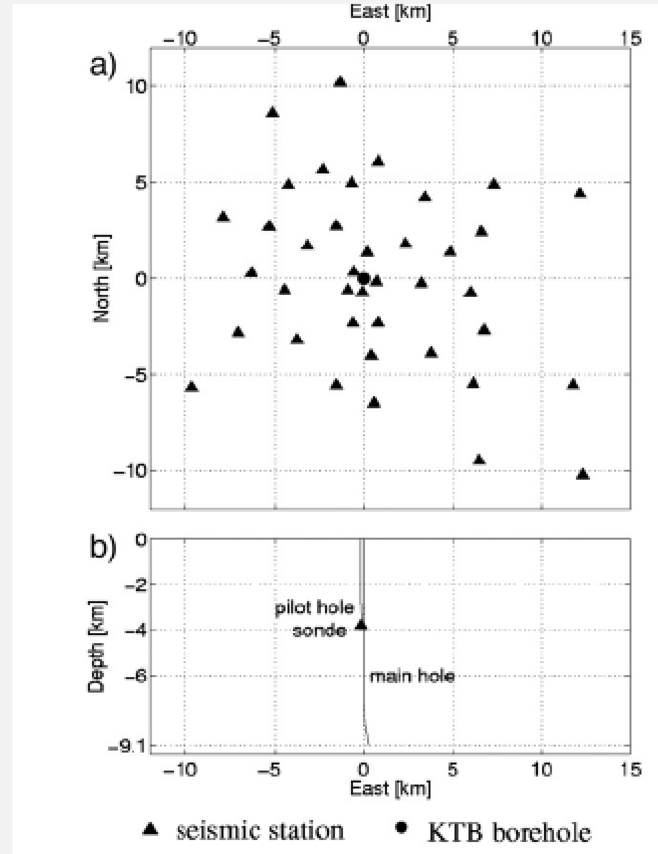

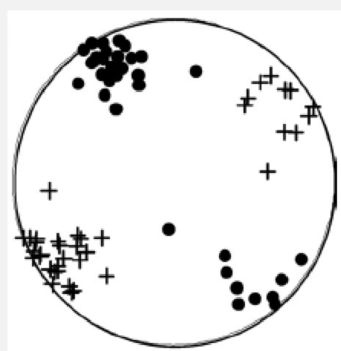

Vavryčuk et al., (Tectonophysics, 2008)

Inversion for stress from focal mechanisms

Assumptions

- homogeneous stress in the area under study
- earthquakes occur on pre-existing faults

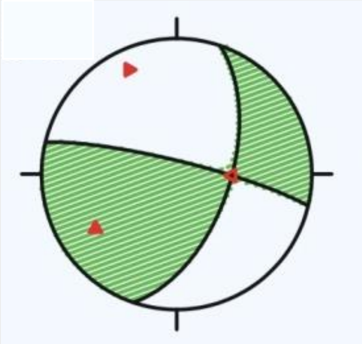

Necessary conditions

- focal mechanisms for a set of earthquakes
- variety of focal mechanisms

Methods

- Gephart & Forsyth (1984) – needs fault orientations
- Michael (1984, 1987) – needs fault orientations
- Angelier (2002)

Output: 4 stress parameters

- directions of principal stress axes
- shape (stress) ratio
- unable to determine the absolute values of stress and trace of stress tensor

$$R = \frac{\sigma_1 - \sigma_2}{\sigma_1 - \sigma_3}$$

Wallace-Bott hypothesis

Wallace-Bott hypothesis: slip is parallel to the shear stress direction on the fault

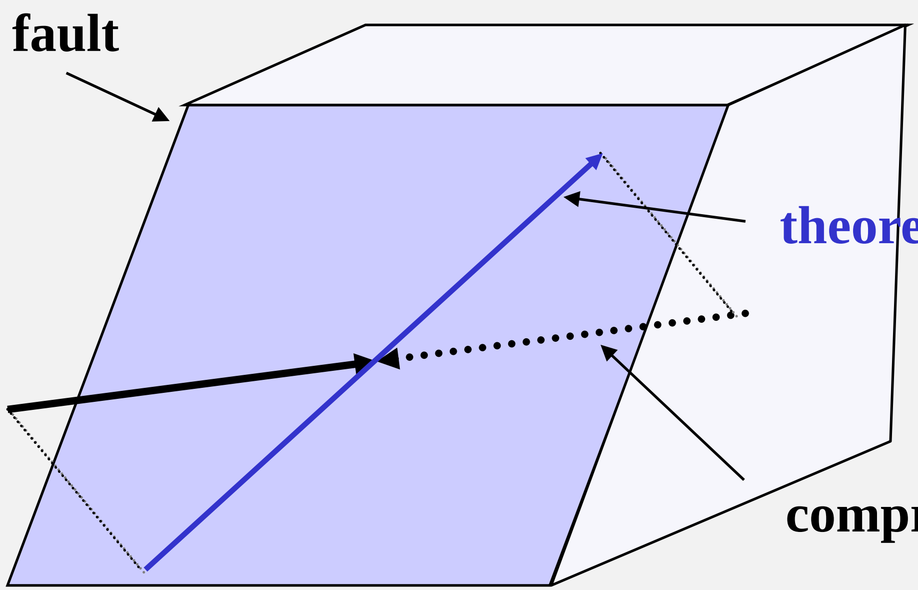

$$T_i = \tau_{ij}\, n_j$$

$$\sigma_n = T_i\, n_i = \tau_{ij}\, n_i\, n_j$$

$$\tau_i = T_i - \sigma_n\, n_i$$

Necessary conditions

- set of focal mechanisms
- variety of focal mechanisms

➡ overdetermined problem
linearly independent equations

Inversion for stress: Gephart & Forsyth (1984)

Wallace-Bott hypothesis: slip is parallel to the shear stress direction on the fault

non-linear inversion

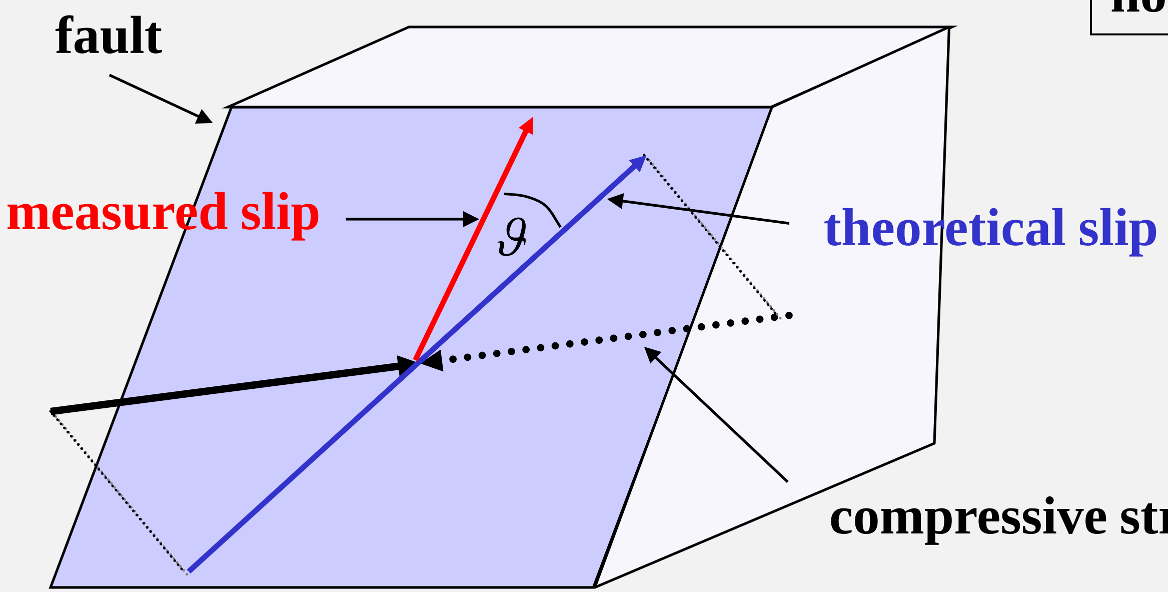

$$T_i = \tau_{ij} n_j$$

$$\sigma_n = T_i n_i = \tau_{ij} n_i n_j$$

$$\tau_i = T_i - \sigma_n n_i$$

Misfit function

$$\sum_{i=1}^{N} |\vartheta_i| = \min$$

theoretical slip – parallel to shear stress

measured slip – determined from focal mechanisms

Inversion for stress: Michael (1984)

Mathematical formulation – linear inversion

$$T_i = \tau_{ij} n_j$$

traction (stress) on the fault

$$\sigma_n = T_i n_i = \tau_{ij} n_i n_j$$

normal stress on the fault

$$\tau N_i = T_i - \sigma_n n_i = \tau_{ij} n_j - \tau_{jk} n_j n_k n_i = \tau_{kj} n_j (\delta_{ik} - n_i n_k)$$

shear stress on the fault

$$\tau_{kj} n_j (\delta_{ik} - n_i n_k) = \tau N_i$$

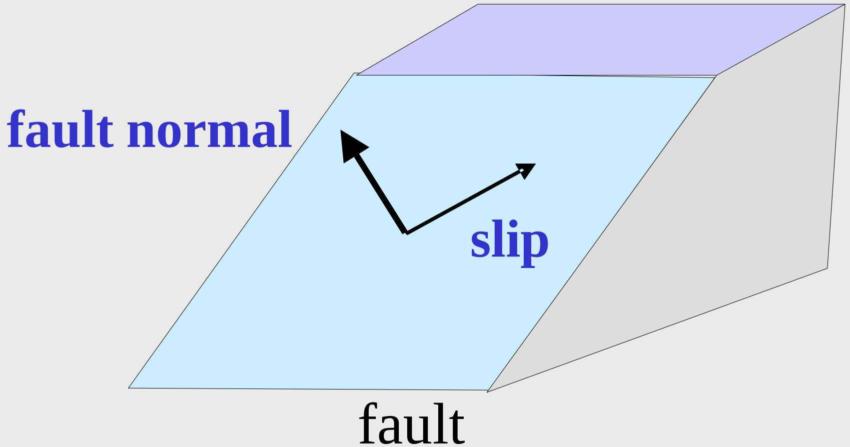

n – fault normal
N – direction of shear stress (assumed to be slip direction)
τ – magnitude of shear stress (assumed to be constant)

$$\mathbf{At} = \mathbf{b} \qquad \mathbf{t} = \mathbf{A}^{-g}\mathbf{b}$$

Fault-choice algorithms: a review

Gephart & Forsyth method (1984)

Fault is that nodal plane which yields a lower misfit between the observed and predicted slip directions.

Michael method (1984, 1987)

Fault is chosen randomly and the inversion is repeated to estimate the errors incurred by using an incorrect fault orientation.

Angelier (2002)

The method is invariant to fault identification. There is no need to identify a fault plane.

Lund & Slunga method (1999)

Fault is that nodal plane which is more unstable in the given stress field.
This criterion is applied to the Gephart & Forsyth method.

Vavryčuk method (2014)

Fault is that nodal plane which is more unstable in the given stress field.
This criterion is applied to the Michael (1984, 1987) method.

Inversion for stress – Angelier (2002)

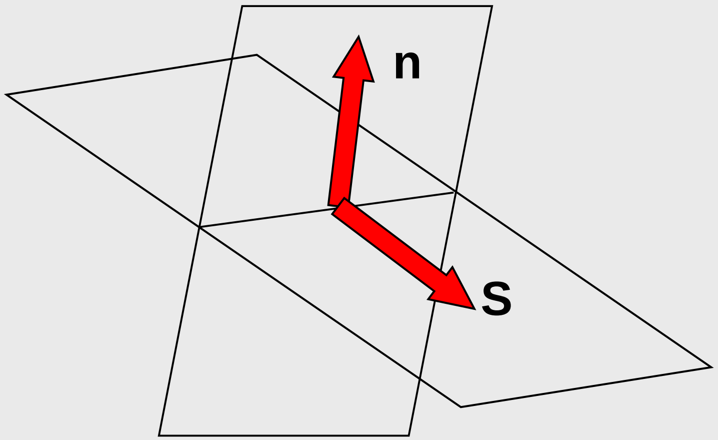

- **invariable of the fault plane identification!**
  (standard methods need an identification of the fault plane)
- shear stress along the slip is maximized (criterion SSSC)
- **non-linear inversion**: grid search

n – fault normal

s – slip vector

τ – stress tensor

$$T = \tau_{ij}\, n_i\, s_j \qquad \mathbf{n} \leftrightarrow \mathbf{s}$$

$T \longleftarrow$ **slip shear stress component (SSSC)**

T is maximized during the inversion

Angelier criterion: physical meaning

Angelier inversion assumes **no friction** on faults

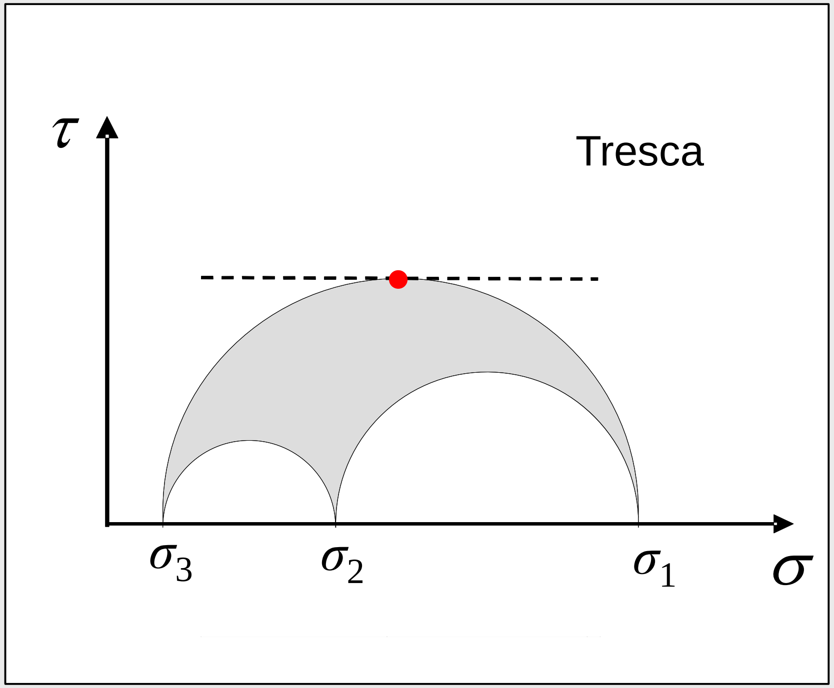

zero friction on faults

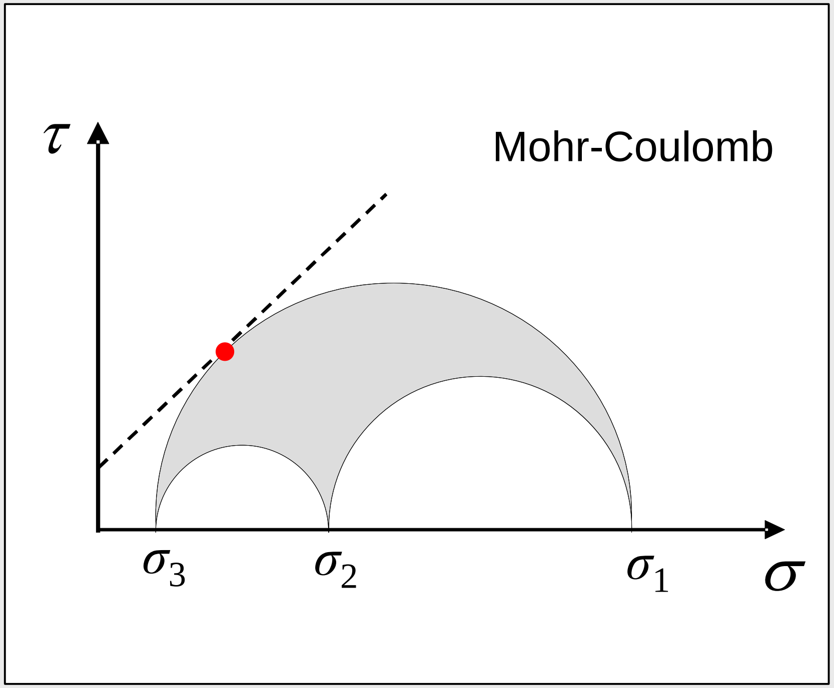

friction on faults: 0.4 - 0.8

Inversion for stress: accuracy

Synthetic data

One-wing data

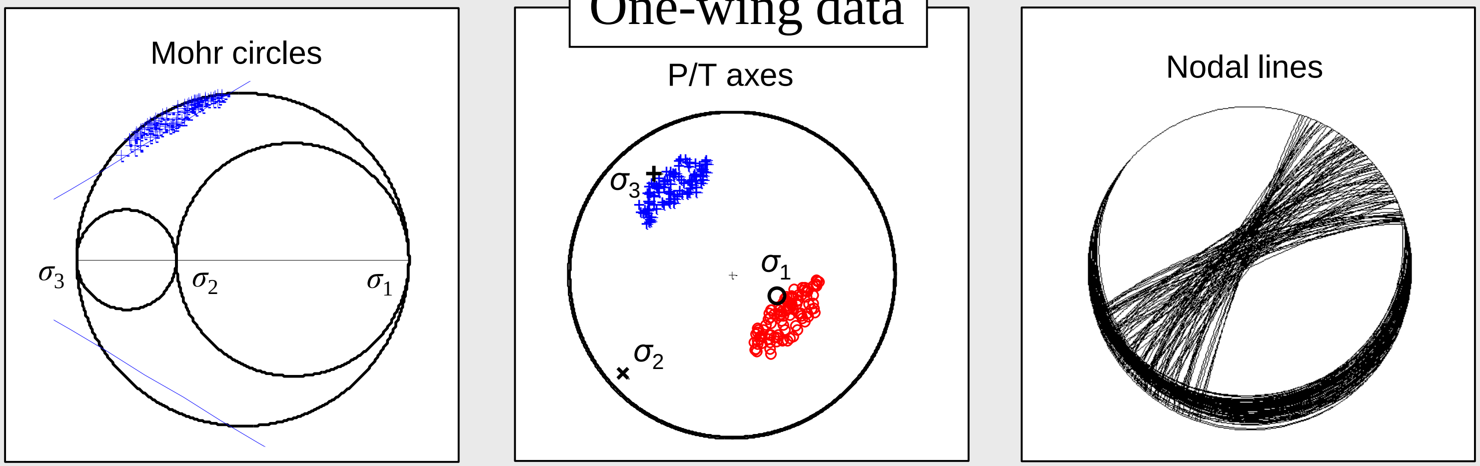

Two-wing data

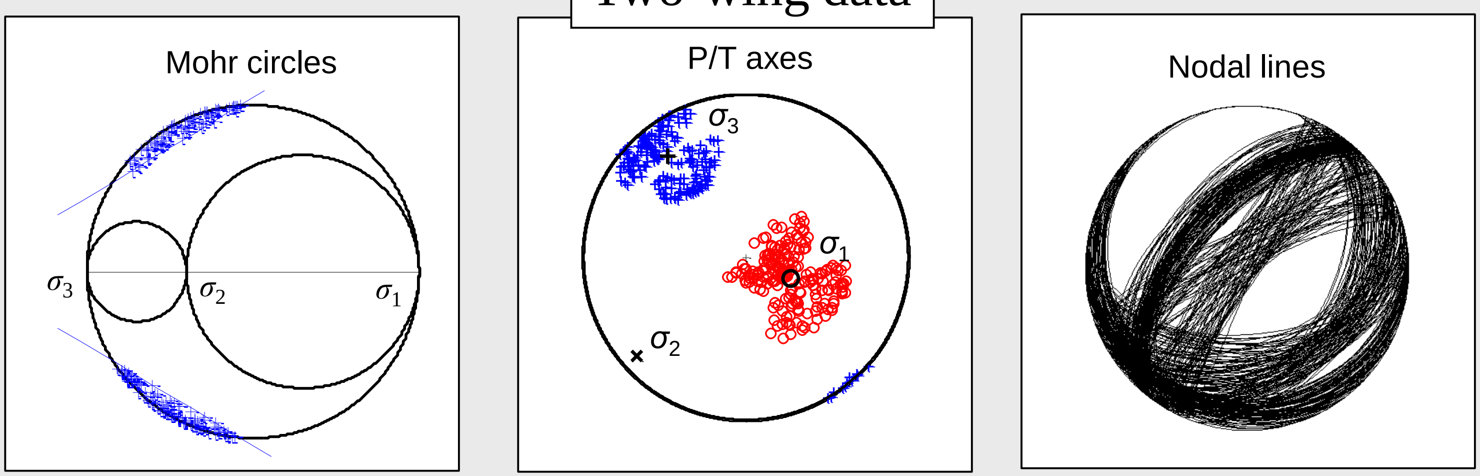

Accuracy of stress inversions

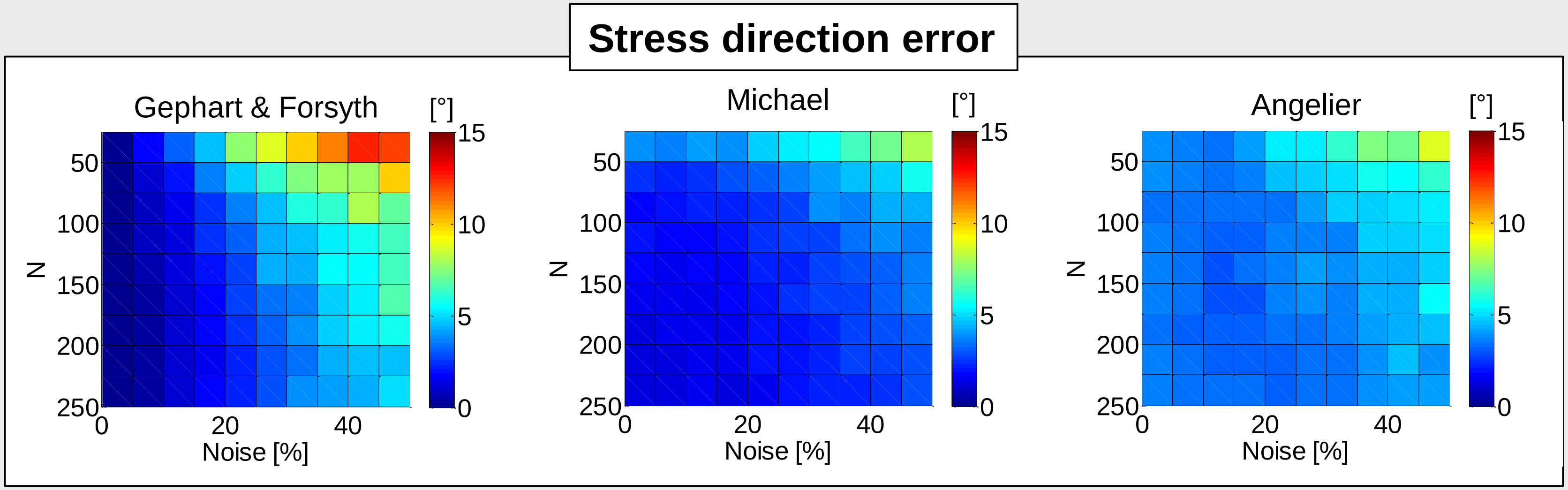

Vavryčuk (Encyclopedia Earth. Eng., 2015)

Accuracy of stress inversions: two-wing data

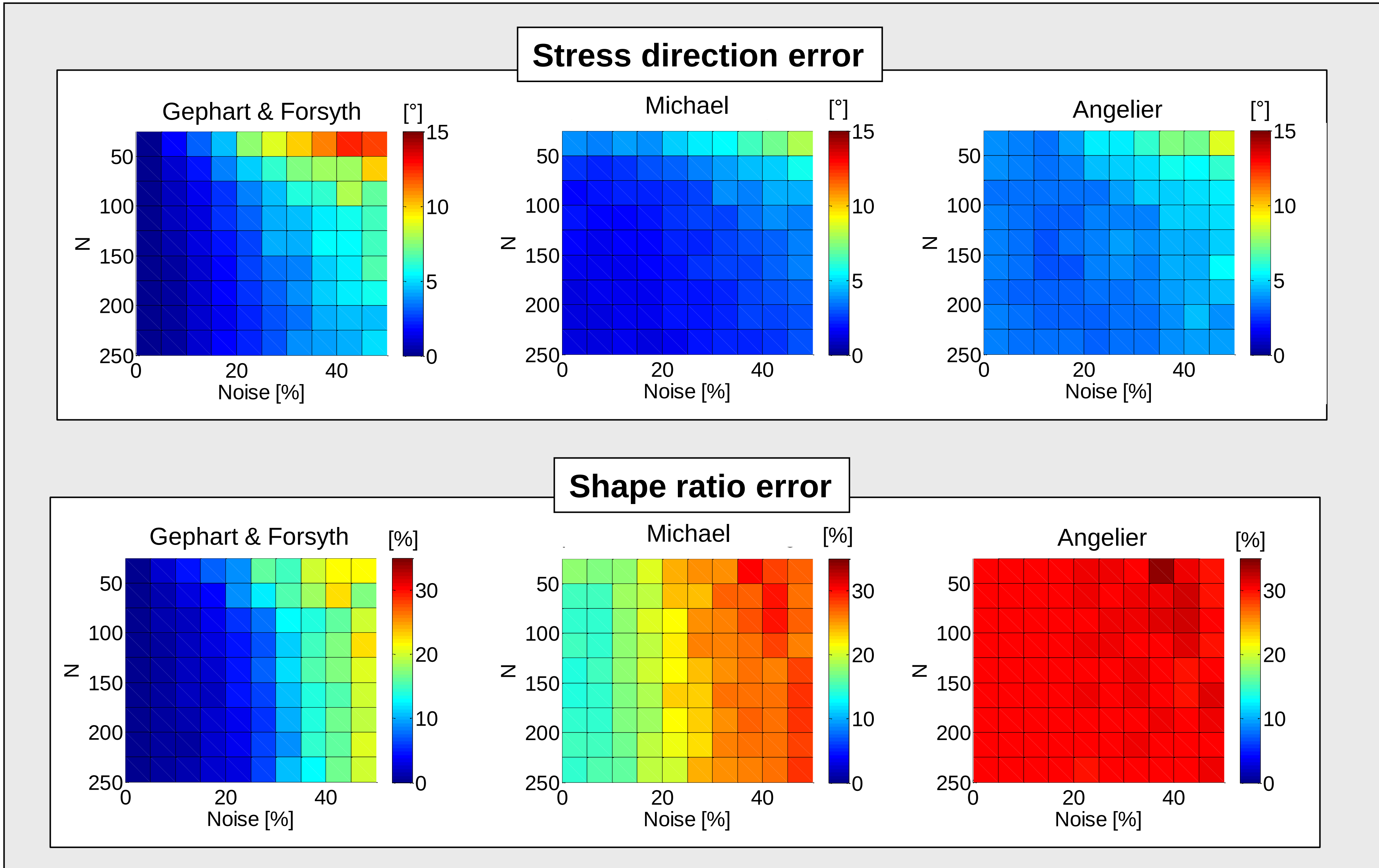

Vavryčuk (Encyclopedia Earth. Eng., 2015)

Accuracy of stress inversions: two-wing data

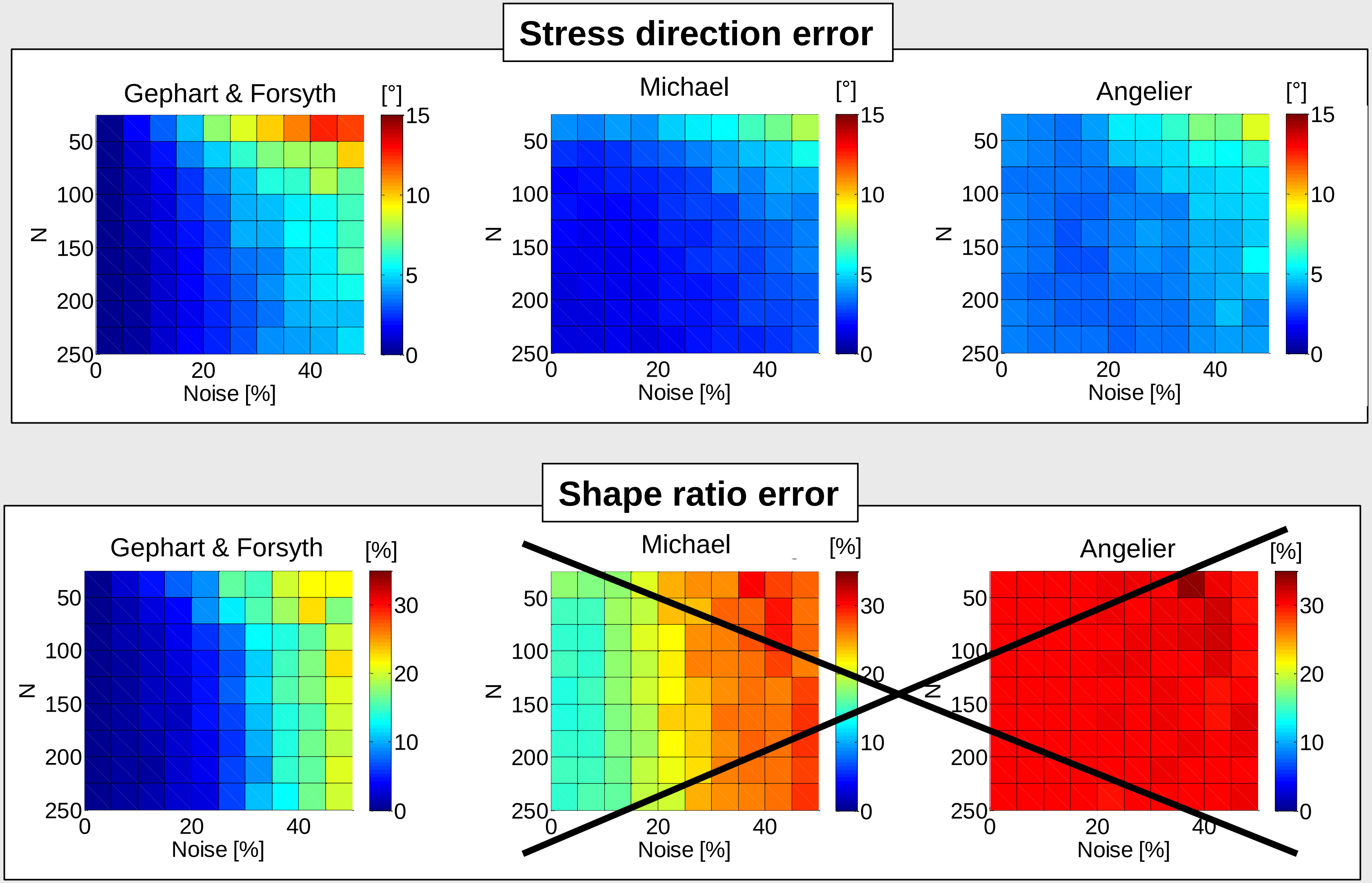

Vavryčuk (Encyclopedia Earth. Eng., 2015)

Fault choice algorithm based on fault instability

Fault-choice algorithms: a review

Ellsworth & Zhonghuai (1980)
Minimize misfit over all possible choices of fault orientations

Gephart & Forsyth method (1984)
Fault is that nodal plane which yields lower misfit between the observed and predicted slip directions

Michael method (1984, 1987)
Fault is chosen randomly and the inversion is repeated to estimate the errors incurred by using an incorrect fault orientation

Lund & Slunga method (1999)
Fault is that nodal plane which is more unstable in the given stress field
This criterion is applied to the Gephart & Forsyth method

Vavryčuk method (2014)
Fault is that nodal plane which is more unstable in the given stress field
This criterion is applied to the Michael method

Mohr-Coulomb failure criterion

$$\tau > \tau_c = S + \mu\big(\underbrace{\sigma_n - p}_{\sigma}\big)$$

τ_c – critical shear traction

S – cohesion

μ – friction

σ_n – normal traction

p – pore pressure

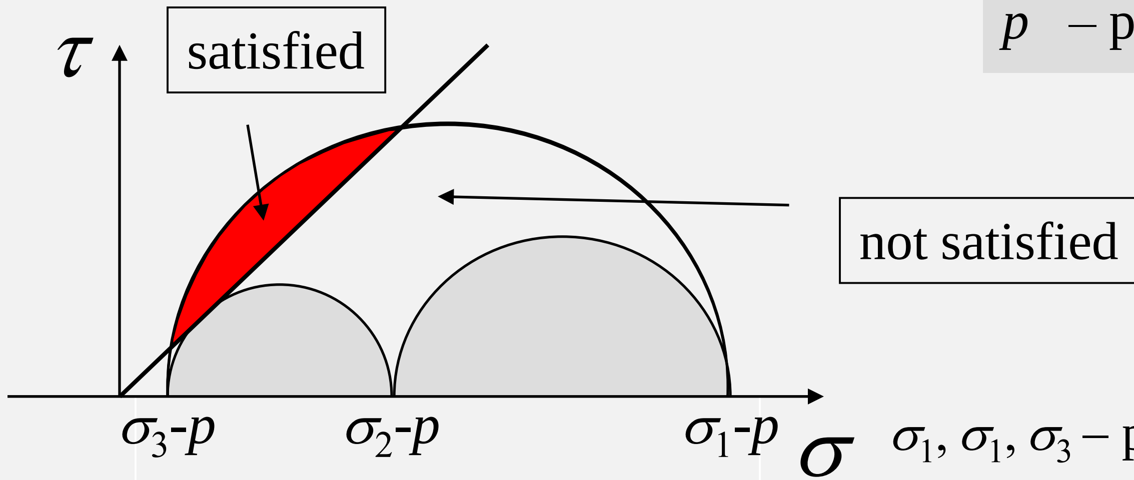

$\sigma_1, \sigma_1, \sigma_3$ – principal stress values

τ - shear traction

σ - effective normal traction

The origin of σ depends on p !

Fault instability: definition

Mohr's circle diagram

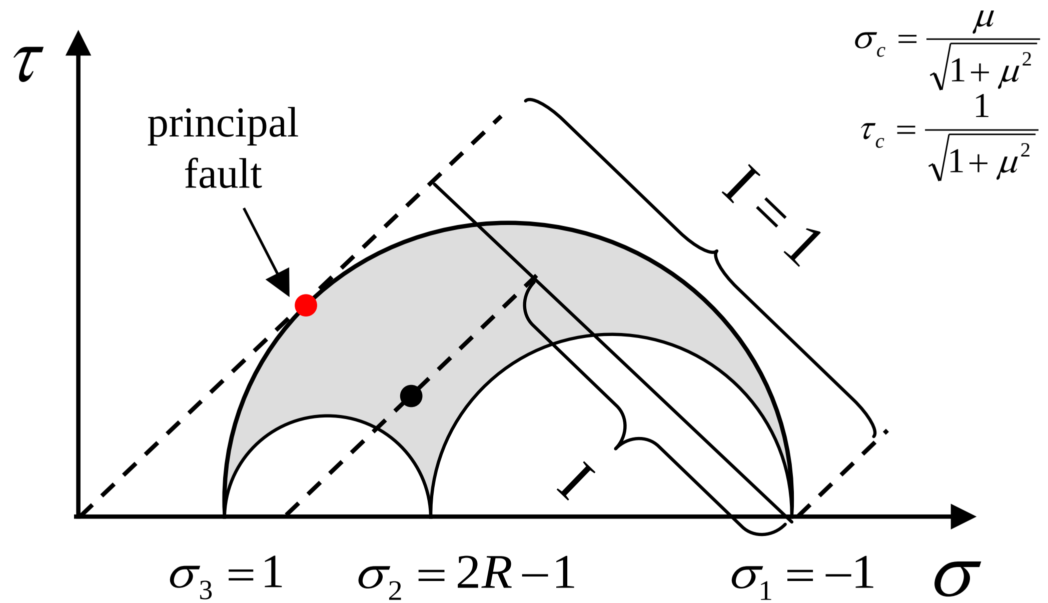

$$I = \frac{\tau + \mu(\sigma + 1)}{\mu + \sqrt{1+\mu^2}}$$

Shape ratio:

$$R = (\sigma_1 - \sigma_2)/(\sigma_1 - \sigma_3)$$

Principal fault is the most unstable fault in the stress field

$$\sigma = -n_1^2 + (2R-1)n_2^2 + n_3^2$$

$$\tau = \sqrt{n_1^2 + (2R-1)^2 n_2^2 + n_3^2 - \left(-n_1^2 + (2R-1)n_2^2 + n_3^2\right)^2}$$

Vavryčuk et al. (Tectonophysics, 2013)

Fault instability: definition

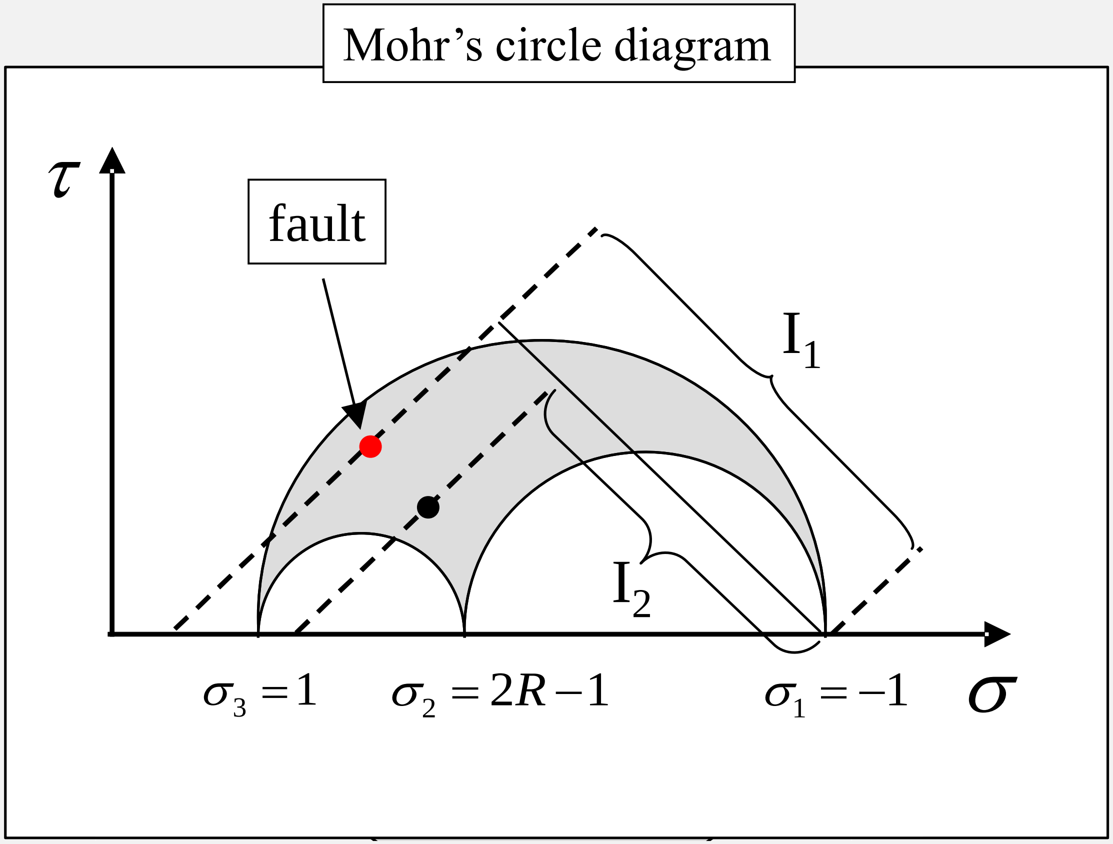

$$I = \frac{\tau + \mu(\sigma + 1)}{\mu + \sqrt{1 + \mu^2}}$$

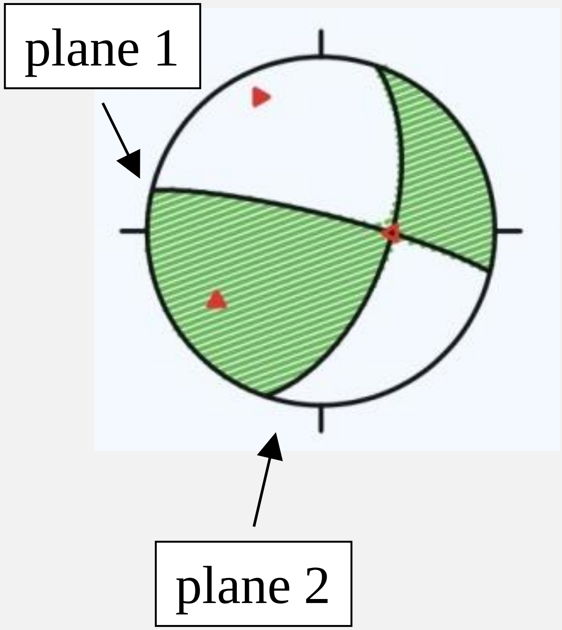

The fault is identified with the nodal plane of the **higher fault instability**

$$I_1 > I_2$$

Vavryčuk et al. (Tectonophysics, 2013)

Joint inversion for stress and fault orientations

Iterative inversion for stress from focal mechanisms

Scheme of the inversion

- **1st iteration:**
  standard Michael's method with fault planes chosen randomly

- **2nd iteration:**
  fault planes are chosen according to the fault instability criterion using stress calculated in the 1st iteration

- **3rd iteration:**
  fault planes are chosen according to the fault instability criterion using stress calculated in the 2nd iteration

The iterative process stops when satisfies some **convergence** criteria

Synthetic tests

Synthetic data

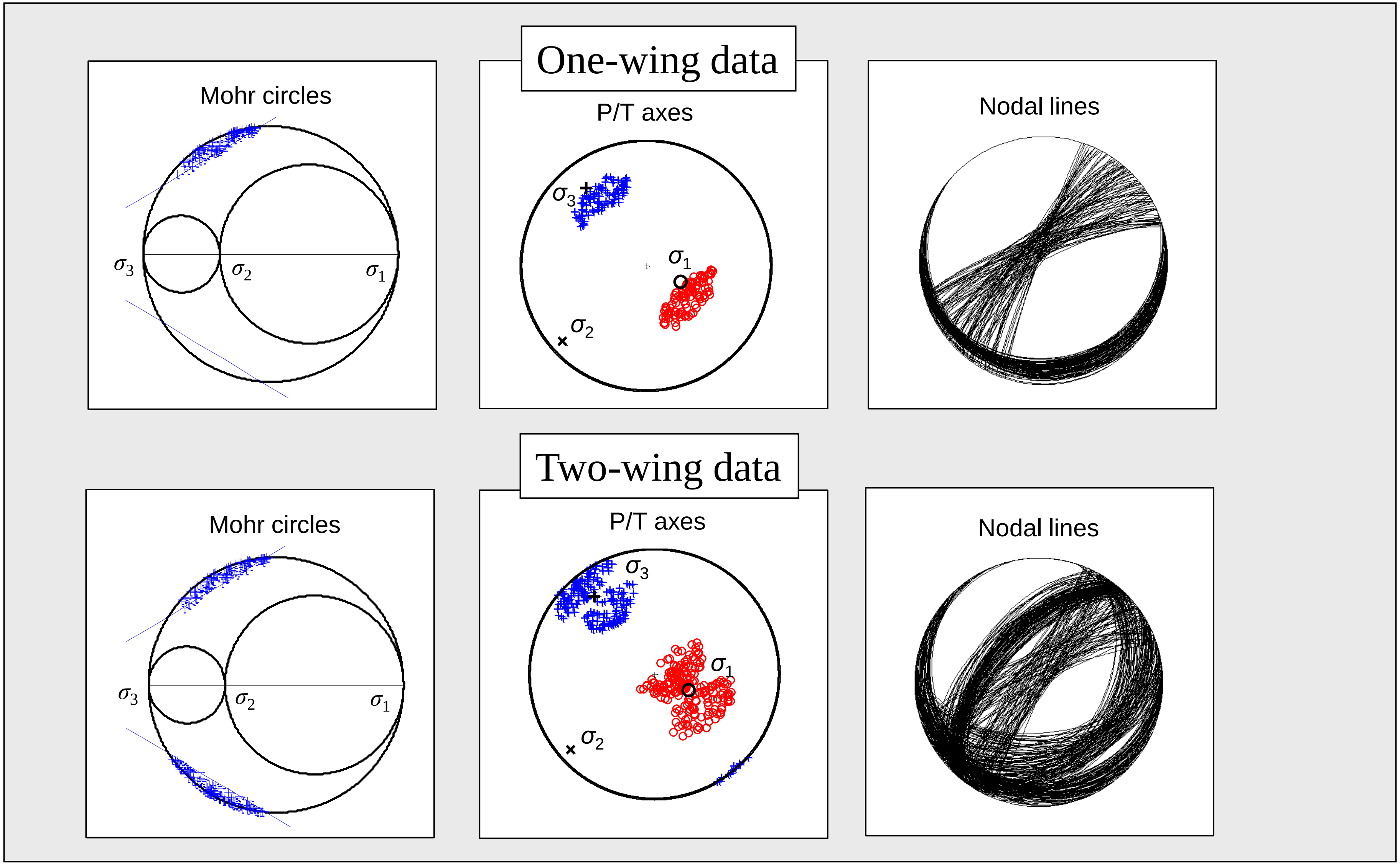

Stress inversion: one-wing data

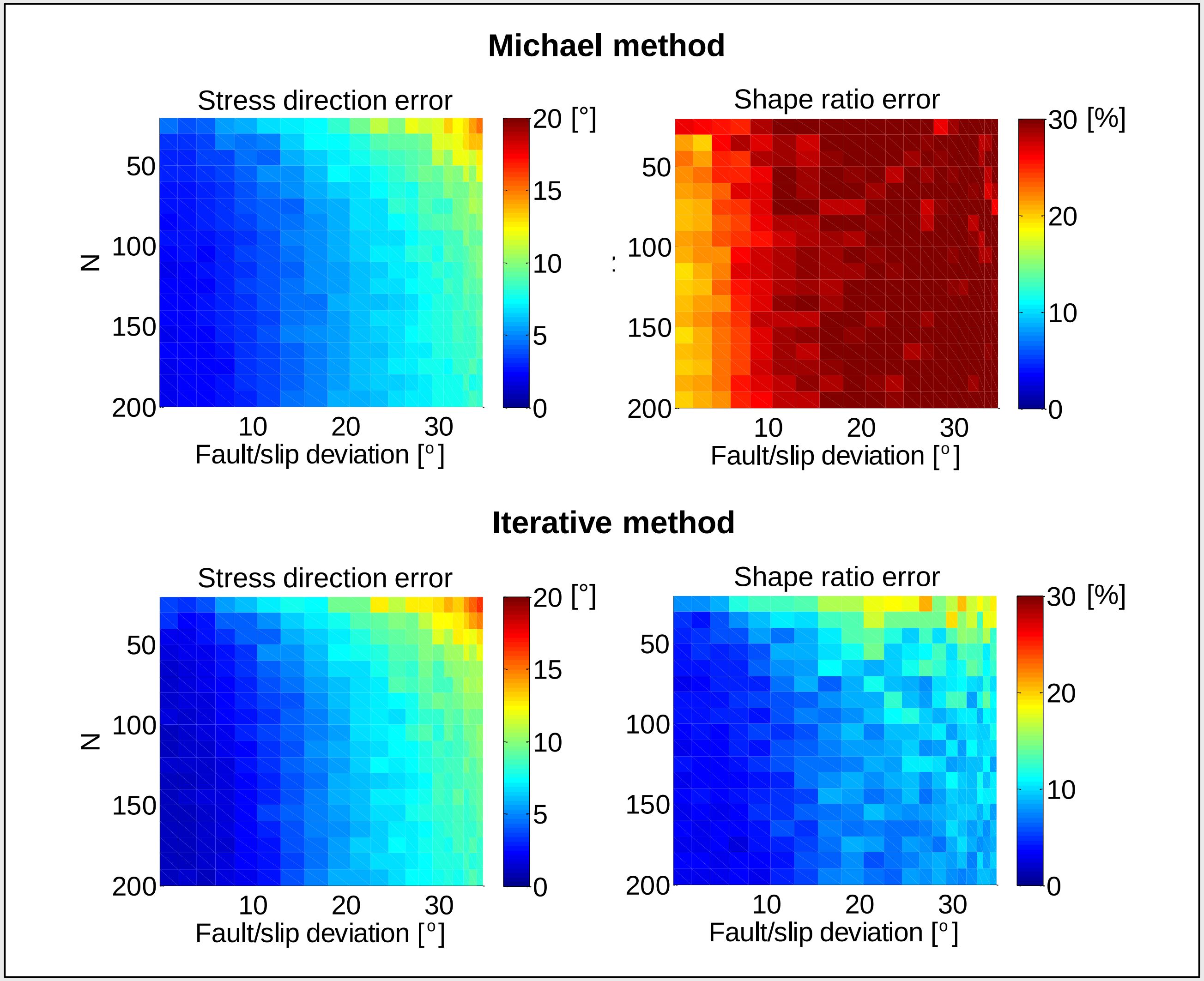

The accuracy
of the shape ratio
is **significantly**
improved!

Stress inversion: two-wing data

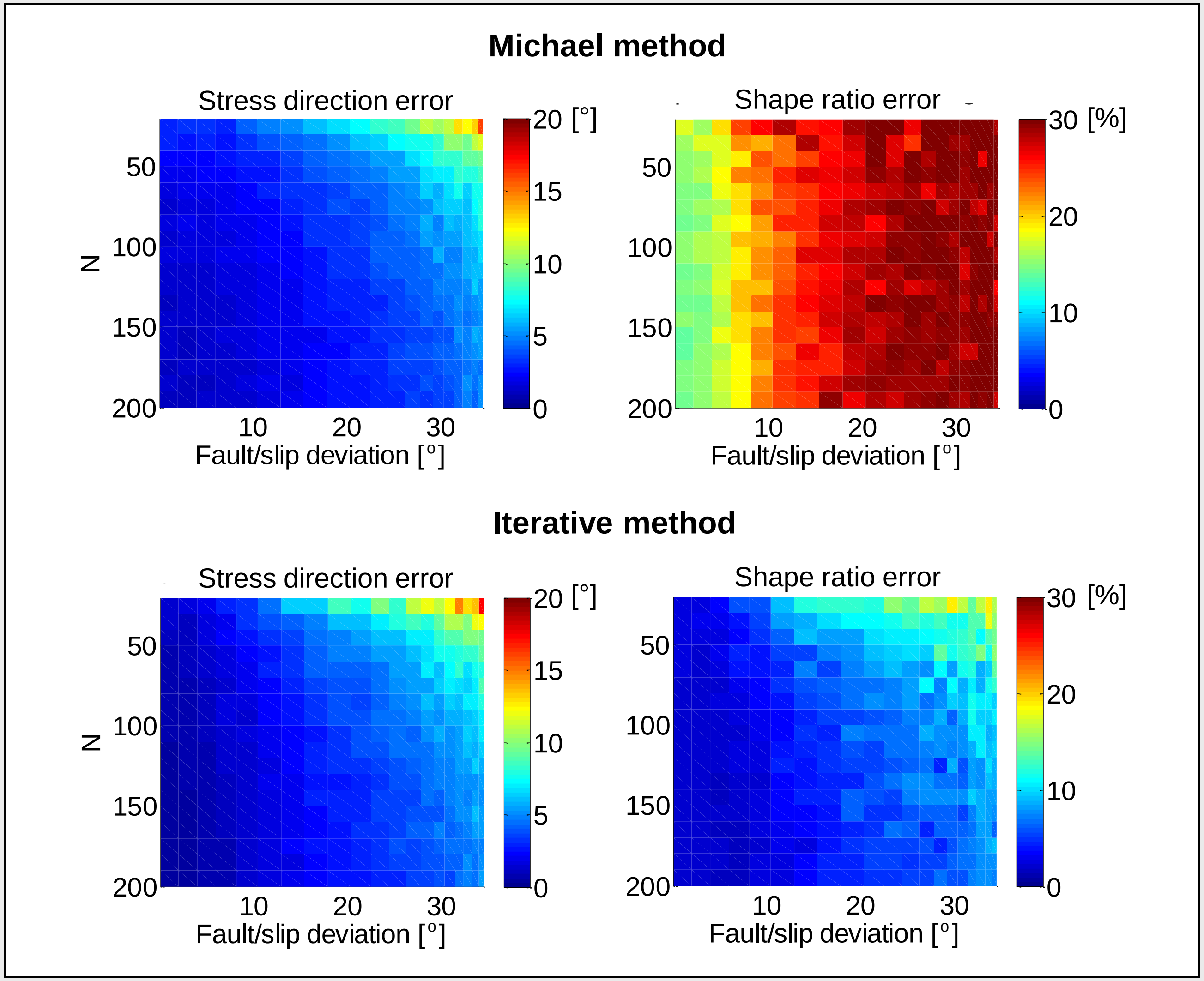

The accuracy of the shape ratio is **significantly** improved!

Stress inversion: identification success and friction

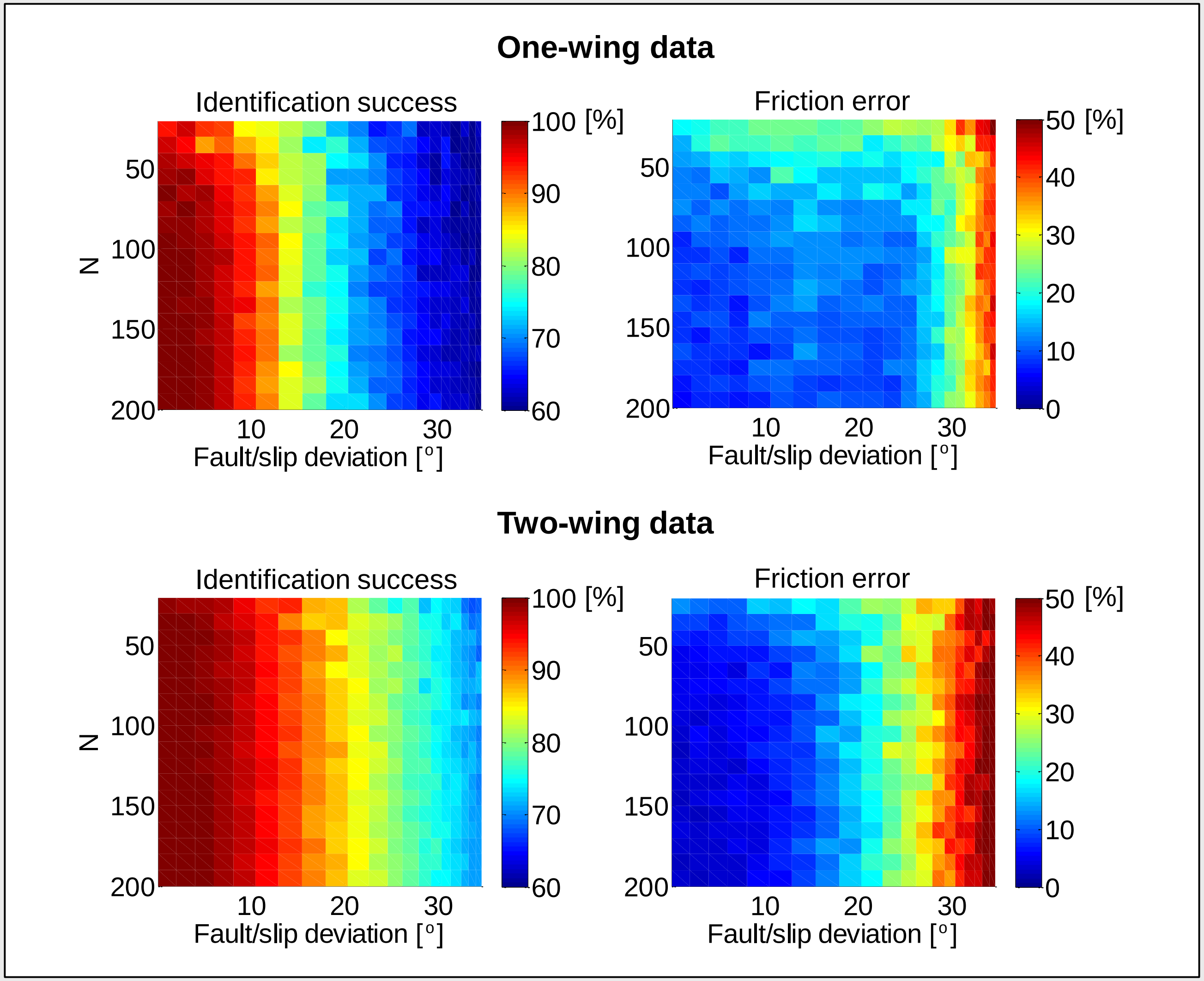

Inversion for shape ratio: Central Crete

Joint inversion for stress and faults: Central Crete

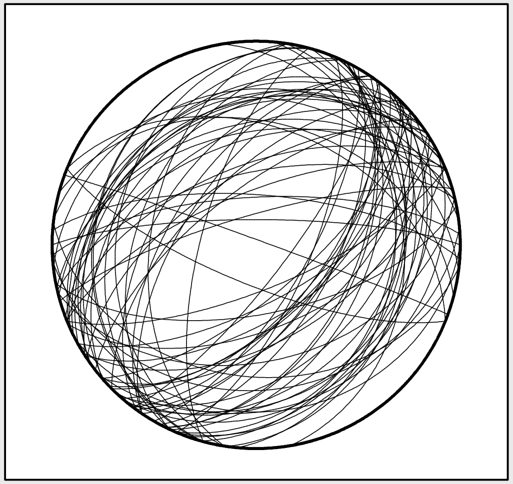

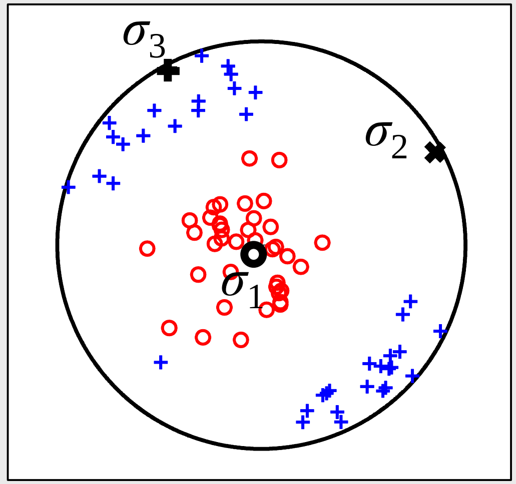

Input data:
38 focal mechanisms with knowledge about the fault orientations

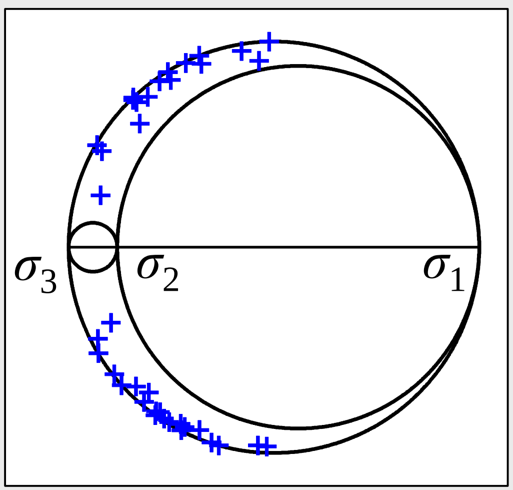

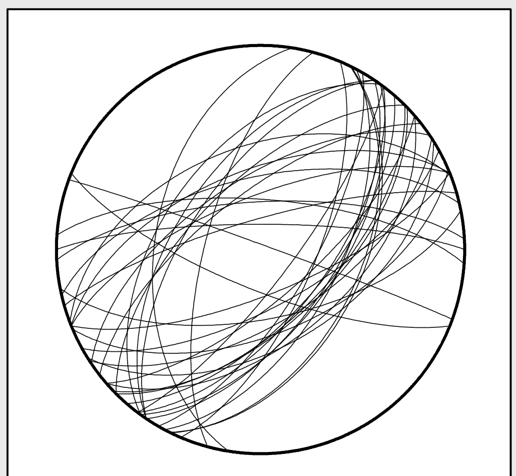

Output of the inversion:

- stress axes
- shape ratio
- fault orientations

36 of 38 faults were successfully identified!

Slickenslide data taken from Angelier (1979) and Michael (1984, 1987)

Vavryčuk (GJI, 2014)

Joint inversion for stress and faults: Central Crete

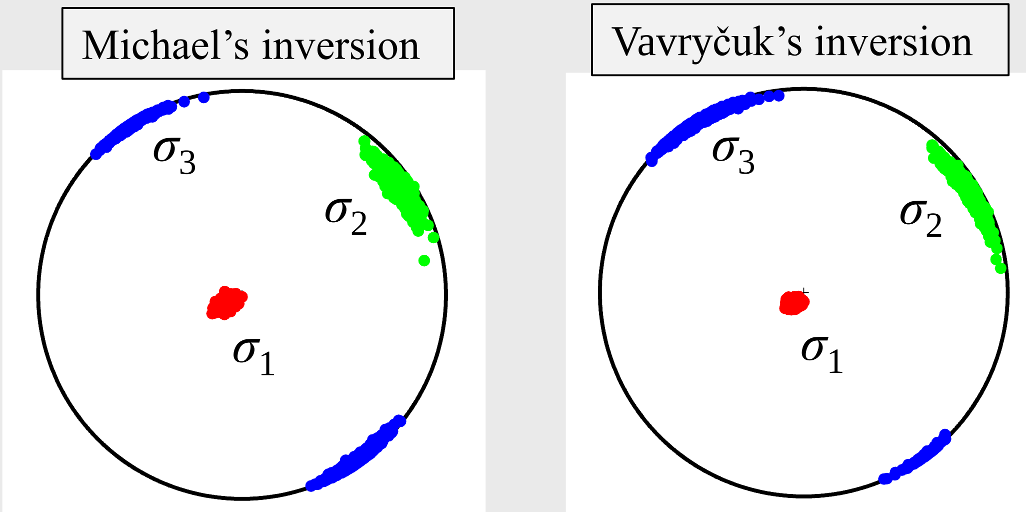

Uncertainties in the stress orientation

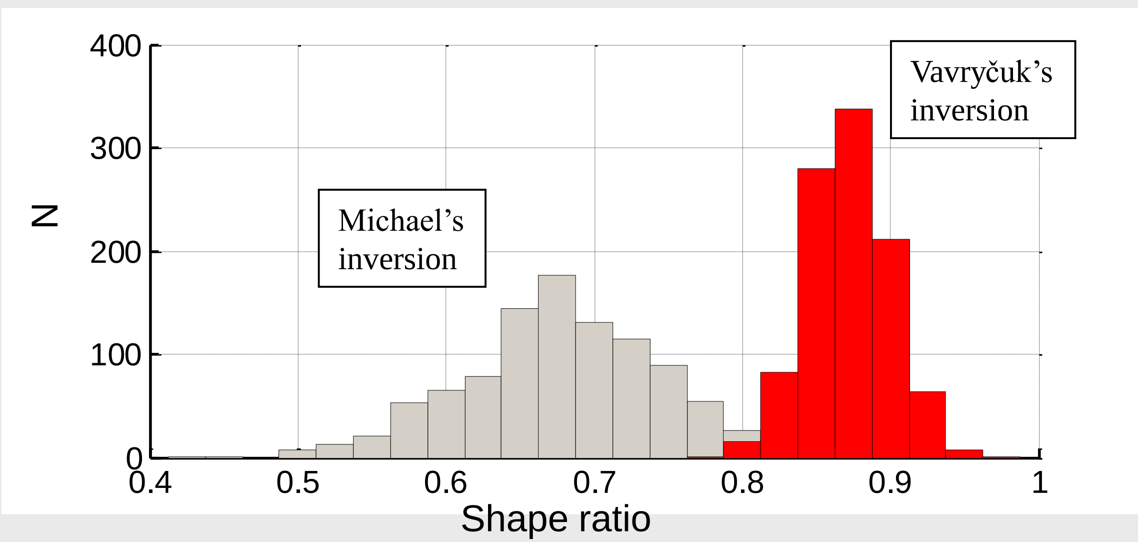

Uncertainties in the shape ratio

$$R = \frac{\sigma_1 - \sigma_2}{\sigma_1 - \sigma_3}$$

Shape ratio is different!

Vavryčuk (GJI, 2014)

Inversion for shape ratio: West Bohemia

Joint inversion for stress and faults: West Bohemia

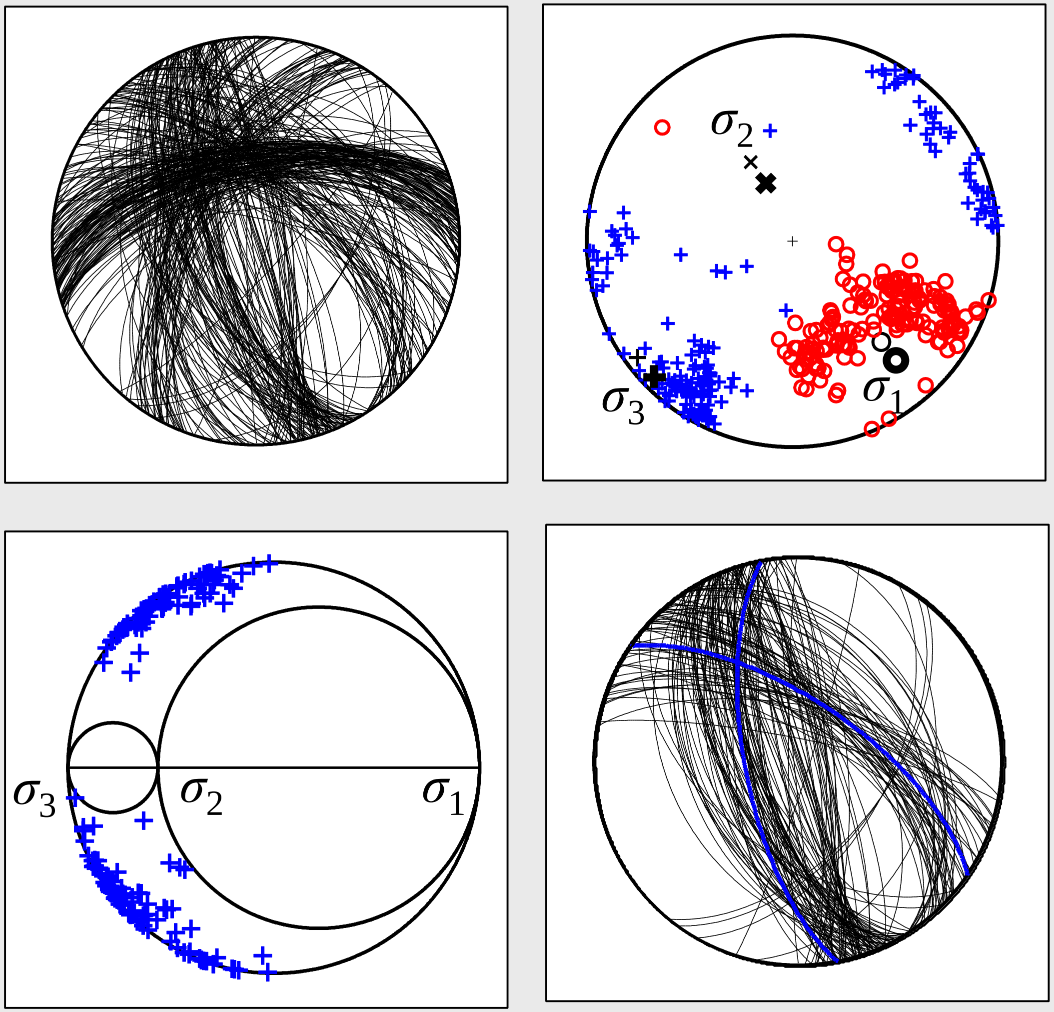

Earthquake swarm in West Bohemia in 2008

Input data:
focal mechanisms
with no knowledge about
the fault orientations

Output of the inversion:

- stress axes
- shape ratio
- fault orientations

Vavryčuk (GJI, 2014)

Joint inversion for stress and faults: West Bohemia

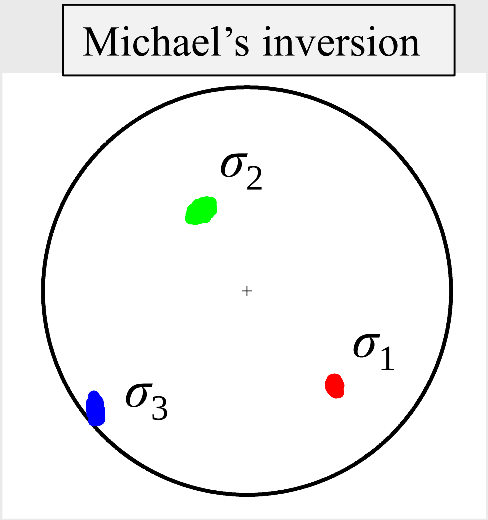

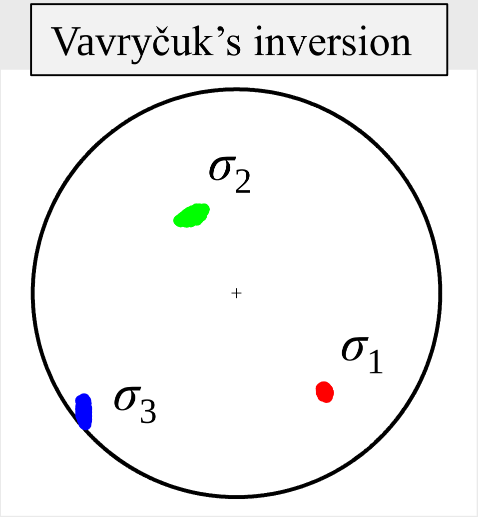

Uncertainties in the stress orientation

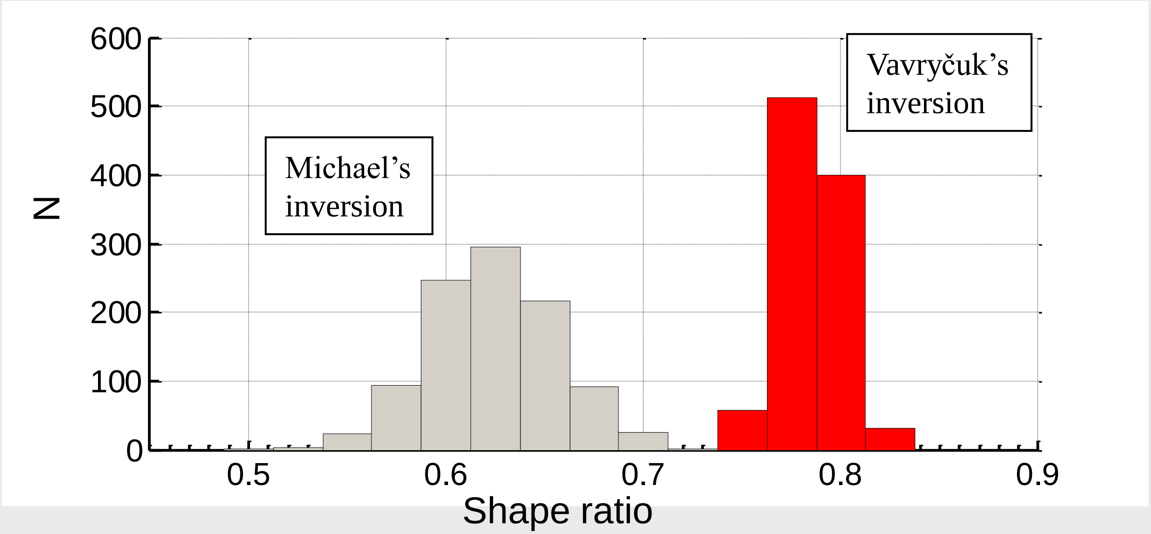

Uncertainties in the shape ratio

$$R = \frac{\sigma_1 - \sigma_2}{\sigma_1 - \sigma_3}$$

Shape ratio is different!

Vavryčuk (GJI, 2014)

Summary

Summary

Focal mechanisms provide key information about stress field

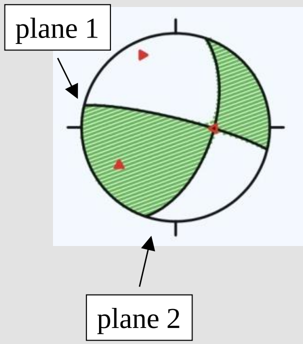

Difficulty in stress inversions is the focal mechanism ambiguity

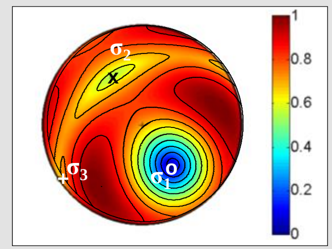

Stress inversion using the instability criterion

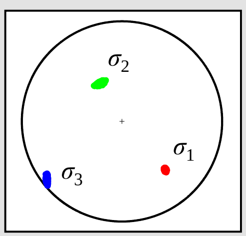

Stress axes do not need knowledge of fault orientations

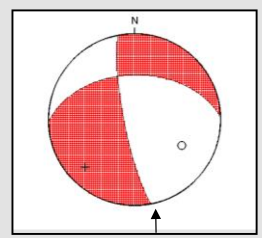

Orientation of faults

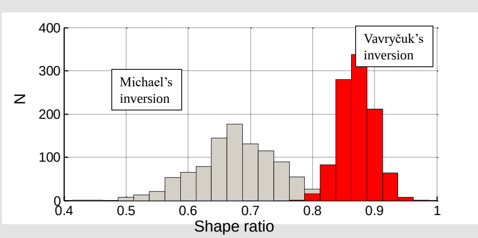

Shape ratio needs knowledge of fault orientations

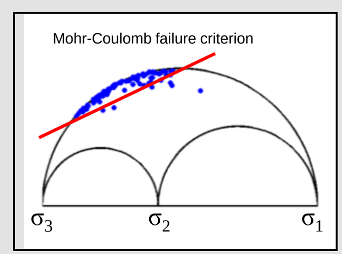

Friction on faults

Stress inversion software

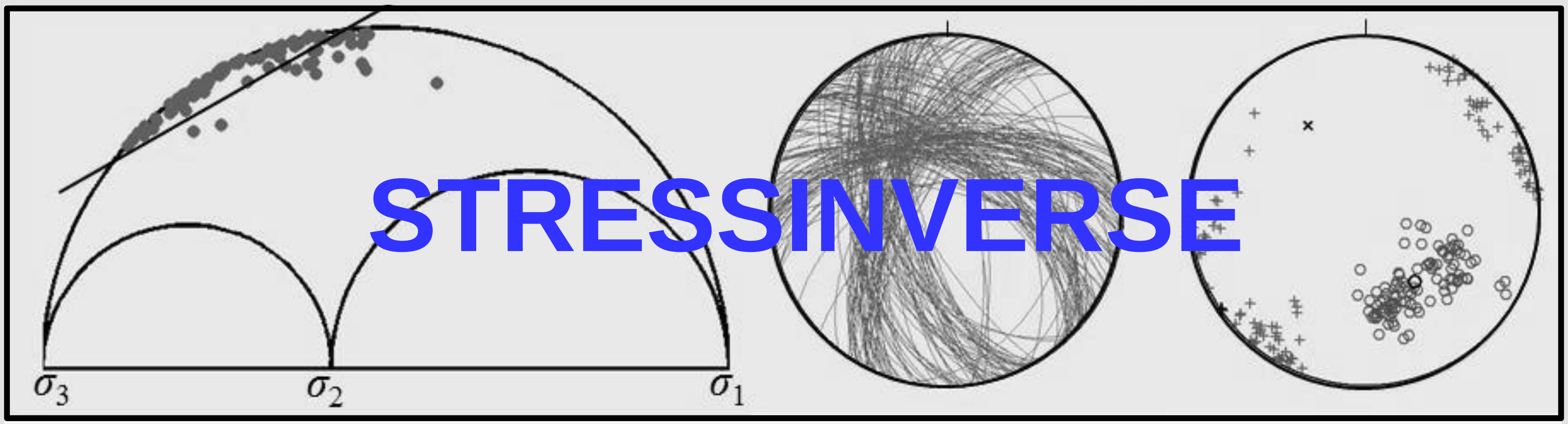

STRESSINVERSE is a free Matlab and Python software package for an iterative joint inversion for stress and fault orientations.

Link: http://www.ig.cas.cz/stress-inverse

Reference:

Vavryčuk, V., 2014. Iterative joint inversion for stress and fault orientations from focal mechanisms, *Geophysical Journal International*, **199**, 69-77.


Thank you
for your attention !

Additional information

Tectonic stress and seismicity

Stress: origin of geodynamic phenomena in the Earth

Basic schematic of different Plate Driving Forces

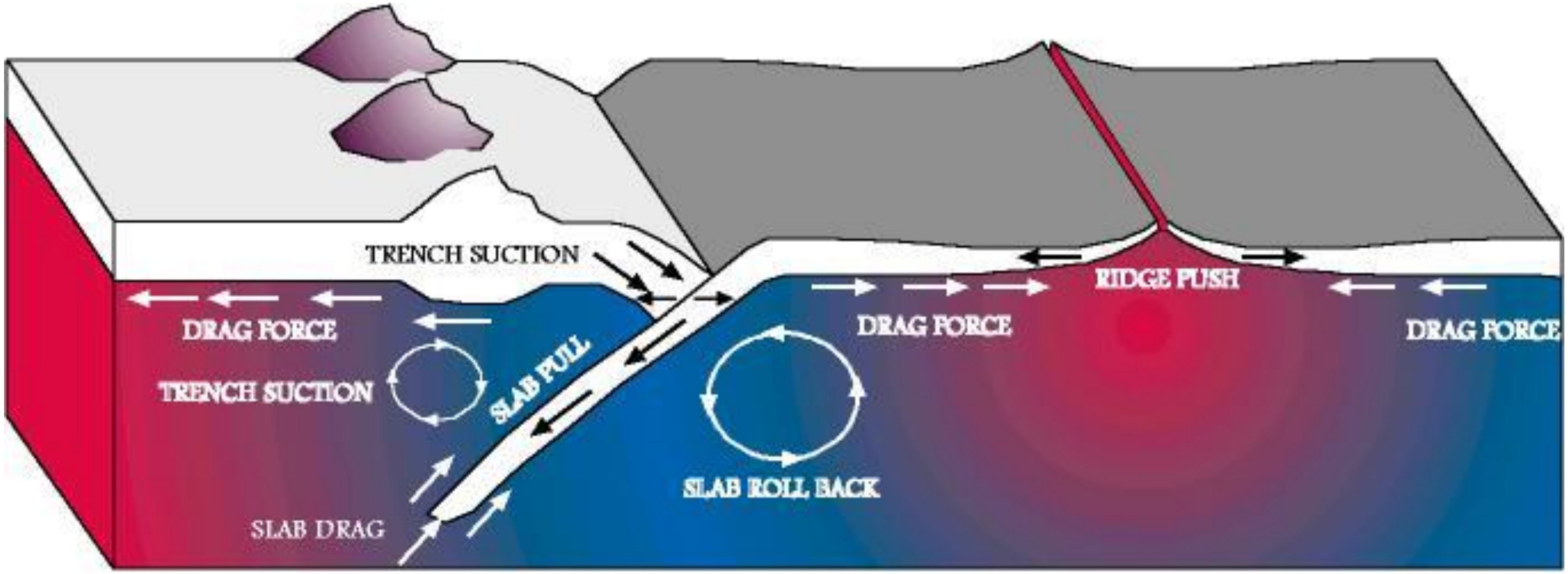

http://websites.umich.edu/~gs265/tecpaper.htm)

Seismic cycles: two alternative scenarios

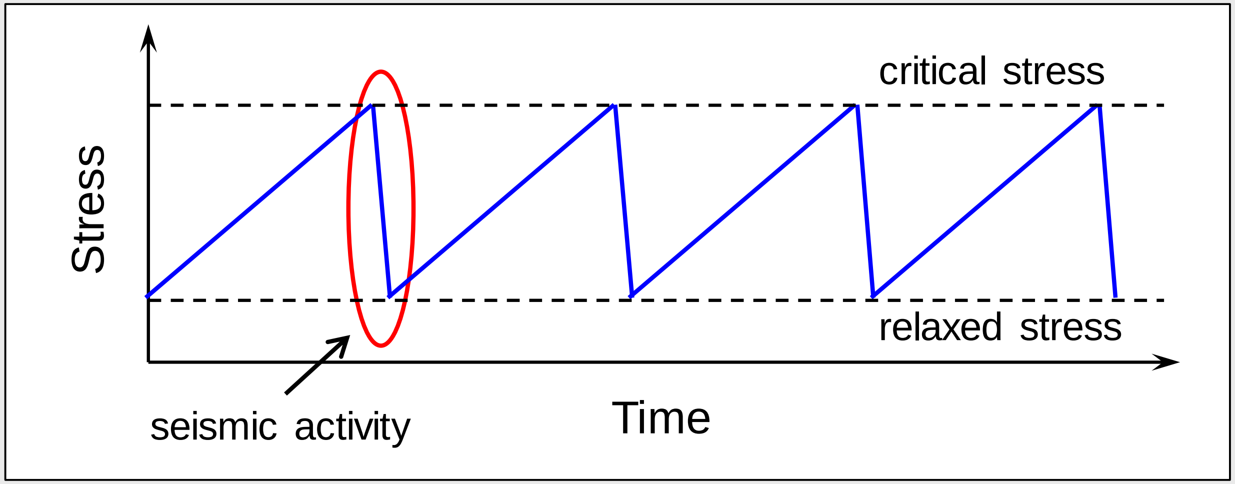

Stress accumulation

(seismicity at margins of continental plates)

mainshock-aftershocks

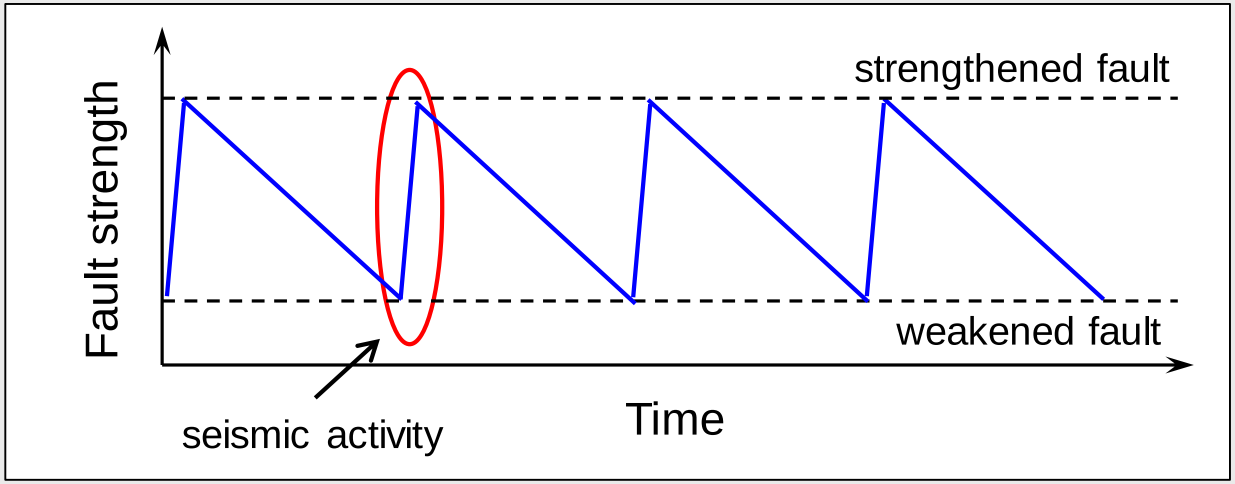

Fault weakening due to fluid erosion

(intraplate seismicity)

earthquake swarms

Vavryčuk & Hrubcová (JGR, 2017)

Fault interaction

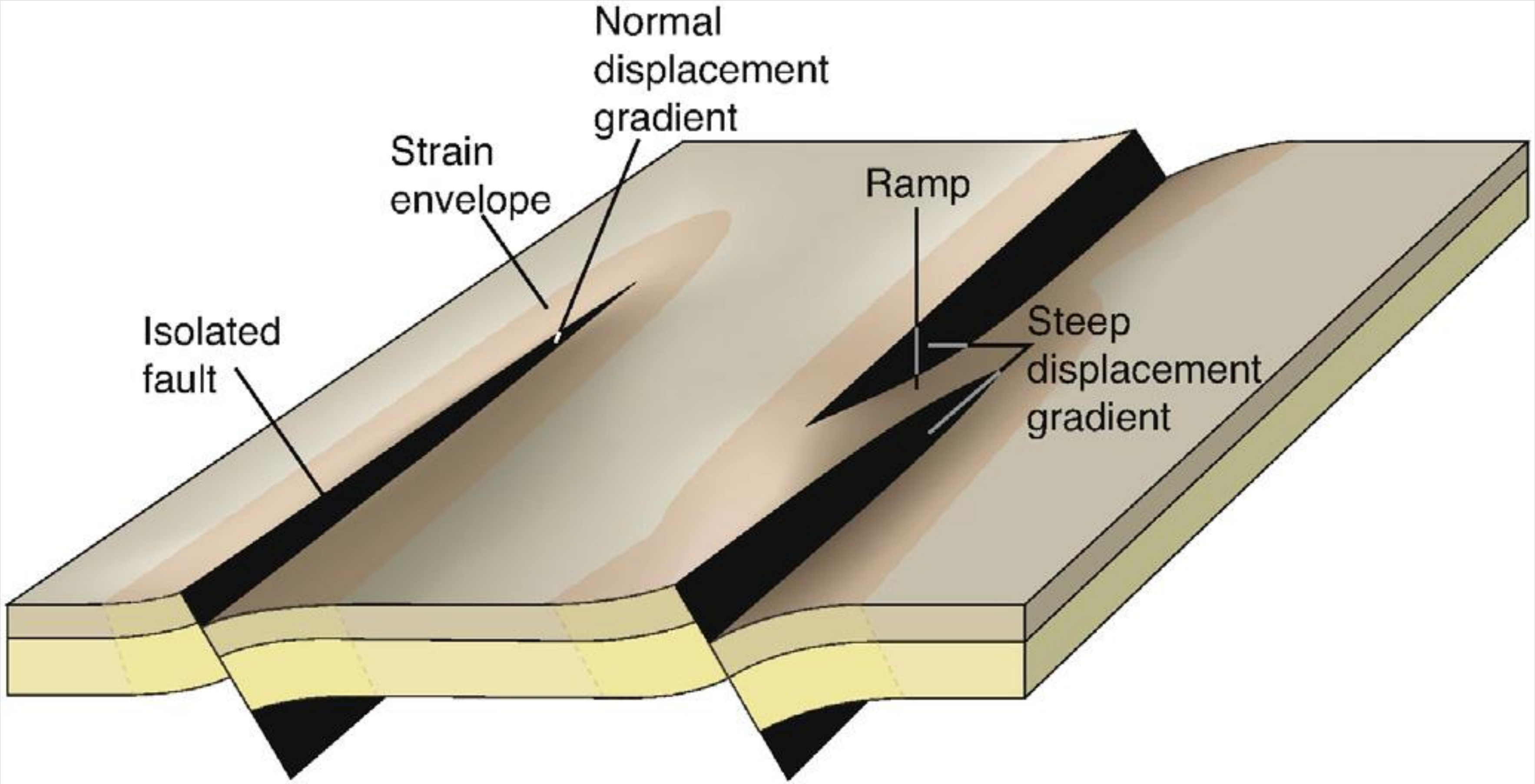

Fossen & Rotevant (Earth Sci. Rev., 2016)

Fault steps and fault linkage

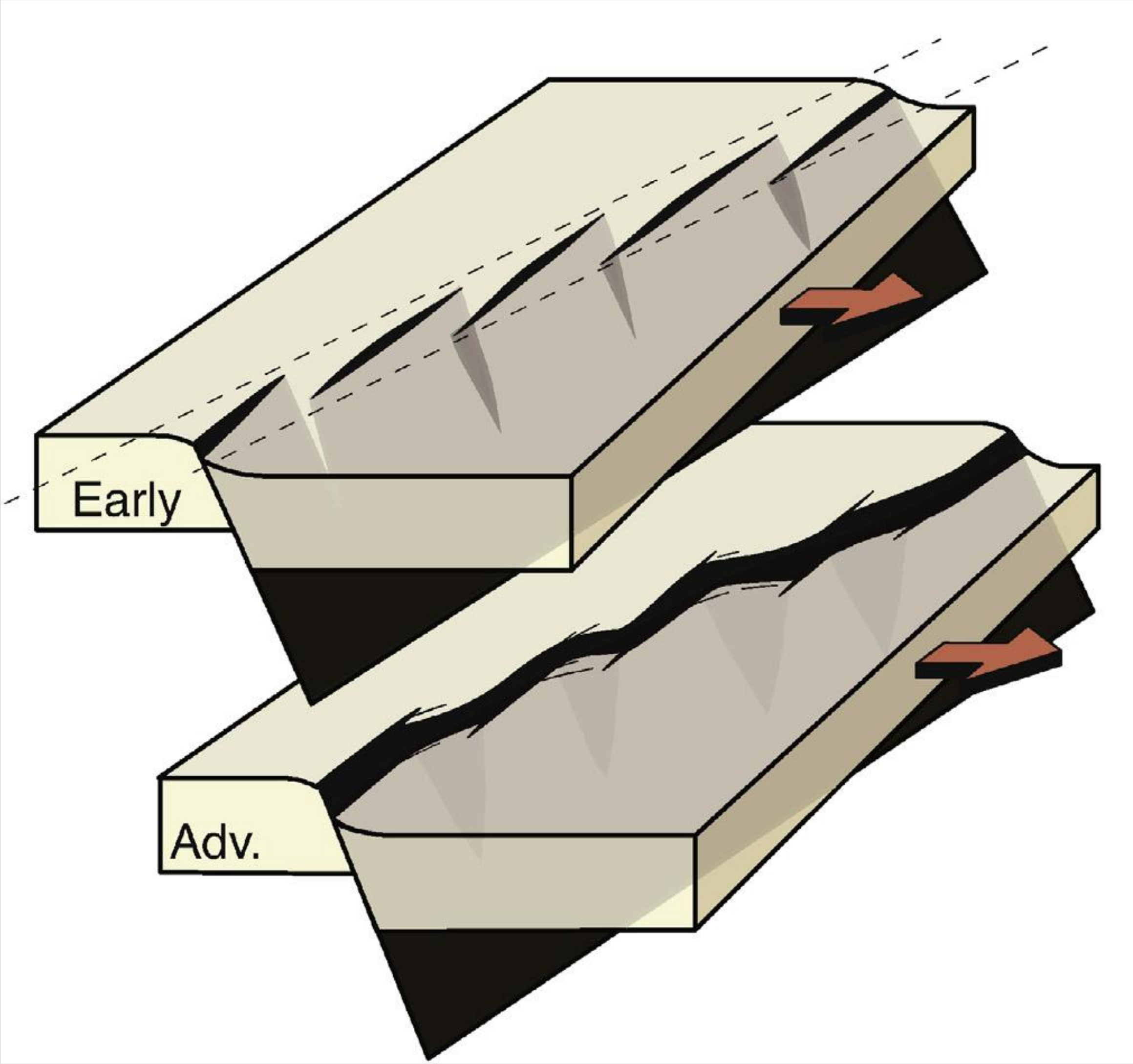

Fossen & Rotevant (Earth Sci. Rev., 2016)

Coulomb stress (CS) modelling

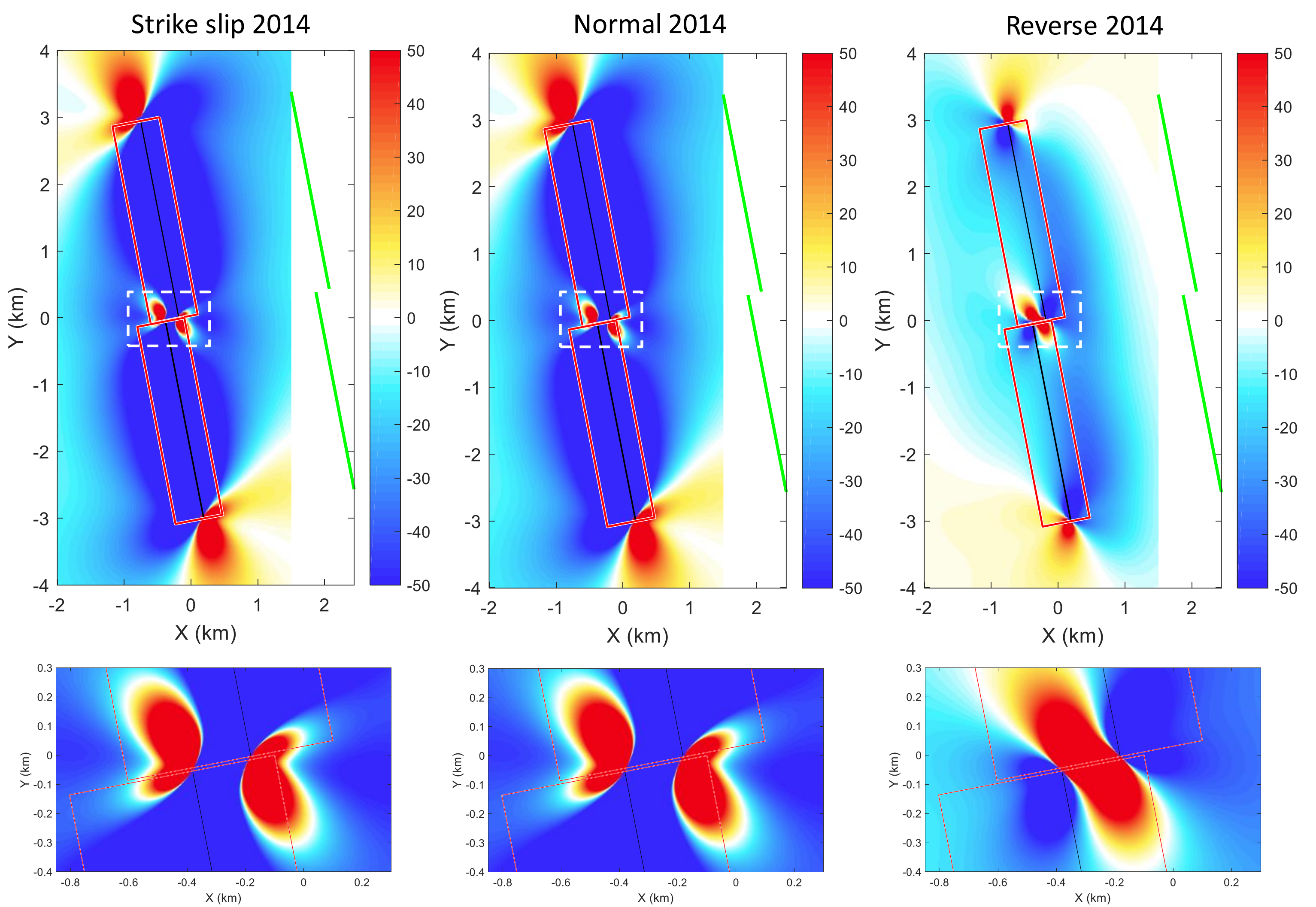

low CS for strike slips

low CS for normal faults

high CS for reverse faults

COULOMB 3.3

Stress variation in a slab

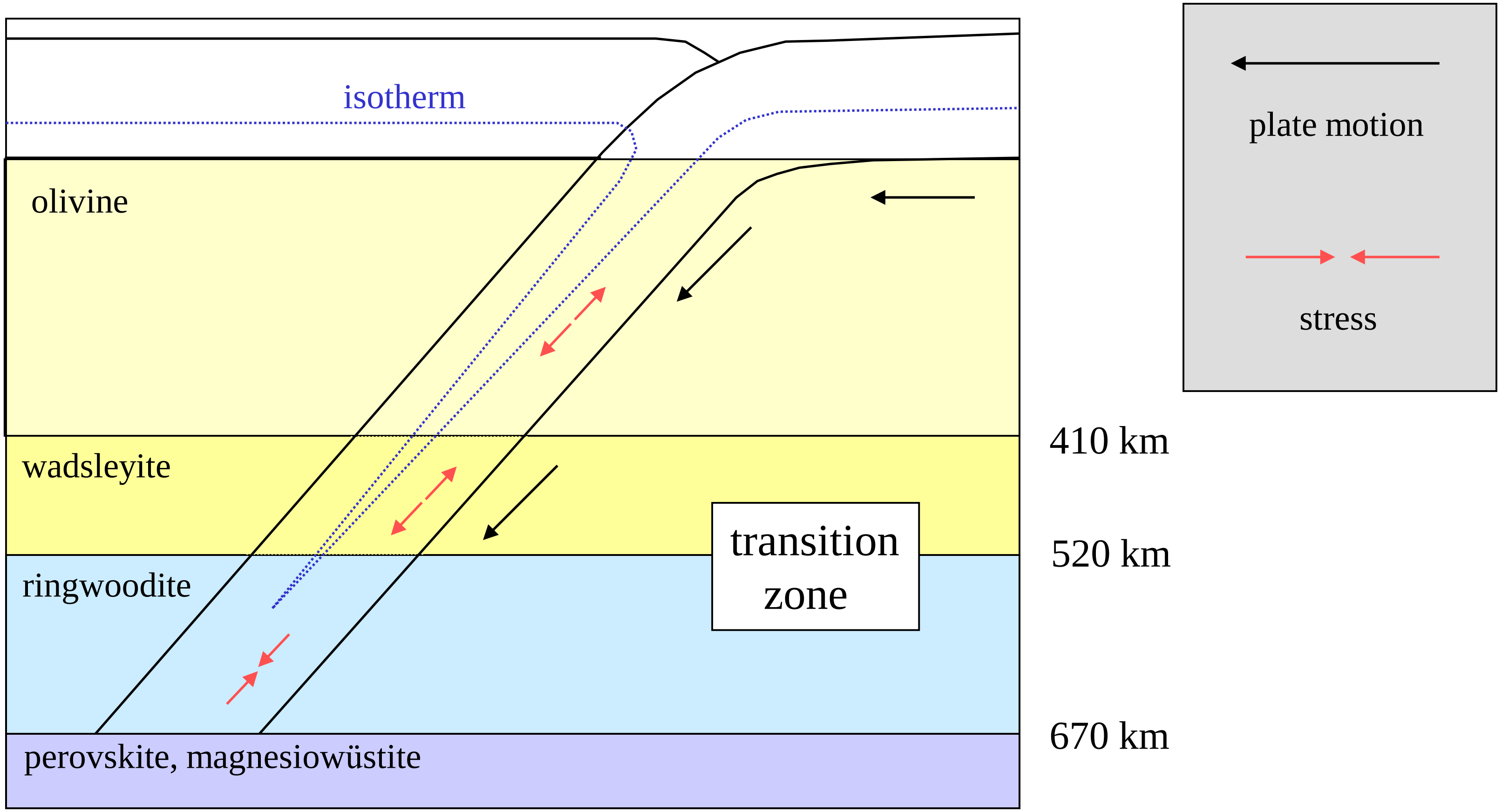

Seismicity in a slab: Tonga subduction zone

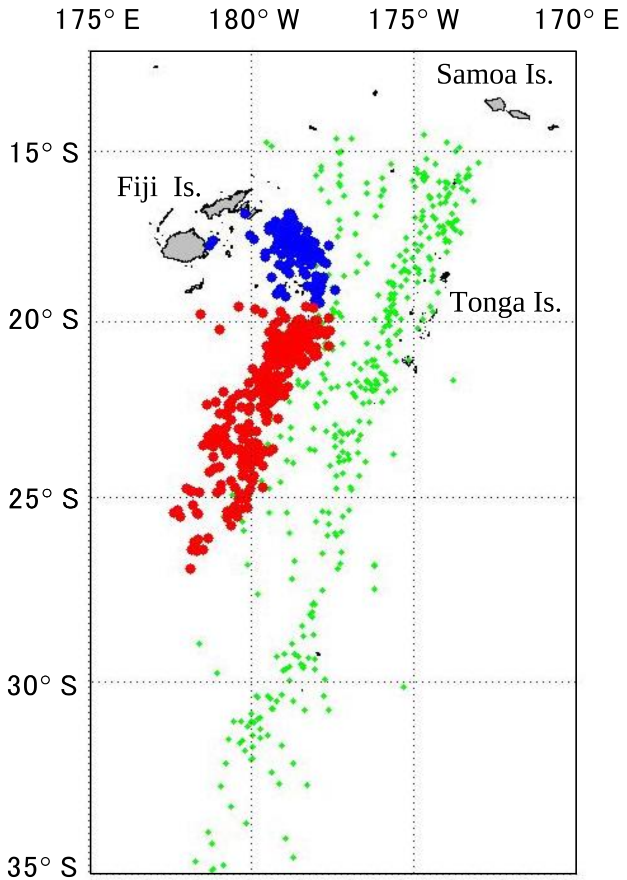

Harvard MT solutions
(M>5, 1980-2002)

Pacific Plate subducts under the Australian Plate

Plate velocity is 10.5 cm/yr

Azimuth of the Tonga Trench is N210°E

Dip of the subducting slab is 60°

The highest deep seismicity in the world

- depth 100-500 km
- **depth 500-700 km, southern cluster**
- depth 500-700 km, northern cluster

Family of accurate focal mechanisms

101 most accurate focal mechanisms

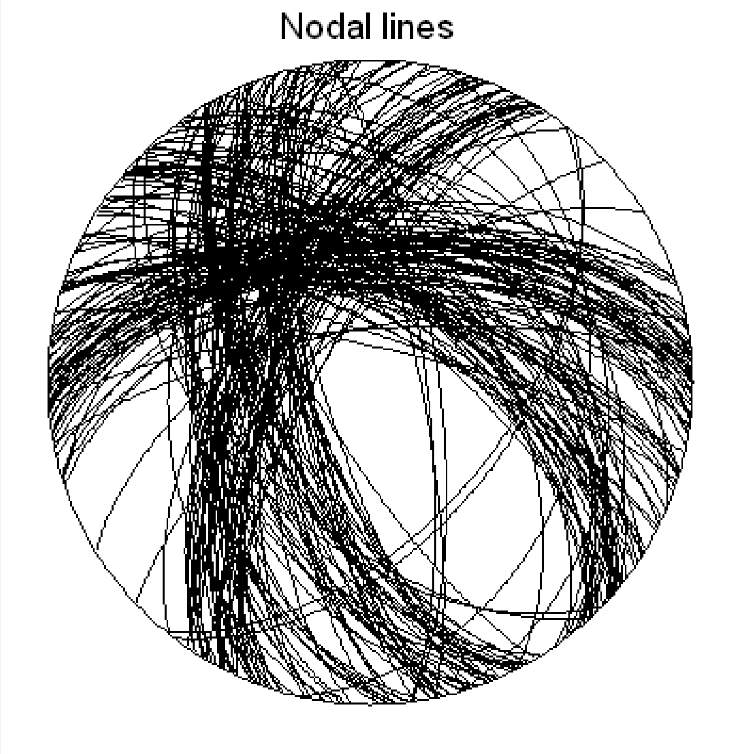

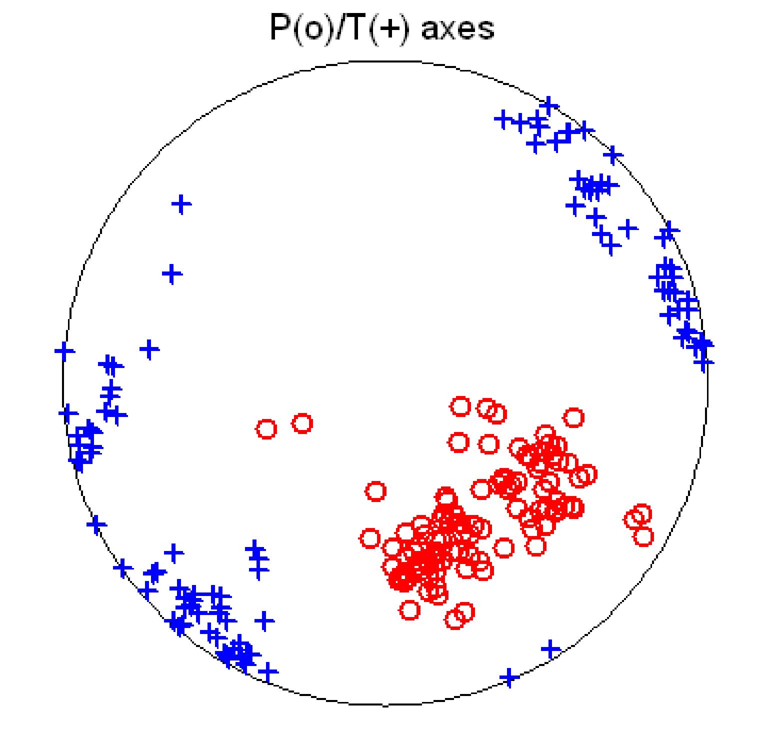

Inversion for stress: Angelier method (2002)

Fit function

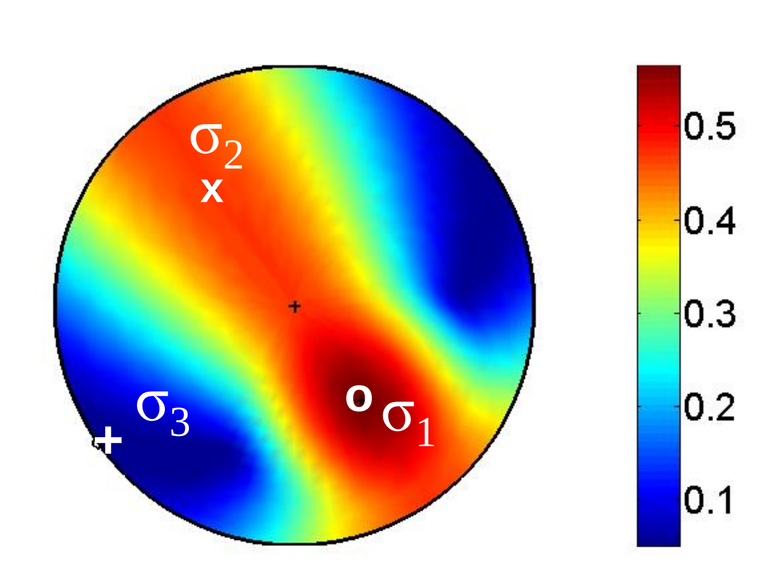

Mohr's diagram

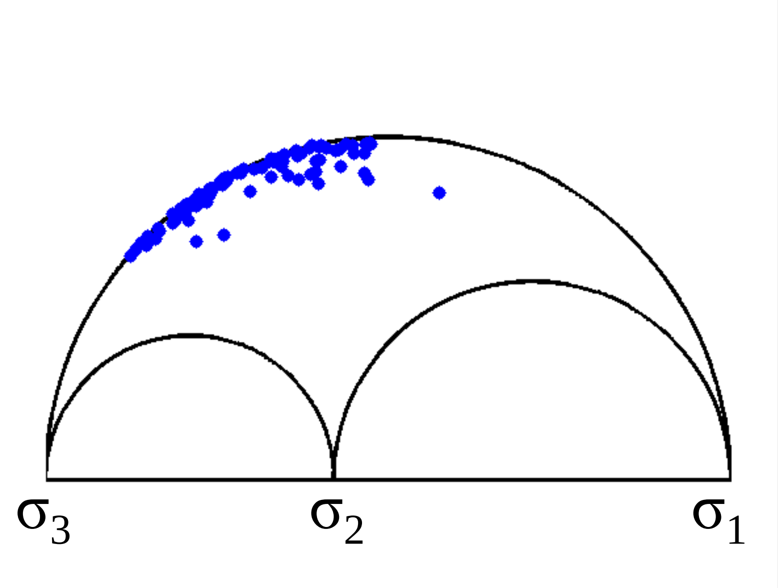

SSSC criterion is maximized

Optimum stress: $\sigma_1 = 50°/145°,\ \sigma_2 = 40°/325°,\ \sigma_3 = 0°/235°,\ R = 0.55$

Inversion for stress: Angelier method (2002)

Misfit function

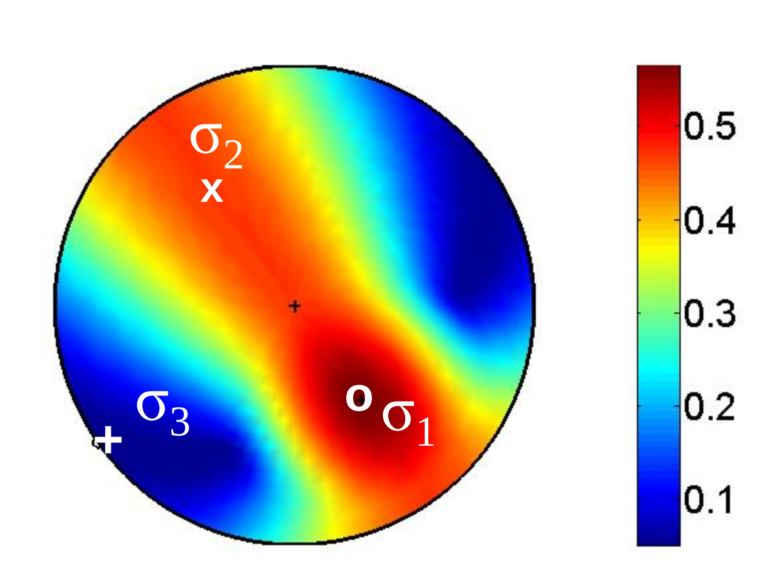

SSSC criterion is maximized

Mohr's diagram

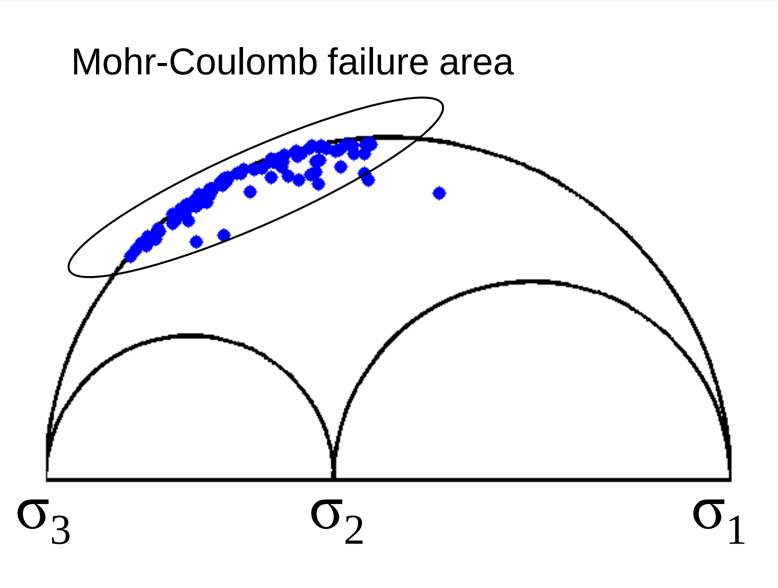

Optimum stress: $\sigma_1 = 50°/145°,\ \sigma_2 = 40°/325°,\ \sigma_3 = 0°/235°,\ R = 0.55$

Inversion for stress: Angelier method (2002)

Misfit function

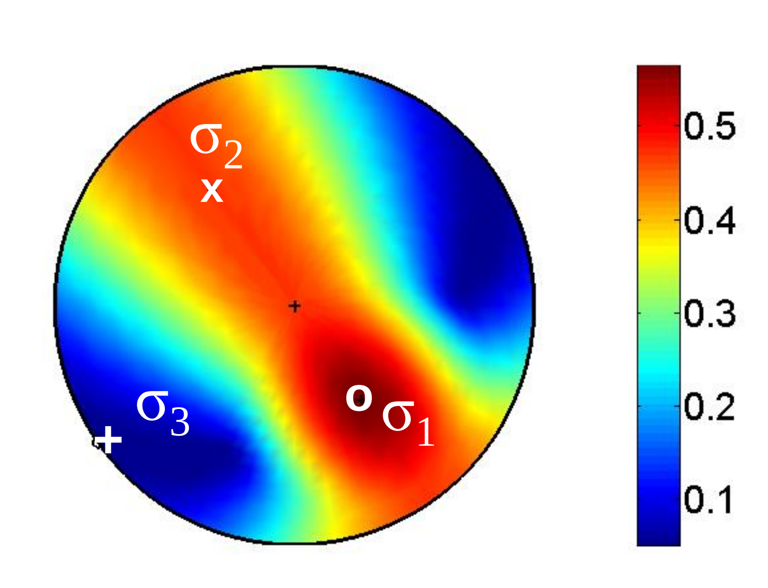

SSSC criterion is maximized

Mohr's diagram

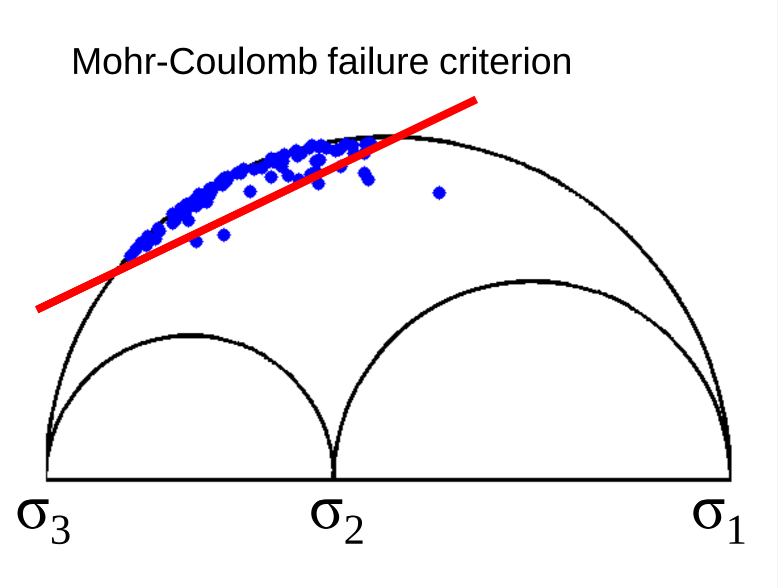

Optimum stress: $\sigma_1 = 50°/145°,\ \sigma_2 = 40°/325°,\ \sigma_3 = 0°/235°,\ R = 0.55$

Forward modelling

Mohr's diagram	Nodal lines	P/T axes	Failure curves

Real data

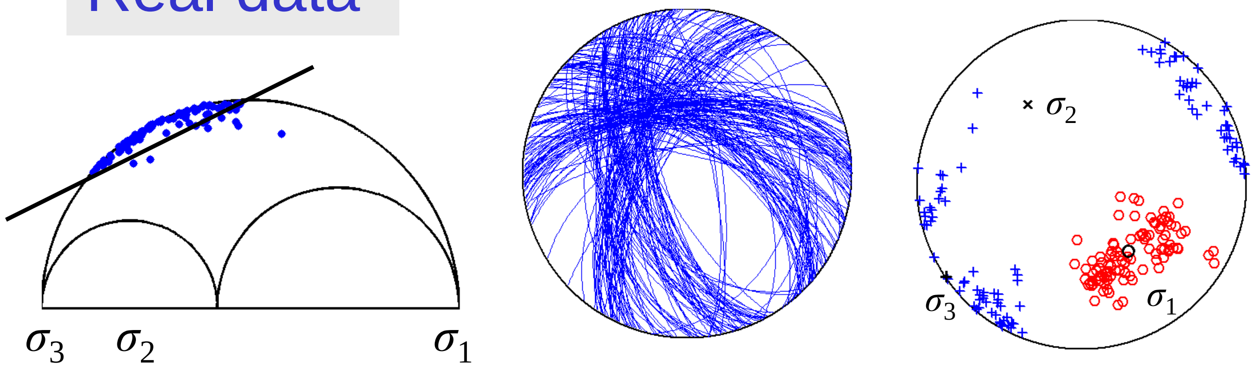

friction = 0.50
shape ratio = 0.55

Synthetic data

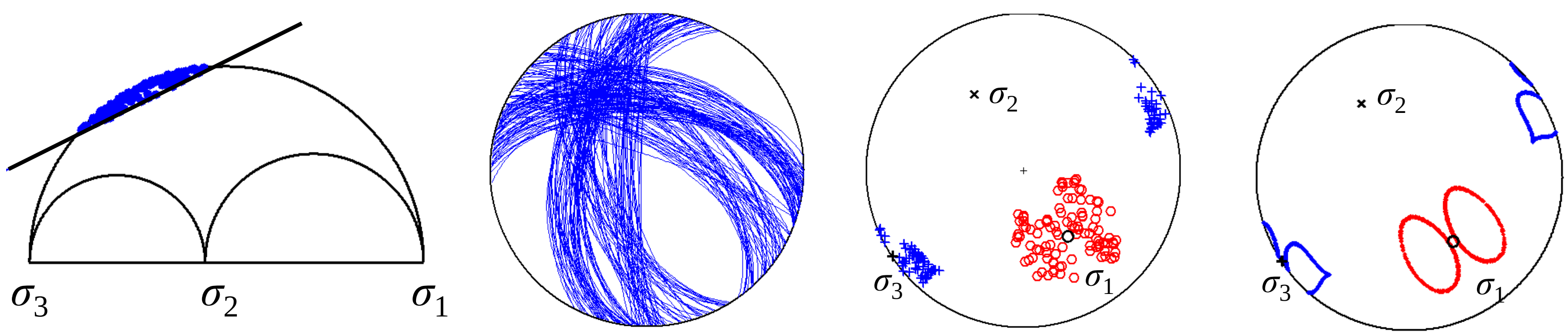

Refining shape ratio I

Mohr's diagram | Nodal lines | P/T axes

friction = 0.6

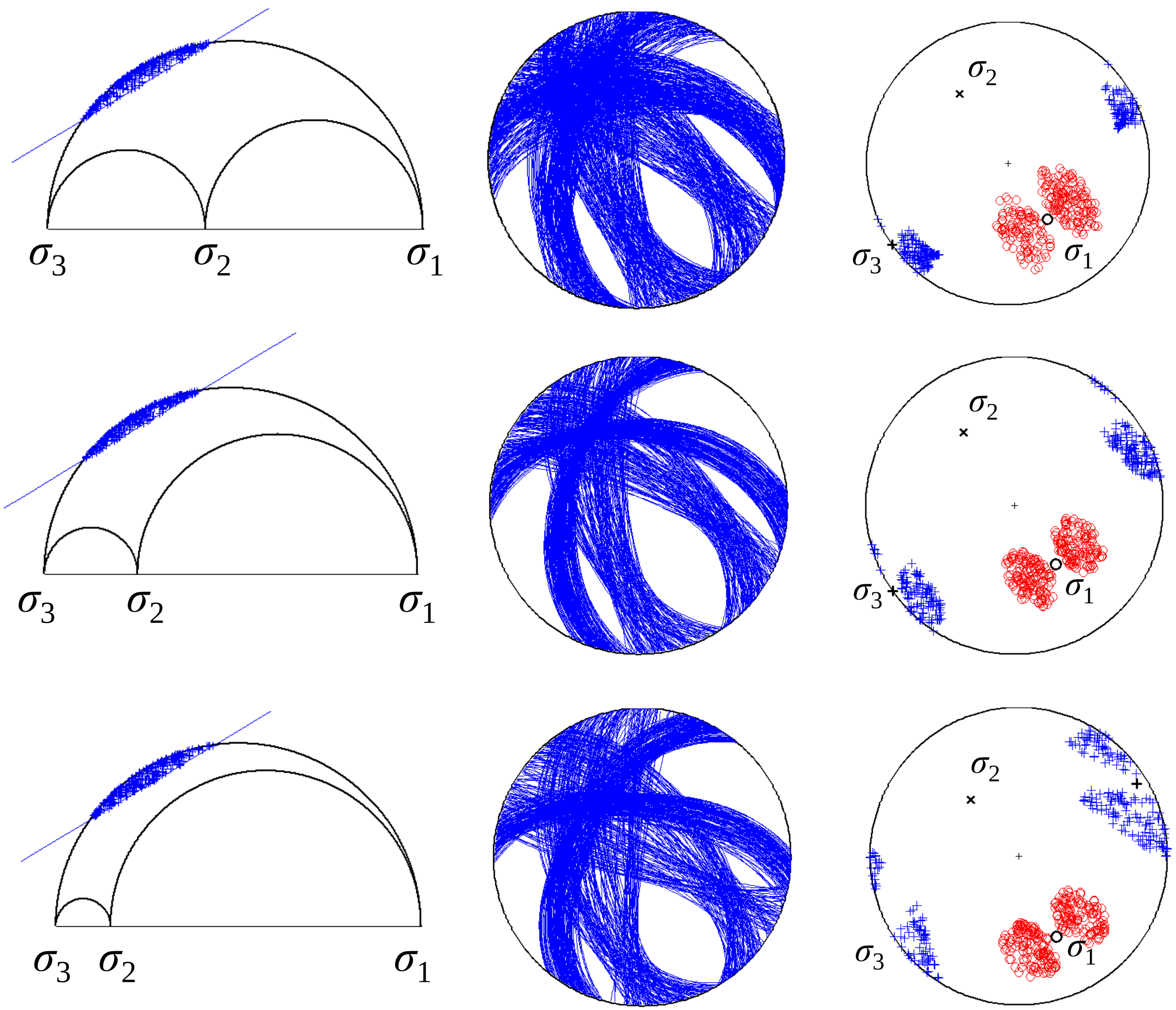

shape ratio = 0.60

shape ratio = 0.75

shape ratio = 0.85

Refining shape ratio II

Mohr's diagram	Nodal lines	P/T axes	Failure curves

Real data

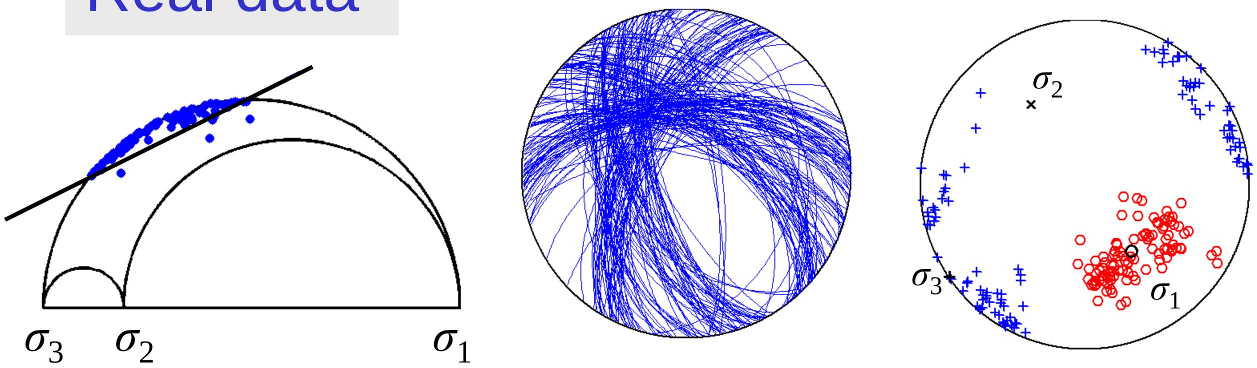

friction = 0.5
shape ratio = 0.8

Synthetic data

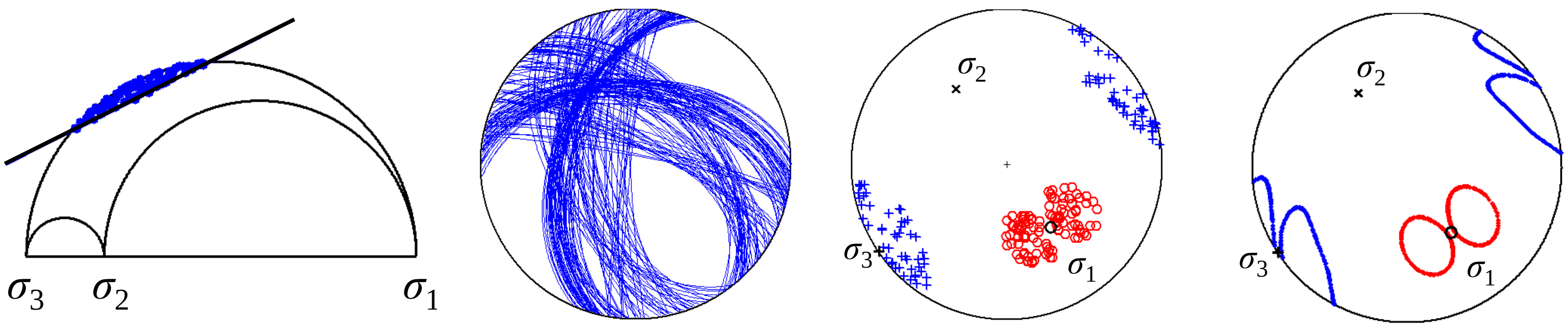

Refining shape ratio III

Original shape ratio

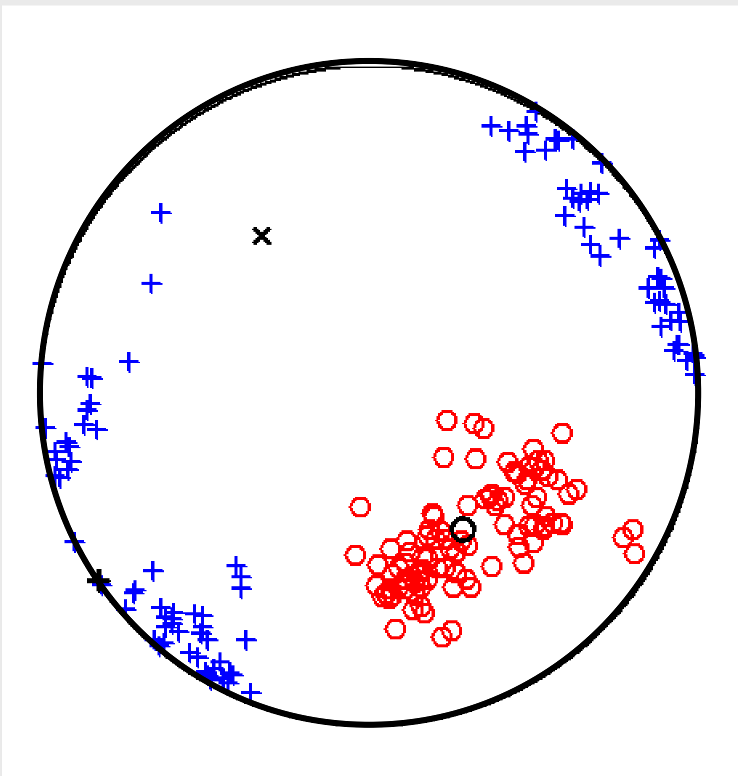

shape ratio = 0.55

Refined shape ratio

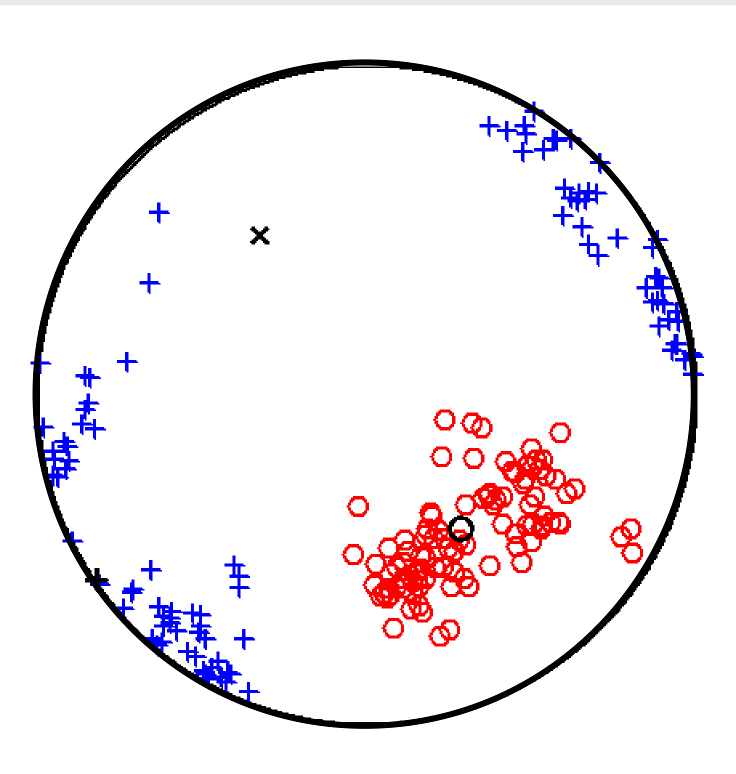

shape ratio = 0.80

Refining shape ratio III

Original shape ratio

Refined shape ratio

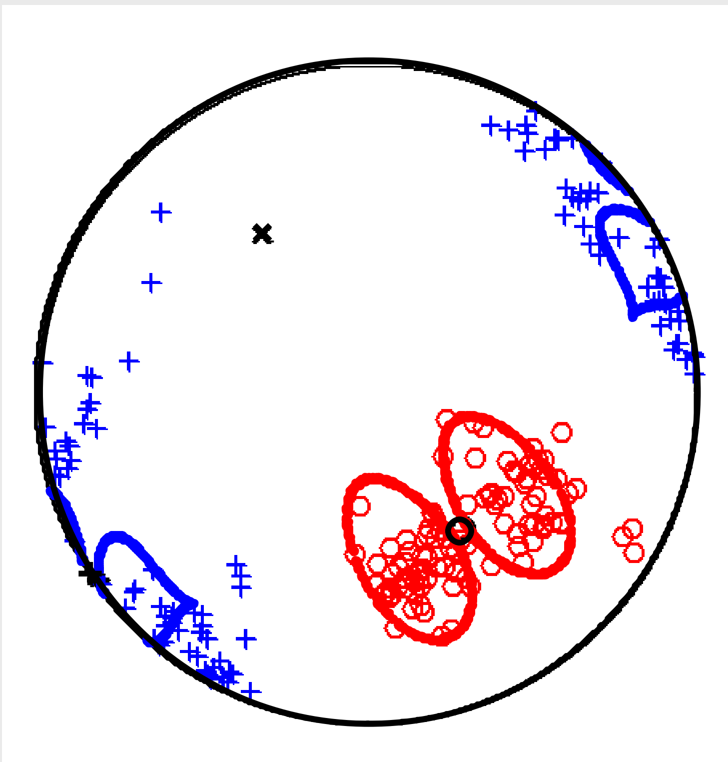

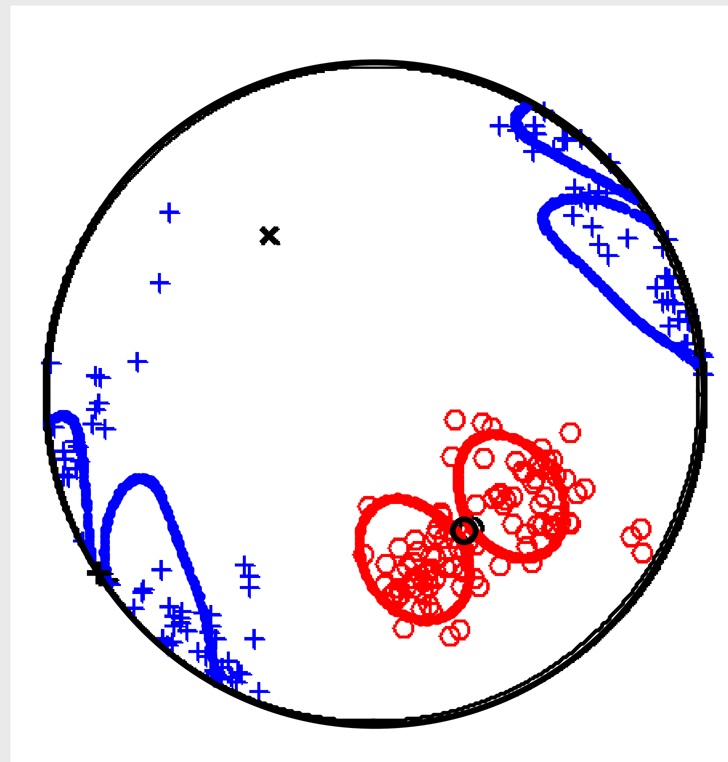

shape ratio = 0.55

shape ratio = 0.80

Tectonic stress and faulting regime

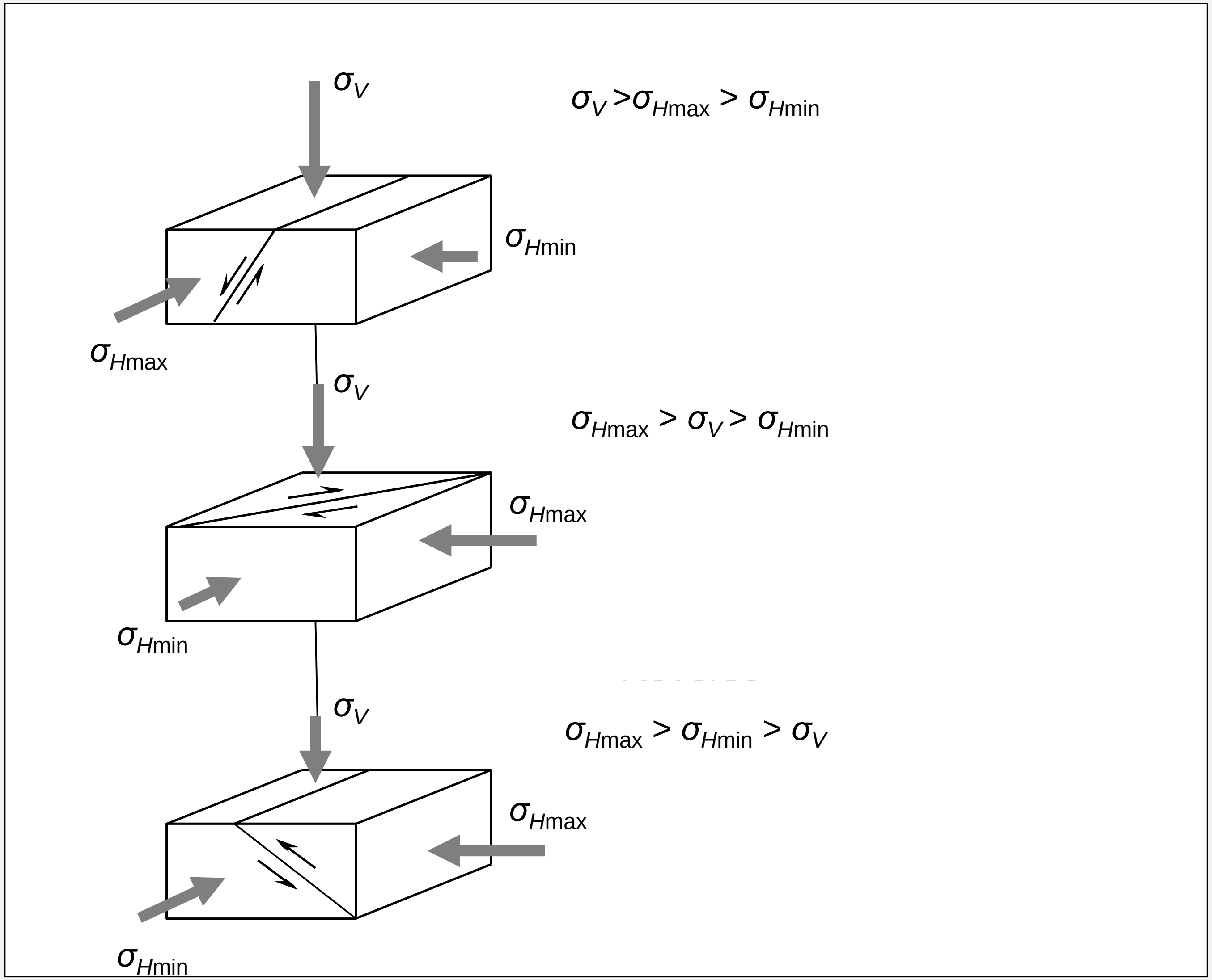

Anderson (1951): The Dynamics of Faulting

Tectonic stress and faulting regime

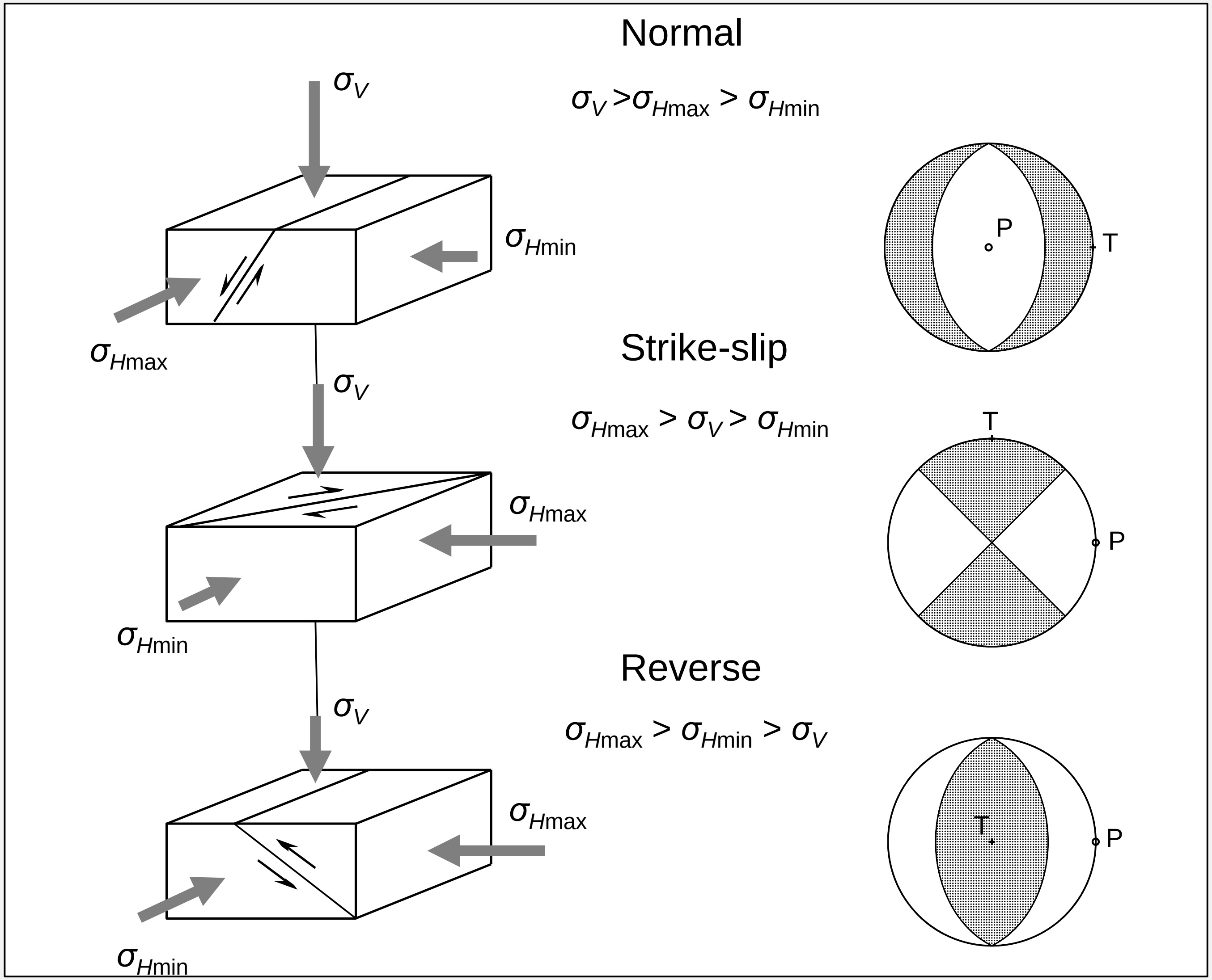

Anderson (1951): The Dynamics of Faulting

Fault instability: visualization

Mohr circles

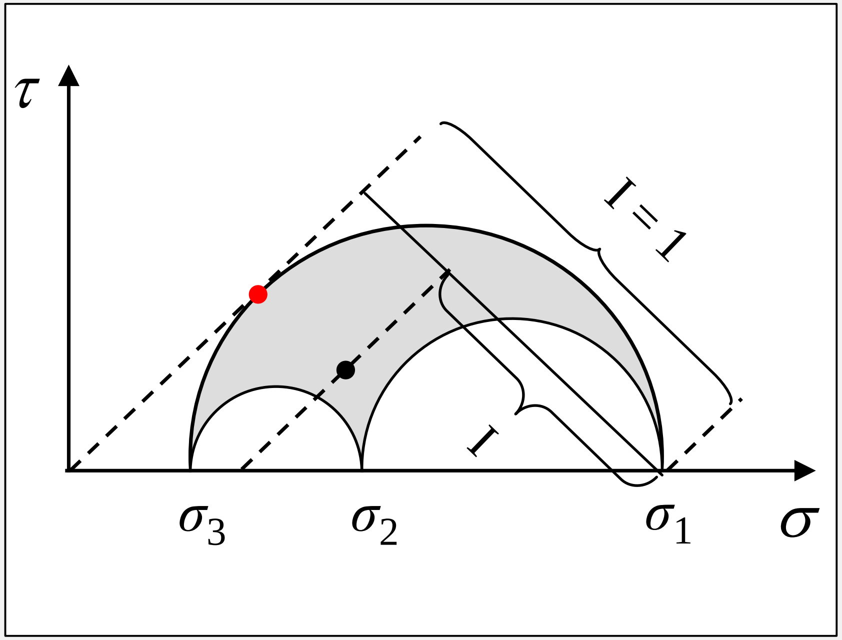

Focal sphere

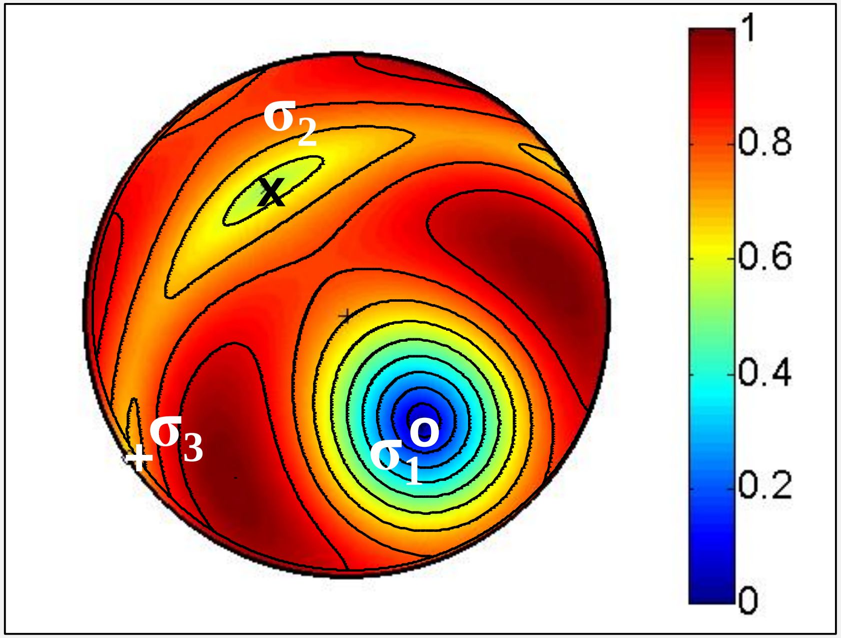

Fault instability & Mohr's diagrams

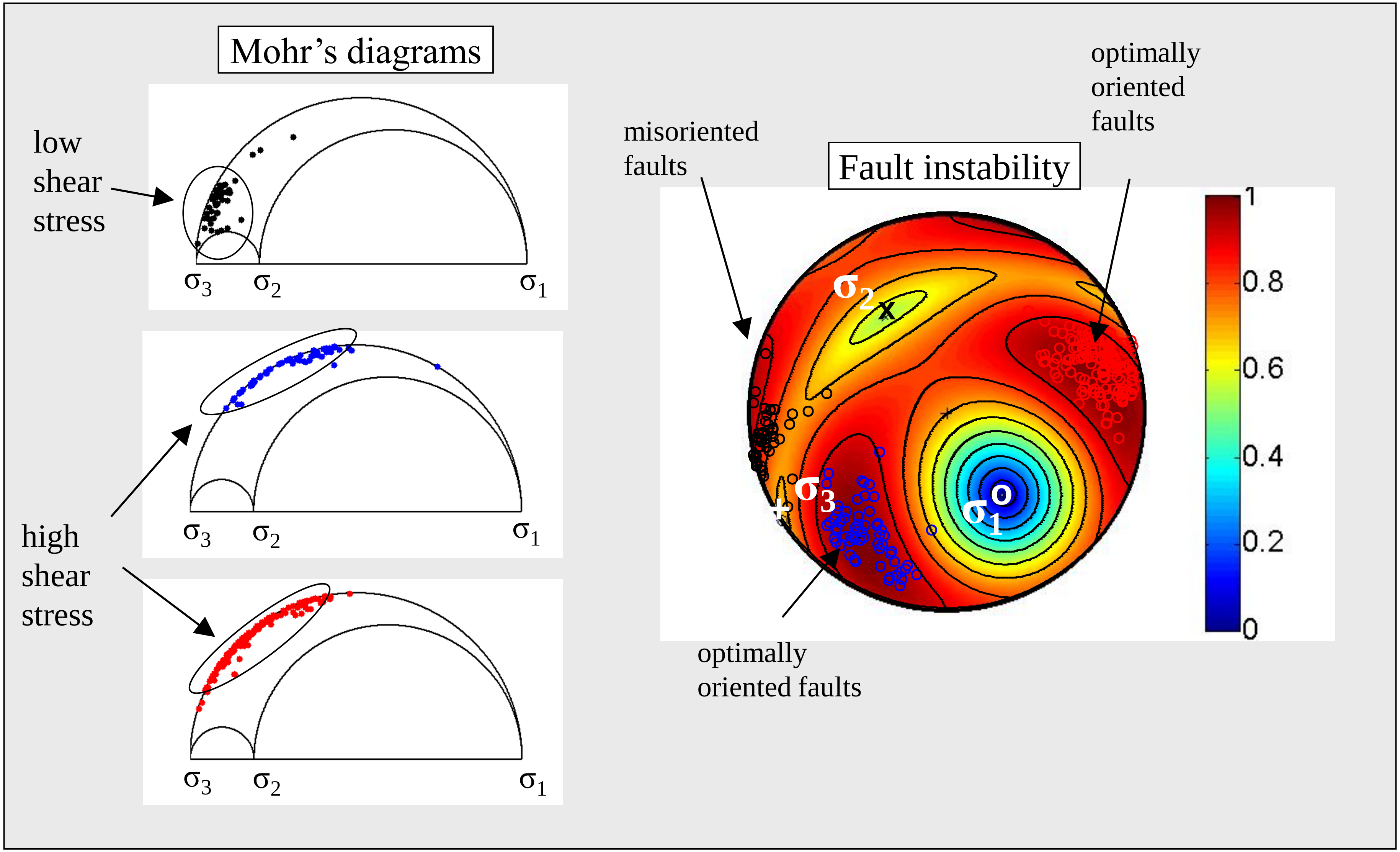

Earthquake activity in West Bohemia in 2008-2018

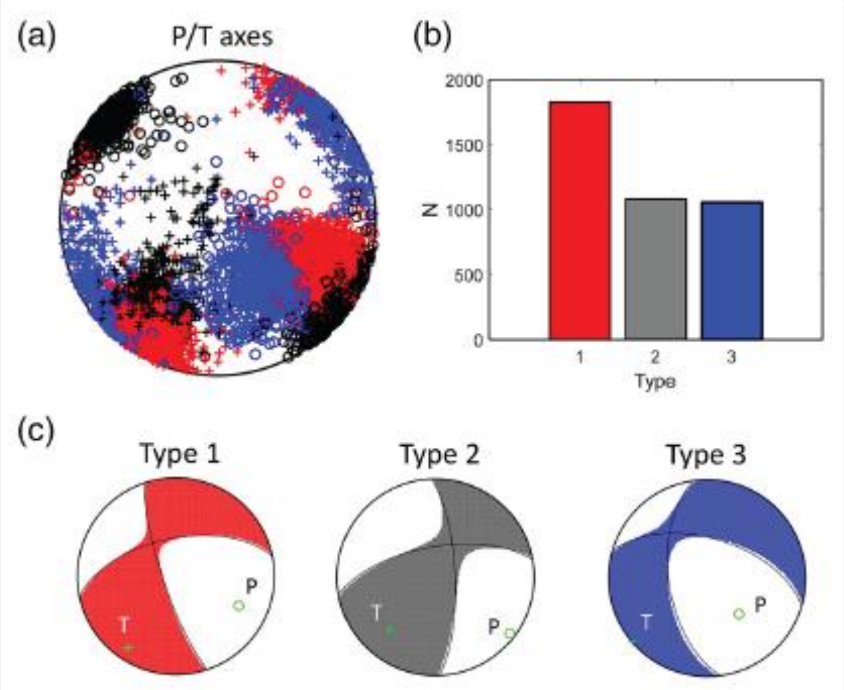

Origins of the FM variety:

- differently oriented preexisting faults
- heterogeneous stress

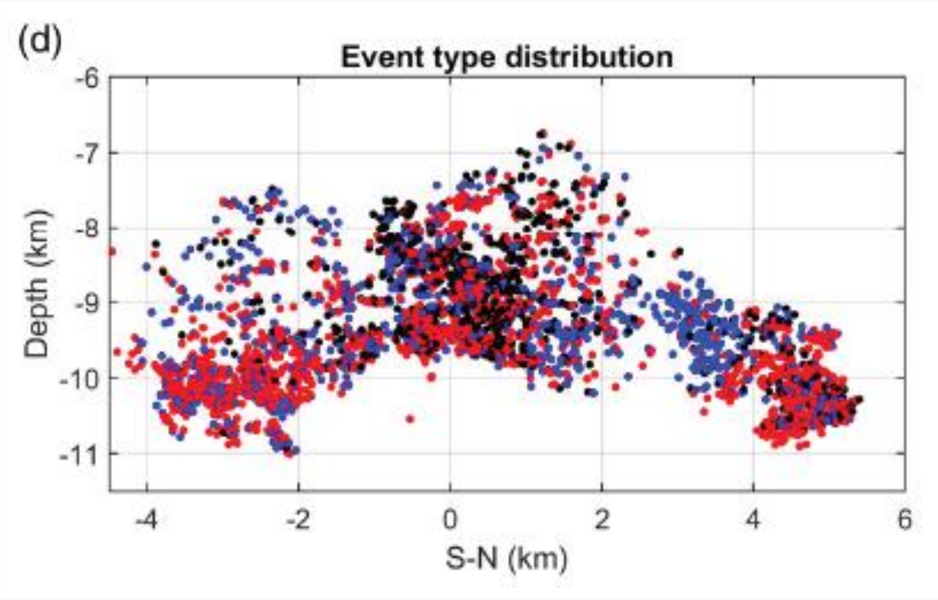

Vavryčuk et al., (Tectonophysics, 2008)

Inversion for stress: example

Fluid injection in KTB: stress inversion

Gephart & Forsyth stress inversion

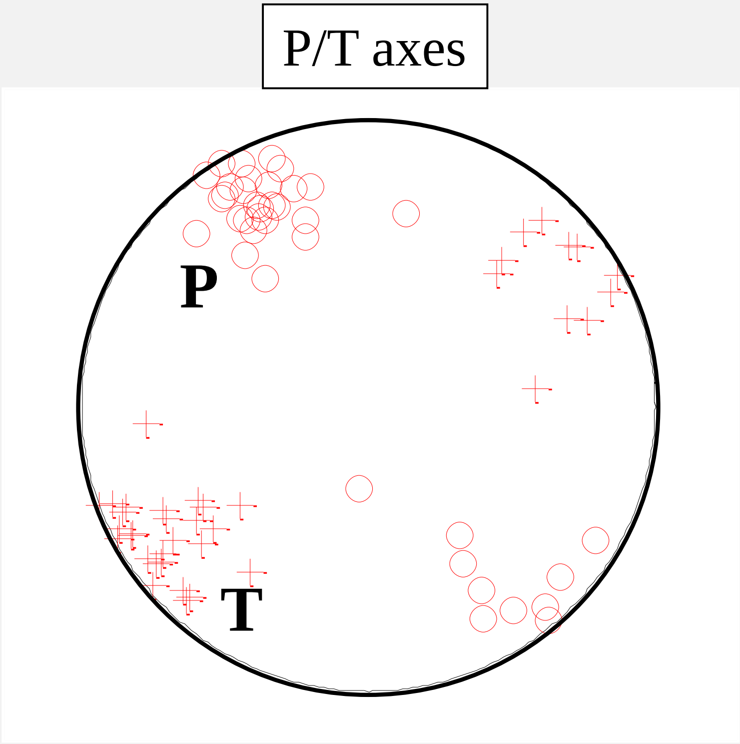

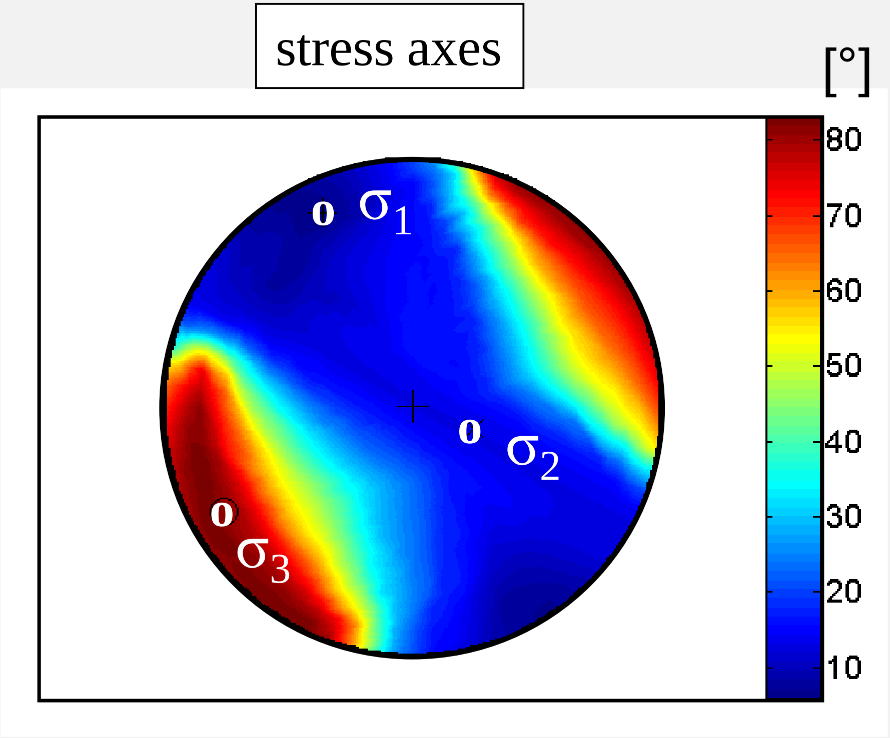

sigma 1 and sigma 3 lie within the P and T clusters

Vavryčuk et al., (Tectonophysics, 2008)

Tectonic stress from focal mechanisms: Applications I

Václav Vavryčuk

Institute of Geophysics, Prague

Swarm activity in West Bohemia

Swarm area in West Bohemia, Czech Republic

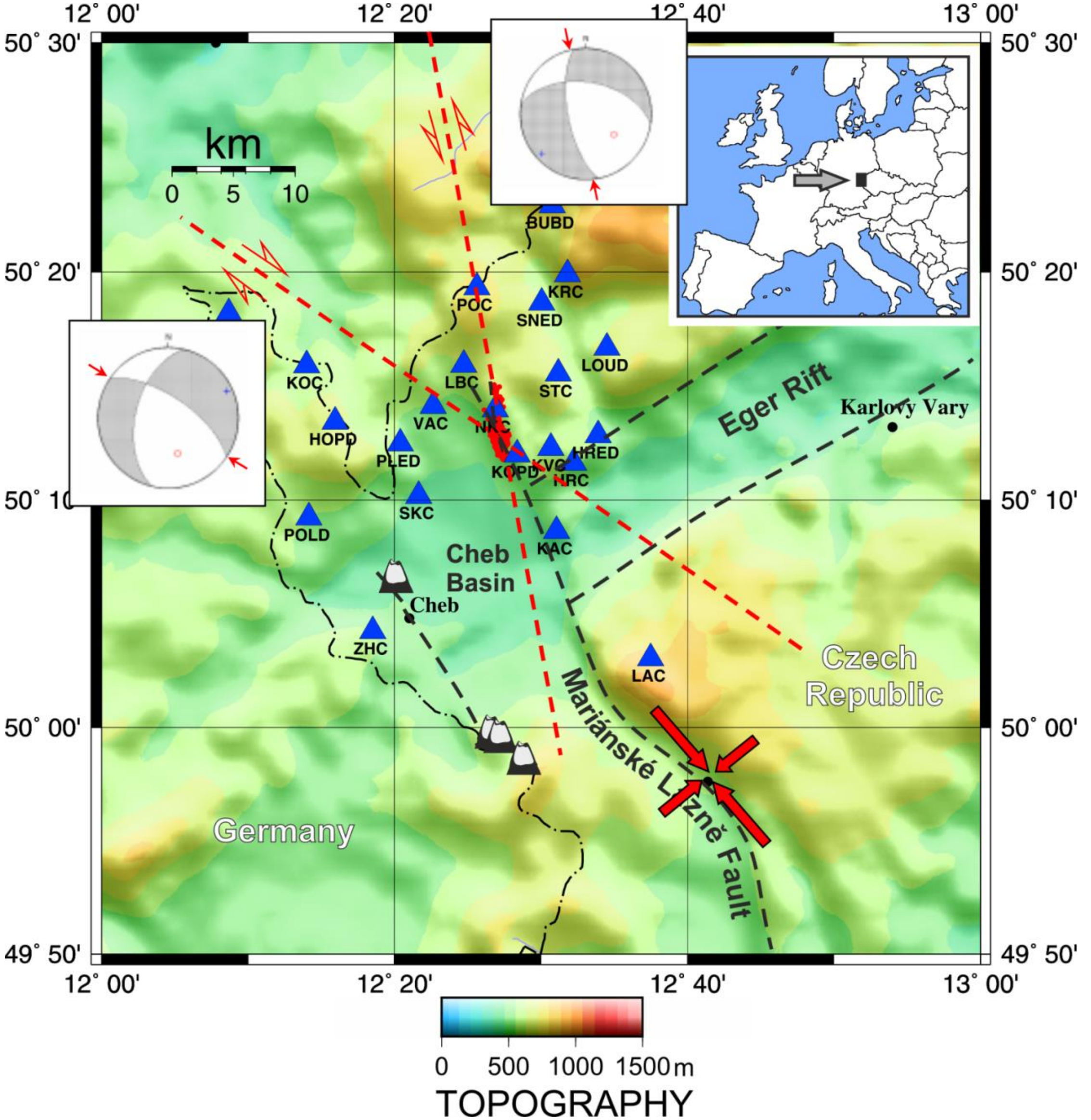

Geodynamically active area:

- Intersection of two major fault systems
- Persistent seismicity
- Emanations of CO_2 rich fluids
- Springs of mineral water
- Quaternary volcanoes

Seismicity in West Bohemia: period 1991-2012

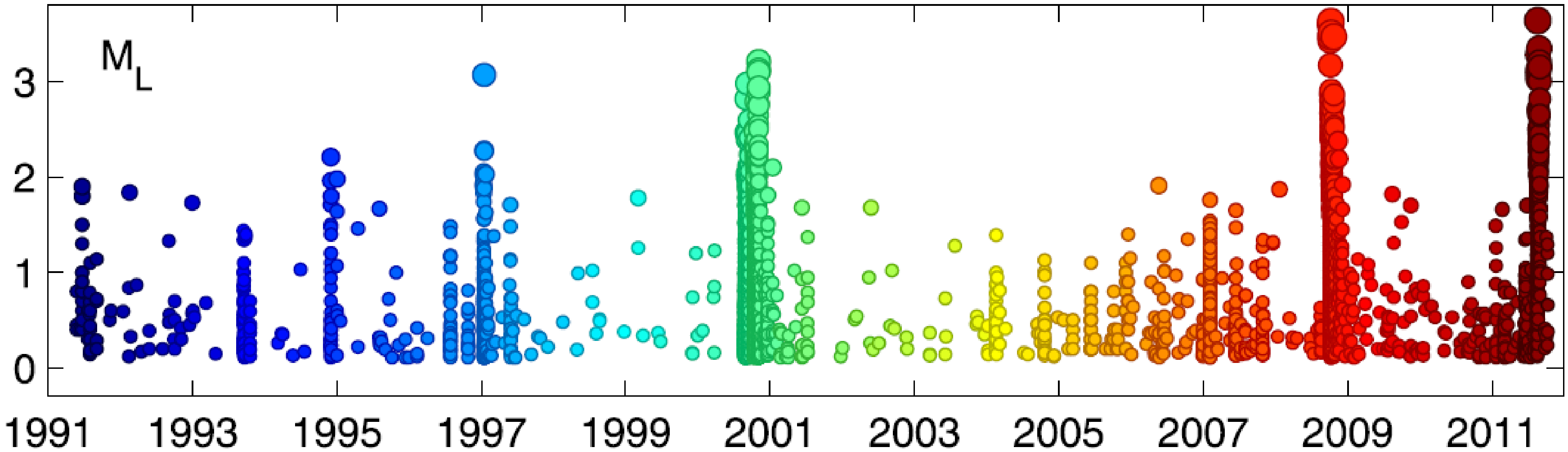

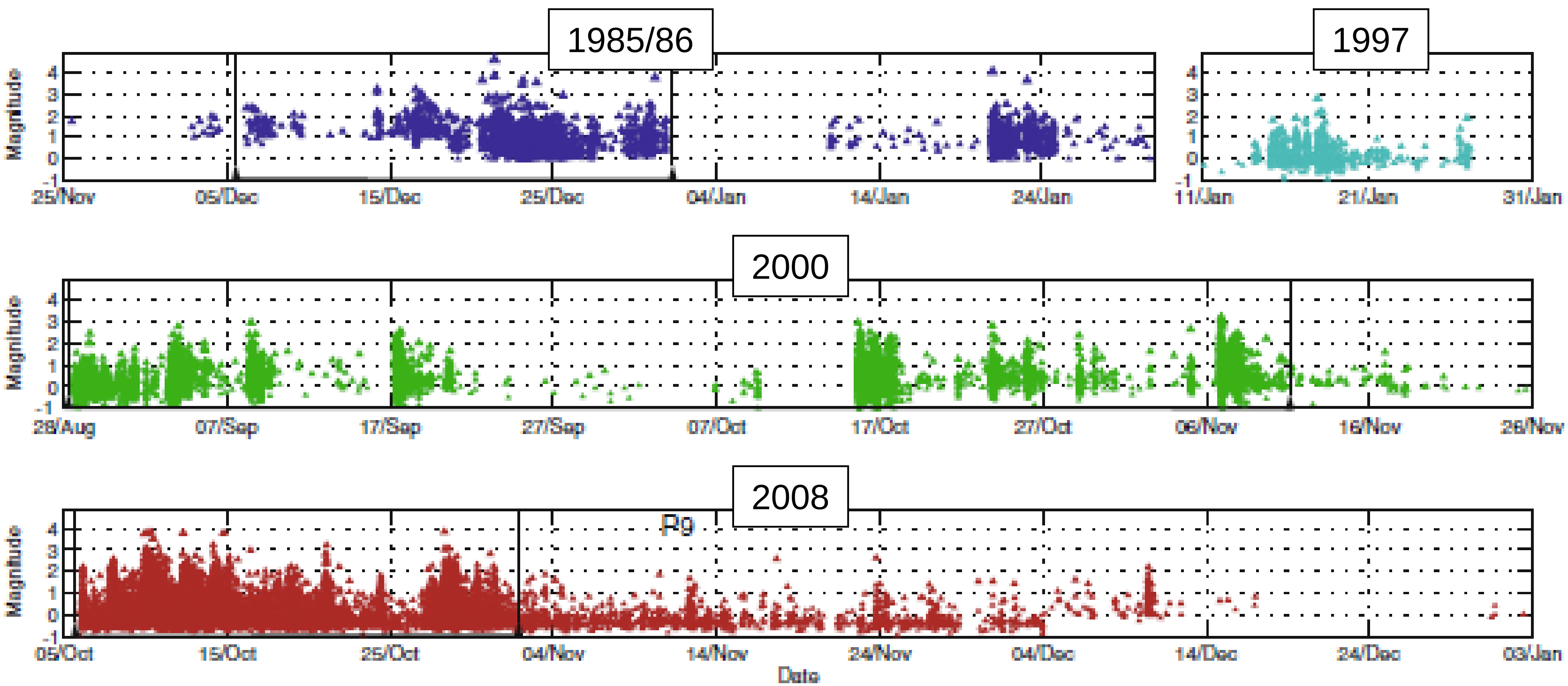

Fluid emanations

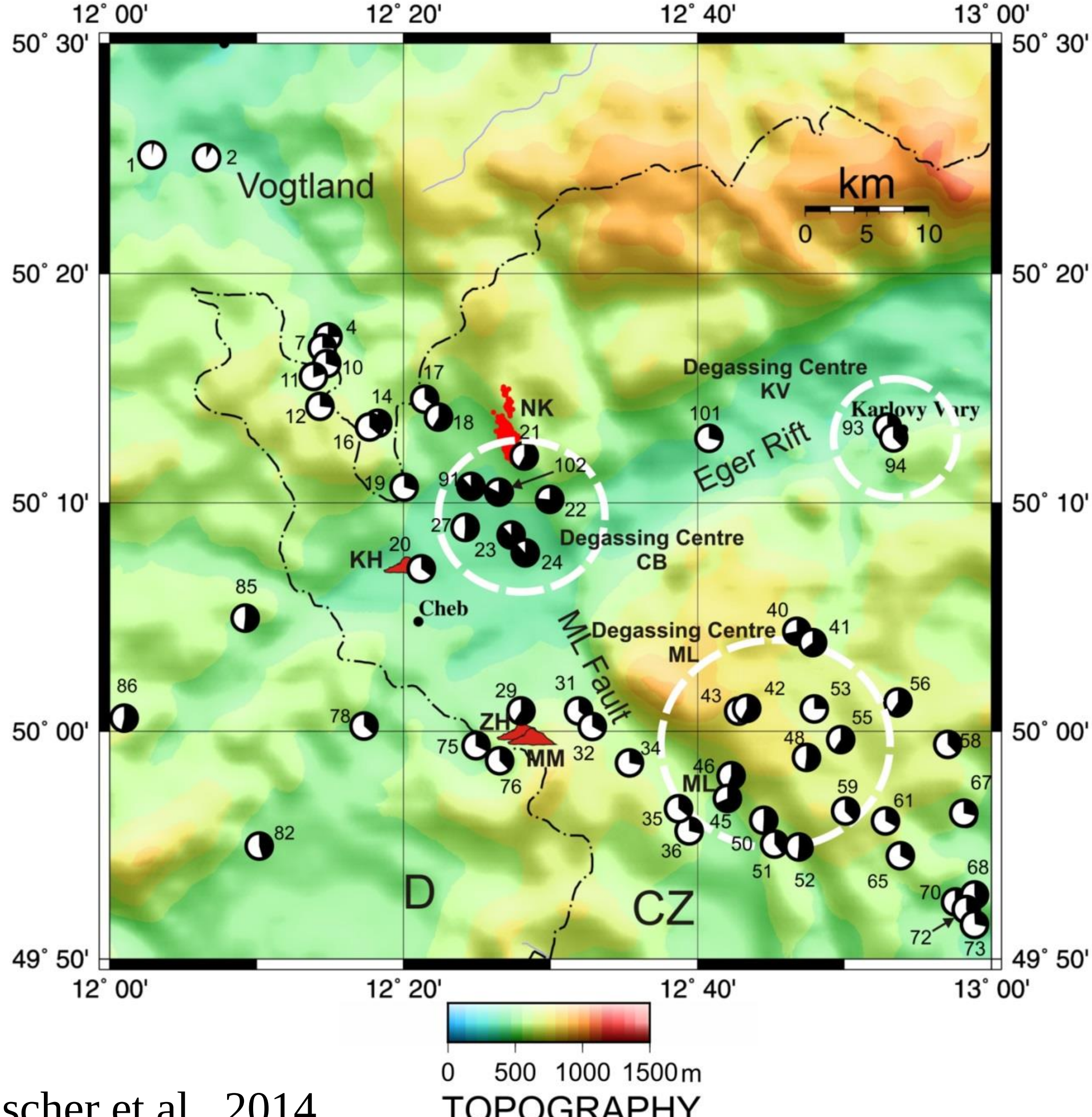

Fischer et al., 2014

Geodynamic activity in West Bohemia/Vogtland

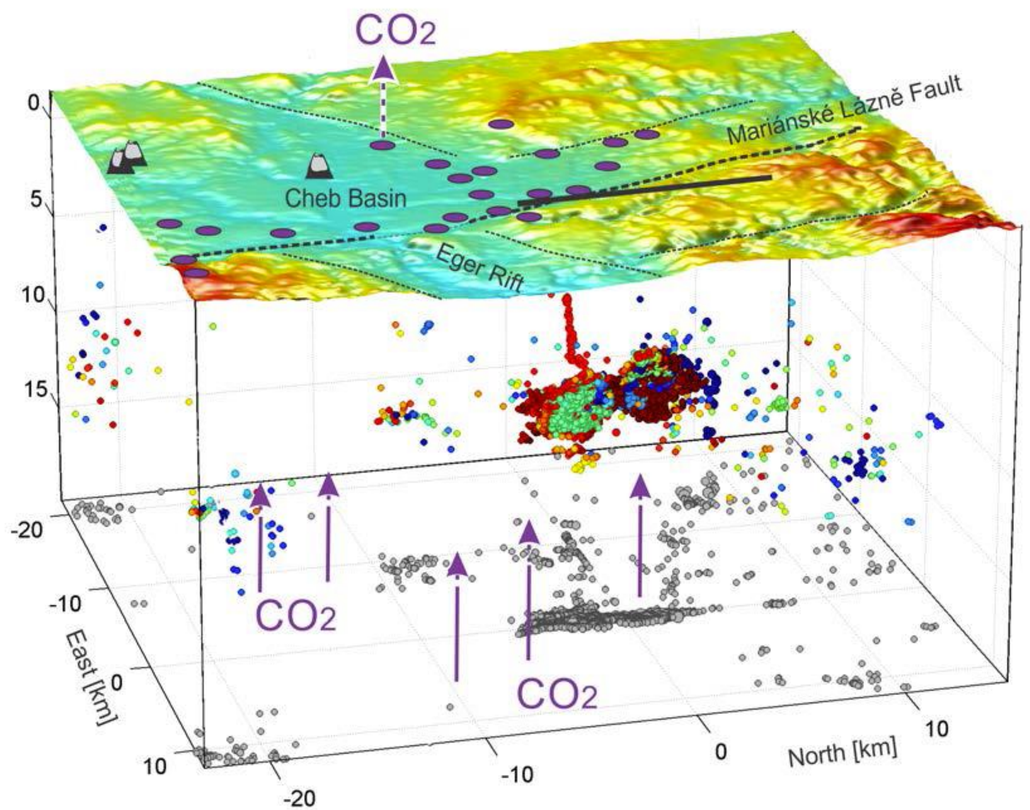

- **repeating earthquake swarms M_L 4+**
- **emanation of fluids**
  - high flow of CO_2 of mantle origin
  - mineral water & wet and dry mofettes
  - $^3He/^4He$, $\delta^{13}C$ – mantle origin of gases
- **3 active Quaternary volcanoes**
  - Scoria cones (Komorní Hůrka, Železná Hůrka)
  - Mýtina Maar

unique European intra-continental area:
mid-crustal, non-volcanic earthquake swarm seismicity and large-scale diffuse degassing of mantle-derived CO_2

Fischer et al., 2014

Foci clustering: period 1991-2011

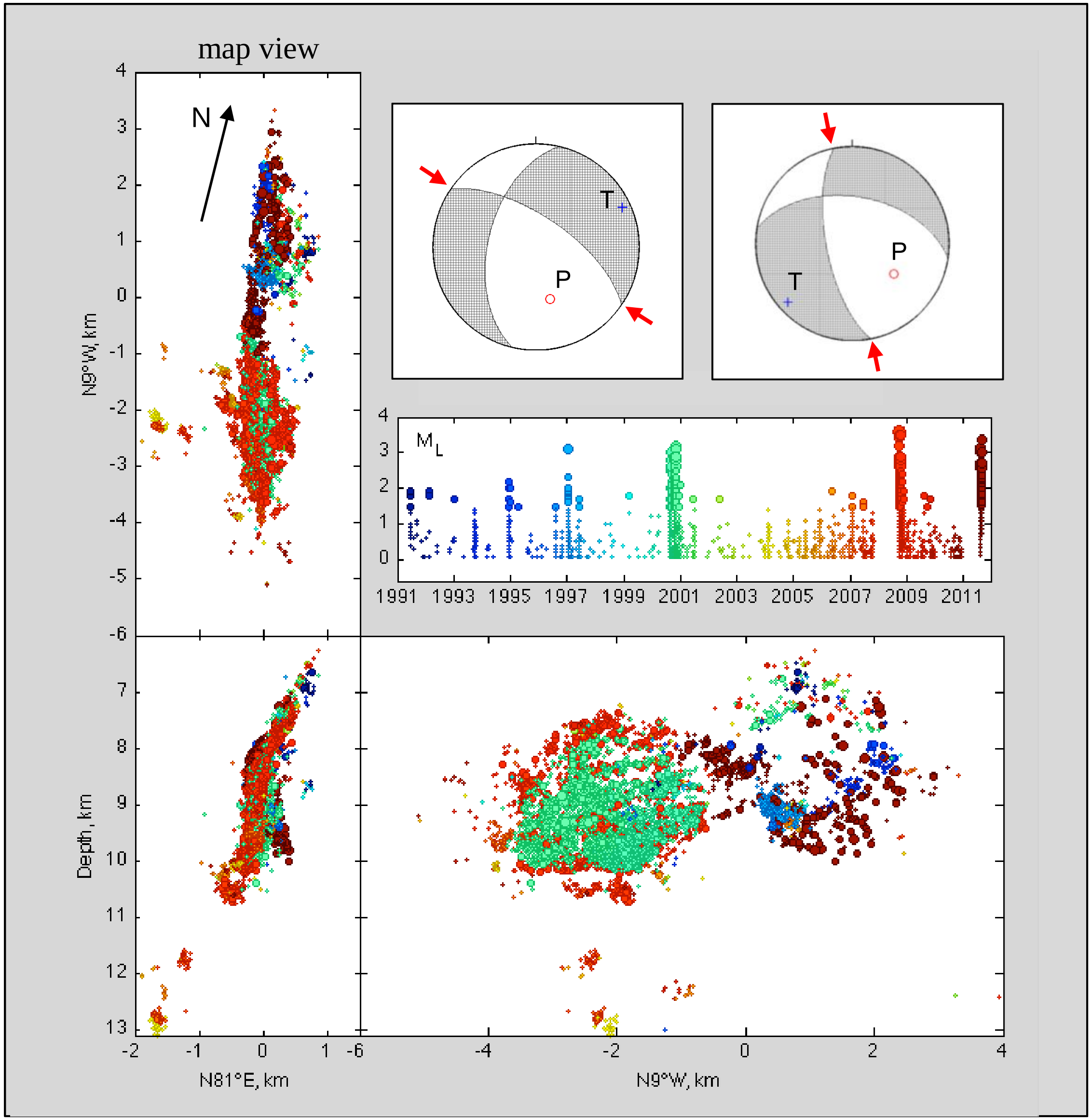

Size of the focal zone:
3 km x 8 km

Detpths:
7 – 13 km

Geometry of the focal zone:
Several differently oriented fault segments

Activity:
Swarms lasting from fiew days to few months

Bouchaala et al., 2013

Principal earthquakes in West Bohemia

Properties of the individual principal faults

Right-lateral faults

Left-lateral faults

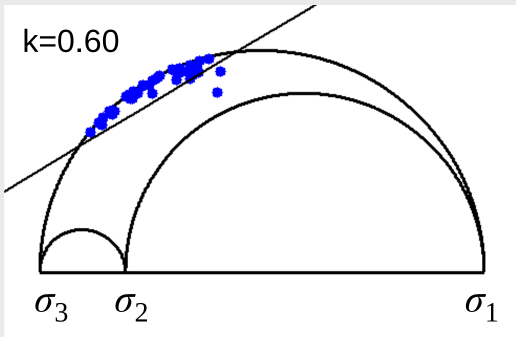

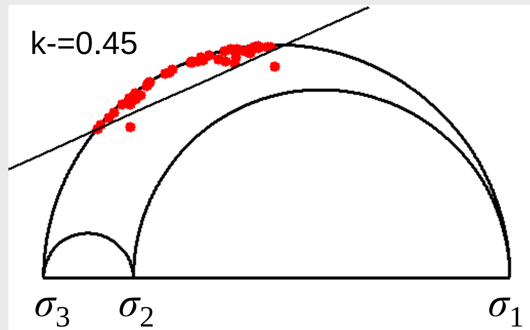

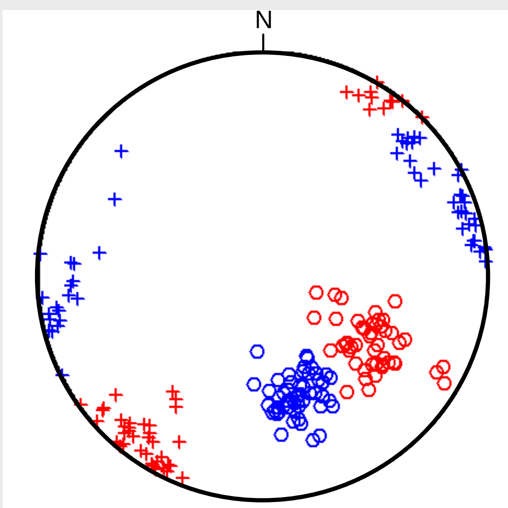

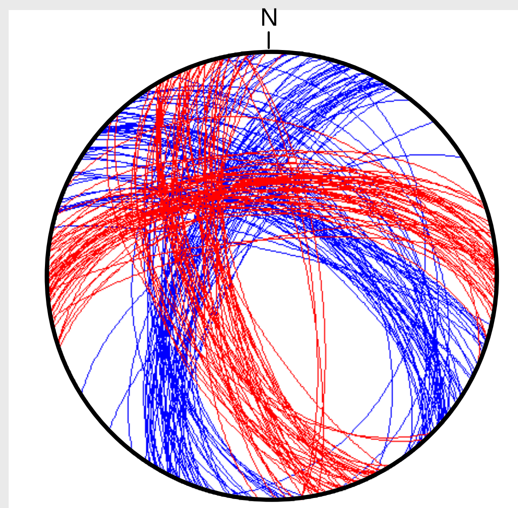

<u>Left-lateral faults</u>:

- most active fault

<u>Right-lateral faults</u>:

- less active

2008 swarm activity

Vavryčuk (EPSL, 2011)

Principal faults versus tectonics in West Bohemia

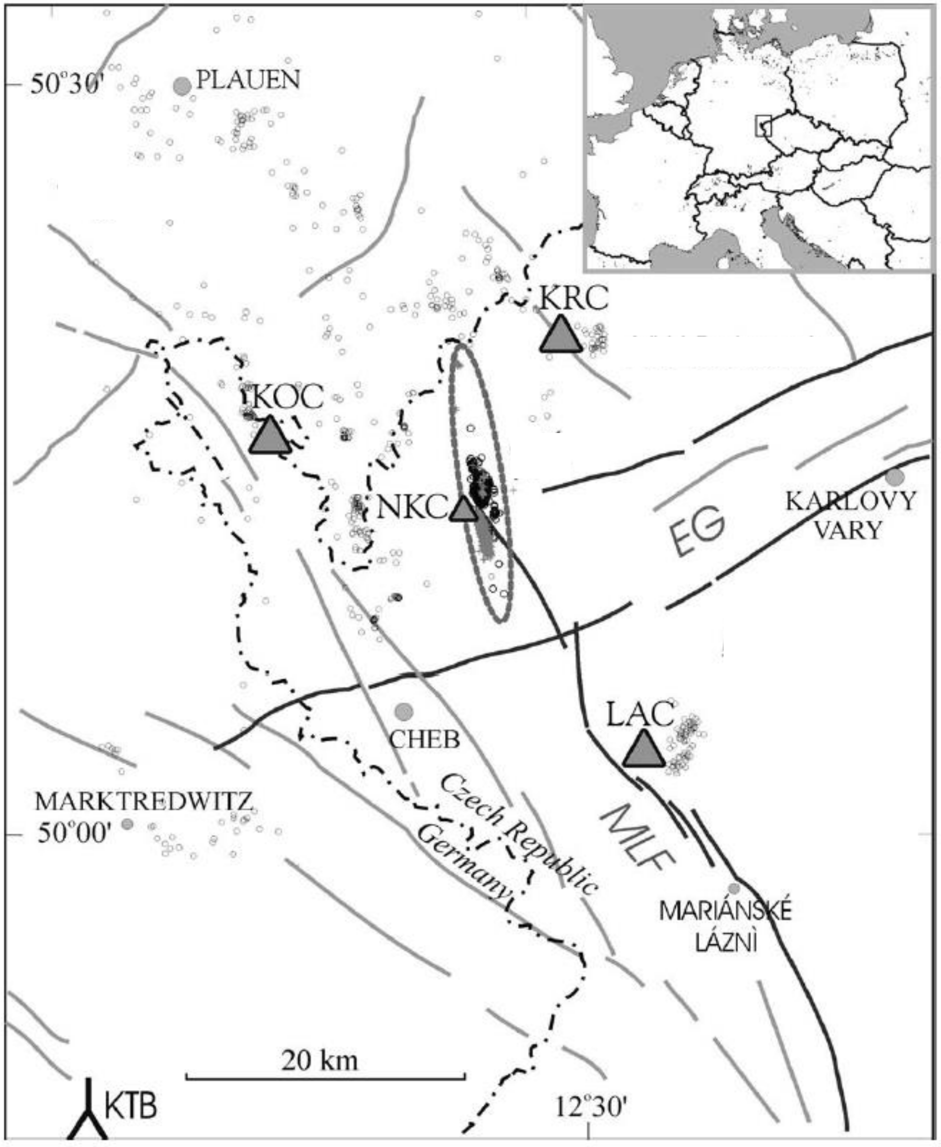

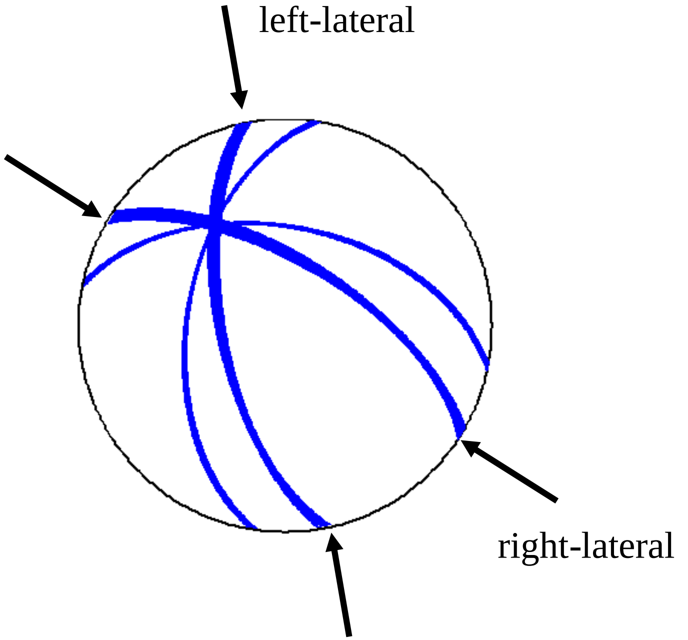

Fischer et al. (2003)

Tectonic sketch and principal faults

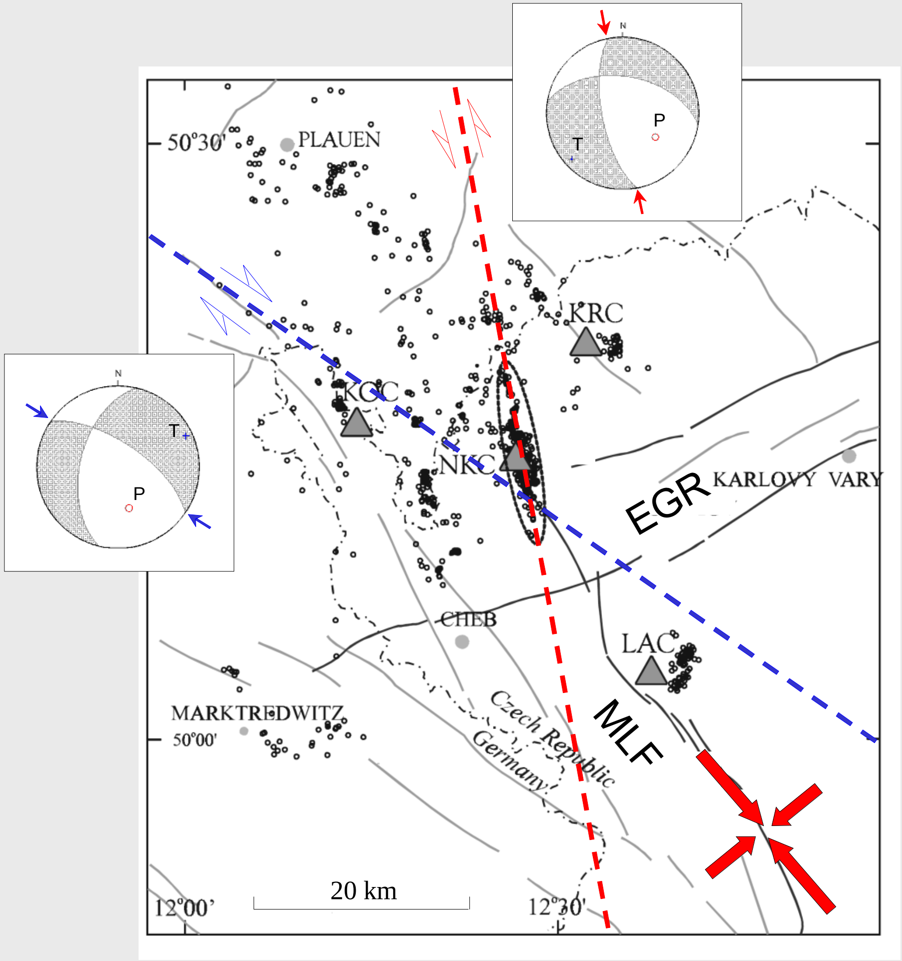

Mohr's diagram

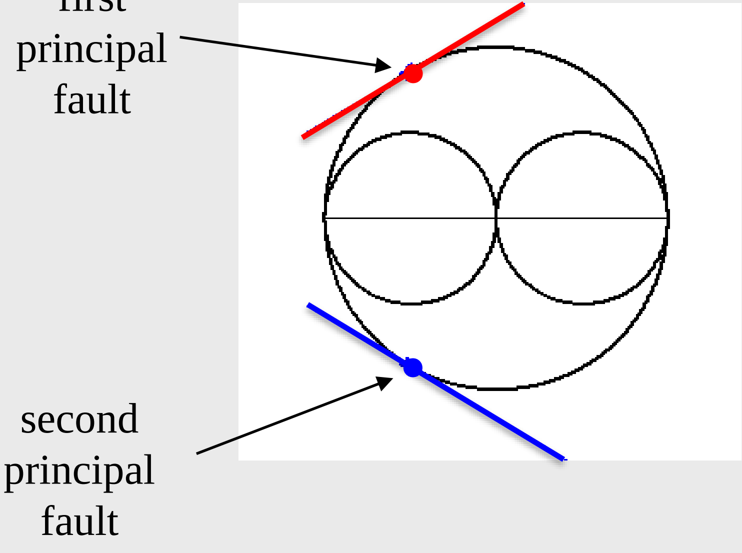

maximum compression coincides with that for western and central Europe

Vavryčuk (EPSL, 2011)

Properties of the individual principal faults

Right-lateral faults

Left-lateral faults

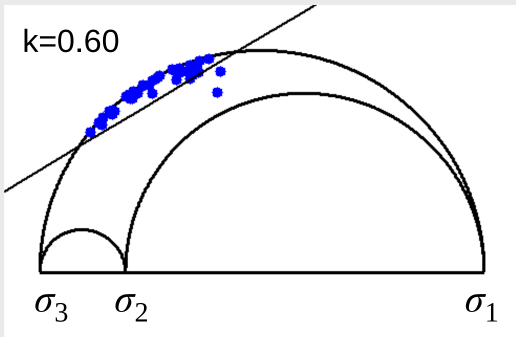

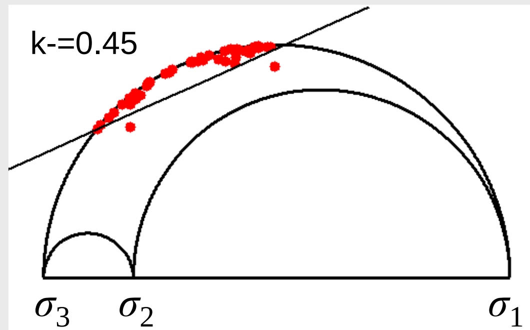

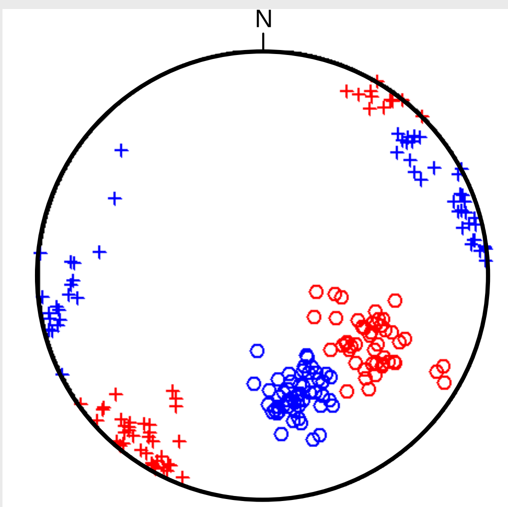

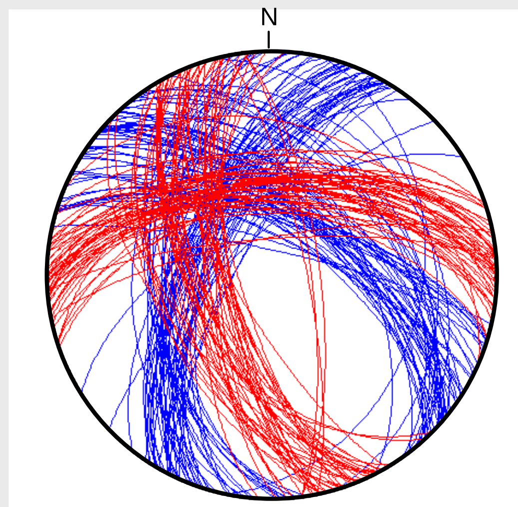

Left-lateral faults:

- friction = 0.45
- most active fault

Right-lateral faults:

- friction = 0.60
- less active

2008 swarm activity

Vavryčuk (EPSL, 2011)

Principal faults versus tectonics in West Bohemia

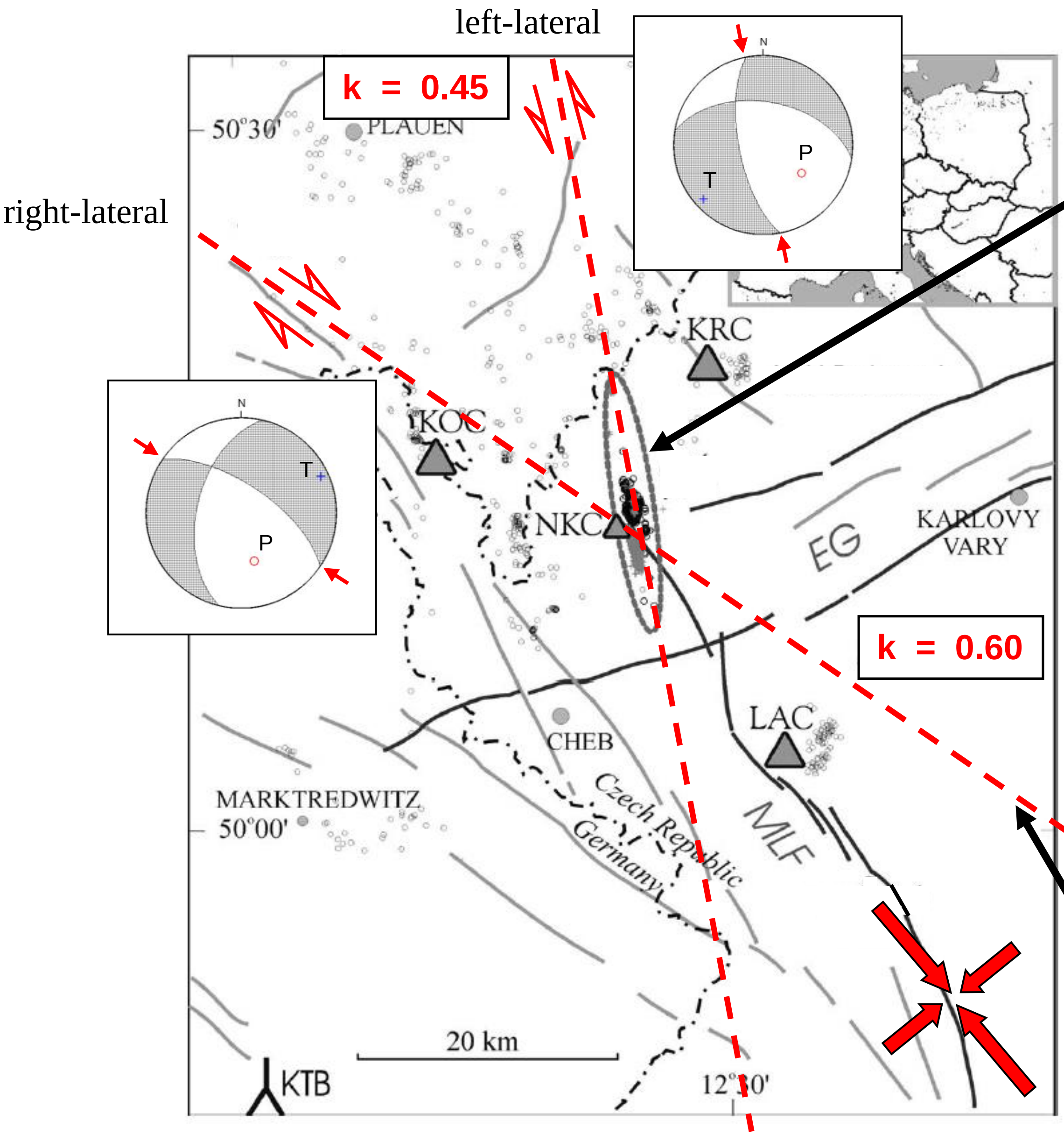

The most active faults
in the recent seismic activity

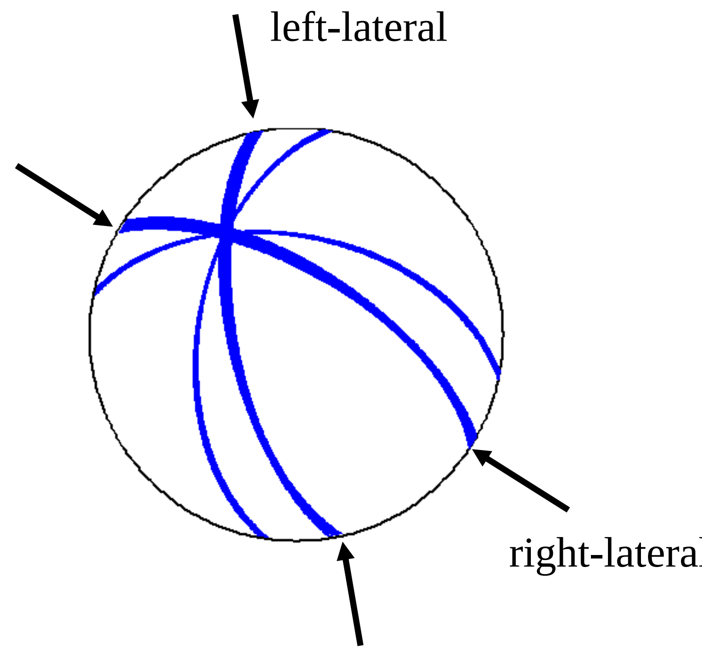

Geologically well pronounced
Fault system in the area

modified figure of Fischer (2003)

Interaction of faults: 2014 seismic sequence

The 2008-2014 seismicity in West Bohemia

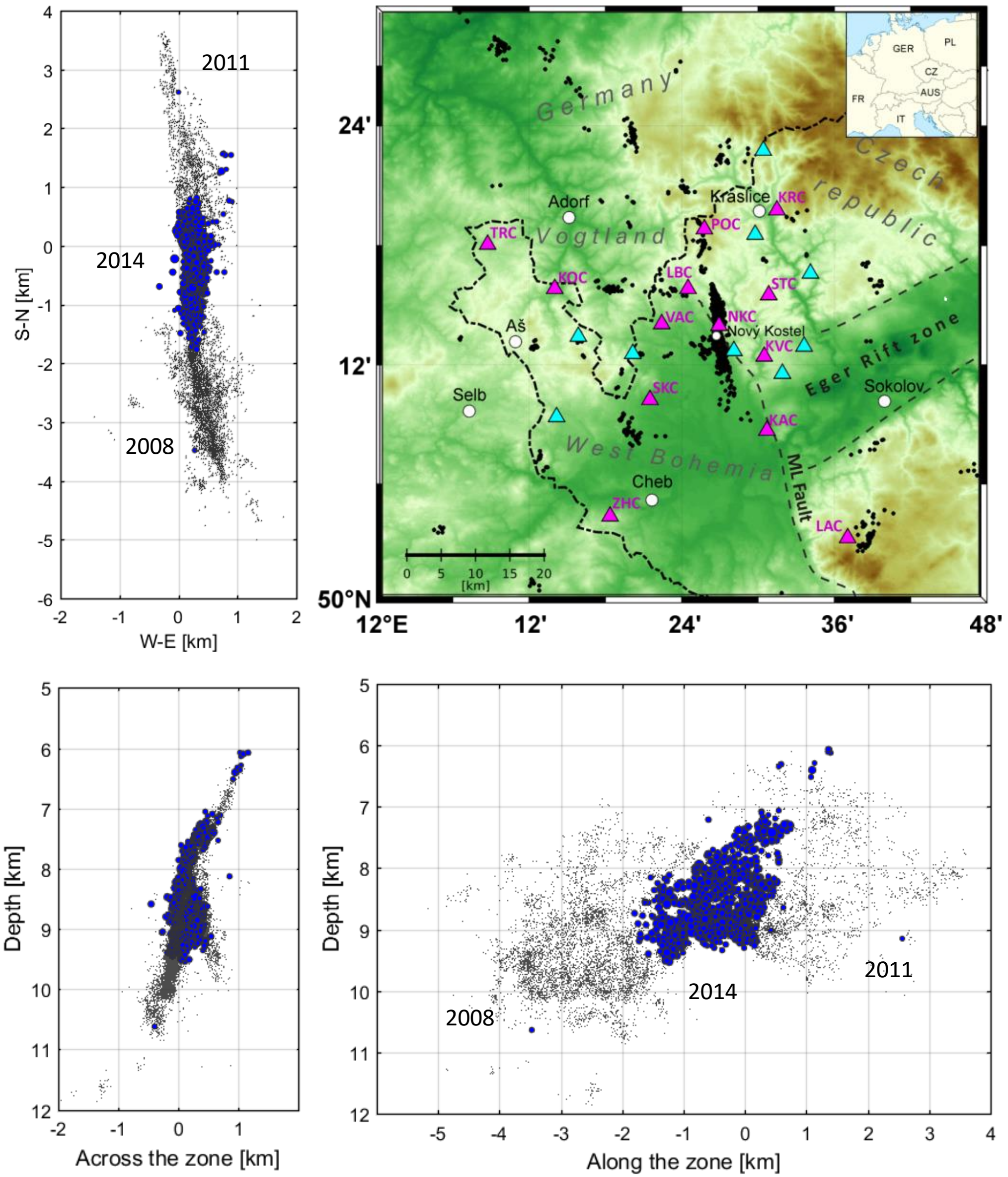

West Bohemia area:

- Geodynamically active area
- Intersection of two major fault systems
- Emanations of CO_2 rich fluids, springs of mineral water
- Persistent seismicity

Seismic observations:

- 22 local 3-component stations
- Sampling frequency 250 Hz
- Flat response 1-60 Hz
- Earthquake swarms
- Strongest event: M_L = 4.6 (1985)
- Depth: 6-12 km

The 2008 and 2011 earthquake swarms

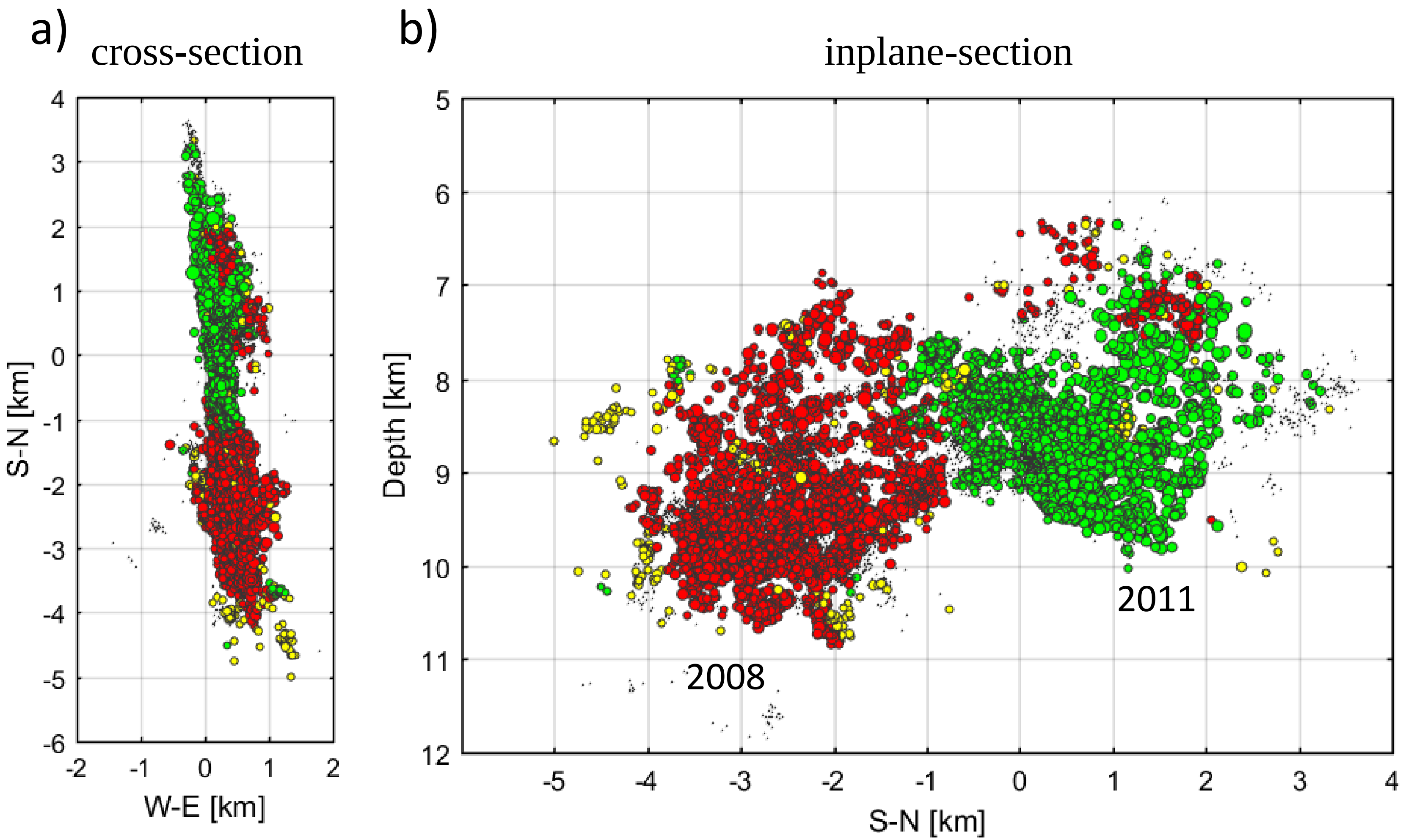

The 2008, 2011 and 2014 earthquake sequences

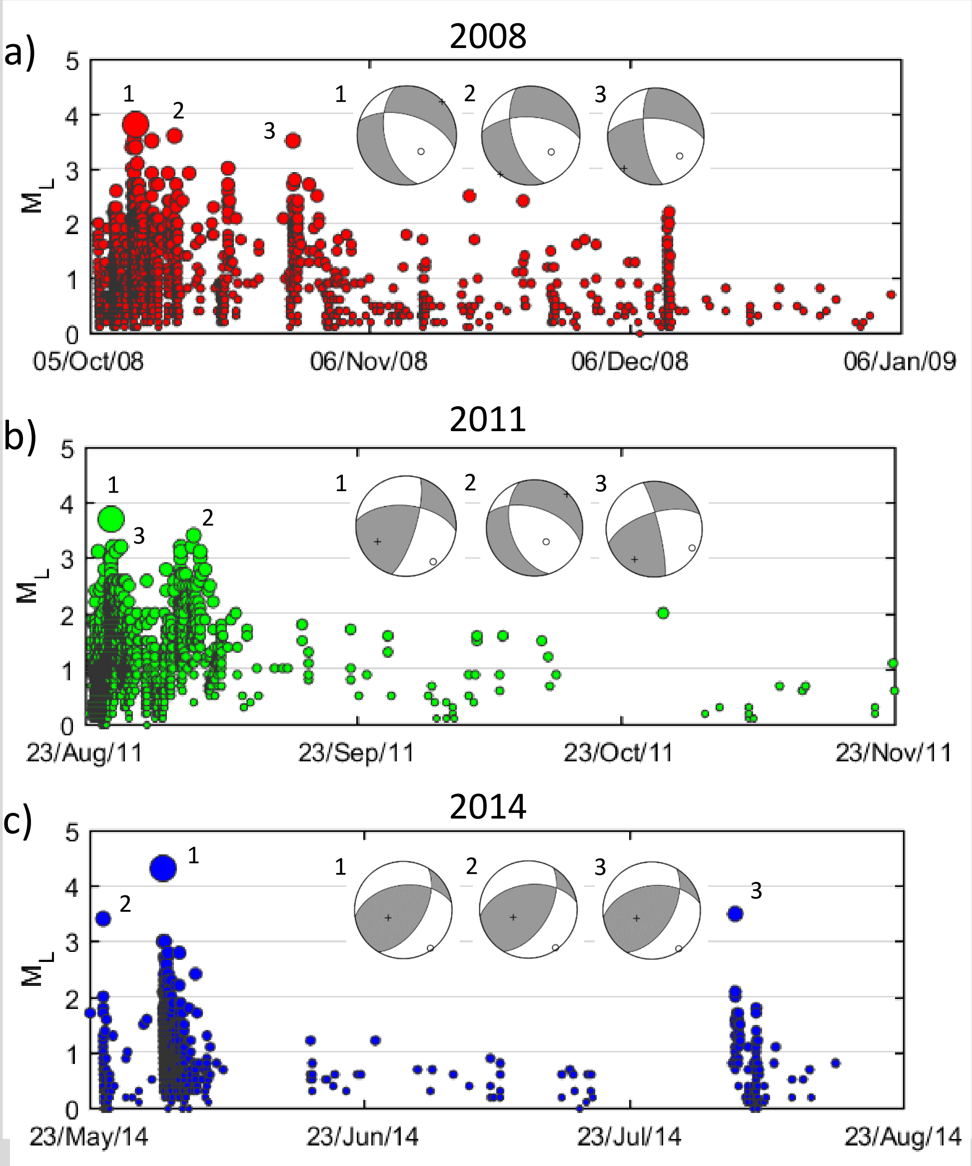

Basic characteristics:

- Duration of about 3 months
- Several distinct phases
- Number of events $M_L > -0.5$:

  2008 – 25000 events
  2011 – 23000 events
  2014 – 7000 events

- Strongest events:

  2008 – $M_L = 3.8$
  2011 – $M_L = 3.7$
  2014 – $M_L = 4.2$

- Energy release:

  2008 – swarm
  2011 – swarm
  2014 – mainshock-aftershock

The 2008, 2011 and 2014 earthquake sequences

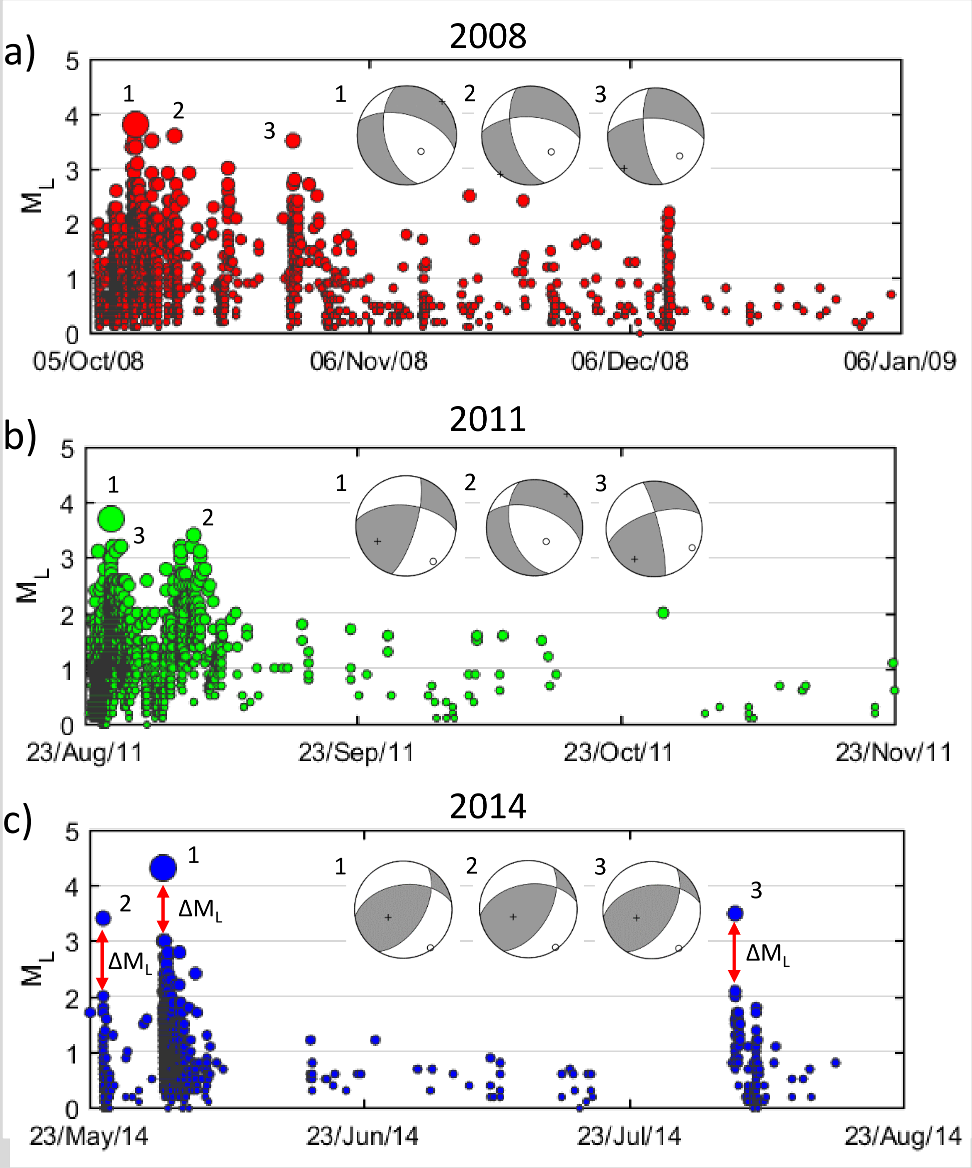

Basic characteristics:

- Duration of about 3 months
- Several distinct phases
- Number of events M_L> -0.5:

  2008 – 25000 events
  2011 – 23000 events
  2014 – 7000 events

- Strongest events:

  2008 – M_L = 3.8
  2011 – M_L = 3.7
  2014 – M_L = 4.2

- Energy release:

  2008 – swarm
  2011 – swarm
  2014 – mainshock-aftershock

Questions related to the 2014 activity to be solved

- **Why repeating reactivation of the fault segments in the NK focal zone?** (Vavryčuk & Hrubcová, JGR, 2017)
- **Why the 2014 activity is just between two patches activated in the previous seismic periods?**
- **Why the activity has an untypical mainshock-aftershock character?**
- **Why the three strongest earthquakes had anomalous reverse focal mechanism?**
- **Why the aftershock decay is very fast?**

Fault geometry: parallel fault steps

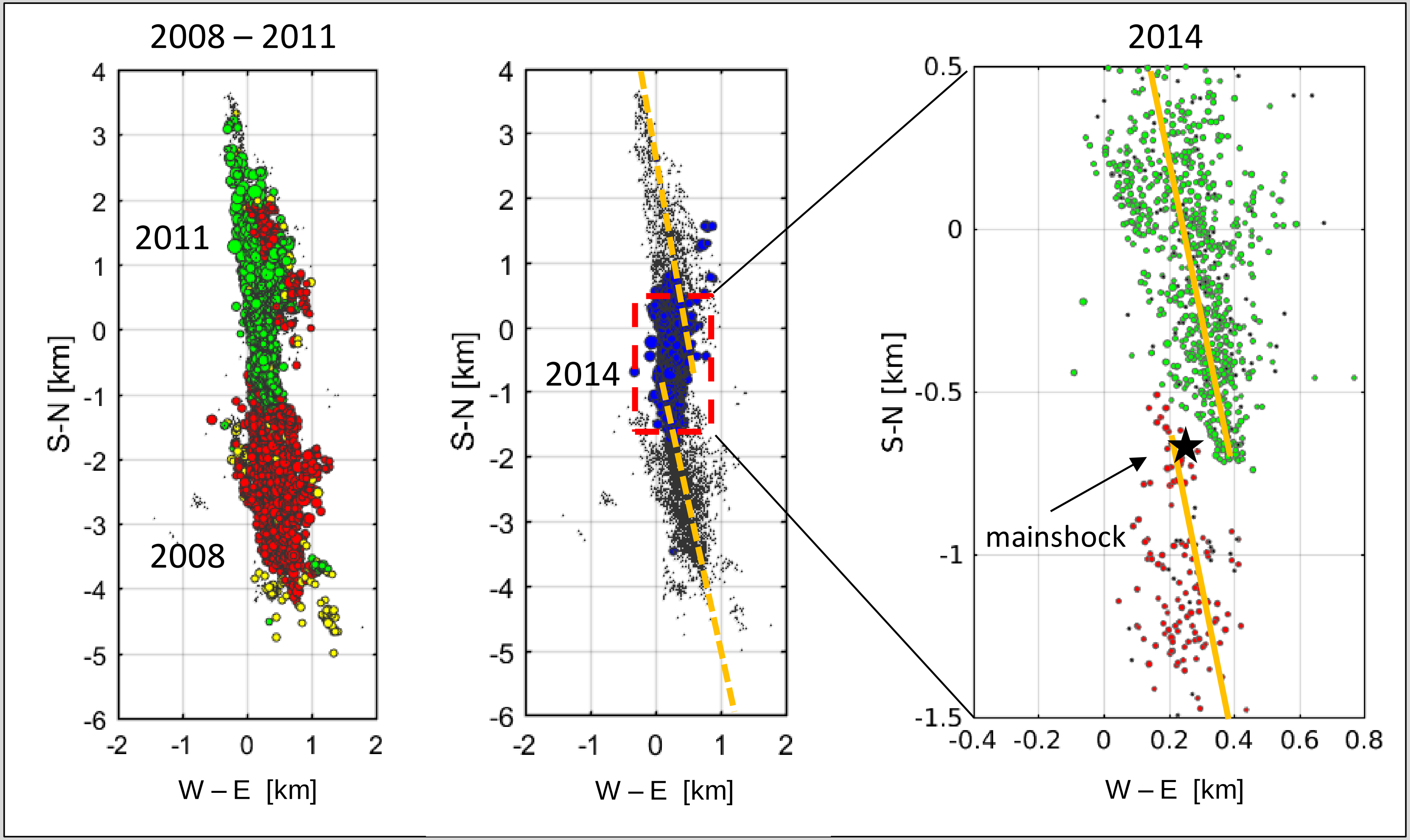

Step width: ~200 m

Fault steps and fault linkage

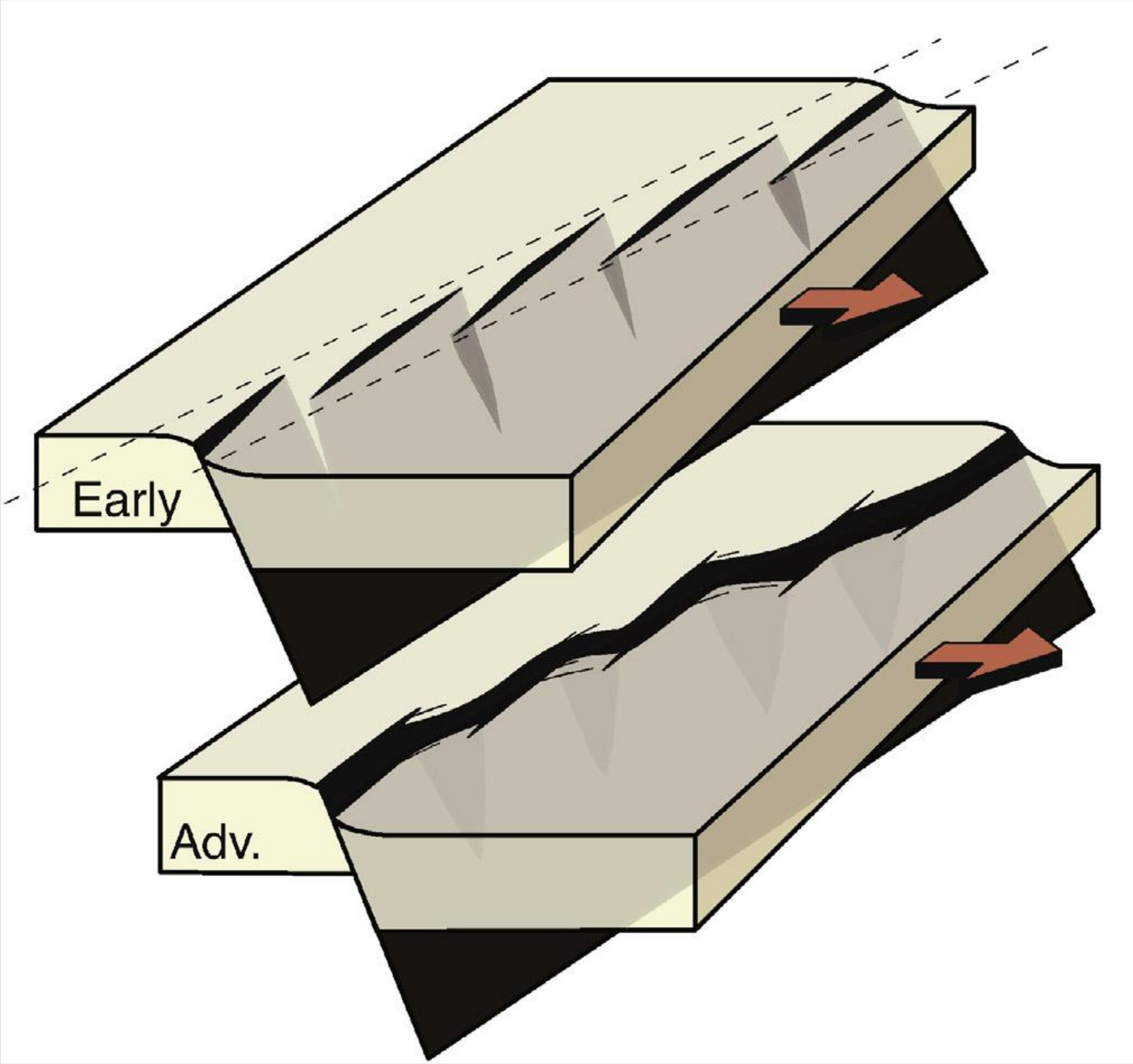

Fossen & Rotevant (Earth Sci. Rev., 2016)

Types of focal mechanisms

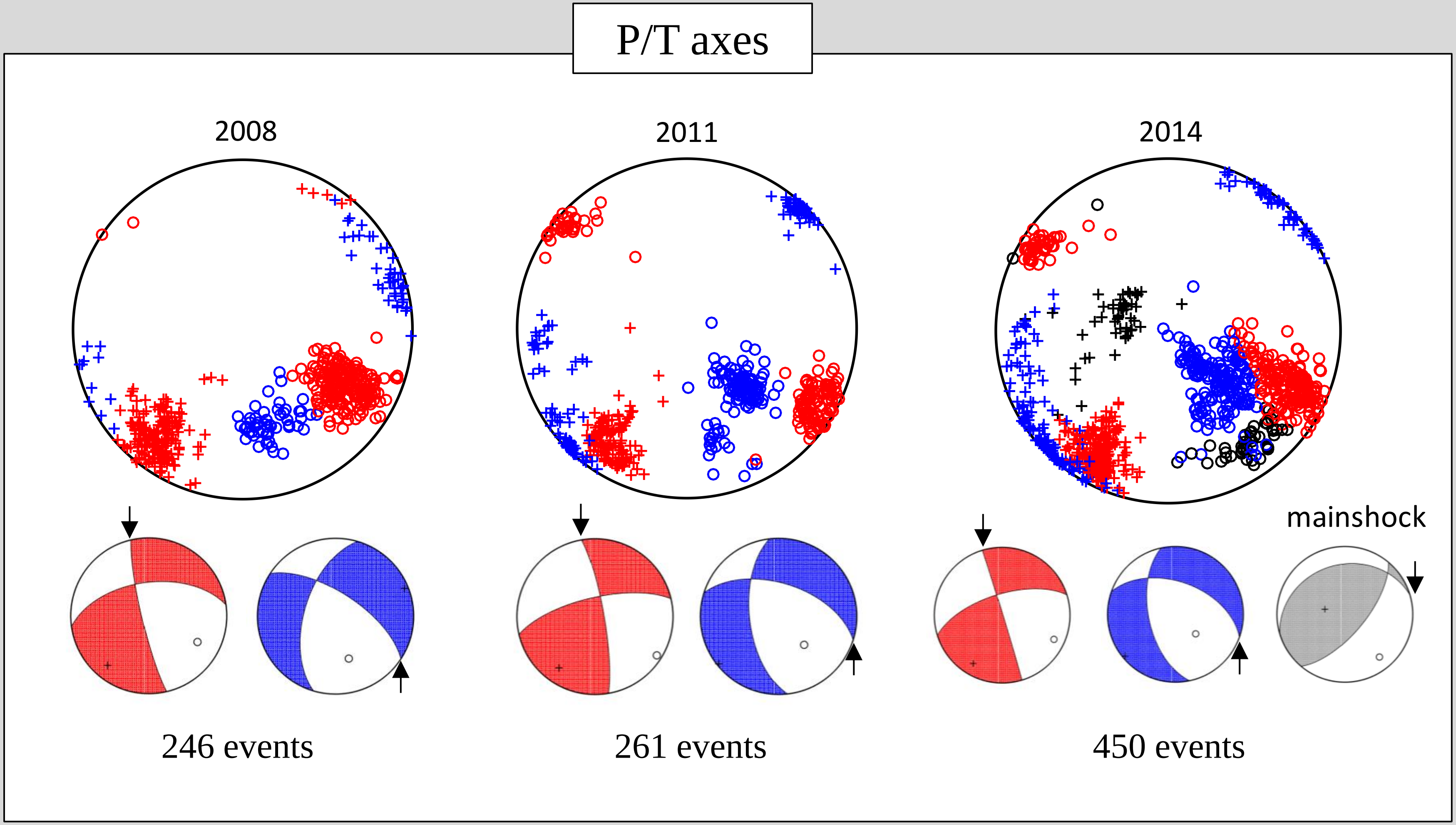

2014 sequence: anomalous reverse mechanisms inconsistent with existing active faults

P axes: ○ ○
T axes: + +

Tectonic sketch of West Bohemia

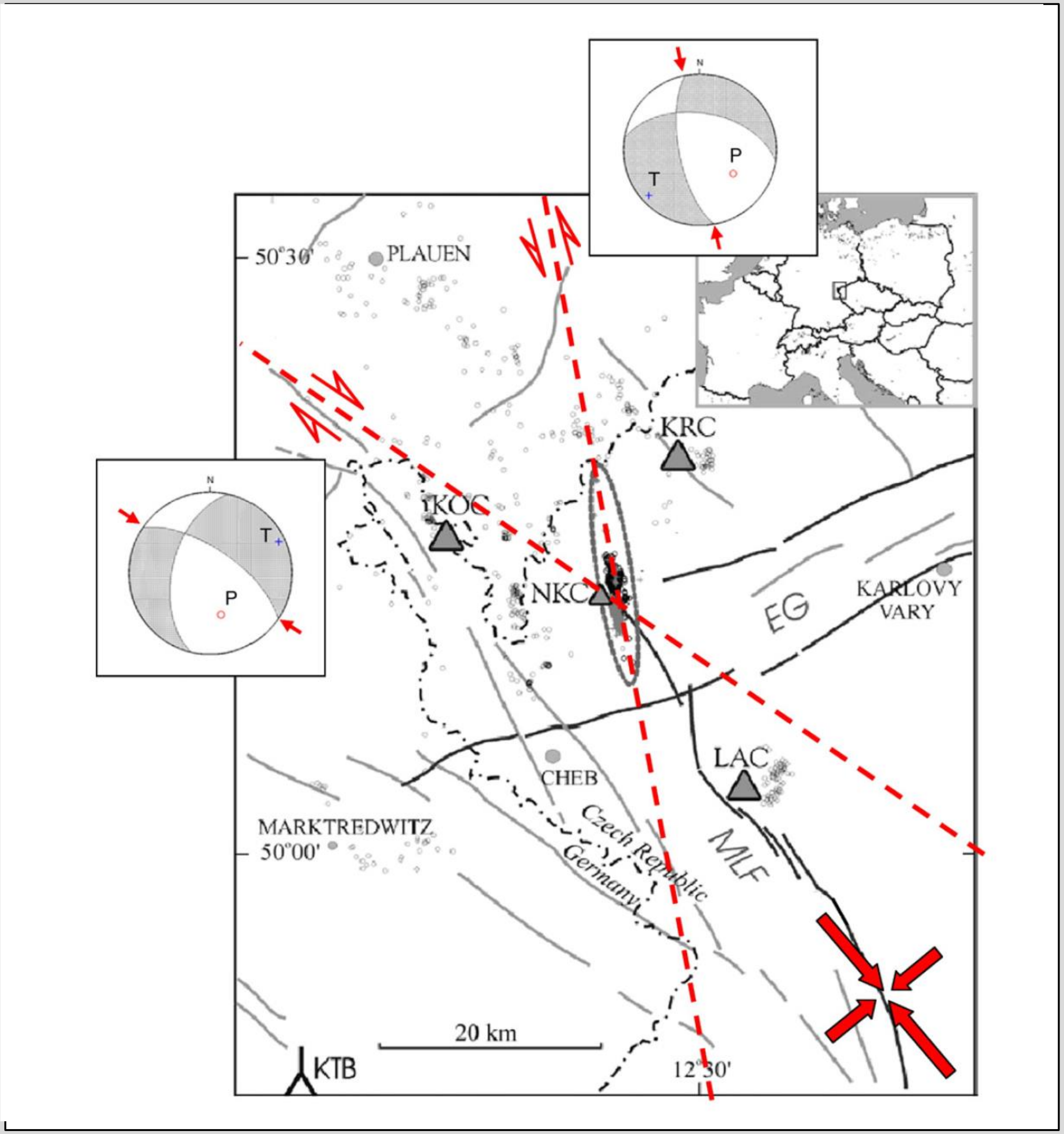

?? unfavourably oriented

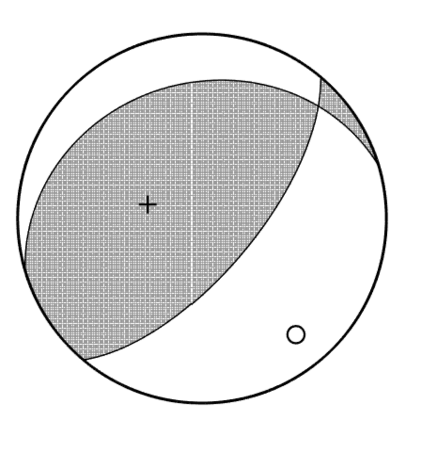

Stress inversion

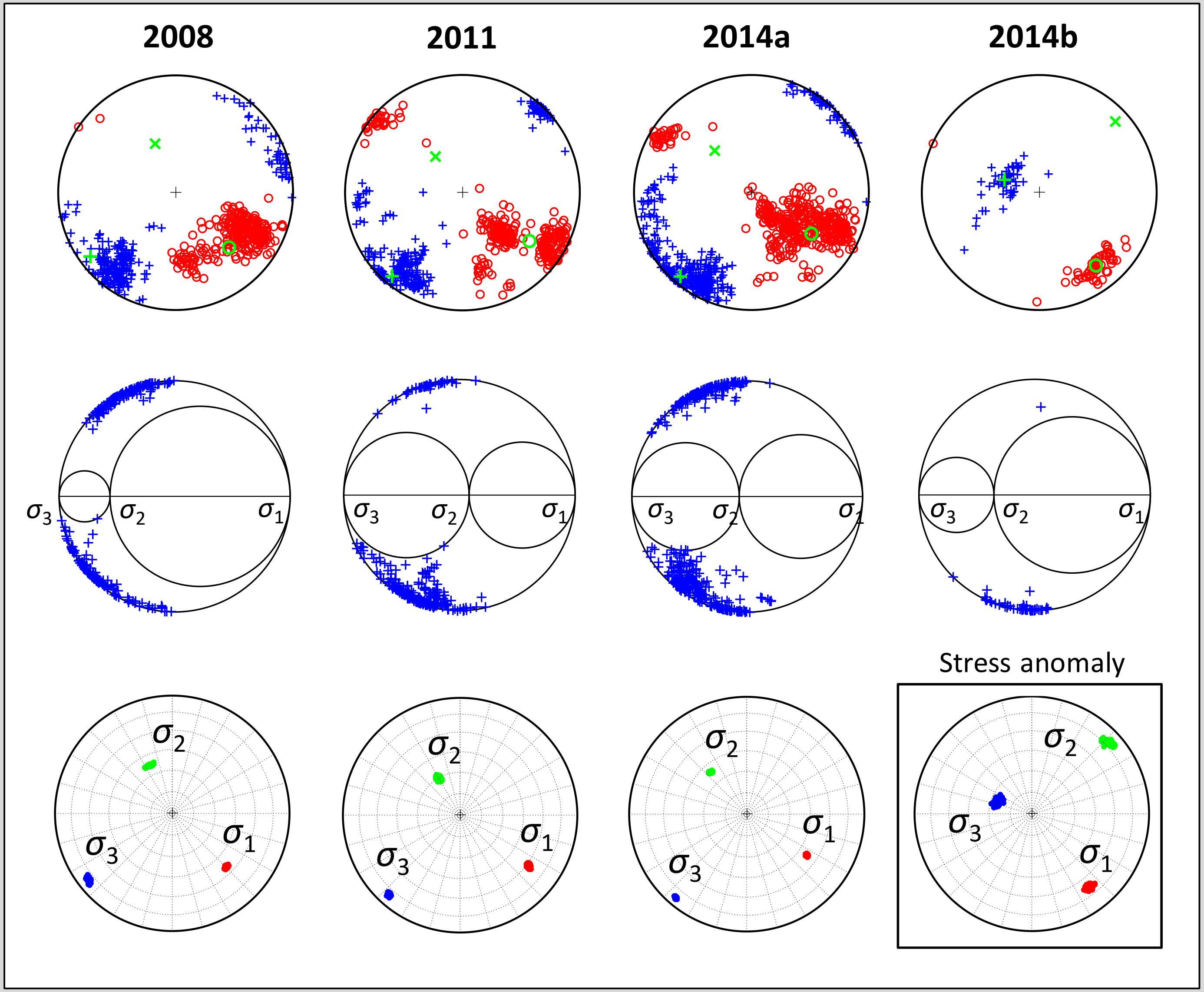

P and T axes

Mohr's circles

Principal stress axes

Locations of events with the reverse mechanism

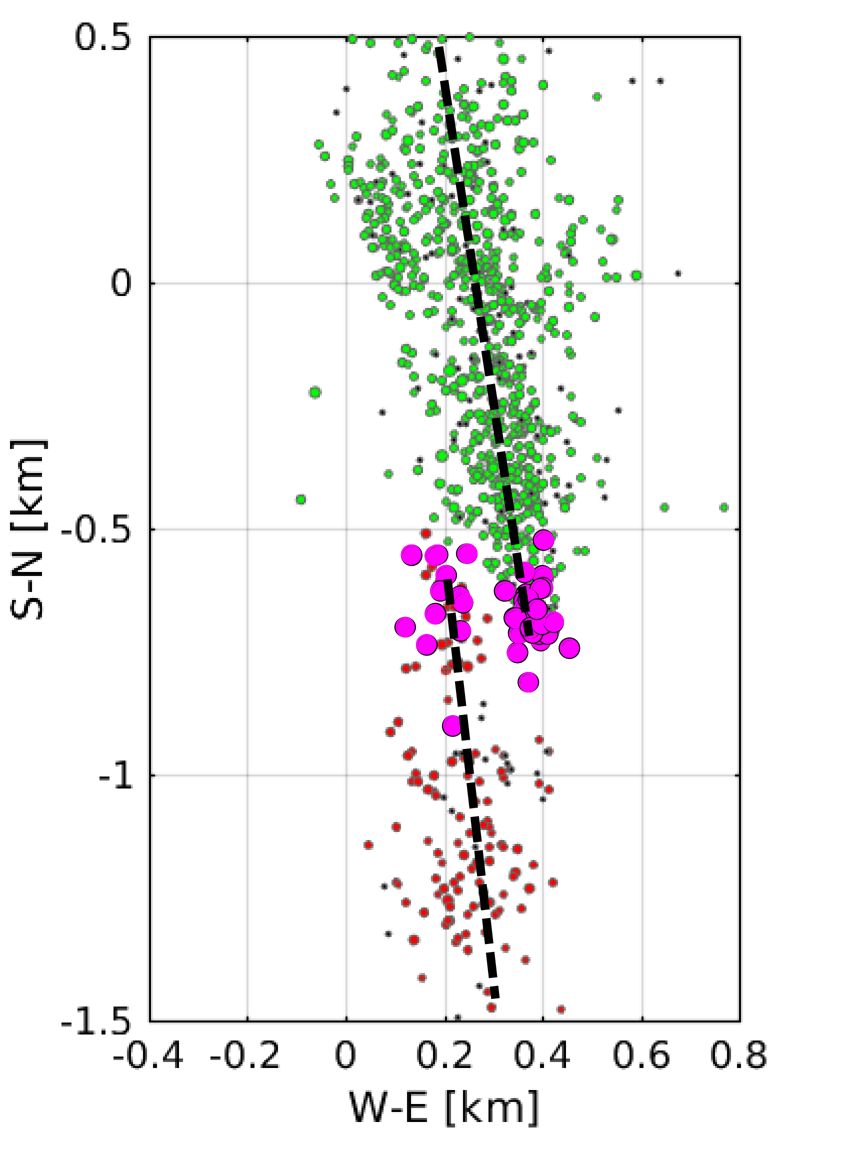

Locations of events with the reverse mechanism define the area of the stress anomaly!

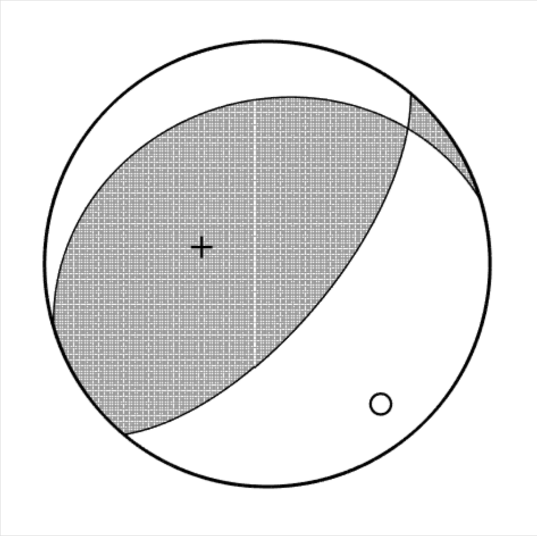

Coulomb stress (CS) modelling

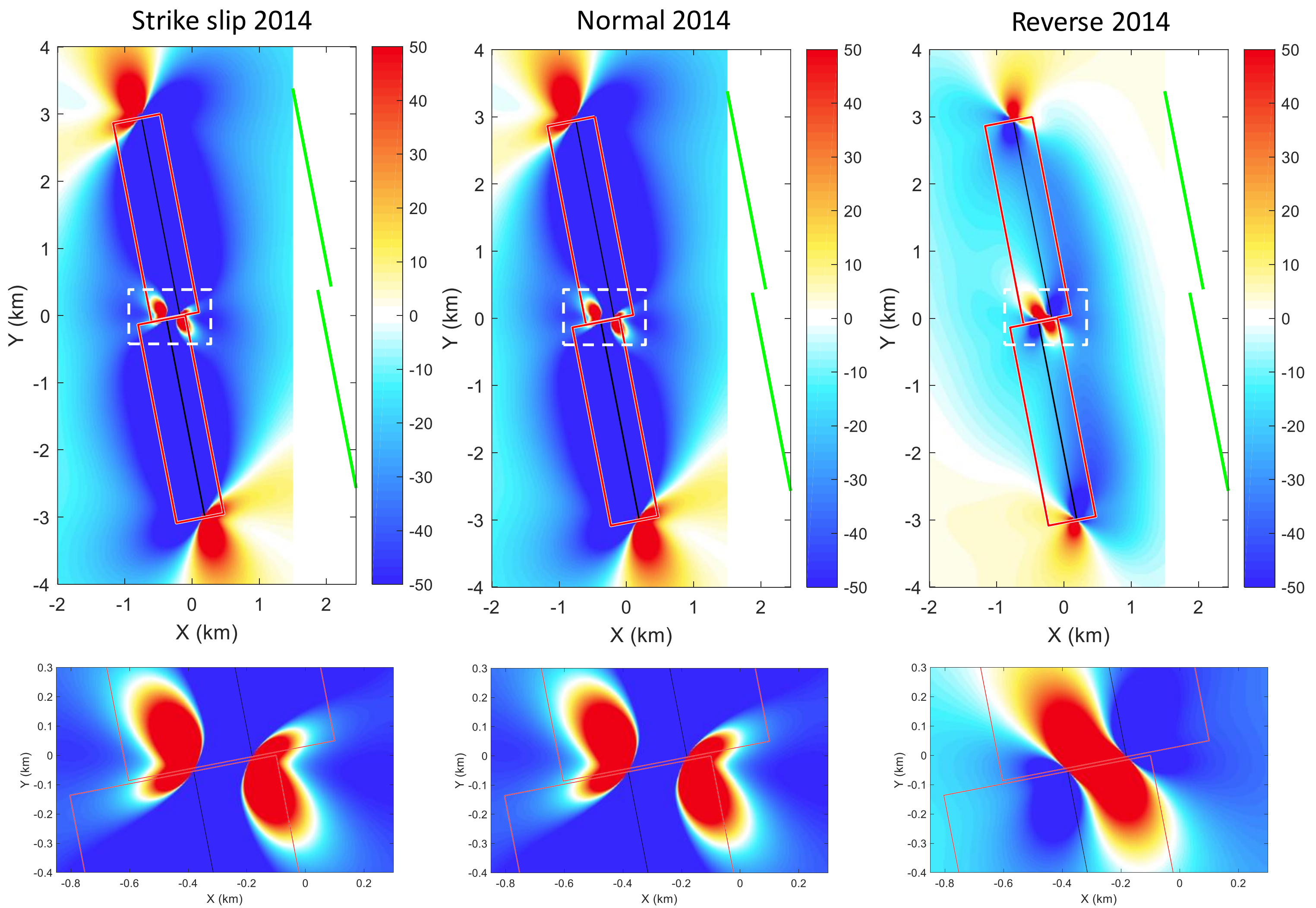

low CS for strike slips

low CS for normal faults

high CS for reverse faults

COULOMB 3.3

Rotation of principal stress axes

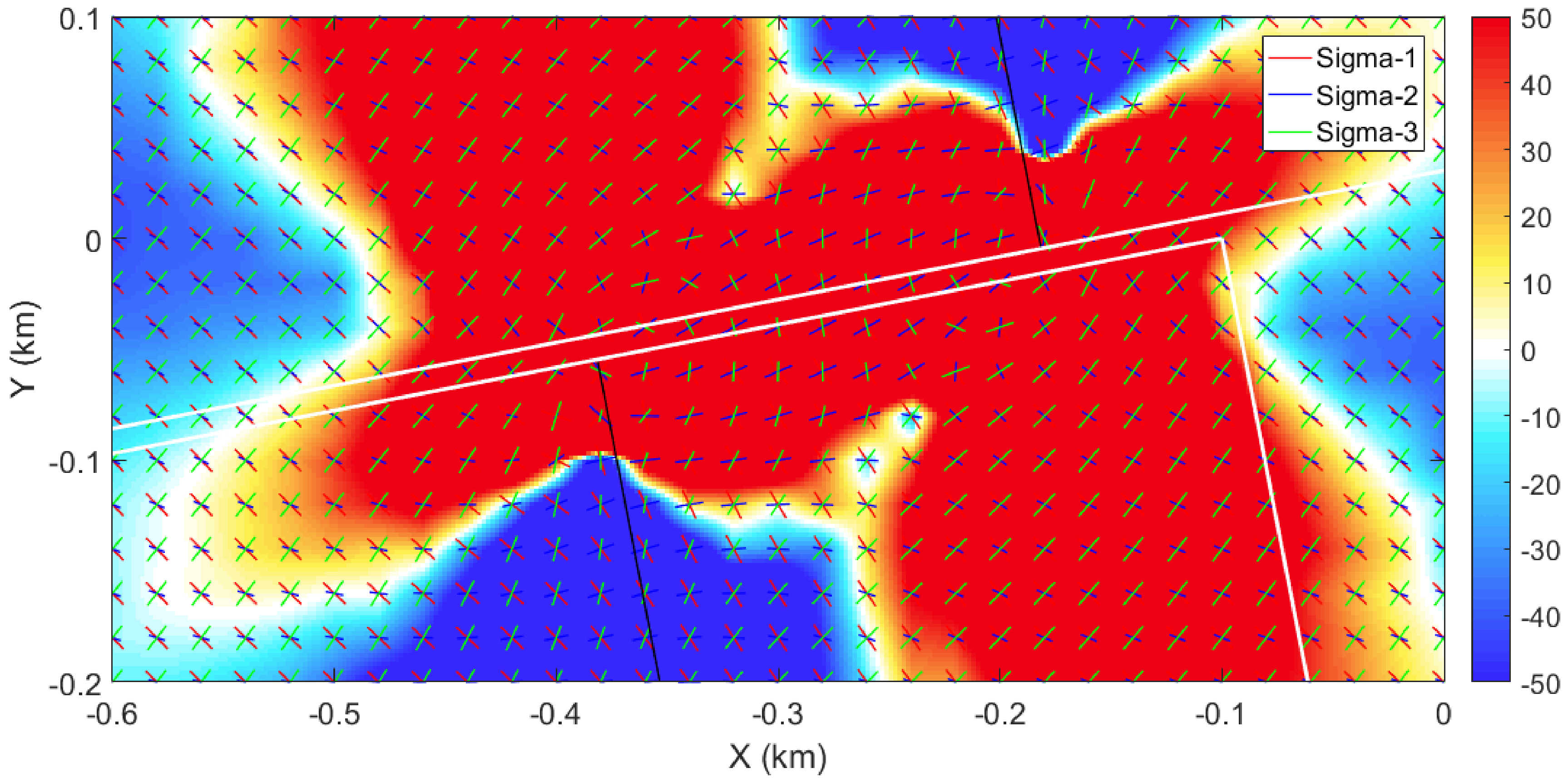

Interaction of faults causes a local stress anomaly between fault tips expressed by rotation of principal stress axes

Aftershock decay in the 2014 sequence

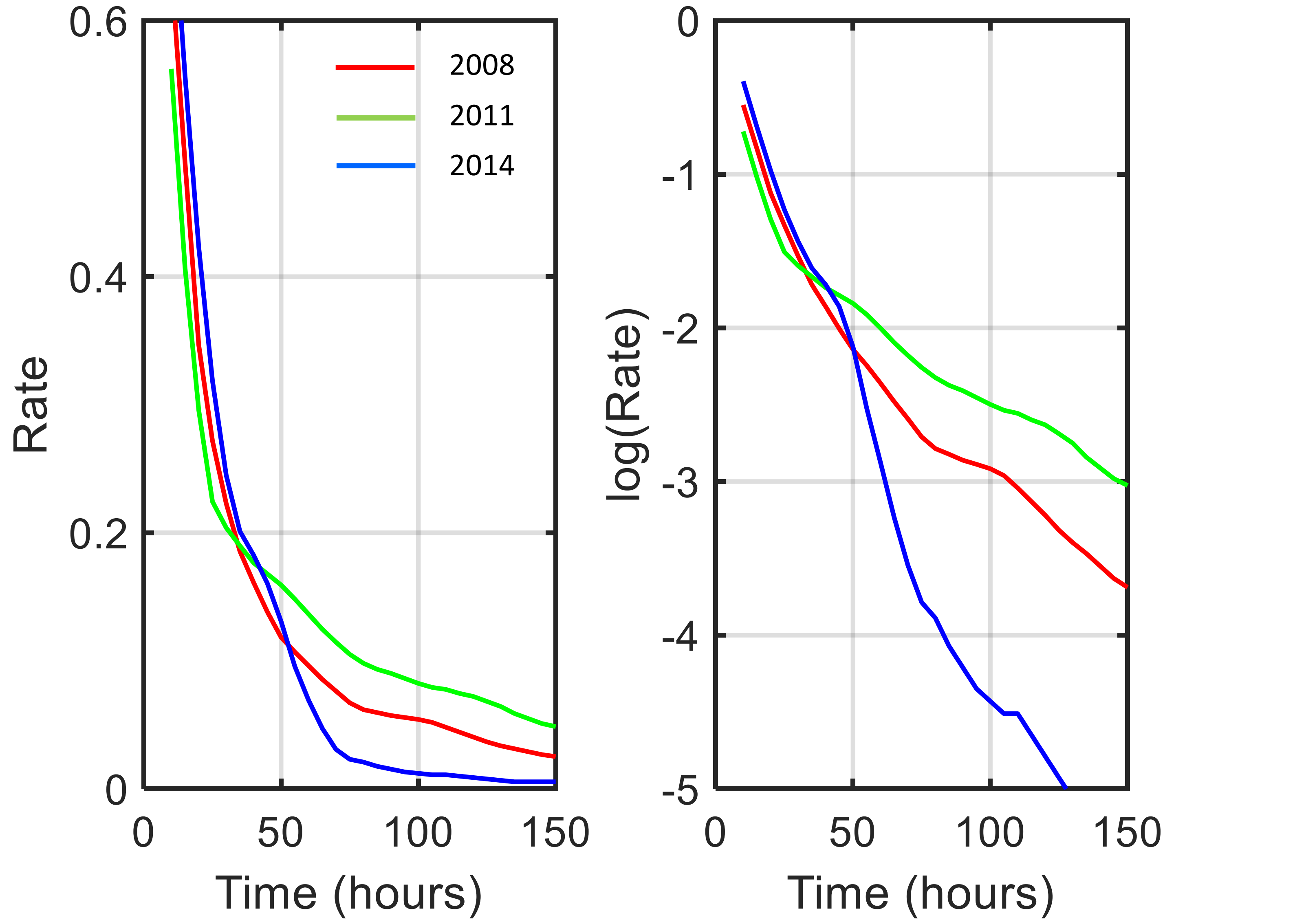

Aftershock decay in other seismogenic regions

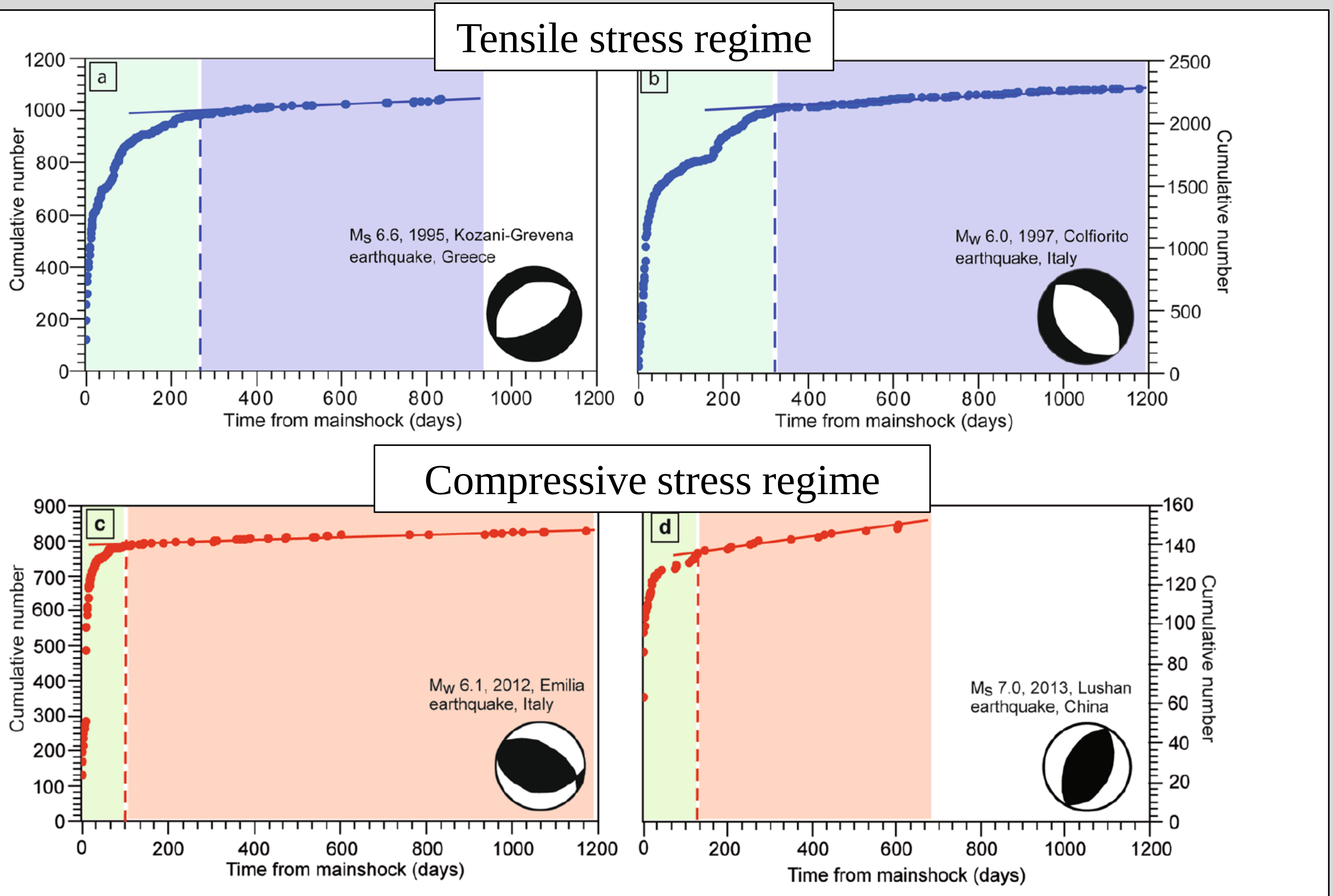

Valerio et al. (Scientific Reports, 2017)

Summary

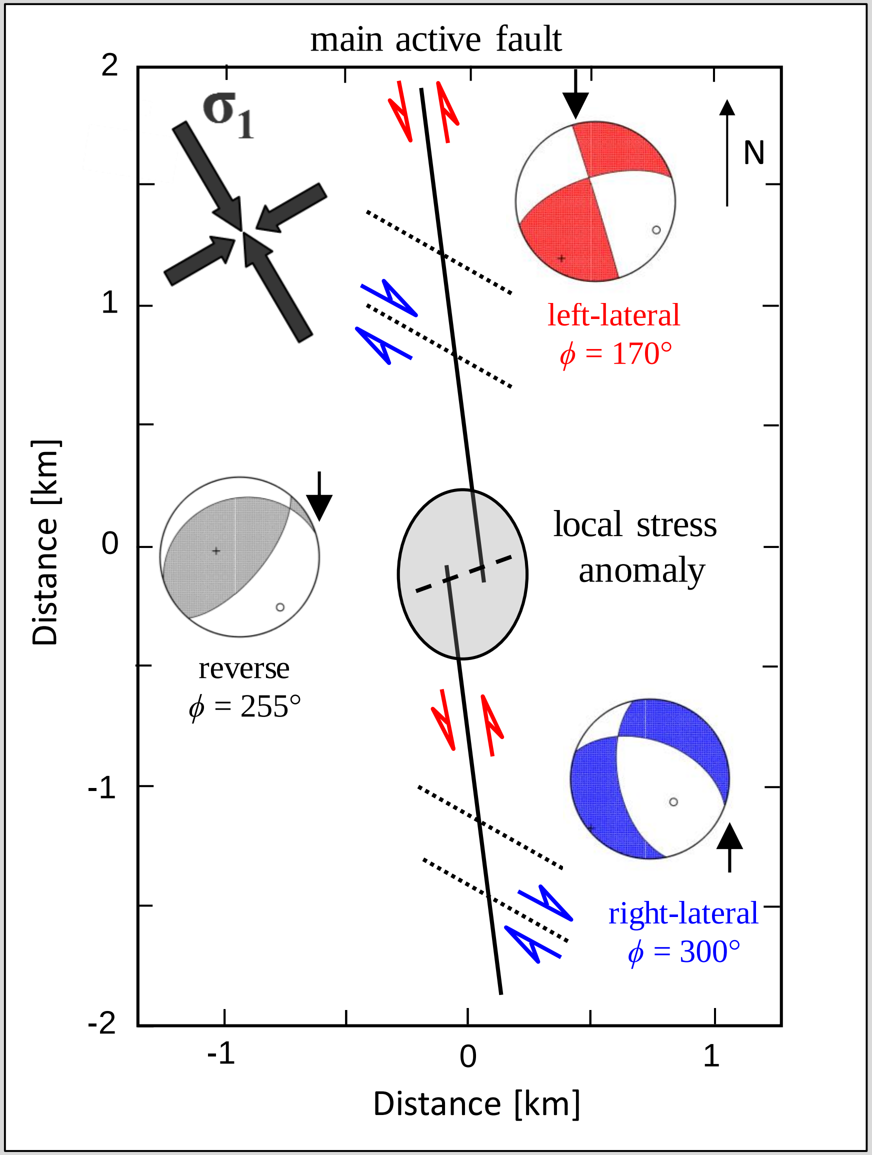

- Identification of compressive fault steps, step width ~ 200 m
- Compressive local stress anomaly between the fault tips due to previous activity – **no fluids** (!)
- Anomalous reverse focal mechanisms – new fractures linking existing faults
- Mainshock-aftershock sequence – **new fractures with no fluids**
- Fast aftershock decay – **compressive stress** regime
- Linking the existing active faults increases the **seismic hazard** in the area from Mw 5.0 to Mw 5.4 (corresponding fracture area – 20 km^2)

Interaction of faults: 2018 seismic sequence

218 seismic sequence

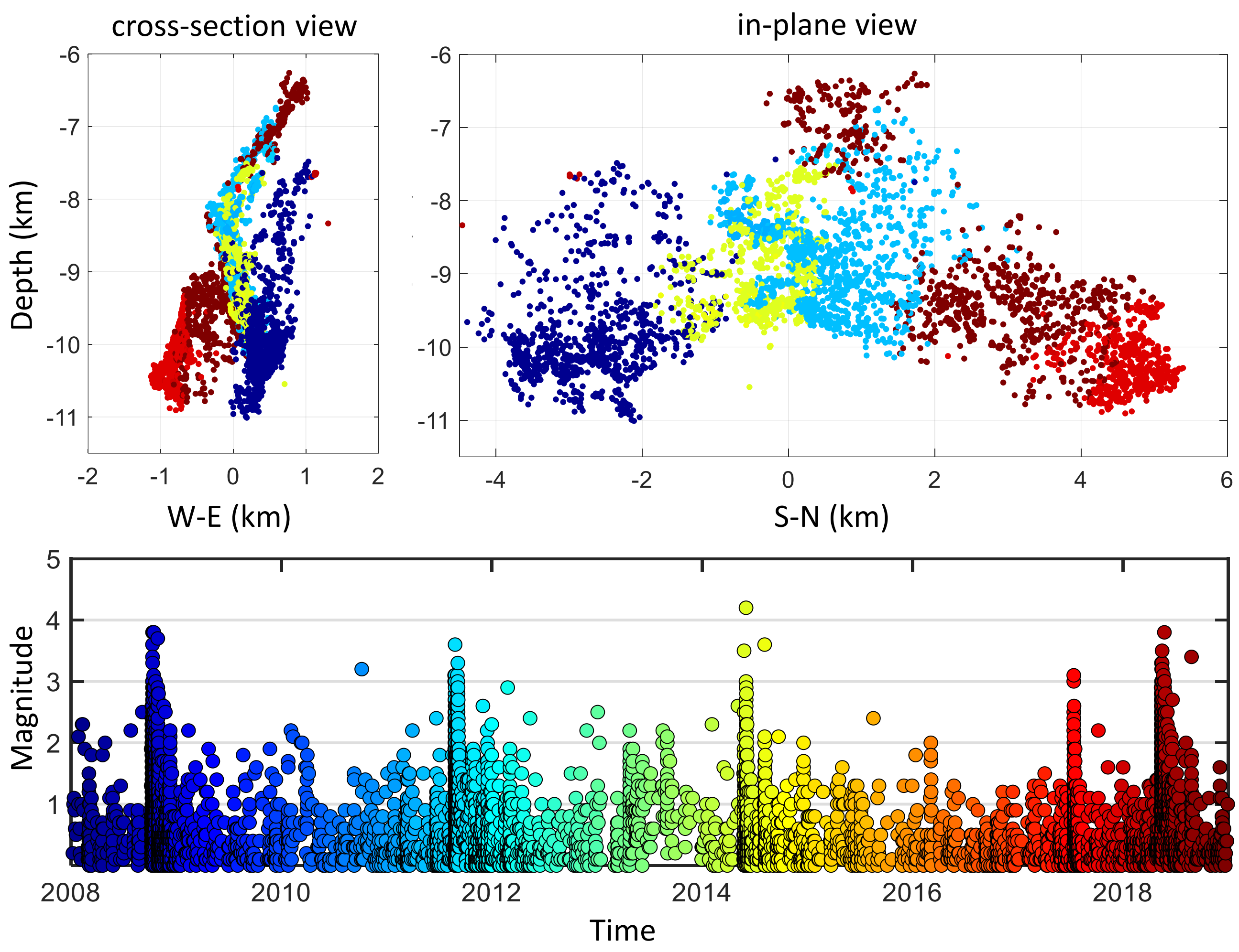

ISO components in the 2018 seismic sequence

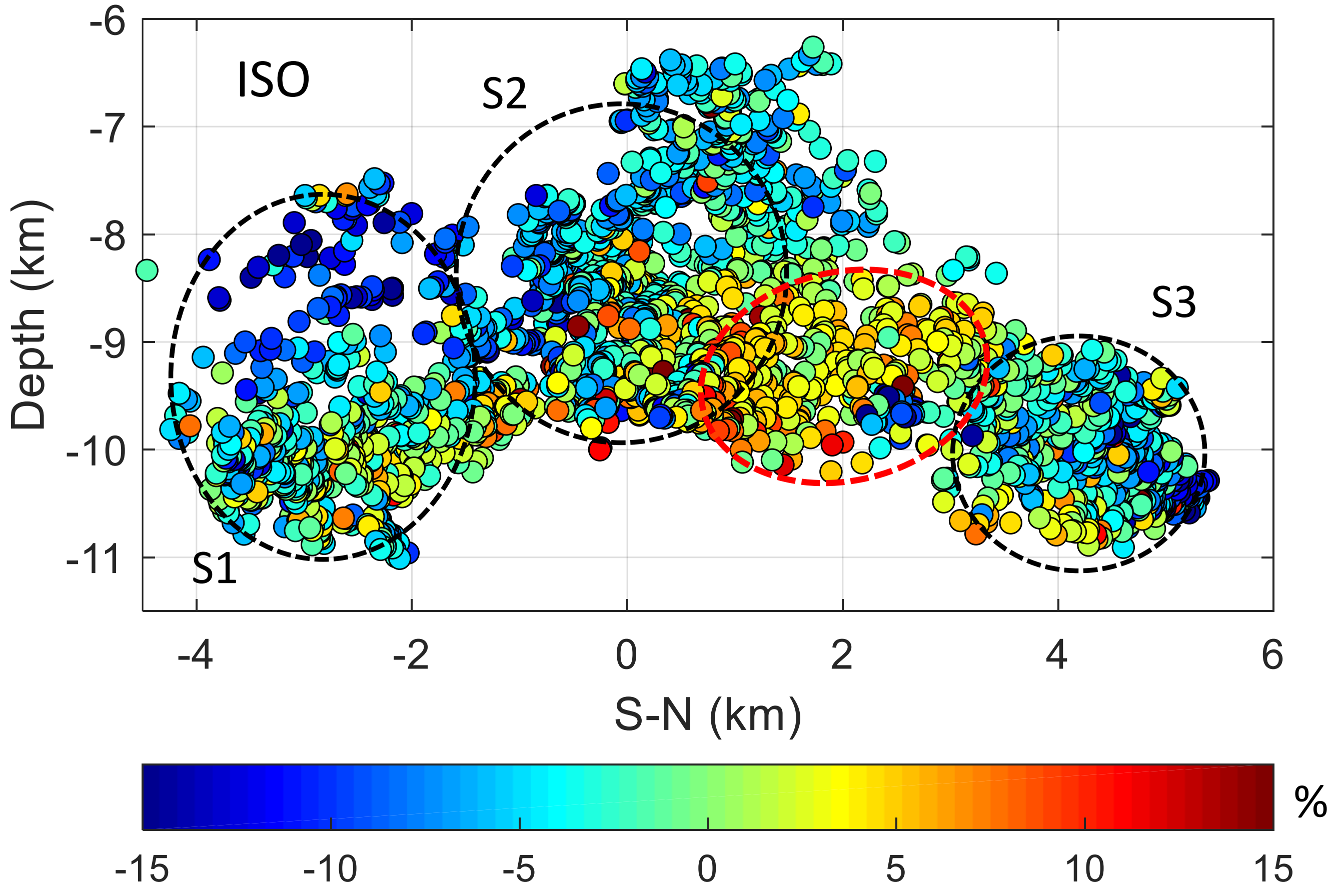

Vavryčuk et al. (JGR, 2021)

Tensile faulting in the 218 seismic sequence

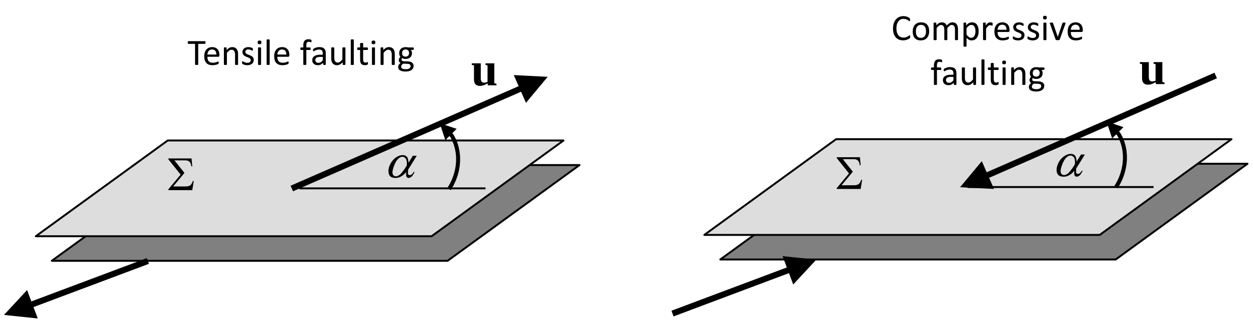

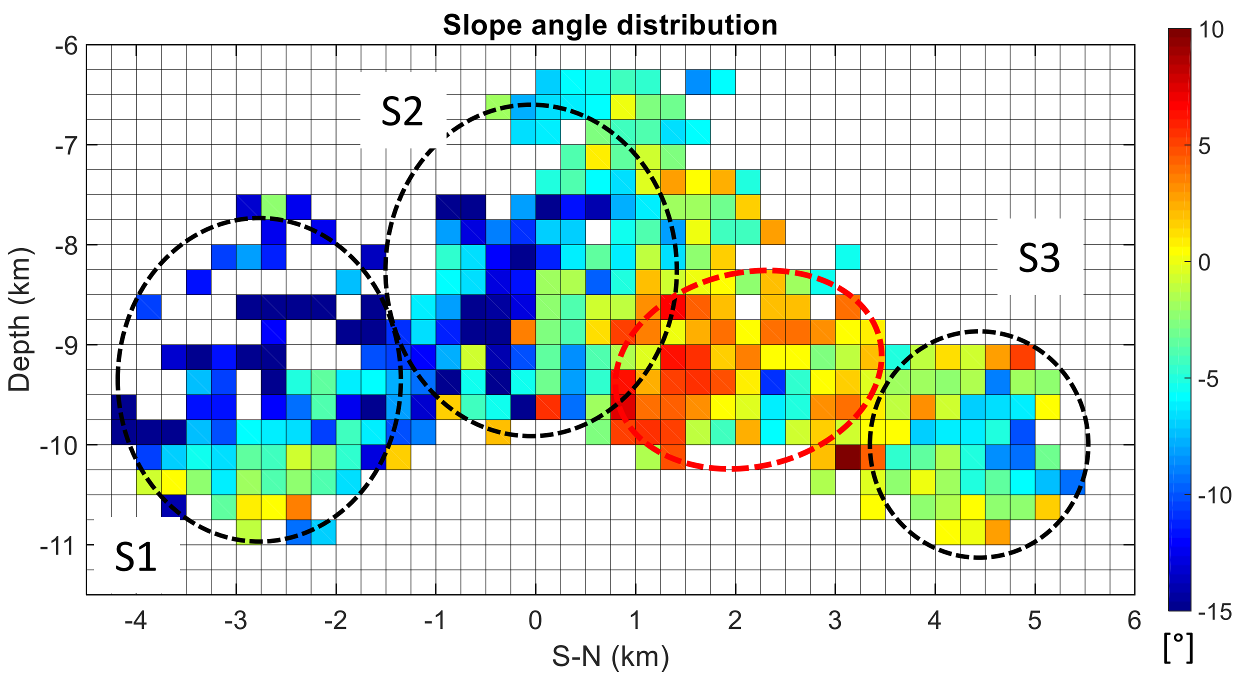

Vavryčuk et al. (JGR, 2021)

Spatial variation of ISO and stress ratio

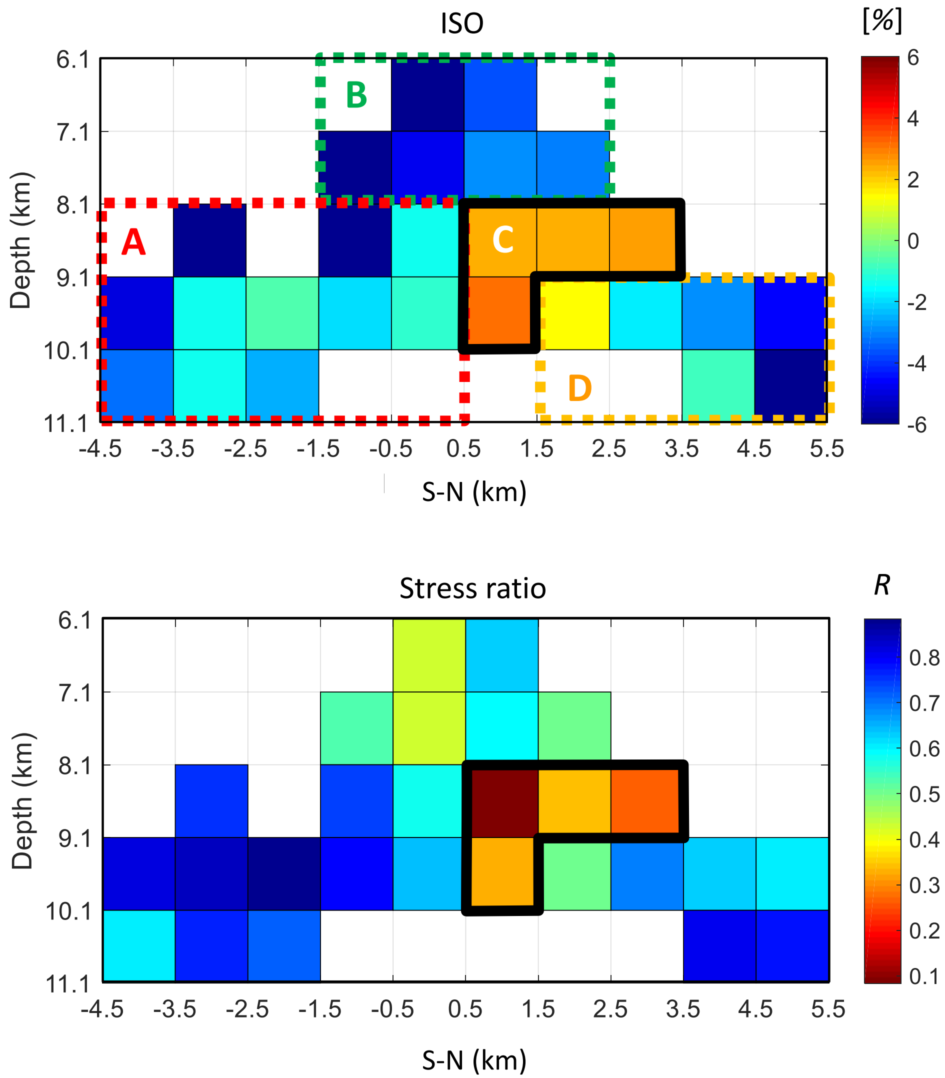

- Spatial variation of ISO maps
  - stress variations
  - changes in fracture mode
- **Negative ISO** indicates compressive regime
- **Positive ISO** indicates tensile regime
- Tensile regime might be an indicator of **fluid flow**

Vavryčuk et al. (JGR, Solid Earth, 2021)

Spatial variation of ISO and stress ratio

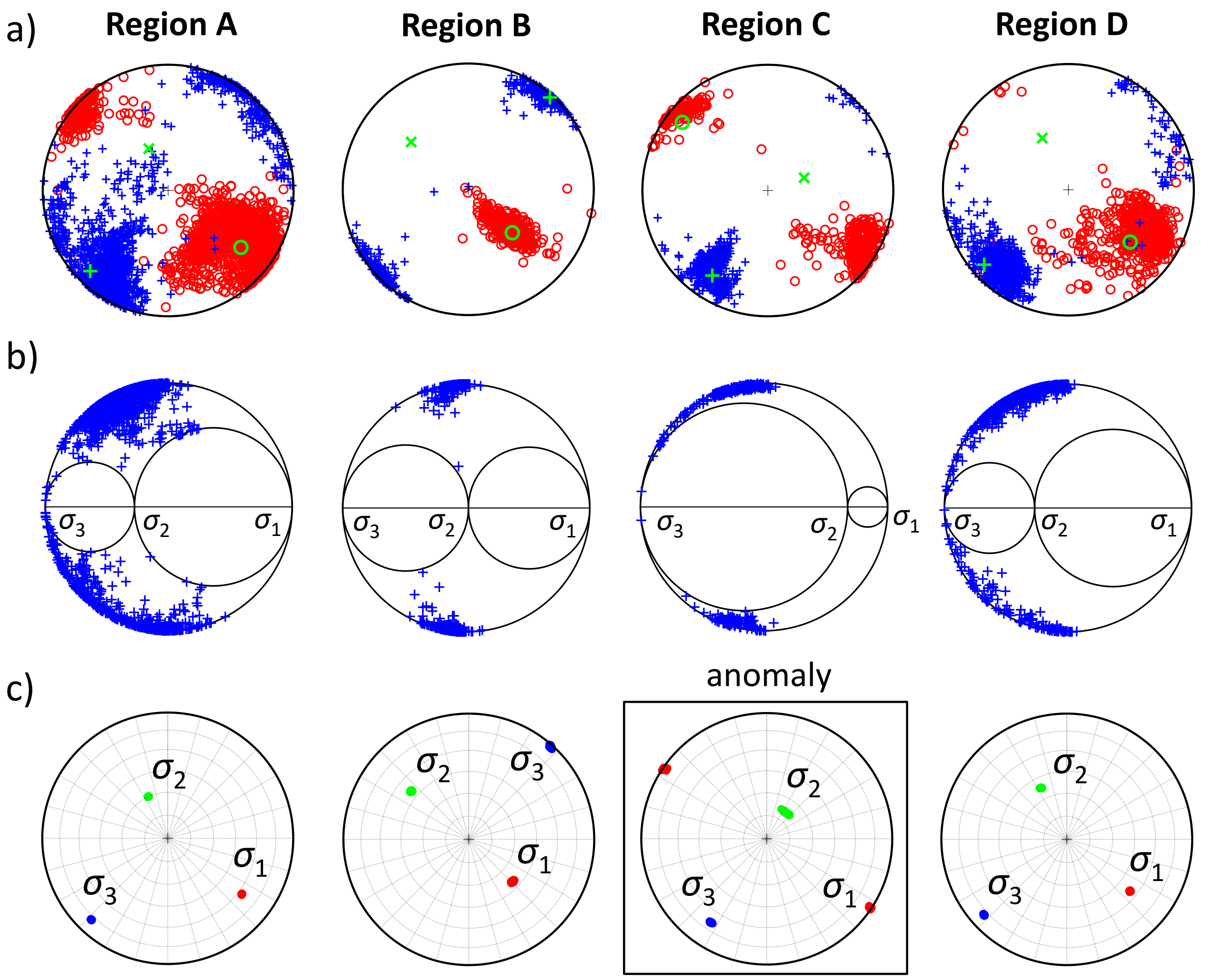

Vavryčuk et al. (JGR, Solid Earth, 2021)

Spatial variation of ISO and stress ratio

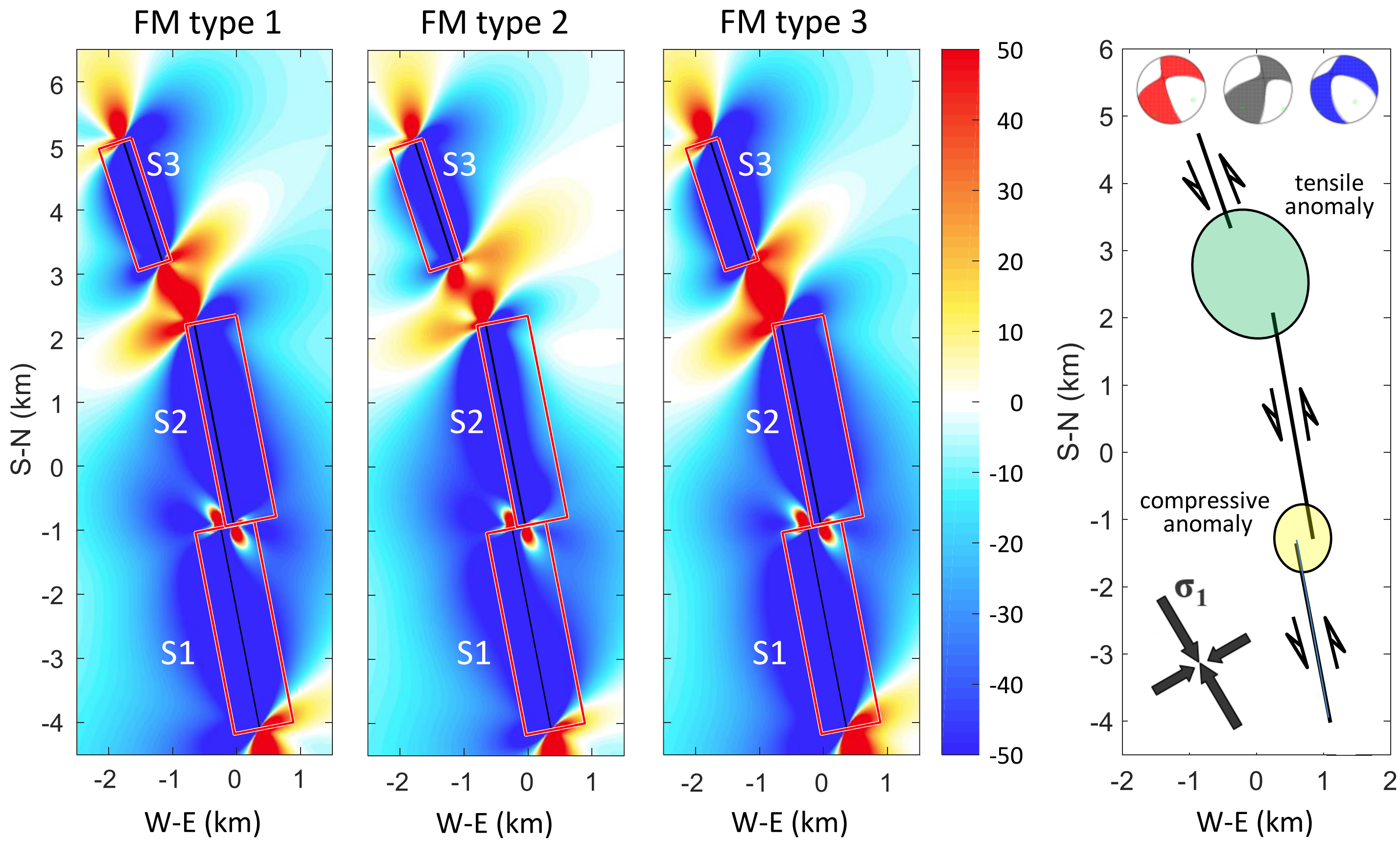

Vavryčuk et al. (JGR, Solid Earth, 2021)

Summary

Summary

Focal mechanisms provide key information about stress field

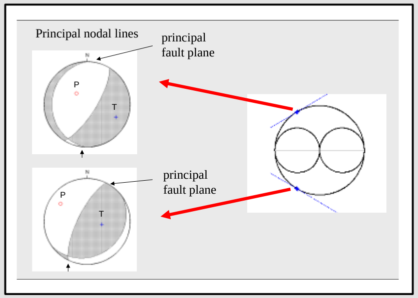

Principal faults and principal earthquakes

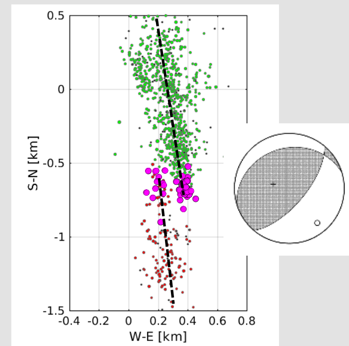

Stress anomaly produces anomalous focal mechanisms

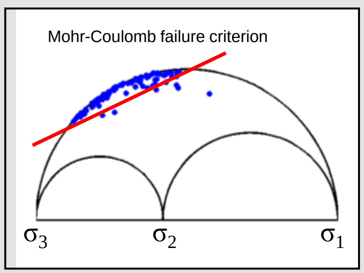

We can determine friction on faults

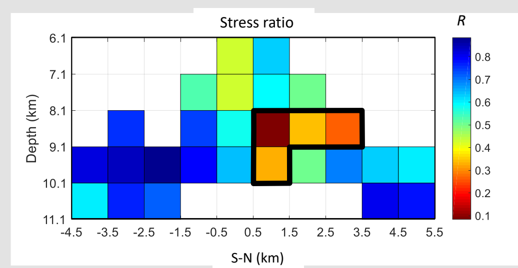

Stress inversion in cells

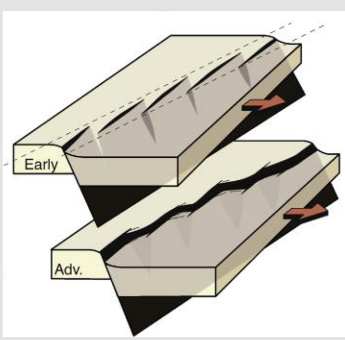

Stress might be heterogeneous due to interaction of faults

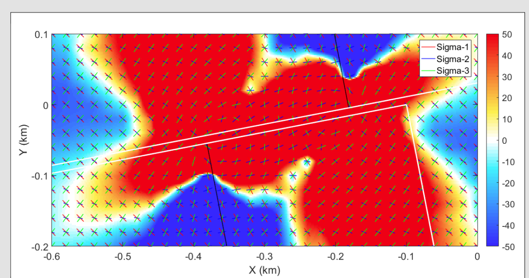

Coulomb stress modelling

Karlovy Vary spa

Thank you for your attention

Reference: Vavryčuk & Adamová (Tectonics, 2018)

Seismic sequences

Standard seismic sequence

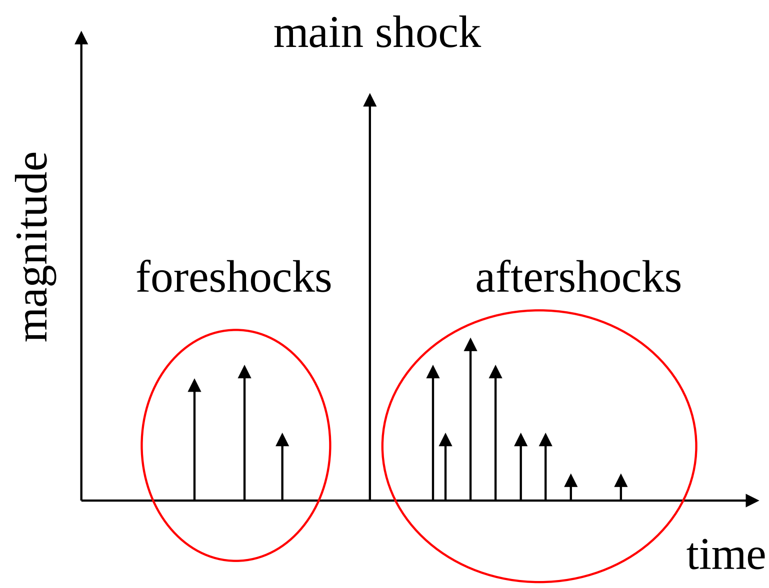

- **foreshocks**
- **main shock**
- **aftershocks**

high fault strength

Earthquake swarm

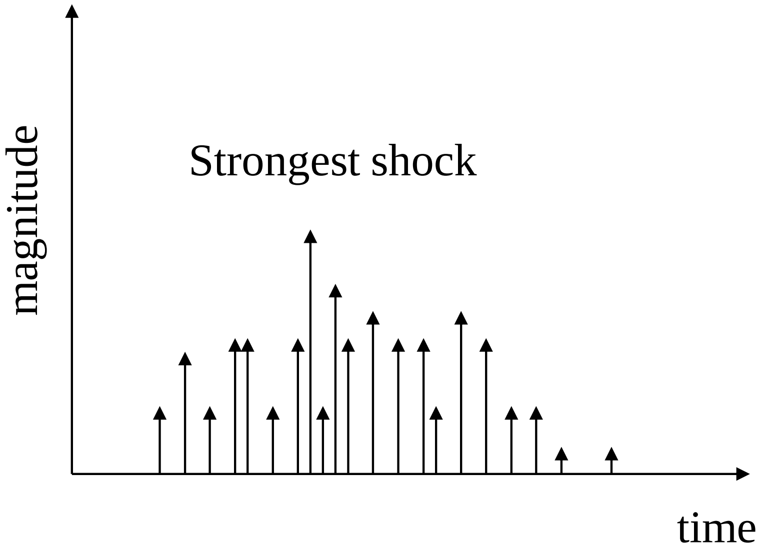

- **many small earthquakes**
- **no main shock**
- **the strongest event is comparable with other events**

low fault strength

Fault interaction

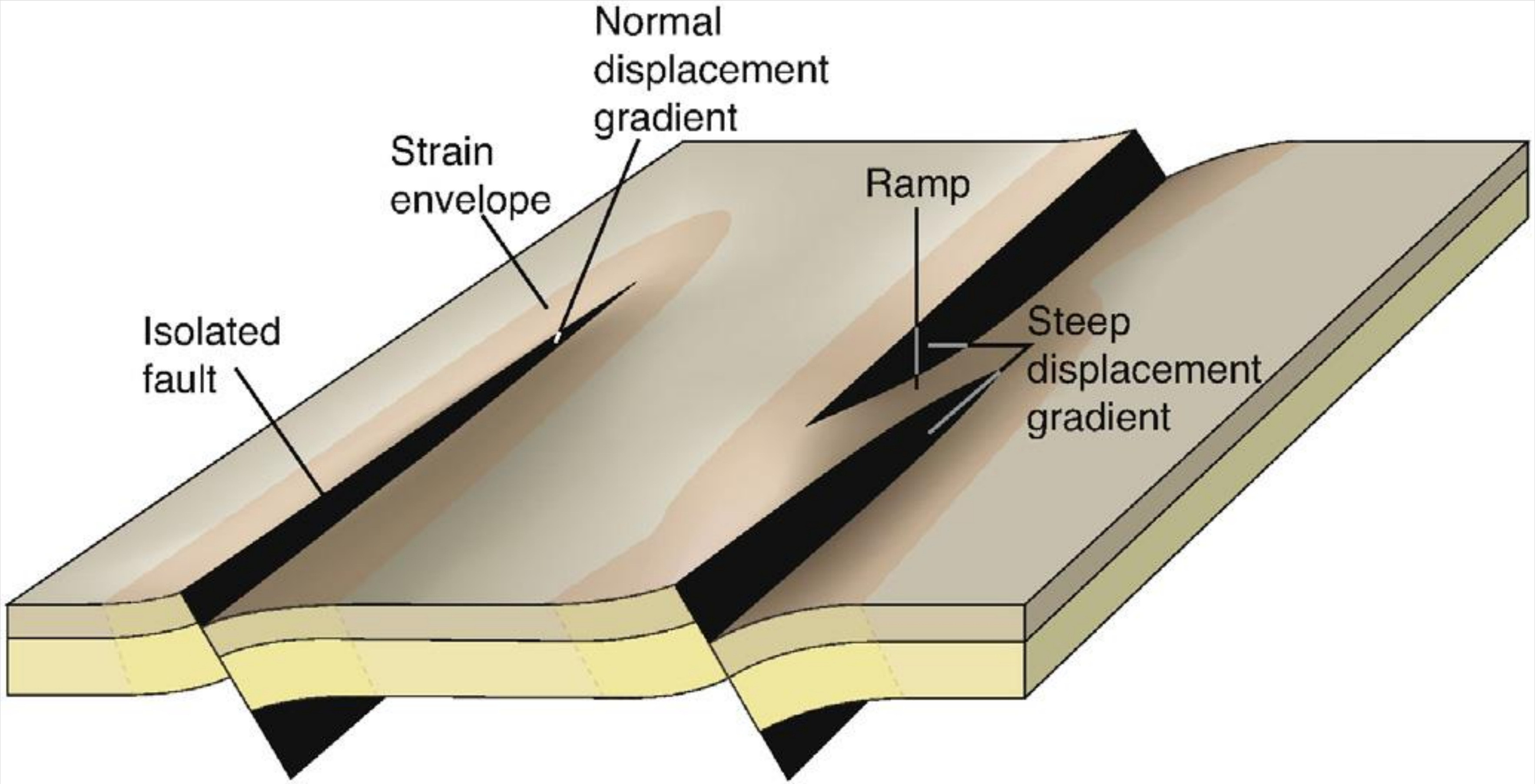

Fossen & Rotevant (Earth Sci. Rev., 2016)

Lessons from the 2014 seismic activity: I

- **Swarm-like activity versus mainshock-aftershock activity**

swarms – high heat flow, elevated temperatures, more 'ductile' rheology
weak faults eroded by long-term rock-fluid interactions
(Vavryčuk & Hrubcová, JGR, 2017)

mainshocks-aftershocks – cold, brittle compact rocks, high-strength faults
(Ben-Zion & Lyakhovsky, 2006; Zaliapin & Ben-Zion, 2013)

mixture of both types of seismicity at the same area is quite unique!

- **Explanation:** focal zone with low-strength as well as high-strength faults

weak faults – eroded by fluids, associated with a long-term seismicity

strong faults – newly created faults or reactivated closed faults
faults with no previous influence of fluids

unfavourably oriented faults with respect to the regional stress
faults inside local compressive anomaly – prevents fluid flow

Lessons from the 2014 seismic activity: II

- **Regional background stress versus local stress anomaly**

background stress – very uniform, homogeneous over large distances
disturbance by individual earthquakes is minor
(stress drop ~ MPa, stress – hundreds of MPa)

local stress anomaly – associated with irregularities on faults
(kinks, step overs, barriers), small in size,
result of many individual earthquakes

- **local stress anomalies are rather exceptions and do not destroy the regional background stress**
- **mainshock can be produced by the local stress anomaly (questions the applicability of the declustering procedure)**
- **the stress anomalies change the magnitudes of principal stresses rather than their directions**
- **variability of focal mechanisms must be studied**

Lessons from the 2014 seismic activity: III

Role of fluids in seismicity

Long-term role

- **high pore fluid pressure** – decrease of effective normal stress
  – destabilizes faults and triggers earthquakes

- **fault weakening by fluids** – affects the type of seismicity (swarms)

Short-term role

- **fluid flow during seismicity** – causes migration of seismicity
  – tensile faulting and overpressure due to fault compaction

However, not everything is caused by fluids!

Hainzl et al. (2016) – fluids are responsible for a fast decay of aftershocks (??)
– fluids trigger mainshock in 2014 on a misoriented fault (??)

Moment tensors and focal mechanisms

Microseismic data

- Complex high-frequency waveforms
- Waveforms are noisy because of low magnitude of events
- Large number of earthquakes requiring automatic processing

Waveform inversion

- Accurate detailed velocity model
- Computing high-frequency waveforms is time consuming (FD method, discrete wavenumber method, reflectivity)

Amplitude inversion

- Simple model is sufficient
- Computing is fast (GF amplitudes calculated by ray theory)
- Many stations, good coverage of the focal sphere
- Sensitive to noise in data

PCA: inversion scheme

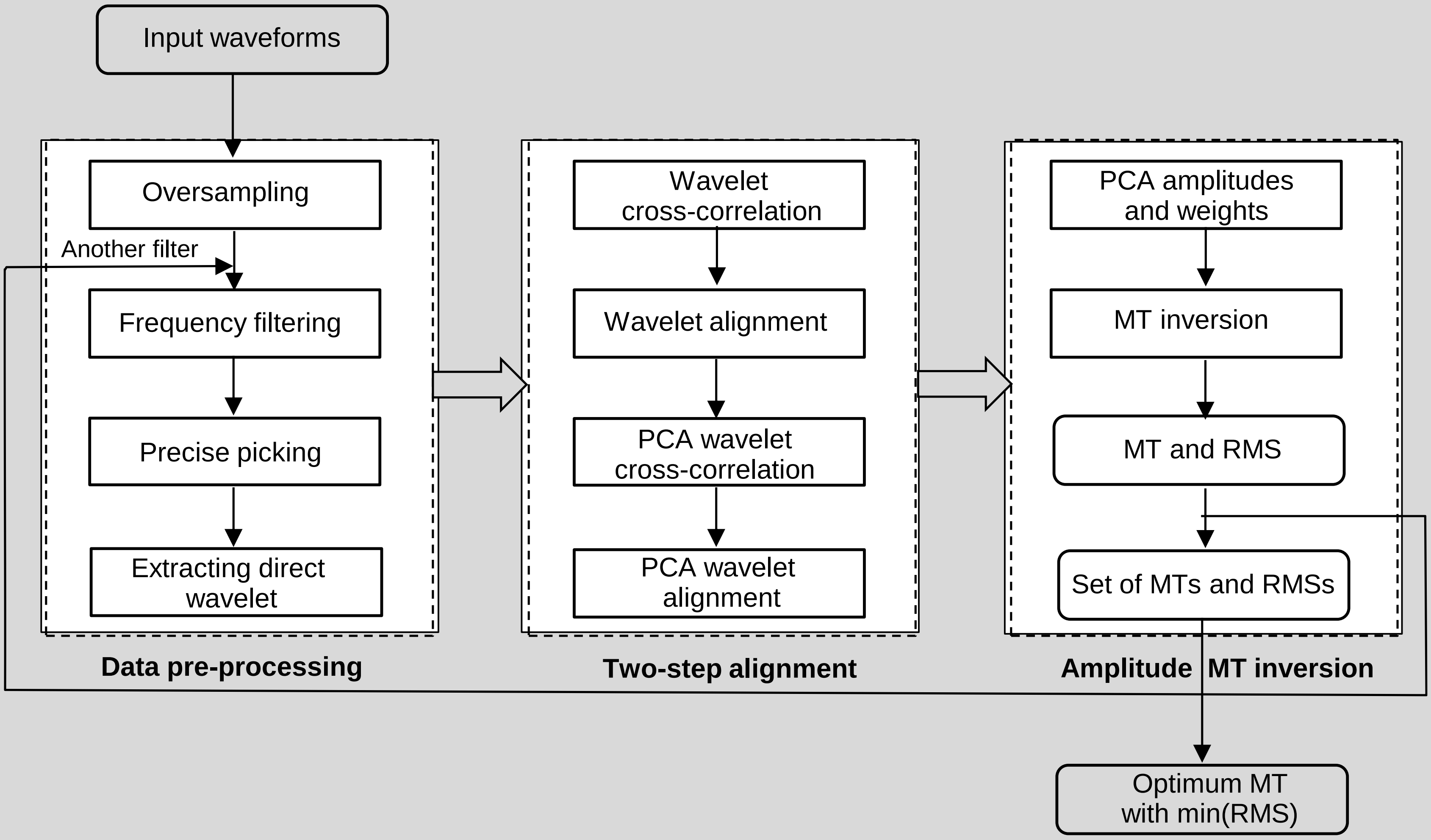

PCA: numerical example II

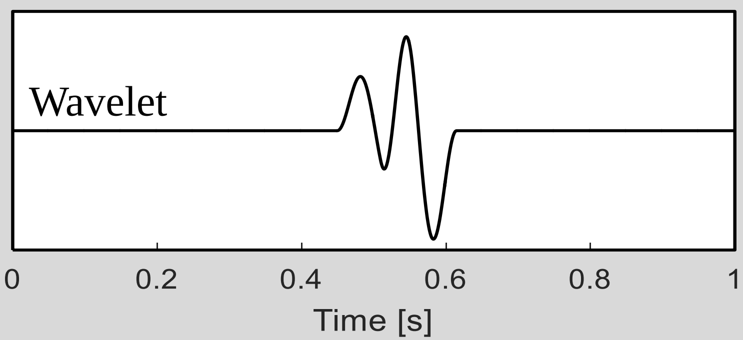

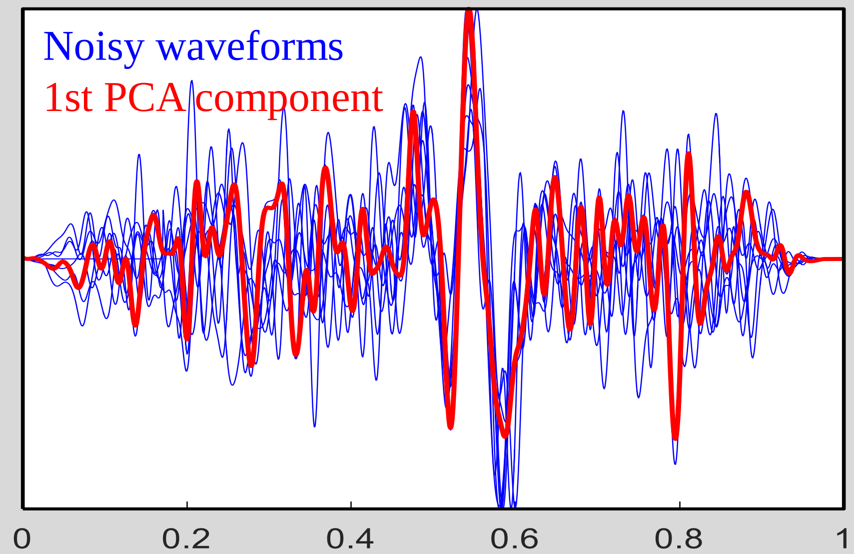

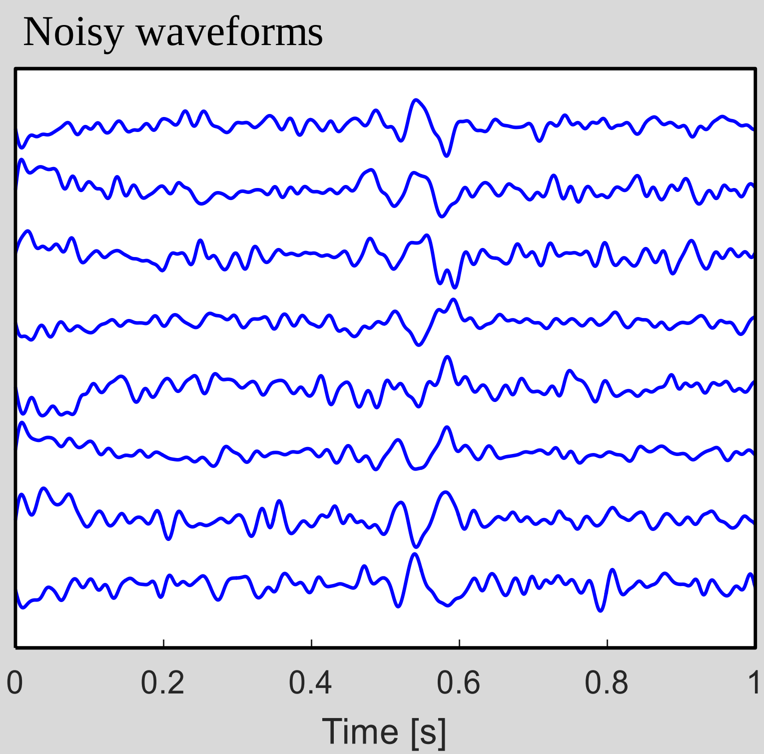

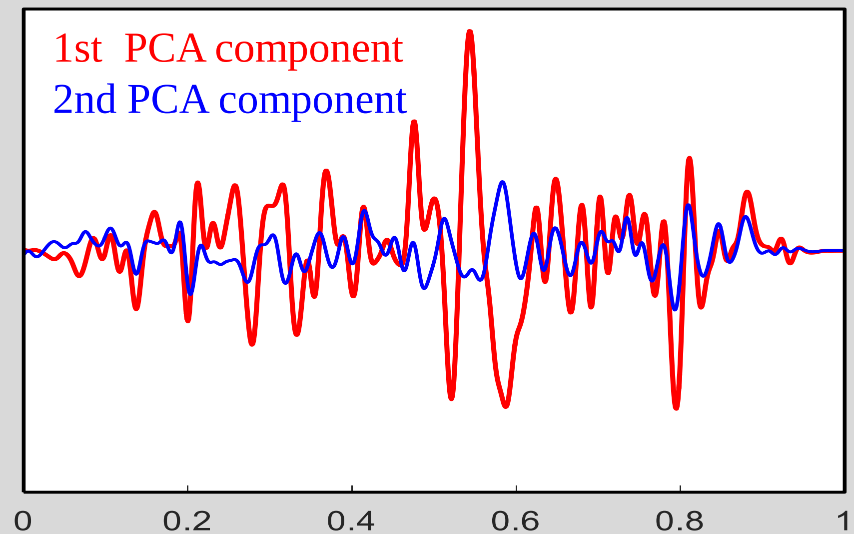

Swarm 2014: non-DC components

CLVD-ISO diamond plot

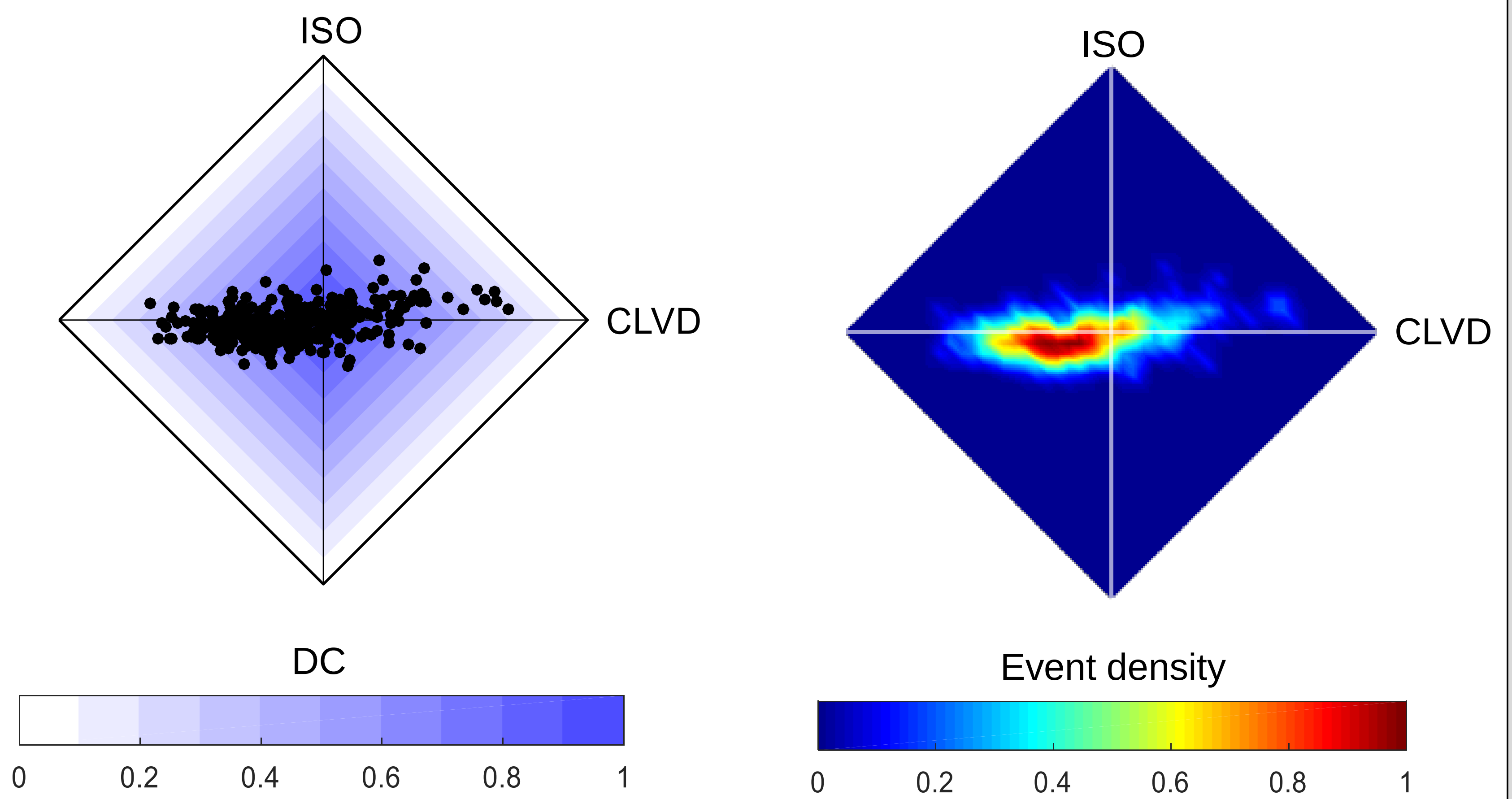

Non-DC components and shear-tensile faulting

Non-DC components

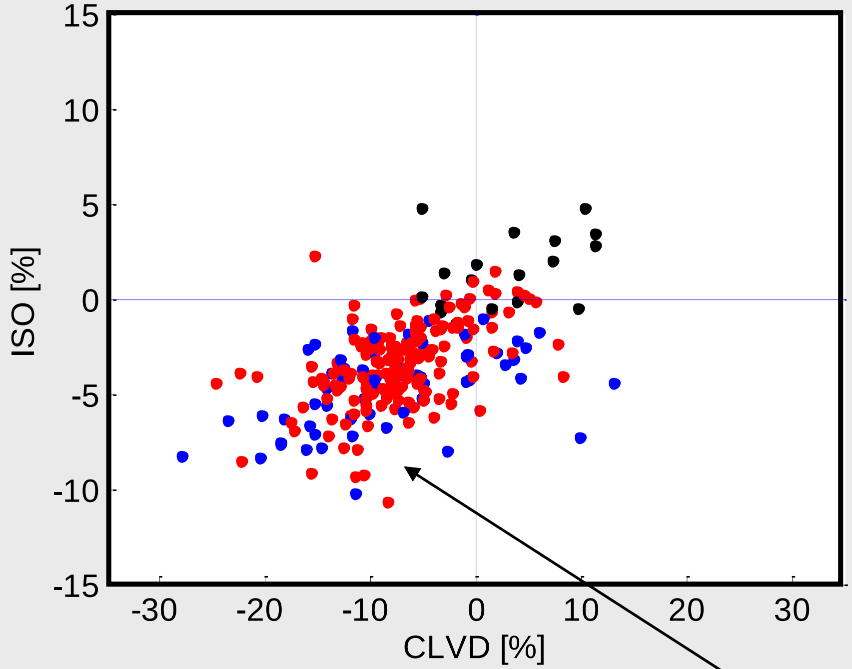

Slip deviation from the fault

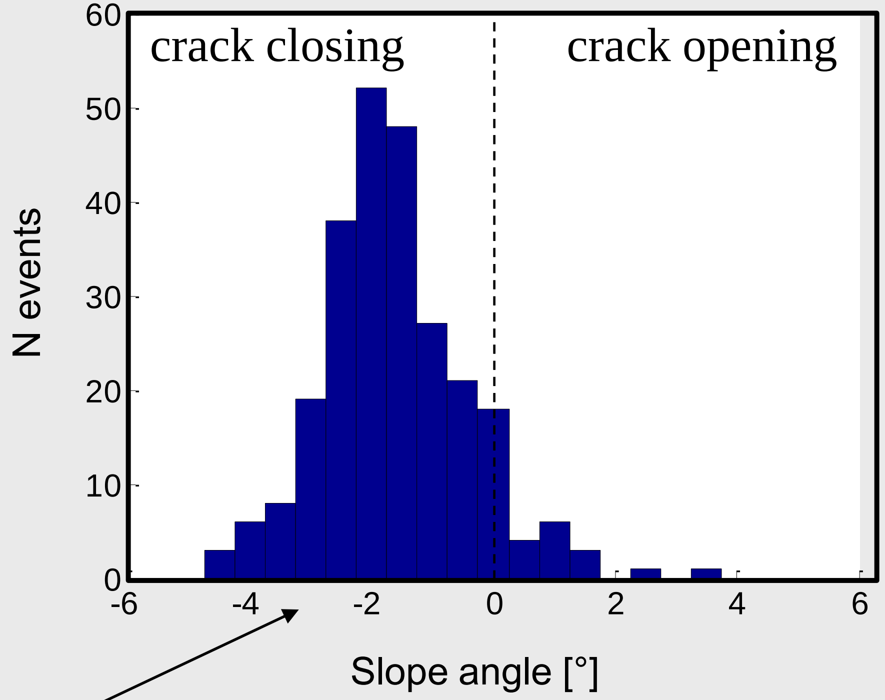

closing of a fault, rock compaction

Data and methods

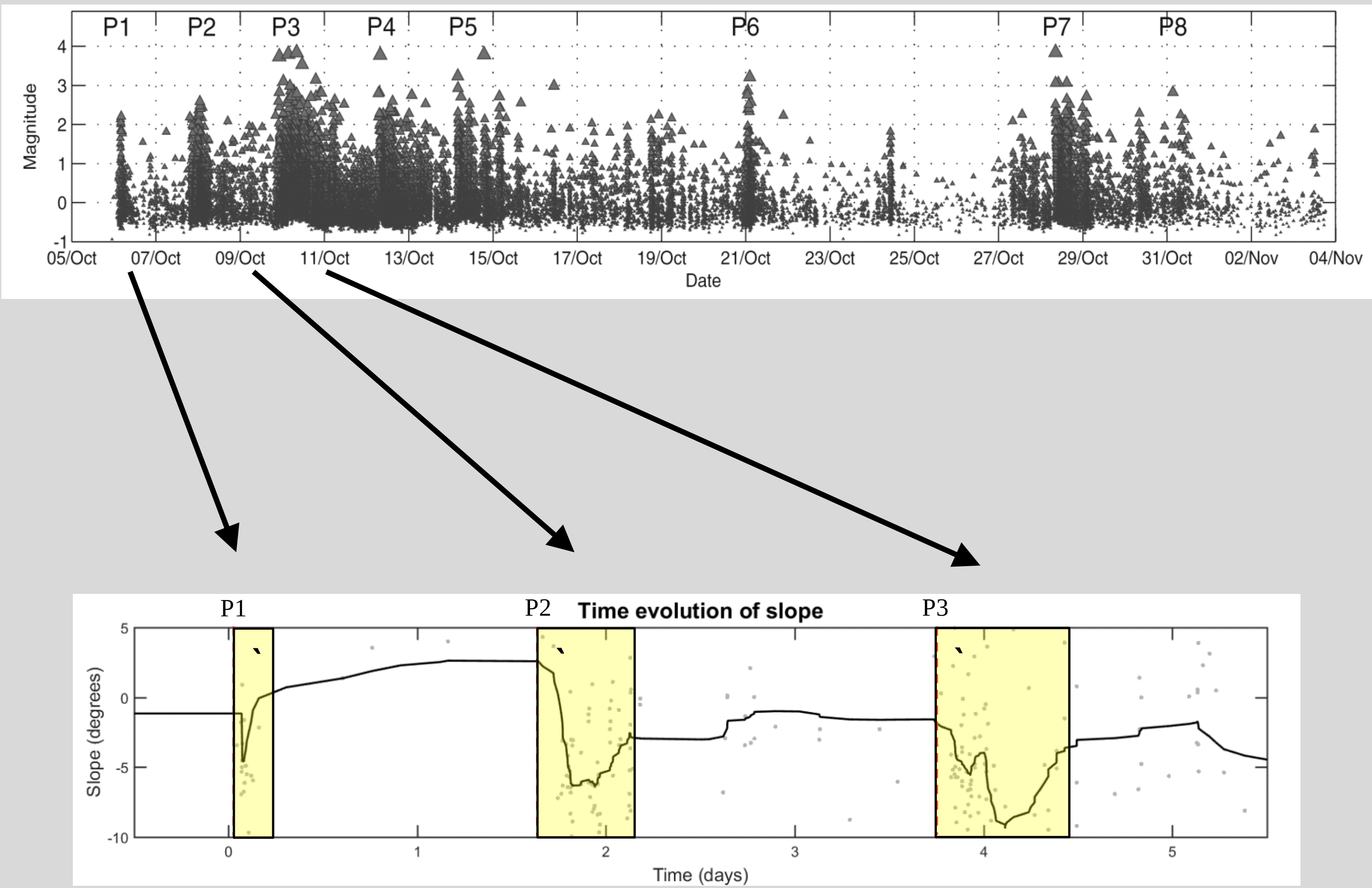

Seismicity in West Bohemia, Czech Republic

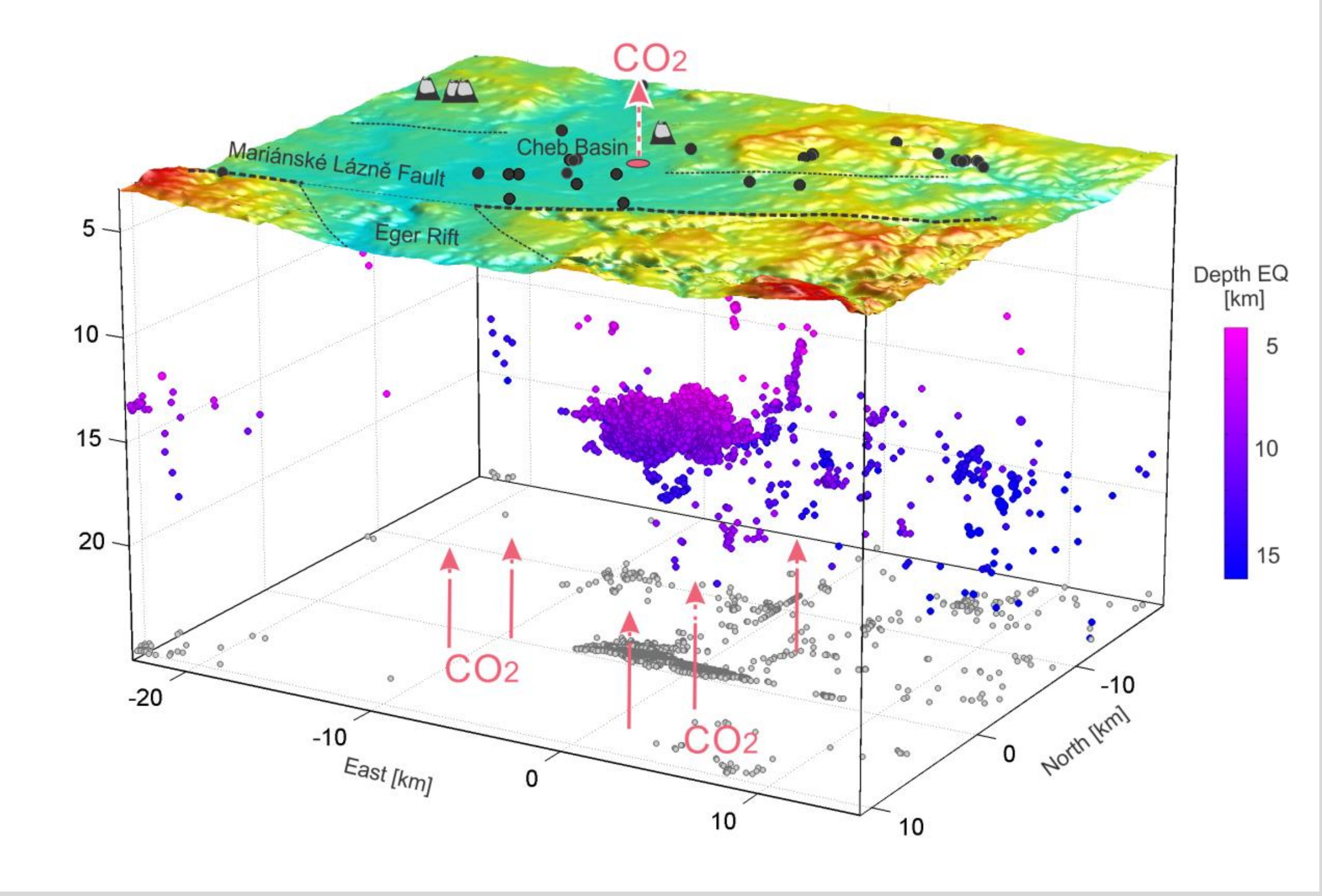

Origins of rock compaction: fluid-rock interaction

- Permanent fluid flow in the Earth's crust
- Hydrothermal alteration of rocks
- Dissolution of minerals
- Transport of dissolved material to the surface
- Fault erosion by fluids

Borehole picture of open fluid-filled fracture at depth of 111 m
The fracture width is 1-2 cm
After Heinicke et al. (2009)

Seismic cycles: two alternative scenarios

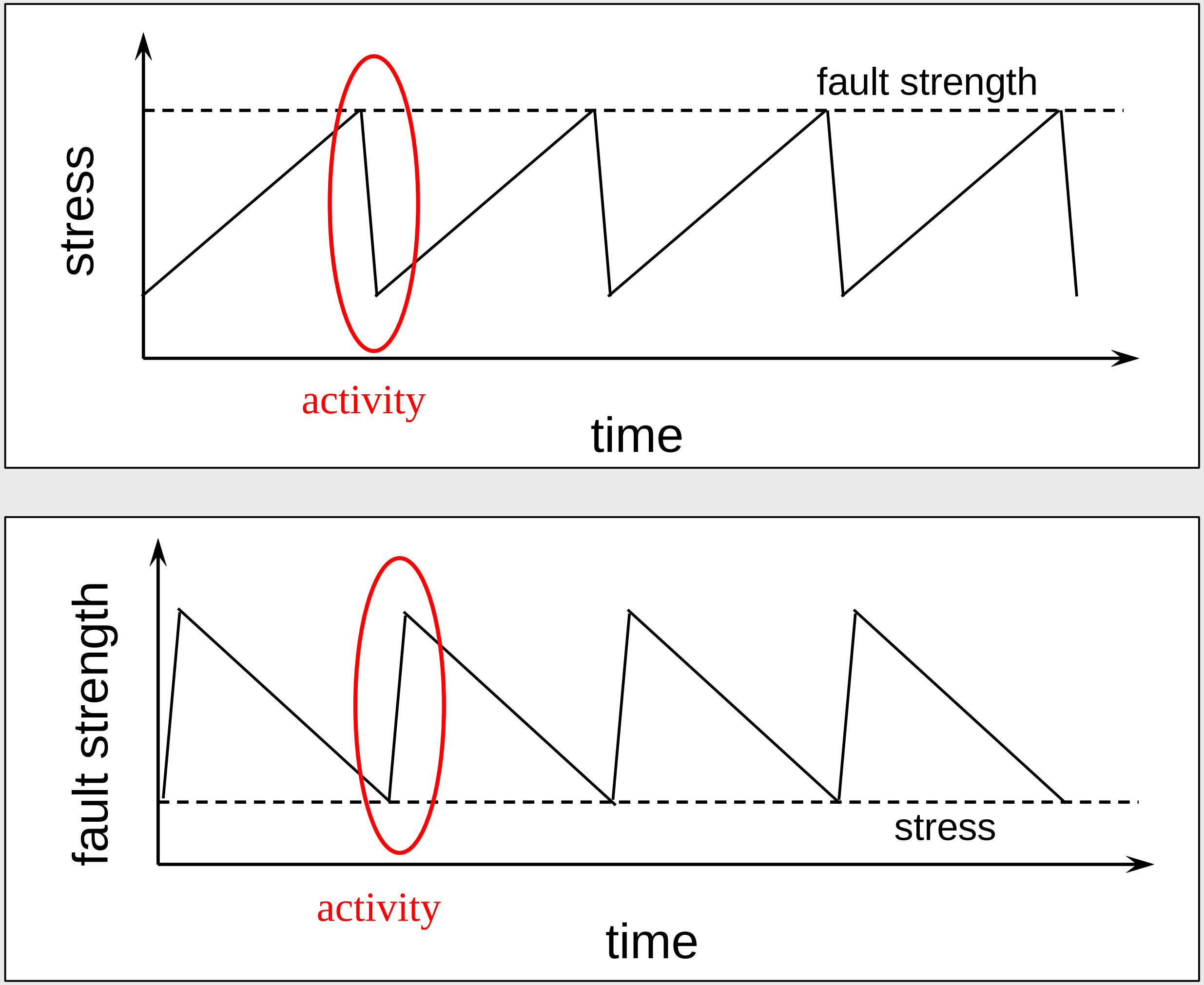

Stress accumulation

(seismicity at margins of continental plates)

Fault weakening

(intraplate seismicity)

Anomalous sequence in 2014

Non-DC components in 2008 swarm

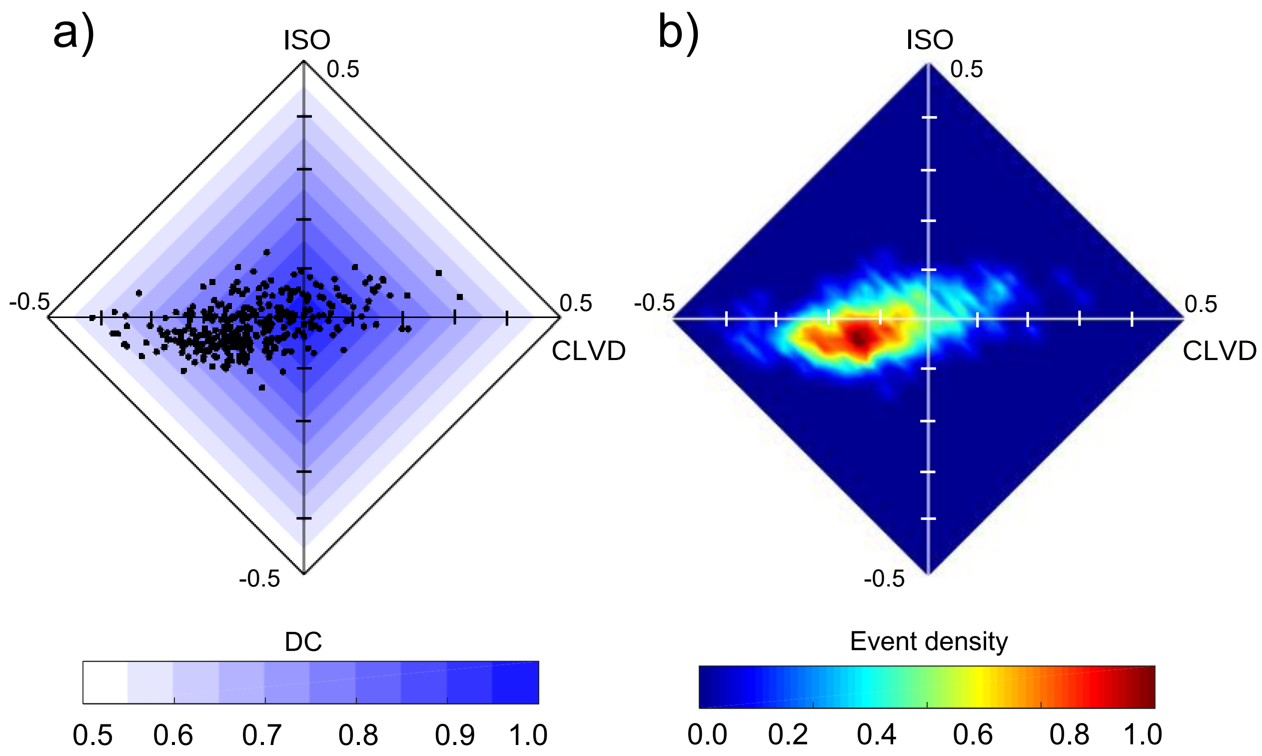

Vavryčuk & Hrubcová (JGR, 2017)

Data and methods

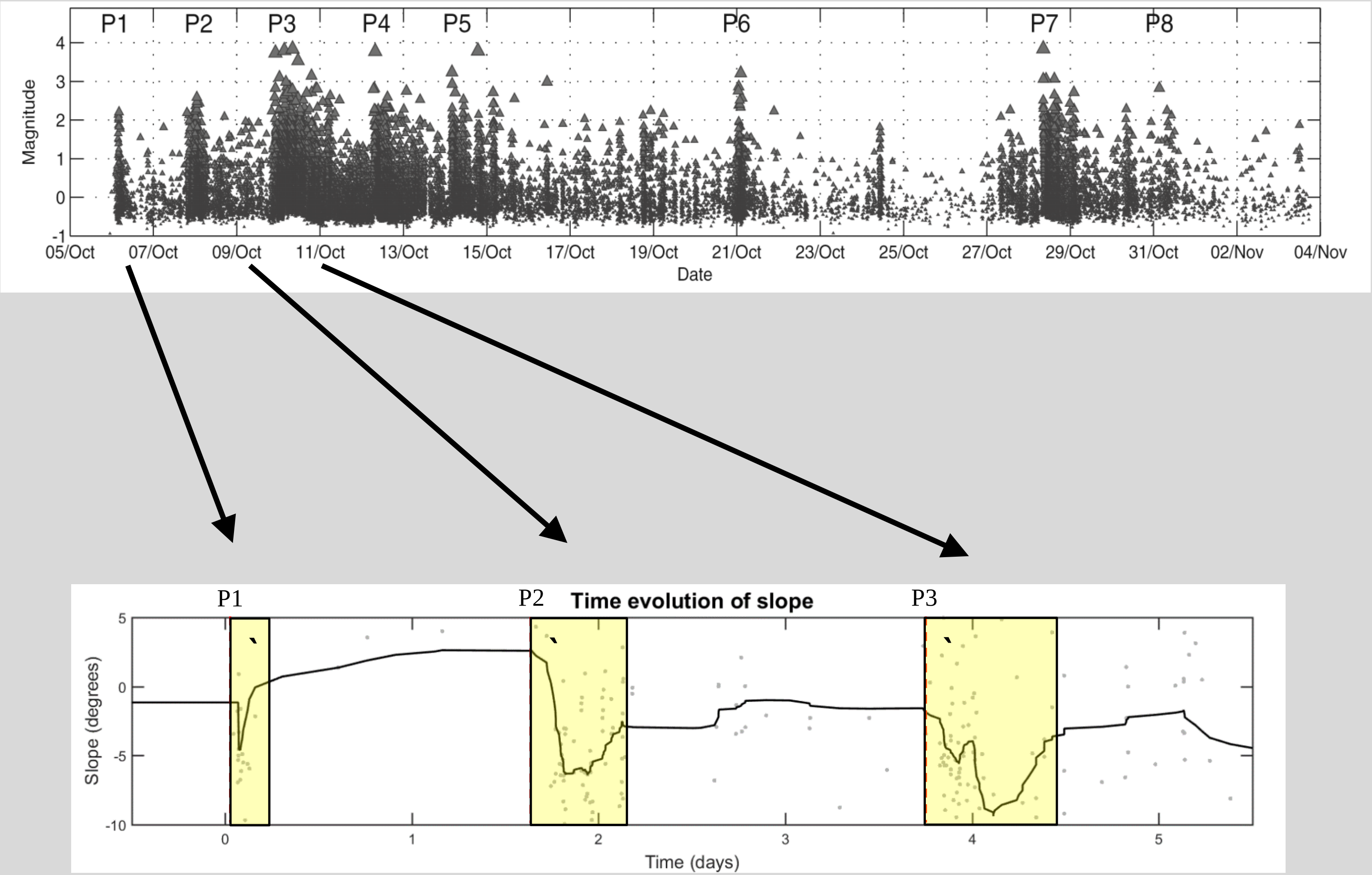

Vavryčuk & Hrubcová (JGR, 2017)

Seismic cycles: two alternative scenarios

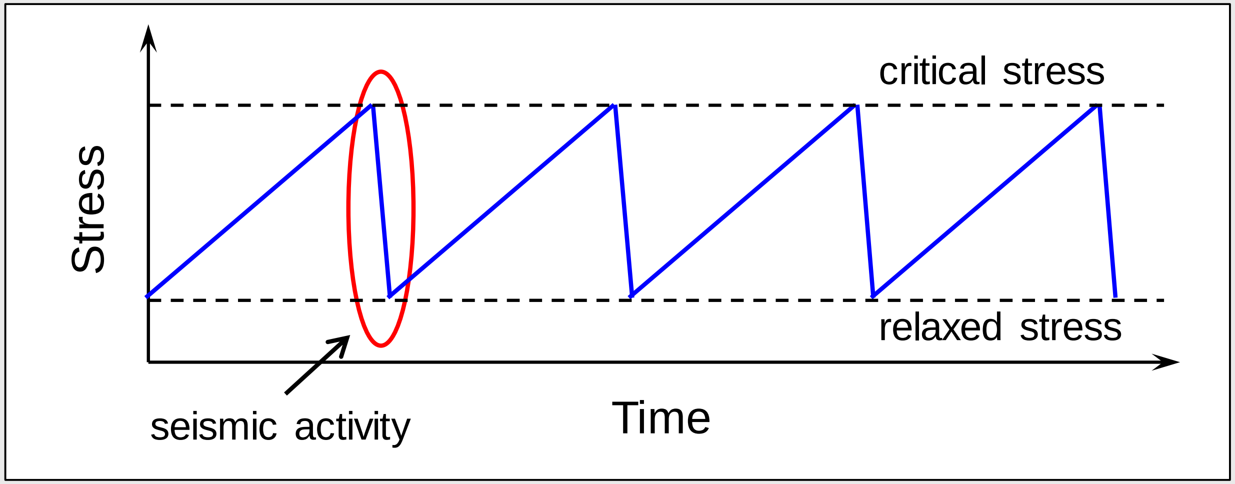

Stress accumulation

(seismicity at margins of continental plates)

mainshock-aftershocks

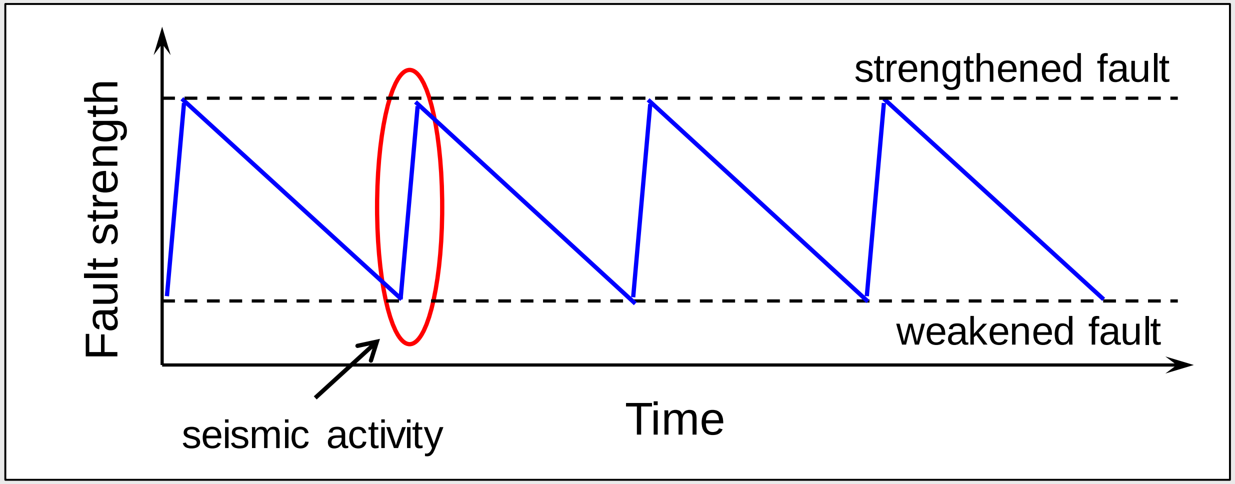

Fault weakening due to fluid erosion

(intraplate seismicity)

earthquake swarms

Vavryčuk & Hrubcová (JGR, 2017)

Inversion for stress – Gephart & Forsyght (1981)

$$\sum_{i=1}^{N} |\vartheta_i| = \min$$

theoretical slip – predicted by stress

measured slip – determined from the mechanism
(by inversion of P and S amplitudes)

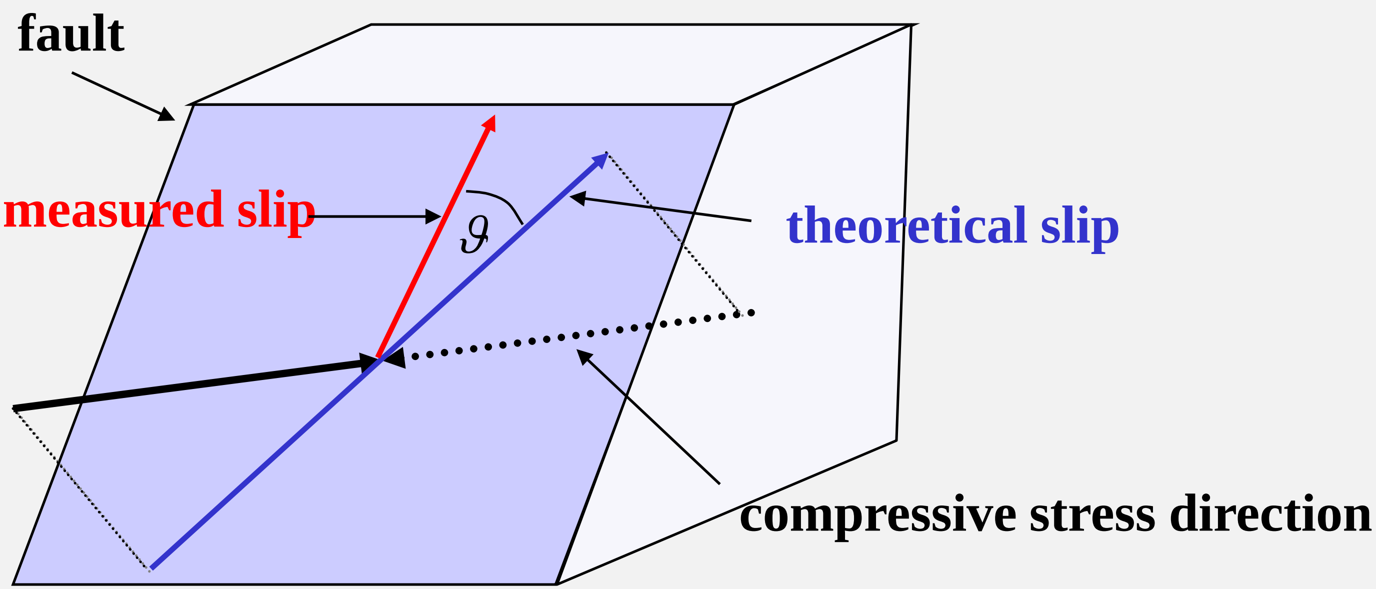

Fault instability: definition

Mohr's circle diagram

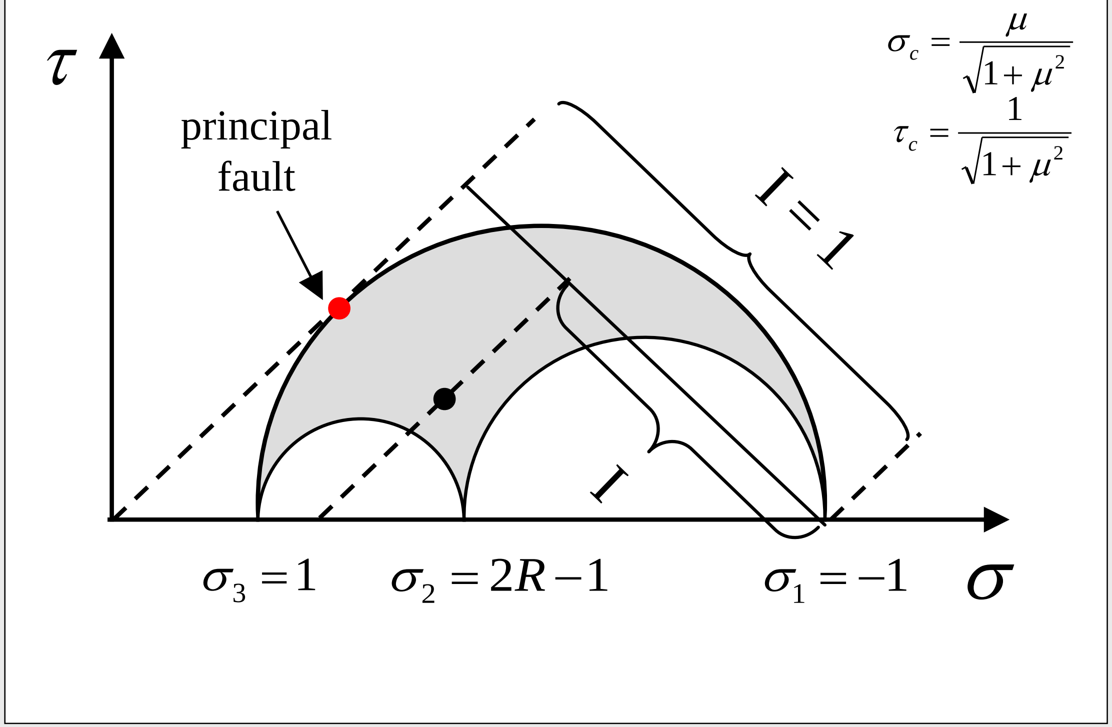

$$I = \frac{\tau + \mu(\sigma + 1)}{\mu + \sqrt{1+\mu^2}}$$

Shape ratio:

$$R = (\sigma_1 - \sigma_2)/(\sigma_1 - \sigma_3)$$

Principal fault is the most unstable fault in the stress field

$$\sigma = -n_1^2 + (2R-1)n_2^2 + n_3^2$$

$$\tau = \sqrt{n_1^2 + (2R-1)^2 n_2^2 + n_3^2 - \left(-n_1^2 + (2R-1)n_2^2 + n_3^2\right)^2}$$

Vavryčuk et al. (Tectonophysics, 2013)

Principal focal mechanisms

Principal focal mechanisms – the mechanisms which occur on the most unstable (optimally oriented) fault planes

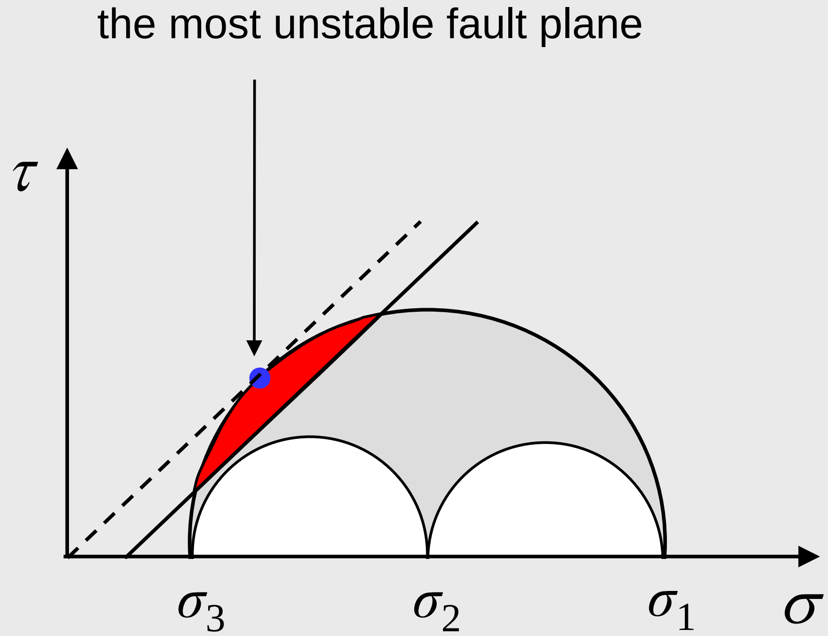

shape ratio = 0.5
friction = 0.6

Principal nodal lines and P/T axes

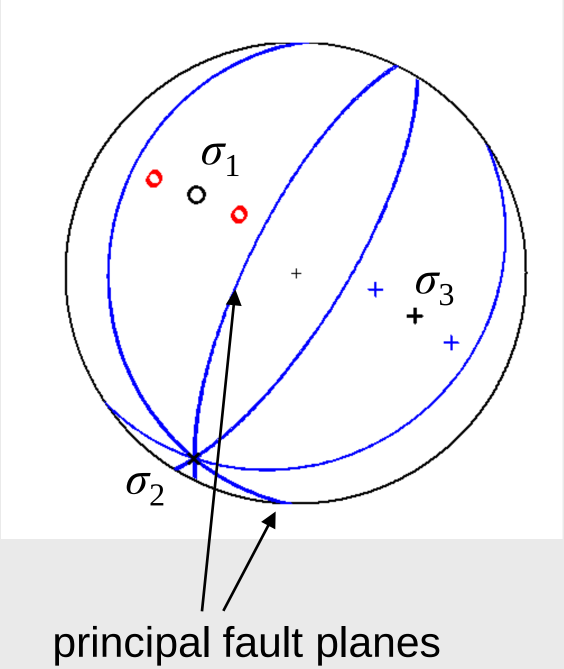

MT inversion - principal component analysis (PCA)

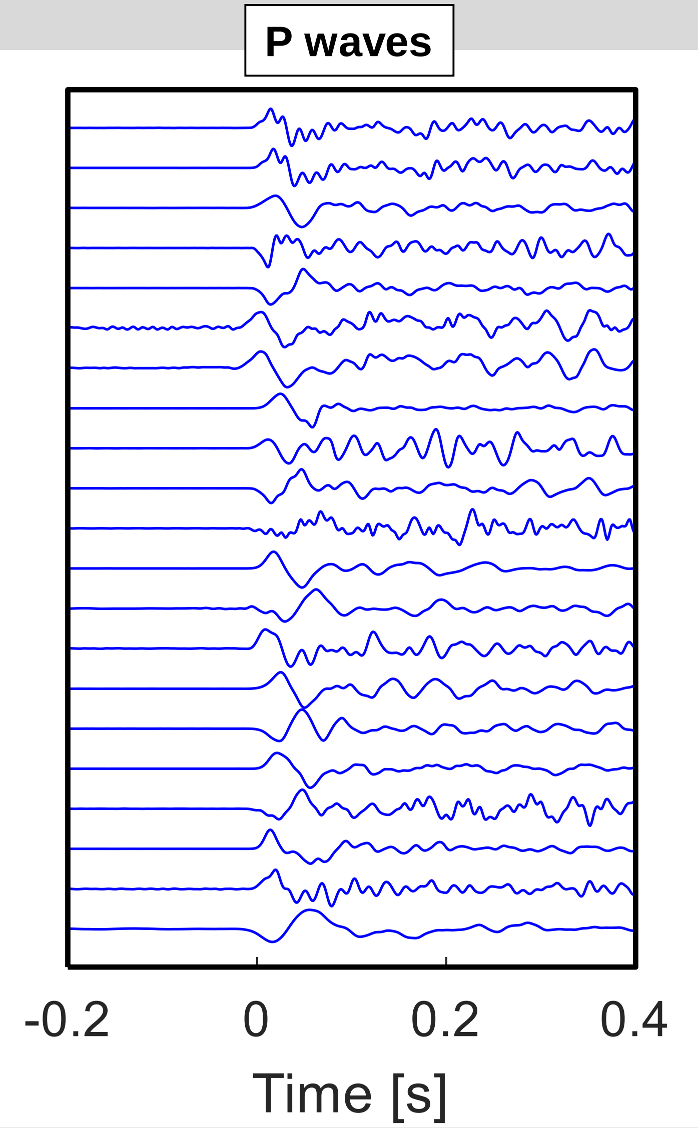

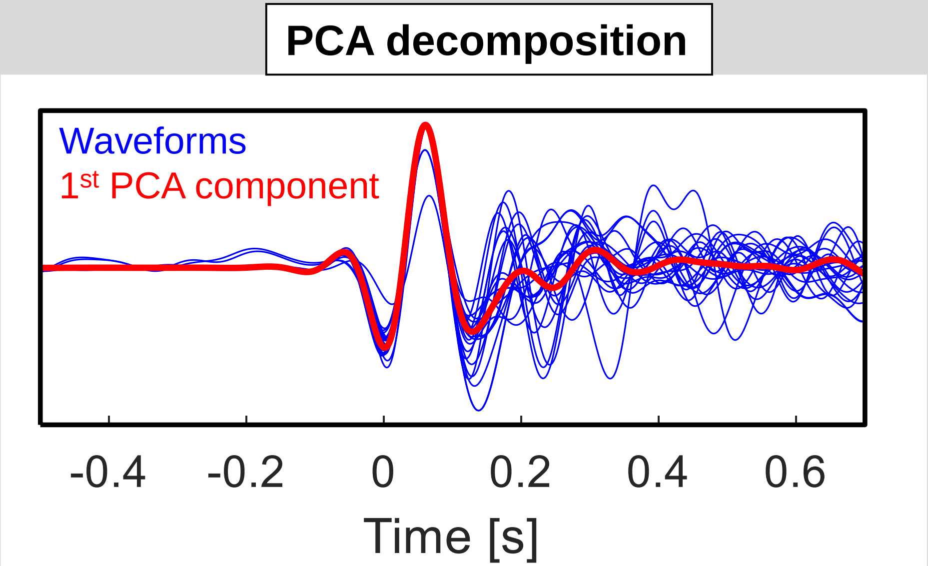

MT inversion of P waves:

- suitable for analysis of large microseismic datasets
- more robust and less sensitive to noise than the amplitude inversion
- more accurate results than for manually processed earthquakes

Vavryčuk et al. (SRL, 2017)

Cluster analysis of 440 focal mechanisms

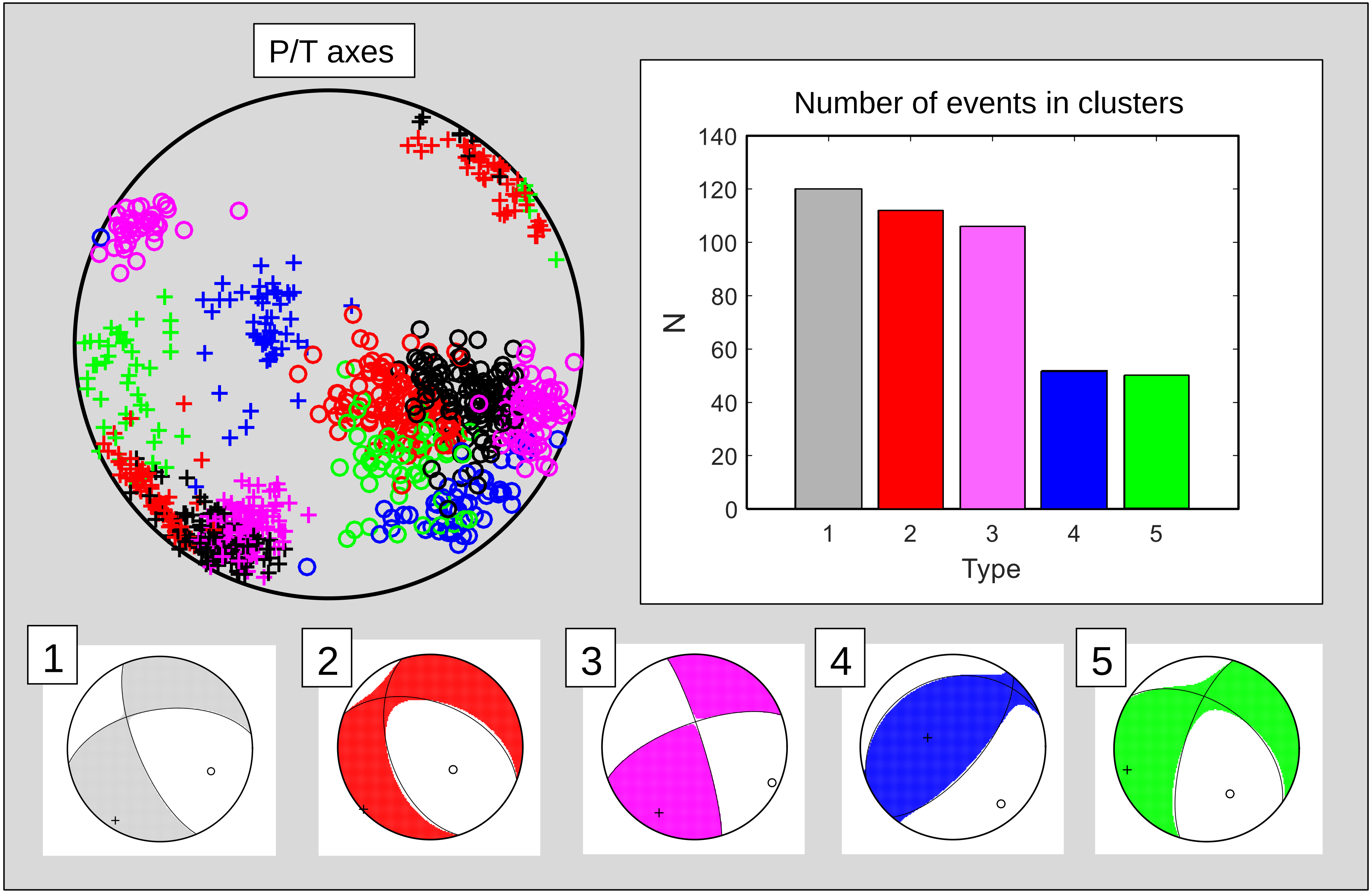

Previous explanations of the 2014 sequence

- **Hainzl, Fischer, Jakoubková, Bachura, Vlček, 2016.** Aftershocks triggered by fluid intrusion: Evidence for the aftershock sequence occurred 2014 in West Bohemia/Vogtland, *J. Geophys. Res., Solid Earth*, *121*, doi:10.1002/2015JB012582

  usage of ‘fluid/fluids’: 29 times

- **Jakoubková, Horálek, Fischer, 2017.** 2014 Mainshock-aftershock activity versus earthquake swarms in West Bohemia, Czech Republic, *Pure Appl. Geophys.*, doi: 10.1007/s00024-017-1679-7

  usage of ‘fluid/fluids’: 5 times

Previous explanations of the 2014 sequence

Jakoubková et al (PAAG, 2017)	Our concept
• Repeating reactivation of the focal zone complex system of fault segments, local fast stress accumulation, fluid pressure increase	Fault weakening due to rock-fluid interaction
• The mainshock activated a barrier between the fault segments	OK, stress accumulated in 2008-2011
• Why mainshock-aftershock sequence? Why the aftershock decay is fast? low stress – swarms, high stress aftershocks, increased stress in the fault zone due to fluids	No fluids in the focal zone! Compressive stress, new fractures.
• The local magnitude ML of the mainshock is 4.4	Our estimate is ML 4.2 Mw = 3.9-4.0
• Maximum expected magnitude ML 4.8	Mw 5.0 ⟶ Mw 5.4 fault linkage

Previous explanations of the 2014 sequence

Hainzl et al. (JGR, 2016)	Comment
• The mainshock is on the jog of the fault segments	Why? Fluid injection exactly on the jog?
• The mainshock occurred on an unfavourable fracture	??, no explanation
• Origin of the mainshock	??
To bring the unfavorably oriented mainshock rupture to failure requires the decrease of the effective normal stress, most likely by high fluid pressure	Fluid injection would activate favourably oriented fractures
• Why mainshock-aftershock sequence? Why the aftershock decay is fast?	??
A strong aseismic driving force with exponential decay – fluid intrusion	Fluids played the key role also in swarm-like activites!

Tectonic stress from focal mechanisms: Applications II

Václav Vavryčuk

Institute of Geophysics, Prague

2017 swarm activity in Iceland

Tectonic setting in Iceland

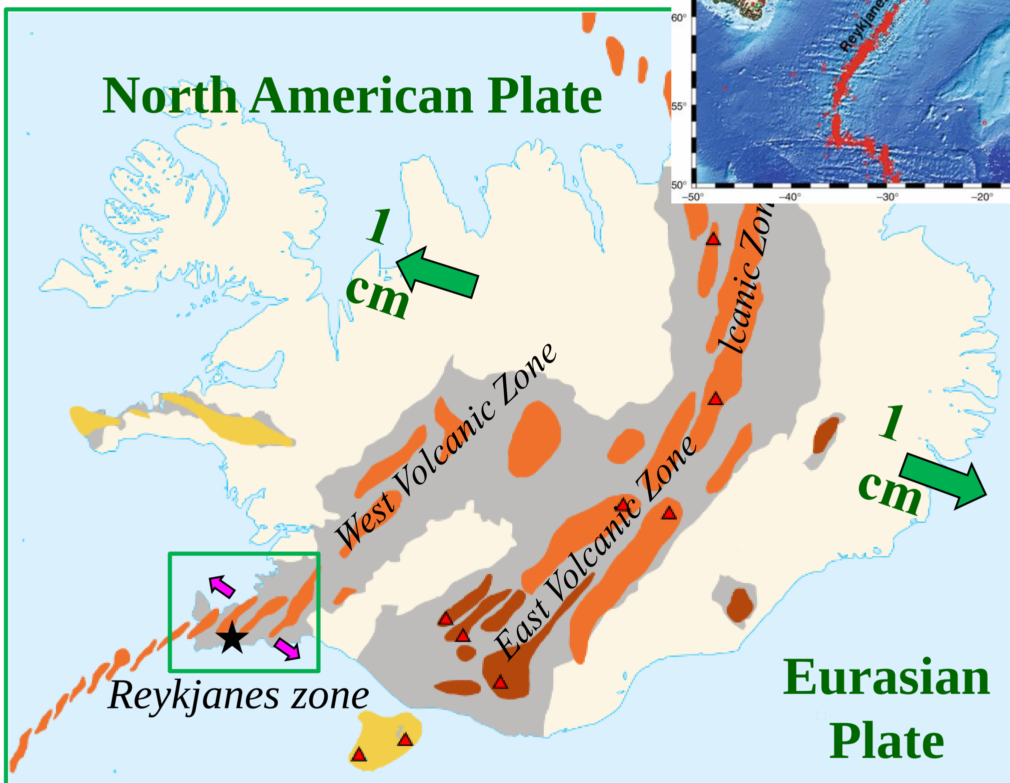

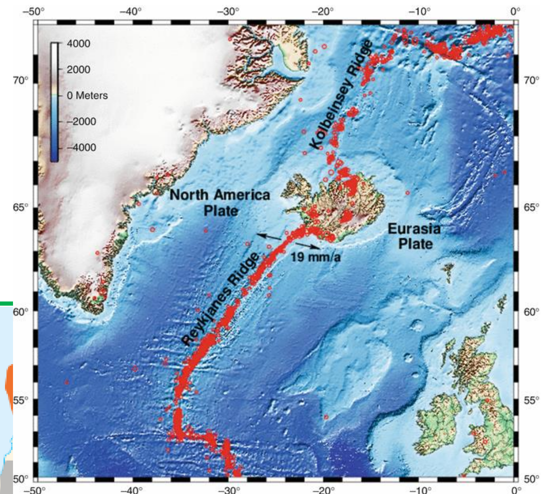

Geodynamically active area:

- Transtensional plate boundary
- Slow-spreading rift
- Spreading rate 1.9 cm/y, ~105°/285°
- Volcanic fissures
- Seismicity, volcanism, geothermal fields
- Mantle plume

2017 swarm in Reykjanes Peninsula

REYKJANET network
(15 BB stations
Guralp CMG-3ESPC)

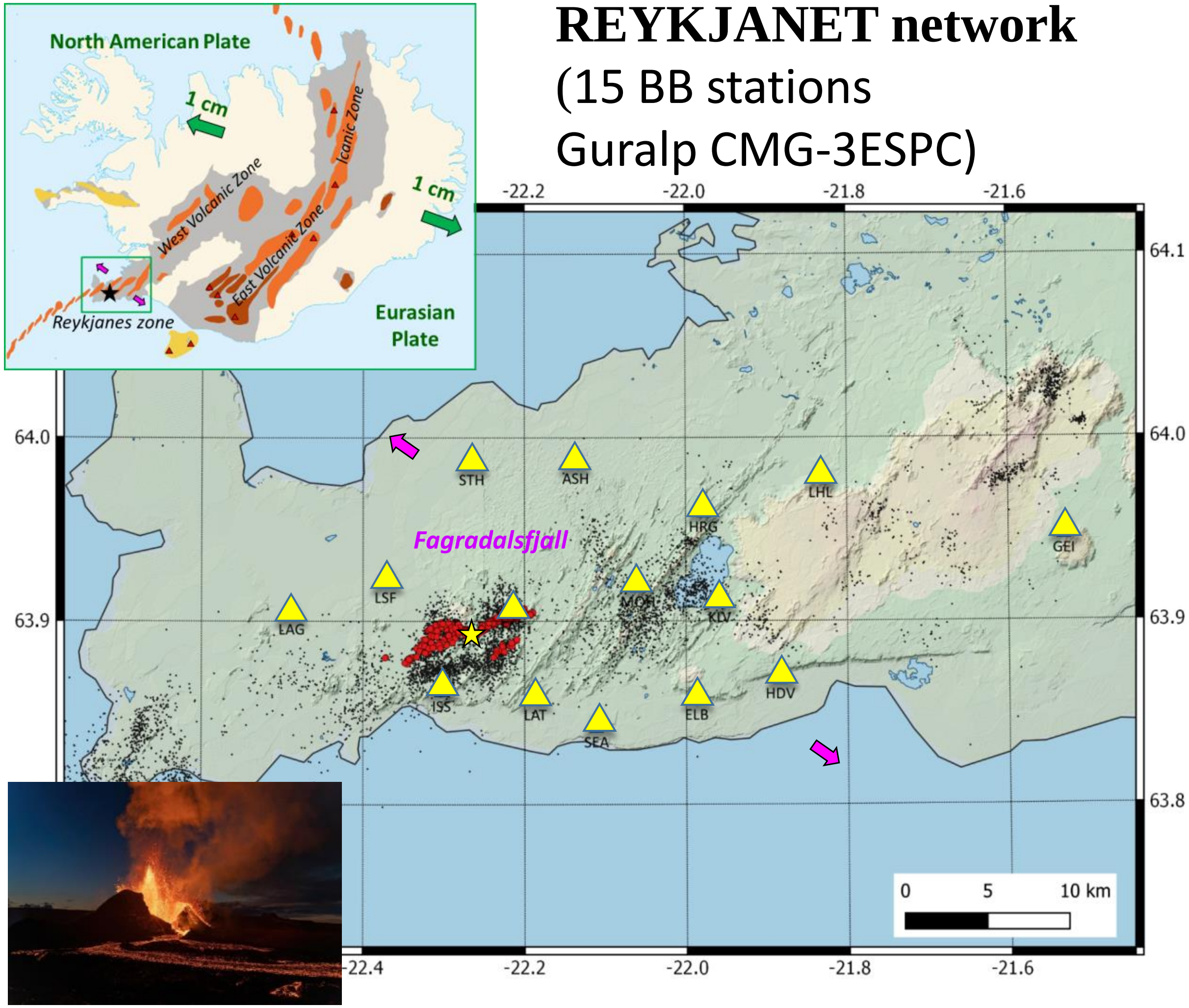

Fagradalsfjall eruption, 19 March 2021

Reykjanes Peninsula:

- High, episodic seismicity
- every ~30 yrs (M < 6)
- 2016, 2017, 2019, 2020-2022
- Swarm duration – few days or weeks
- Fagradalsfjall volcano-tectonic segment

Hrubcová et al. (EPSL, 2021)

2017 swarm: spatiotemporal evolution

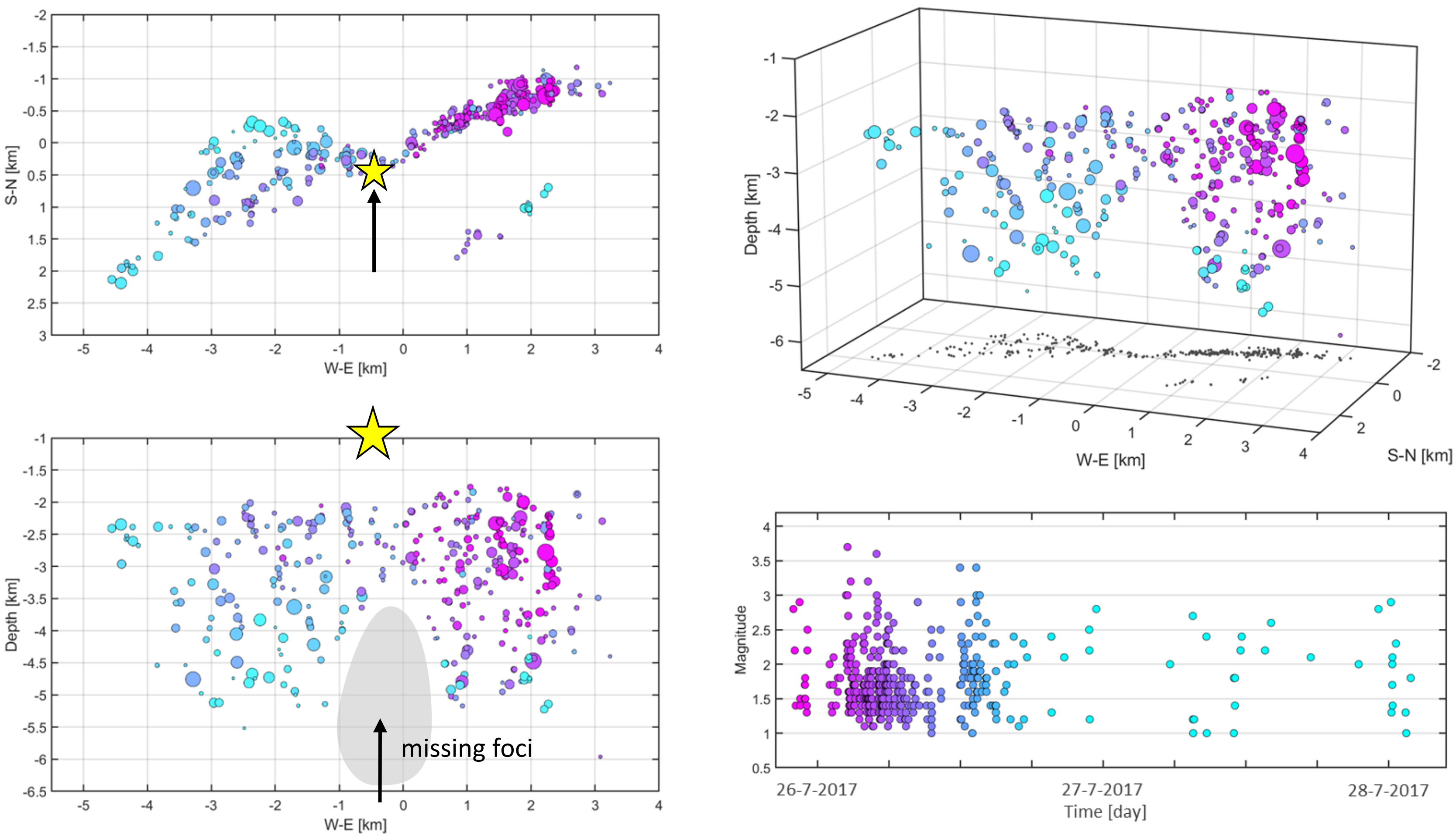

Duration: July 26-28, 2017
Size: 9 km long cluster
Strongest shock: ML=3.7

Mote than 2000 earthquakes with ML > 1.0
389 events with DD-locations

Hrubcová et al. (EPSL, 2021)

PCA moment tensor inversion

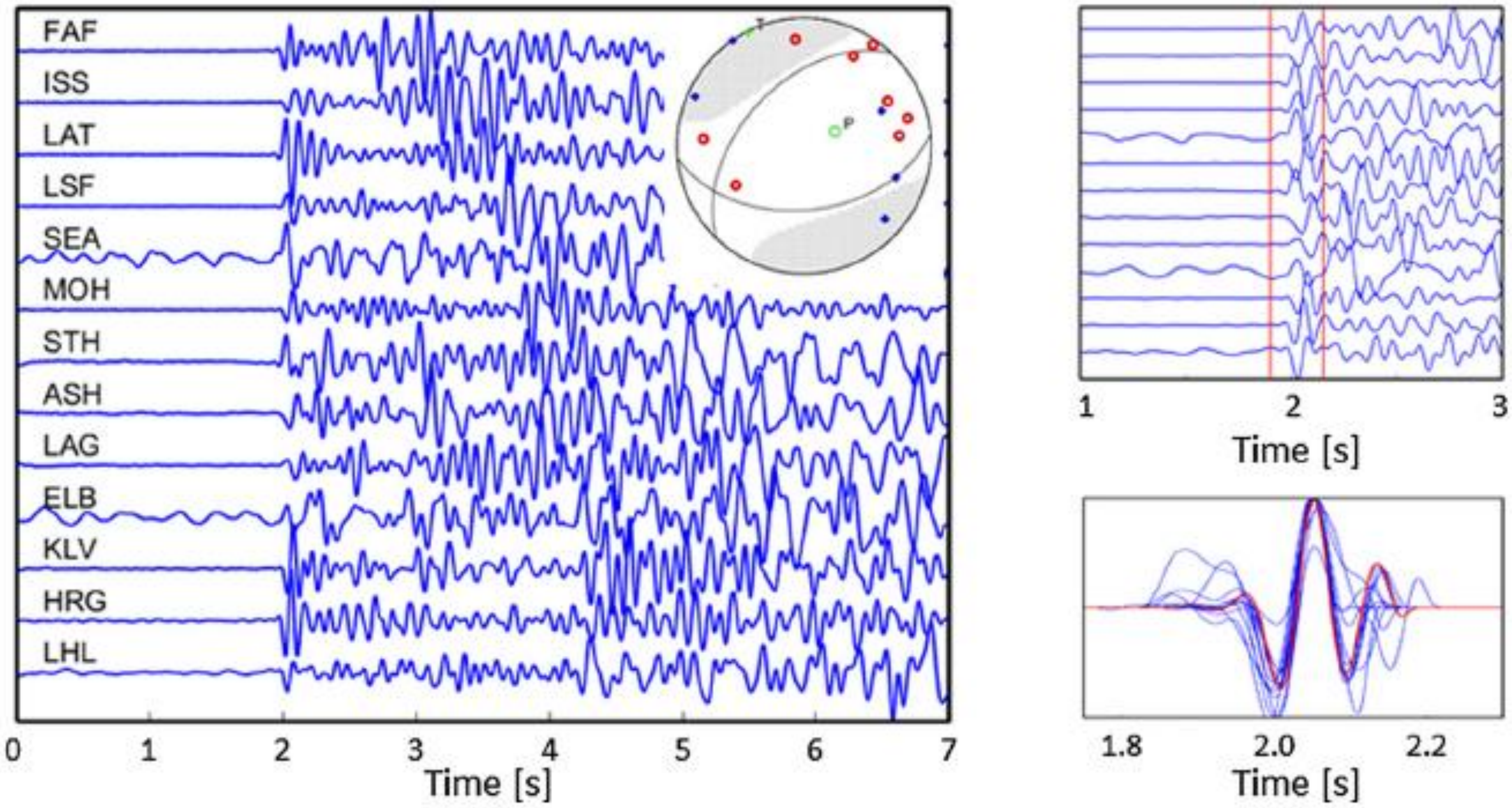

Input: Z-components of P wavelets
Method: inversion for full moment tensors using the PCA analysis

Focal mechanisms of selected 251 events

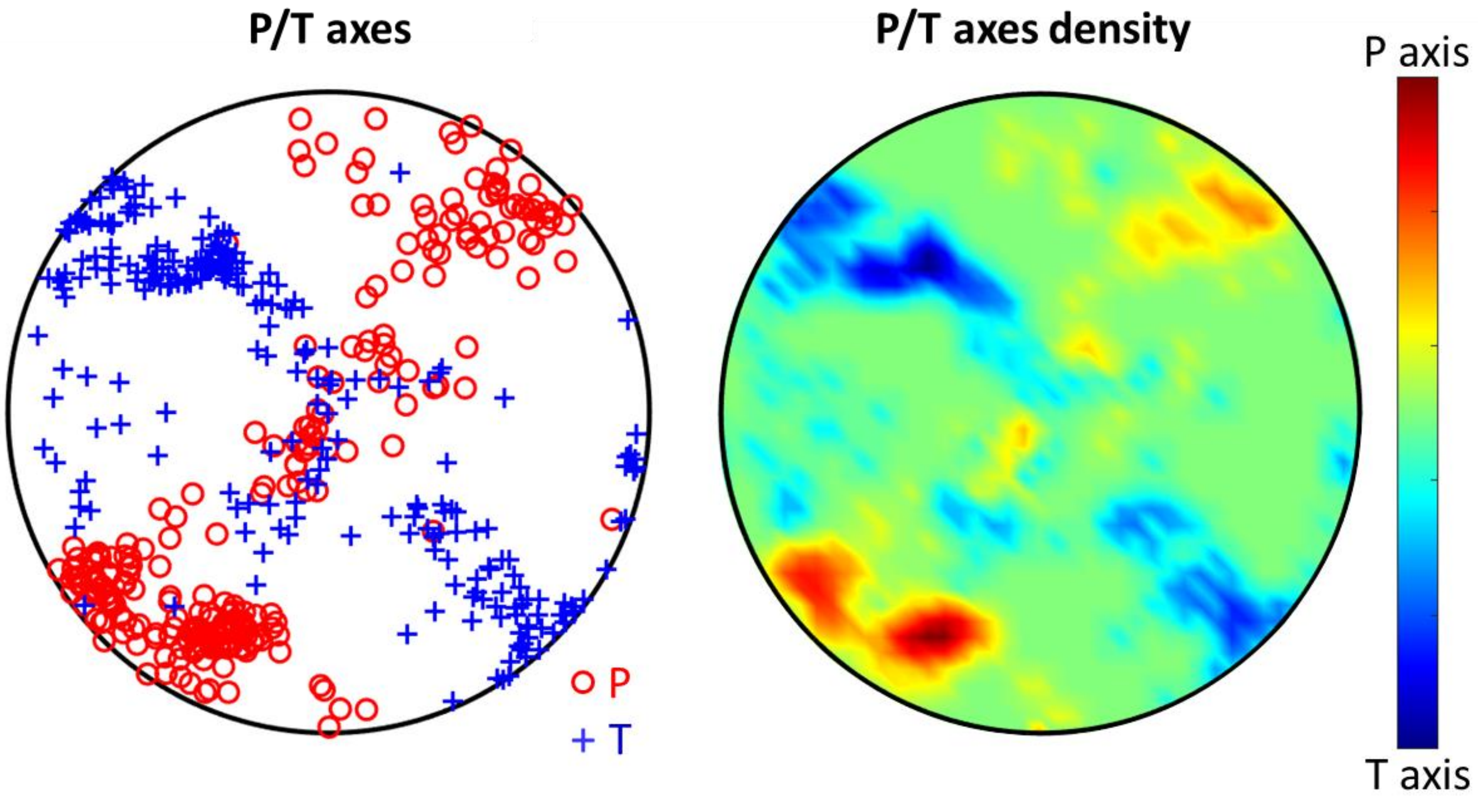

Reliable MTs criteria:

Number of stations > 10
RMS < 0.3
P/T axes deviation < 12°
ISO error < 12%

P/T axes are well-separated
mixed only in near-vertical directions

Hrubcová & Vavryčuk (Tectonophysics, 2023)

Classification of focal mechanisms

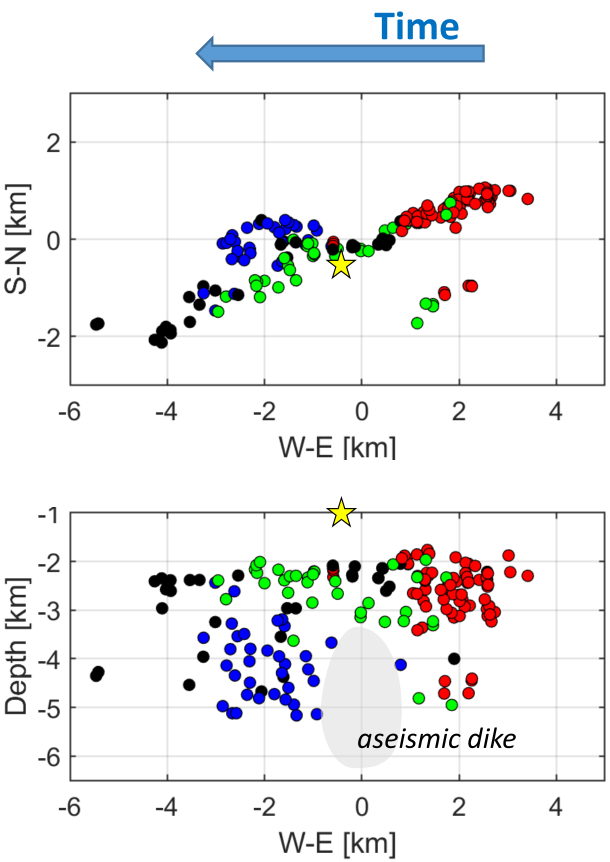

P/T axes

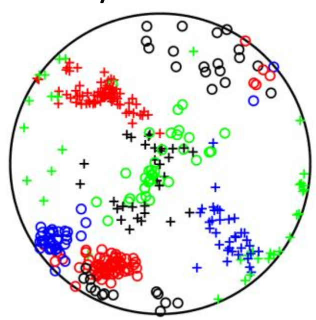

Volumetric components

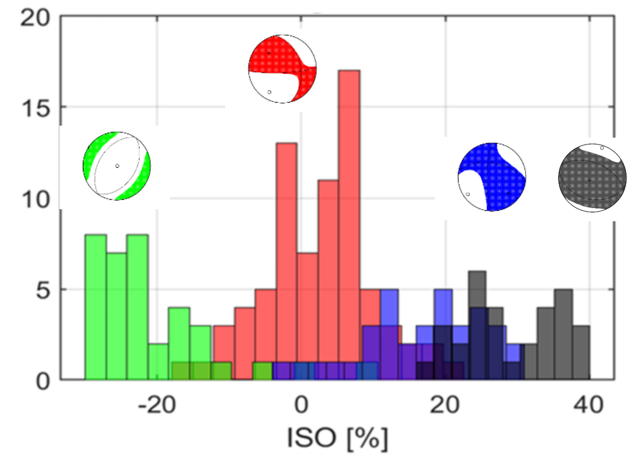

Distribution of events

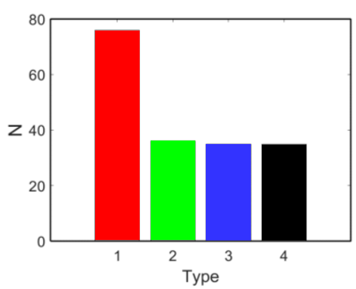

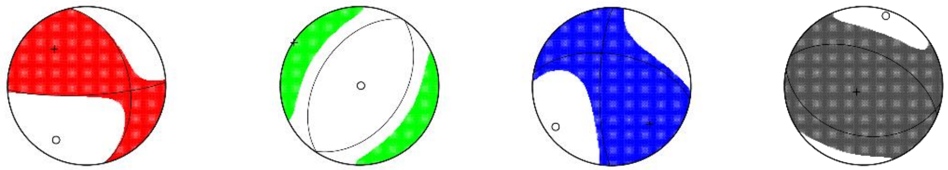

Focal mechanisms

- Shear (strike slips)
- Tensile (reverse)
- Compressive (normal)

Hrubcová & Vavryčuk (Tectonophysics, 2023)

Inversion for stress

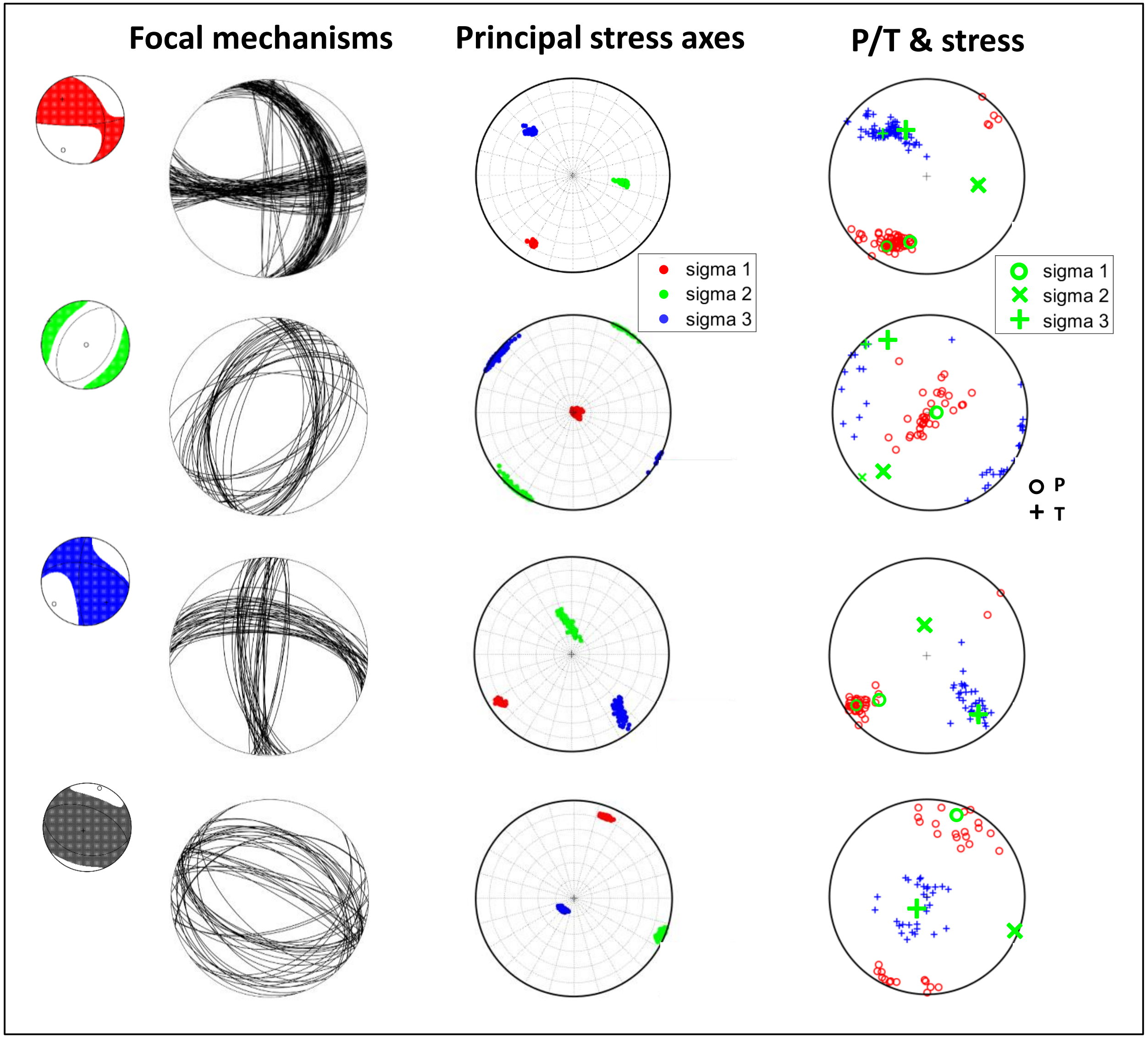

Stress pattern

- Strongly heterogeneous
- Stable principal stress directions
- Stress axes are switching
- Strike/reverse/ normal regimes
- Dominant stable extension (σ_3)

Hrubcová & Vavryčuk (Tectonophysics, 2023)

Tectonic interpretation

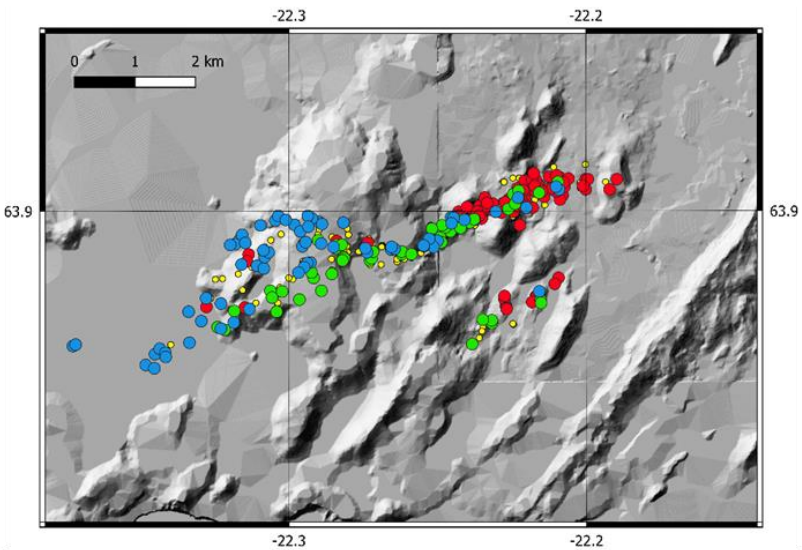

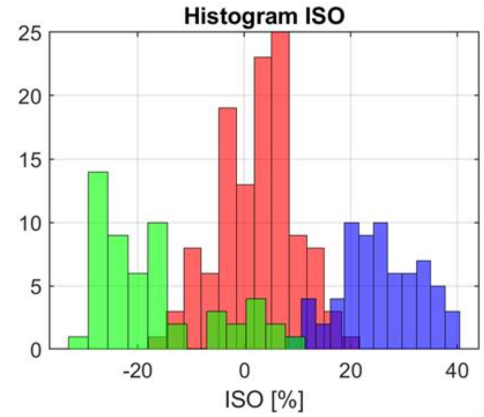

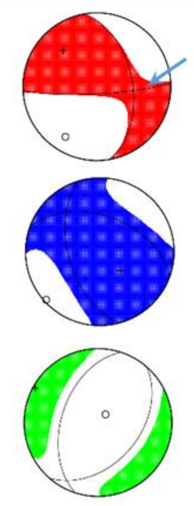

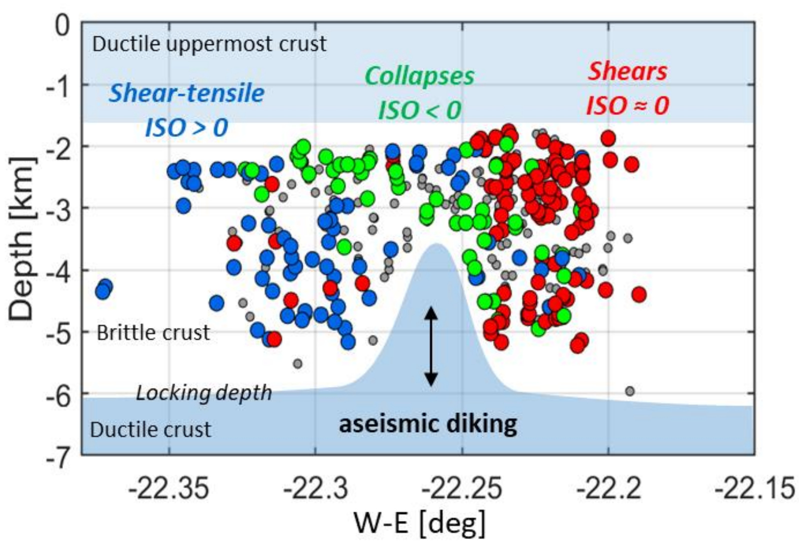

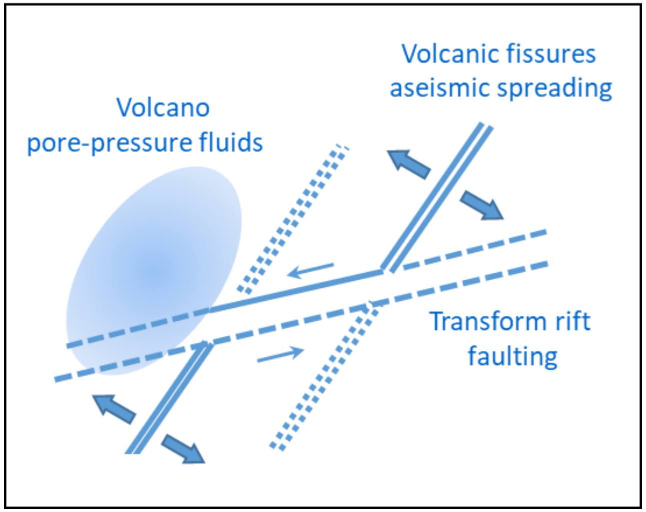

Hrubcová & Vavryčuk (Tectonophysics, 2023)

Summary
Iceland seismicity

Summary

Focal mechanisms provide key information about stress field

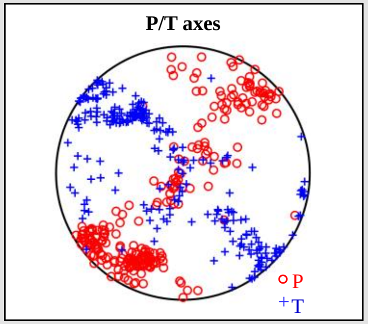

Diversity of FMs indicates heterogeneous stress pattern

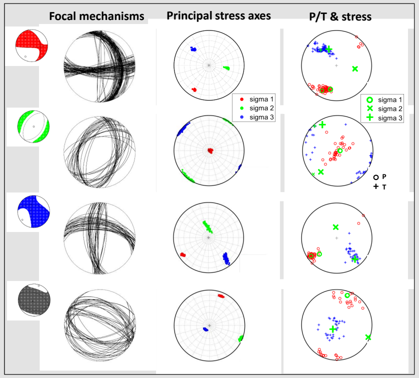

Stress inversion must be done for individual types of FMs

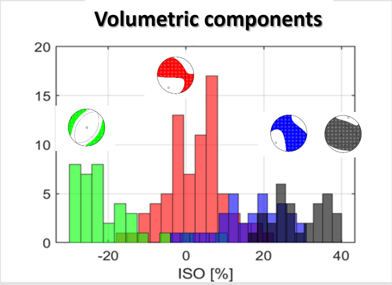

The presence of extensional/ compressional fracturing

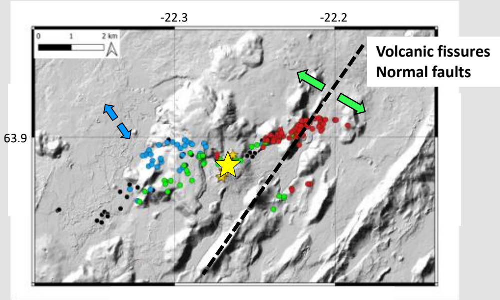

Stress directions are stable, but stress axes can switch

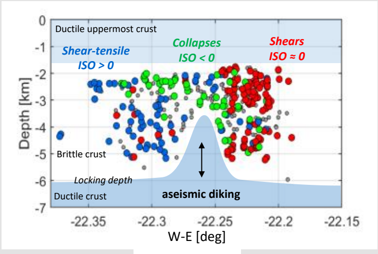

Seismicity delineated an aseismic dike activated in 2021

Stress variations in Tonga derived from deep earthquakes

Tonga subduction zone

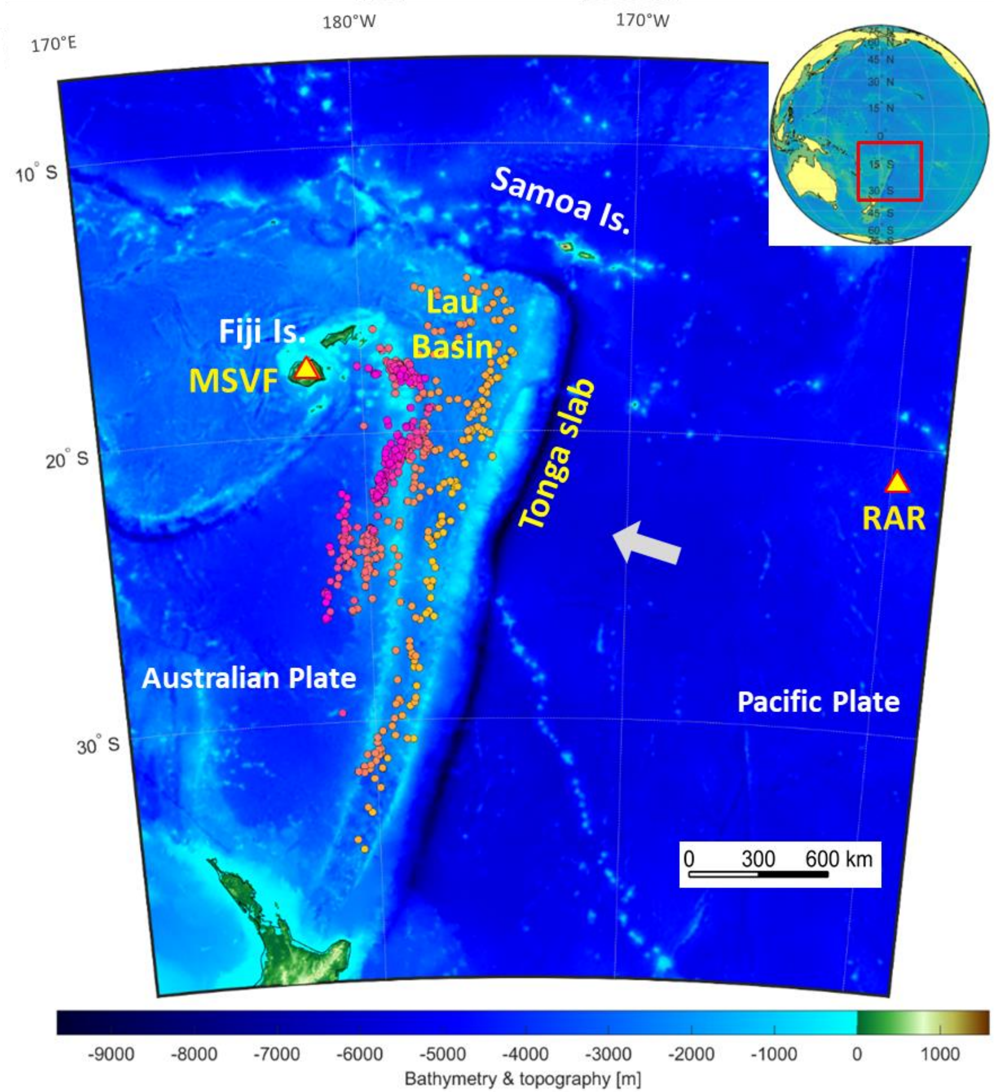

Tectonic setting:

- Collision of Pacific & Australian plates
- Fastest convergent boundary (24 cm/yr)
- The most active deep seismicity
- Complex geometry due to the interaction with the Samoa plume

Hrubcová et al. (JGR, 2023, submitted)

Data – Harvard CMT catalogue

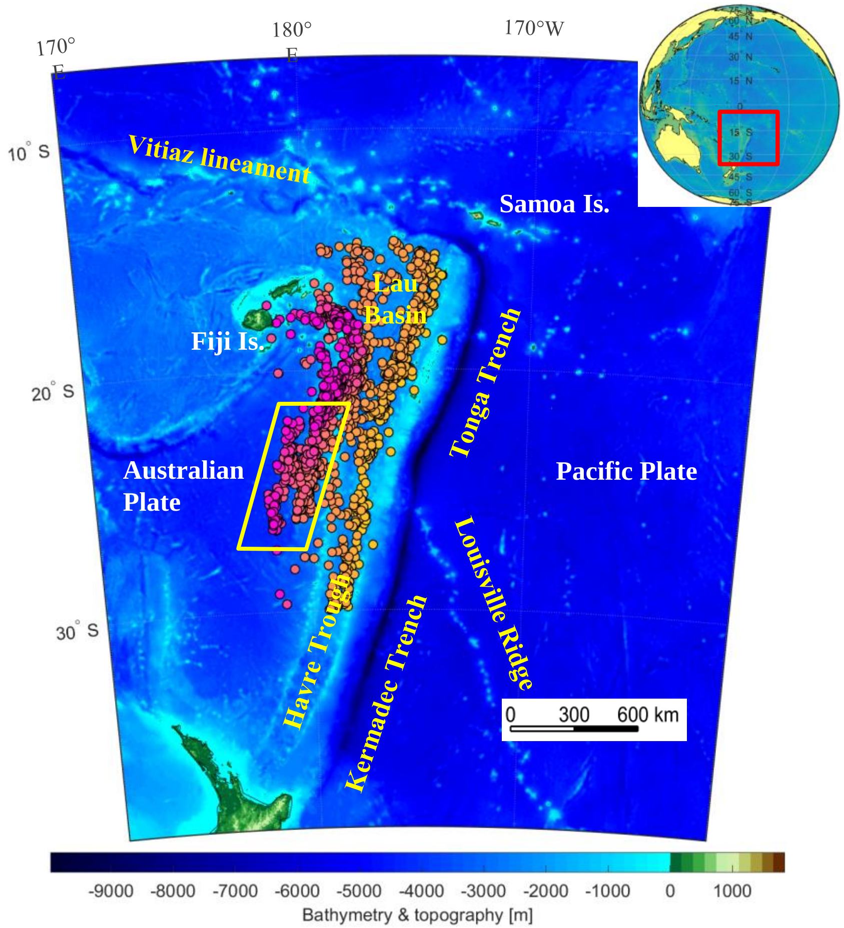

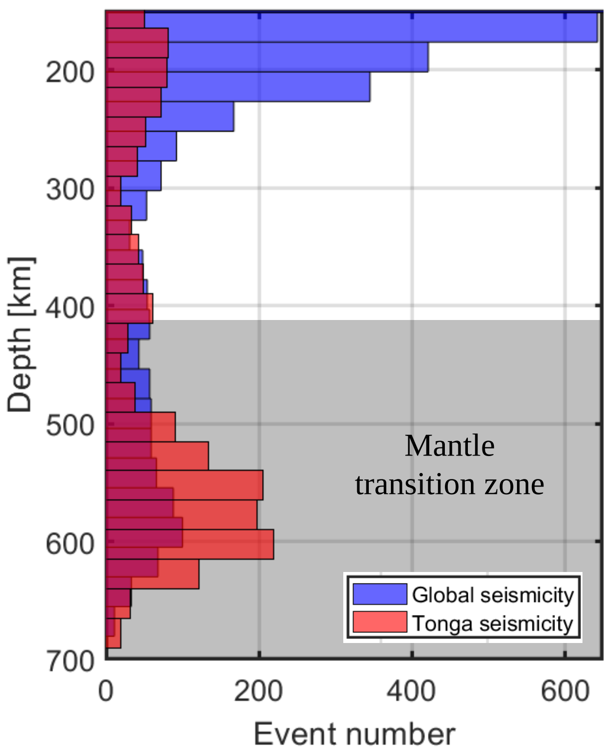

Hrubcová et al. (JGR, 2023, submitted)

Locations & focal mechanisms

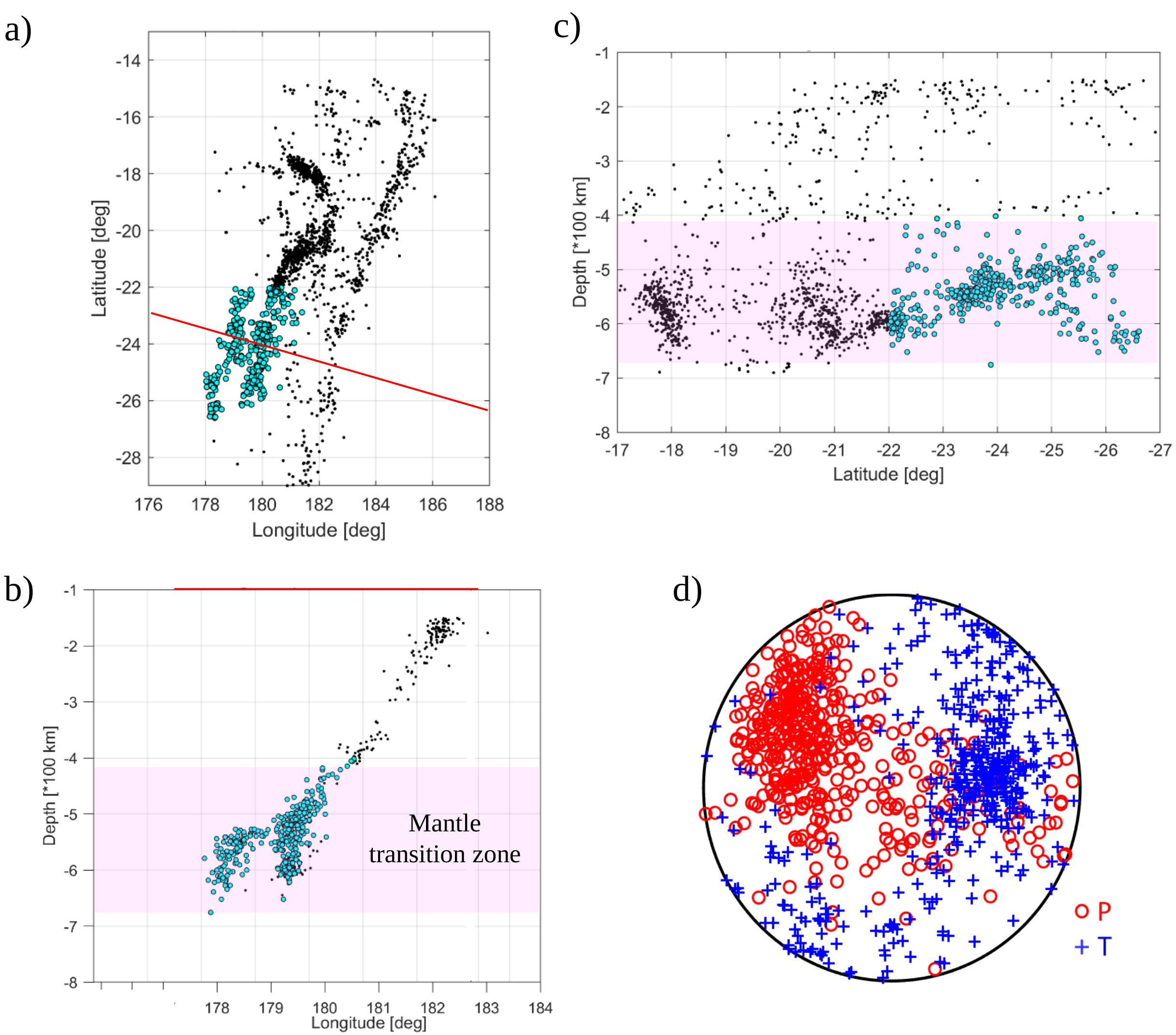

Global CMT Catalog

- Double seismic zone
- 430 earthquakes
- depths of 400-700 km
- mb >= 4.8
- period of 1976-2022
- Complex pattern of P/T axes

Hrubcová et al. (JGR, 2023, submitted)

Classification of focal mechanisms

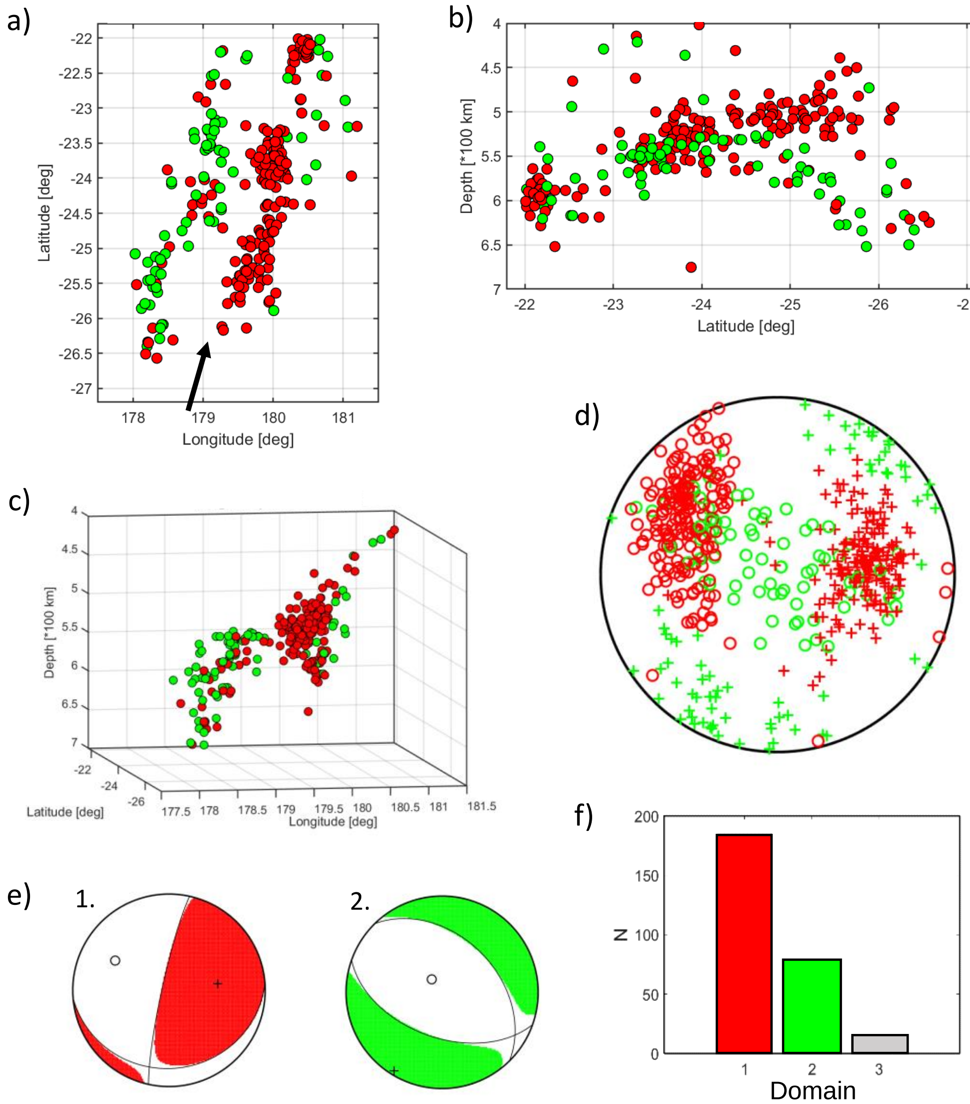

Clustering of FMs

- Double seismic zone
- 277 earthquakes with most reliable MTs
- Two domains separated in space
- Two different stress regimes

Hrubcová et al. (JGR, 2023, submitted)

Inversion for stress

P/T axes | **Mohr's diagram**

Domain 1

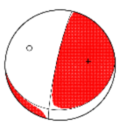

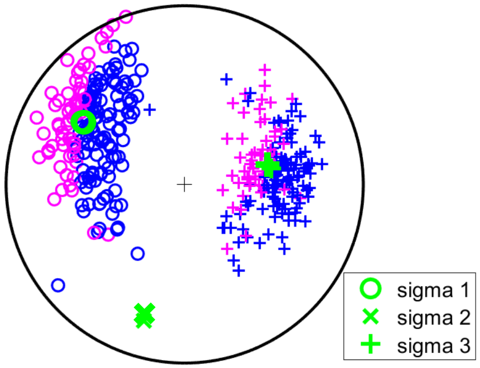

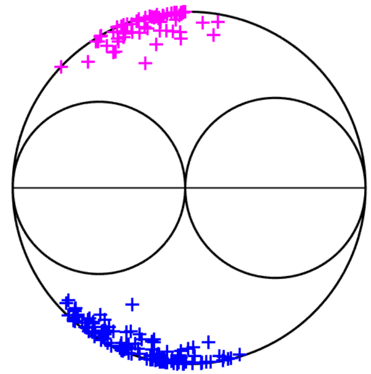

Domain 2

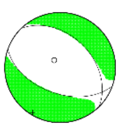

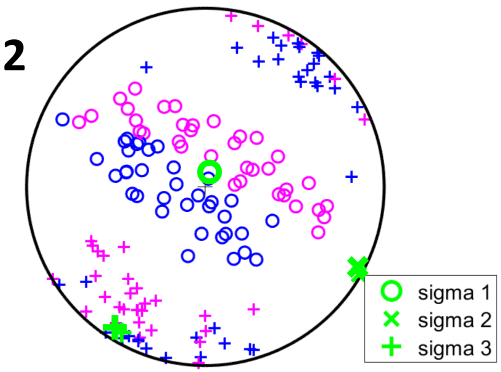

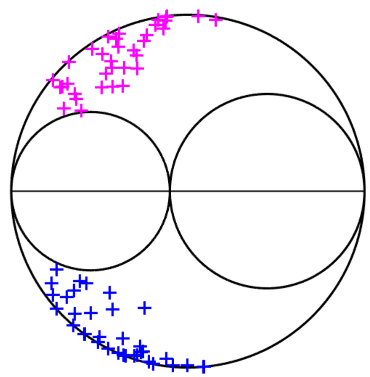

Domain 1

- condensed clusters of P/T axes
- low friction

Domain 2

- separated but scattered clusters of P/T axes
- high friction

Hrubcová et al. (JGR, 2023, submitted)

Orientation of fault planes

Nodal lines | **Fault plane solutions**

Domain 1

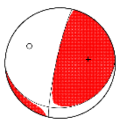

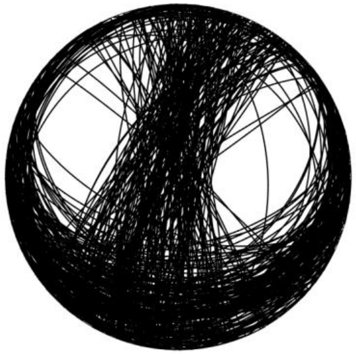

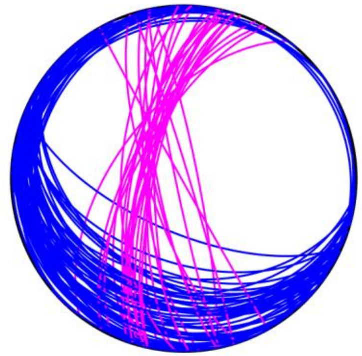

Domain 2

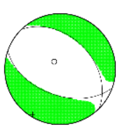

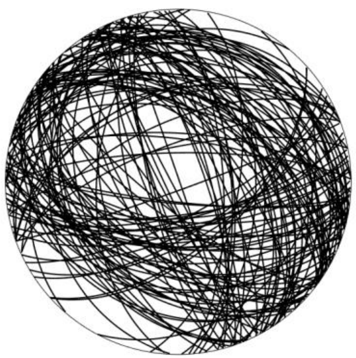

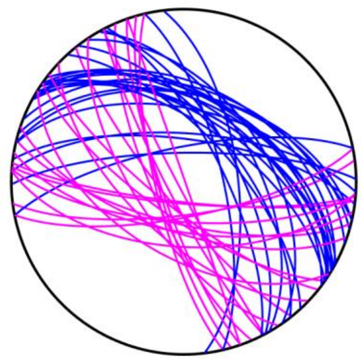

After instability
I > 0.8

After instability contrasts
ΔI > 0.15
Well-constrained

Domain 1

- Near-vertical or near-horizontal faults
- Near-horizontal faults prevail

Domain 2

- Faults planes are significantly inclined

Hrubcová et al. (JGR, 2023, submitted)

Tectonic interpretation

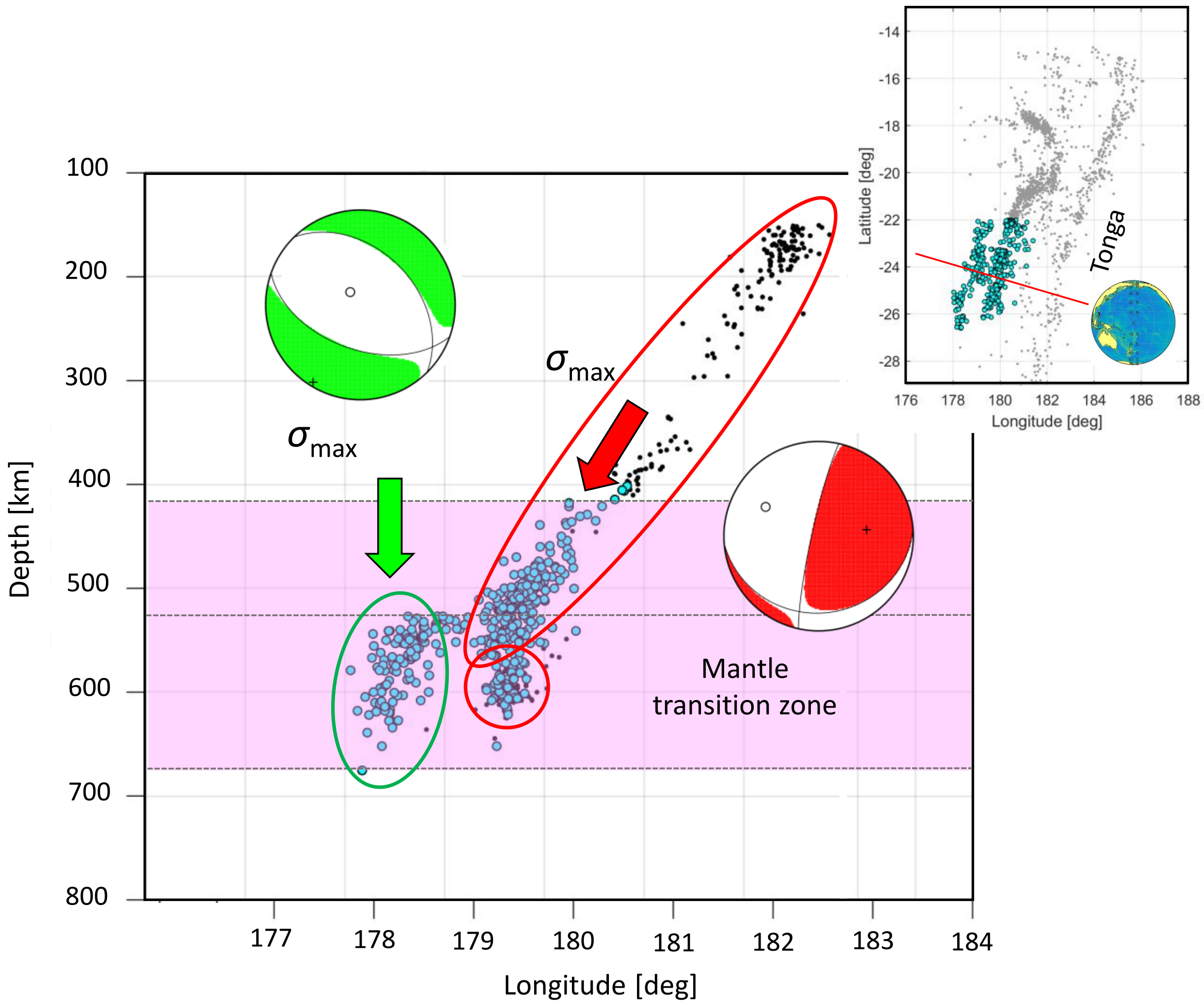

Domain 1

- Integral part of the slab
- Max. compression is along the down dip motion

Domain 2

- Detached slab segment
- Max. compression is vertical (lithostatic)

Hrubcová et al. (JGR, 2023, submitted)

Summary
Tonga deep seismicity

Summary

Focal mechanisms provide key information about stress field

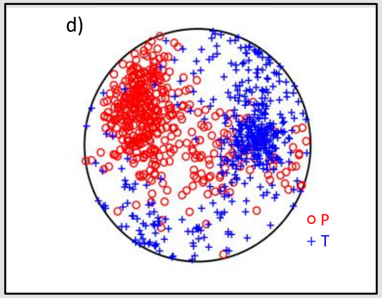

Diversity of FMs indicates heterogeneous stress pattern

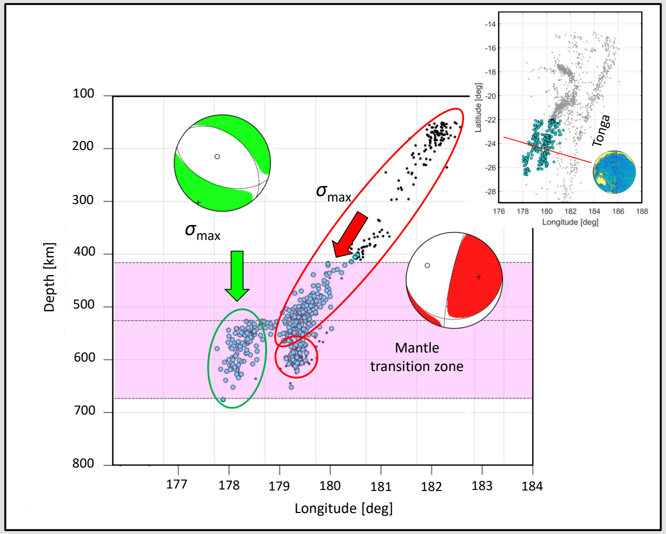

Stress inversion revealed a detached slab segment

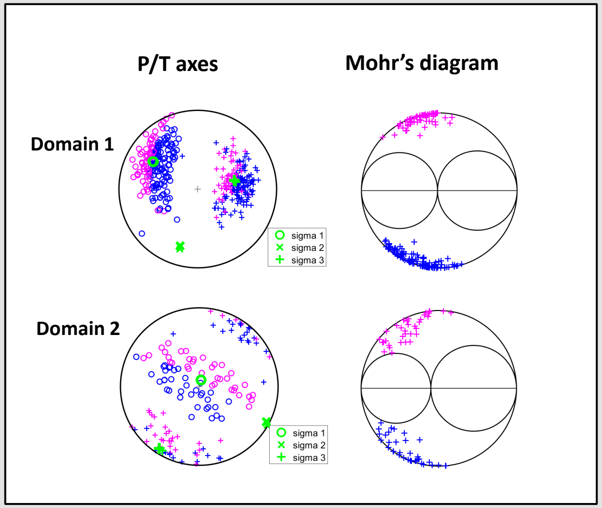

Two types of FMs and two different stress domain


Fagradalsfjall eruption – 19 March 2021
Thank you for attention

Attenuation of seismic waves in the area of REYKJANET (Iceland)

Jiří Málek and Lucia Fojtíková

Institute of Rock Structure and Mechanics CAS,
Department of Seismotectonics,
V Holešovičkách 41, 182 09, Prague, Czech Republic
Malek@irsm.cas.cz* , *Fojtikova@irsm.cas.cz

Prague, December, 2023

Overlook:

- Motivation
- Selection of seismograms
- Amplitude determination
- Method
- P-wave attenuation
- S-wave attenuation
- Local magnitude for REYKJANET
- Amplitude tomography (preliminary results)

Motivation:

Attenuation model is necessary for seismic hazard assessment
Site-specific Ground Motion Prediction Equations (GMPE)

Attenuation anomalies of S-waves can be connected with partially melted rocks and with a high-temperature localities

The same method could be used also for Vrancea region

Selection of seismograms:

- **December 2019 – October 2020 - before erruption**
- **Wide range of magnitudes 0.2 – 5.6 (IMO type 1)**
- **Sharp P-wave onsets at seismograms**
- **Detectable S-wave onsets,**

  we use only seismograms with both P and S onsets
- **Epicenters distributed inside REYKJANET**

Selection of seismograms:

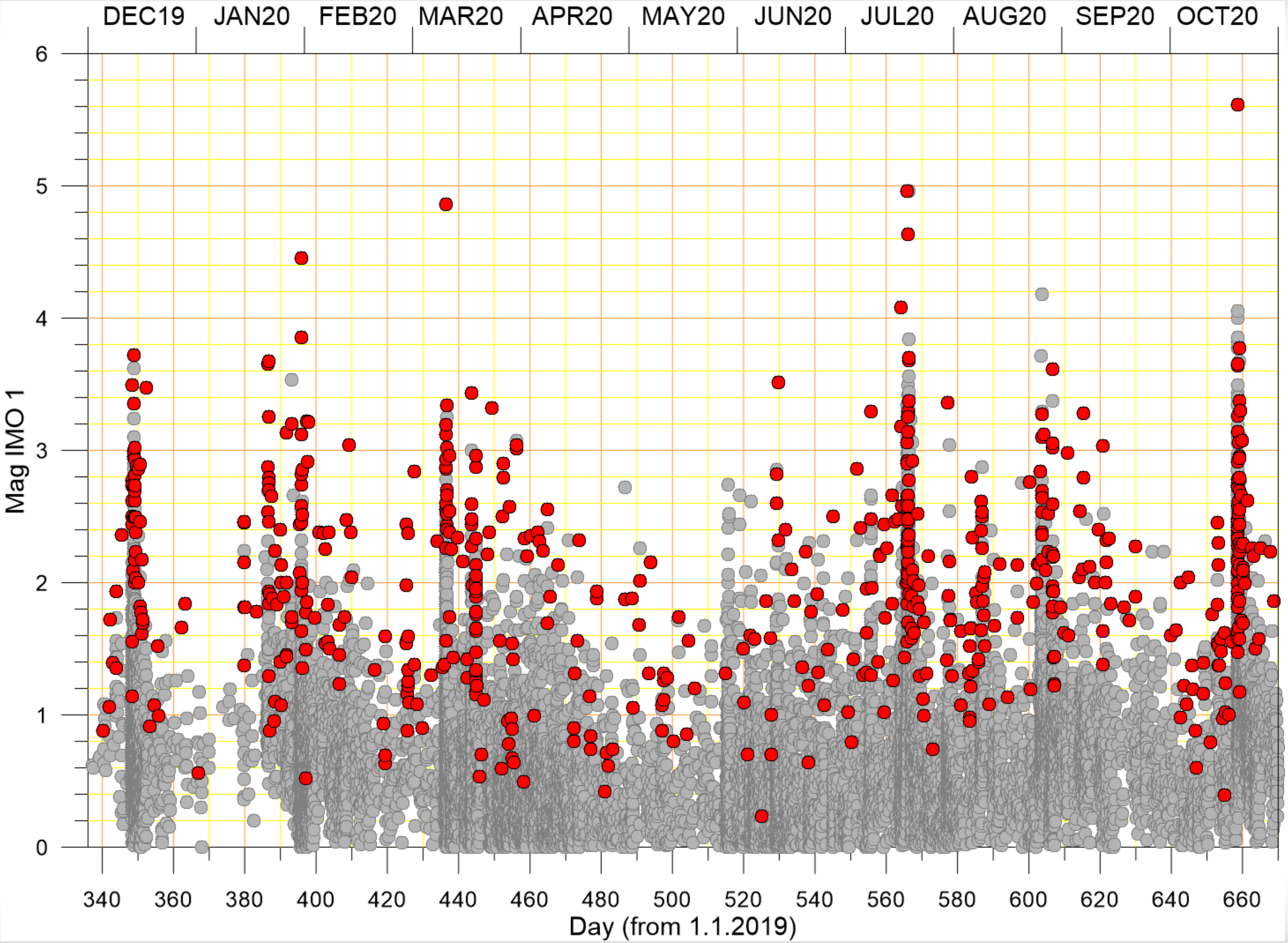

Selection of seismograms:

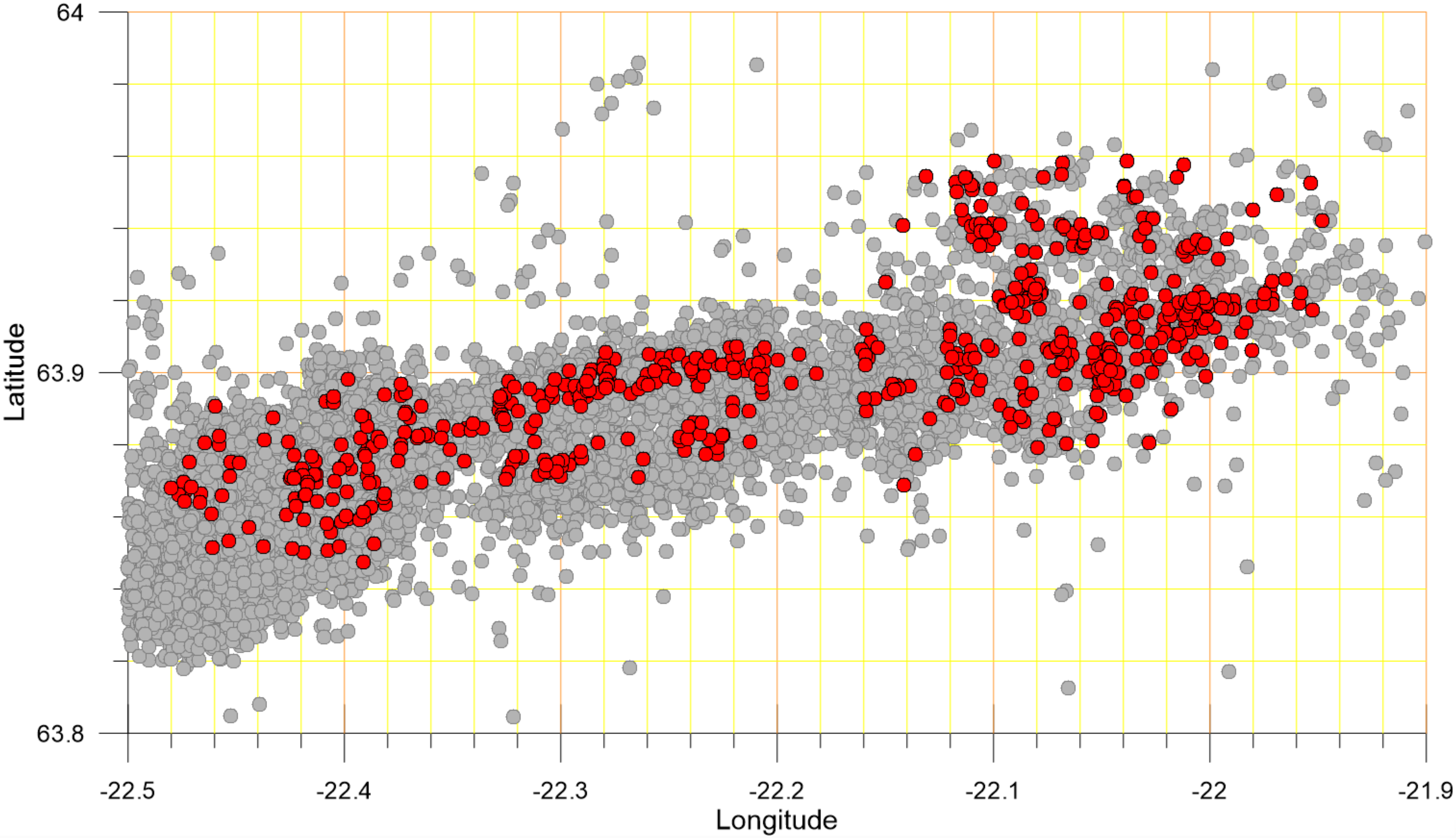

Selection of seismograms:

681 Earthquakes

14 REYKJANET stations

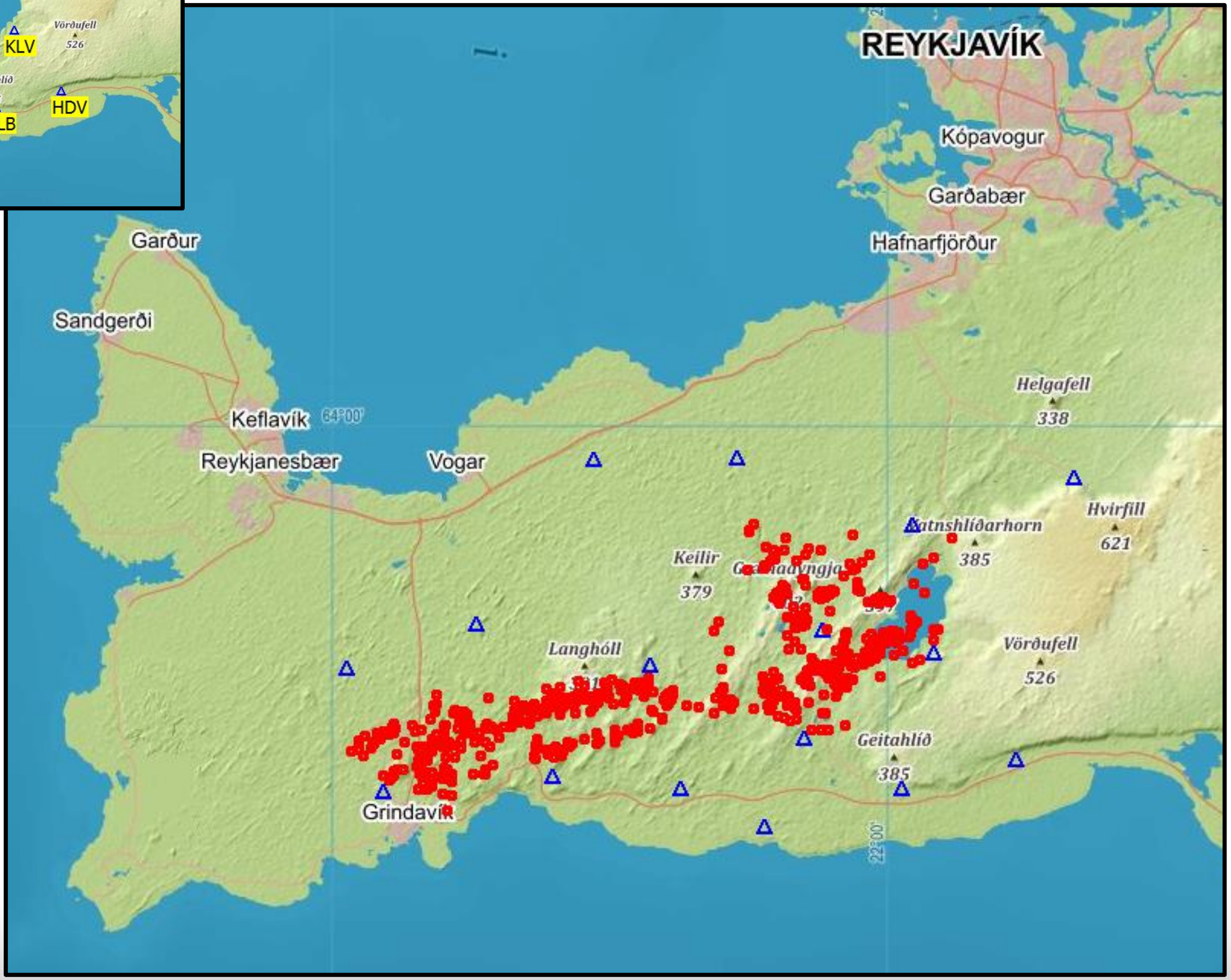

Selection of seismograms:

681 Earthquakes

14 REYKJANET stations

8614 Seismograms 90 %

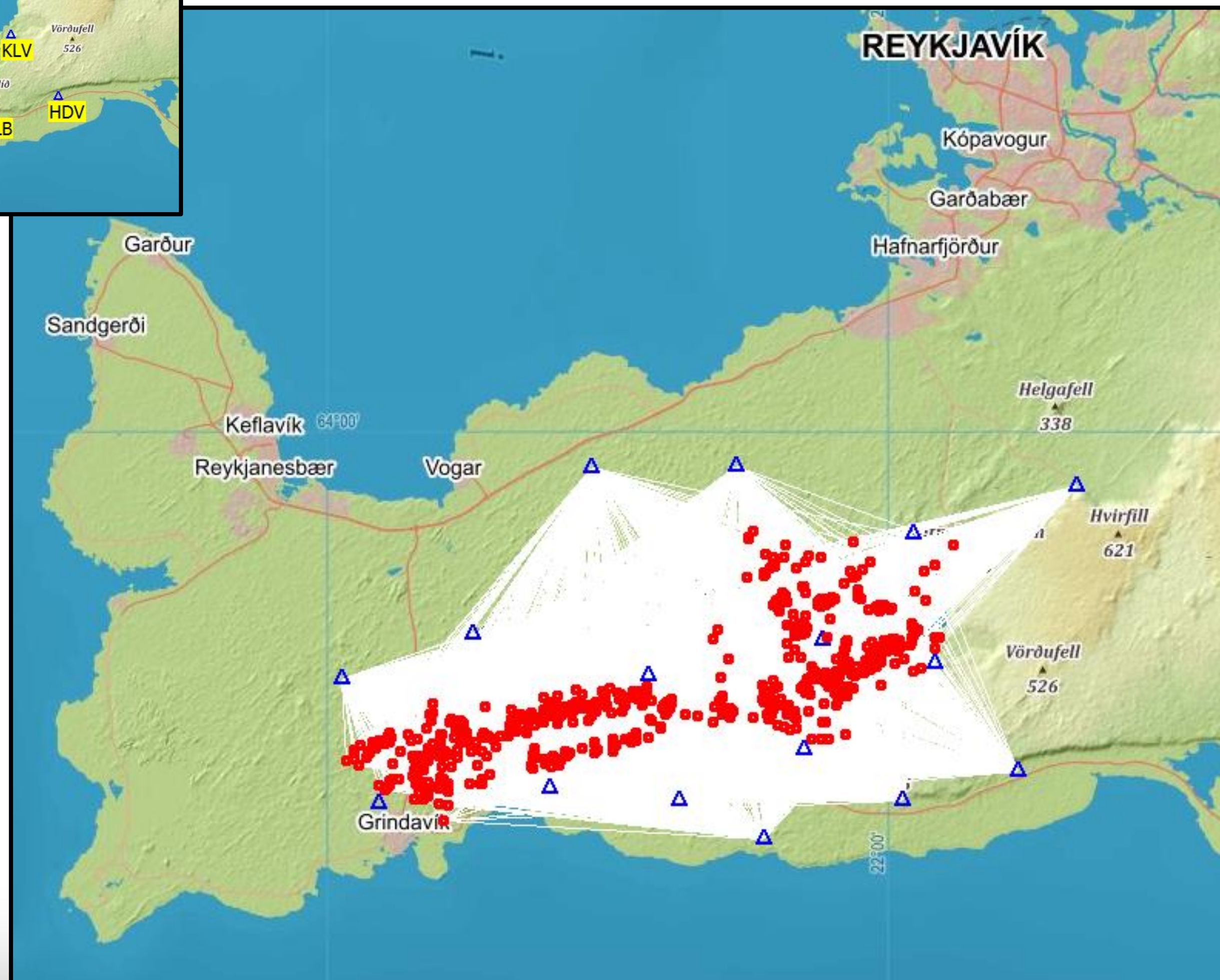

Attenuation of seismic waves in the area of REYKJANET

Amplitude determination:

APZ **Maximum amplitude of the velocity of P wave, vertical component, the first peak after onset polarity**

ASZ **Maximum amplitude of the velocity of S wave group, vertical component, the maximum in window from S-onset, length Ts-Tp without polarity, only absolute value**

High-pass filter from 1 Hz (to avoid microseisms)
Automatic mode

Amplitude determination:

FAF 15.12.2019 20:15:20

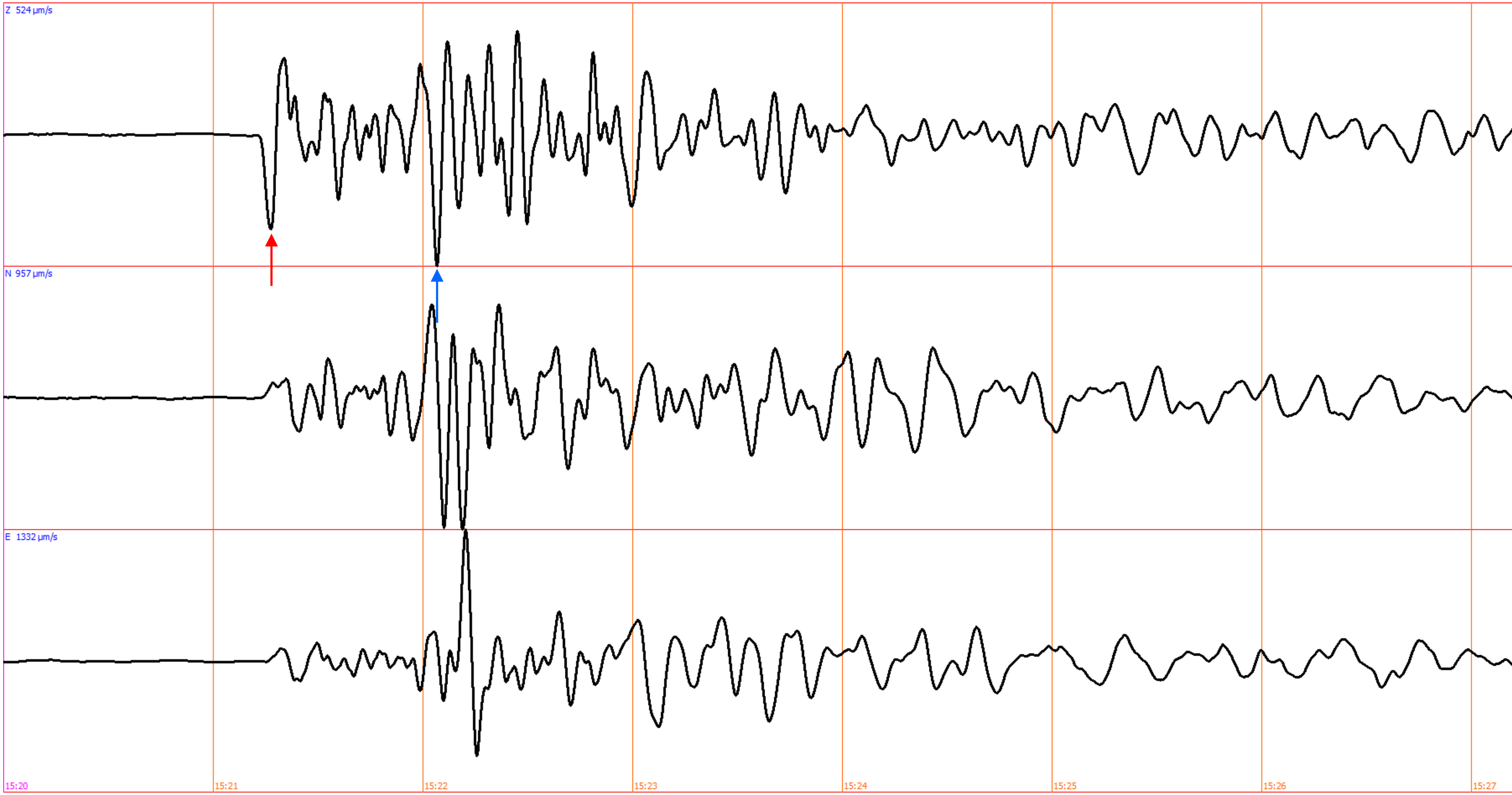

Amplitude determination:

LAG 15.12.2019 20:15:22

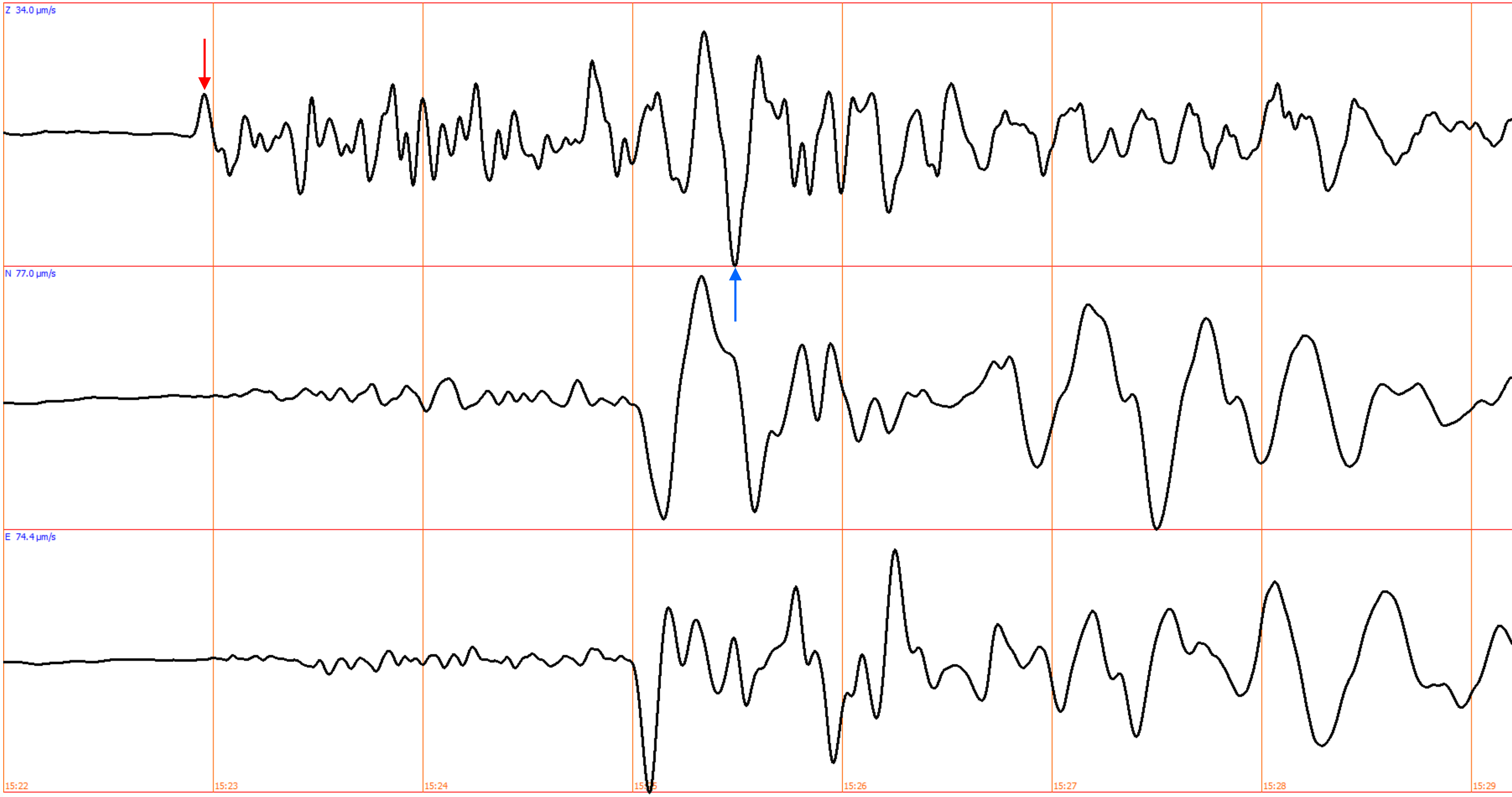

Amplitude determination:

KLV 15.12.2019 20:15:22

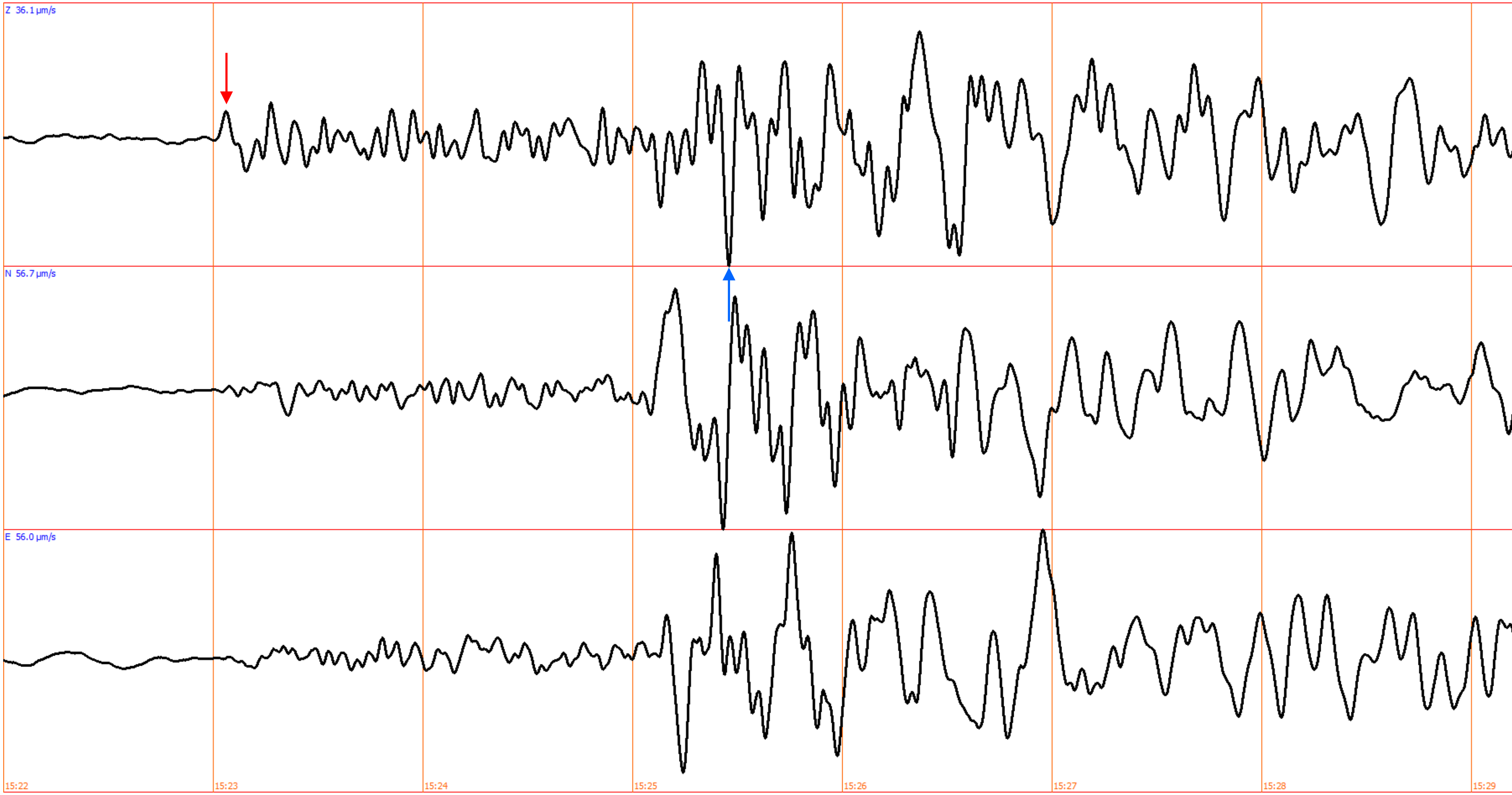

Amplitude determination:

KLV 15.7.2020 15:34:40

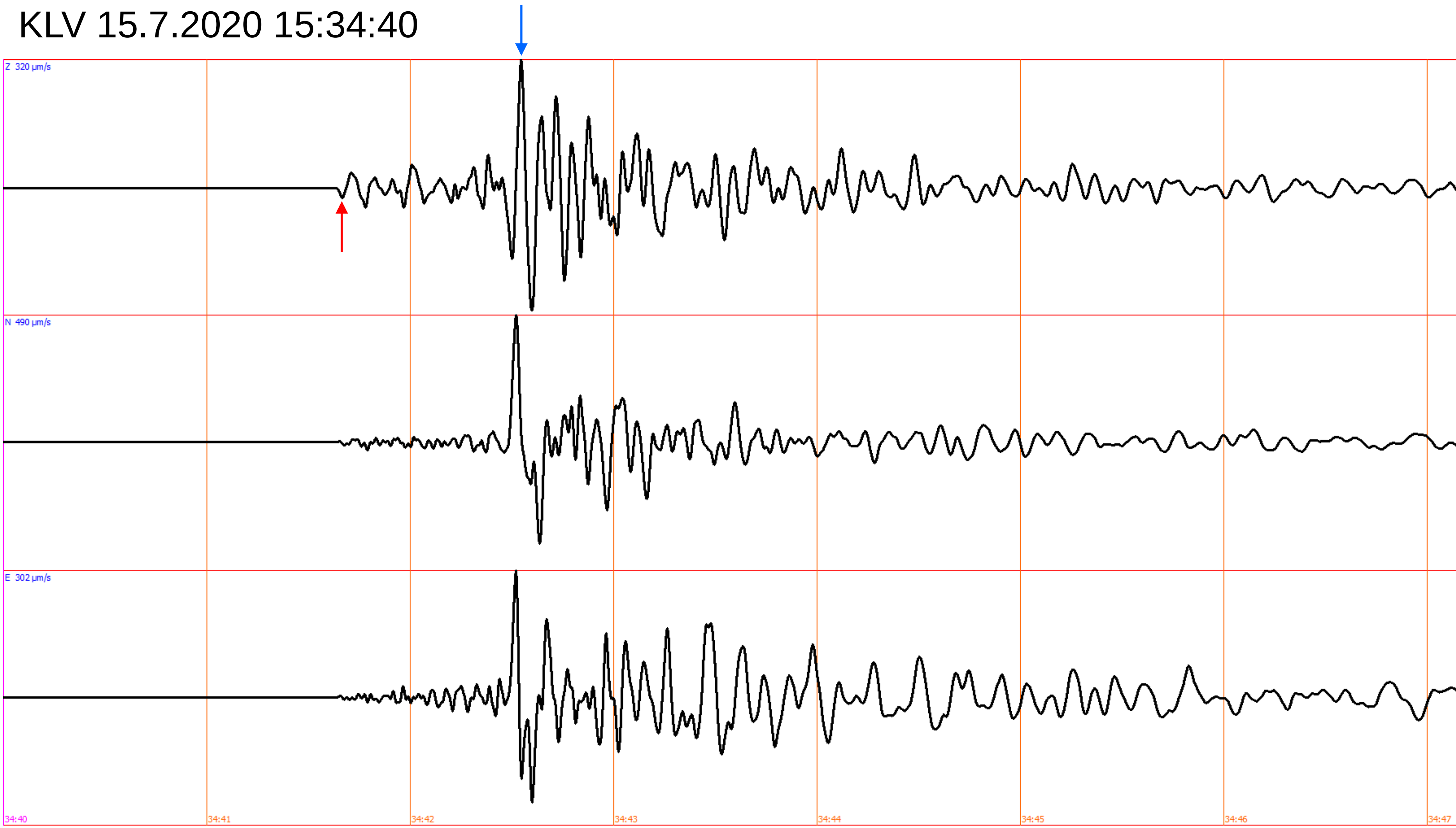

Amplitude determination:

SEA 15.7.2020 15:34:41

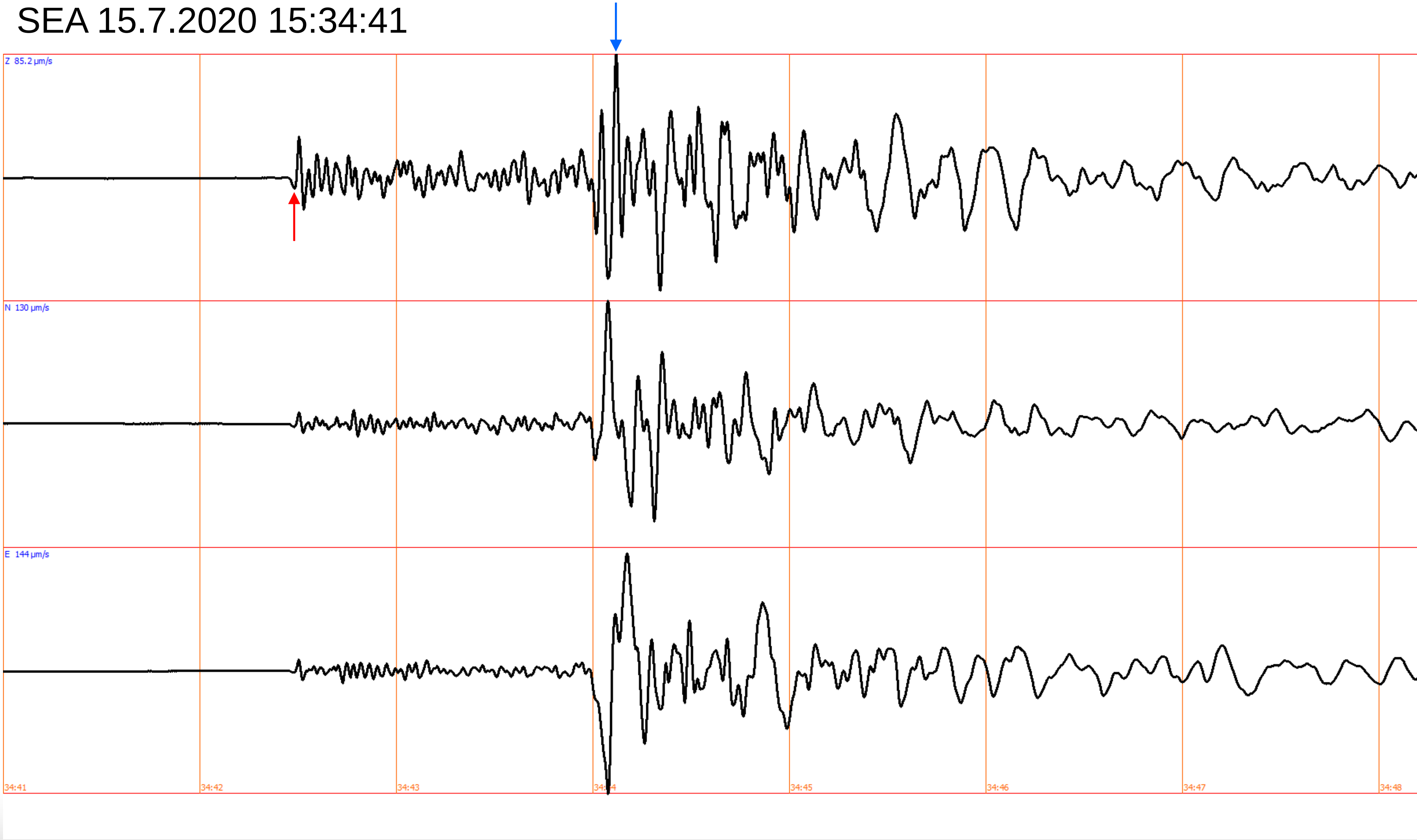

Amplitude determination:

LAT 15.7.2020 15:34:41

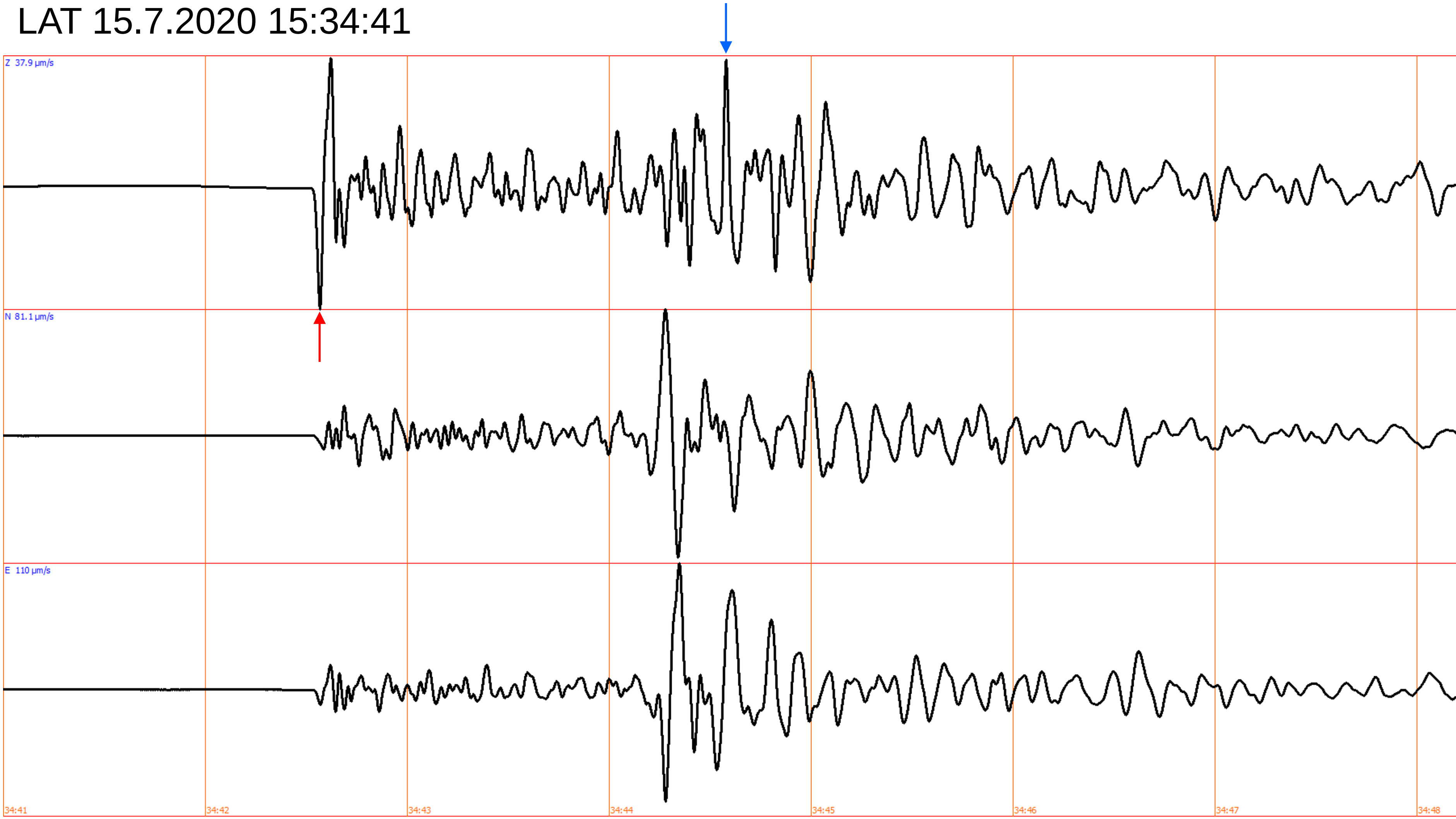

Method: overdetermined inverse problem solution

$$A_i^j = A_0\, 10^{M_i - \alpha(r_H - r_0)}\, G\, S^j\, V_i$$

$$\log(A_i^j) = \log(A_0^j) + M_i - \alpha(r_H - r_0) + \log(G) + \log(S^j) + \log(V_i)$$

A_i^j	Measured amplitude for i-th earthquake at j-th station	Data (8614)
r_H	Hypocentral distance	
r_0	Reference distance 10 km	
A_0	Amplitude for magnitude 0 at reference distance	Parameter
M_i	Magnitude of i-th earthquake	
G	Geometrical spreading r_0/r_H	
α	Attenuation coefficient	Parameter
S^j	Local amplification constant for j-th station	
V_i	Radiation pattern for i-th earthquake (only for APZ)	

P-Wave (APZ) attenuation

$$\log(A_i^j) - \log(A_0) - M_i = -\alpha(r_H - r_0) + \log(G) + \log(S^j) + \log(V_i)$$

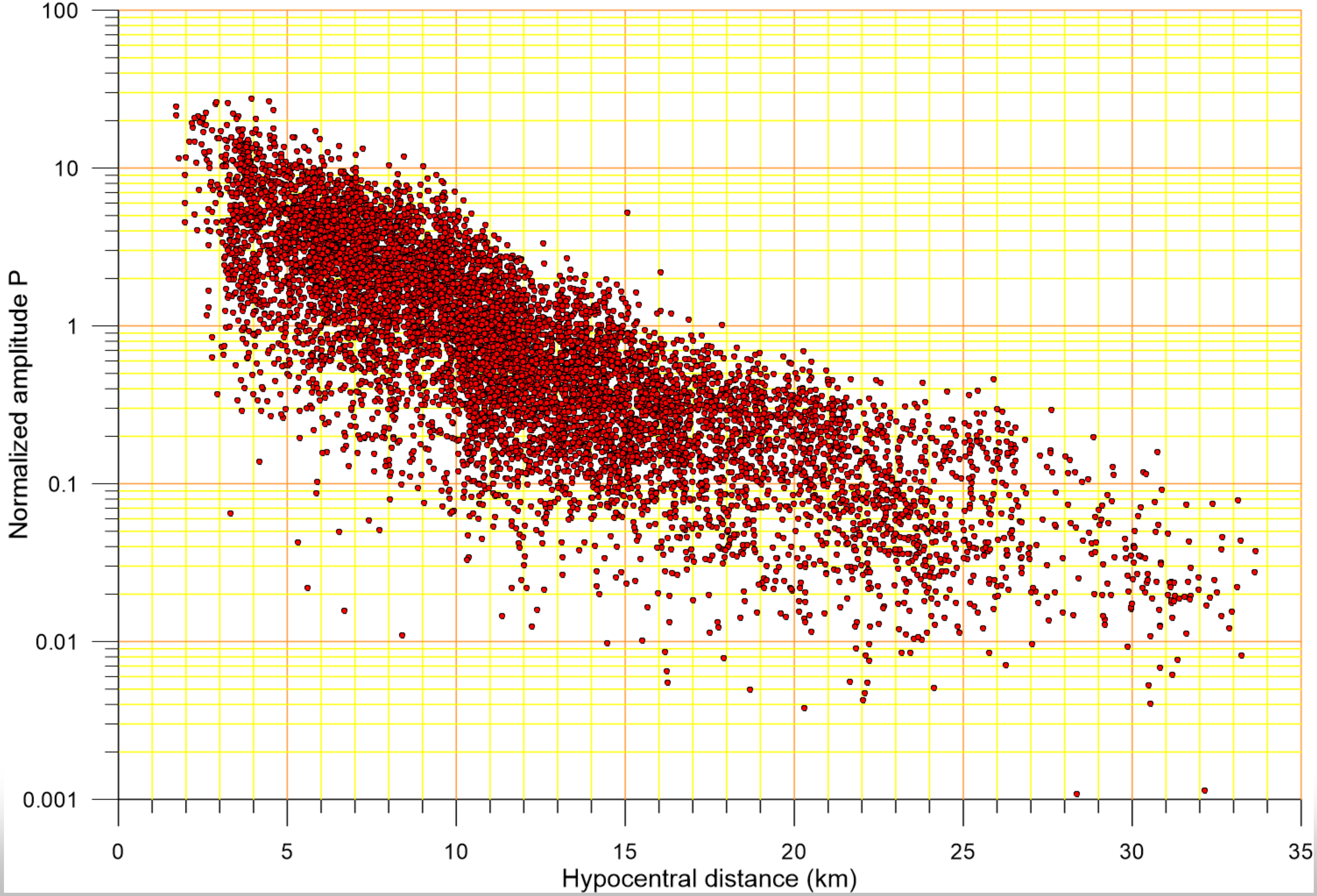

P-Wave (APZ) attenuation

$$\log(A_i^j) - \log(A_0) - M_i - \log(S^j) = -\alpha(r_H - r_0) + \log(G) + \log(V_i)$$

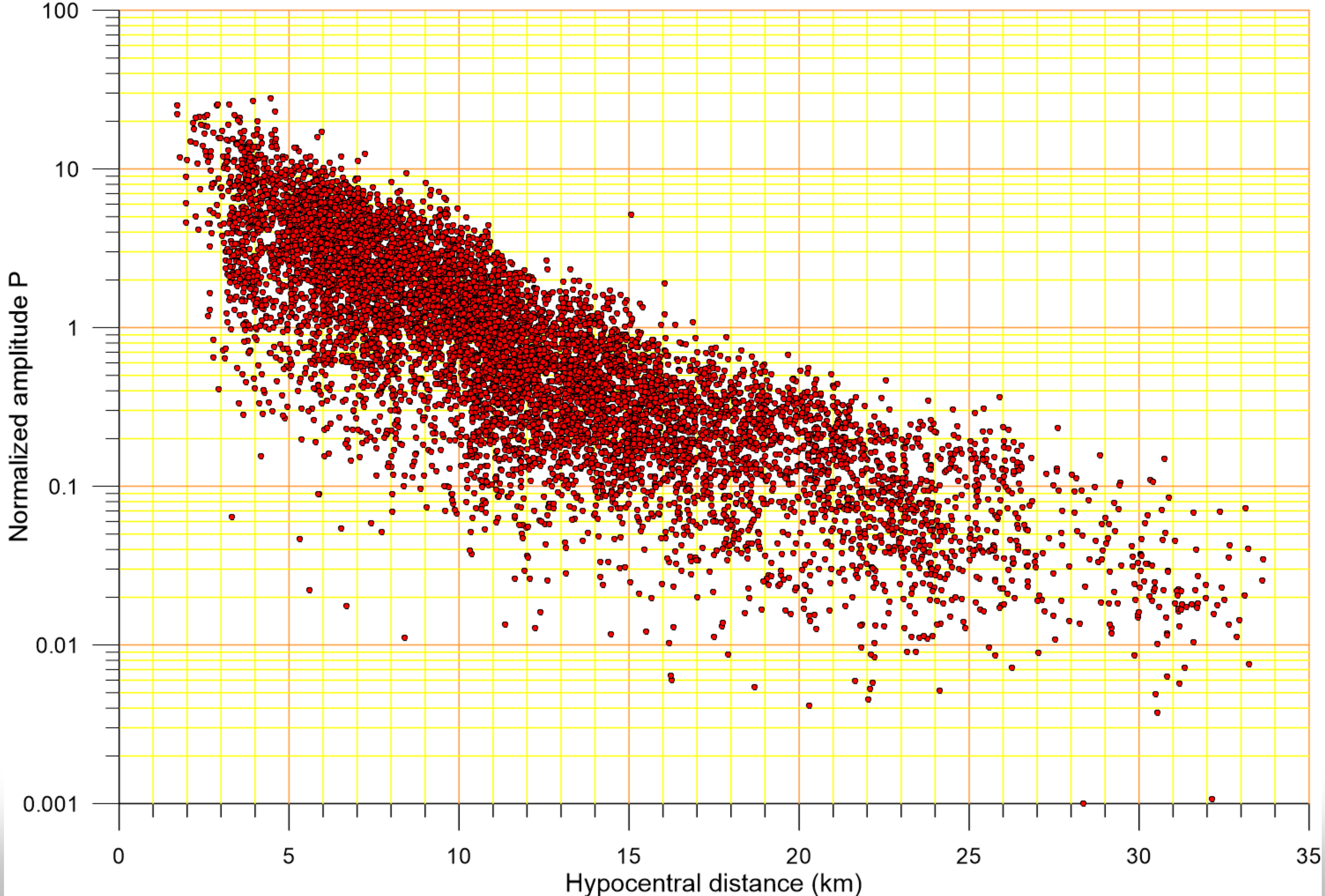

P-Wave (APZ) attenuation

$$\log(A_i^j) - \log(A_0) - M_i - \log(S^j) - \log(G) = -\alpha(r_H - r_0) + \log(V_i)$$

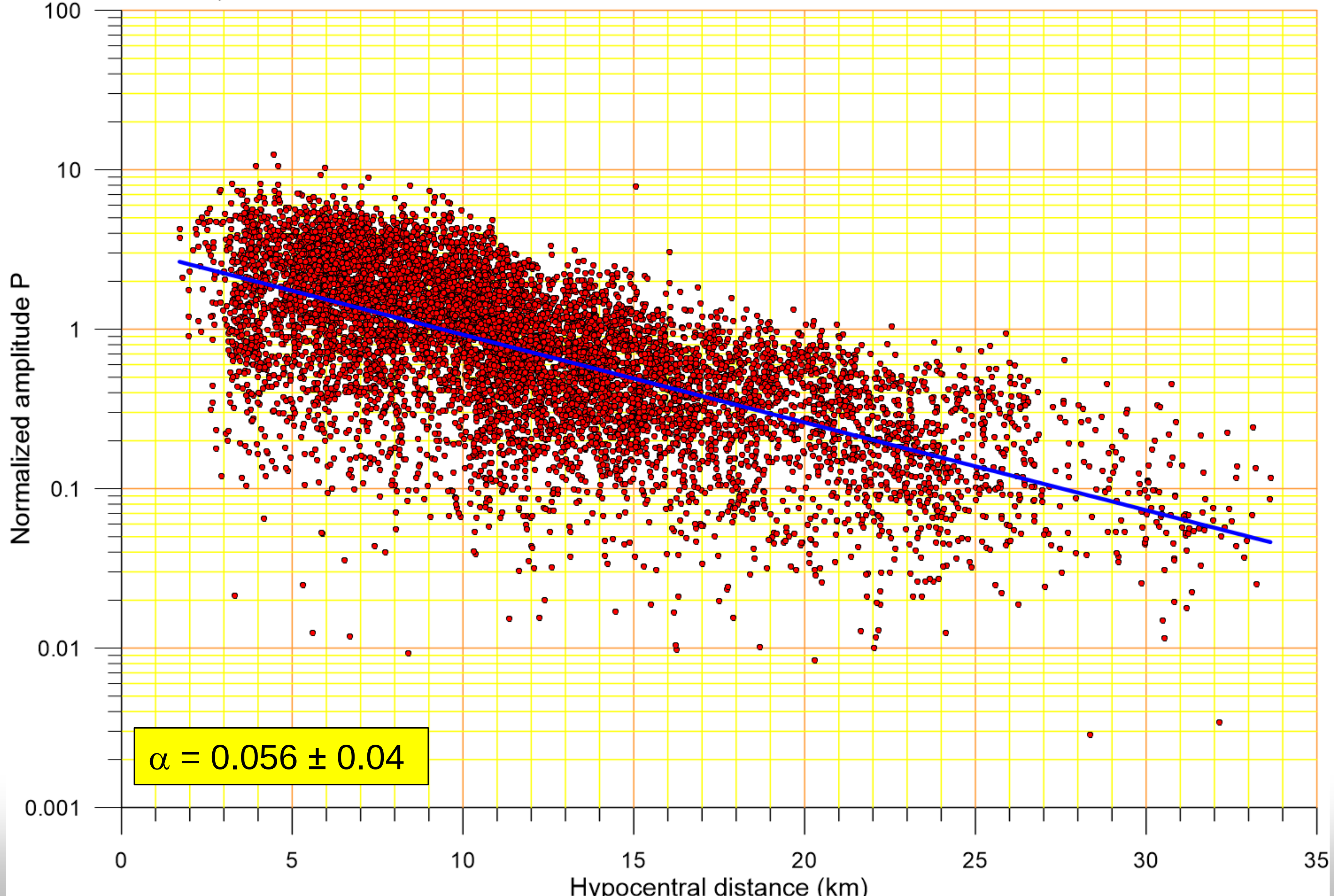

P-Wave (APZ) attenuation

$$\log(A_i^j) - \log(A_0) - M_i - \log(S^j) - \log(G) - \alpha(r_H - r_0) = \log(V_i)$$

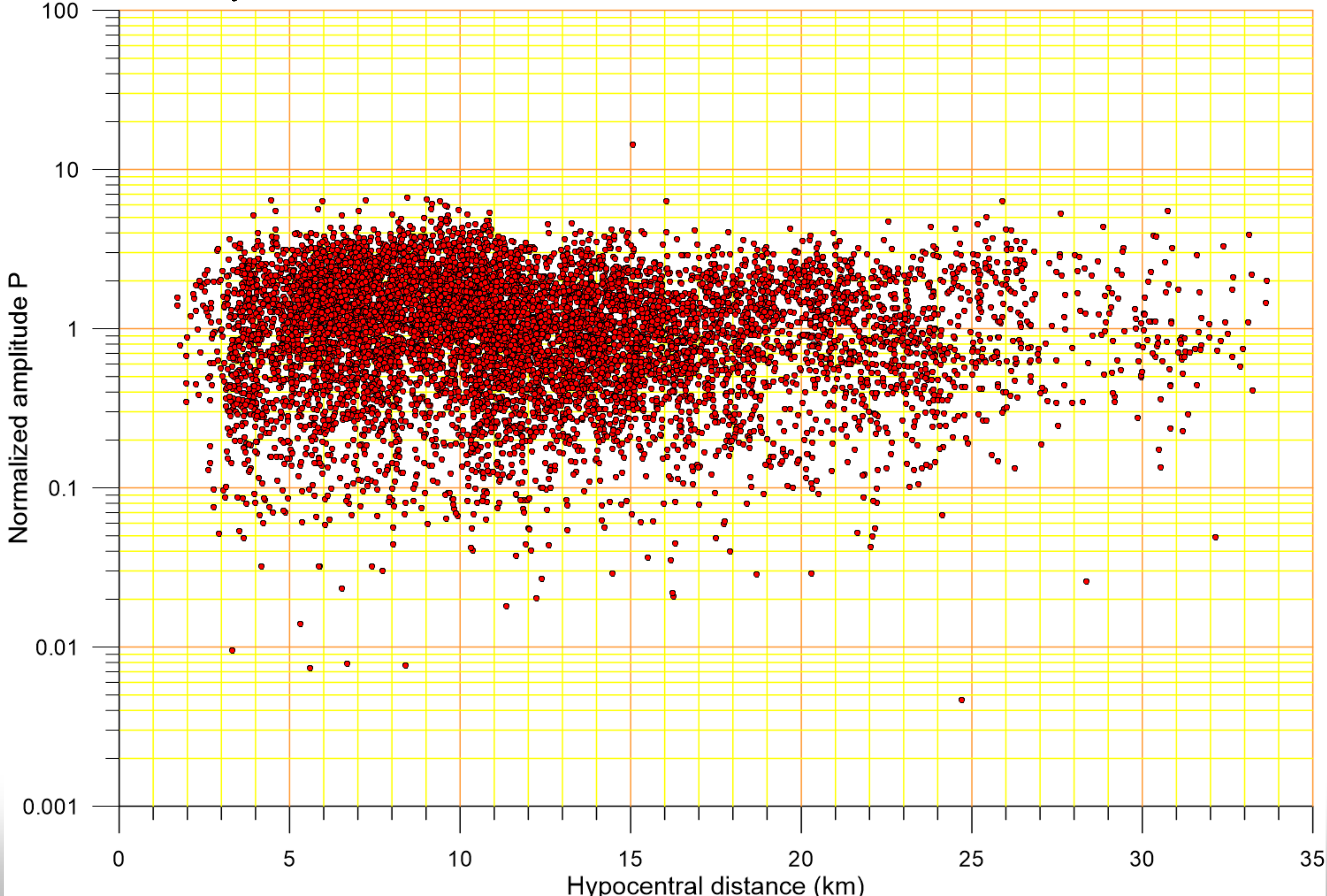

P-Wave (APZ) attenuation

$$\log(A_i^j) - \log(A_0) - M_i - \log(S^j) - \log(G) - \alpha(r_H - r_0) - \log(V_i) = 1$$

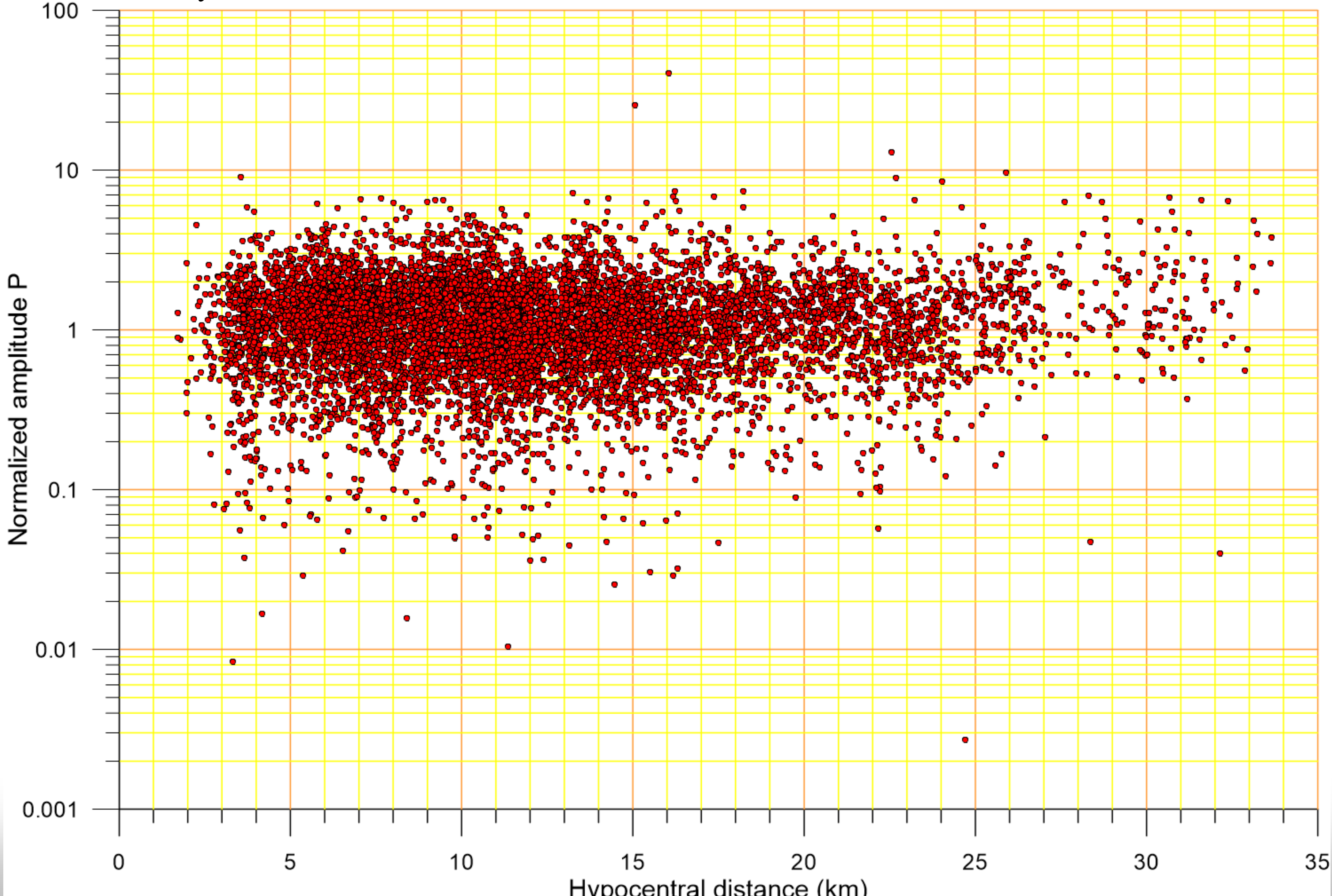

S-Wave (ASZ) attenuation

$$\log(A_i^j) - \log(A_0) - M_i = -\alpha(r_H - r_0) + \log(G) + \log(S^j)$$

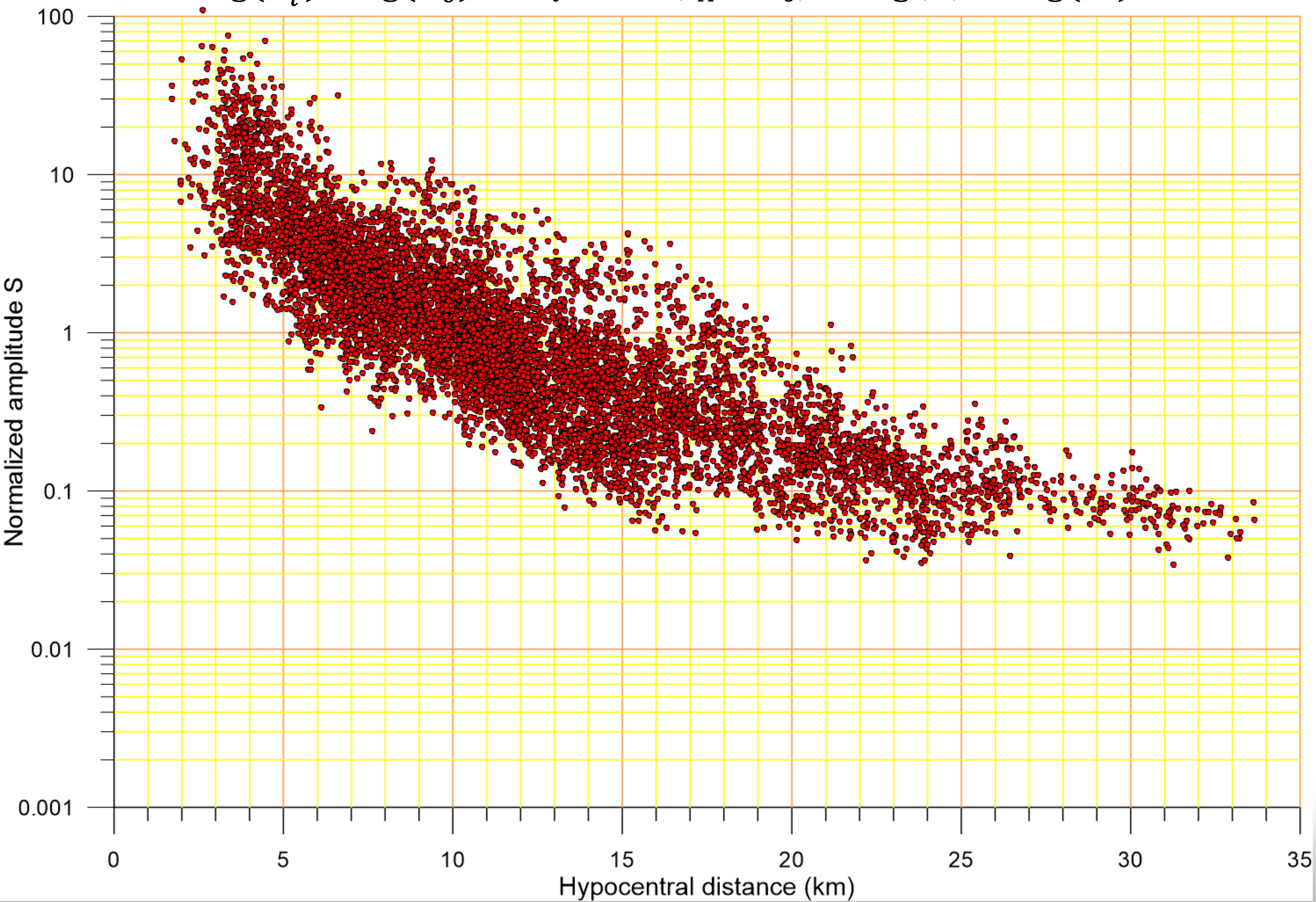

S-Wave (ASZ) attenuation

$$\log(A_i^j) - \log(A_0) - M_i - \log(S^j) = -\alpha(r_H - r_0) + \log(G)$$

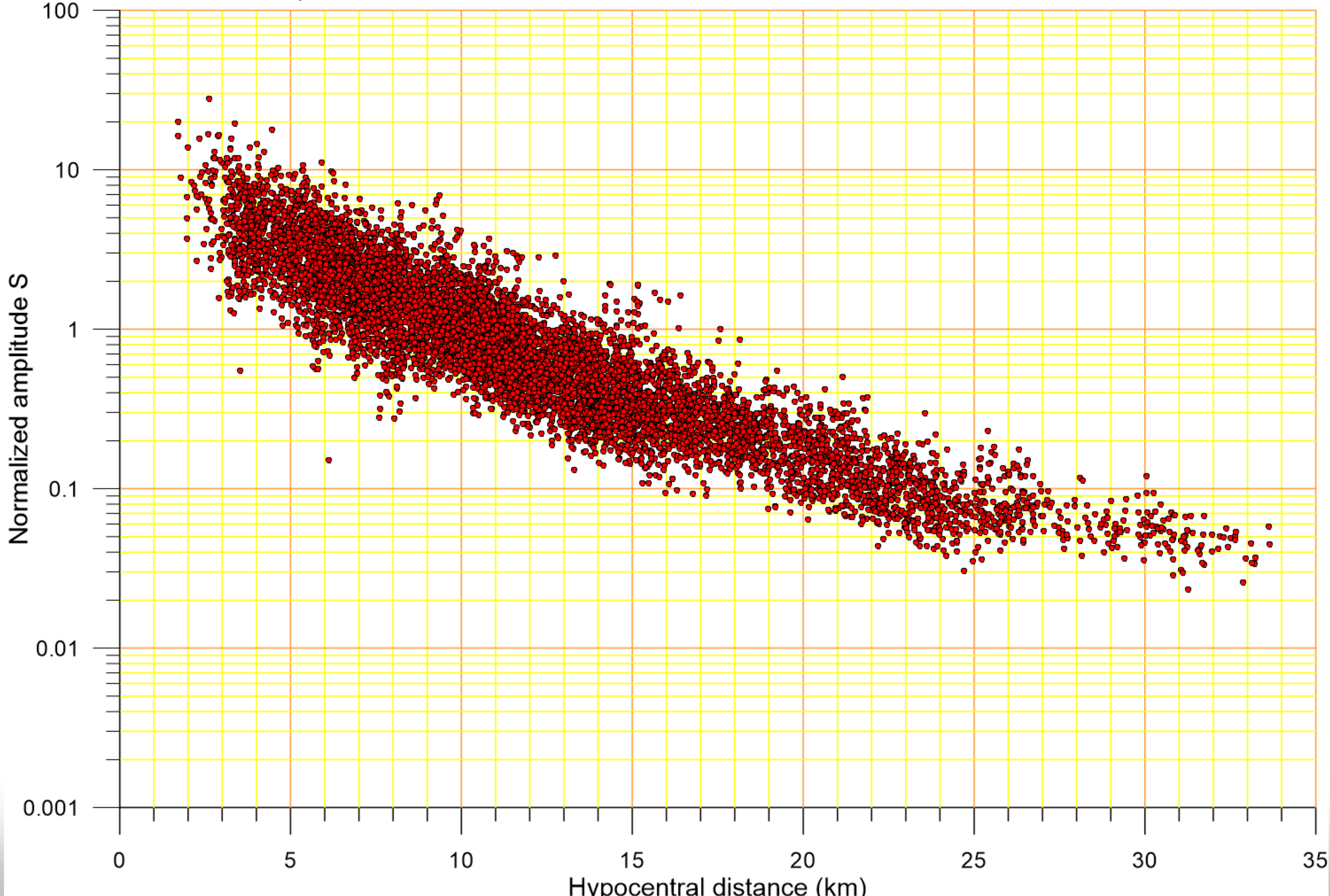

S-Wave (ASZ) attenuation

$$\log(A_i^j) - \log(A_0) - M_i - \log(S^j) - \log(G) = -\alpha(r_H - r_0)$$

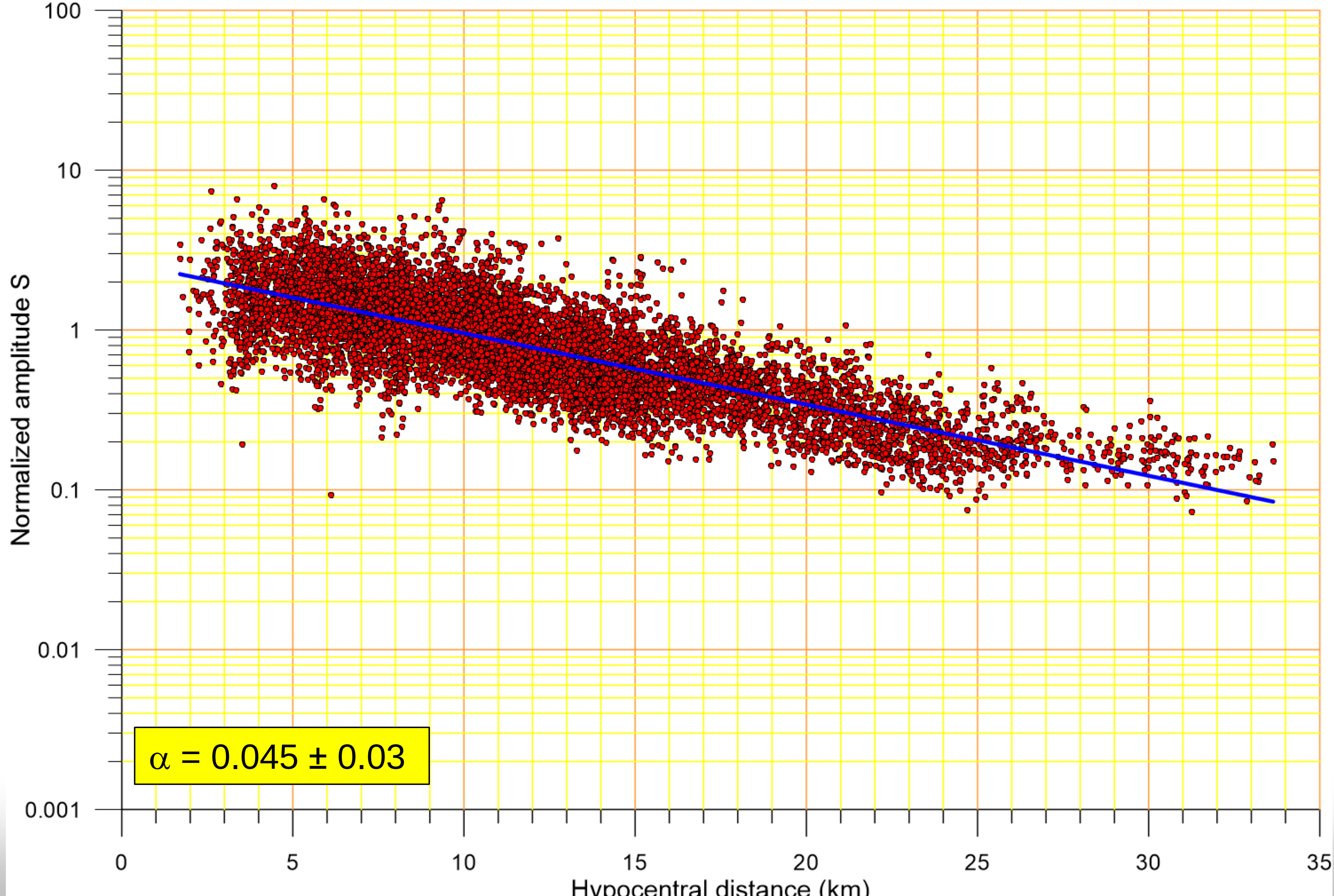

S-Wave (ASZ) attenuation

$$\log(A_i^j) - \log(A_0) - M_i - \log(S^j) - \log(G) - \alpha(r_H - r_0) = 1$$

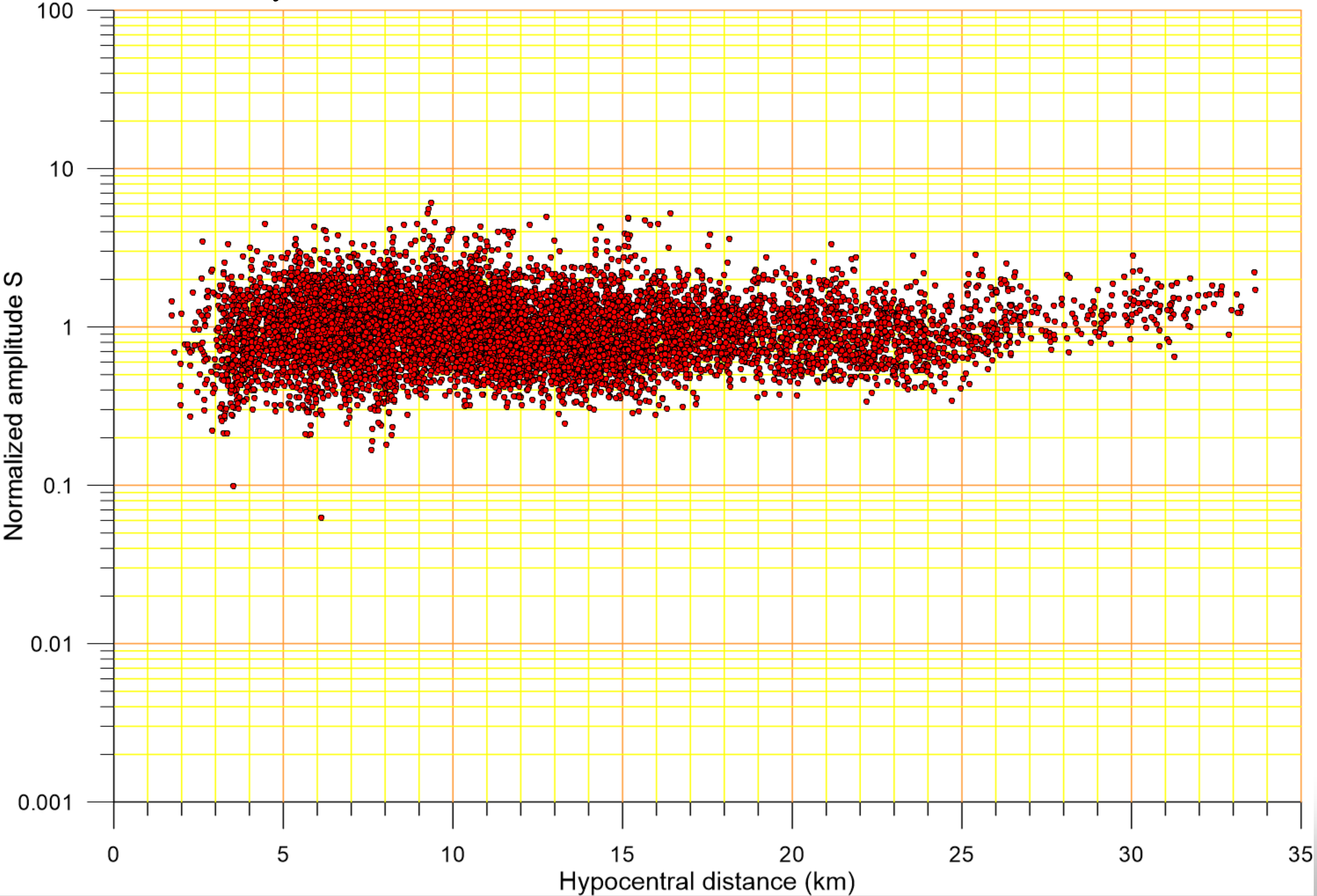

S-Wave (ASZ) attenuation

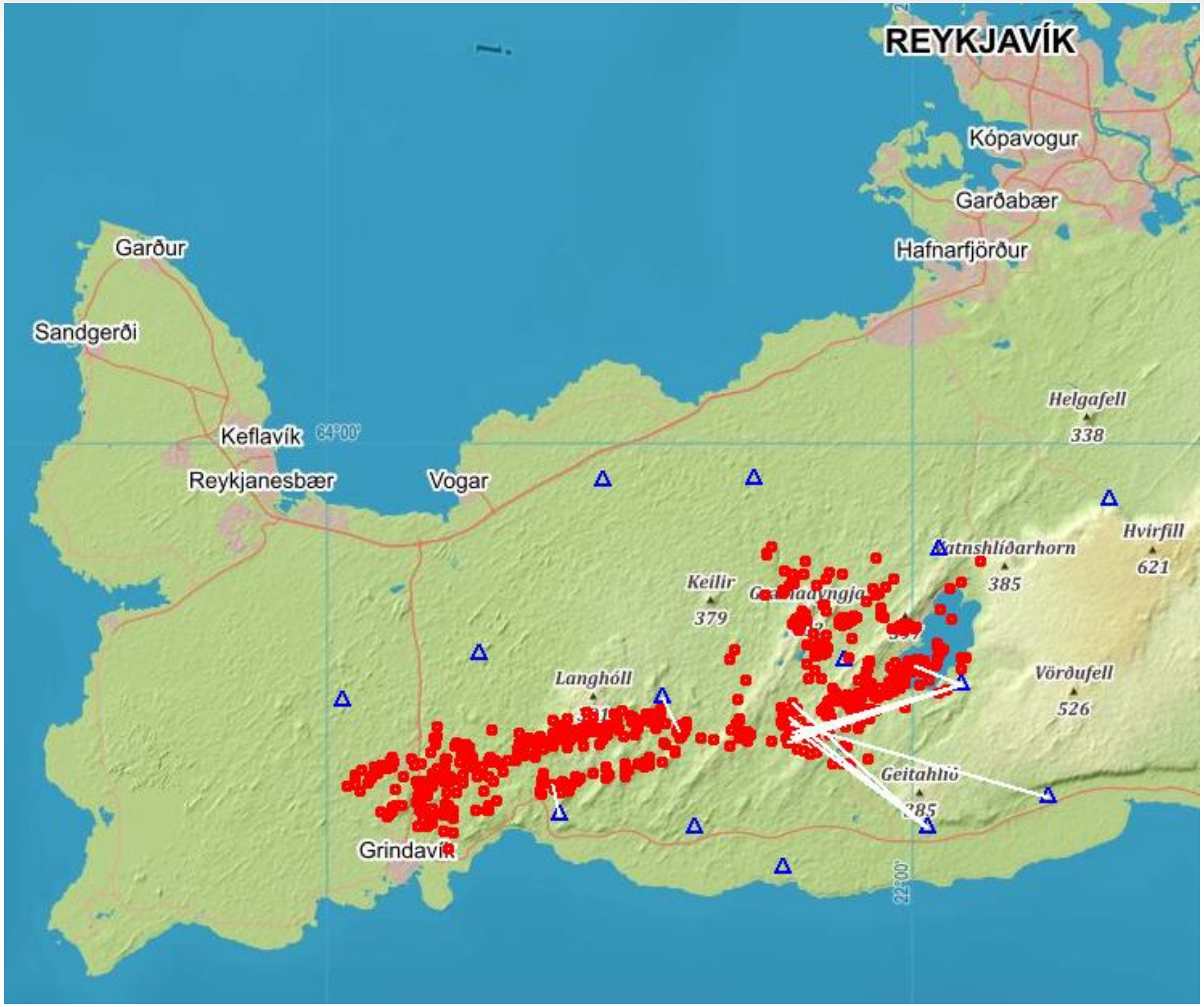

Fig. 11 Anomalous rays (white lines) with high attenuation (small amplitudes)

S-Wave (ASZ) attenuation

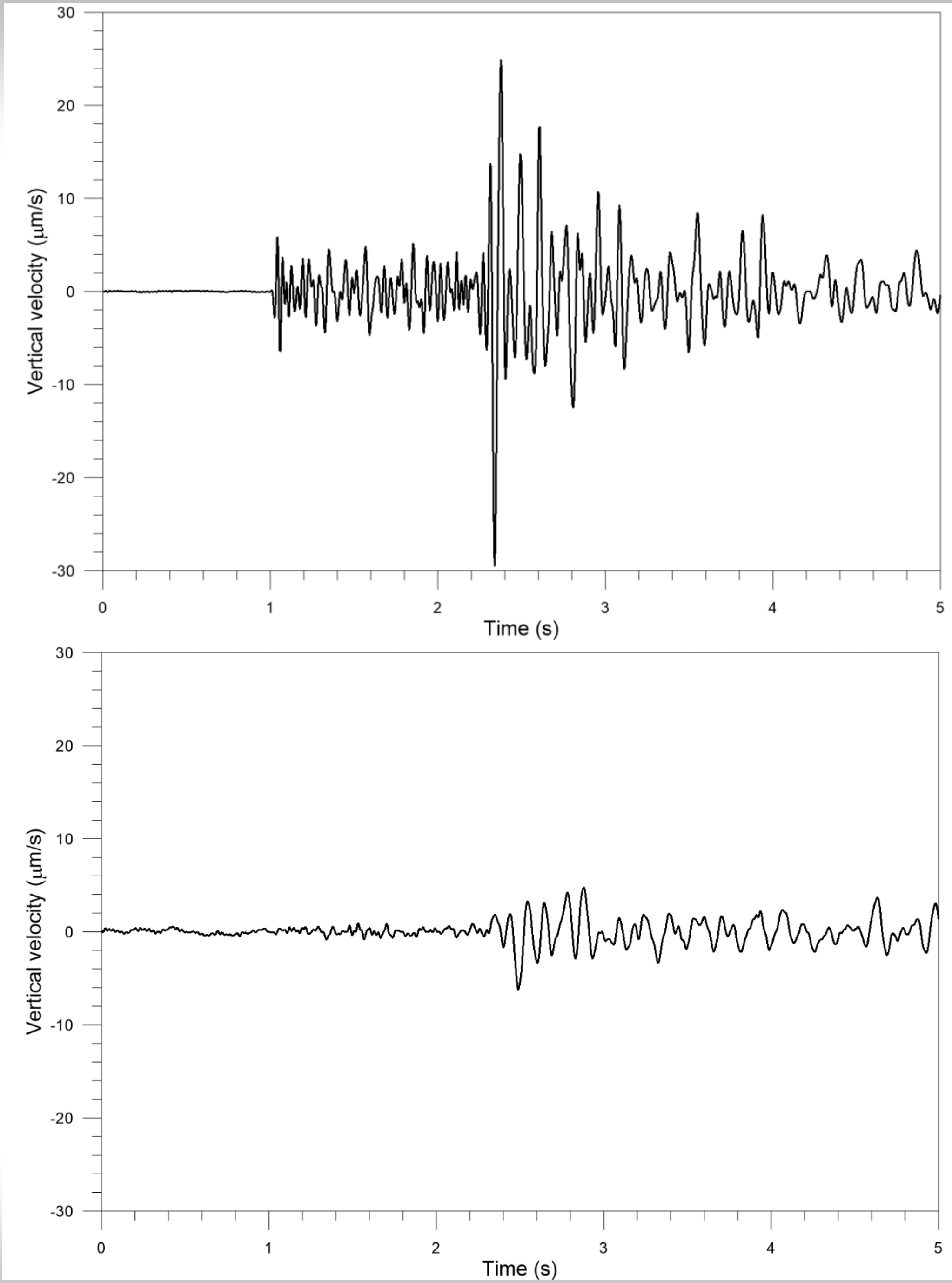

Fig. 12 Comparison of two vertical seismograms at KLV station.

A) Magnitude 1.1 at the hypocentral distance 8.05 km

B) Magnitude 1.0 at the hypocentral distance 8.04 km coming from Krýsuvík volcanic system with high attenuation.

Frequency dependence

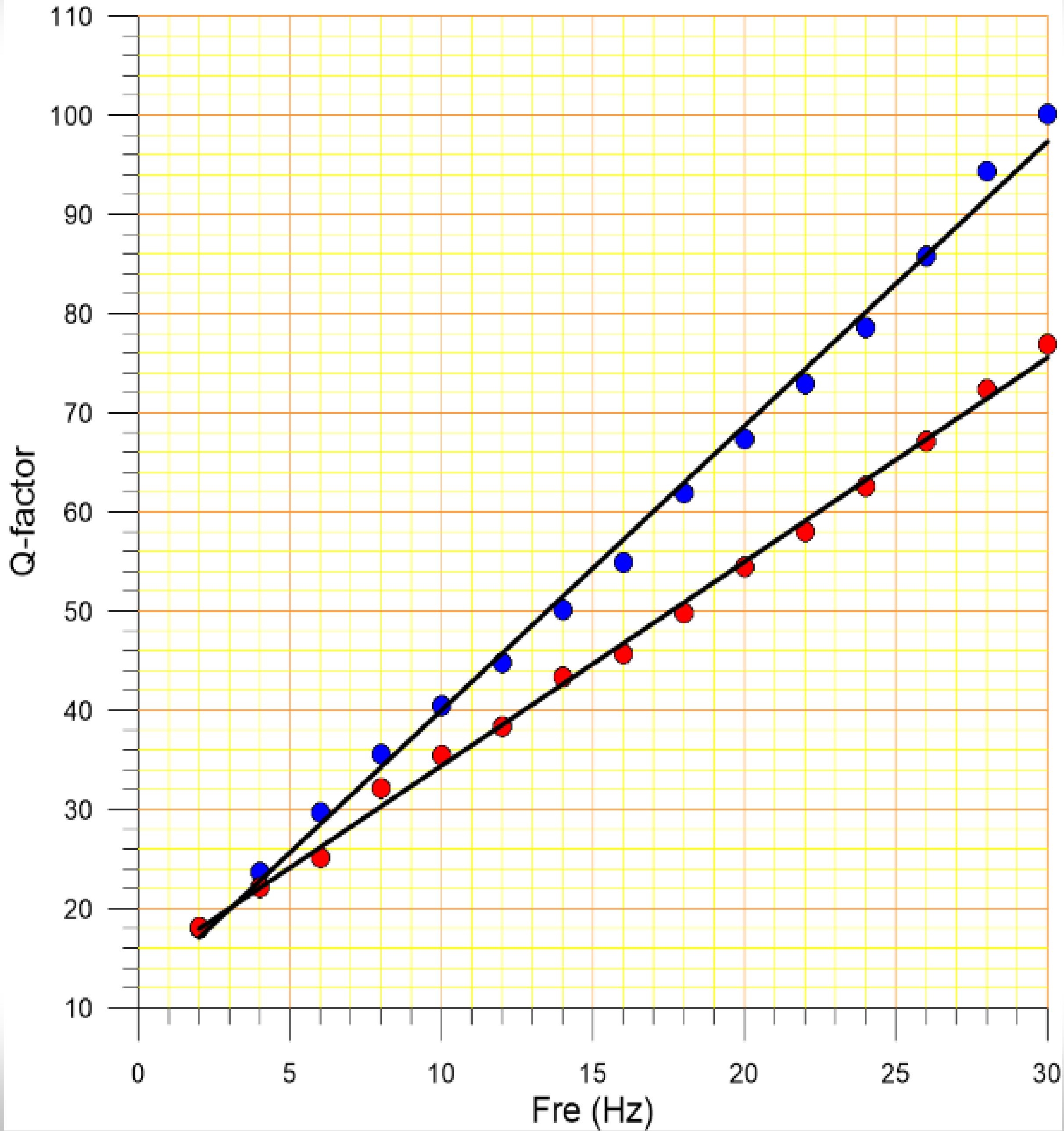

Dependence of S-waves attenuation (Q-factor) on frequency. Blue dots represent vertical component, red dots represent the component in the horizontal plane.

2 types of magnitude in IMO catalogue

Local magnitude IMO 1
from seismic moment

```
(1) m = log10(Mo) - 10
    M = m                                 if           M <= 2.0
    M = 2.0 + (m-a)*0.9                          2.0 < M <= 3.0
    M = 3.0 + (m-a-b)*0.8                        3.0 < M <= 4.6
    M = 4.6 + (m-a-b-c)*0.7                      4.6 < M <= 5.4
    M = 5.4 + (m-a-b-c-d)*0.5                    5.4 < M <= 5.9
    M = 5.9 + (m-a-b-c-d-e)*0.4                  5.9 < M >= 6.3
    M = 6.3 + (m-a-b-c-d-e-f)*0.35               6.3 < M

    where Mo = seismic moment in Nm and
          a = 2,  b = 1/0.9,  c = 1.6/0.8,  d = 0.8/0.7,  e = f = 1
```

Local magnitude IMO 2
from maximun amplitude and distance

```
(2) M = log10(amp) + 2.1 * log10(dist.-in-km) - 4.8,

    where amplitude is estimated in a 10 second window around the S arrival.
```

2 types of magnitude in IMO catalogue

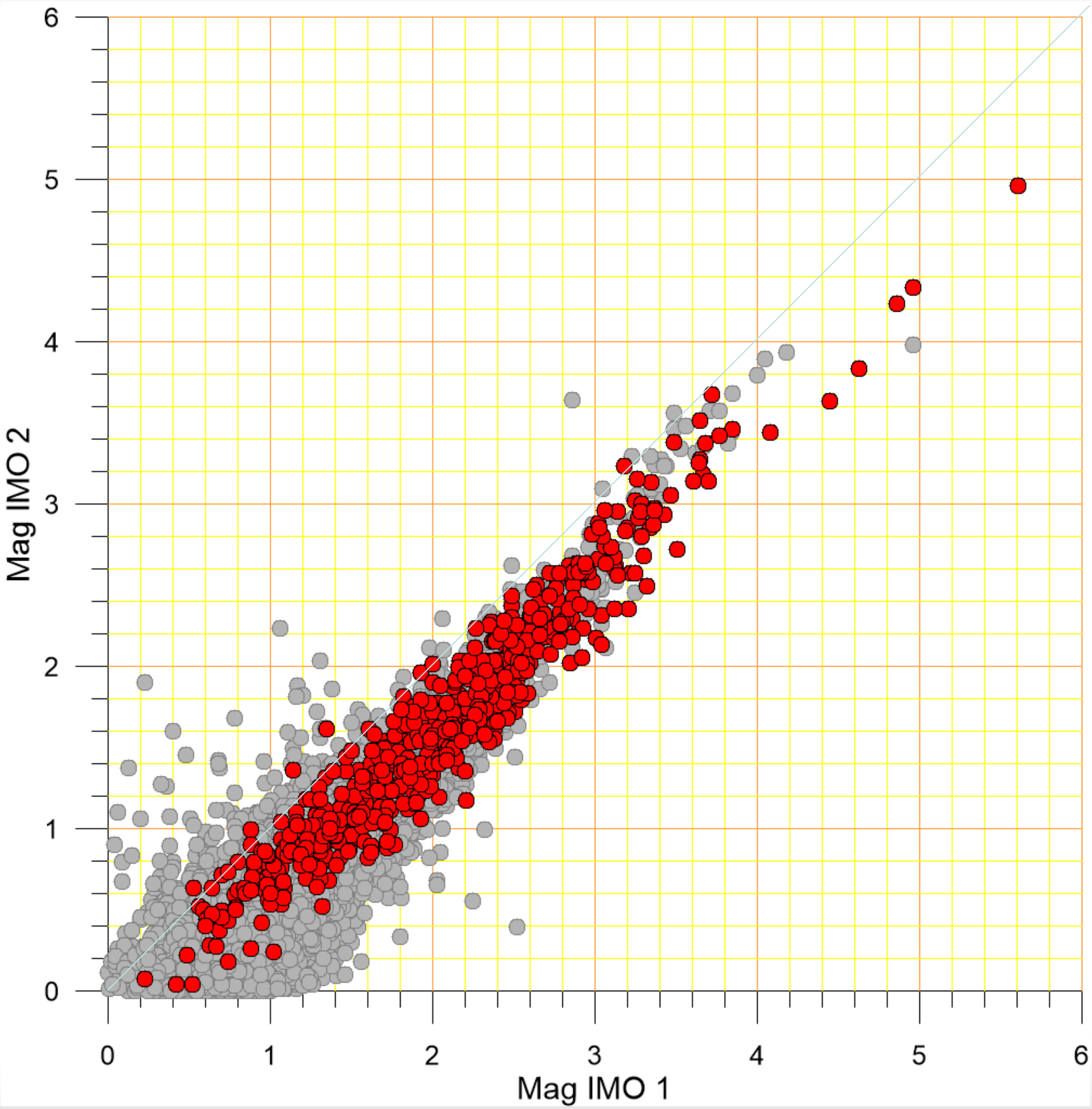

Attenuation of seismic waves in the area of REYKJANET

New local magnitude from REYKJANET

$$M^j = \log(A_{ZS}^j) - \log(A_0) + \alpha\left(r_H^j - r_0\right) - \log\left(r_0/r_H^j\right) - \log(S^j)$$

$$M = median(M^j)$$

A_{ZS}^j is maximum Z-velocity after S-wave onset at j-th station,

r_H^j is hypocentral distance at j-th station

S^j station constant at j-th station

A_0 = 0,6838 μm/s, α = 0.0447, r_0 = 10 km,

Station	$\log(S^j)$	Station	$\log(S^j)$
ASH	-0.288	LAG	-0.197
ELB	-0.169	LAT	-0.081
FAF	0.180	LHL	0.096
HDV	0.190	LSF	0.044
HRG	-0.120	MOH	0.568
ISS	0.075	SEA	-0.043
KLV	0.169	STH	-0.424

New local magnitude from REYKJANET

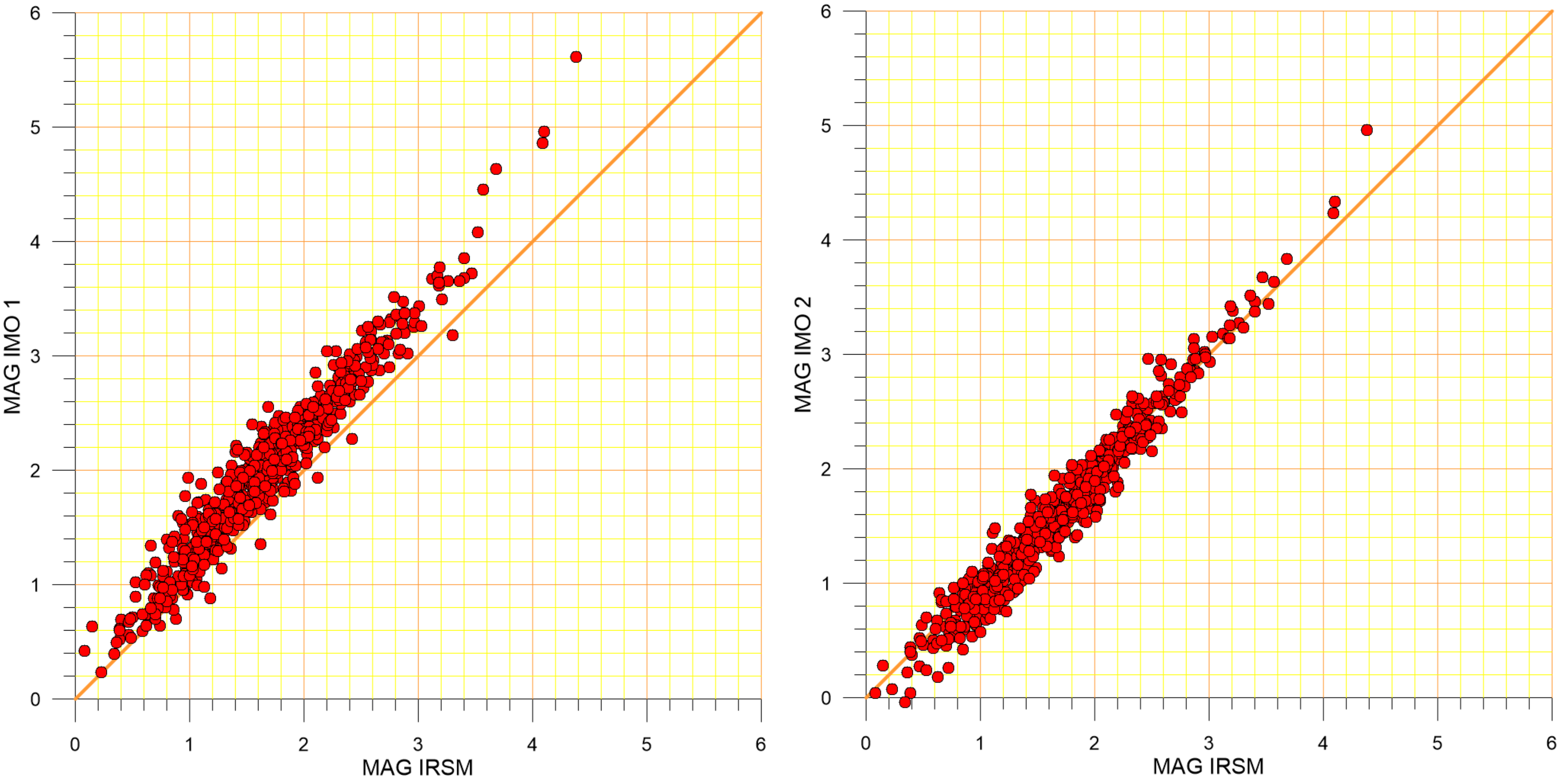

New local magnitude from REYKJANET

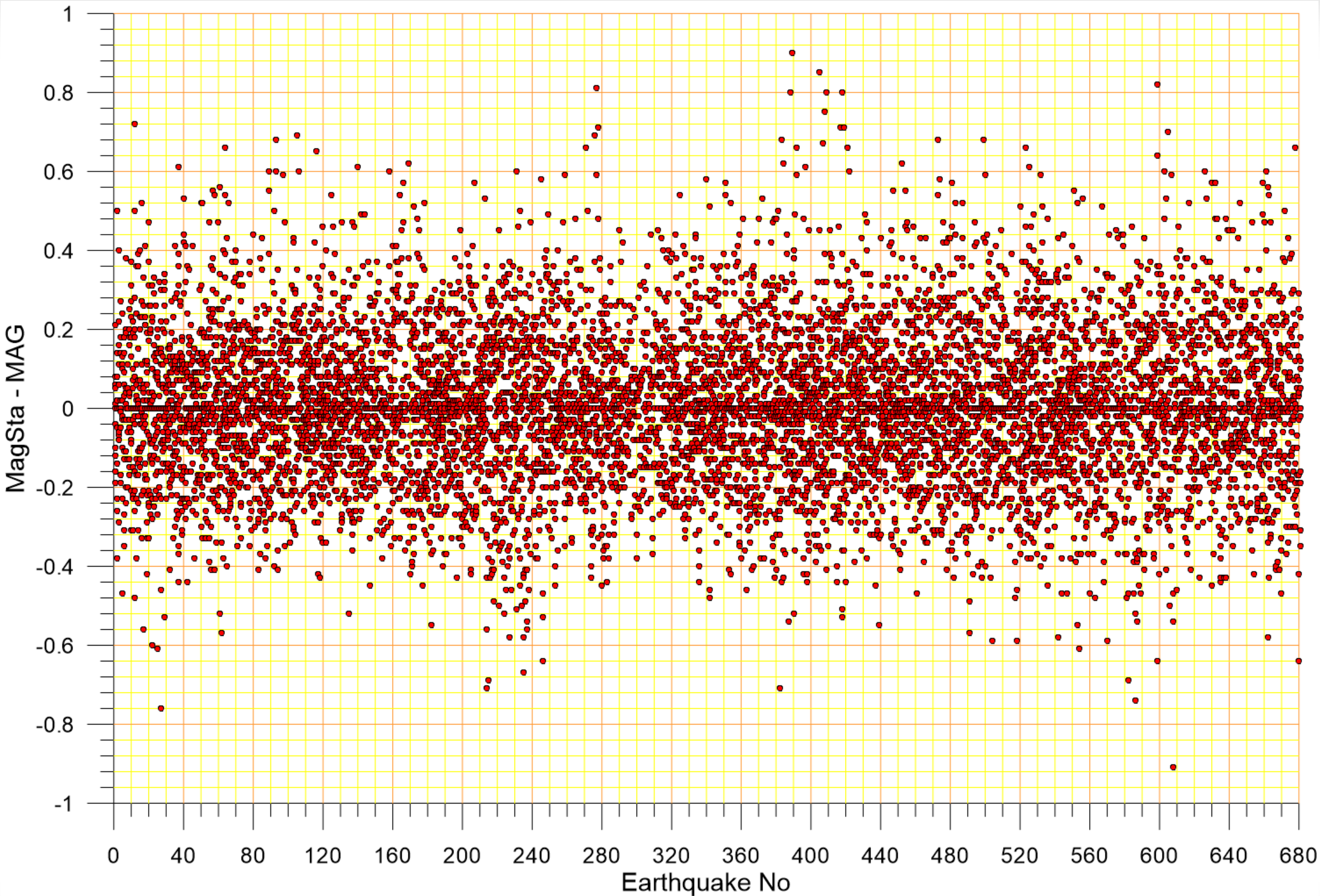

Average absolute value of difference is **0.148**

Attenuation of seismic waves in the area of REYKJANET

Amplitude Tomography

$$\log(A_i^j) = \log(A_0^j) + M_i - \alpha(r_H - r_0) - \sum_{k=1}^{n} \Delta\alpha_k p_k + \log(G)$$

$\Delta\alpha_k$ difference of attenuation coefficient in k-th cell

p_k length of the path of the ray in k-th cell

Overdetermined linear inverse problem – Newton’s method

Amplitude Tomography - chess-board test +-10%, more than 5 rays

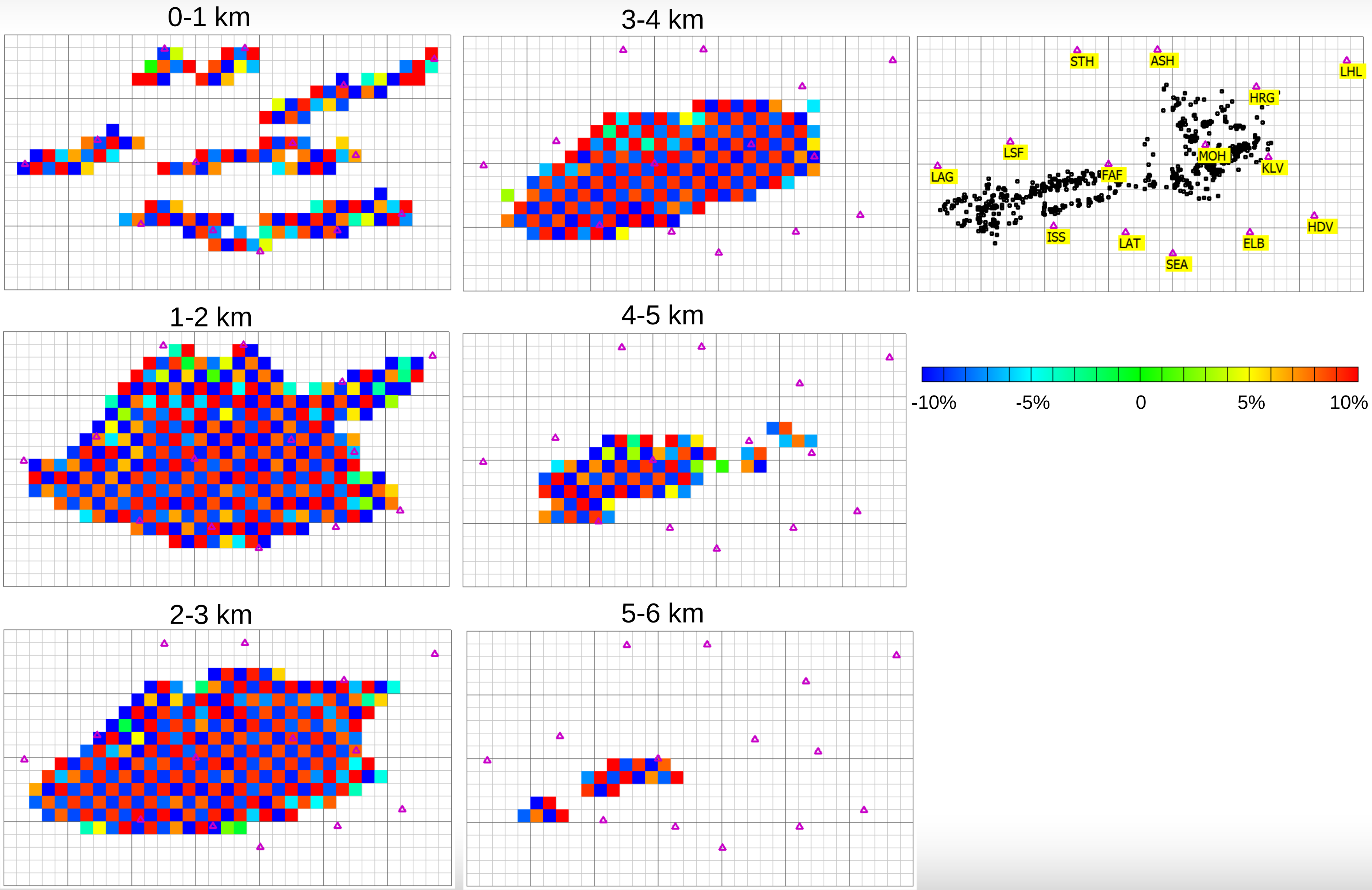

Attenuation of seismic waves in the area of REYKJANET

Amplitude Tomography S-waves

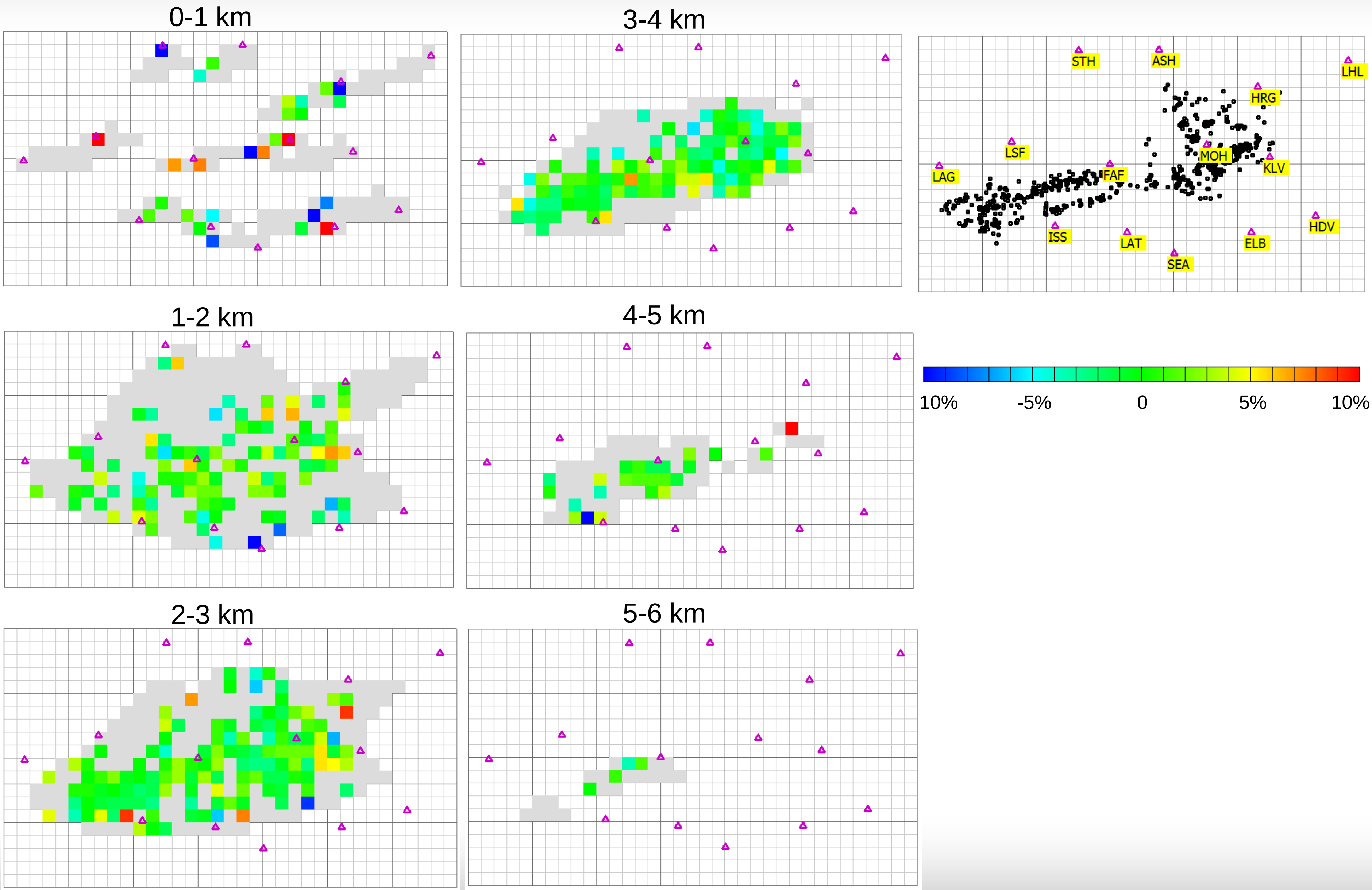

Attenuation of seismic waves in the area of REYKJANET

CONCLUSIONS:

- Average attenuation at the area of REYKJANET was estimated. Attenuation of P-waves (α = 0.056) is higher than attenuation of S-waves (α = 0.045).
- New type of local magnitude from REYKJANET was proposed.
- Amplitude tomography revealed several localities with S-waves high-attenuation anomaly.

PLANS FOR FUTURE:

- To add KRI and GRV stations
- To improve resolution (more earthquakes, more stations)
- To compute attenuation also from horizontal components - it is important for seismic hazard
- To investigate acceleration and displacement
- To find frequency dependence of attenuation
- To improve radiation patterns and geometrical spreading

Picking of rock samples at Fagradalsfjall volcano, June 7, 2021

SVH station, June 2023

BLF station, June 2023

ÚSTAV VIED O ZEMI
SLOVENSKEJ AKADÉMIE VIED

USMH Ústav struktury a mechaniky hornin AV ČR, v.v.i.

Seismic Activity and the event Oct 9th, 2023, M5.0 in Slovakia

Lucia Fojtíková, Kristian Csicsay, Andrej Cipciar, Peter Pažák, Jozef Kristek, Miriam Kristeková, Róbert Kysel, Martin Gális, Renata Lukešová, Luděk Vecsey, Hana Kampfová Exnerová, Petr Jedlička, Dmytro Malytsky

Earthquake Oct 9th, 2023, M5.0 in Slovakia

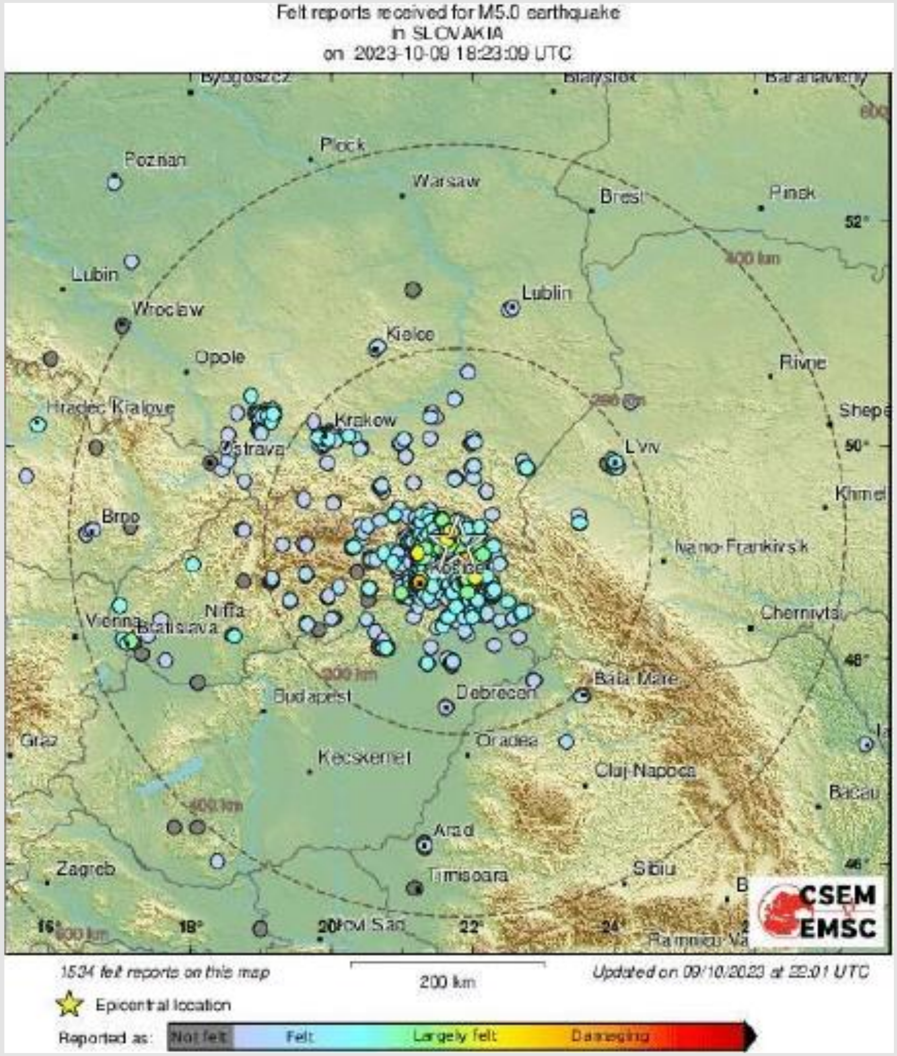

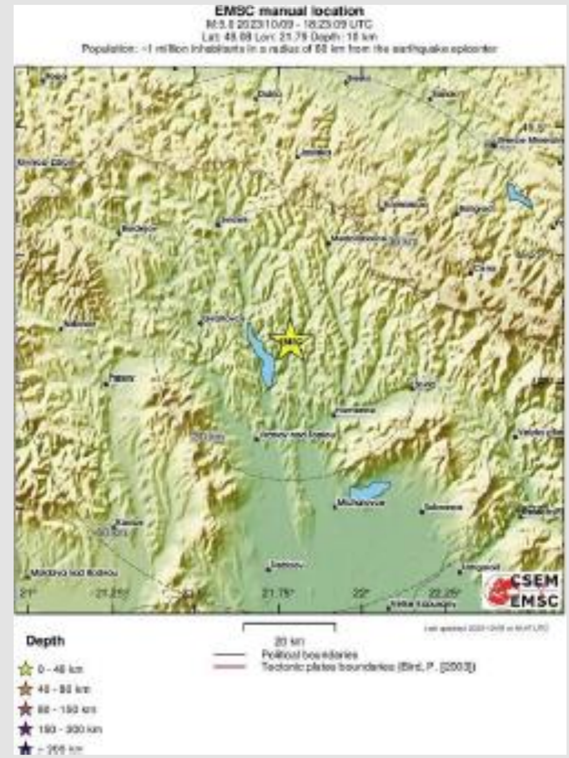

Seismic stations on the territory of Slovakia

- 2 local seismic networks around the nuclear power plants Mochovce and Jaslovské Bohunice
- 5 seismic stations in cooperattion between Progseis, ESI SAV and IRSM ASCR
- 2 seismic networks in international cooperation under the ADRIA Array initiative

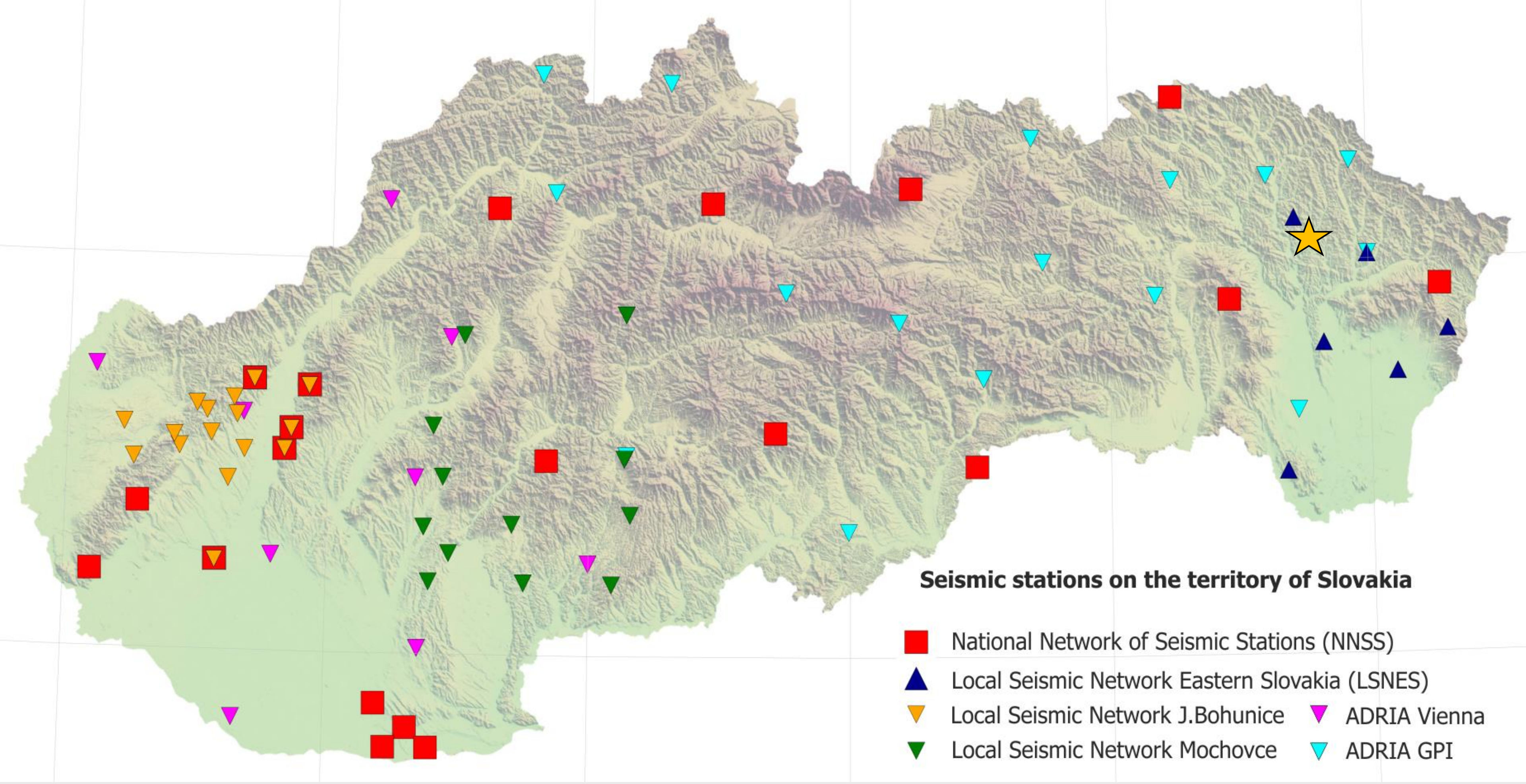

Seismic stations on the territory of Slovakia

- ❑ 2 local seismic networks around the nuclear power plants Mochovce and Jaslovské Bohunice
- ❑ 5 seismic stations in cooperattion between Progseis, ESI SAV and IRSM ASCR
- ❑ 2 seismic networks in international cooperation under the ADRIA Array initiative

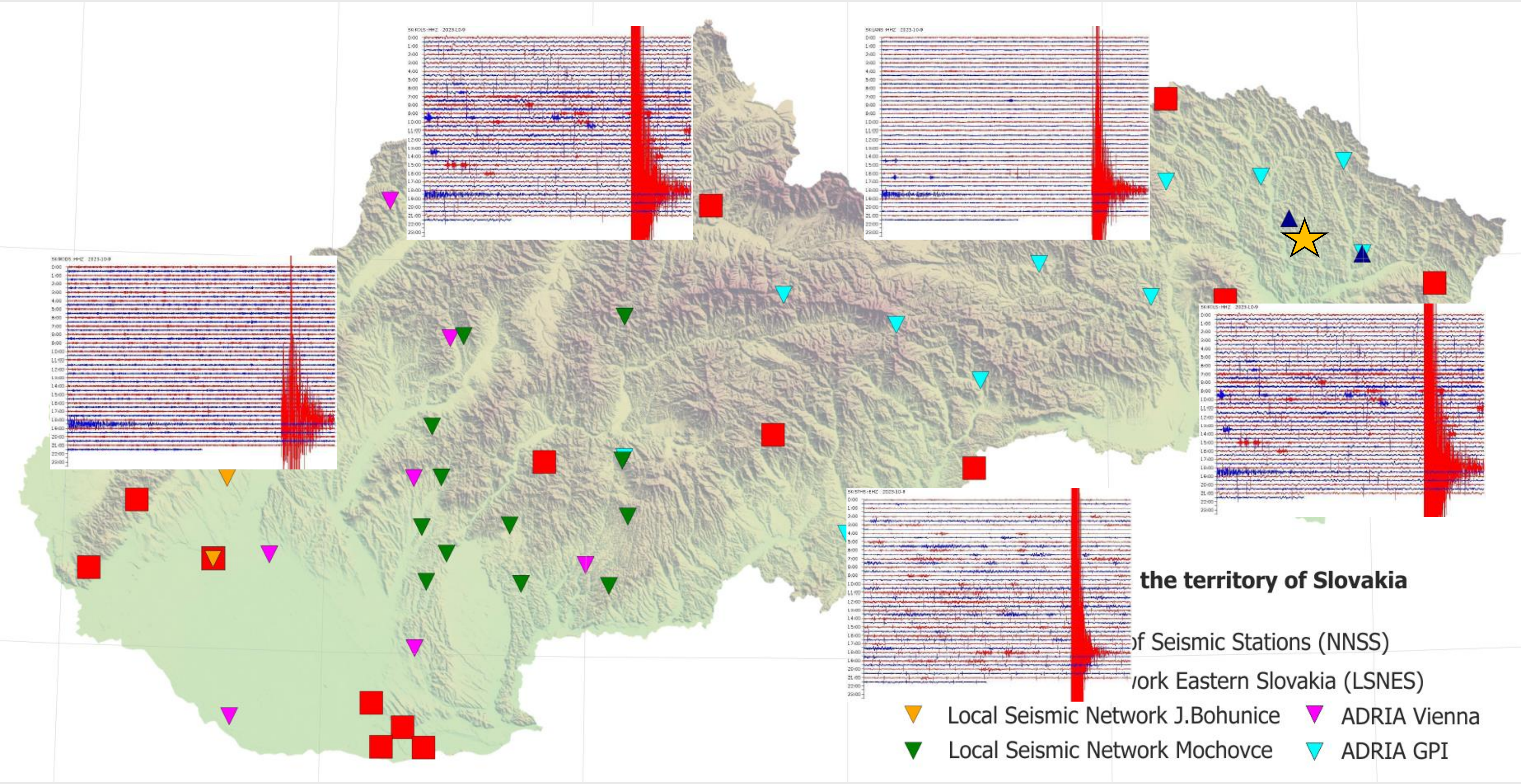

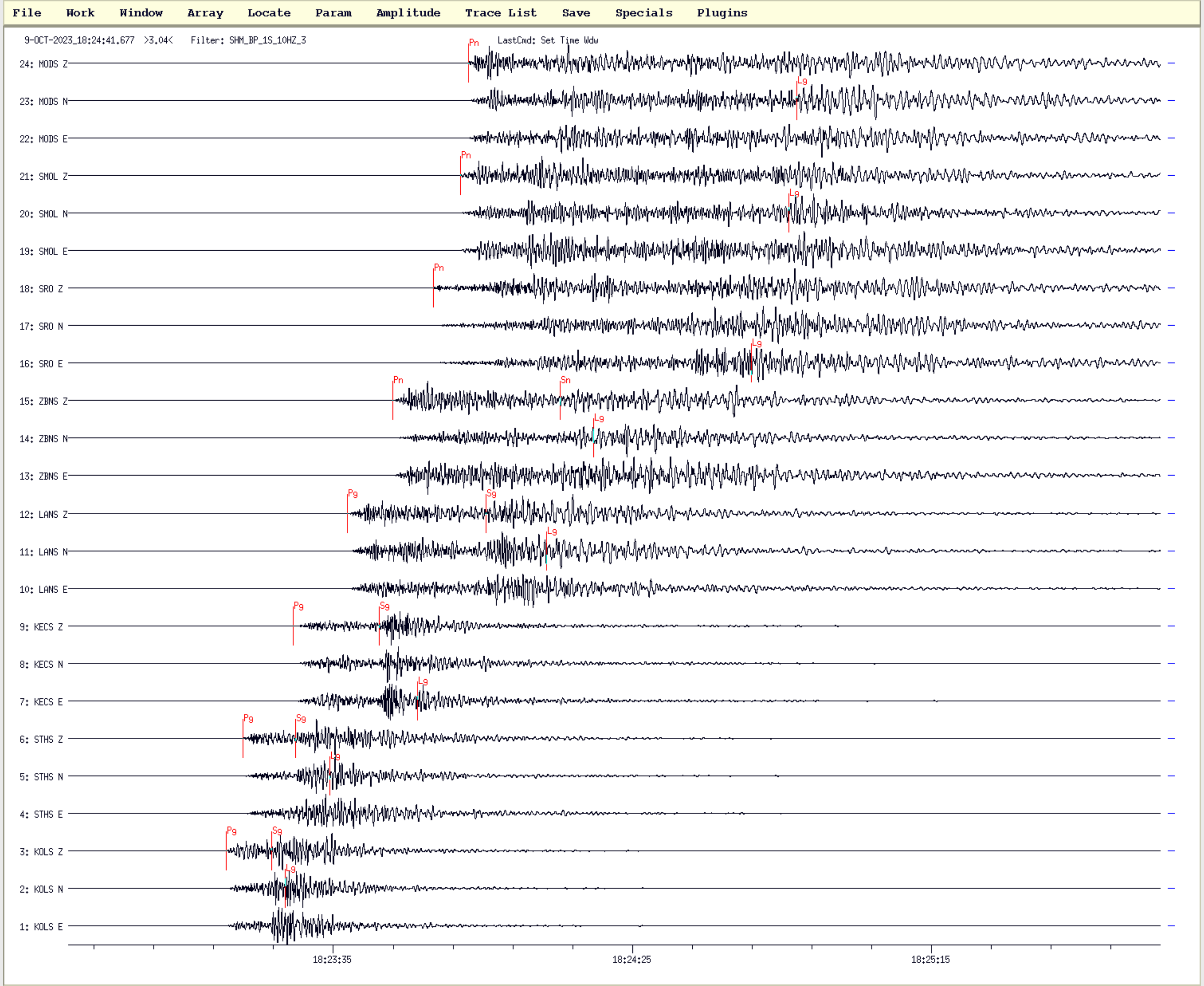
File Work Window Array Locate Param Amplitude Trace List Save Specials Plugins
9-OCT-2023_18:24:41.677 >3.04< Filter: SHM_BP_1S_10HZ_3
LastCmd: Set Time Wdw
24: MODS Z
23: MODS N
22: MODS E
21: SMOL Z
20: SMOL N
19: SMOL E
18: SRO Z
17: SRO N
16: SRO E
15: ZBNS Z
14: ZBNS N
13: ZBNS E
12: LANS Z
11: LANS N
10: LANS E
9: KECS Z
8: KECS N
7: KECS E
6: STHS Z
5: STHS N
4: STHS E
3: KOLS Z
2: KOLS N
1: KOLS E
Pn
Sn
Pg
Sg
Lg
18:23:35
18:24:25
18:25:15

Earthquake Oct 9th, 2023, M5.0 in Slovakia

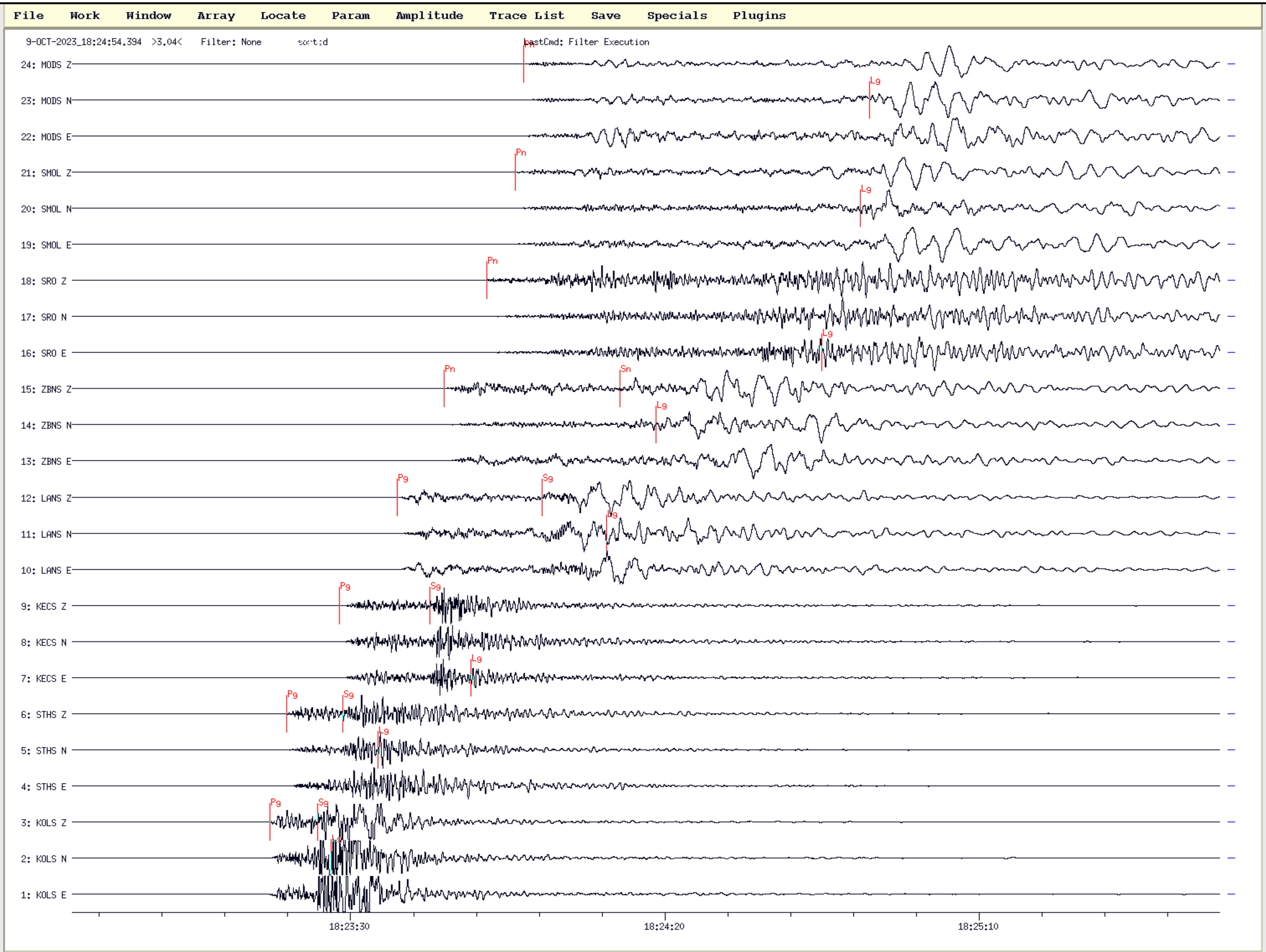

Earthquake Oct 9th, 2023, M5.0 in Slovakia

KOLS

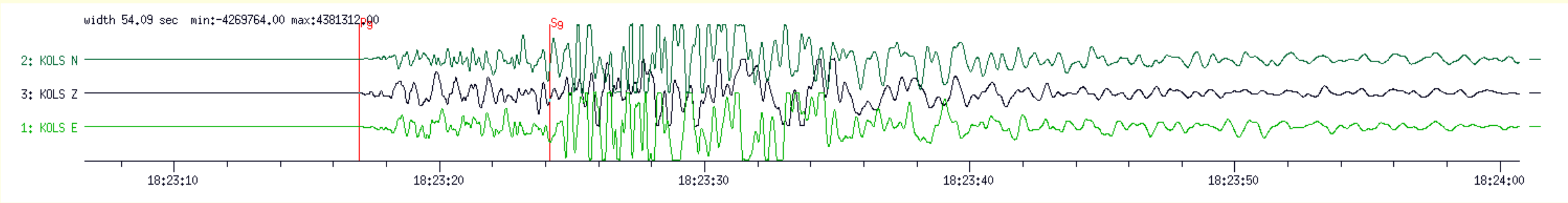

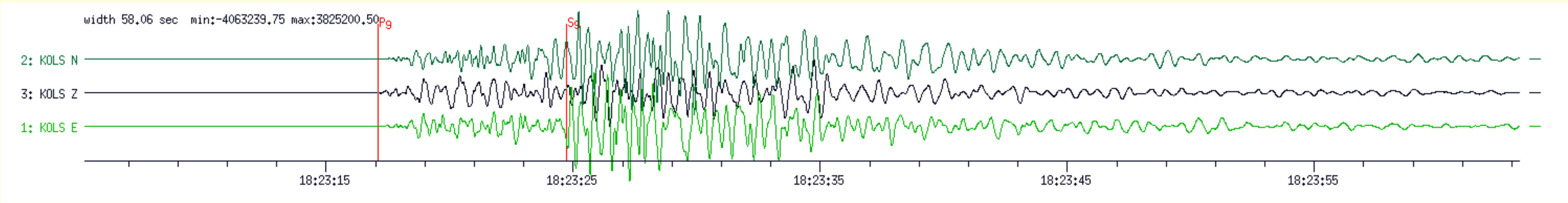

Earthquake Oct 9th, 2023, M5.0 in Slovakia

LOKÁLNE ZEMETRASENIA

Lokalizácie z Národnej siete seizmických staníc

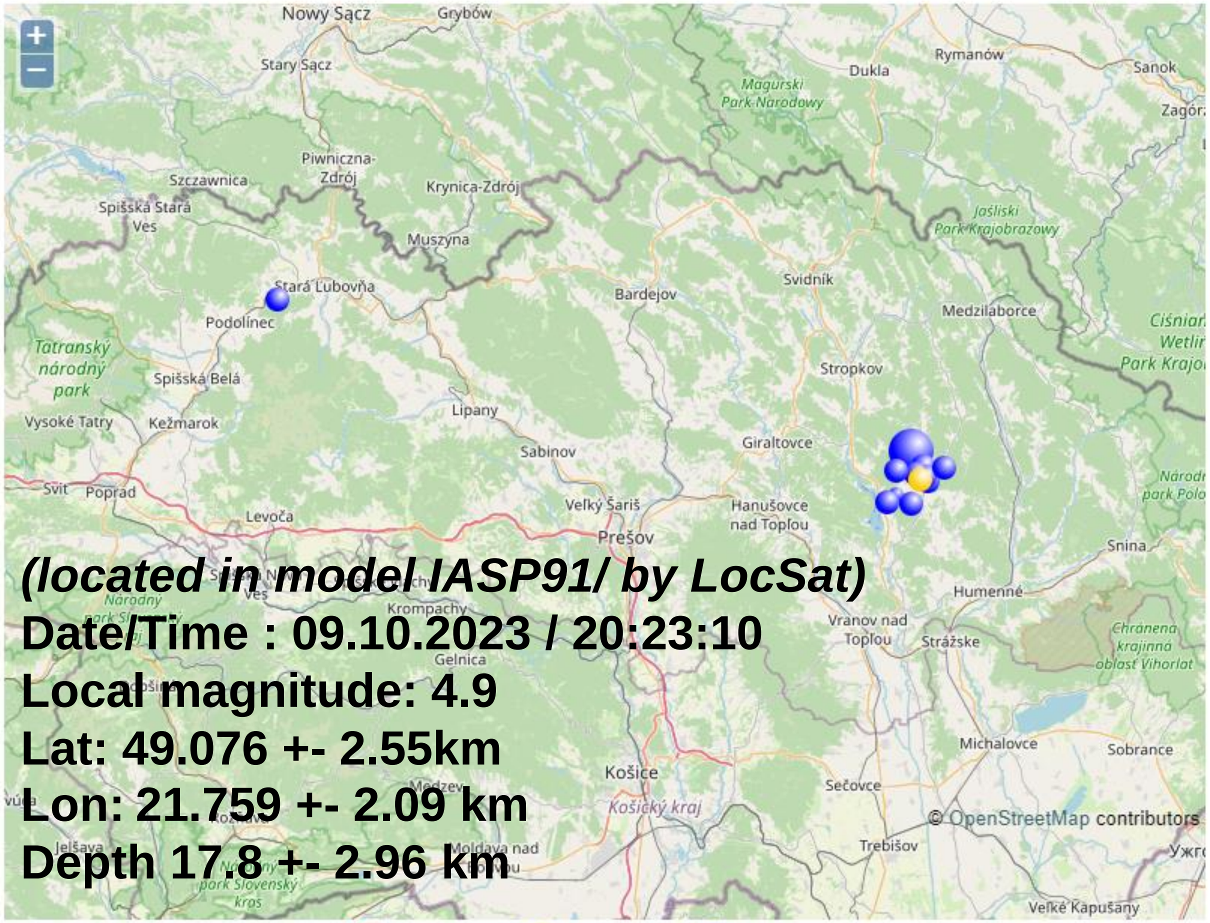

(located in model IASP91/ by LocSat)

Date/Time : 09.10.2023 / 20:23:10

Local magnitude: 4.9

Lat: 49.076 +- 2.55km

Lon: 21.759 +- 2.09 km

Depth 17.8 +- 2.96 km

Zoznam lokálnych zemetrasení:
dátum, lokálny čas, magnitúdo

09.11.2023, 12:44:04, Ml = 2.1
08.11.2023, 16:24:45, Ml = 1.3
06.11.2023, 00:37:37, Ml = 1.2
30.10.2023, 14:59:14, Ml = --
29.10.2023, 05:04:01, Ml = 1.1
26.10.2023, 07:43:26, Ml = 1.1
25.10.2023, 22:51:52, Ml = -0.1
25.10.2023, 09:50:45, Ml = 1.3
21.10.2023, 07:10:39, Ml = 0.5
18.10.2023, 23:03:37, Ml = 1.2
18.10.2023, 03:20:36, Ml = 0.9
17.10.2023, 21:28:07, Ml = 1.4
17.10.2023, 08:00:04, Ml = 1.5
16.10.2023, 06:23:29, Ml = 2.8
11.10.2023, 23:04:17, Ml = 3.2
11.10.2023, 04:15:36, Ml = 1.5
09.10.2023, 20:39:49, Ml = 1.3
09.10.2023, 20:23:10, Ml = 4.9
07.10.2023, 14:59:25, Ml = 1.9
28.09.2023, 13:34:11, Ml = 1.4
28.09.2023, 05:37:10, Ml = 1.4
27.09.2023, 10:51:02, Ml = 1.2
23.09.2023, 19:26:18, Ml = 1.0
13.09.2023, 01:24:55, Ml = 2.1

last 2 days | last 2 weeks | last 2 months

local magnitude: below 1 | 1 - 2 | 2 - 3 | 3 - 4 | more than 4

AdriaArray

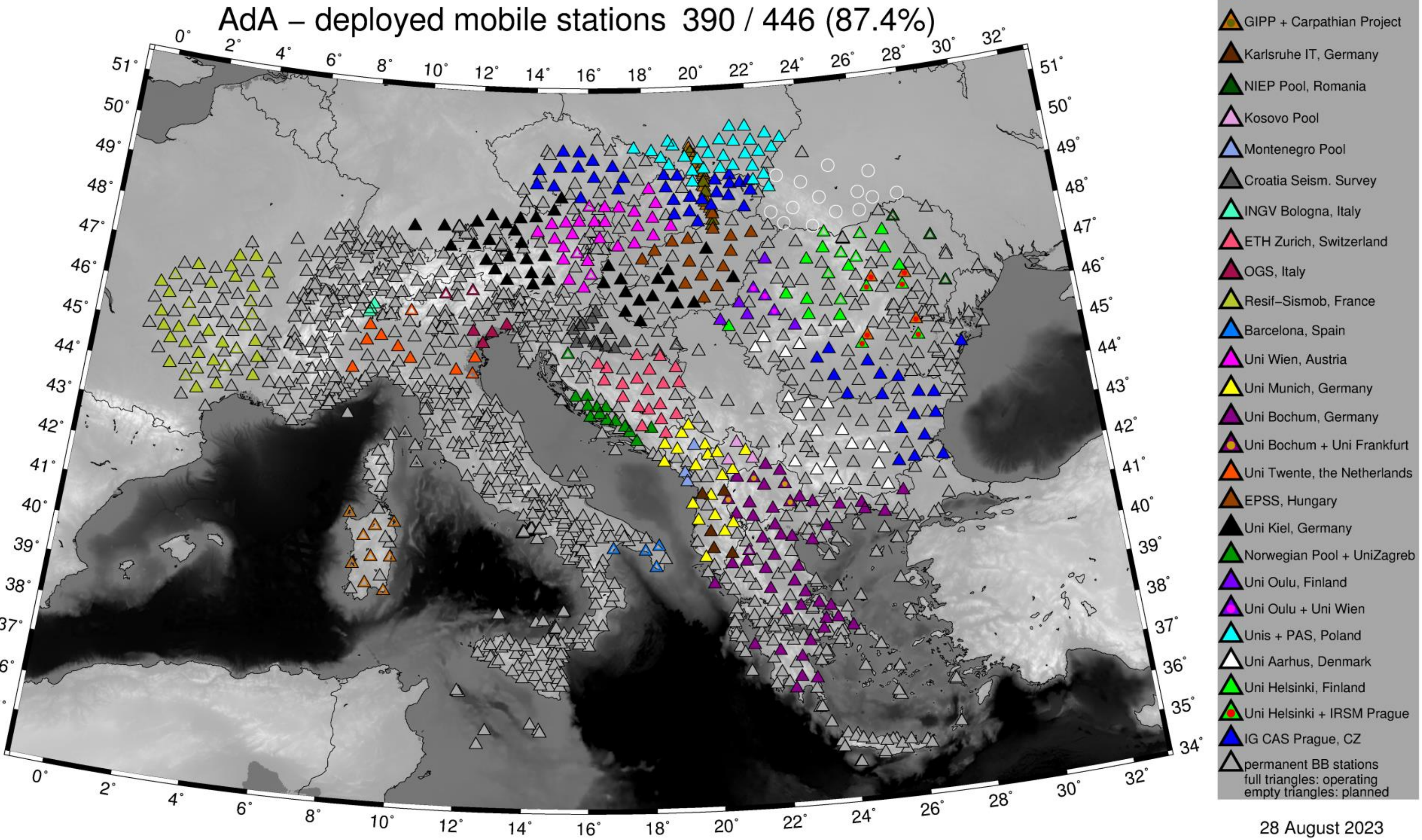

28 August 2023

Earthquake Oct 9th, 2023, M5.0 in Slovakia

Z component

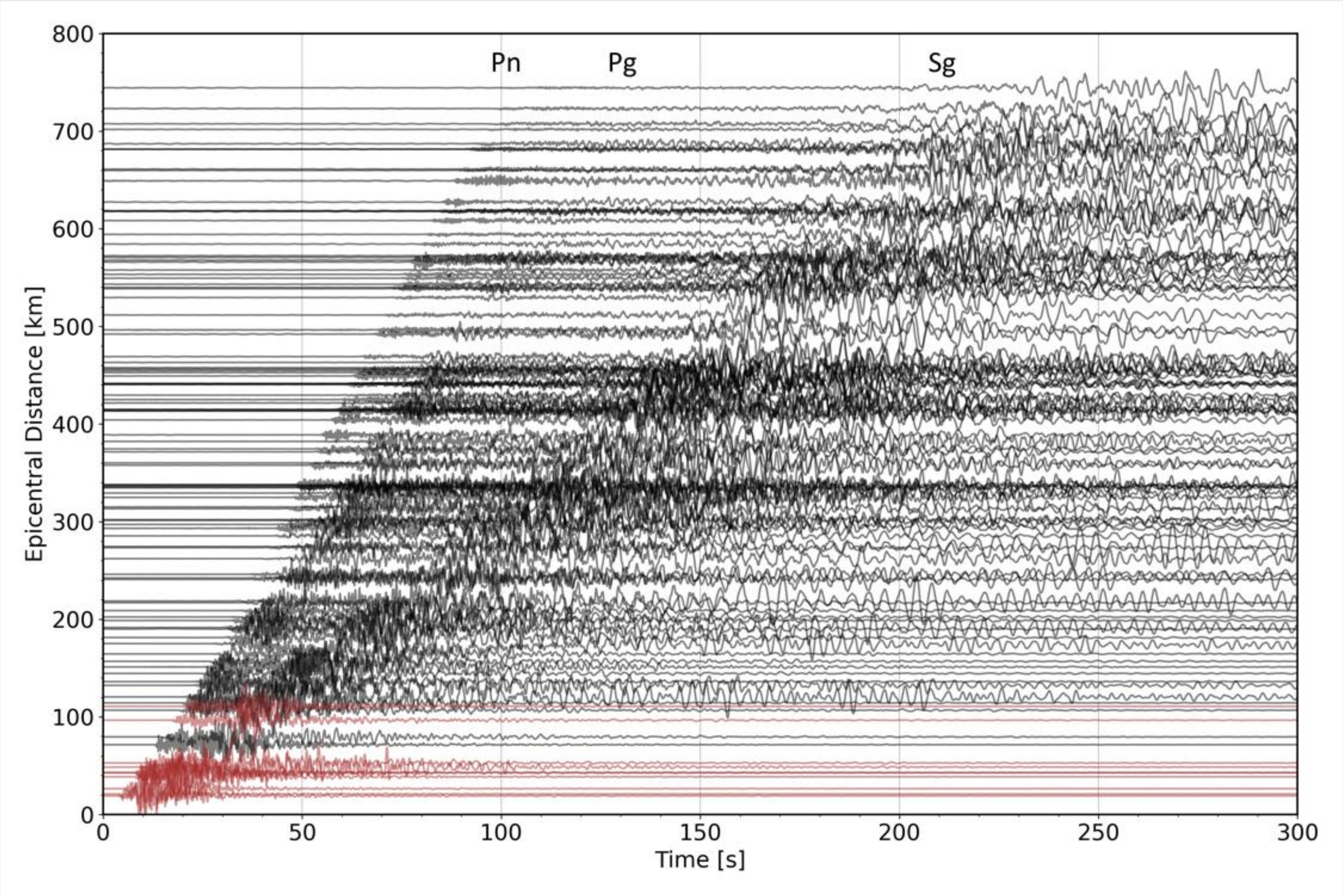

Schlömer et al., 2023 (in review)

Earthquake Oct 9th, 2023, M5.0 in Slovakia

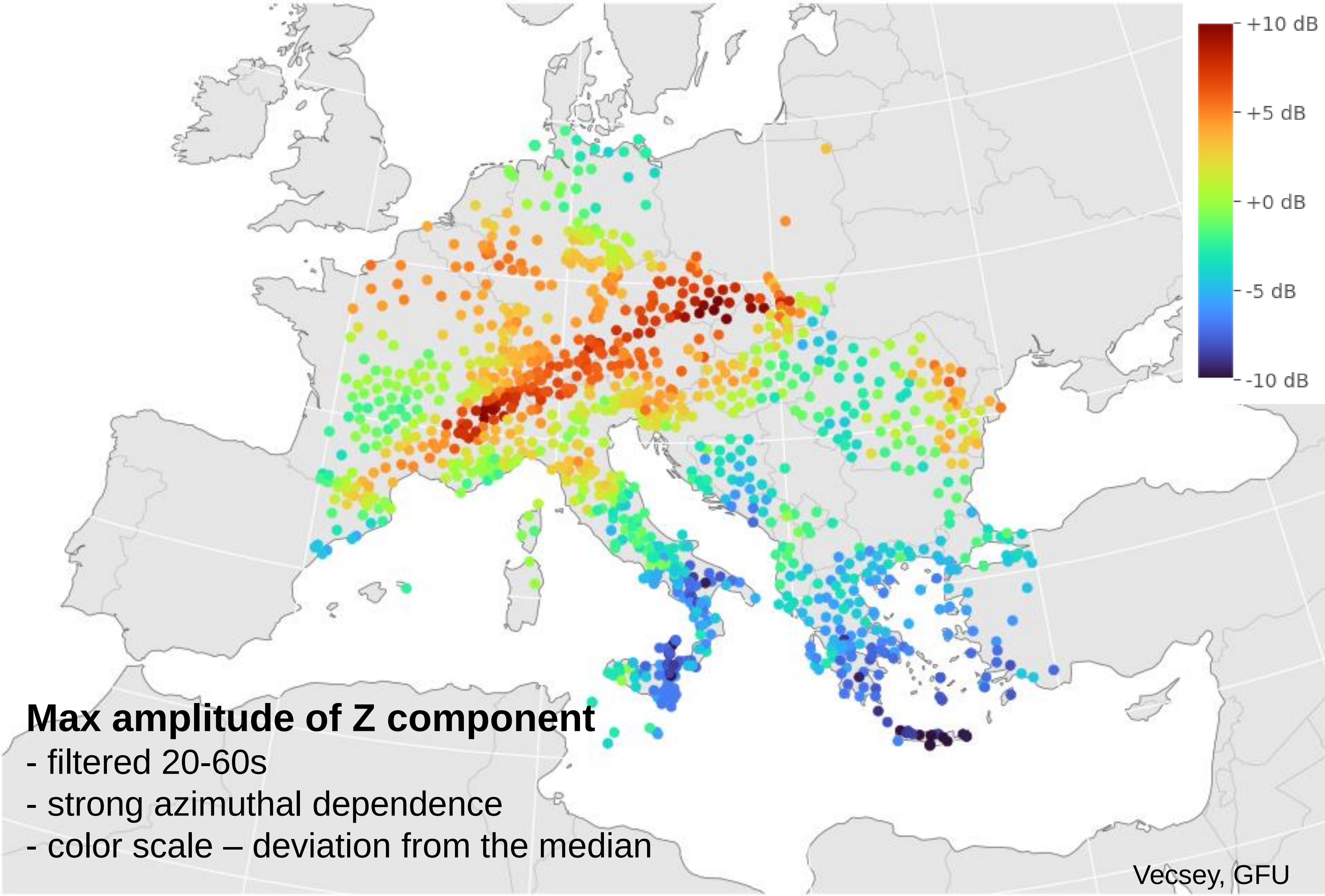

Max amplitude of Z component
- filtered 20-60s
- strong azimuthal dependence
- color scale – deviation from the median

Vecsey, GFU

Earthquake Oct 9th, 2023, M5.0 in Slovakia

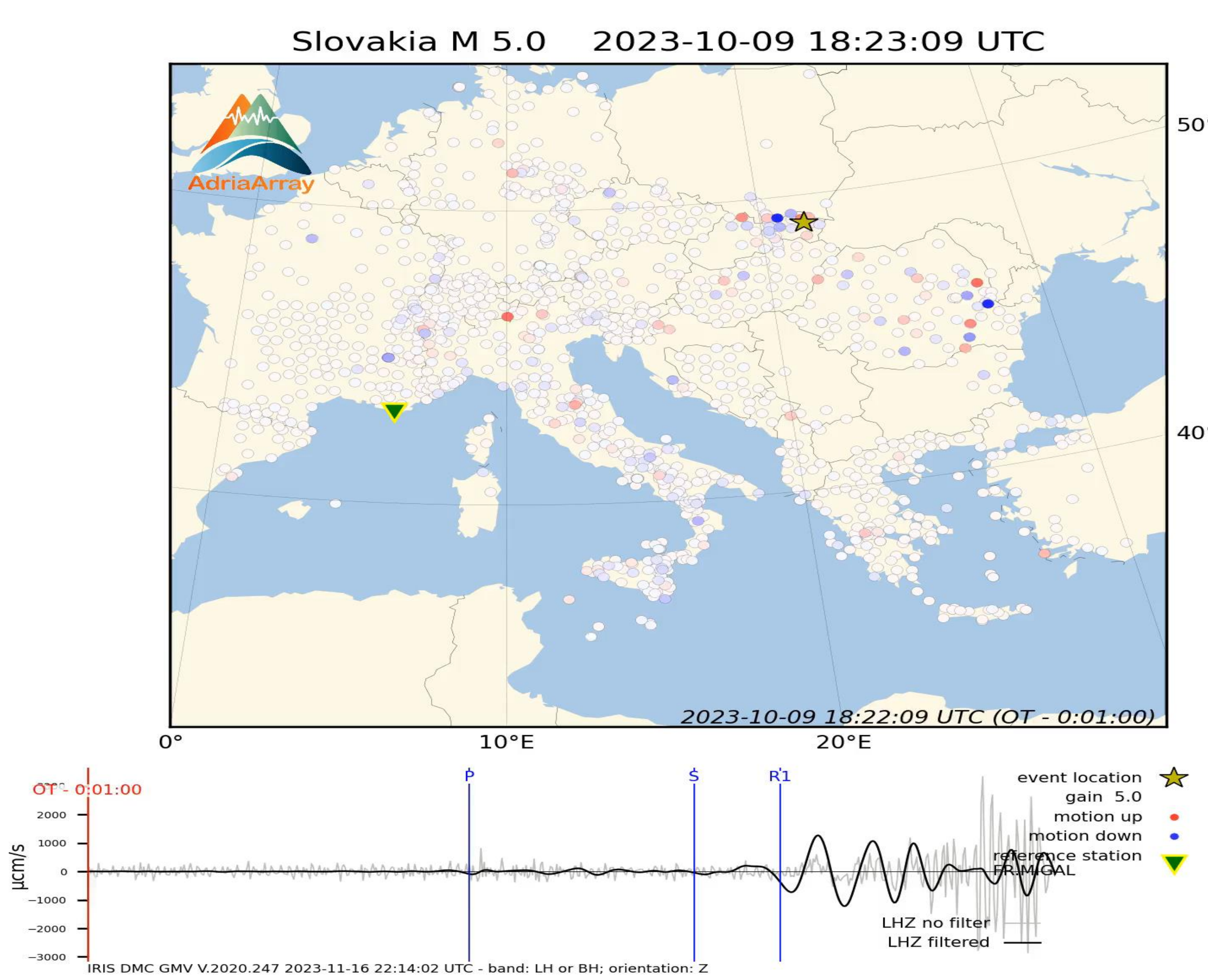

IRIS DMC (2010), Data Services Products: GMV; modified

Earthquake Oct 9th, 2023, M5.0 in Slovakia

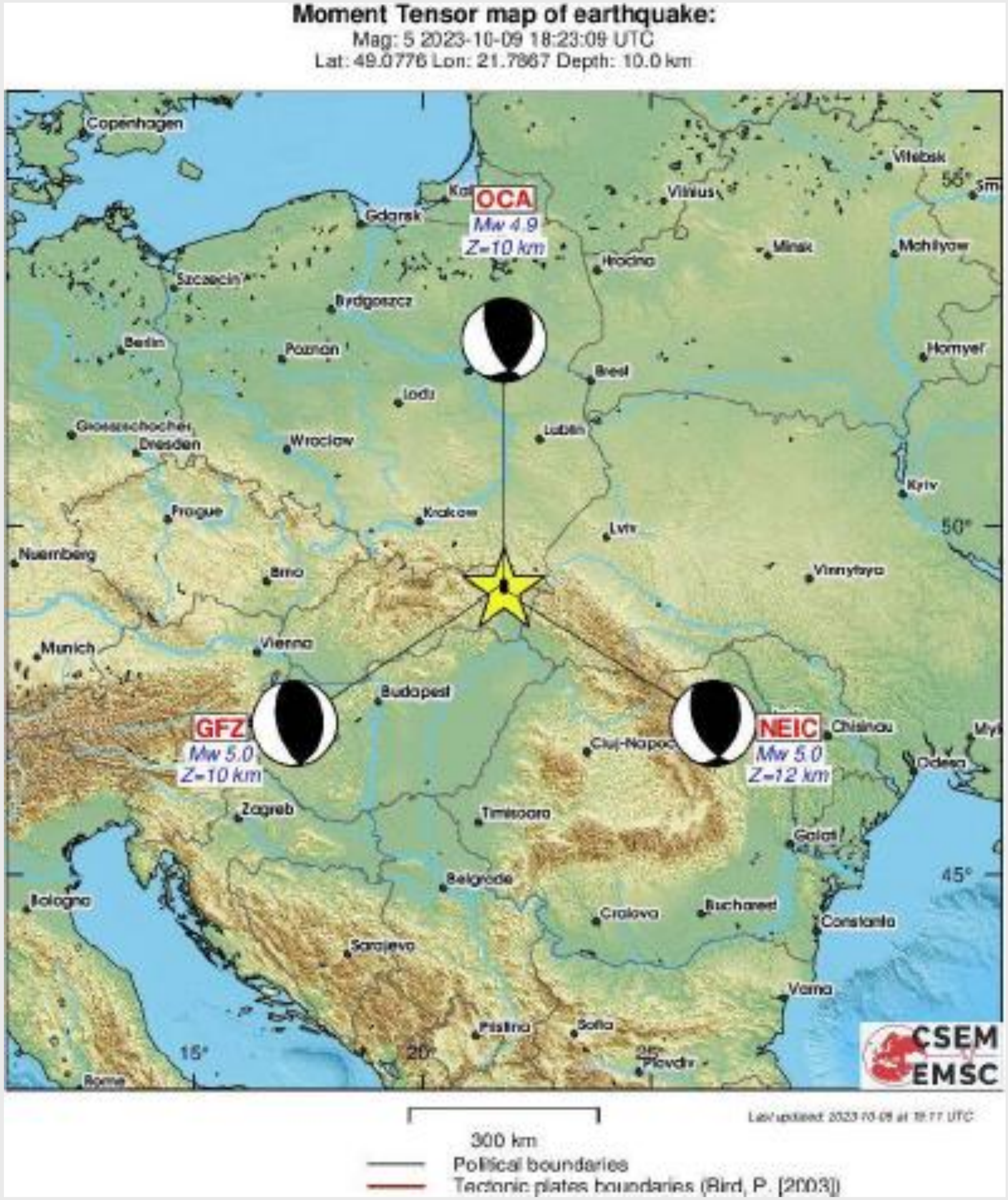

Earthquake Oct 9th, 2023, M5.0 in Slovakia

Location by PACASE – AdriaArray stations

(located in local model derived from CELL06 and CELL11 / by fastHYPO)

Date/Time : 09.10.2023 / 20:23:08.9

Local magnitude: 4.9

Lat: 49.0575+- 0.8556km

Lon:21.7173+- 0.7508km

Depth 7.32+- 2.02km

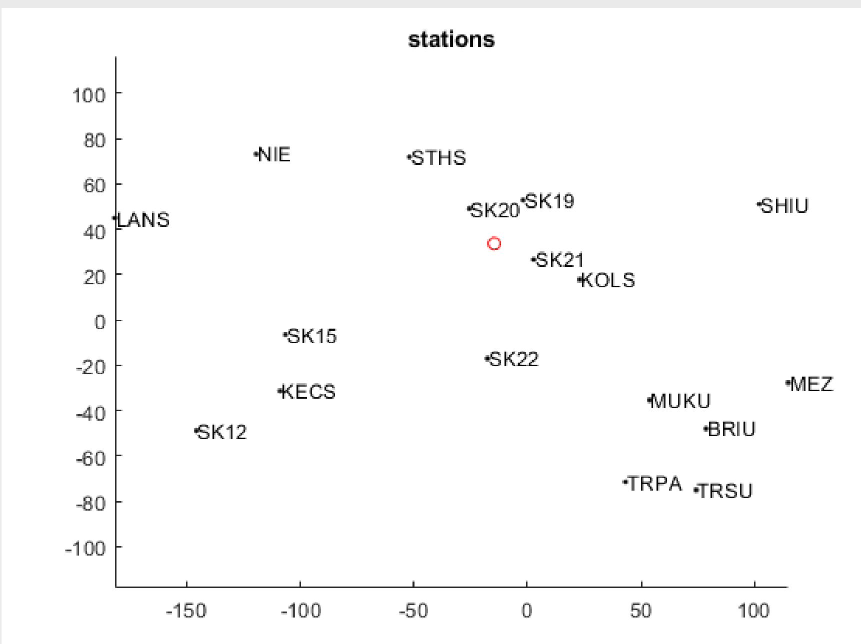

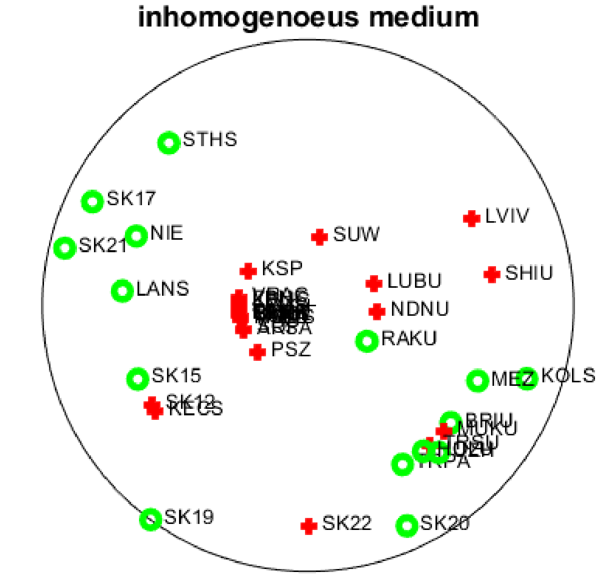

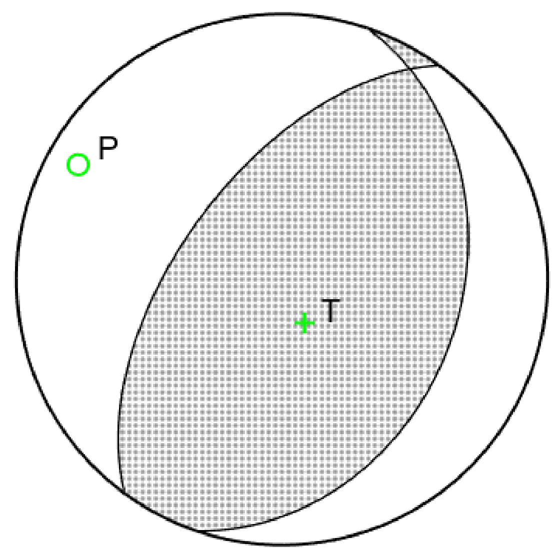

Earthquake Oct 9th, 2023, M5.0 in Slovakia

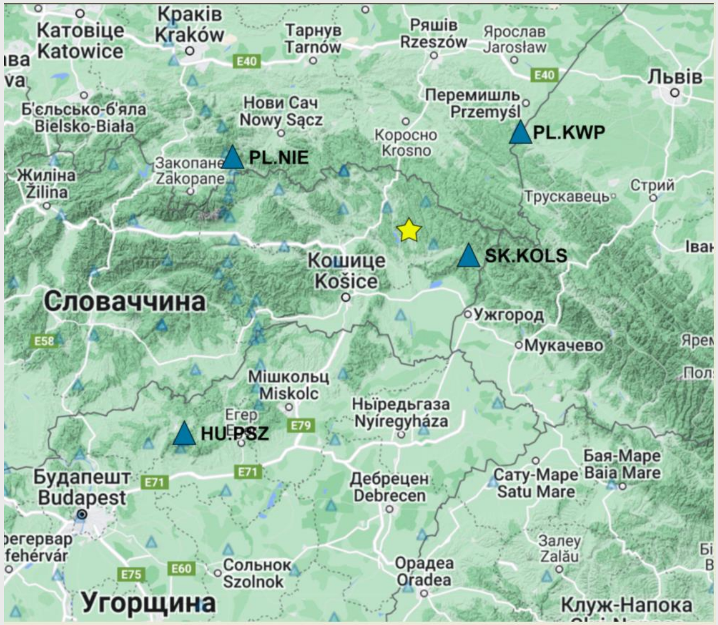

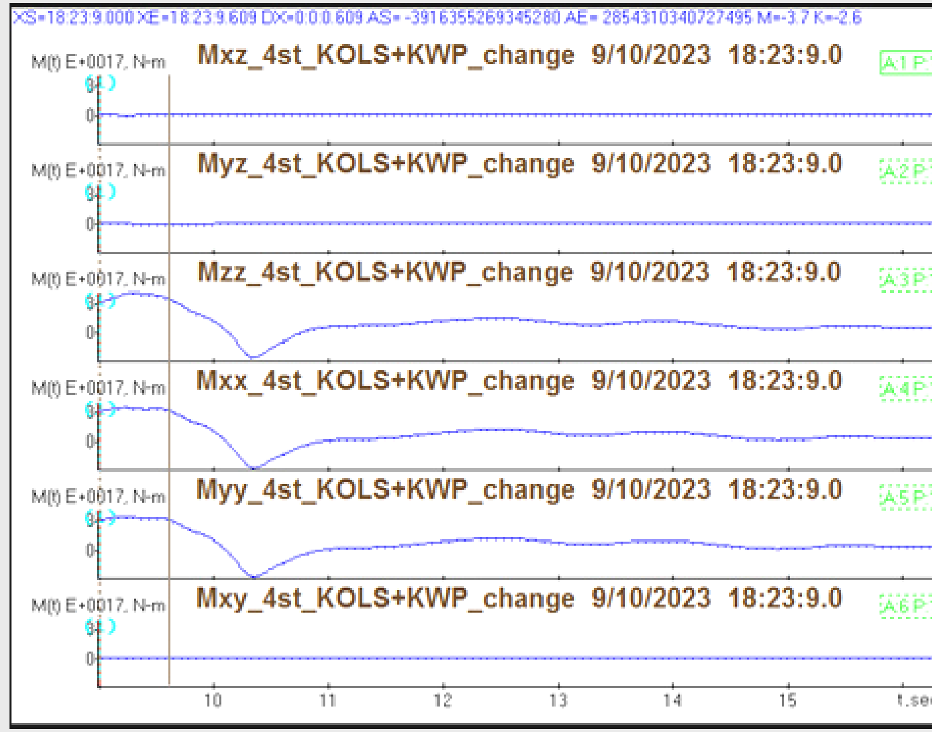

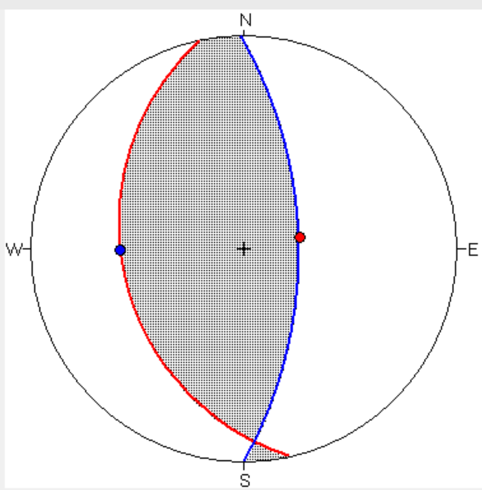

EventID: 100

Plane 1: (168, 30, 80)

Plane 2: (359, 60, 95)

CSIR

Exit

W-phase Moment Tensor (Mww)

Moment	3.470e+16 N-m
Magnitude	4.96 Mww
Depth	11.5 km
Percent DC	71%
Half Duration	0.79 s
Catalog	US
Data Source	US [1]
Contributor	US [1]

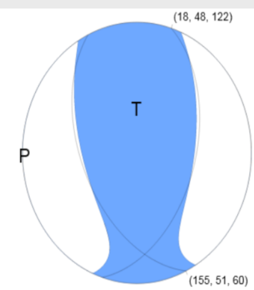

Malytsky – in preparation

Earthquake Oct 9th, 2023, M5.0 in Slovakia

Slovak katalog – 1643-2020

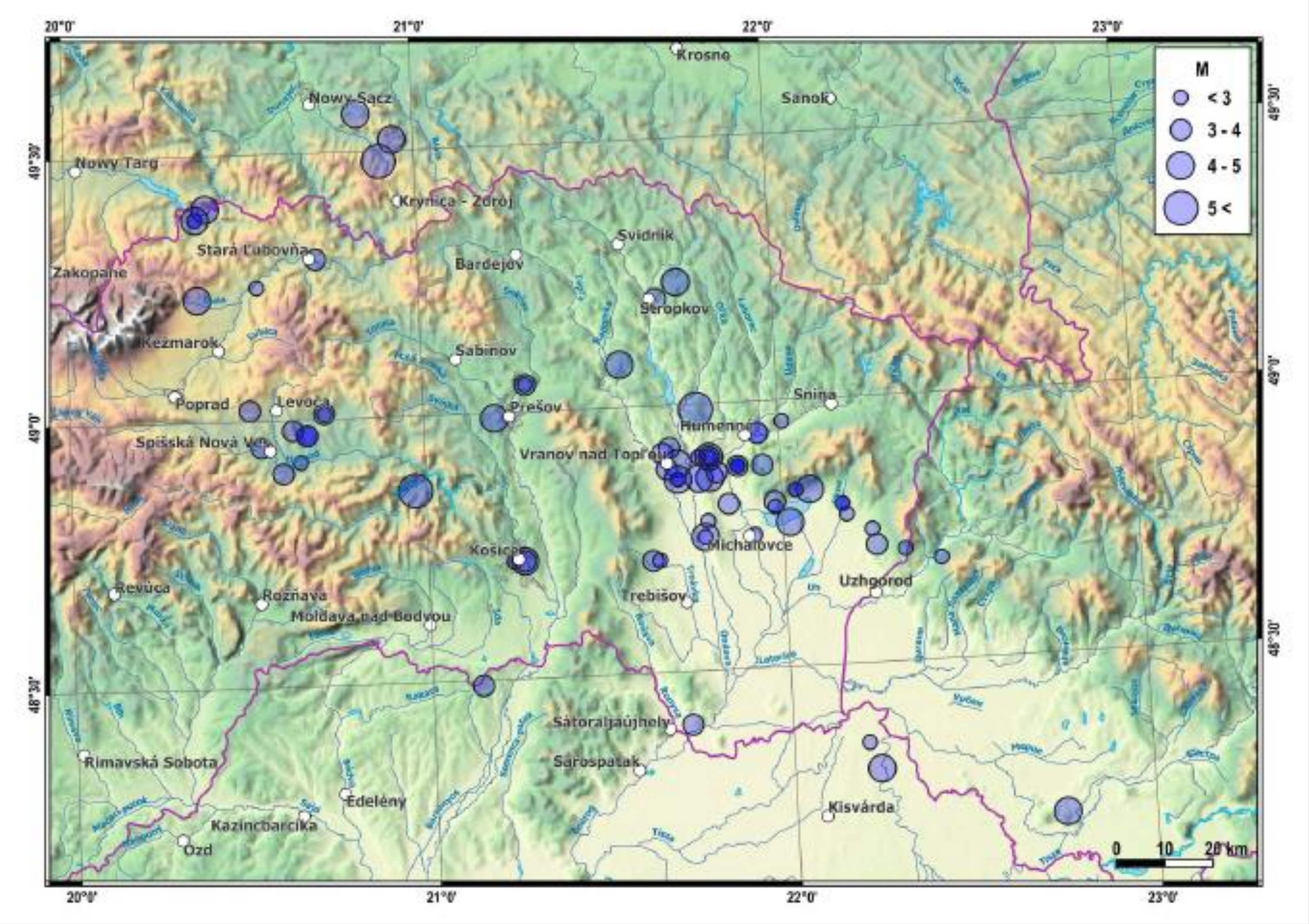

Earthquake Oct 9th, 2023, M5.0 in Slovakia

Slovak katalog – 1643-2020

1	cislo zt	year	mounth	day	hour	min	sec	latitude	longitude	depth	I0	M(I0)	ML	region
2	27	1643	6	5	11			49,23	20,37		6	4,1		Spis
3	29	1652	3	7				48,72	21,27		5	3,6		Kosice
4	32	1656						49,01	20,72		5	3,6		Spis
5	35	1669	2	27				48,95	20,54		5	3,6		Spis
6	36	1676	3	26				48,72	21,27		7	4,6		Kosice
7	41	1703	7	28				48,86	20,97		8	5,2		Gelnica
8	44	1724	3	10	21			48,97	20,67		5	3,6		Spis
9	45	1724	3	12				48,97	20,67		5	3,6		Spis
10	46	1724	3	13	7			48,97	20,67		5	3,6		Spis
11	47	1724	6	12				48,9	20,6		5	3,6		Spis
12	48	1724	6	13				48,98	20,63		5	3,6		Spis
13	118	1778	12	19	8			48,99	21,77	12	7	5		HUMENNE - VRANOV
14	122	1778	12	23	6			48,86	21,71		7	4,8		HUMENNE - VRANOV
15	123	1779	4	6	3	15		48,86	21,77		7	4,8		HUMENNE - VRANOV
16	128	1780	4	4	2			48,94	21,94		5	3,7		HUMENNE - VRANOV
17	162	1787	7	12				48,4	21,72		5	3,7		Slovenske Nove Mesto
18	176	1809	11	17	21	40		48,99	21,2		7	4,8		Saris
19	224	1840	4	23				49,38	20,37		7	4,8		Spis
20	349	1885	8	17	18	35		48,89	21,71		6	4,3		HUMENNE - VRANOV
21	360	1890	12	28	11	32		48,9	21,8	10	6,5	4,6		HUMENNE - VRANOV
22	367	1893	4	15	4	48		49,23	21,73	9	6,5	4,6		HUMENNE - VRANOV
23	377	1901	10	21	1	20		49,4	20,4		6,5	4,5		Spis
24	505	1914	5	26	20	29		49,08	21,56		7	4,8		HUMENNE - VRANOV
25	556	1932	2	18	23	15		48,75	21,78	9	5,5	4,1		HUMENNE - VRANOV
26	565	1941	6	5	2	49	57	48,86	21,8	3	7	4,4		HUMENNE - VRANOV
27	566	1941	6	5	5	15		48,87	21,82		5	3,7		HUMENNE - VRANOV
28	624	1978	3	22	19	20		48,91	21,67	6	5	3,3		HUMENNE - VRANOV
29	625	1978	7	19	0	57		48,88	21,68		5	3,7		Puste Cemerne - East Slovakia
30	630	1982	7	1	5	50	1	48,3	22,24	7	6	4		Ukraina
31	651	1992	6	28	23	19	30,6	49,57	20,84	24	5	4,2		Poland - Krynica
32	652	1992	6	29	0	29	47,6	49,52	20,94	14	5,5	4,2		Poland - Krynica
33	654	1992	9	22	8	24	42,5	48,88	21,95	11	5	3,9		HUMENNE - VRANOV
34	655	1993	3	1	7	42	39,2	49,48	20,9	12	7	5		Poland - Krynica
35	703	2003	5	20	20	13	39,8	48,83	22,09	4,5	6,5	4,3	3,7	EASTERN SLOVAKIA - Vihorlat
36	723	2006	11	23	7	15	20,4	48,2	22,75	21	6,5	4,9	4,3	UKRAJINA
37	787	2020	4	23	23	18	27,21	48,77	22,02	16	5,5	4,2	3,3	Vihorlatské vrchy

Earthquake Oct 9th, 2023, M5.0 in Slovakia

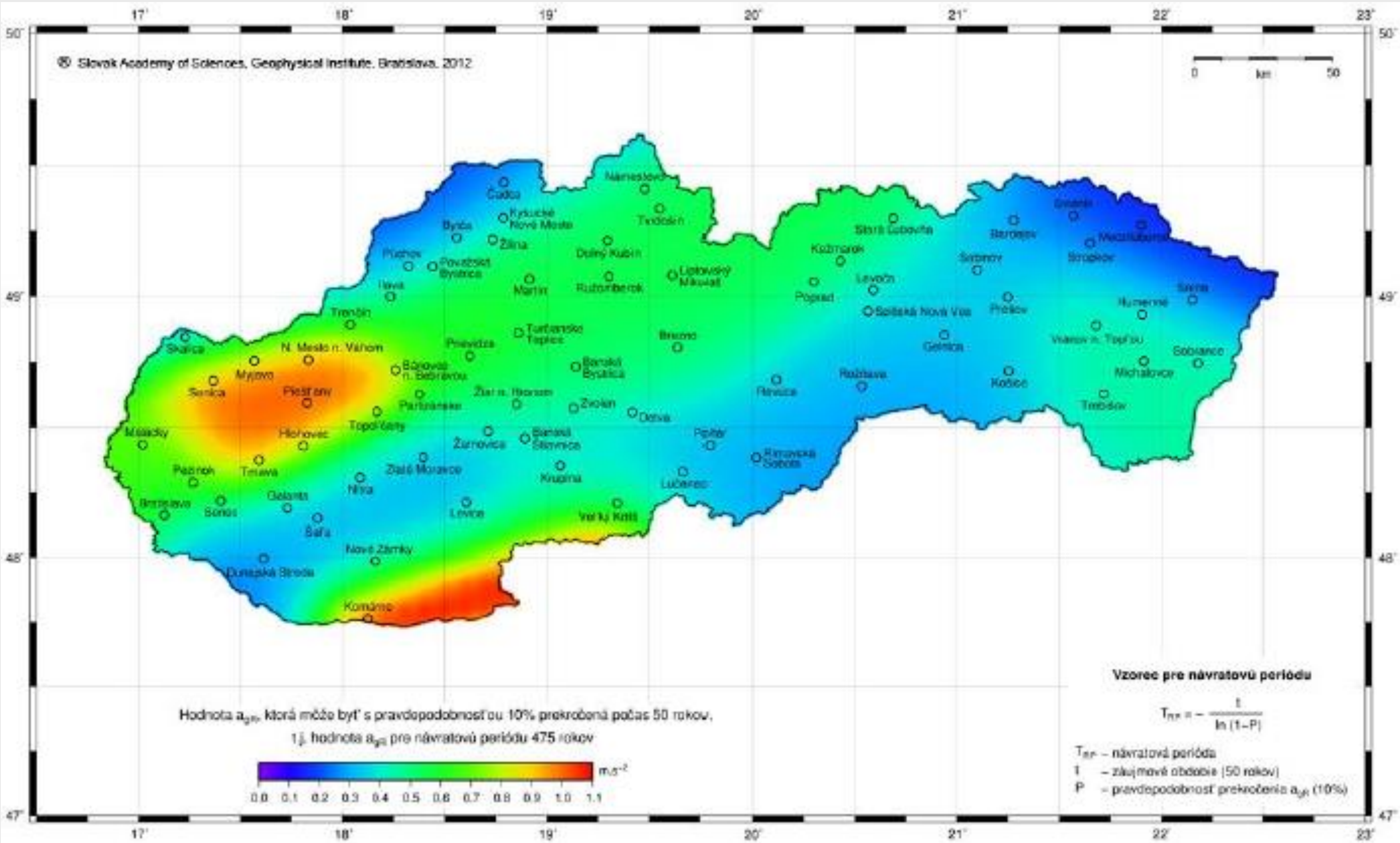

Earthquake Oct 9th, 2023, M5.0 in Slovakia – Macroseismic Intensity EMS-98

www.seismology.sk

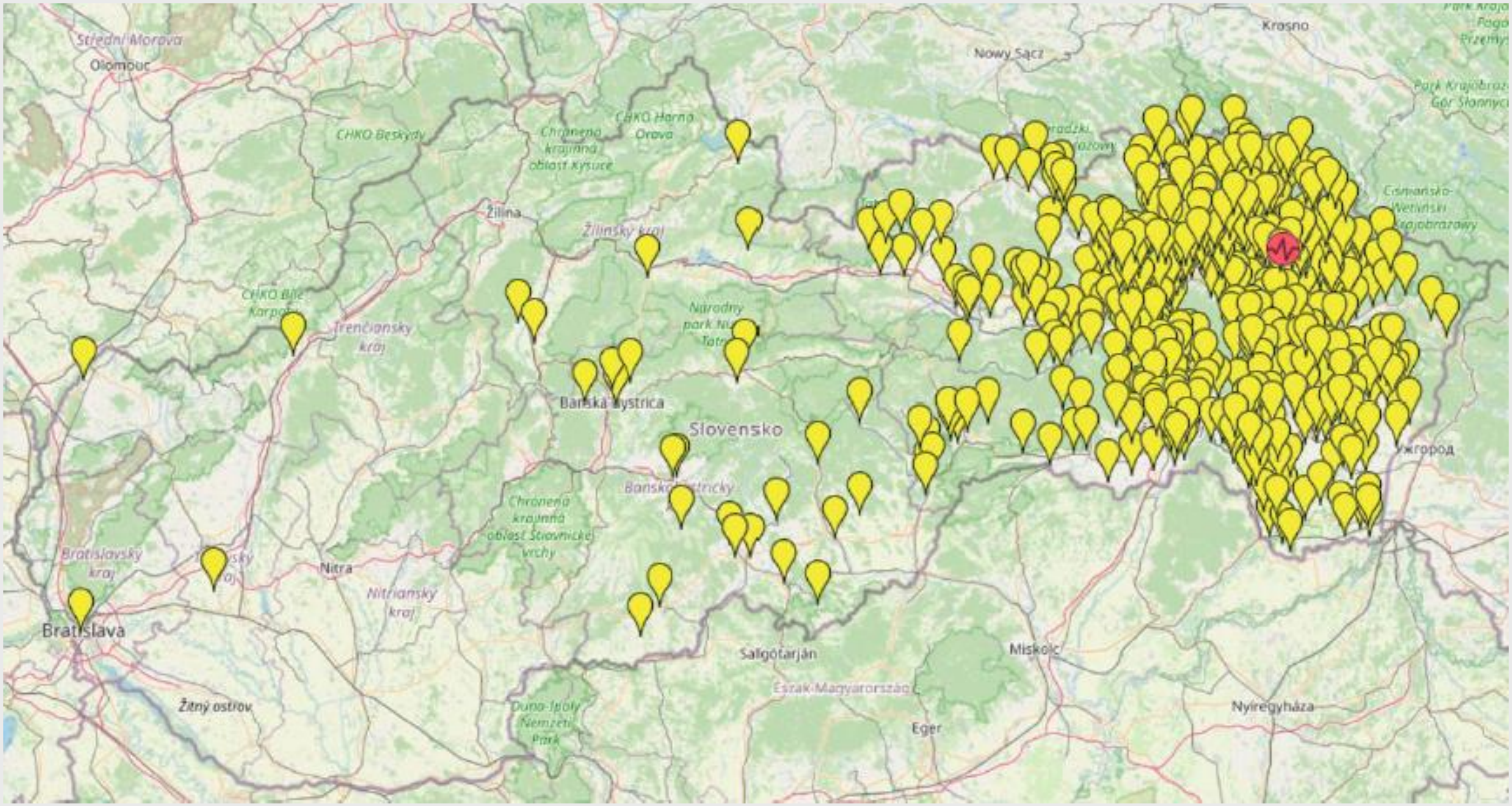

Earthquake Oct 9th, 2023, M5.0 in Slovakia – Macroseismic Intensity EMS-98

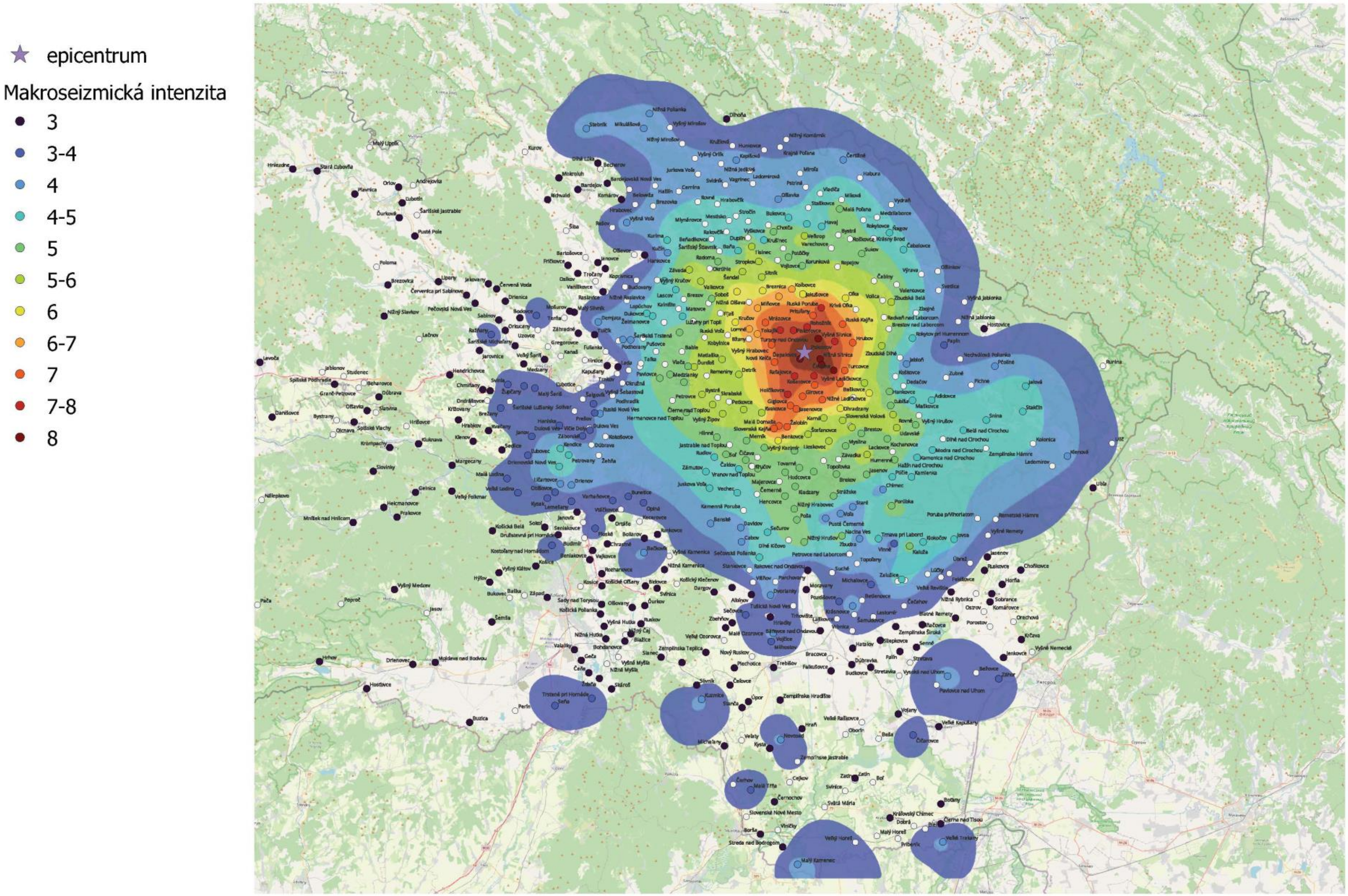

Earthquake Oct 9th, 2023, M5.0 in Slovakia

Earthquake Oct 9th, 2023, M5.0 in Slovakia

Earthquake Oct 9th, 2023, M5.0 in Slovakia

Earthquake Oct 9th, 2023, M5.0 in Slovakia

Earthquake Oct 9th, 2023, M5.0 in Slovakia

Earthquake Oct 9th, 2023, M5.0 in Slovakia

Earthquake Oct 9th, 2023, M5.0 in Slovakia

Earthquake Oct 9th, 2023, M5.0 in Slovakia

Earthquake Oct 9th, 2023, M5.0 in Slovakia

Earthquake Oct 9th, 2023, M5.0 in Slovakia

Earthquake Oct 9th, 2023, M5.0 in Slovakia

Earthquake Oct 9th, 2023, M5.0 in Slovakia

Earthquake Oct 9th, 2023, M5.0 in Slovakia

Earthquake Oct 9th, 2023, M5.0 in Slovakia

Earthquake Oct 9th, 2023, M5.0 in Slovakia

Earthquake Oct 9th, 2023, M5.0 in Slovakia

Earthquake Oct 9th, 2023, M5.0 in Slovakia

Earthquake Oct 9th, 2023, M5.0 in Slovakia

Earthquake Oct 9th, 2023, M5.0 in Slovakia

Earthquake Oct 9th, 2023, M5.0 in Slovakia

Nižná Sitnca

Earthquake Oct 9th, 2023, M5.0 in Slovakia

Nižná Sitnca

Earthquake Oct 9th, 2023, M5.0 in Slovakia

Earthquake Oct 9th, 2023, M5.0 in Slovakia

Earthquake Oct 9th, 2023, M5.0 in Slovakia

Earthquake Oct 9th, 2023, M5.0 in Slovakia

Earthquake Oct 9th, 2023, M5.0 in Slovakia

Earthquake Oct 9th, 2023, M5.0 in Slovakia

Earthquake Oct 9th, 2023, M5.0 in Slovakia

CONCLUSION

- the earthquake verified the team work of (not only) Slovak seismologists

- AdrriaArray stations played a key role in the determination of the earthquake parameters

- www.seismology.sk

CONCLUSION

- the earthquake verified the team work of (not only) Slovak seismologists

- AdrriaArray stations played a key role in the determination of the earthquake parameters

- www.seismology.sk

Thank you for you attention

Empirical Green's functions method to calculate Apparent Source Time functions (ASTFs)

Vladimir Plicka

Charles University

Czech-Romanian Seismology Workshop: AdriaArray local experiment in Vrancea (Romania), December 5th – 6th 2023

AdriaArray

Overview

- History
- New method based on Non-Negative least square technique
- Software description
- Earthquake implementation
  - The 2020 Samos (Aegean Sea) M7 earthquake
  - The 2021 shallow earthquake in the Western Corinth Rift
  - Deep China earthquake
- Conclusion
- Future plans

Empirical Green function

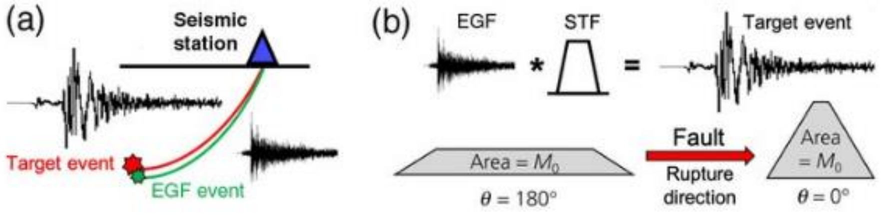

Lui and Huang (2019)

The first application by Hartzell (1978), and many followers: Mueller (1985), Fukuyama and Irikura (1986), Mori and Frankel (1990), Ammon et al. (1993), Courboulex et al. (1997), Plicka and Zahradnik (1998), Vallee, 2004, Vallee and Douet (2014), ….

- Earthquake source inversions require a **good knowledge of the medium** along the source-station propagation path.
- **Weak earthquake** having similar focal mechanism and located close to the "**Target event**" can be considered as an **Empirical Green function**.

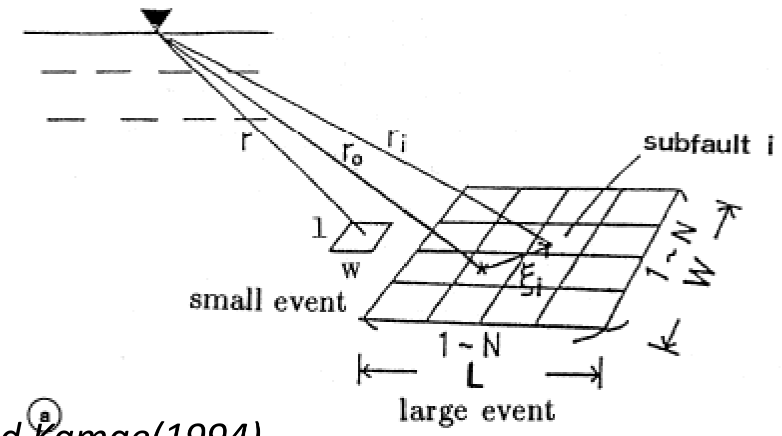

Irikura and Kamae(1994)

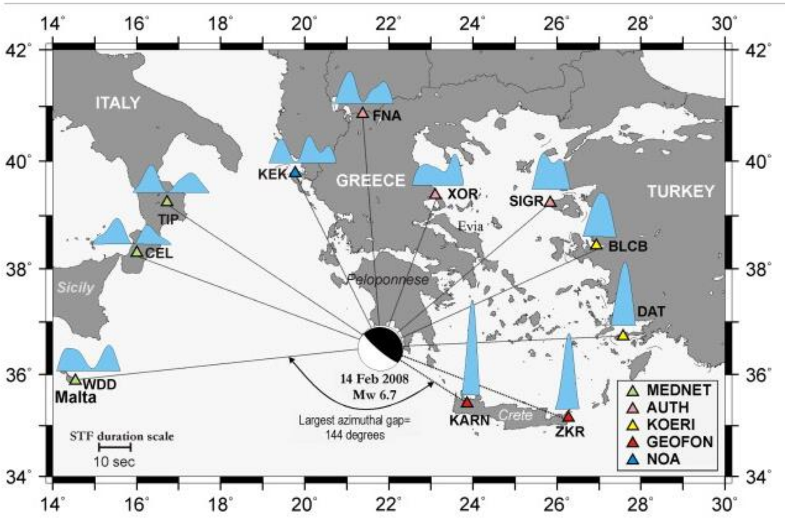

Roumelioti (2009)

How to retrieve ASTF?

- The idea is to **deconvolve** the mainshock from the smaller event, called the empirical Green function (EGF), to obtain a relative (apparent) source time function at each considered station (RSTF, ASTF).
- Deconvolution process is not stable (dividing by small numbers in the frequency domain) => different techniques (Damping factor deconvolution, Water level deconvolution, …)

$$\hat{f}(\omega) = \frac{d(\omega)w^*(\omega)}{w(\omega)w^*(\omega) + \delta}$$

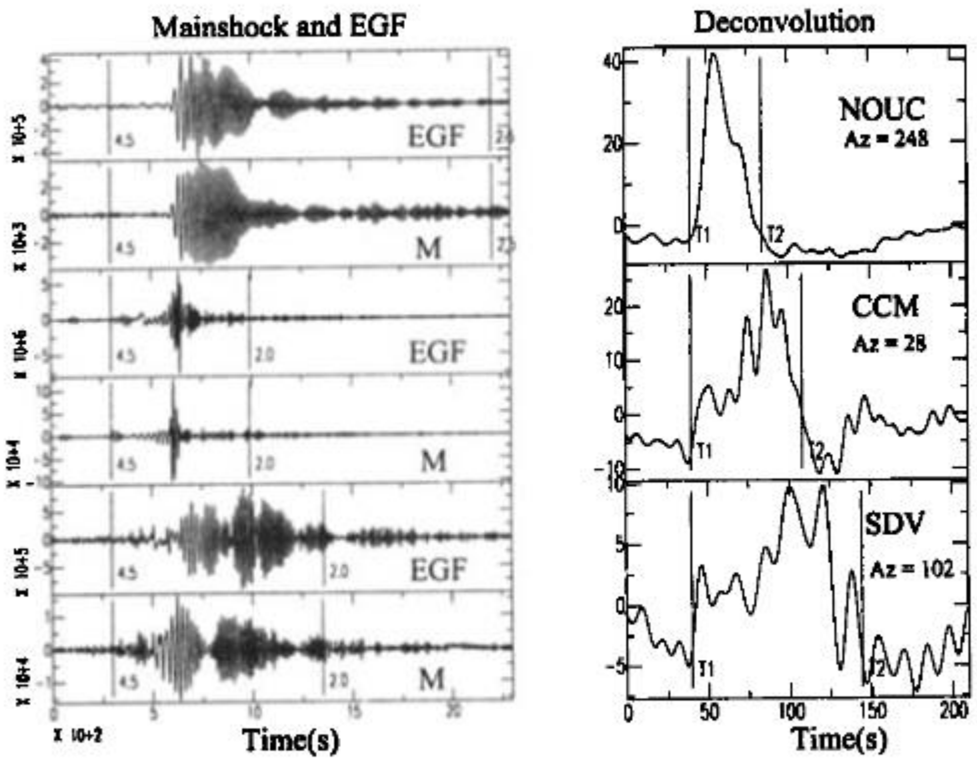

Courboulex et al. (1997)

- Deconvolution technique comes with some nonphysical features of RSTFs:

1. **There are some negative parts.**
2. **There is some acausal signal, that is, some signal arrives before the assumed beginning of the source time**
3. **There is some signal after the assumed duration of the source time functions.**
4. **The area of the source time function, the relative moment between the mainshock and the EGF, is different from one station to another.**

New method based on Non-Negative least square technique

Plicka et al., 2022

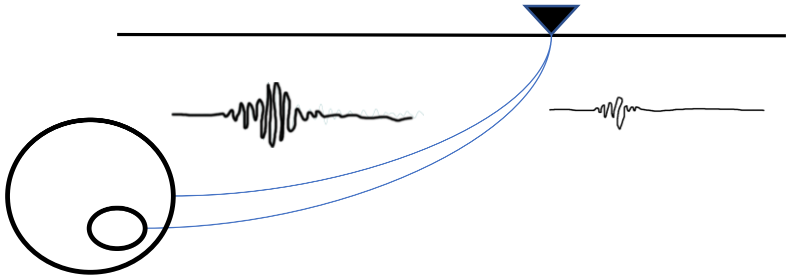

$s(t) = m(t) * g(t)$, EGF waveform

$S(t) = M(t) * g(t)$, Mainshock waveform

$M(t), m(t)$ moment rate functions

$m(t)$ can be expressed as an isosceles triangle, centered at time t=0, whose duration is shorter than the duration of $M(t)$

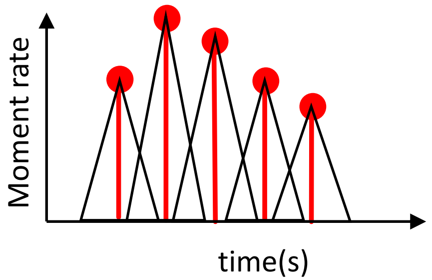

$M(t)$ is expressed as a set of equidistantly shifted functions $m(t)$, where w_i are the unknown weights.

$$M(t) = \sum_{i=1}^{N} m(t - \tau_i) w_i$$

$$S(t) = [\sum_{i=1}^{N} m(t - \tau_i) w_i] * g(t) = \sum_{i=1}^{N} s(t - \tau_i) w_i$$

Weighted sum of the EGF shifted records

$$M_0 = \sum_{i=1}^{N} m_0 w_i, \ \frac{M_0}{m_0} = \sum_{i=1}^{N} w_i$$

The ratio of the scalar moments of the mainshock and the EGF event (the relative moment) provides a constraint for the weights.

$$
\begin{pmatrix}
s(t_1-\tau_1) & s(t_1-\tau_1) & \cdots & s(t_1-\tau_N) \\
s(t_2-\tau_1) & s(t_2-\tau_2) & \cdots & s(t_2-\tau_N) \\
. & . & . & . \\
s(t_M-\tau_1) & s(t_M-\tau_2) & \cdots & s(t_M-\tau_N) \\
1 & 1 & \cdots & 1
\end{pmatrix}
\begin{pmatrix}
w_1 \\ w_2 \\ . \\ w_N
\end{pmatrix}
=
\begin{pmatrix}
S_1 \\ S_2 \\ . \\ S_M \\ \frac{M_0}{m_0}
\end{pmatrix}
$$

Nonnegative least-squares inversion (NNLS)
Lawson & Hanson (1974)

Assumption

The elementary assumptions of the EGF method must be met

Similar focal mechanism and similar location

The outputs: In case of quality data, the software provides an ASTF, which is:

- Non-negative (by definition).
- Causal, i.e. starting generally at origin time (t=0); we allow small signals before t=0.
- Stable, i.e. having generally only small artifacts beyond the major ASTF part.
- The area of ASTF is proportional to the relative moment (Mo/mo) at each station.

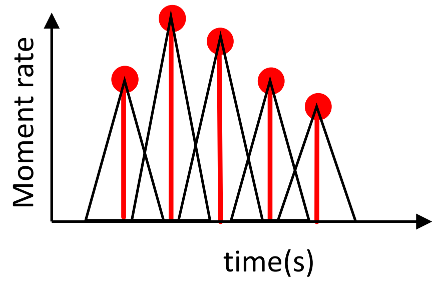

- The time shift value $\tau_i = (i-1)\Delta\tau$ and their number N are predefined.
- The waveforms are filtered with a band-pass filter (Harris, 1990) at a frequency band (Fmin, Fmax). The duration of the triangle $m(t)$ is defined as 1/Fmax.
- The quality of the inversion is measured by the fit between the real and synthetic record, quantified by a variance reduction.

Running the program and data pre-processing

- A Fortran code and Gnuplot graphics scripts have been developed to perform the inversion and to automatically visualize the results.

- Pre-processing of the data
  - 3-components ASCII waveforms of the mainshock and EGF.
  - No instrumental correction is needed in case of the same instrument.
  - Before the first code run, both seismograms are aligned to have the same P-wave arrival times.
  - The S-wave alignment can be different because the locations of the mainshock and EGF are not exactly identical => Therefore, if inverting the whole record, or only S waves, we must allow for a possible start of the resulting ASTF before t=0, mentioned above as the small acausal effect.

Graphical outputs

The result of the inversion
The weights obtained by Non Negative least square method in predefined time interval.

Moment rate
obtained by summation of triangles with predefined duration (T_1 = 1/fmax)

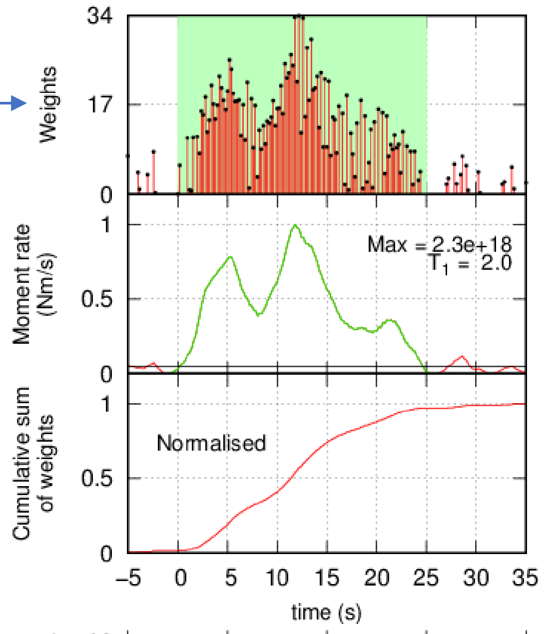

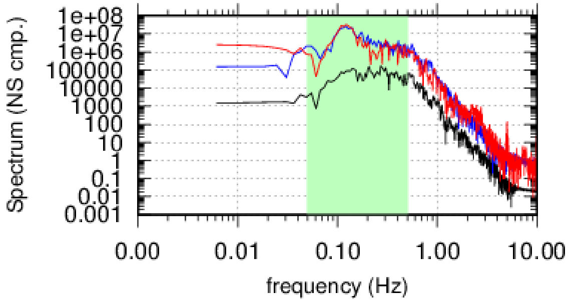

Amplitude spectrum of NS comp.
Black … EGF
Blue … observed mainshock
Red … synthetic mainshock

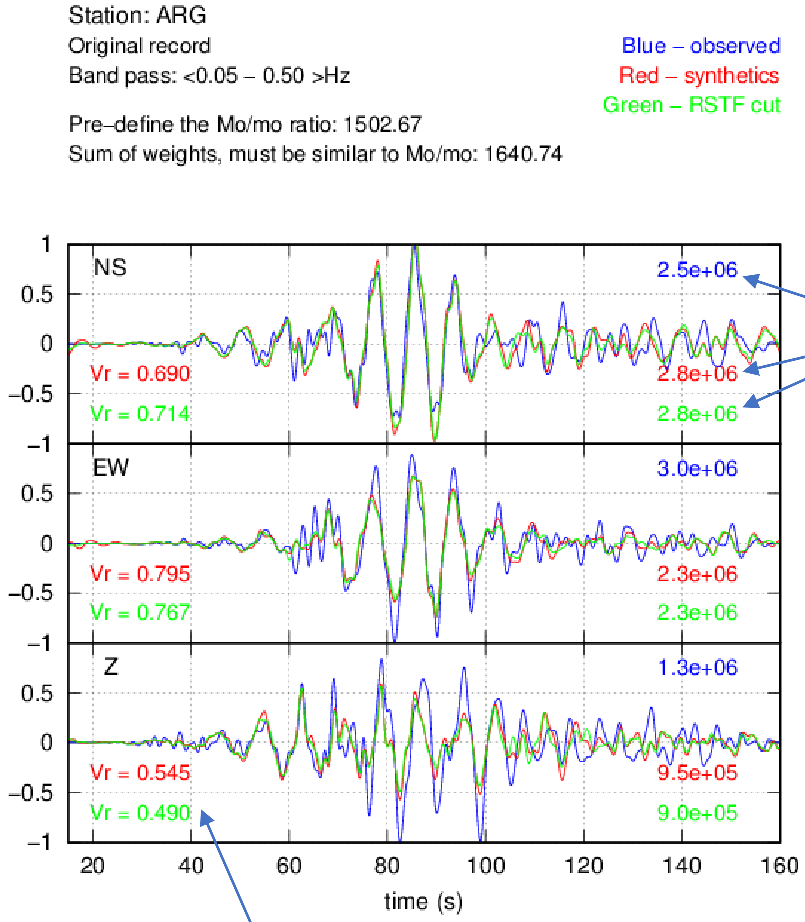

Maximum amplitudes, here in counts

Variance reduction

Graphical outputs

The three-component normalized waveforms

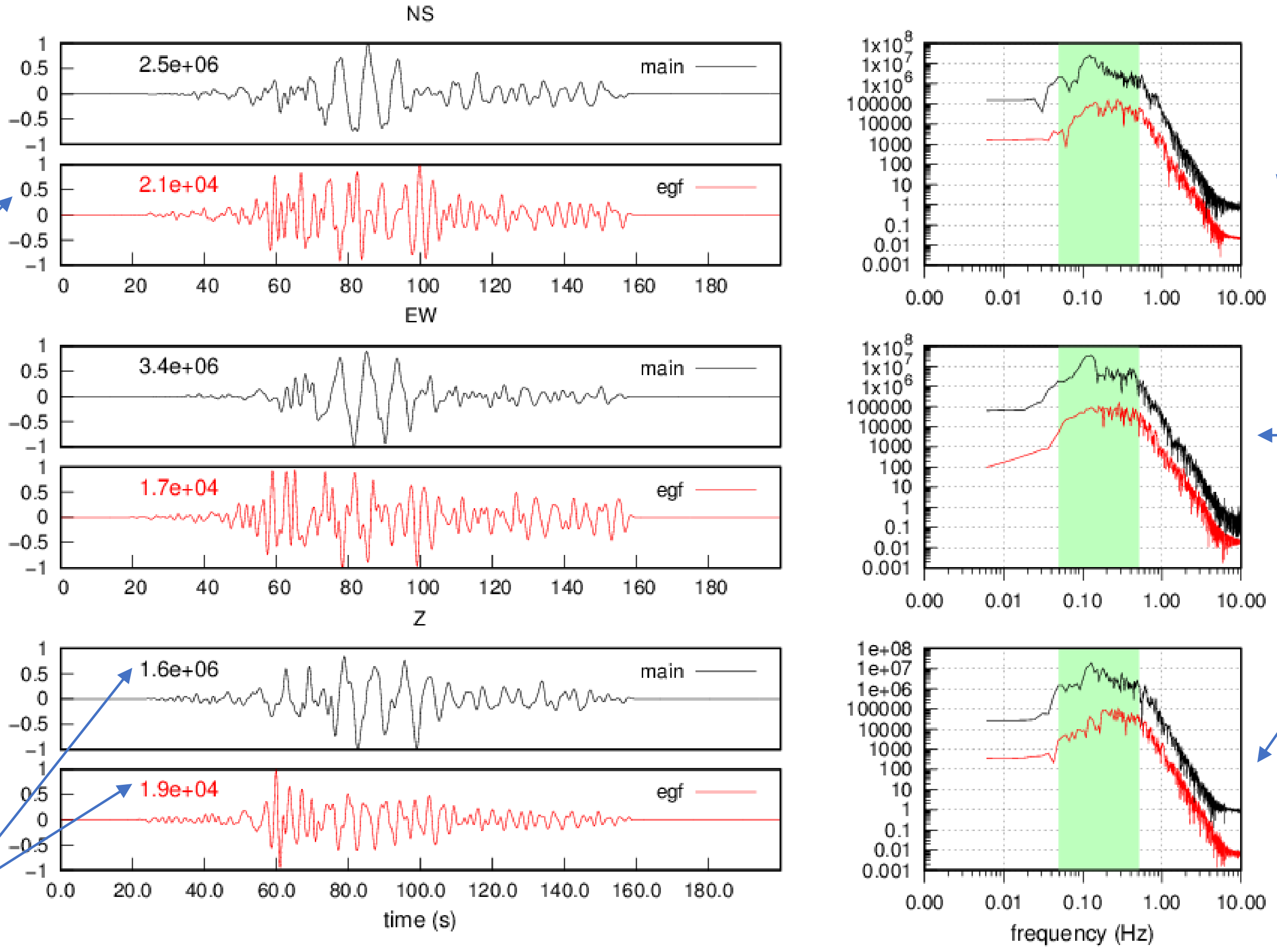

The amplitude spectra of the mainshock and EGF

The true amplitudes

The 2020 Samos (Aegean Sea) M7 earthquake

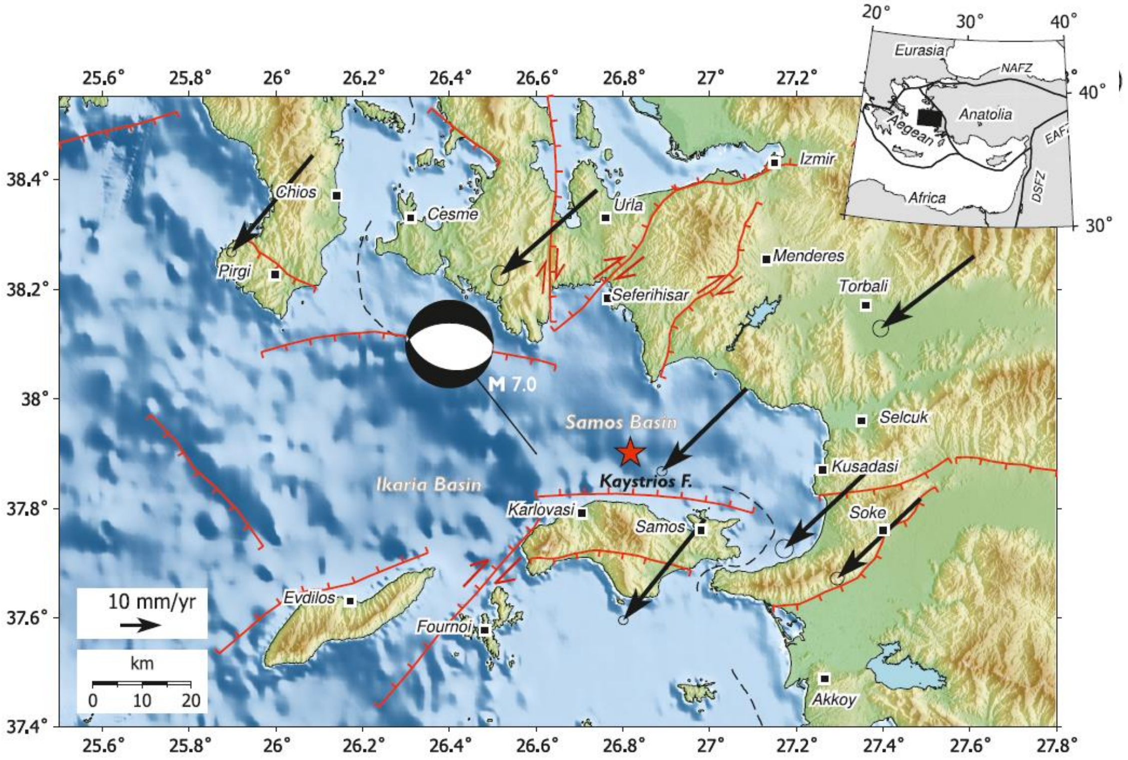

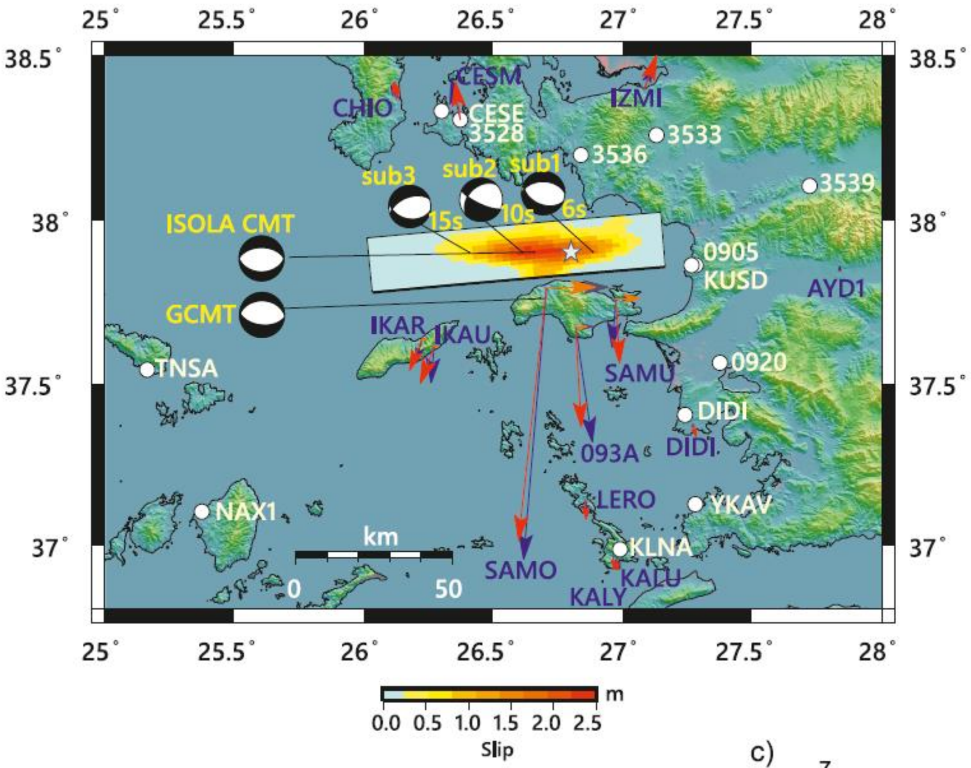

(Plicka et al., 2022)

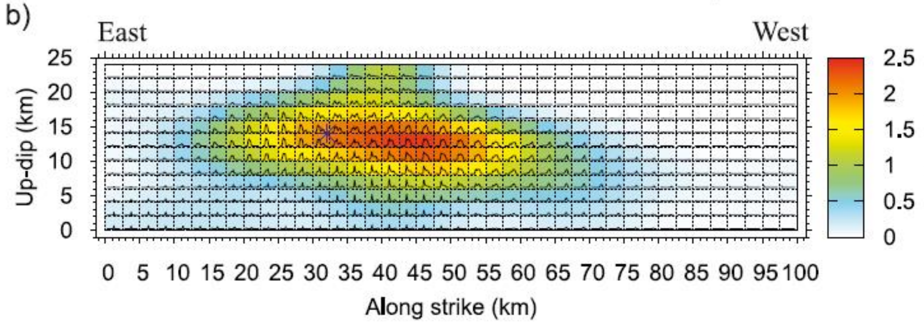

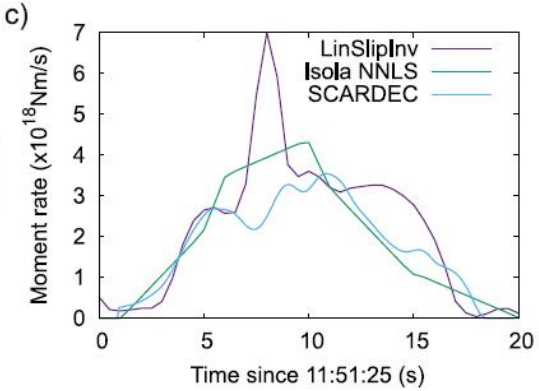

The 2020 Samos (Aegean Sea) M7 earthquake

Two aftershocks selected as EGFs to see the inversion stability.

1. Mw5 aftershock (Oct. 31, 2020, 05:31 UTC).
2. Mw5.1 aftershock (Ovt. 30, 2020, 13:00 UTC).

- BB and SM seismograms at **12 regional stations** *(NOA and ORFEUS EIDA nodes)*
- The full seismogram, including P and S waves and all three components were inverted.
- The frequency band of inversion: **20s - 0.5 Hz**
- The ASTFs are searched in a time interval from -5s to 35s relative to origin time, i.e. **40s** in total.

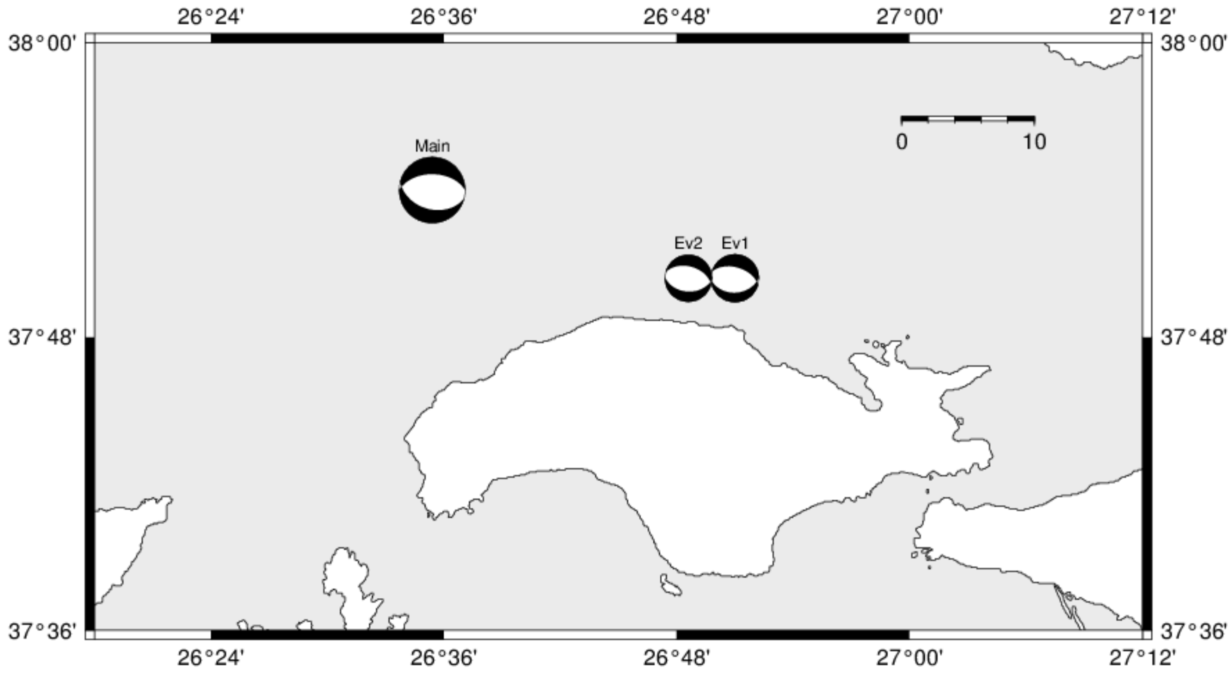

Rupture Directivity

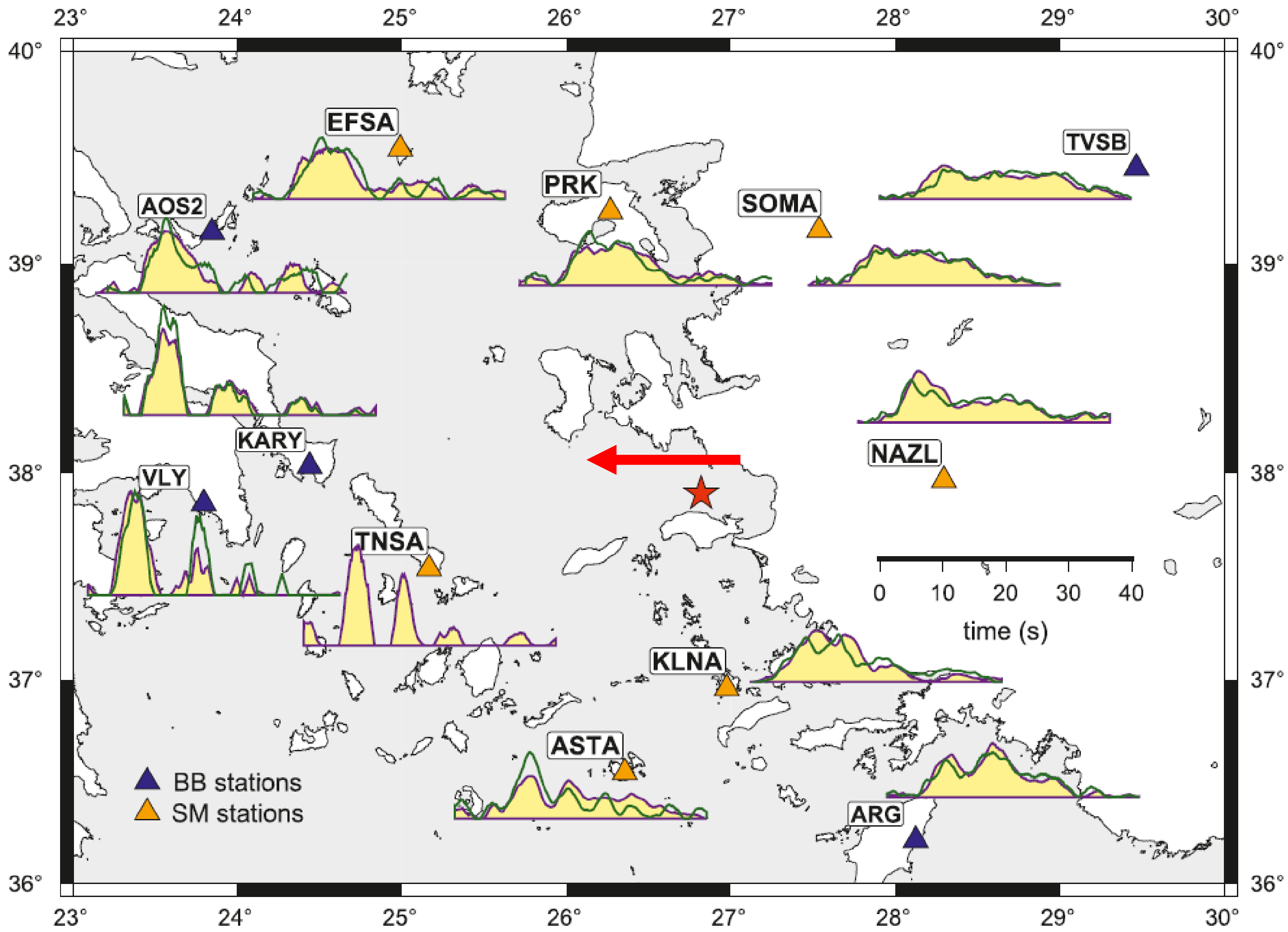

The inferred ASTFs from stations located orthogonal to the fault strike **(=270deg**) (EFSA, PRK, SOMA, TVSB in the north and KLNA, ASTA, ARG in the south) depict longer pulse duration and lower amplitudes, compared to those located along strike (KARY, VLY, TNSA in Greece and NAZL in Turkey), which supports **westward rupture propagation**.

More specifically, NAZL lies in the backward direction of rupture propagation, whereas KARY, VLY and TNSA in the forward direction, exhibiting narrow, high-amplitude pulses.

Assuming a **horizontal rupture propagation** featuring a **unilateral rupture propagation** on a part of the fault, apparent duration $\tau(f)$ as a function of station azimuth f can be described by

$$\tau(f) = T_1 + T_2\left(1 - \frac{V_R}{V_{P,S}}\cos(f-\alpha)\right) = T_D - \frac{L_2}{V_{P,S}}\cos(f-\alpha)$$

$T_D = T_1 + T_2$, ... total rupture duration
T_1, ... rupture duration corresponding to nondirective part of the fault
$T_2 = \frac{L_2}{V_R}$, ... rupture duration of the fault portion L_2 with assumed unilateral rupture propagation at speed V_R
$V_{P,S}$ ...P or S wave velocity
α...the rupture directivity azimuth

Green line:
$\alpha = N265°$ fixed from fault slip model
$T_D = 22s \pm 2s$
$\frac{L_2}{V_{P,S}} = 7s$, $L_2 = 24.5\ km$ for $V_S = 3.5\ km/s$

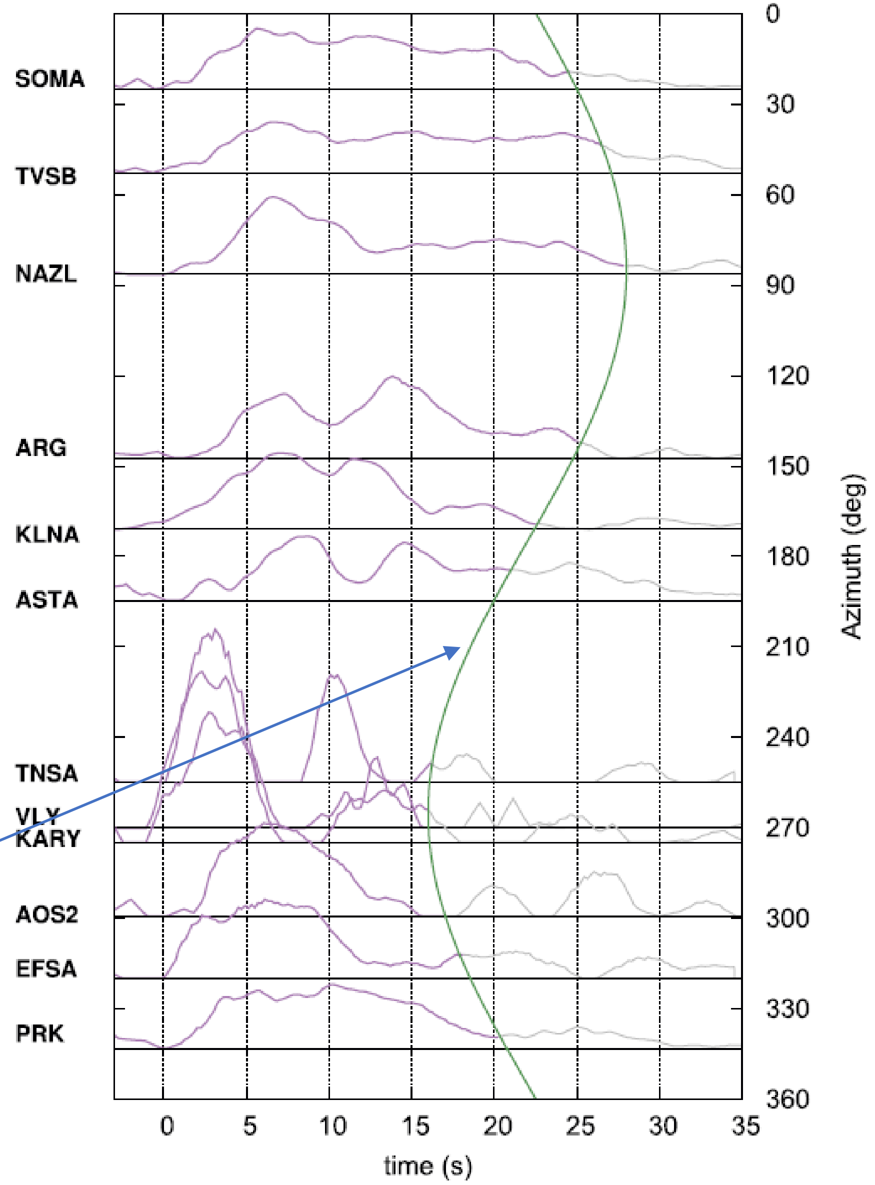

CRL crisis 2021

Kaviris, G., P. Elias, V. Kapetanidis, A. Serpetsidaki, A. Karakonstantis, V. Plicka, L. De Barros, E. Sokos, I. Kassaras, V. Sakkas, I. Spingos, S. Lambotte, C. Duverger, O. Lengliné, Ch. Evangelidis, I. Fountoulakis, O.-J. Ktenidou, F. Gallovič, S. Bufféral, E. Klein, El M. Aissaoui, O. Scotti, H. Lyon-Caen, A. Rigo, P. Papadimitriou, N. Voulgaris, J. Zahradnik, A. Deschamps, P. Briole and P. Bernard (2021). **The western Gulf of Corinth (Greece) 2020–2021 seismic crisis 1062 and cascading events: First results from the Corinth Rift Laboratory Network,** *The Seismic Record*, 1 (2), 85–95. doi: 10.1785/0320210021.

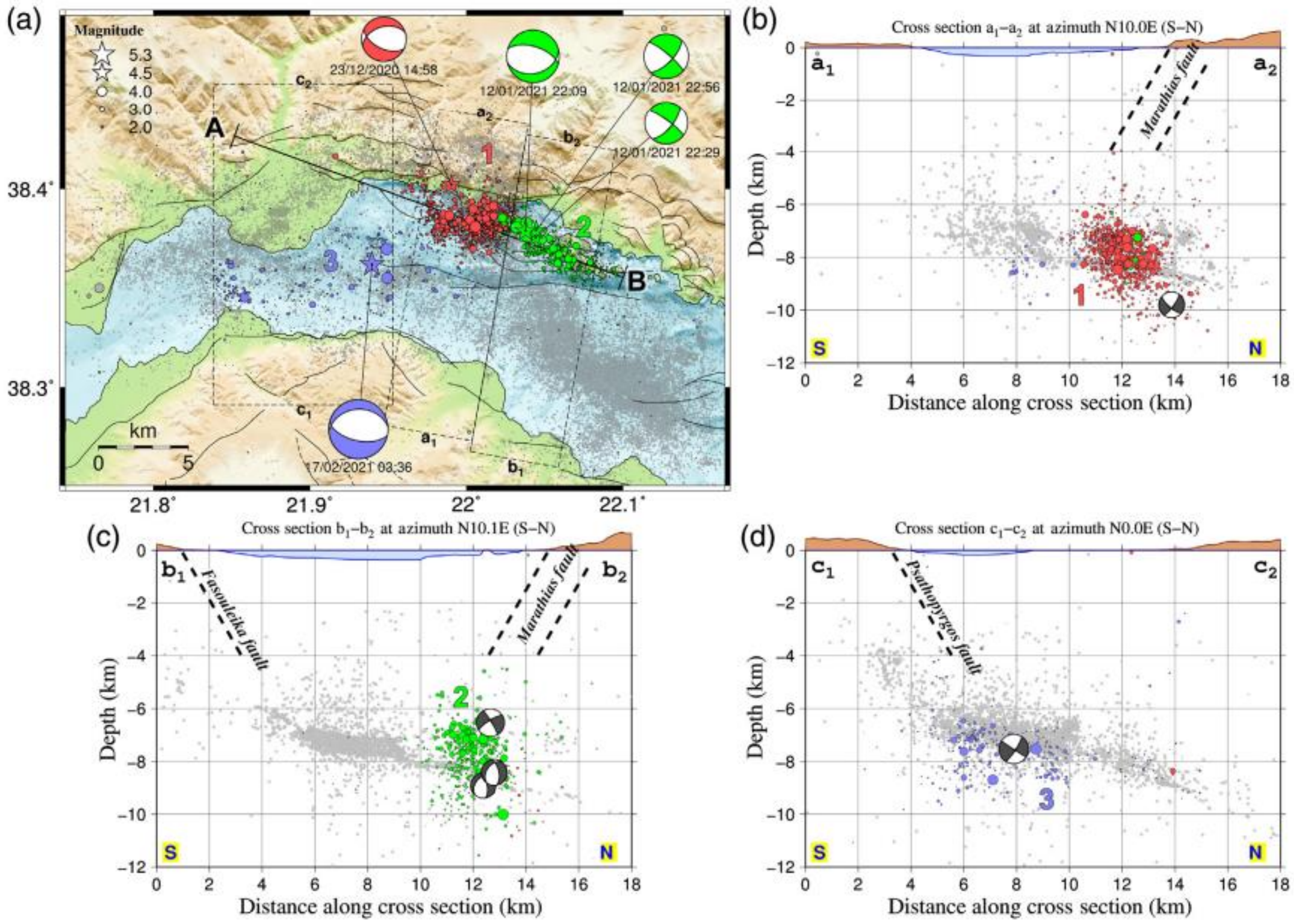

CRL crisis 2021 - continue

Zahradnik et al, 2022

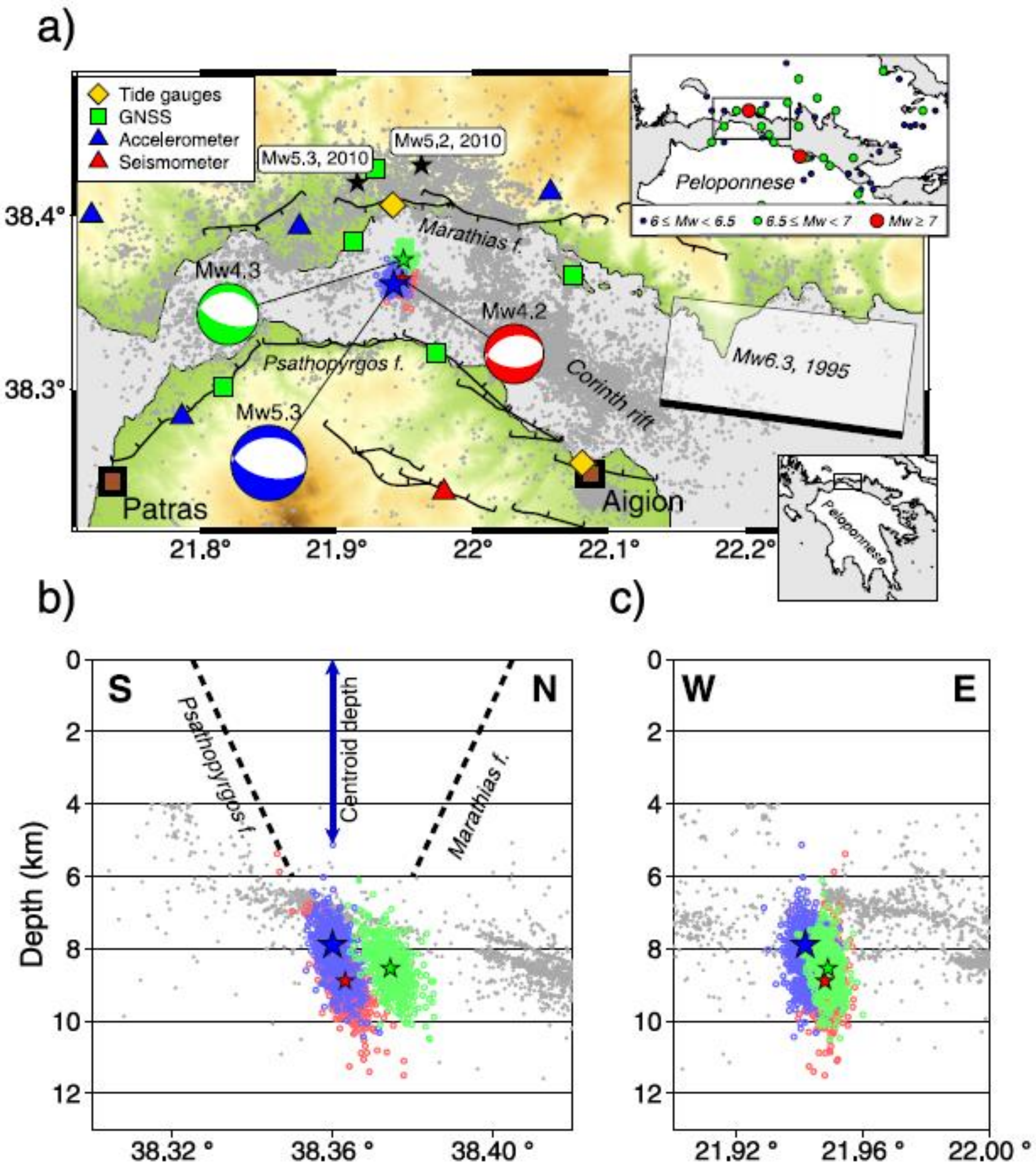

Multiple-point source (MPS) modeling

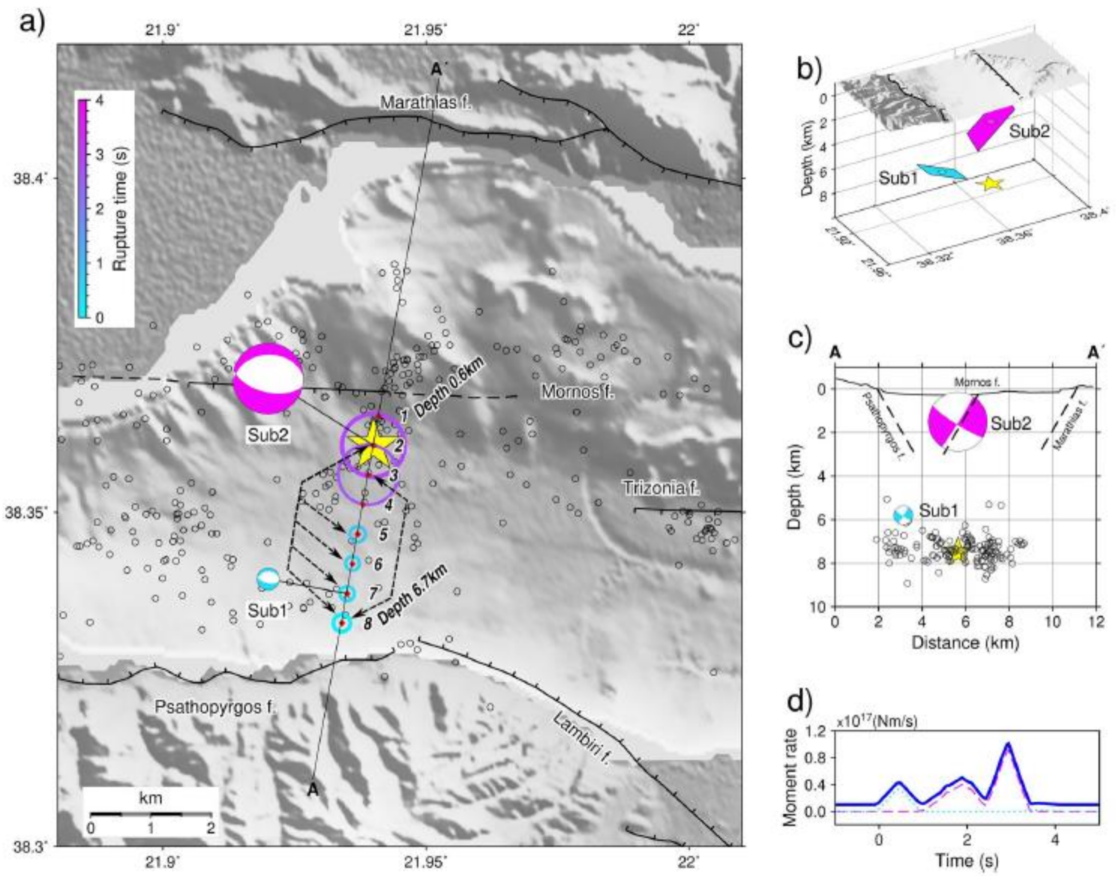

Finite-extent modeling of the shallow rupture.

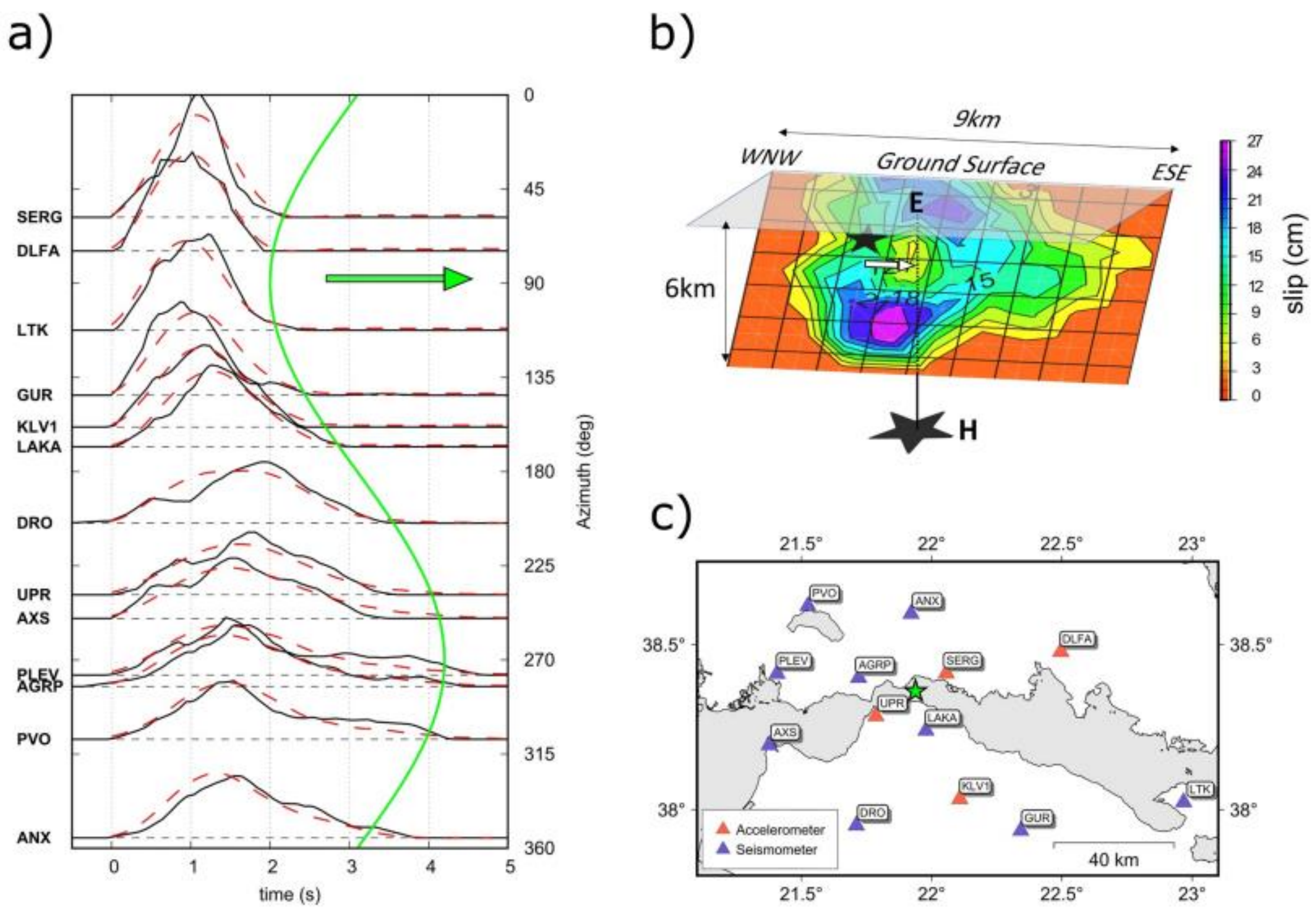

ASTF for frequencies up to 1 Hz (0.1–1.0 Hz)

Azimuthal variation of the durations around a ~3-second - compatible with MPS

Eastward-directivity model, N80°E - N100°E

Slip patch derived by inverting the ASTFs on a south-dipping plane. The mean slip is ~15 cm

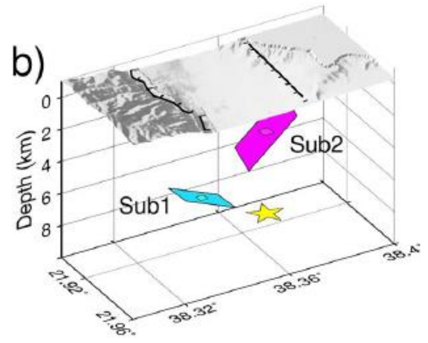

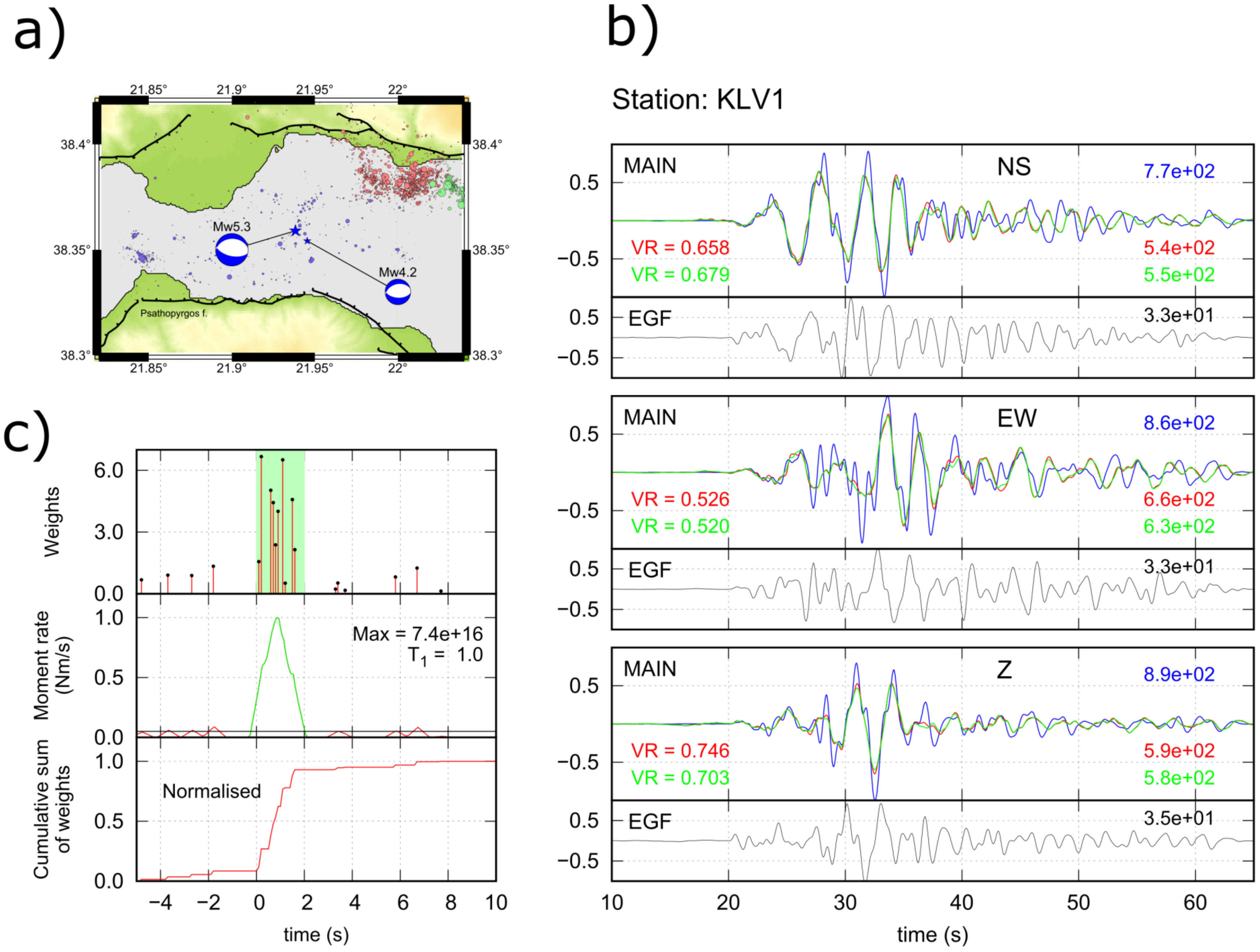
a)
b)
c)
21.85°
21.9°
21.95°
22°
38.4°
38.35°
38.3°
Mw5.3
Mw4.2
Psathopyrgos f.
Station: KLV1
MAIN
NS
7.7e+02
VR = 0.658
VR = 0.679
5.4e+02
5.5e+02
EGF
3.3e+01
MAIN
EW
8.6e+02
VR = 0.526
VR = 0.520
6.6e+02
6.3e+02
EGF
3.3e+01
MAIN
Z
8.9e+02
VR = 0.746
VR = 0.703
5.9e+02
5.8e+02
EGF
3.5e+01
time (s)
Weights
Moment rate (Nm/s)
Max = 7.4e+16
T1 = 1.0
Cumulative sum of weights
Normalised
time (s)

Conclusions

- EGF method was developed a based on NNLS technique, fully operating in time domain.
- ASTF is implicitly positive (NNLS).
- ASTF is causal, small acausal signals are allowed.
- Seismic moment is constant across the stations.
- The software package contains the Fortran code and gnuplot scripts for visualization.
- The code is freely available at: http://geo.mff.cuni.cz/~vp/ASTFs/

Future plans

- Make Pre-processing of the data more simple
  - ObsPy
  - Direct Data access from EIDA
  - Including STA/LTA to automatic align to P waves
- Selecting EGF based on known FM or automatically check waveform similarity
- Make it fully automated????

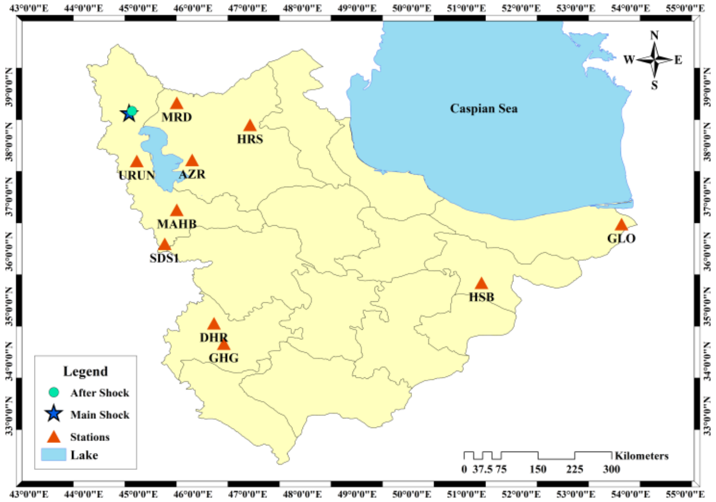

TURKEY-IRAN BORDER REGION

Mainshock: M5.9, 2023-01-28 18:14:47.2 UTC
Aftershock: M4.5, 2023-01-28 20:09:58.9 UTC

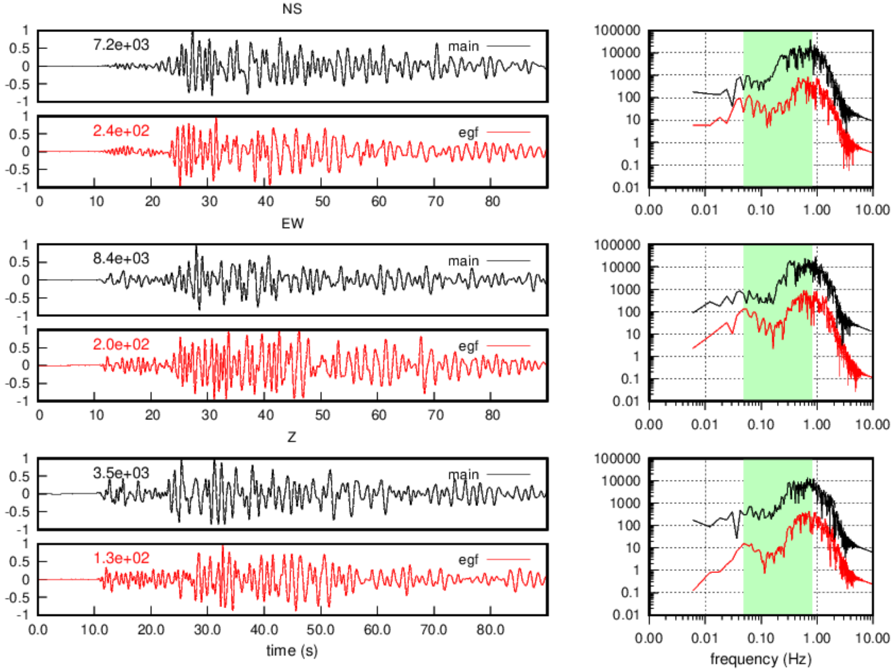

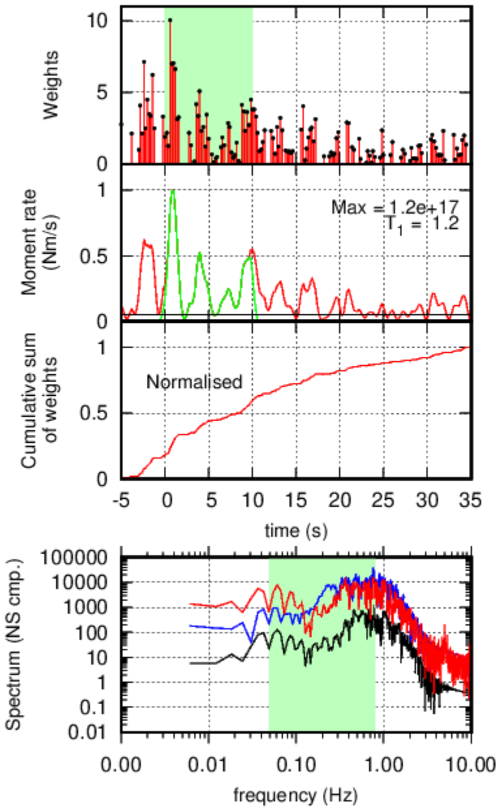

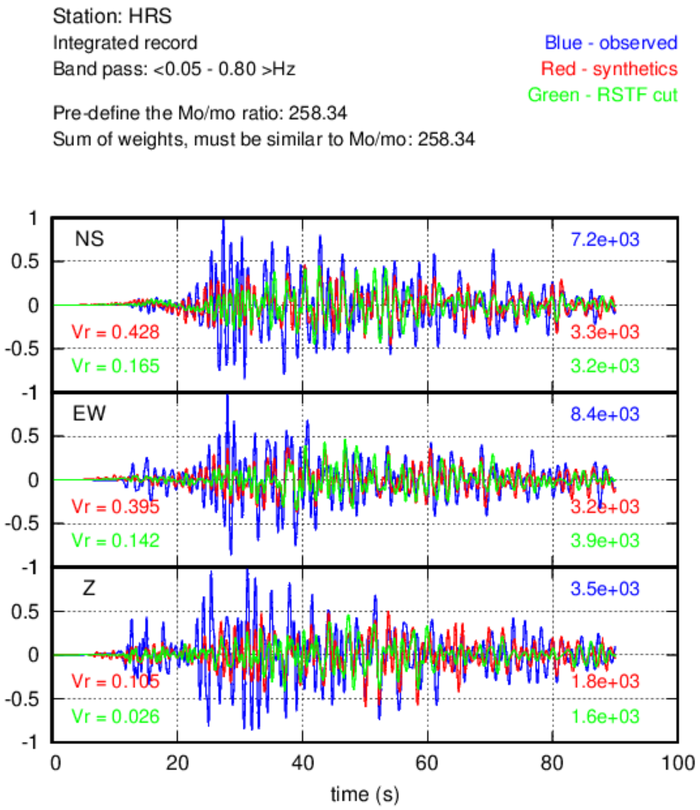

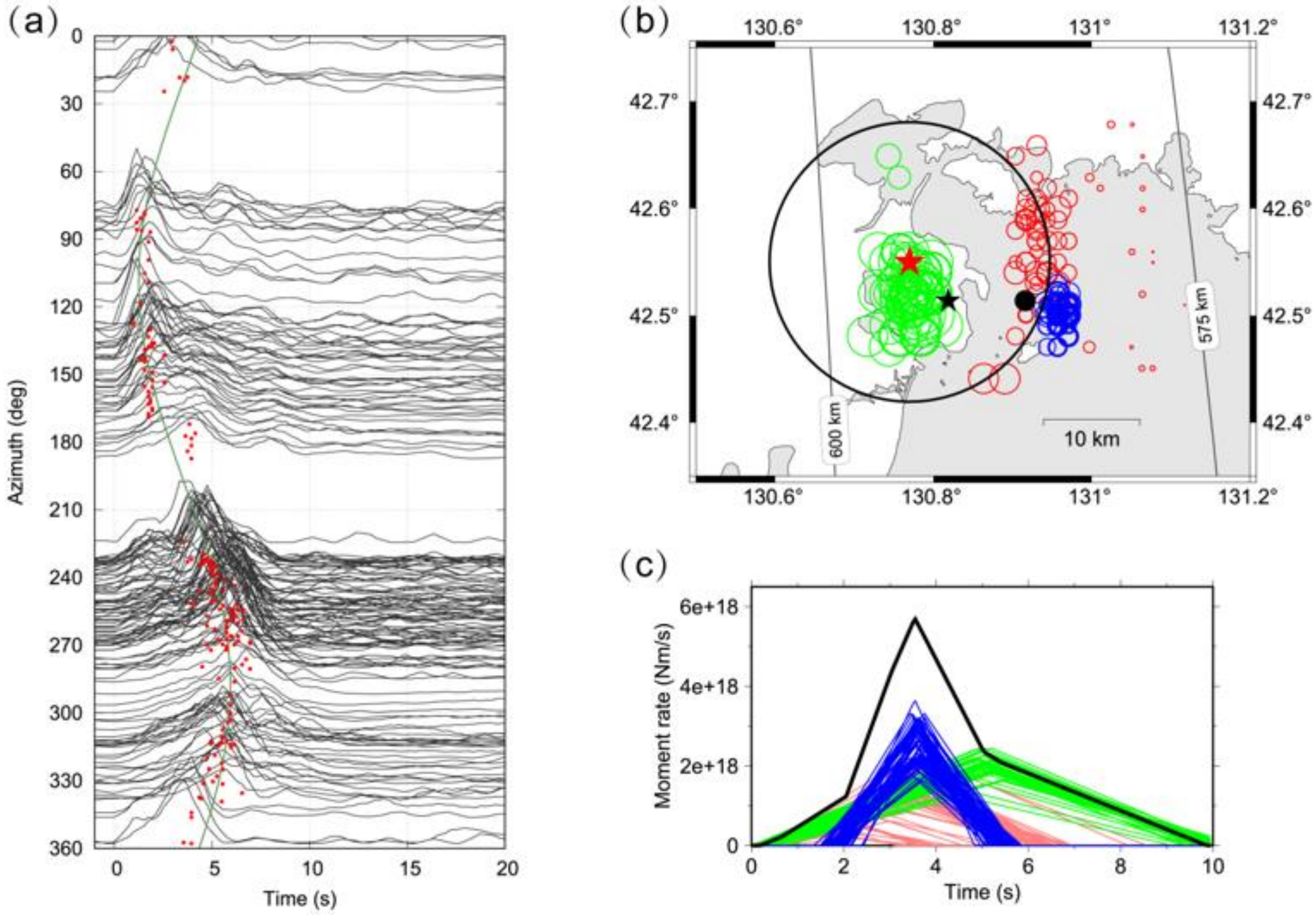
(a)
Azimuth (deg)
Time (s)
(b)
130.6°
130.8°
131°
131.2°
42.7°
42.6°
42.5°
42.4°
600 km
575 km
10 km
(c)
Moment rate (Nm/s)
6e+18
4e+18
2e+18
Time (s)

Thank you